Evaluation and Optimization of the Fire Safety of Concrete Elements Strengthened with NSM Reinforcement

Evaluatie en optimalisatie van de brandveiligheid van betonelementen versterkt met groefwapening

Aniello Palmieri

Promotor: prof. dr. ir. S. Matthys
Proefschrift ingediend tot het behalen van de graad van
Doctor in de Ingenieurswetenschappen: Bouwkunde

Vakgroep Bouwkundige Constructies
Voorzitter: prof. dr. ir. L. Taerwe
Faculteit Ingenieurswetenschappen en Architectuur
Academiejaar 2012 - 2013

UNIVERSITEIT GENT

ISBN 978-90-8578-575-0
NUR 955
Wettelijk depot: D/2013/10.500/8

Supervisor

Prof. dr. ir. Stijn Matthys

Research institute

Magnel Laboratory for Concrete Research
Department of Structural Engineering
Faculty of Engineering
Ghent University, Belgium

Examination committee

Prof. dr. ir. Luc Taerwe (chairman)
Ghent University – Faculty of Engineering and Architecture

Prof. dr. ir. Nele De Belie (secretary)
Ghent University – Faculty of Engineering and Architecture

Prof. dr. ir. Stijn Matthys (supervisor)
Ghent University – Faculty of Engineering and Architecture

Prof dr. ir. Philippe Van Bogaert
Ghent University – Faculty of Engineering and Architecture

Prof. dr. ir. Bart Merci
Ghent University – Faculty of Engineering and Architecture

Prof. dr. ir. Emidio Nigro
Università degli Studi di Napoli Federico II (Napoli, Italy) – Faculty of Engineering

Prof. dr. ir. Mark Green
Queen's University (Kingston, Canada) – Faculty of Engineering

Research funding

The author would like to thank FWO Flanders for the financial support through the research project number G.0069.08N

Acknowledgements

Here I am…. At the end of one of the most wonderful and often overwhelming experiences of my life….the end of my PhD. Looking back, it seems amazing to think how many people I have met, how many places I have visited and how many things I have learned. First of all, I am deeply grateful to my supervisor Prof. Stijn Matthys for his support and guidance during my PhD research. His enthusiasm, valuable remarks and the useful discussions we had were of great help and highly improved the quality of my thesis. Also I am thankful for the international dimension he gave to this research project, resulting in my participation to several conferences, workshop and membership in international task group. I would like also to thank Prof. Luc Taerwe, director of the Magnel Laboratory for Concrete research, who gave me the opportunity of becoming part of the "Magnel Team". The time and effort in reading and reviewing this thesis by all the jury members of the doctoral committee is also highly appreciated.

With respect to the experimental work, I am very grateful to the technical staff of the Magnel Laboratory who contributed and assisted during the testing program. A special word of thanks is addressed to Dieter Hillewaere who helped me with setting up the experiments, building the test set-up, for the application of the different insulation systems and who was able to find always a practical solution for any of my ideas during testing. But first of all for his friendship and the pleasant talks during and after working. Special acknowledgments to Marijke, Christel and Viviane: thank you for your friendly and unconditional help. I also wish to say thanks to all my colleagues of the Magnel Laboratory for the great time I had during my PhD. I especially wish to thank Anibal and Dorleta for making this experience so unique. Special thanks as well to Emmanuel and Ruben for the interesting discussions concerning the analytical part of my doctoral research.

Finally, I want to thank my family and close friends who encouraged and supported me in a more personal way. To my mother and my father who have always expressed how proud they are of me and how much they love me. To Gianluca, Luca and Francesco, thanks so much for making me feel at home and to be as brothers more than friends. I wish to thank as well Yeczain and Vanessa, for your encouragement, support and most of all your humor. Most important, I would like to thank my wife Vittoria for her understanding and patience during all the weekends I had to work on my thesis. She supported and encouraged me during all those years, for which I'm very, very grateful.

Table of contents

List of abbreviations and symbols

1. Abbreviations

ACI	American Concrete Institute
AFRP	Aramid Fibre Reinforced Polymer
AR	Alkali Resistance
BFRP	Basalt Fibre Reinforced Polymer
CFRP	Carbon Fibre Reinforced Polymer
CSH	Calcium Silicate Hydrates
CTE	Coefficient of Thermal Expansion
DMA	Dynamic mechanical analysis
DSC	Differential Scanning Calorimetry
EBR	Externally Bonded Reinforcement
EC2	Eurocode 2
FRP	Fibre Reinforced Polymer
GFRP	Glass Fibre $reinforced Polymer
ISO	International Organization for Standardization
LVDT	Linear Variable Displacement Transducer
NSM	Near Surface Mounted
PAN	Polyacrylnitrile
PC	Prestressed Concrete
RC	Reinforced Concrete
RH	Relative Humidity
TGA	Thermo Gravimetric Analysis

2. Symbols

Roman letters

a	thermal diffusivity or deflection at midspan	m^2/s or mm
a_i	area element i	mm^2
A_c	cross-sectional area of concrete	mm^2
A_f	cross-sectional area of FRP reinforcement	mm^2
A_s	cross-sectional area of longitudinal tensile steel reinforcement	mm^2
A'_s	cross-sectional area of longitudinal compressive steel reinforcement	mm^2
b_f	width of the FRP laminate	
$c_{aest.}$	specific heat capacity Aestuver	J/kg°C
c_p	specific heat capacity concrete	J/kg°C
$c_{p,HPC.}$	specific heat capacity HPC	J/kg°C
$c_{p,OM}$	specific heat capacity Omega Fire	J/kg°C
$c_{p,WR.}$	specific heat capacity WR-typeC	J/kg°C
$c_{pr,H}$	specific heat capacity Promat-H	J/kg°C
c_s	specific heat capacity of steel reinforcement	J/kg°C
c_v	concrete volumetric heat capacity	$J/m^3°C$
$c_{v,HPC.}$	volumetric heat capacity HPC	$J/m^3°C$
$c_{v,OM.}$	volumetric heat capacity Omega Fire	$J/m^3°C$
$c_{v,WR.}$	volumetric heat capacity WR-typeC	$J/m^3°C$
d_f	diameter of FRP bar	mm
d_s	effective depth of the member	mm
d'_s	distance between compression face and compressive steel reinforcement	mm
du	infinitesimal displacement	mm
d_x	element length	mm
E_a	Young's modulus of adhesive	N/mm^2
E_c	Young modulus of concrete	N/mm^2
E_f	Young modulus of FRP reinforcement	N/mm^2
$E_{f,\theta}$	Young modulus of FRP at temperature θ	N/mm^2

E_s	Young modulus of steel reinforcement	N/mm^2
F	geometrical parameter, depending on the dimensions and relative positions of the objects	-
f_a	tensile strength of adhesive	N/mm^2
f_c	cylinder compression strength of concrete	N/mm^2
$f_{c,\theta}$	cylinder compression strength of concrete in function of the temperature θ	N/mm^2
$f_{c,cub}$	compression strength of concrete measured on cubes	N/mm^2
$f_{c,\theta}$	cylinder compression strength of concrete at temperature θ	N/mm^2
$f_{c,tb}$	flexural tensile strength of concrete	N/mm^2
$f_{c,ts}$	tensile strength of concrete measured with splitting tests	N/mm^2
f_f	tensile strength of FRP reinforcement	N/mm^2
$f_{f,\theta}$	tensile strength of FRP at temperature θ	N/mm^2
f_s	tensile strength of steel reinforcement	N/mm^2
$f_{s,\theta}$	tensile strength of steel at temperature θ	N/mm^2
$f_{s,u}$	tensile strength of steel reinforcement	N/mm^2
$f_{s,y}$	yield strength of steel reinforcement	N/mm^2
$f_{sp,\theta}$	proportionality limit of steel at temperature θ	N/mm^2
F_u	failure load FRP bar/strip	kN
$F_{u,20°C}$	failure load FRP at room temperature	kN
$F_{u,T}$	failure load FRP at temperature T	kN
G	Shear modulus	N/mm^2
h	total depth of the member or convection coefficient	mm or $W/m^2°C$
$h_{c,ef}$	effective height	mm
$h_{fictitious}$	fictitious coefficient for convection and radiation effect	$W/m^2°C$
k	constant of Stefan-Boltzman	$W/m^2°C^4$
k_E	temperature reduction factor of FRP's Young modulus	-
k_{el}	slip modulus of τ-slip relationship	N/mm^3
k_f	temperature reduction factor of FRP's tensile strength	-
$k_{G,i}$	shear stiffness	N/mm^3
l_b	bond length of FRP	mm

L_i	Length of the segment i	mm
l_t	transfer length	mm
M	moment	kNm
$\overline{M}$	moment line of a beam with a point load Q=1 at midspan	kNm
M_{cr}	cracking moment	kNm
N_f	axial force FRP	kN
P_{frp}	Force in the FRP reinforcement	kN
qc	heat transfer by convection	W/m^2C
Q_{cr}	cracking load	kN
Q_{k1}	service load, from ultimate state	kN
Q_{k2}	service load, from stress limitation	kN
Q_{k3}	service load, from crack width limitations crack width	kN
Q_{k4}	service load, from deflection limitations	kN
qr	heat transfer by radiation	W/m^2C
Q_{serv}	service load	kN
Q_u	ultimate load strengthened member	kN
$Q_{u,1}$	ultimate load (analytical verification) assuming full composite action	kN
$Q_{u,2}$	ultimate load (analytical verification) assuming debonding	kN
$Q_{u,ref}$	ultimate load reference member	kN
$Q_{u,residual}$	ultimate load residual strength tests	kN
$Q_{u,str}$	ultimate load strengthened member	kN
$Q_{u,unstr}$	ultimate load unstrengthened member	kN
$1/r_i$	curvature	mm^{-1}
s(x)	local slip FRP	mm
t	time	min
T	temperature	°C
T_0	ambient temperature	°C
t_a, t_g	thickness of the adhesive	mm
$T_{adhesive}$	temperature at adhesive/FRP interface	°C
T_{concr}	temperature of concrete	°C
t_f	thickness of FRP reinforcement	mm

T_g	glass transition temperature	°C
T_{gas}	temperature of combustion gases	°C
t_r	reference loading duration time	min
T_s	surface temperature of the element	°C
T_{steel}	temperature of bottom longitudinal steel reinforcement	°C
u_f	perimeter of the FRP bar/strip	mm
$u_{(X)}$	slip at FRP/concrete interface	mm
x	depth of the compression zone or distance	mm
y	distance from the uppermost concrete fiber to the discretized element i	mm

Greek letters

α	constant	
α_c	thermal expansion coefficient concrete	/°C
α_f	thermal expansion coefficient FRP or E_f/E_c	/°C or -
α_s	thermal expansion coefficient steel or E_s/E_c	/°C or -
γ_i	shear strain	-
δ_G	stress block centroid coefficient	mm
δ_{slip}	Relative slip between FRP and concrete	mm
$\Delta a,t$	increase of deflection at midspan under fire exposure	mm
$\Delta\varepsilon_{c,cr}$	creep strain concrete for temperatures 500°C<T≤800°C	°C
ΔN_f	difference in FRP axial forces	kN
Δ_{ref}	max deflection at midspan of unstrengthened beams/slabs	mm
ΔT, $\Delta\theta$	temperature change	°C
$\Delta\tau_f$	extra bond shear stresses	N/mm^2
Δ_u	max deflection at midspan of strengthened beams/slabs	mm
ε	relative emissivity	-
ε_0	initial concrete strain at the extreme tension fibre	-
ε_c	concrete strain at the extreme compression fibre	-
$\varepsilon_{c1,\theta}$	concrete strain at peak stress at temperature θ	-

$\varepsilon_{c,cr}$	creep strain of concrete	-
$\varepsilon_{c,\sigma}$	mechanical (or instantaneous stress- related strain) of concrete	-
$\varepsilon_{c,th}$, $\varepsilon_{\Delta T}$	free thermal strain concrete	-
$\varepsilon_{c,tot}$	total strain of concrete	-
$\varepsilon_{c,tr}$	transient strain of concrete	-
ε_{cu}	ultimate concrete strain at the extreme compression fibre	-
$\varepsilon_{cu,\theta}$	ultimate concrete strain at temperature θ	-
ε_{f}	FRP reinforcement strain	-
ε^{*}_{f}	FRP reinforcement strain (structural analysis at fire exposure)	-
$\varepsilon_{f,cr}$	creep strain of FRP	-
$\varepsilon_{f,ext}$	FRP strain induced by internal restrain	
$\varepsilon_{f,lim}$	FRP reinforcement strain limitation	-
$\varepsilon_{f,Qu}$	FRP strain at ultimate load	-
$\varepsilon_{f,\sigma}$	instantaneous stress-related strain of FRP	-
$\varepsilon_{f,th}$	free thermal strain of FRP	-
$\varepsilon_{f,tot}$	total strain of FRP	-
$\varepsilon_{f,u}$	ultimate strain of FRP	-
$\varepsilon_{f,}(x)$	thermal strains FRP/concrete interface	-
ε_{s}	steel reinforcement strain	-
$\varepsilon_{s,cr}$	creep strain of steel reinforcement	-
ε_{slip}	slip strain of FRP	-
$\varepsilon_{sp,\theta}$	steel strain corresponding to the proportionality limit at temperature θ	-
$\varepsilon_{s,\sigma}$	mechanical (or instantaneous stress- related strain) of steel reinforcement	-
$\varepsilon_{s,th}$	free thermal strain of steel reinforcement	-
$\varepsilon_{s,tot}$	total strain of steel reinforcement	-
$\varepsilon_{sy,\theta}$	yield strain of the steel reinforcement at temperature θ	-
$\varepsilon_{su,\theta}$	ultimate strain of the steel reinforcement at temperature θ	-
θ	temperature	°C

λ	constant	-
λ_{aest}	thermal conductivity Aestuver	W/m°C
λ_c	thermal conductivity of concrete	W/m°C
λ_{HPC}	thermal conductivity HPC	W/m°C
$\lambda_{OmegaFire}$	thermal conductivity Omega Fire	W/m°C
$\lambda_{pr,H}$	thermal conductivity Promat-H	W/m°C
$\lambda_{pr,L\text{-}500}$	thermal conductivity Promat-L500	W/m°C
λ_s	thermal conductivity of steel reinforcement	W/m°C
λ_{WR}	thermal conductivity WR-typeC	W/m°C
ν_c	Poisson ratio of the concrete	-
ν_a	Poisson ratio of the adhesive	-
ρ_c	density of concrete	kg/m^3
σ_c	stress in the concrete	N/mm^2
σ_f	stress in the FRP	N/mm^2
σ_s	stress in the steel reinforcement	N/mm^2
$\tau(x)$	thermal shear stresses at FRP/concrete interface	N/mm^2
τ_{av}	average bond shear stresses of FRP reinforcement	N/mm^2
τ_f	bond shear stresses of FRP	N/mm^2
τ^*_f	bond shear stresses of FRP (structural model at fire exposure)	N/mm^2
τ_{max}	peak value of bond shear stresses of FRP	N/mm^2
$\tau_{max,T}$	peak value of bond shear stresses of FRP at temperature T	N/mm^2
ψ	stress block area coefficient	-
ω	constant	-

Abstract

The deterioration of buildings and infrastructure and the changing demands to existing buildings are some of the most pressing concerns facing today's civil engineering community. Demolishing and rebuilding these structures is not an economically viable option. Strengthening of a structure is in most cases less expensive and less interfering compared to rebuilding. One of the developments during the last decade is the use of fiber reinforced polymer (FRPs) bars and strips, as near surface mounted (NSM) reinforcement to strengthen existing concrete structures.

Despite the increasing success in applying the FRP strengthening system in reinforced concrete structures during the past decade, the weak performance of this strengthening technique under elevated temperatures, as might be experienced in a fire, has hindered their application in some cases. The main concerns in implementing FRP materials in buildings, for which fire risk is not negligible, is the deterioration of mechanical properties of FRPs, as well as a reduction of bond strength at the concrete-adhesive interface under elevated temperatures and fire exposure. The deterioration of the mechanical properties of the FRP is primarily due to deterioration of the polymer matrix. Indeed as the temperature of the polymer matrix approaches the glass transition temperature, T_g, the matrix transforms to a soft, rubbery material with reduced strength and stiffness. Thus for epoxy resins often used as primer, adhesive and matrix for FRP strengthening systems the degree of reduction of the mechanical properties at temperatures close to their T_g (the glass transition temperature of ambient cured epoxies is usually in the range of 50-90°C) is of relevant importance for the strengthened structures, mostly in relation to the bond performance. Indeed the overall performance of the FRP strengthened members depends on the properties of the FRP-adhesive and the adhesive-concrete bond interface.

With these issues in mind and considering that, so far, limited research has been carried out on the behavior of NSM FRP strengthening systems at elevated temperatures, this doctoral research program has main focus on two aspects: 1) the influence of elevated temperatures on the debonding behaviour at the NSM FRP-concrete bond interface; 2) the performance of NSM FRP strengthened and insulated members (beams ad slabs) under and after fire exposure, trying to develop practical methods for protecting FRP during fire in order to achieve a wider acceptance of these polymer based strengthening systems in buildings.

First the effect of elevated service temperatures on the bond behavior of NSM FRP strengthening systems is investigated with bond tests. To that extent a series of 20 double bond shear tests at different temperatures has been performed. Four different temperatures are used: 50°C, 65°C, 80°C and 100°C. The temperature level is chosen in relation to the glass transition temperature of the utilized epoxy resin which equals 65°C, based on DSC (differential scanning calorimetry). From the experimental outcomes it is observed that increasing the temperature up to 50°C resulted in an increase of failure load and bond stresses, while further increase of temperature (up to 100°C for the presented research program) resulted in a decrease of failure load and change of failure mode. At and/or above the adhesive glass transition temperature, the type of failure changed from debonding at the concrete/resin interface with varying degrees of concrete damage, depending on the FRP bar surface configuration, to debonding of the FRP NSM bars at the adhesive/bar interface (pull-out of the bar). This was accompanied by reduced bond strength, although no complete degradation of bond strength is observed up to 1.5 T_g for all the tested specimens. It is moreover, observed that the transfer length increased by increasing the temperature, with a consequent more linear distribution of strains over the FRP bond length. Based on the analysis of the shear stresses it was concluded that the increasing failure load at 50°C was mainly due to thermal shear stresses, induced by the difference of coefficient of thermal expansion between the FRP and the concrete. Above this temperature the softening and strength reduction of the adhesive are governing over a possible positive effect of thermal stresses induced by heating of the specimens.

Before investigating the performance of near surface mounted FRP strengthened elements under fire exposure, their behaviour at ambient temperature has been investigated. The experiments have been conducted on near surface mounted FRP strengthened beams and slabs, varying several parameters with respect to the type of FRP bars, the FRP's shape, the FRP surface configuration and the type of adhesive used to embed the FRPs into the grooves. This study forms the basis for studying the behaviour at and after fire exposure. Based on the experimental work, an insight is obtained in the structural behaviour of the near surface mounted FRP strengthened members. The feasibility and efficiency of near surface mounted FRP reinforcement to strengthen concrete structures is clearly demonstrated. By means of an analytical study, existing models have been verified to predict the influence of near surface mounted FRP reinforcement. These calculation models deal with both the ultimate state and serviceability behaviour. It appears that the structural behaviour of the strengthened concrete members can be predicted in an accurate way.

Following these reference tests, the performance of near surface mounted FRP strengthened and insulated members (beams and slabs) under and after fire exposure has been investigated. The complete fire testing program consists in 4 fire test series and involved the design and fabrication of 20 full-scale NSM FRP strengthened and insulated beams and 4 full-scale NSM FRP strengthened and insulated slabs. All the specimens have been pre-loaded to the service load and subsequently exposed to a standard fire. A time exposure of two hours and one hour has been chosen. The performance of the NSM FRP strengthened and insulated beams and slabs under fire exposure is investigated varying several parameters with respect to insulation materials type and thickness, insulation configuration and type of adhesive for embedding the FRP bars/strips into the grooves. The effect of bond degradation at temperatures moderately higher than the adhesive glass transition temperature is also investigated (in order to do this a time of 1 h of fire exposure was choose to avoid loss of composite action due to an excessive heating of the adhesive). Moreover, the fire resistance effectiveness of the FRP strengthening system after fire exposure has been investigated by structural testing up to failure. The experimental results have demonstrated the feasibility of providing 2h of fire endurance rating under service load, even after the adhesive temperature exceeds excessively the glass transition temperature and loss of the FRP reinforcement can be assumed. No obvious dysfunction of the FRP in terms of stress transfer between the FRP and the RC member during and after fire is observed if adequate protection against fire is provided. The residual strength tests have demonstrated that, if the insulation is able to maintain the adhesive temperature at relatively low temperature ($T_{adhesive}$=100 °C to 130 °C and $T_{adhesive}$=167 °C for epoxy resin and expansive mortar respectively) the FRP is able to retain bond strength to the concrete and the beams and slabs are still able to retain considerably part (up to 84% and up to 92% for 2h and 1 h of fire exposure respectively) of the flexural capacity of the FRP strengthened beam at room condition.

Finally a numerical model, for evaluating the thermal and structural behaviour of the NSM FRP strengthened beams and slabs exposed to fire, is developed. The predicted behaviour is compared with experimental data and predictions of the model are presented and discussed. The model accounts for temperature dependent thermal and mechanical properties of the constituent materials (concrete, steel FRP and insulation system) as well as for the effect of bond degradation at FRP/adhesive interface with increasing temperature. By modeling the combined effects of temperature dependent adhesive strength and stiffness reduction with the distribution of shear stresses at the FRP/adhesive interface the analysis tentatively predicts the time of FRP loss of composite action (bond failure) during fire exposure. It appears that the model is able to simulate the experiments both qualitatively and quantitatively. Moreover results from this study demonstrated that for FRP strengthened and insulated members, if stresses in the FRP are low (as is generally the case for service load levels) during fire exposure, no debonding is experienced at the FRP/adhesive interface even if the glass transition temperature is moderately exceeded. This is valid since the bond shear stresses along the FRP bond length, given the applied load and the fire insulation protection, are below the temperature-dependent adhesive bond strength.

Samenvatting

De veroudering van gebouwen en infrastructuur en de veranderlijke eisen die gesteld worden aan het bestaande patrimonium vormen vandaag de dag een belangrijke uitdaging voor de bouwindustrie. Het slopen en herbouwen van constructies is immers in de meeste gevallen geen economisch haalbare optie. Het herstellen en/of versterking van constructies zal daarentegen meestal minder duur zijn en minder verstorend dan bij wederopbouw. Eén van de ontwikkelingen van de laatste tien jaar, met betrekking tot het versterken van bestaande betonconstructies, is het gebruik van vezelcomposietstaven of strippen als groefwapening. Vezelcomposieten worden gangbaar aangeduid met de afkorting FRP (fibre reinforced polymer). Groefwapening wordt in de internationale literatuur aangegeven als NSM (near surface mounted) wapening.

Ondanks het toenemende succes van FRP versterkingssystemen voor gewapend beton, wordt de inzetbaarheid van deze versterkingstechniek voor een stuk belemmerd door de zwakke prestaties van FRP of haar verlijming bij hoge temperaturen of brand. Dit is het gevolg van de afname in mechanische eigenschappen van FRP materialen, evenals de afname in aanhechtsterkte van de FRP-lijm-beton interface, bij verhoogde temperaturen. De oorzaak ligt in hoofdzaak bij de polymeermatrix gebruikt voor FRP materialen of voor de verlijmingsinterface. Immers, als de temperatuur van de polymeermatrix de glasovergangstemperatuur (T_g) benadert, dan transformeert deze tot een zacht, rubberachtig materiaal met verminderde sterkte en stijfheid. De mate waarin zich dit voordoet voor epoxy, gangbaar toegepast als primer, lijm of matrix van FRP versterkingssystemen, is van groot belang bij toepassing van FRP groefwapening of andere versterkingssystemen met een gelijmde verbinding. Immers, de glasovergangstemperatuur van epoxy (die verwerkt wordt bij omgevingstemperatuur) heeft een grootteorde van 50-90°C. Aangezien het gedrag van betonconstructies versterkt met FRP groefwapening mede bepaald wordt door de FRP-lijm-beton interface, is vooral de invloed op het aanhechtingsgedrag van belang.

Vanuit deze problematiek en gezien het feit dat nog weinig onderzoek gedaan is naar het gedrag van FRP groefwapening bij verhoogde temperaturen, is in dit doctoraatsonderzoek ingegaan op twee aspecten: 1) de invloed van hoge temperaturen op het aanhechtingsgedrag tussen het beton en de FRP groefwapening, 2) het gedrag van gewapend betonbalken en platen versterk met FRP groefwapening en voorzien van een brandbescherming, tijdens en na blootstelling aan brand. Dit vanuit het oogpunt om praktische methoden voor de bescherming van FRP tijdens

brand te ontwikkelen, en zodoende een bredere inzetbaarheid te bereiken van deze polymeer gebaseerde versterkingstechniek.

Het aanhechtingsgedrag tussen FRP groefwapening en beton is onderzocht door middel van hechtproeven. Proeven zijn uitgevoerd op 20 proefstukken bij verschillende temperaturen: 50°C, 65°C, 80°C en 100°C. De temperatuur is gekozen in functie van de glasovergangstemperatuur van de toegepaste epoxy. Deze laatste bedraagt 65°C, bepaald via DSC (differential scanning calorimetrie). Op basis van de experimentele resultaten is vastgesteld dat het verhogen van de temperatuur tot 50°C resulteert in een toename van breuklast en hechtsterkte, terwijl verdere verhoging van de temperatuur (tot 100°C voor het uitgevoerde onderzoeksprogramma) resulteerde in een afname van de hechtsterkte, evenals in een wijziging van het breukaspect. Waar het breukaspect gekenmerkt is door onthechting ter hoogte van de beton/epoxy interface, met een zekere graad van schade aan het beton, afhankelijk van het type FRP oppervlaktetextuur, wijzigt het breukaspect bij verhoogde temperatuur in onthechting ter hoogte van de FRP/epoxy interface. Dit gaat gepaard met een verminderde hechtsterkte, hoewel geen volledig verlies van de hechtcapaciteit wordt waargenomen tot 1,5 T_g (voor het uitgevoerde onderzoeksprogramma). Tevens is waargenomen dat de overdrachtslengte toeneemt met stijgende temperatuur, met als gevolg een meer lineaire verdeling van de rekken langsheen de FRP overdrachtslengte. Gebaseerd op een analyse van de schuifspanningen is geconcludeerd dat de sterkteverhoging bij 50°C kan verklaard worden aan de hand van de thermische schuifspanningen, veroorzaakt door het verschil in thermische uitzettingscoëfficiënt tussen de FRP en het beton. Bij hogere temperaturen is de degradatie van de sterkte en de stijfheid van de epoxy meer bepalend t.o.v. de positieve invloed van de thermische schuifspanningen.

Voorafgaand aan de studie van de brandveiligheid van gewapend betonelementen versterkt met FRP groefwapening is eerst hun buigingsgedrag bij omgevingstemperatuur onderzocht. De proeven zijn uitgevoerd op gewapend beton balken en platen versterkt met FRP groefwapening, en waarbij verschillende parameters onderzocht zijn: het type FRP, de vorm van de staaf, de oppervlaktetextuur van de staaf en het type verlijmming gebruikt om de FRP in de groeven aan te brengen. Op basis van de buigingsproeven is inzicht opgebouwd in het constructief gedrag van de betonelementen versterkt met FRP groefwapening. De haalbaarheid van deze versterkingstechniek en de efficiëntie ervan zijn duidelijk aangetoond. Tevens is een analytische verificatie uitgevoerd van de experimentele resultaten aan de hand van bestaande modellen voor de bezwijktoestand en voor het gedrag bij gebruiksbelasting. Het constructief gedrag van de versterkte elementen kan op goede wijze voorspeld worden.

Vervolgens is het buigingsgedrag bestudeerd van gewapend betonbalken en platen versterkt met FRP groefwapening en voorzien van een brandbescherming, tijdens en na blootstelling aan een standaardbrand. Het proefprogramma bestond uit een serie van 4 brandproeven op in het totaal 24 grootschalige betonelementen (20 balken en 4 platen). Alle proefstukken worden belast tot hun gebruiksbelasting, dewelke dan aangehouden wordt tijdens de één of twee uur durende brandproef. Binnen het kader van dit proefprogramma zijn de volgende parameters onderzocht: het type brandbeschermingsisolatie, de dikte ervan, de configuratie van de brandbescherming, en het type verlijming gebruikt om de FRP in de groeven aan te brengen. De invloed van de verhoogde temperatuur op de aanhechting tussen beton en FRP is hierbij eveneens bestudeerd (hierbij is uitgegaan van een 1 uur brandblootstelling om de temperatuur in de lijmlaag niet bovenmatig hoog te laten oplopen). Verder is ook de residuele sterkte na brand bestudeerd, door buigproeven tot breuk na het beëindigen van de brandproef. De experimentele resultaten hebben aangetoond dat het haalbaar is een brandweerstand van 2 uur te bekomen, zelfs als de temperatuur in de lijm de glasovergangstemperatuur overschrijdt en onthechting kan verondersteld worden. Echter, geen significant verlies in aanhechting kon vastgesteld worden tussen de FRP groefwapening en het gewapend beton, indien voldoende brandbescherming voor handen is. Residuele sterkteproeven hebben aangetoond dat bij beperkte temperatuursverhoging in de lijm ($T_{adhesive}$ = 100°C tot 130°C voor epoxyhars en $T_{adhesive}$ = 167°C voor lijmmortel), de FRP in staat is om zijn hechting met het beton in belangrijke mate te behouden (residuele buigsterkte tot 84% en tot 92% voor een brandduur van respectievelijk 2 uur en 1 uur).

Tot slot is een numeriek model ontwikkeld, om het thermisch en constructief gedrag te voorspellen van de gewapend beton balken en platen versterkt met FRP groefwapening blootgesteld aan brand. Een vergelijking tussen het voorspelde gedrag en de proefresultaten wordt uitgebreid besproken. Het model houdt rekening met de temperatuursafhankelijke thermische en mechanische eigenschappen van de samenstellende materialen (beton, staal, FRP en brandisolatie), evenals met de temperatuursinvloed op de aanhechting in de FRP/lijm interface. Door het modelleren van de gecombineerde effecten van temperatuursafhankelijke reductie van de sterkte en stijfheid van de lijm en wijzigende distributie van schuifspanningen in de FRP/lijm interface, laat het model toe een afschattende voorspelling te doen van de brandduur waarop verlies aan composietwerking tussen de FRP groefwapening en het gewapend beton optreedt. Het model is in staat de experimentele resultaten zowel kwalitatief als kwantitatief te simuleren. Bovendien tonen de resultaten van deze studie aan dat voor FRP versterkte betonelementen voorzien van een goede brandbescherming, indien de trekspanningen in de FRP voldoende laag zijn (zoals meestal het geval is bij gebruiksbelasting), geen onthechting wordt waargenomen tijdens brand, zelfs niet indien de temperatuur in de lijmlaag de glasovergangstemperatuur licht overschrijdt. Dit is te verklaren omdat de aanhechtingsschuifspanningen langsheen de FRP de temperatuursafhankelijke hechtsterkte van de lijm niet overschrijdt, voor de van toepassing zijnde gebruiksbelasting en toegepaste brandisolatie.

Chapter 1

INTRODUCTION

1.1 General

Strengthening of existing structures has become increasingly important in the construction industry nowadays and is being applied more and more often due to several reasons, such as durability problems (e.g. the corrosion of the embedded steel reinforcement), or the need for increasing the structural capacity due to a change in the use and function of the structure, or may be due to the increased load requirements, among other factors. Demolishing and rebuilding these structures is not economically a viable option. Strengthening of a structure is in most cases less expensive and less interfering compared to rebuilding.

In recent years, strengthening technologies for Reinforced Concrete (RC) structures using Fiber Reinforced Polymer (FRP) composites have been gaining widespread interest and growing acceptance in the civil engineering industry. FRP materials consist of high strength fibers (typically carbon, glass, aramid or basalt) embedded in a polymer matrix (typically epoxy or vinylester). The favorable intrinsic properties possessed by these materials (extremely high strength to weight ratio, good corrosion resistance, electromagnetic neutrality) can be successfully exploited for strengthening and/or rehabilitation of concrete as well as steel, masonry and timber structures, emerging as an alternative over conventional materials (e.g. steel) and systems. Furthermore, the decreasing material cost due to the market expansion is making FRP-based construction or strengthening techniques more and more economically competitive.

Nowadays use of FRP composites to strengthen existing reinforced concrete structures can be distinguished in two main categories: (1) the Externally Bonded Reinforcement (EBR) technique, that consist of bonding, with an high strength adhesive, an FRP laminate/textile onto the surface of the concrete element, and (2) the Near Surface Mounted (NSM) technique, that consist in grooving the surface of the member and embedding the FRP bars into the grooves with a high strength adhesive.

Whereas the first technique is well known [1-2] and widely used in practical applications, the use of FRP bars as near surface mounted reinforcement is, in the last decade, emerging as a promising and alternative strengthening technique with respect to the more common EBR technique [3-17]. The NSM technique is relatively simple and considerably enhances the bond of the FRP reinforcement, thereby using the material more efficiently. Moreover, NSM reinforcement is particularly attractive for the flexural strengthening in negative moment regions of slabs and decks, where external reinforcement would be subjected to mechanical and environmental damage and would require protective cover.

However, concerns around the performance of FRP strengthening systems in fire and/or under elevated service temperatures still hinder their application in those situations, where structural fire resistance ratings are required by regulators and building officials.

1.2 Problem statement

When designing structural members in buildings, fire safety is taken into consideration by providing protective steps to ensure that fire and smoke do not spread, and to prevent structural collapse. These objectives can be achieved in part by providing adequate fire resistance to the building components. Fire resistance has been defined as the time to failure of a (fire insulated) structural member when subjected to a standard fire. Failure of an element is defined as loss of load bearing capacity, loss of fire separation characteristics, or unacceptable temperature rise at the unexposed surface of floors and walls [18].

Despite the increasing success in applying FRP reinforcing materials in reinforced concrete structures during the past decade, the comparatively poor mechanical properties of FRPs and adhesives as well as the reduction of bond strength at the concrete-adhesive interface at elevated temperatures, as might be experienced in a fire, have hindered their application in buildings. This gives potential concerns regarding the structural integrity of FRP strengthened concrete structures during fire exposure. As the temperature of the polymer matrix approaches its glass transition temperature, T_g, the matrix transforms to a soft, rubbery material with reduced strength and stiffness. Thus for epoxy resins, currently used as primer, adhesive and matrix for FRP strengthening systems the reduction of the mechanical properties at temperatures close to their T_g (the T_g of ambient cured epoxies is usually in the range of 50-90 °C) is of relevant importance for the strengthened structures, mostly in relation to the bond performance [19-22]. Indeed, the overall performance of the FRP strengthened member significantly depends on the properties of the FRP-adhesive-concrete bond interface.

Due to the degradation of FRP materials at high temperature, guidelines for design of FRP strengthened structures [1-2] required that the strength of the FRP is ignored unless a fire-protection system is used that can maintain the FRP temperature below its critical temperature (defined as the lowest T_g of its components). Thus, the use of FRP strengthening systems is mainly limited to applications where fire aspects are not critical or where loss of the FRP under service loads in fire can be shown not to be critical for the structural integrity [2].

A number of research projects around the world have investigated the influence of elevated service temperature on the bond between the FRP EBR strengthening system and the concrete [23-28]. These investigations have shown that the failure load and type of failure are affected by temperature changes (see Chapter 2). Researchers [29-33] have also shown that with an appropriate insulation, concrete structures strengthened with FRPs (EBR and/or NSM strengthening technique) can achieve a satisfactory fire endurance rating though contribution of the FRP is generally assumed as lost during fire exposure (see Chapter 2). This occurs because an insulation system can improve the overall fire rating of the reinforced concrete member by providing protection to the concrete and the reinforcing steel. Kodur et al. [34] have presented a numerical model for evaluating the fire performance of EBR FRP RC strengthened beams under fire conditions and concluded that supplemental fire insulation is often needed to satisfy fire resistance requirements.

However, the performance of FRP strengthening systems among which NSM reinforcement under elevated temperature and/or fire exposure has yet to be fully addressed and more research is required in this area to quantify the degree of FRP bond loss and/or adhesive bond degradation at temperatures higher than the adhesive's glass transition temperature.

1.3 Aim of the thesis and research objectives

Related to the problem statement given in the previous section the aim of this research project is to obtain a better insight in the behaviour of NSM FRP strengthened systems at elevated temperatures and/or fire exposure in order to achieve a wider acceptance of these polymers based strengthening systems in buildings and infrastructure. The research program objectives are defined as follows. To investigate:

- the bond behaviour of the NSM FRP strengthened system under elevated service temperature , at or beyond the glass transition temperature;

- the fire endurance of NSM FRP strengthened and insulated reinforced concrete members under fire exposure;
- the fire insulation system configuration, material type and thickness which is more optimal in order to develop practical methods for protecting FRPs during fire exposure;
- the adhesive bond degradation at temperatures higher than the glass transition temperature for members under fire exposure;
- the influence of using, an expansive mortar, alternative to epoxy based adhesive;
- the residual strength of the FRP NSM strengthening system during and after fire exposure
- the modeling of the thermal and structural behaviour of the NSM FRP strengthened and insulated beams and slabs exposed to fire.

1.4 Outline of the thesis

Following the first chapter in which a brief overview of the scope and objective of the research project is given, in Chapter 2 a description is given of FRP materials, including properties of the constituent materials and techniques for flexural strengthening with externally bonded reinforcement and near surface mounted reinforcement. A discussion then follows on the concerns of the FRP during fire and a detailed overview is given of previous research studies on the behaviour of FRP strengthened members at elevated temperature and under fire exposure.

In Chapter 3 the effects of temperature on the thermal and mechanical properties of the concrete, internal steel reinforcement, polymer matrix, FRP reinforcement and fire insulation system is given with reference to the literature. Details on the glass transition temperature and an overview of the bond degradation of the polymer matrix is also given.

The influence of temperature at/or beyond the adhesive glass transition temperature, on the bond behaviour of the FRP-adhesive-concrete interface for the NSM FRP strengthening technique is described in Chapter 4. Test results of the experimental work are presented and discussed together with an analytically study.

In Chapter 5 the flexural behaviour of NSM FRP strengthened beams and slabs at ambient temperature have been investigated. This study forms the basis for investigating the behaviour of NSM FRP strengthened beams at and after fire exposure. The increase of flexural strength capacity, failure mode, load-deflection response and cracking of the tested specimens is presented and discussed in details. Moreover experimental results have been, also, analytically verified based on existing models for the structural behaviour of FRP strengthened RC members. These calculation models deal with both the ultimate state and serviceability state.

The experimental program of the full-scale fire tests performed in order to analyze the fire endurance of NSM FRP strengthened and insulated beams and slabs is described in Chapter 6. A detailed description of the testing program is given, including test set-up, instrumentation and parameters investigated. The results of the full-scale fire tests are presented and discussed in details. The fire resistance effectiveness of the FRP strengthening system after fire exposure, obtained by residual strength testing at ambient temperature, is also presented and discussed in Chapter 6.

In Chapter 7 a numerical model, for evaluating the thermal and structural behaviour of the NSM FRP strengthened and insulated beams is presented. This chapter begins with the development of the analytical model, followed by comparison between the experimental data and predictions. The effect of bond degradation at the FRP/adhesive interface with increasing temperature is also analyzed in Chapter 7.

Finally in Chapter 8 the main conclusions of the research project are summarized and recommendations for future research are given.

1.5 References

1. *fib* Task Group 9.3 (2001). "Externally bonded FRP reinforcement for RC structures". *International Federation for Structural Concrete*, *fib* Bulletin 14.
2. American Concrete Institute (ACI) (2008). "Guide for the Design and Construction of Externally Bonded FRP System for Strengthening Concrete Structures". *ACI 440.2R-2008*, ACI Committee 440, 80 pp.
3. De Lorenzis L., Lundgren K., Rizzo A. (2004). "Anchorage length of near-surface mounted FRP bars for concrete strengthening – Experimental investigation and numerical modeling". *ACI Structural Journal*, 101(2), 269-278.
4. De Lorenzis L., Nanni A. (2002). "Bond between NSM fiber-reinforced polymer rods and concrete in structural strengthening". *ACI Structural Journal*; 99(2), 123-132.
5. De Lorenzis L., Teng J.G. (2007) "Near-surface mounted FRP reinforcement: an emerging technique for structural strengthening". *Composite Part B: Eng*; 38, 119-143.

6. De Lorenzis L., Rizzo A., La Tegola A. (2002). "A modified pull-out test for bond of near surface mounted FRP rods in concrete". *Composites Part B: Eng*; 33 (8), 589-603.

7. Kotynia R. (2005). "Strain Efficiency of Near-Surface Mounted CFRP-strengthened Reinforced Concrete Beams". *Proc. of International Conference on Composites in Construction*, Lyon, 35-42.

8. Palmieri A., Matthys S., Taerwe L. (2010). "Strengthening with Near Surface Mounted Reinforcement: Structural and Fire behavior". *Proc. of 3rd fib International Congress* (fib-2010), Washington DC.

9. Sena Cruz J.M., Barros. J. (2004). "Bond between Near Surface Mounted Carbon-Fiber-Reinforced Polymer Laminate Strips and Concrete", *J. Compos. Constr.*, ASCE, 8(6), 519-527.

10. Seracino R., Saifulnaz M.R.R., Oehlers D.J. (2007). "Generic Debonding Resistance of EB and NSM Plate-to-Concrete Joints". *J. Compos. Constr.*, ASCE, 11(1), 62-70.

11. Teng J.G., De Lorenzis L., Wang Bo., Rong Li., Wong T.N., Lik Lam (2006). "Debonding failures of RC beams strengthened with near surface mounted CFRP strips". *J. Compos. Constr.*, ASCE, 10(2), 92-105.

12. Ceroni F., Pecce M., Bilotta A., Nigro M. (2012). "Bond behavior of FRP NSM systems in concrete elements". *Composites Part B: Eng*, 43, 99-109.

13. Blaschko, M. (2003). "Bond behaviour of CFRP strips glued into slits". *Proc. of 6th Int. Symposium on FRP Reinforcement for Concrete Structures (FRPRCS-6)*, K. H. Tan, ed., World Scientific, Singapore, pp. 205–214.

14. El Hacha R., Rizkalla S.H. (2004). "Near-Surface-Mounted Fiber-Reinforced Polymer Reinforcement for Flexural Strengthening of Concrete Structures". *ACI Structural Journal*, 101(5), 717-726.

15. Barros J.A.O., Fortes A.S. (2004). "Flexural strengthening of concrete beams with CFRP laminates bonded into slits". *Cement & Concrete Composites*, Elsevier, 27 (1), 471-480.

16. Palmieri A., Matthys S., Taerwe L. (2012). "Bond Behaviour between NSM FRP Rods and Concrete: Experimental and Numerical Investigation". *Proc. in 12th International Conference on Recent Advances in Concrete Technology and Sustainability Issues*, Prague, 14 pp.

17. Hassan T., Rizkalla S., (2003). "Investigation of bond in concrete structures strengthened with near surface mounted carbon fiber reinforced polymer strips". *J. Comp. Constr.*, ASCE, 7(3), 248-257.

18. Buchanan A., (2001). “Structural Design for Fire Safety”. *John Wiley & Sons*, 444 pp.

19. Blontrock H., Taerwe L., Matthys S. (1999). “Properties of Fibre Reinforced Plastics at Elevated Temperatures with Regard to Fire Resistance of Reinforced Concrete Members”. *ACI Structural Journal*, 188(5), 43-54.

20. Kodur V., Bisby L., Green, M.F. (2007). “Guidance for the design of FRP-strengthened concrete members exposed to fire”. *Journal of Fire Protection Engineering*, 17 (5), 5-16.

21. Wang Y.C., Wong P.M.H., Kodur V. (2007). “An experimental study of the mechanical properties of fibre reinforced polymer (FRP) and steel reinforcing bars at elevated temperatures”. *Composite Structures*, 80(1), 131-140.

22. Foster S.K., Bisby L.A. (2008). “Fire Survivability of Externally- Bonded FRP strengthening Systems”. *J. Compos. Constr.*, ASCE, 12(5), 553-561.

23. Di Tommaso A., Neubauer U., Patruso A, Rostasy F.S, (2001). “Behaviour of adhesively bonded-concrete joints at low and high temperatures”. *Mechanics of Composite Materials*, 37(4): 327-338

24. Blontrock H. (2003). “Analyse en modellering van de brandweerstand van betonelementen uitwendig versterkt met opgelijmde composietlaminaten (in Dutch)”. *Ph-D Thesis*, Faculty of Engineering, Department of Structural Engineering, Ghent University, Belgium, 412 pp.

25. Wu. Z.S., Iwashita K., Yagashiro S., Ishikawa T., Hamaguchi Y. (2004). “Temperature effect on bonding and debonding behavior between FRP sheets and concrete”. *Proc. of the 2nd International Conference on FRP Composites in Civil Engineering- CICE 2004*, Adelaide, Australia.

26. Klamer E.L. (2009). “Influence of Temperature on Concrete Beams Strengthened in Flexure with CFRP”. *PhD thesis*, Department of architecture, building and planning, Eindhoven University of Technology, the Nederlands, 250 pp.

27. Leone M., Matthys S., Aiello M.A. (2009). “Effect of elevated service temperature on bond between FRP EBR systems and concrete”. *Composites Part B: Eng*, 40(1), 85-93.

28. Nigro E., Manfredi G., Cosenza E., Zappoli M., (2006). “Effects of High Temperature on the Performance of RC Bridge Decks strengthened with Externally Bonded FRP Reinforcement”. *International Federation for Structural Concrete - Proc. of the 2nd International Congress*, Naples, Italy.

29. Blontrock H., Taerwe L., Vandevelde P. (2001). "Fire Testing of Concrete Slabs Strengthened with Fibre Composite Laminates". *In Proc. of FRPRCS-5*, London, 547-556.

30. Burke P.J. (2007). "Low and High Temperature Performance of Near Surface Mounted FRP Strengthened Concrete Slabs". *M.Sc. Thesis*, Queen's University, Canada, 210 pp.

31. Rein G., Abecassis Empis C., Carvel R. (2007). "The Dalmarnock Fire Tests: Experiments and Modelling". *School of Engineering and Electronics*, University of Edinburg.

32. Williams B., Kodur V., Green M., Bisby L. (2008). "Fire endurance of Fiber-Reinforced Polymer Strengthened Concrete T-Beams". *ACI Structural Journal*, 105(1), 60-67.

33. Bisby L.A., Burke P.J., Green M.F. (2008). "Comparative Performance of Externally- Bonded and Near Surface Mounted FRP Strengthening Systems at High Temperatures". *In Proc. of 5th International Conference on Advanced Composite Materials in Bridge and Structures (ACMBS)*, Winnipeg, Canada, 10 pp.

34. Kodur V., Ahmed A. (2010), "Numerical Model for tracing the Response of FRP-Strengthened RC Beams Exposed to Fire". *J. Comp. Constr.*, ASCE, 14(6), 730-742.

Chapter 2
LITERATURE REVIEW

2.1 Introduction

In this chapter a brief overview is given of FRP materials, including properties of the constituent materials, and the techniques for flexural strengthening with FRP EBR and FRP NSM. A discussion then follows on the concerns of the use of FRP during fire. Finally a detailed overview is given of previous research studies on the behavior of FRP strengthened members at elevated temperature and under fire exposure.

2.2 Fibres Reinforced Polymer (FRP) Materials

From military applications in the 1940s to the industrial and manufacturing industries in the 1950s, the use of fibre reinforced polymer (FRP) composites became an important material group in several sectors of the industry, including aerospace, marine, automotive, recreation and construction [1-2]. FRP evolved into architectural applications, starting with the restoration of historical buildings in the late 1950s [3]. The technology entered the infrastructure markets in Europe, Japan and United States in the 1970s and 1980s, with the rehabilitation of bridge columns, decks and beams as well as tunnel and marine pier repairs [2-3]. Due to the technological evolution in the different industries and the decreasing cost of the materials, FRP continues to grow for retrofitting and strengthening of reinforced concrete buildings and bridge structures.

FRPs are a subgroup of the class of materials referred to as composites. Composites are defined as materials created by the combination of two or more materials on a macroscopic scale, to form a new and useful material with enhanced properties that are superior to those of its constituents [4]. FRP is a two component material and consists of a high number of small, continuous, directionalized, non-metallic fibres (with diameter between 5-25 μm) with advanced characteristics, embedded in a polymer matrix. The latter guarantees the union between the fibres, allows transfer and distribution of the stresses as well as a smooth transfer of load from a broken fibre to nearby intact fibres to prevent failure of the overall FRP composite. In case of bonded reinforcements, a polymer is also used as an adhesive. In addition, the matrix protects the fibres to a certain extent against mechanical damage and environmental attack. The fibres confer strength and stiffness to the composite material. Therefore, the mechanical properties of FRP materials depend strongly on the orientation and amount of fibres embedded in the matrix (fibre volume fractions up to about 60% to 70% are common). In the following the constituent materials of FRP are briefly discussed, more information can be found in [4-6].

2.2.1 Fibres

The most commonly fibres used as structural reinforcement for concrete are: glass fibres (GFRP), carbon fibres (CFRP) and aramid fibres (AFRP). The main differences between these types of fibres are the resistance against aggressive environments and the mechanical properties. Depending on their chemical composition glass fibres are classified for the envisaged applications into three types: E-glass fibres, S-glass fibres and AR-glass fibres. E-glass fibres, which are based on calcium-aluminoborosilicate glass are low cost fibres (with respect to other fibre composite materials), they have a good electrical resistance and strength but a low alkali resistance. S-glass (which is based on magnesium-aluminosilicate glass) fibres have higher strength, stiffness and thermal stability than E-glass, but still not resistant to alkali. To prevent glass fibre from being eroded by cement alkali, a considerable amount of zircon is added to produce alkali resistance (AR) glass fibres; such fibres have mechanical properties similar to E-glass. Although characterized by high tensile strength, good electrical resistivity, good thermal resistance and low price, glass fibres are known to degrade to some extent in the presence of water, acid and alkaline solutions. Also, they exhibit a considerable creep and stress rupture behavior, meaning that the tensile strength gradually decreases under high constant stress.

Carbon fibres are produced from polyacrylnitrile (PAN), pitch or rayon. Isotropic pitch and rayon are used to produce low modulus carbon fibres. High modulus/high strength carbon fibres are made from PAN or liquid crystalline pitch. More information about the carbon fibres composition can be found in [5-6]. Carbon fibres are in most cases preferred in the construction industry, as they have excellent mechanical properties (carbon fibres are the stiffest and strongest reinforcing fibres for polymer composites), good resistance to creep and fatigue and an excellent resistance against UVlight, moisture and chemical influences. As the fibres are electrically conducting, they can give galvanic corrosion in contact with metals.

Aramid fibres show high tensile strength, high energy absorption and toughness (as no other fibres), good vibration damping and fatigue resistance, low thermal conductivity, good thermal stability and moderate chemical resistance. With respect to durability, aramid fibres generally exhibit a low or moderate resistance against acids, a moderate resistance against alkalis and are sensitive to moisture. Because of these aspects, the fibres should be embedded in a matrix which is carefully chosen to provide additional protection.

In addition to the type of fibres described above, basalt fibres are recently gaining increasing interest to apply in concrete construction [7]. Basalt is a volcanic rock, from which fibres can be manufactured in a single stage process by melting (melting point above 1400°C) crushed basalt stone. Basalt fibres are non-corrosive, non-magnetic, have good resistance against corrosion, posses resistance against low and high temperatures and are superior to others fibres in terms of thermal stability. They possess high insulating characteristics, vibration resistance and durability. Additionally, basalt fibres are naturally resistant to ultraviolet (UV) light and have a good resistance against high energy electromagnetic radiation and acids. They offer also the opportunity to modulate the mechanical properties over a wide range modifying the chemical composition. In this way it is possible to develop fibres having an elastic modulus higher than conventional glassy ones and a very high bio-solubility. Basalt fibres have high fire resistance and are cheaper than carbon fibres (yet more expensive than E-glass). The use of basalt FRP reinforcement is currently in the research and development phase.

FRP fibres have a tensile strength which is higher than that of steel and are linear elastic up to tensile failure. The physical and mechanical properties vary considerably between the different fibre types and may vary significantly for a given type of fibre as well. Some typical properties are given in Table 2.1. The tensile stress-strain behavior of the fibres is shown in Figure 2.1.

Table 2.1 – Typical properties of fibres [5]

Fibre type	Tensile strength [N/mm^2]	Modulus of elasticity [kN/mm^2]	Ultimate strain [%]	Density [kg/m^3]	Fibre diam. [mm]
E-glass	1800-2700	70-75	3.0-4.5	2550-2600	5-25
S-glass/AR-glass	3400-4800	85-100	4.5-5.5	2550-2600	5-25
Carbon-Pitch HM	3000-3500	400-800	0.4-1.5	1900-2100	9-18
Carbon-PAN HM	2500-4000	350-700	0.4-0.8	1800-2000	5-8
Carbon-PAN HT	3500-5000	200-260	1.2-1.8	1700-1800	5-8
Aramid-IM	2700-4500	60-80	4.0-4.8	1400-1450	12-15
Aramid-HM	2700-4500	115-130	2.5-3.5	1400-1450	12-15
Basalt	1600-4840	70-100	2.2-3.5	2700-2800	9-23

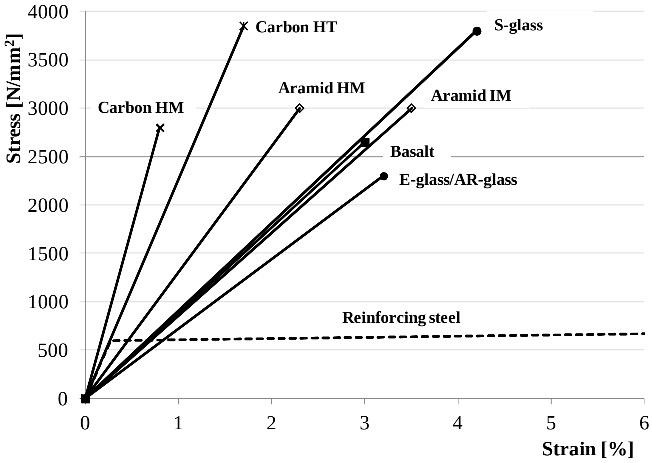

Figure 2.1 – Stress-strain behavior of reinforcing fibers [5]

2.2.2 Matrix

Polymer matrix materials for FRPs can be grouped in two categories: thermosetting resins and thermoplastic resins. Thermosetting resins are the most commonly used matrix materials for production of FRP materials. They are usually available in a partially polymerized state with fluid or pasty consistency at room temperature. When mixed with a proper reagent, they polymerize to become a solid, vitreous material irreversibly. Thermosetting resins have low viscosity that allow for a good fibre wet-out without applying high pressure or temperature, good adhesive properties, good thermal stability and chemical resistance. Disadvantages are a limited range of operating temperatures, with the upper bound limit given by the glass transition temperature, brittle behavior and sensitivity to moisture during applications. Thermosetting resins include epoxies, polyesters and vinyl esters. Epoxy resins are more expensive than polyesters and vinyl esters, but are largely used in high-performance composites as they generally have the best mechanical properties, good adhesion properties and excellent resistance to chemicals and solvents.

The thermoplastic resins include such polymer compounds as polyethylene, nylon and polyamides. These resins are characterized by more linear macromolecules and can be repeatedly softened when heated and hardened when cooled. The shape of each component may be modified by simply heating the material at a suitable temperature (hot forming). Because thermoplastic polymers are more ductile and tough, they have higher impact strength, fracture resistance and microcracking resistance than thermosetting polymers. Other advantages are the shorter fabrication time, better resistance to environmental factors and the long storage life. However, as they are very viscous, incorporation of continuous fibres to thermoplastic matrices and hence composite production is difficult and requires complex and costly working equipment.

2.3 FRP as construction materials

FRP materials are used in the civil engineering industry as strengthening materials in a variety of forms, such as bars, laminates, fabrics, grids and ropes (see Figure 2.2).

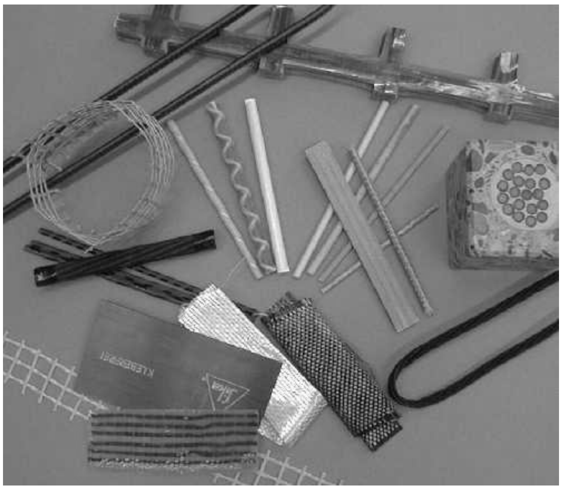

Figure 2.2 – Type of FRP reinforcements [9]

Several manufacturing methods exist for the production of FRP composites, among which lay-up techniques, moulding techniques (e.g. injection, compression, resin transfer, vacuum bag and autoclave moulding), pultrusion, braiding, weaving and filament winding. FRP reinforcement is commonly fabricated in a pultrusion process (see Figure 2.3). The bundled fibers or rovings or mats are pulled through a resin bath and through a heated shaping die. The die is usually tapered to achieve some compaction. As the element emerges from the shaping die, it passes through a curing chamber where the resin is allowed to harden. The pultrusion process allows considerable latitude in the selection of a structural shape: rods, strips, profiles, etc. Longitudinal rovings are necessary to provide sufficient strength for pulling the material through the die, although mats and fabrics with fibre angles between 0 and

90 degrees are frequently added to obtain some transverse stiffness and strength. The pultrusion process is compatible with all the high modulus fibres and with a wide variety of resins. Pultrusion is one of the most economical manufacturing processes for fibre composites. Also grids are produced (by filament winding technique), which are made of continuous impregnated fibres alternating in two directions to form a cross laminate grid structure. More information about other manufacturing methods can be found in [5].

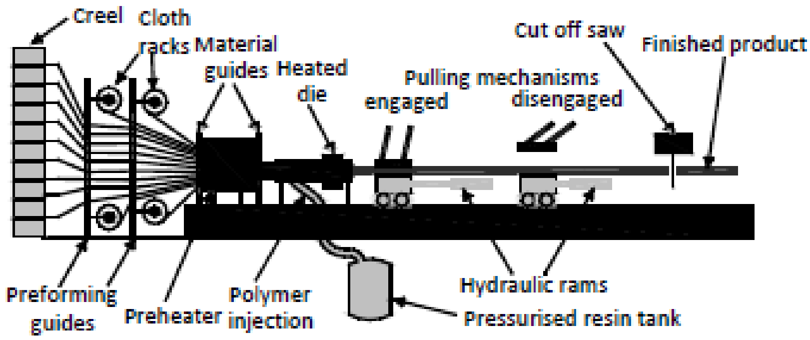

Figure 2.3 – Pultrusion process for laminates [10]

The use of FRPs in civil engineering applications has emerged over the past 20 years and FRPs have gradually emerged as a possible alternative to conventional materials (e.g. concrete and steel) in both new construction, and particularly for repair and strengthening of existing structures. Some of the advantages of using FRPs as strengthening materials for reinforced concrete members can be summarized as follows. The light weight of FRP allows for their quick installation on the structure without the need for heavy equipment or extensive labor. Due to this low weight, the dead weight of the structure is hardly increased. No additional fixation of the FRP is required during hardening of the structural epoxy. The FRPs are non corrosive, have a very good resistance against aggressive environments, electrochemical attack and they do not posses magnetic properties. FRP can be manufactured with no limitations concerning the length. Hence no overlap between different strips is necessary if long lengths of the reinforcement are required. There are however, a number of disadvantages in using FRPs. Some of the most pressing concerns include the high material costs in comparison with steel (nevertheless, taking into account the more simple applications methods and efficiency of use, the overall costs is often lower than alternative techniques); low strain at failure; extremely low lateral load capacity due to the relatively poor mechanical properties of the matrix; excessive creep and relaxation in some cases, particularly for aramid FRPs; the potential of ultra-violet (UV) degradation of polymer matrices in external applications; although FRPs are not susceptible to corrosion and are inert to various aggressive solutions, they may be negatively affected by some environmental conditions (e.g. aramid FRPs appear to be moisture sensitive and glass FRPs are sensible to alkaline environments); reduced mechanical properties and bond properties at elevated temperatures, as would be expected in the case of fire.

The advantages of FRP materials have, however, led to their increasing use both for reinforcing new concrete structures (FRP bars have been used for internal flexural reinforcement replacing the use of steel reinforcing bars to avoid corrosion in highly aggressive environments, like marine environments and in the chemical industry, and in situations where electromagnetic neutrality is required, like for magnetic railway systems and scanning facilities in hospitals) and for strengthening existing reinforced concrete (RC) and prestressed concrete (PC) structures, such as beams, slabs, columns and walls. The main FRP strengthening techniques are externally bonded reinforcement (EBR) and near-surface mounted reinforcement (NSM). In the following a brief description of these two techniques is given.

2.3.1 Externally Bonded Reinforcement (EBR)

The Externally Bonded Reinforcement (EBR) technique consists of bonding, with a high strength adhesive (usually an epoxy), a laminate/textile onto the surface of the concrete element. FRP EBR can be applied for the strengthening of existing structures, enhancing the flexural capacity and shear capacity or to strengthen by means of confinement. To obtain a good bonding between the FRP EBR and the substrate, specific preparations of both the strengthening material and concrete surface are needed. The concrete surface needs to be roughened by means of gritblasting or grinding with special equipment. The surface of the FRP material needs to be degreased before the application. Different FRP EBR systems exist related to the constituent materials, the form and the technique of the FRP strengthening. In general these can be grouped in wet lay-up system and prefab or pre-cured system. Typical applications of the wet lay-up and prefabricated systems are illustrated in Figure 2.4 and Figure 2.5. Wet lay-up systems consist of dry unidirectional or multidirectional fiber sheets or fabrics that are impregnated with a saturating resin on-site. The saturating resin, along with the compatible primer or putty, is used to bond the sheets to the concrete surface. Pre-preg FRP systems consist of uncured unidirectional or multidirectional fiber sheets or fabrics that are pre-impregnated with a saturating resin off-site in the supplier’s facility. Such systems are bonded to the concrete surface with or without an additional resin application depending upon specific system requirements. Pre-preg systems are saturated off site and, like wet lay-up systems, cured in place.

Pre-cured FRP systems consist of a wide variety of composites shapes manufactured off-site in the system supplier's facility and shipped to the job site. Typically, a thixotropic adhesive along with the primer and the putty is used to bond pre-cured shapes to the concrete surface. Three common types of pre-cured systems are: unidirectional laminate sheets, typically delivered to the site in the form of large flat stock or as thin ribbon strips coiled in a roll; and shells, typically delivered to the site in the form of shell segments cut longitudinally so they can be opened and fitted around colums or other elements.

Figure 2.4 – Application of a prefab FRP EBR system [6]

Figure 2.5 – Application of a wet lay-up FRP EBR system [5]

In the case of concrete beams and slabs strengthened in flexure or shear with FRP EBR, the FRP materials are bonded to the tension face (flexural strengthening applications) or side faces (shear strengthening applications) in such a way to supplement the tensile reinforcement provided by the internal reinforcing steel. In the case of concrete columns, FRP sheets are applied to the exterior of reinforced concrete columns in either the longitudinal directions (to provide additional flexural capacity) or in the circumferential direction (to provide additional confining reinforcement which increases both the ductility and the compressive strength).

The mechanical behavior of EBR systems depends strongly on the bond stress transfer at the reinforcement-concrete interface. The design of a FRP strengthened structure is, in most cases, governed by debonding of the FRP reinforcement. Debonding failure can occur within the concrete, between the concrete and the adhesive, in the adhesive, at the FRP reinforcement-adhesive interface or even within the FRP reinforcement [6]. Figure 2.6 shows the different types of bond failure.

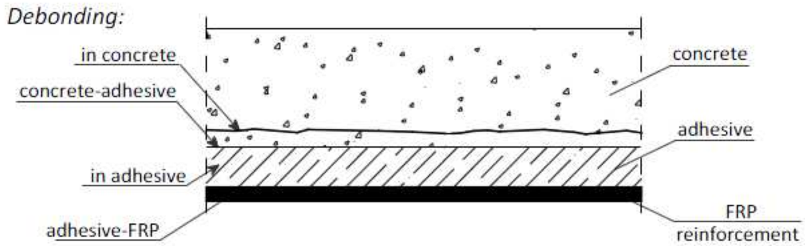

Figure 2.6 – Different types of bond failure [6]

Debonding can initiate at several places along the length of a beam as shown in Figure 2.7 (1-7). The failure modes that can be distinguished in literature are [5-6]: 1) debonding at flexural cracks; 2) debonding due to high shear stresses; 3) debonding at shear cracks; 4) debonding at the end anchorage; 5) plate end shear failure; 6) concrete cover rip off; 7) debonding due to the unevenness of the concrete surface. The FRP reinforcement is generally ended at some distance from the support, which results in stress concentrations in the concrete at the end of the FRP reinforcement. Besides anchorage failure, these stress concentrations could also result in a vertical crack that propagates further as a shear crack or along the level of the internal steel reinforcement, ripping of the concrete cover (Figure 2.7 (5 and 6)). These types of failure are not related to the debonding failure of the concrete-adhesive-FRP joint, as the bond between the materials stays intact.

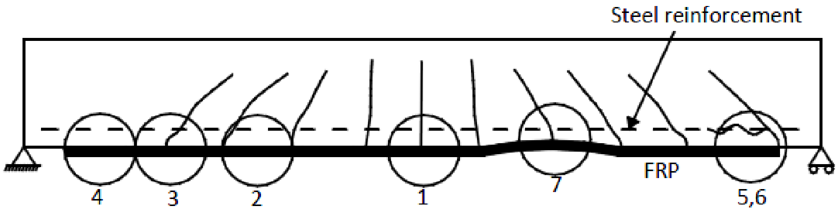

Figure 2.7 – Bond failure modes of a concrete member with EBR [11]

In addition to the above mentioned bond failures modes, in RC beams strengthened by EBR systems two other failure modes can occur: steel yielding/concrete crushing (in this failure mode, the concrete reaches its crushing strain, at the top of the beam, prior to either FRP rupture or some form of bond failure) and the steel yielding/FRP rupture (in this failure mode the member strengthened with FRP EBR can fail due to the rupture of the reinforcement when the geometry is such that concrete crushing is prevented and the strengthening system has proper strength to delay the debonding failure). More information regarding the failure types of EBR strengthened members and the analytical calculation can be found in [5-6].

Despite the popularity of the FRP EBR strengthening technique, they have a number of important limitations in practice. The main limitation is that the bond between the concrete and the FRP, which is critical for adequate performance in most cases, is often unable to develop the full tensile strength of the FRP, resulting in premature debonding failures. The result is that design procedures for these systems often impose strain limits that can make use of FRPs uneconomical. Also because the FRP strengthening system is located on the external surface of the members in these applications, the FRP and epoxy adhesive are exposed to environmental effects, fire and possibly vandalism.

2.3.2 Near Surface Mounted reinforcement (NSM)

In the recent years the use of FRP bars as near surface mounted (NSM) reinforcement is emerging as a promising and alternative strengthening technique with respect to the more common EBR strengthening technique [11-30]. Embedment of the FRP bars is achieved by grooving the surface of the member to be strengthened along the desired direction and to the desired depth and width. The groove is filled half-way with a high strength adhesive (epoxy or cementitious mortar), the FRP bars is then placed into the groove and lightly pressed, so forcing the adhesive to flow around the bar and completely fill the space between the bar and the sides of the groove. The groove is then filled with more adhesive if needed and the surface is leveled. A typical application of FRP bars as NSM strengthening is shown in Figure 2.8.

Figure 2.8 – Application of NSM strengthening system [31]

Similar to externally bonded FRP reinforcement, the NSM technique has been originally developed for steel reinforcement bars embedded with cement mortar (the earliest reference that could be found in the literature dates back to 1949 [32]) but has been replaced by FRP reinforcement and epoxy resin. The advantages of using FRP are primarily the better resistance to corrosion, the ease and speed of application due to the lightweight properties, and the optimization of the grooving process. Due to the high tensile strength of the FRP, rods with smaller diameters can be used for a given required tensile force, which reduces the groove size needed for embedment. Further reduction in depth is due to the better corrosion resistance and possibly to the better bond behavior of ribbed FRP rods with respect to steel rebars.

In existing research on NSM FRP reinforcement, FRP bars of various shapes have been used, including round, square, or rectangular bars as well as narrow strips. In particular, the latter have been shown to be the least prone to debonding from the concrete substrate [18-19,23] for two main reasons: 1) they maximize the ratio of surface to cross sectional area, which minimizes the bond stresses associated with a given tensile force in the FRP reinforcement and 2) the normal stresses, which in case of NSM round bars tend to split the epoxy cover and the surrounding surface layer of concrete, act in this case mainly towards the thick lateral concrete [11,22] so that splitting failure becomes less likely.

Compared to the FRP EBR strengthening technique, the NSM system can resolve some drawbacks discussed above. For instance the NSM strengthening technique enhances the bond of the FRP reinforcements, thereby using the material more efficiently (debonding typically occurs at 70-80% of the FRP ultimate strain, which is at higher strain levels than typically obtained for externally bonded reinforcement [16,24]). NSM bars can be more easily anchored into adjacent members to prevent debonding failures; this feature is particularly attractive in the flexural strengthening of beams and columns in RC frames, where the maximum moments typically occur at the ends of the member. Moreover NSM is particularly attractive for the flexural strengthening in negative moment regions of slabs and decks, where external reinforcement would be subjected to mechanical and environmental damage and would require protective cover. The aesthetic of the strengthened structure is virtually unchanged. Finally it has been suggested in literature that the NSM strengthening technique offers a better fire performance if compared to externally bonded laminates, due to the protection provided by the embedment in the concrete cover.

Although the NSM FRP strengthening technique is less susceptible to debonding than the externally bonded systems, the strength of RC beams with NSM FRP is still likely to be governed by debonding mechanism. RC beams strengthened with NSM FRP bars in general exhibit similar failure modes as observed in RC beams with externally bonded FRP, including concrete crushing, rupture of the FRP bars and debonding of the FRP strengthening system. Previous studies [11-14,18,19,21,27-30] have shown that a large number of parameters affect the bond behavior of the NSM systems such as: the mechanical properties of the materials, the surface properties of FRP reinforcement and the groove, the external NSM FRP reinforcement ratio, the geometry of the strengthening system (rods or strips), the tensile strengths of both the epoxy and the concrete, the dimension of the groove and the depth of the FRP reinforcement into the grooves. The current understanding of the mechanism of debonding is however still limited. Based on the available experimental evidence, the possible bond failure modes of beams flexurally strengthened with NSM FRP reinforcement can be grouped in: 1) interfacial debonding between the NSM bar and the epoxy adhesive [13,17,24] and 2) concrete cover separation. For the latter case, in many tests, bond cracks formed on the soffit of the beam inclined at approximately 45 degrees to the beam axis. Upon reaching the edges of the beam soffit, these cracks may propagate upwards on the beam sides maintaining a 45-degree inclination within the cover thickness, and then propagate horizontally at the level of the internal steel reinforcement. Therefore, debonding may occur, depending on the subsequent evolution of the crack pattern, in the following modes:

- Bar end cover separation: If the NSM FRP reinforcement is terminated at a significant distance from the supports, separation of the concrete cover typically starts from the cut-off section and propagates inwards [20,22,23,24,28]. This mode is similar to the concrete cover separation failure mode observed in RC beams strengthened with FRP EBR.
- Localized cover separation: Bond cracks within or close to the maximum moment region joined with pre-existing flexural and/or flexural-shear cracks may isolate triangular or trapezoidal concrete wedges, of which one or more are eventually split off [28].
- Flexural crack-induced cover separation: Separation of the concrete cover can occur in correspondence of flexural cracks almost simultaneously over a long portion of the NSM reinforcement, often involving one of the shear spans and the maximum moment region [13,17,25]. This mode is similar to the failure induced by an intermediate crack observed in RC beams with and externally bonded FRP laminate.
- Flexural-shear crack induced cover separation: Like in the EBR technique, the shear sliding and the crack opening movements of a flexural shear critical crack promotes the concrete cover separation [29].
- Beam edge cover separation: When the FRP NSM bars are located near the edges, the detachment of the concrete cover along the edges can occur.

2.4 Concerns of FRP in fire

Despite the increasing success in applying the FRP strengthening system in reinforced concrete structures during the past decade, the weak performance of this strengthening technique under elevated temperature and/or fire exposure has hindered their application in buildings. The main concern in implementing FRP materials in buildings for which fire risk is not negligible is the deterioration of mechanical properties of FRPs, as well as a reduction of bond strength at the concrete-adhesive interface under elevated temperature and fire exposure [33-38]. The deterioration of the mechanical properties of the FRP is primarily due to deterioration of the polymer matrix. Indeed as the temperature of the polymer matrix approaches its glass transition temperature, T_g, the matrix transforms to a soft, rubbery material with reduced strength and stiffness. Thus for epoxy resins, currently used as primer, adhesive and matrix for FRP strengthening systems the degree of reduction of the mechanical properties at temperatures close to their T_g (the glass transition temperature of ambient cured epoxies is usually in the range of 50-90°C) is of relevant importance for the strengthened structures, mostly in relation to the bond performance. Indeed the overall performance of the FRP strengthened member depends on the properties of the FRP-adhesive and the adhesive-concrete bond interface.

A second possible concern related to the use of FRP strengthening materials, under fire exposure, is the combustion of the polymer matrix. Many polymer composites ignite when exposed to high heat flux, releasing heat that can, in some circumstances, contribute to the growth of the fire. Significant quantities of smoke and toxic fumes may also be released limiting the visibility and posing a health hazard. Smoke toxicity is obviously most critical in cases where the FRP is installed on the exterior of the concrete member. Flame spread, smoke generation and toxicity considerations, while important are not addressed in detail in the current thesis, which focuses on the structural fire endurance of FRP strengthened concrete members under elevated temperature and fire exposure. More information about the effect of heat release, smoke generation and toxicity can be found in [39-41]. It has to be noted that in [39,41] it was found that flame spread and smoke generation can be reduced, therefore increasing the performance of FRP under fire exposure, by applying different type of intumescent coatings or/and barrier treatments.

While the effect of elevated temperature on the thermal and mechanical properties of FRPs and polymer matrix materials will be discussed further in chapter 3, in the following sections the effect of elevated temperatures on the bond behavior of the FRP strengthening system and the endurance of FRP strengthening systems under fire exposure, are discussed based on a literature review. It has to be noted that, although this thesis is mainly focused on the NSM FRP strengthening technique, due to the few number of research projects on NSM FRP systems under fire exposure, the behavior of EBR strengthened members under elevated temperatures and fire exposure is also reviewed.

2.5 Bond properties at elevated temperature: state of art

The main aspect governing the design of an FRP strengthening application is the debonding of the FRP. External application of FRP requires them to develop and transfer shear forces through the bond interface between the FRP and the concrete. The bond performance of the FRP strengthening system is likely to be affected with increasing temperature, which will eventually lead to a loss of interaction between FRP and concrete. Knowledge about the decrease of the bond properties of the FRP-concrete interface at elevated temperatures is currently limited.

2.5.1 Bonded steel plates at elevated temperature

In [42] the influence of elevated service temperature on the bonding of steel plates to concrete by means of epoxy resin was studied. The bond behavior of three different concrete grades (concrete cube compressive strength equal to 27.9 MPa, 44.4 MPa and 74.0 MPa) was investigated at 20°C, 30°C, 60°C, 90°C and 120°C. It has to be noted that no information about the glass transition temperature of the epoxy resin was reported. The authors, performing double shear tests (see Figure 2.9) observed a relevant decrease of failure load by increasing the temperature. The double bond shear tests indicated that the bond of steel plates to high-strength concrete by means of epoxy resin was more sensitive to variations in temperature than such a bond with lower-strength concrete (see Figure 2.10). Referring to the specimens tested at room temperature the reduction of the bond strength was in the range of 0.9-31.7% at 30°C, 48.6-55.3% at 60°C, 72.2-75.7% at 90°C and 91.1-92.7% for the specimens tested at 120°C.

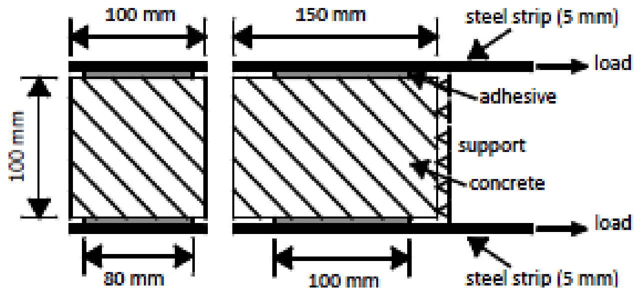

Figure 2.9 – Bond shear test set-up (Tadeu and Branco 2000) [11]

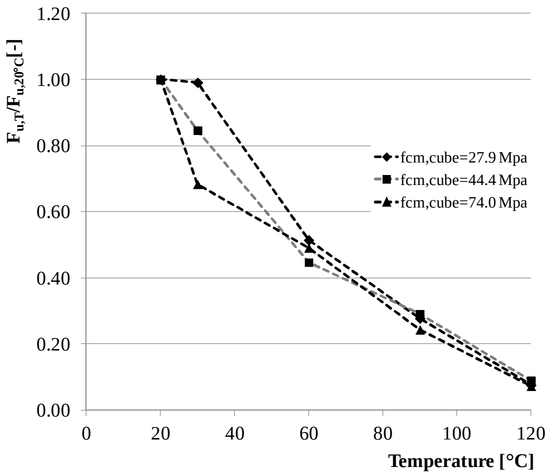

Figure 2.10 – Normalized load as a function of temperature [42]

The authors observed, moreover, a change in the type of failure mode with increasing temperature. For temperatures up to 30°C, the steel concrete bond failed through rupture of the concrete, while for higher temperatures failure at the interface between adhesive and steel plate was observed. At 120°C, film water was observed on the surface of the concrete, in addition to the deterioration of the resin. This was caused by release of free water present within the concrete by evaporation at 100°C. The migration of water caused the appearance of pressures on the bond, contributing to the failure.

2.5.2 Bonded FRP strips at elevated temperature

A different trend of failure load was obtained in [43], performing double bond shear tests on concrete elements strengthened with externally bonded CFRP laminates at different temperature values (20°C, 40°C, 55°C and 70°C). The specimen (nominal dimensions 150 x 150 x 800 mm) was composed of two concrete blocks (150 x 150 x 400 mm) as shown in Figure 2.11. Only one block is the test region, with a bond length of 300 mm. To prevent bond failure in the second concrete block extra clamp anchorages were used. The glass transition temperature of the epoxy adhesive was 62°C, as reported by the manufacturers.

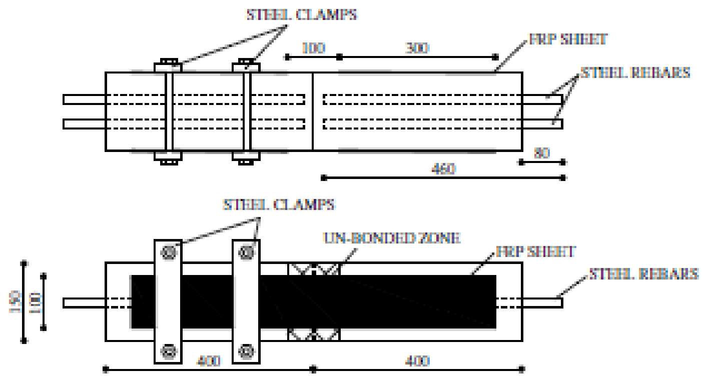

Figure 2.11 – Double bond shear test set-up [43]

Experimental outcomes showed that, considering the test at 20°C as reference, the ultimate load increased for the test at 40°C and 55°C (41% and 24% respectively) while it decreased at 70°C (19%) as shown in Figure 2.12. The author concluded that no complete degradation of bond strength was observed increasing the temperature up to 1.12 times T_g. Therefore, although the bond behavior is clearly affected by increasing the temperature, it still retains some strength even at temperatures higher than the adhesive glass transition temperature. Moreover the author mentioned two possible causes for the initial bond strength increase (which differs compared to [42], section 2.5.1). A first reason relates to the different dimensions of the specimens with a significant larger bond surface (300 x 100 mm^2) for [43] compared to [42] (100 x 80 mm^2). This resulted in a different failure mode. For the EBR FRP strengthening system the failure load was due to debonding of the FRP with a concrete layer with approximately 1 mm thickness, while in case of externally bonded steel plates, failure of concrete was observed with a depth approximately equal to 30 mm from the bonded surface. The second reason is the difference in coefficient of thermal expansion between the FRP and concrete (for steel and concrete the coefficient of thermal expansion is almost the same). This induced thermal stresses between the CFRP and the concrete which could have affected the load capacity. These stresses had a positive effect on the load capacity up to 55°C. Further increase of temperature up to 70°C resulted in a decrease of failure load, caused by the softening of the adhesive.

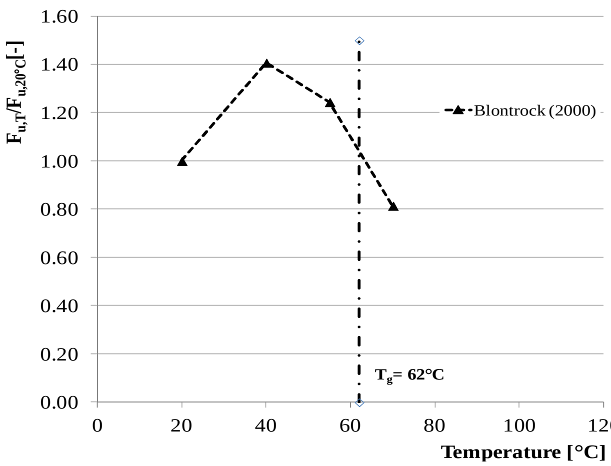

Figure 2.12 – Normalized load as a function of temperature [43]

A similar test set-up was adopted in [44] for testing CFRP and GFRP fabrics (wet lay-up) and prefabricated CFRP laminates at various temperatures up to and including 80°C. The glass transition temperature of the adhesive was equal to 55°C. The glass transition temperature was experimentally evaluated, on three epoxy samples, using a Differential Scanning Calorimetry (DSC) method. Each sample was held for 1.0 minute at 5°C and subsequently heated in a nitrogen atmosphere from 5°C to 200°C at 10°C/min. The trend of the recorded failure load was in agreement with the experimental results reported in [43] for the CFRP fabrics. For instance, increasing the temperature to 50°C and 65°C the failure load increased (24% and 7% respectively) while it decreased at 80°C (11%) as shown in Figure

2.13. The GFRP fabrics were tested only at ambient temperature and at 80°C, at which temperature a decrease of failure load, equal to 20% with respect to that at ambient temperature, was observed (see Figure 2.13). For the CFRP laminates, at 50°C a lower failure load was observed with respect to that at room temperature, while at 80°C a higher failure load was observed. The authors concluded that the different behavior of CFRP laminates with respect to that of CFRP fabrics could be explained considering the lower concrete quality of these specimens and the eccentricities that were observed in the tests.

The bond stress-slip curves with increasing service temperature showed that the stiffness at the FRP-concrete interface decreased besides the decay of the maximum bond stress (see Figure 2.14 as reference).

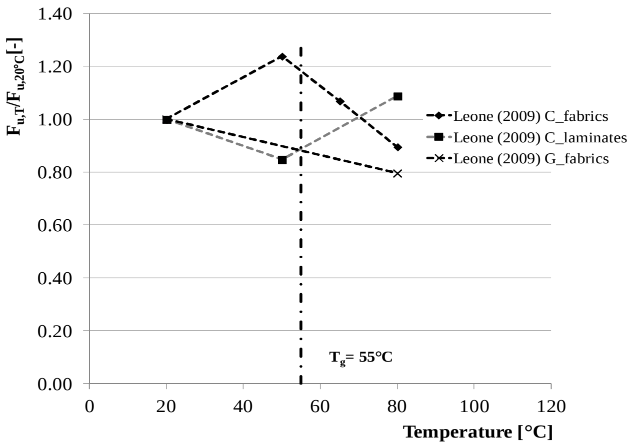

Figure 2.13 – Normalized load as a function of temperature [44]

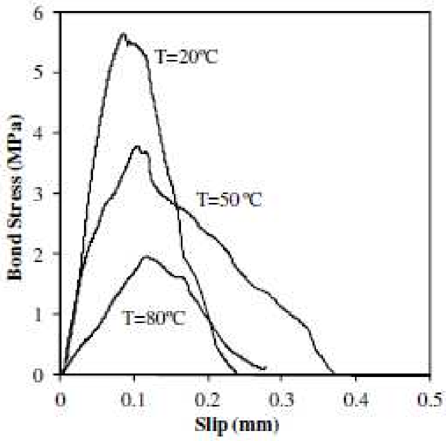

Figure 2.14 – Bond stress-slip curves at different temperatures for CFRP laminates [44]

The type of failure changed with increasing test temperatures. Specimens tested at 50°C showed cohesion failure within the concrete, while increasing the temperature an adhesion failure at the adhesive-FRP interface was observed. The transfer length (assumed as the distance from the loaded end to the point where the strain reaches almost zero) increases with the test temperature while the maximum forces remain almost constant. In particular the transfer length at 80°C increased 2.5-3 times with respect to that at 20°C. Finally, as in [43], experimental outcomes showed no complete bond degradation by increasing the temperature up to $1.5T_g$.

Double bond shear tests (see Figure 2.15) have been carried out also in [45]. The influence of temperature on the bond behavior between CFRP fabrics and concrete has been investigated, making use of both ordinary epoxy and a new developed thermo-resistant epoxy (with a higher glass transition temperature). First an epoxy primer was applied to the concrete surface, followed by the epoxy adhesive for bonding the CFRP. The glass transition temperature for the two epoxies was equal to 34°C for ordinary epoxy and 40°C for thermo-resistant epoxy, according to ISO 11359-2 [46]. The specimens were tested under load and a temperature ranging between 26°C and 60°C.

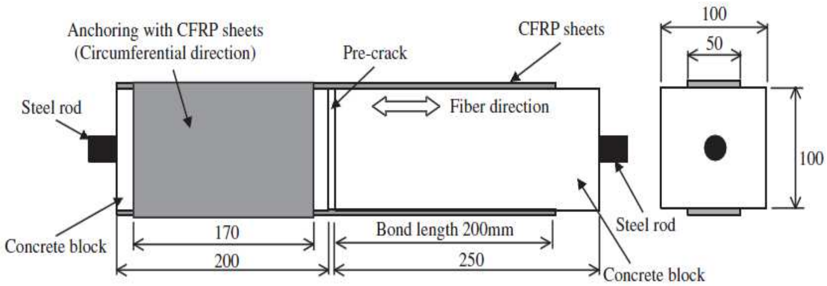

Figure 2.15 – Double bond shear test set-up [45]

The authors in [45] observed a decreasing failure load with increasing temperatures for both types of epoxy adhesives (see Figure 2.16). The decrease of failure load was more significant for the ordinary epoxy resin than for the thermo-resistant epoxy. The different trend of results for increasing temperature, in terms of failure load, with respect to [43-44] could be related to the reduced bond capacity of the primer-adhesive interface at elevated temperature rather than that of the adhesive-FRP interface. For instance it was observed that, for both epoxy adhesives the failure mode changed from a mixed type of failure in the concrete and in the primer-adhesive interface at 26°C and 30°C to failure in the primer-adhesive interface at 40°C and above. Moreover, in accordance with the experimental results obtained in [44], it was observed that the transfer length increased with the test temperature. Figure 2.17 shows the variation of transfer length as a function of temperature for the two different epoxy adhesives.

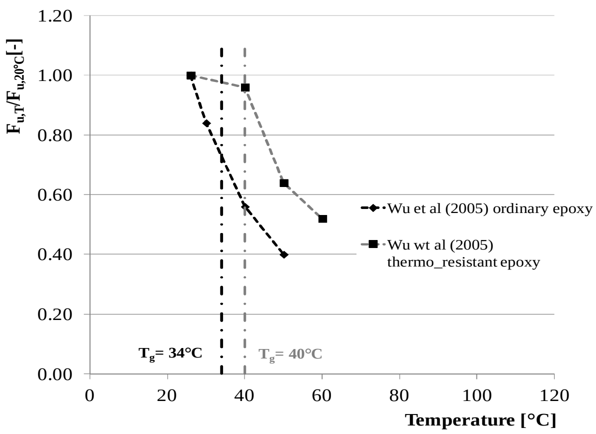

Figure 2.16 – Normalized load as a function of temperature [45]

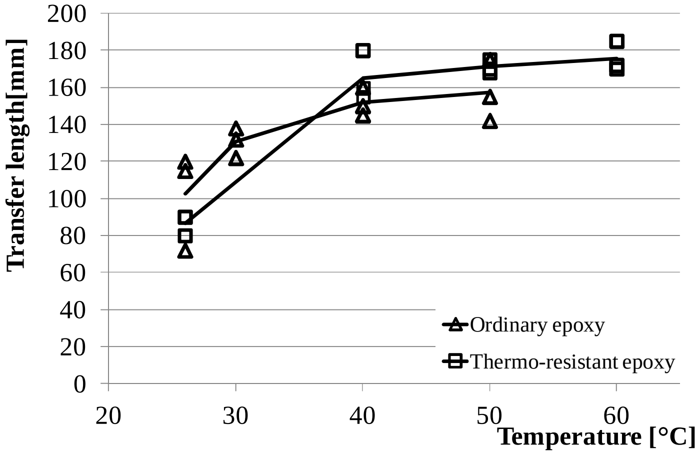

Figure 2.17 – Transfer length as a function of temperature [45]

In Klamer [11] the influence of increasing the temperature on the bond strength of the epoxy adhesive was investigated through two different test set-ups: a double bond shear test set-up (Figure 2.18) and a three point bending test set up (Figure 2.19).

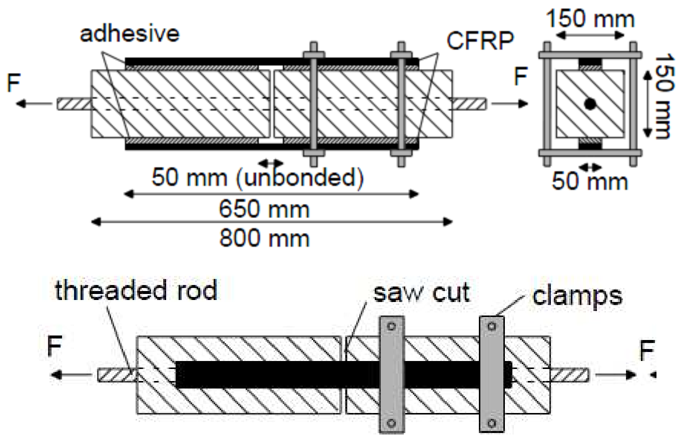

Figure 2.18 – Double bond shear test set-up [11]

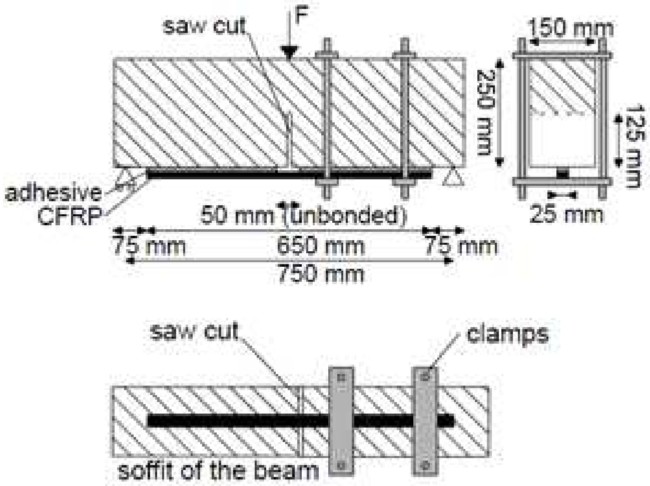

Figure 2.19 – Three point bending test set-up [11]

The double bond shear test set-up was similar to that adopted in [43-44] with a difference in the CFRP laminate dimensions (half of the width was adopted for the CFRP laminate) and only one threaded rod was used to make the connection of the specimen to the loading device. Moreover for the three point bending test set-up the width of the CFRP laminate was half that used in the double bond shear test set-up. The influence of temperature on the bond behavior in shear was investigated at several temperatures (in the range from -20°C up to 100°C for the double bond shear test set up and from -20°C up to 90°C for the three point bending test set-up), for two different concrete grades with a mean cubic compressive strength of 41.1 MPa and 70.8 MPa respectively. The experimental test results in terms of failure load as a function of the temperatures are given in Figure 2.20 for the double bond shear test set-up and Figure 2.21for the three point bending test set-up respectively.

The trend of the recorded failure load was in agreement with previous research studies. For instance, for both test set-ups, for temperatures up to the glass transition temperature of the adhesive (T_g= 62°C, as reported by the manufacturer), the tendency turned out to be an increasing failure load with increasing temperature, while for higher temperatures than the T_g, a decreasing failure load with increasing temperature was found. As demonstrated in previous studies [42], the experimental results indicate that bond of FRP strips to high-strength concrete was more sensitive to variations in temperature than for with lower-strength concrete.

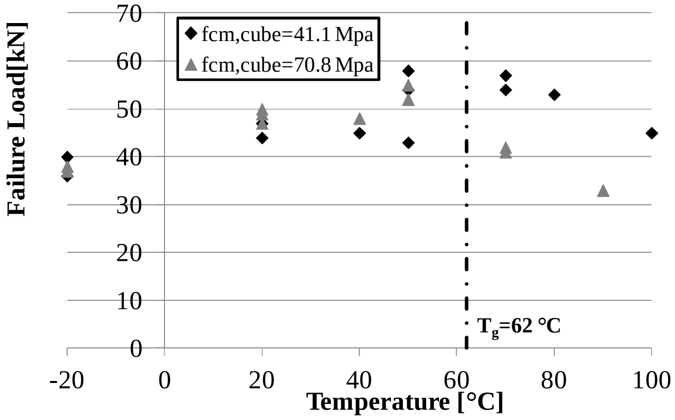

Figure 2.20 – Failure load of double bond shear test as a function of temperature [11]

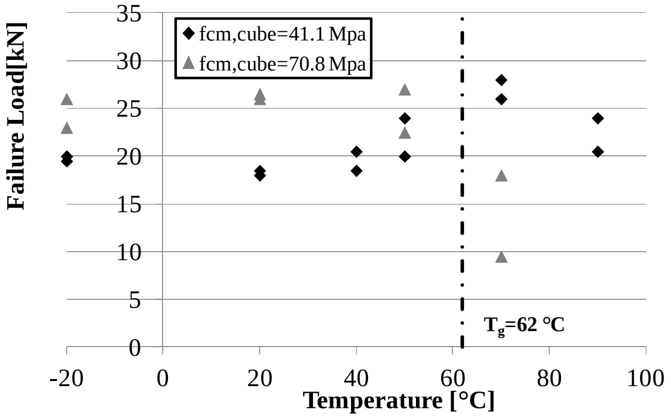

Figure 2.21 – Failure load of three point bending test as a function of temperature [11]

It was concluded that the decreasing failure load was caused by the changed type of bond failure above 50°C (specimens tested up to 50°C showed failure in the concrete adjacent to the interface, leaving a small layer of concrete attached to the adhesive; while increasing the temperature, debonding occurred in the concrete-adhesive interface without leaving any concrete attached to the adhesive) and the corresponding decreased bond strength of the concrete-adhesive interface with increasing temperature. It was also demonstrated, that at higher temperatures strains were distributed more linear over the length of the laminate, which implies that the shear stresses in the concrete are more equally distributed. Moreover, it was analytically and numerically demonstrated that the tendency of an increasing failure load with increasing temperatures up to T_g was related to the difference in coefficient of thermal expansion between concrete and CFRP and/or the reduced Young's modulus of the adhesive. For instance the difference in the coefficient of thermal expansion between the concrete (α_c= 10x10^{-6} /°C) and the CFRP (α_f= 0x10^{-6}/°C in the fiber direction) will result in the development of strains and thermal stresses in the FRP and concrete when changing the temperature. In [11] these thermally induced strains and stresses were determined analytically according to a kinematic model developed by Di Tommaso et al. [47]. The model was modified considering also the shear stiffness of the adhesive layer, which was not included in [47], in order to take the effect of the reduced Young's modulus of the adhesive at elevated temperature into account. The CFRP thermal strains, $\varepsilon_f(x)$, and thermal shear stresses, $\tau_c(x)$, in the concrete were determined by the equations 2.1 and 2.2:

$$\varepsilon_f(x) = \left[\frac{\varepsilon_{\Delta T}}{\cosh\left(\omega \cdot \frac{l}{2}\right)} \cosh(\omega \cdot x) - \varepsilon_{\Delta T}\right] \tag{2.1}$$

$$\tau_c(x) = E_f \cdot t_f \cdot \omega \cdot \frac{\varepsilon_{\Delta T}}{\cosh\left(\omega \cdot \frac{l}{2}\right)} \cdot \sinh(\omega \cdot x) \tag{2.2}$$

Where:

- E_f is the Young's modulus of the FRP reinforcement
- $\varepsilon_{\Delta T} = \alpha_c \Delta T$ is the thermal strain of the concrete
- α_c is the coefficient of thermal expansion of concrete
- $\omega^2 = \frac{k_G}{E_f t_f}$
- $\frac{1}{k_G} = \frac{1}{k_{Gc}} + \frac{1}{k_{Ga}}$
- $k_{Gc} = \frac{E_c(T)}{2 \cdot (1 + \nu_c) \cdot h_{c,ef}}$ is the shear stiffness of the concrete
- $k_{Ga} = \frac{E_a(T)}{2 \cdot (1 + \nu_a) \cdot t_a}$ is the shear stiffness of the adhesive
- $E_c(T)$ is the young modulus of the concrete at temperature T
- $h_{c,ef}$ is the effective height equal to 50 mm or two times the maximum aggregate size
- $E_a(T)$ is the Young modulus of the adhesive at temperature T

- t_a is the thickness of the adhesive layer
- t_f is the thickness of the FRP laminate
- ν_c and ν_a are the Poisson ratio of the concrete and the adhesive
- *l* is the bonded length
- x is the distance from the middle of the bonded length

The shear stress distributions along the bond length, for the double bond shear test set-up, are plotted in Figure 2.22 for different load levels (similar behavior was observed for the three point bending test set-up). It was observed that, at the end of the bonded length (loaded end) the direction of the shear stress due to a temperature increase (thermal shear stresses; Figure 2.22a) were opposite to the direction of the shear stress due to the loading (Figure 2.22 b and c). Shear stresses due to the loading had first to compensate the thermal stresses at this end. The increasing failure load with increasing temperature was related to the lower shear stress at the loaded end with increasing temperature (Figure 2.22 b).

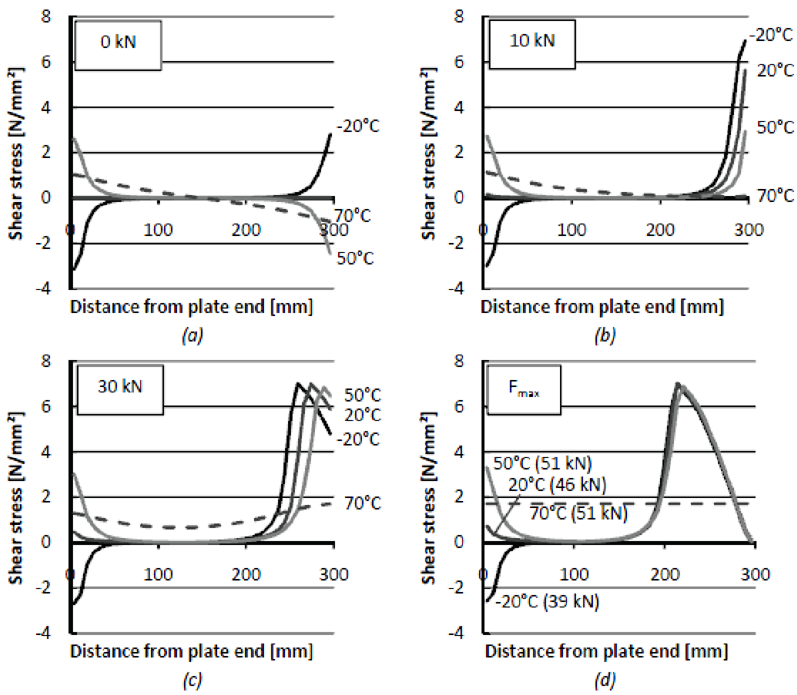

Figure 2.22 – Shear stresses at the interface at a) 0 kN, b) 10kN, c) 30 kN and d) the failure load for double bond shear test set-up [11]

For temperatures higher than T_g the reduction of the bond strength of the adhesive governed over the beneficial effect induced by the difference of thermal expansion and resulted in a reduction of failure loads and change in failure modes.

2.5.3 Residual bond strength after exposure to elevated temperature

In [48] the residual bond properties of externally bonded CFRP (wet lay-up) after exposure to elevated temperature (up to 250°C) were investigated. The double bond shear test set-up is shown in Figure 2.23. The CFRP strips were applied to the opposite sides of the blocks with bonded length of 102 mm. To promote debonding at the predetermined location, additional 102 mm square patches of FRP were applied laterally on the top of the longitudinal FRP strips on the other side of the concrete block. The glass transition temperature of the epoxy adhesive was experimentally evaluated by Differential Scanning Calorimetry (DSC) according to ASTM D3418 [49] and was equal to T_g=78°C.

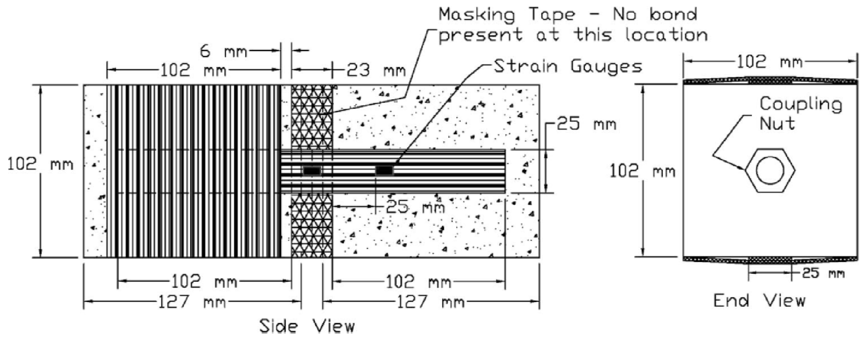

Figure 2.23 – Double bond shear test set-up [48]

The residual bond properties of the CFRP system were investigated at different temperatures: 20°C, 100°C, 140°C, 180°C, 195°C and 250°C. Thermal exposures were accomplished by placing the specimens in a programmable electric furnace and heating to the predetermined temperature at a rate of approximately 10°C/min, a soak time of 3h and slow natural cooling to ambient conditions after heating. After cooling, the specimens were tested in tension up to failure. Experimental results in terms of normalized residual bond strength at different temperatures are shown in Figure 2.24.

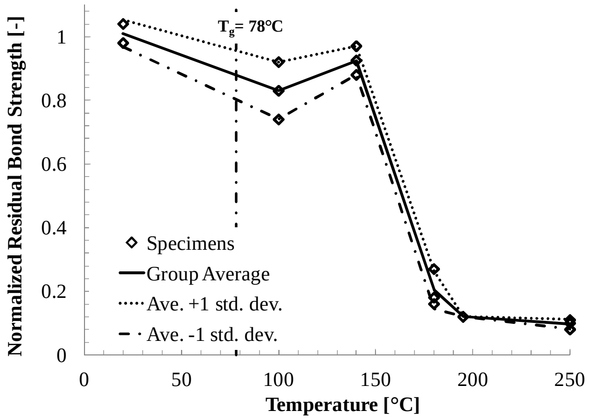

Figure 2.24 – Normalized residual bond strength as a function of the temperature [48]

An average bond strength reduction of less than 20% was observed for specimens exposed to 100°C (1.28 T_g) and 140°C (1.80 T_g), while almost complete loss of average bond strength was observed at higher temperatures. Changes in failure mode also occurred for increasing exposure temperatures. Specimens tested at room temperature and up to 140 °C failed by shear/tensile failure of the substrate concrete beneath the FRP-concrete interface, indicating that the bond strength was limited by the strength of the substrate concrete as opposed to the adhesive. Specimens exposed to 180°C, 195°C and 250°C exhibited bond failure in the adhesive at FRP/concrete interface due to the decrease of the adhesive bond strength. The author in [38] concluded that the retention of bond strength in pure shear failure is highly affected by temperature exposure due mainly to the degradation of the adhesive bond strength properties. Moreover, it was concluded that contribution to the loss of bond shear strength may be, also, due to the moisture evaporation from the concrete substrate, which is known to occur at temperatures above 100°C, causing damage to the adhesive layer.

2.5.4 Conclusions on bond strength at elevated temperature

Bond tests at elevated temperatures have shown that the bond behavior of FRP strengthening systems is clearly affected by temperatures close to the adhesive glass transition temperature; although no complete bond degradation was observed for all the reviewed research projects. The failure mode and transfer length are also affected by increasing temperature. Moreover for some of the reviewed tests an initial increase of load capacity is observed for temperatures below or/at the adhesive glass transition temperature. This behavior is attributed to the beneficial effect of induced thermal stresses, due to the difference in thermal expansion between the CFRP and the concrete and the reduction of adhesive Young's modulus. Both effects have been experimentally and analytically investigated in [11]. However, for temperatures higher than the glass transition temperature, the reduction of bond strength of the adhesive governed over the beneficial effect induced by the difference in thermal expansion and resulted in a reduction of failure loads and a change in failure mode. Finally, the residual CFRP to concrete bond properties after exposure to elevated temperature have shown the possibility to retain a high percentage of the room temperature bond strength up to an exposure to 140ºC (equal to $1.80T_g$ for the reviewed research). Increasing the temperature further a drastic reduction on bond strength in pure shear was observed. This behavior is attributed not only to the strength degradation of the adhesive but also to the influence of the moisture evaporation from the concrete substrate, which occurs at temperatures above 100°C, causing damage to the adhesive layer.

2.6 Fire endurance of FRP strengthened concrete structures: state of art

Figure 2.25 shows, schematically, the interaction between fire resistance, strength and service load with increasing temperature of an FRP strengthened reinforced concrete structure and un-strengthened concrete structure. During a fire, the specific performance of the FRP system is not critical if the strengthened structural member can resist failure, for the required duration of fire, under the acting service load of the strengthened structure under fire (failure of the member would occur when the ultimate strength drops below the acting load).

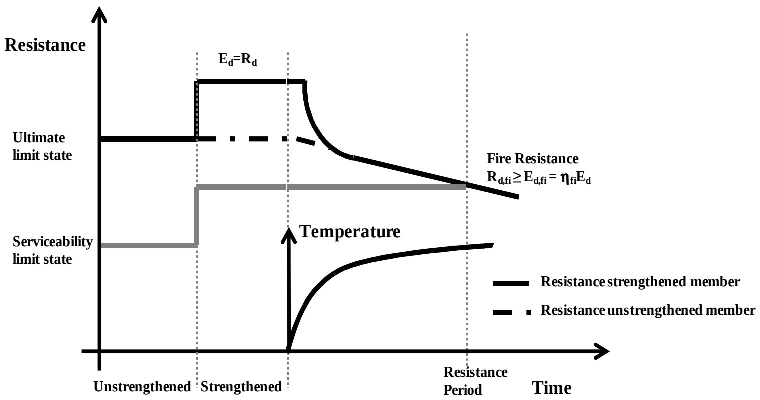

Figure 2.25 – Interactions between fire resistance, strength and temperature for an FRP strengthened member [50]

2.6.1 Fire endurance of FRP EBR RC members strengthened in flexure

A limited number of research projects have shown that, with an appropriate insulation, concrete structures strengthened with FRPs can achieve a satisfactory fire endurance rating though contribution of the FRP is generally assumed as lost during fire exposure. In [51] six fire tests were executed to determine the behaviour of FRP externally strengthened beams under fire exposure. The configurations of the tested beams (dimensions 300 mm x 400 mm x 5.3 m) were: a beam without external reinforcement (reference beam), one strengthened with a bonded steel plate, and four strengthened with CFRP sheets. For these CFRP strengthened beams two were protected with calcium silicate insulating plates. The insulation material was mechanically fixed (screws type M6 each 250 mm) at the underside of the beams for their entire length. Two different insulation thicknesses (40 mm and 60 mm) were tested. The longitudinal lower reinforcement of the control beam consisted of six steel rebars with diameter 12 mm for a length equal to 5.3 m and three steel rebars with diameter 12 mm for a length equal to 5.05m, while the longitudinal lower steel reinforcement of the others beams consisted of six steel rebars with diameter 12 mm for a length equal to 5.3 m. The longitudinal upper reinforcement consisted, for all the beams, of four steel rebars with diameter 10 mm for a length equal to 5.2 m. All the beams were pre-loaded, in four point-bending, to a constant load equal to 2 x 47 kN which was kept constant during the fire test. All the beams were heated, in a furnace, according to the ISO 834 [52] standard fire curve. Experimental outcomes showed that, during the fire test, interaction between steel plates and concrete was lost approximately at 10 minutes into the test, while interaction between CFRP laminates and the concrete was lost within 20 minutes for the unprotected beams. The higher number of longitudinal steel reinforcement of the control beam with respect to the unprotected beams strengthened with bonded steel plate and bonded CFRP lead to a smaller increase of deflection with increasing temperature. Insulated beams experienced loss of interaction between the CFRP and the concrete after approximately 1 h of fire exposure, at which time the temperature of the CFRP was approximately 83°C for the beams insulated with 60 mm of calcium silicate board and 85°C for the beams insulated with 40 mm of calcium silicate board. Figure 2.26 shows the time-deflection curves during the fire tests for all the tested beams.

It was concluded that composites sheets without protection behave better than steel plates without protection because of the much lower heat conduction in the fibre direction and their smaller weight. Moreover the results demonstrated the need for thermal insulation of the FRP plates in order to reach a sufficient fire resisting capacity.

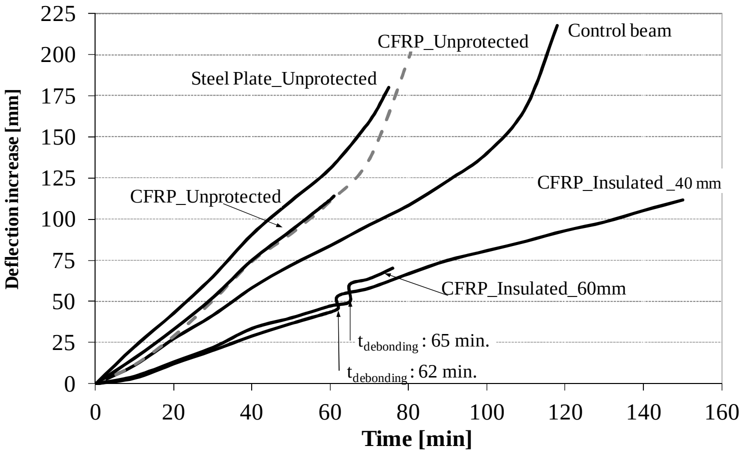

Figure 2.26 – Time-deflections curves fire tests in [51]

Furnace tests in [43] investigated the performance of FRP strengthened concrete beams and slabs, to evaluate their fire endurance. A total of 8 beams and 16 slabs were tested including: unstrengthened versus strengthened and unprotected versus protected specimens. The configurations of the tested beams (200 mm x 300 mm x 3150 mm) were: two unprotected and unstrengthened beams and six strengthened and protected beams. The protection schemes were different for all six protected beams and consisted of gypsum board/rock wool combinations. The parameters investigated were the different insulation board thickness, the location (protection at the bottom side of the beam or U-shaped form), length (for one beam the protection board was installed only at the FRP anchorage zone) and bonding method (for one beam the insulation was anchored only by adhesive, while all the others were mechanically fixed by screws). All the beams have the same geometry, longitudinal steel reinforcement and FRP reinforcement. Figure 2.27 shows some details of the strengthened beam and some insulation schemes as reference. The configurations of the tested slabs (400 mm x 150 mm x 3150 mm) were: two unprotected and unstrengthened slabs and 14 strengthened and protected slabs. The protection schemes were different for all 14 protected slabs and consisted of gypsum board with or without rock wool. The parameters investigated were the type of fire protection board (two different type of gypsum fire protection boards were investigated), the board thickness and the length of the fire protection boards. All the slabs have the same geometry and longitudinal steel reinforcement. Two different type of FRP reinforcements were used to strengthened the slabs as shown in Figure 2.28, in which some details of the strengthened slabs and the different insulation scheme are also reported. All the specimens (beams and slabs) were pre-loaded in four points bending to their unstrengthened and strengthened service loads, as calculated according to Eurocode 2 [53] for the unstrengthened/unprotected and strengthened/protected beams and slabs respectively. The load was kept constant for all the duration of the fire test. A maximum of two hour of fire exposure was chosen for all the tests. The fire endurance tests were conducted in accordance to EN 1363-1 [54] standard fire testing; the furnace temperature was controlled to follow the standard ISO 834 [52] curve.

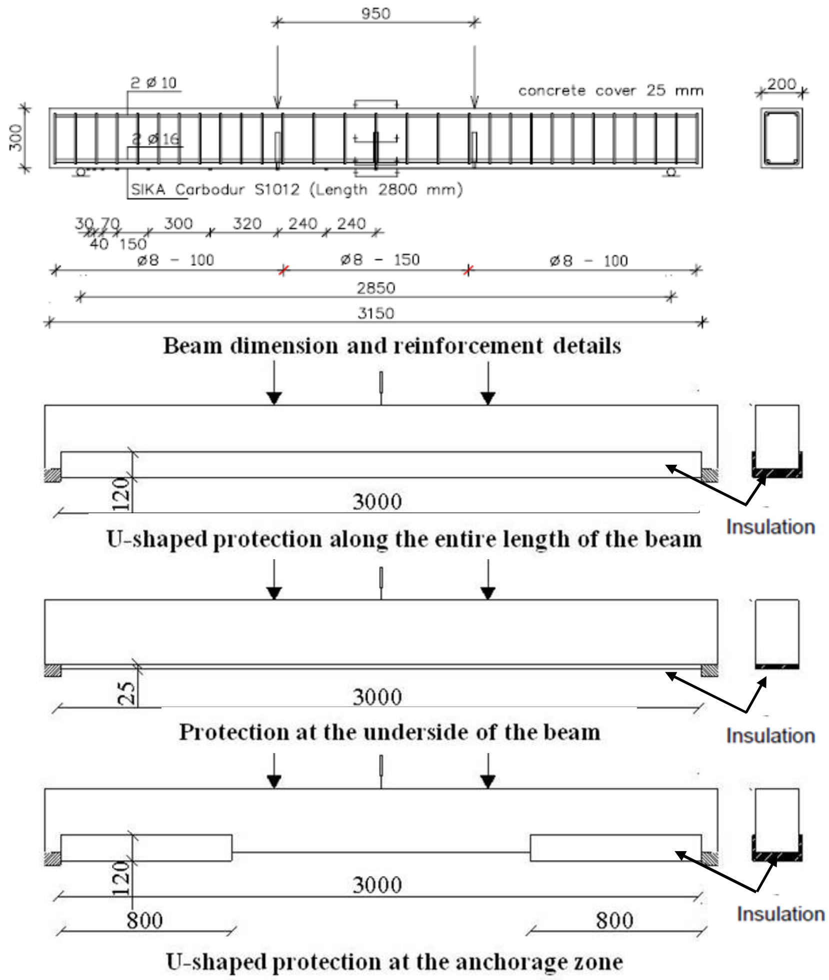

Figure 2.27 – Details of beams specimens [43]

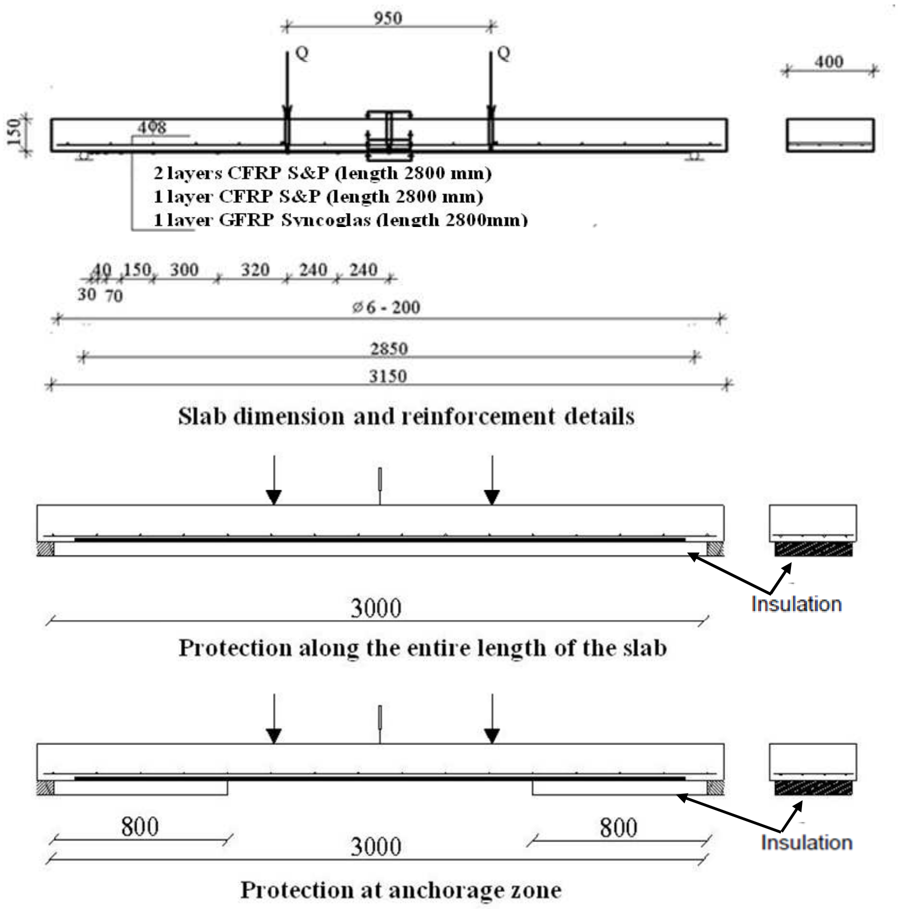

Figure 2.28 – Details of slabs specimens [43]

As for previous research studies the loss of interaction between the concrete and the FRP strengthened system was recorded by monitoring the sudden increase of deflection. Experimental outcomes in terms of time – increase of deflection at midspan are reported in Figure 2.29 and Figure 2.30. It was concluded that all the tested elements achieved satisfactory fire endurance, depending on the applied fire protection scheme, although temperature and deflection measurements indicated reduced bond integrity (lost of composite action) after 10-60 min for the beams and 24-56 min for the slabs. The temperature in the adhesive, when interaction between FRP and concrete was lost, was in the range of 66°C - 81°C for the beams and 47°C-

69°C for the slabs. Thermal protection is required in order to maintain the interaction between the FRP plates and the concrete. However, all the insulations schemes were able to limiting the increase of temperature of the concrete and longitudinal steel reinforcement, thus improving the fire endurance of the beams and slabs even in combination with loss of FRP bond interaction. The U-shaped protection performed better than that applied only at the underside of the beam, due to the additional protection of the internal reinforcing steel. The performance of the partial protection of the FRP strengthening system (protection applied only at the anchorage zone) was observed to be similar to that in which the protection was applied for the entire length of the beams and slabs. This showed that protecting the anchorage zones of the FRP would be able to maintain interaction between the FRP and concrete.

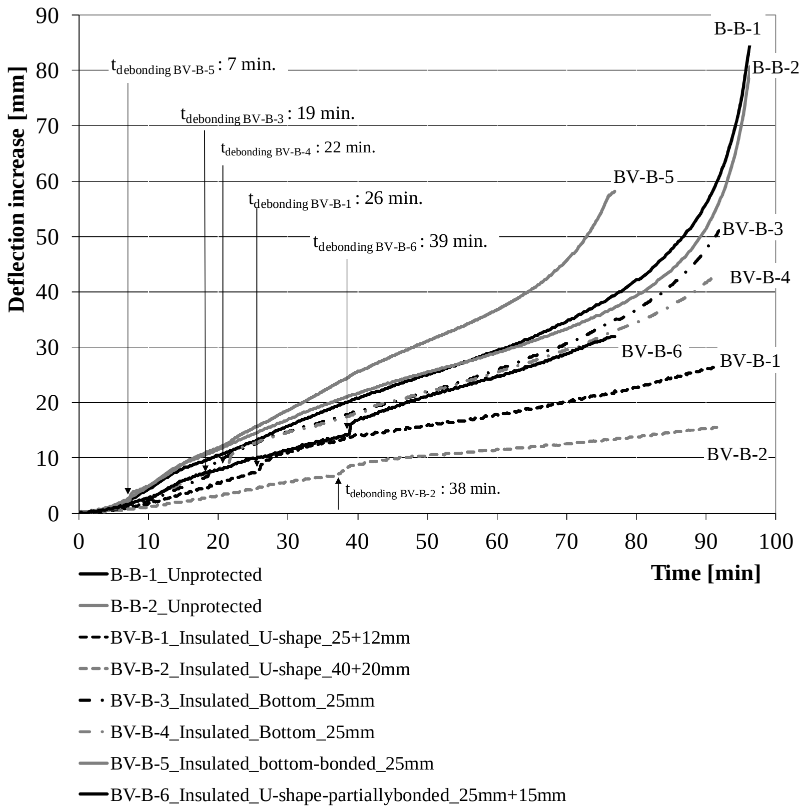

Figure 2.29 – Time-increase of deflection at midspan of beams [43]

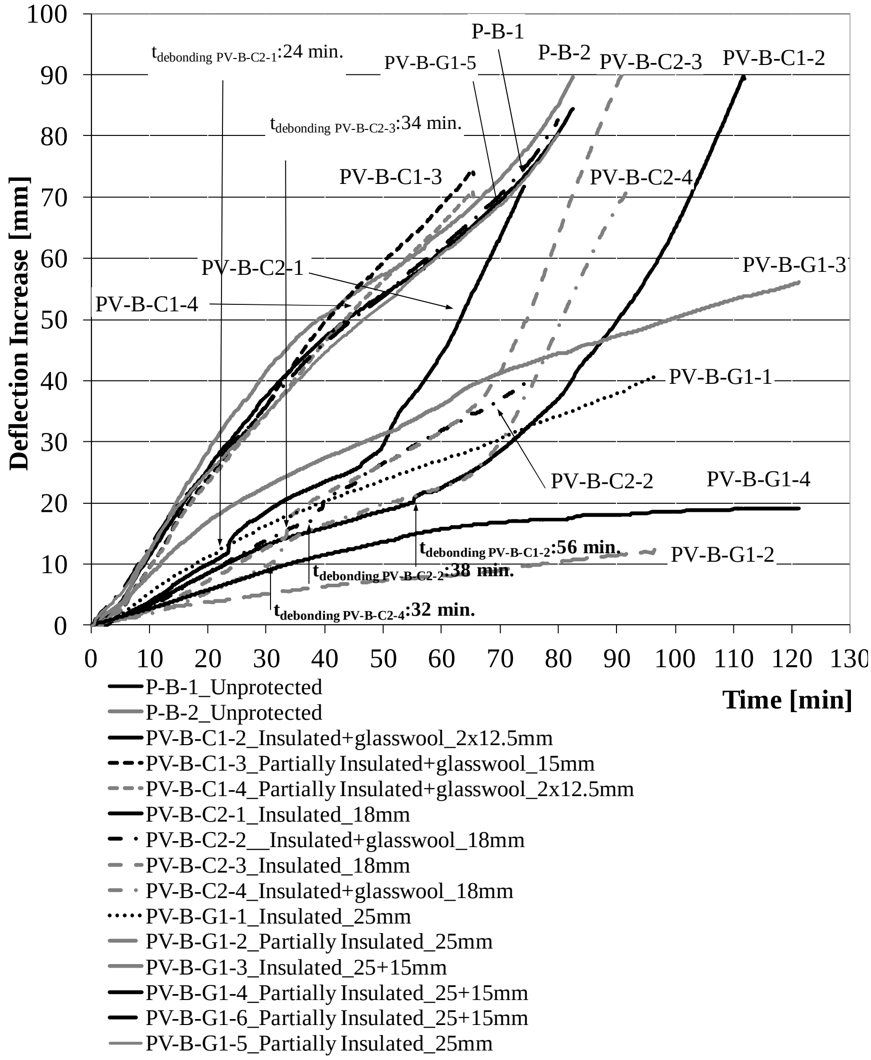

Figure 2.30 – Time-increase of deflection at midspan of slabs [43]

In [55-56] full scale fire tests were conducted on T-beams strengthened with CFRP sheets. A total of 4 T-beams with a length of 3.9 m were investigated; Figure 2.31 shows the cross section of the beams. Prior to fire tests, beams 1 and 2 were strengthened in flexure with a single layer of 100 mm wide CFRP system and beams 3 and 4 with a single layer of 200 mm wide CFRP system on the soffit of the beams' web. In addition, for anchorage of the flexural sheets at their ends, GFRP U-wraps were provided at the ends of beams 1 and 2, and CFRP U-wraps at the ends of beams 3 and 4, over a distance of 600 mm in both cases. More information about the FRP strengthened systems can be found in [55-56]. The fire protection system for all four beams was a patented two-component system developed specifically for these applications by an industrial partner and was applied as shown in Figure 2.31. The fire protection system of beam 1 and 2 consisted of 25 mm and 38 mm thick spray-applied gypsum based mortar along with an impermeable surface-hardening topcoat, with a thickness of 0.13 mm. Beams 3 and 4 were protected with a spray-applied mortar insulation of 38 mm and 25 mm thickness respectively. All the beams were pre-loaded to their service load, calculated from the ultimate capacity of the FRP strengthened beams in accordance to ACI 440-2R [57] and assuming a dead to live load ratio of 1.0. Based on these calculations, a sustained uniformly distributed load of 34 kNm and 35 kNm was applied to beams 1 and 2 and beams 3 and 4 respectively.

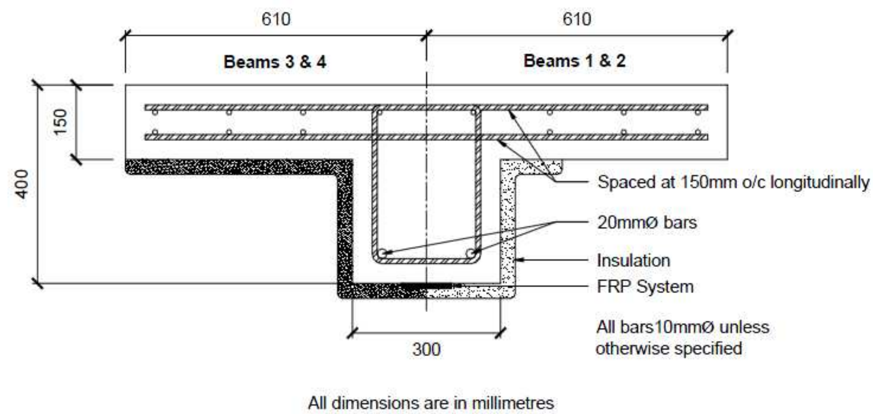

Figure 2.31– Cross – sectional dimensions of T-beams [55-56] reported in [58]

Figure 2.32 shows the experimental results in terms of time-temperature curves at various locations in the four beams including the unexposed face, the primary steel longitudinal rebars and the FRP temperatures. The insulation system applied over the FRP of beams 1 and 2 stayed attached to the beams for all the duration of the 4 h of fire exposure (although some cracks were observed during the tests), while that applied over the FRP of beams 3 and 4 debonded locally near 80 min into the fire tests (see Figure 2.32). The temperature in the FRP exceeded the glass transition temperature, T_g of 93°C (beams 1 and 2) and T_g of 71°C (beams 3 and 4) at 36 min into the test for beam 1, 79 min into the test for beam 2 and 20 min into the test for beams 3 and 4. The FRP started to lose strength and its bond to the concrete when the glass transition temperature was exceeded, and was probably ineffective during the fire test. The experimental outcomes showed that all the four beams were able to carry the applied load for more than 4 h of exposure to the standard fire, and all four beams achieved the 4 h of fire endurance ratings even after the adhesive temperatures exceeded the glass transition temperature. At approximately 4 h of fire exposure, the load applied to the beams was increased to almost twice the original intensity (the maximum capacity of the test frame) and no impending failure was observed.

The authors concluded that the insulation systems provided good thermal protection and were effective in increasing the fire endurance of reinforced concrete members strengthened with FRP by keeping the temperatures in the internal longitudinal reinforcement and unexposed side of the concrete below critical levels (these critical levels were assumed to be equal to $T_{steel} \leq 593°C$ and $T_{concr.} \leq 139°C$ in accordance to [59] for the longitudinal steel reinforcement and the concrete at the unexposed side respectively) so that the strength of the preexisting members could be relied upon to carry the loads even when the FRP-strengthening system may be rendered ineffective. After fire exposure, since the beams did not fail under the increased load, they were tested to failure at room temperature [60]. The residual strength of the beams was found to be close to the strength of the beams without the FRP. Once again, the insulation systems were demonstrated to be effective in protecting the original strength of the reinforced concrete member.

In addition to the testing program, numerical heat transfer models have been developed to predict temperatures at various points within the cross section of an FRP-strengthened and insulated beam [55-56]. The model employed an explicit finite difference formulation that discretizes the beam into nodal points and subsequently applies thermal equilibrium equations to each node to determine the temperature at each successive time step. Comparison between the predicted temperatures and experimental data resulted to be in reasonably agreement.

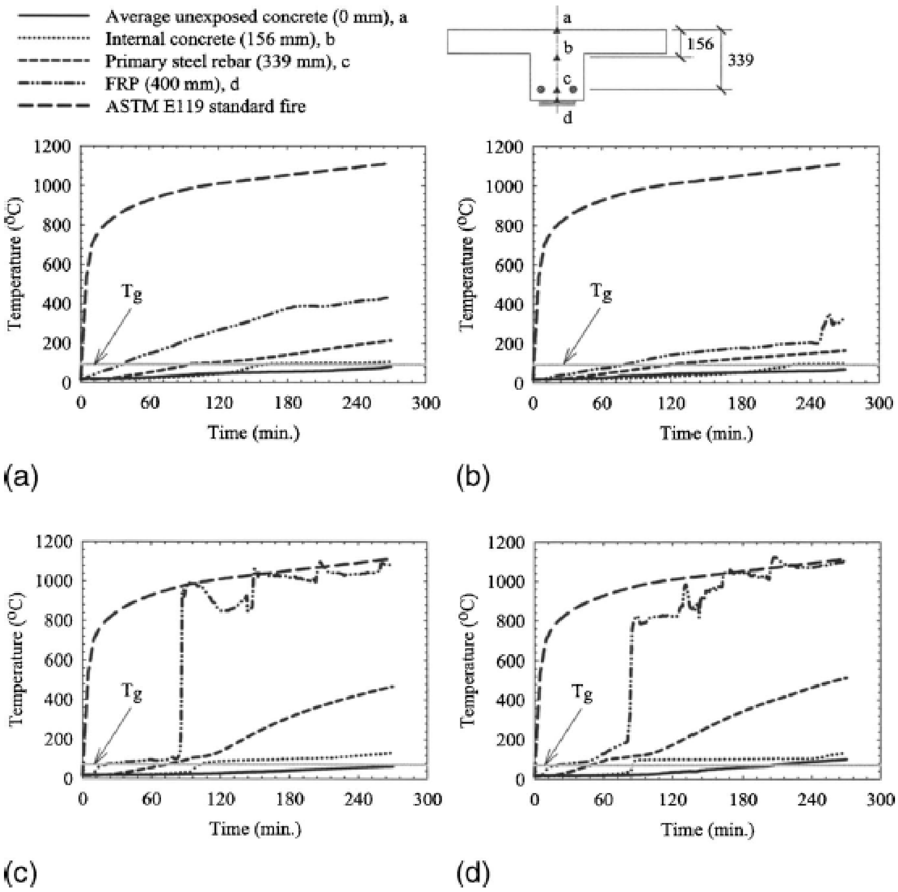

Figure 2.32 – Temperatures recorded at various locations in (a) Beam 1; (b) Beam 2; (c) Beam 3; (d) Beam 4 tested by Williams et al. (2008) and Chowdury (2005) [60]

A numerical model, initially developed for predicting the behavior of RC beams under fire exposure [61], has been extended in [62-63] to evaluating the fire performance of FRP RC strengthened beams under fire conditions up to collapse under fire. In a first stage [62] the behavior of FRP strengthened beams under fire exposure was modeled considering perfect bond between the FRP and concrete. In a second stage [63], the model was improved by considering also the effect of bond degradation between the FRP and the concrete (the second model is an extension of the first one). An overview of the model developed in [63], is given in the following focusing mainly in the analysis of the bond degradation between the FRP and the concrete.

This fire resistance model takes into account the properties of the constituent materials as a function of the temperature, to generate moment-curvature relationships for different beams segments at various time steps. In the analysis, the total fire exposure time is divided into a number of time steps and at each time step, the response of the beam is evaluated. The beam is idealized by dividing it into a number of segments along its length (see Figure 2.33 b) and the middle of each segment is assumed to represent the overall behavior of the segment. The mid-section is further discretized into a number of elements (see Figure 2.33 e). At each time step, thermal analysis was carried out to determine the temperature distribution within the cross-section of each segment, from know time-temperature curves for standard or any other specific design fire scenario, utilizing thermal properties of constituent materials (concrete, steel, FRP, insulation). Detailed information about the thermal analysis can be found in [62-63].

The computed cross sectional temperatures form the input for the strength analysis wherein time dependant moment-curvature relationships are generated for each beam segment. To generate the moment-curvature relationship the strains of each constituent material (concrete, steel and FRP) are defined as follows (equations 2.3-2.5):

$$\varepsilon_{c,\sigma} = \varepsilon_{c,tot} - \varepsilon_{c,th} - \varepsilon_{c,cr} - \varepsilon_{c,tr} \qquad \text{(for concrete)} \qquad (2.3)$$

$$\varepsilon_{s,\sigma} = \varepsilon_{s,tot} - \varepsilon_{s,th} - \varepsilon_{s,cr} \qquad \text{(for steel)} \qquad (2.4)$$

$$\varepsilon_{f,\sigma} = \varepsilon_{f,tot} - \varepsilon_{f,th} - \varepsilon_{f,cr} + \varepsilon_{f,bi} + \varepsilon_{slip} \qquad \text{(for frp)} \qquad (2.5)$$

Where $\varepsilon_{i,tot}$ is the total strain, $\varepsilon_{i,th}$ is the thermal strain, $\varepsilon_{i,\sigma}$ is the mechanical strain, $\varepsilon_{i,cr}$ is the creep strain, ε_{tr} is the transient strain, ε_{bi} is the initial strain at the soffit of the beam at the time of retrofitting with FRP and ε_{slip} is the strain slip that takes into account the bond degradation at the interface FRP-concrete during fire exposure (more information regarding these different strains can be found in chapter 3). The subscript ‘c’, ’s’ and ‘frp’ represent the concrete, the steel and the FRP respectively. At each time step, the total strain, ε_{tot}, in each element of concrete, steel and FRP is computed for an assumed value of the concrete strain at the top most fiber (ε_c) and curvature (1/r) by equation 2.6:

$$\varepsilon_{tot} = \varepsilon_c + \frac{1}{r}\, y \qquad (2.6)$$

where ε_{tot} is the total strain, ε_c is the strain at the top most concrete fiber, 1/r is the curvature and y is the distance from the uppermost concrete fiber to the center of the considered discretized element (see Figure 2.34).

In equations 2.3-2.5, creep strains for both concrete and steel and transient strain in concrete are computed based on the models proposed by [64-65] and [66] respectively. For FRP, creep strain can be considered negligible and therefore not accounted for the analysis and the initial strain (ε_{bi}) can be evaluated based on dead loads at time of retrofitting. For computing the bond slip-strain due to the bond degradation at the FRP-concrete interface the following assumptions are made. Considering a small elemental length “dx” of the adhesive (see Figure 2.33 c) the displacement (du) due to the slip is determined by equation 2.7:

$$du = \frac{\tau}{G} t_g \tag{2.7}$$

where τ is the shear stress, G is the shear modulus and t_g is the adhesive thickness. For each beam segment i, the average shear stress, τ_i, at the FRP concrete interface is determined by equation 2.8 (see Figure 2.33 b):

$$\tau_i = \frac{P_{frp(i+1)} - P_{frp(i)}}{L_i \; b} \tag{2.8}$$

where $P_{frp(i)}$ is the force in the FRP reinforcement for segment i, L_i is the length of the segment i and b is the width of the beam.

With increasing temperature due to the fire, the adhesive softens and experiences a significant reduction in its shear modulus (G). This softening effect results in a relative slip (δ_{slip}) between the FRP and the concrete. In the model the slip in a segment i is calculated with equation 2.9 (see Figure 2.33 c).

$$\delta_{slip,i} = \gamma_i t_g \tag{2.9}$$

where t_g is the adhesive thickness and γ_i is the shear strain in segment i, calculated by equation 2.10

$$\gamma_i = \frac{\tau_i}{G} \tag{2.10}$$

Substituting γ_i in equation 2.9 and considering the relative strain as the ratio between the change in length and the original segment length, the bond slip strain ε_{slip} can be computed, at each exposure time, by equation 2.11:

$$\varepsilon_{slip} = \frac{\delta_{slip,i}}{L_i} = \frac{P_{frp(i+1)} - P_{frp(i)}}{L_i^2 b} \frac{t_g}{G} \tag{2.11}$$

The variation of the adhesive shear modulus (G) as a function of the temperature was evaluated based on experimental results on double bond shear tests at elevated temperatures performed in [44] (see section 2.5.2). The variation of shear stresses (see equation 2.8) is a function of the distance from FRP plate ends (peak shear stresses occurs near FRP plate end and varies exponentially towards center of the beam). The beam segment with peak shear stress was assumed to be a critical segment of the FRP strengthened beam, since delamination of FRP was assumed to start at this segment. For simplification the author assumed the shear stress, evaluated in the critical segment, consistent in all beam segments for a given time step.

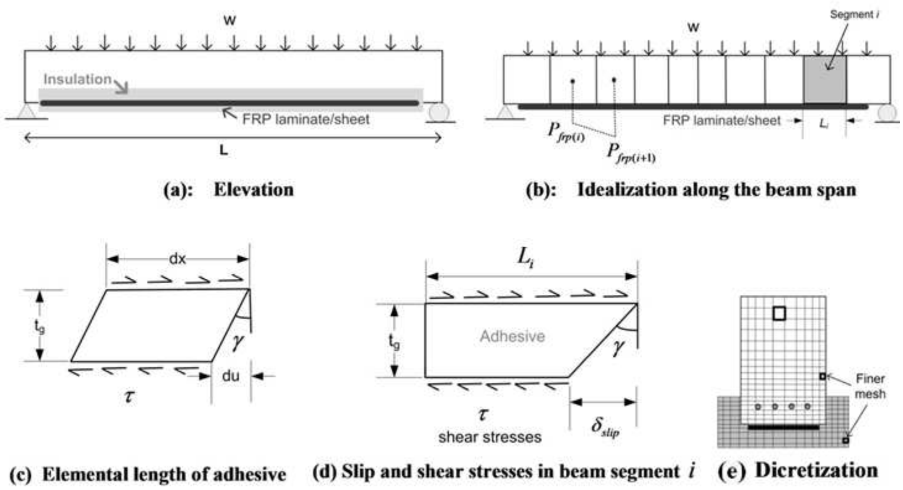

Figure 2.33 – Layout of typical FRP strengthened RC beam, its idealization, development of shear stresses and bond slip and its discretization [63]

Once the mechanical strains are calculated, stresses in each of the concrete, steel and FRP elements are obtained through temperature dependent stress-strain relationships and thereafter also the respective forces. As shown in Figure 2.34, at each time step the computed forces are used to check the force equilibrium. For instance, for an assumed total strain at the top layer of concrete ε^t_c, the curvature κ is iterated until force equilibrium is satisfied. This iterative procedure is repeated till equilibrium, compatibility and convergence criterion are satisfied. Once these conditions are satisfied, moment and curvature corresponding to that strain are computed. Given the calculated moment curvature relationships, deflections of the beam at each time step are derived through an iterative procedure described in [67] by evaluating the average stiffness of the beam.

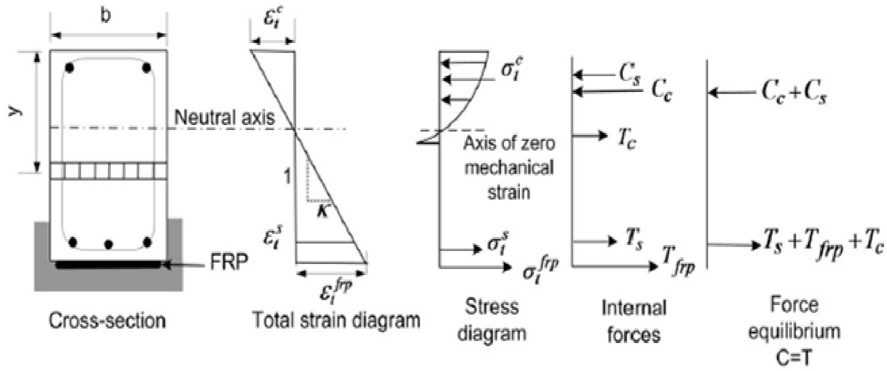

Figure 2.34 – Variations of strains, stresses and internal forces in a beam cross-section exposed to fire [63]

The model was validated by comparing predictions with experimental data of FRP strengthened beams under fire exposure tested in [43, 64]. The authors concluded that the model was capable to predict the overall thermal and structural response of FRP-strengthened beams. Predicted temperatures and deflections in comparison with experimental data of the beam tested in [43] are reported in Figure 2.35 as reference. Moreover the study concluded that in computing moment capacity of a fire exposed insulated FRP strengthened RC beam, a perfect bond can be assumed till the temperature at the FRP-concrete interface (adhesive) reaches T_g, after which point the FRP contribution can be taken as zero for the moment capacity.

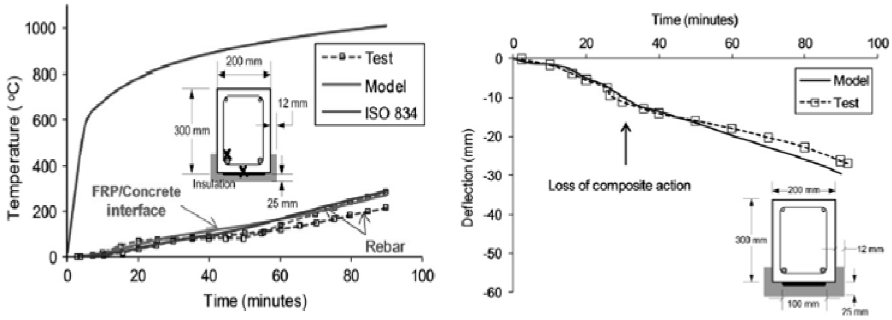

Figure 2.35 – Measured and predicted temperatures and deflection of beam tested in Blontrock 2003 [63]

2.6.2 Fire endurance of FRP NSM RC members strengthened in flexure

In [69] the flexural performance of NSM FRP strengthened concrete slabs at elevated temperature was investigated. A total of 13 slabs were tested, 2 of which were not strengthened (control specimens) and 11 of which were strengthened in flexure with a single strip of CFRP NSM strengthening system (see Figure 2.36). The slabs were tested either at room temperature up to failure (two control specimens and four NSM FRP strengthened slabs), or under sustained load with increasing surface temperature up to failure (seven NSM FRP strengthened slabs).

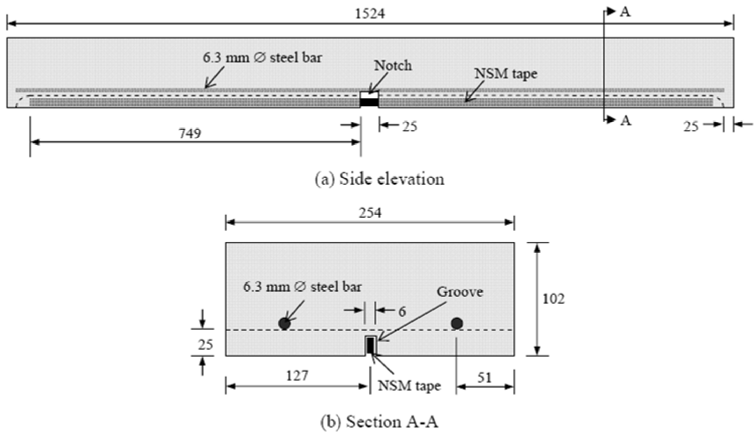

Figure 2.36 – Details slab specimens [69]

Two different adhesives, an epoxy adhesive (T_g = 51°C) and a cementious grout, were used to embed the NSM FRP strengthening system into the grooves. Differential Scanning Calorimetry (DSC) was used to determine the glass transition temperature of the epoxy resin according to ASTM E1356 [70]. Both epoxy and grout adhesive were tested to examine their different behavior at elevated temperature. The NSM FRP strengthened slabs were pre-loaded to a sustained load of 20 kN. This load was based on results at room temperature and was selected to be higher than the failure load of the unstrengthened slab (the average failure load of the two unstrengthened slab was equal to 12 kN). Once the load was achieved the slabs were heated, by a heating blanket, up to either 100°C or 200°C keeping the load constant. The temperature was held constant up to failure of the specimens. The temperature of 100°C and 200°C were selected based on FRP EBR surface thermal histories recorded during full scale fire tests of insulated FRP EBR strengthened members conducted in [71]. The temperature of 200°C was also the maximum temperature reachable by the heating blanket.

Experimental results in terms of time-midspan deflection curves (including the midspan deflection recorded during initial loading up to 20 kN, before turning on the heating system) are shown in Figure 2.37 and Figure 2.38 for slabs tested at 100°C and 200°C respectively.

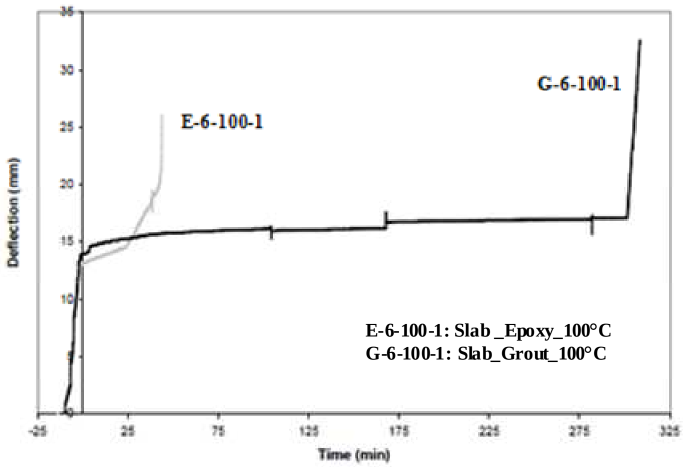

Figure 2.37 – Midspan deflection time curves specimens tested at 100°C [69]

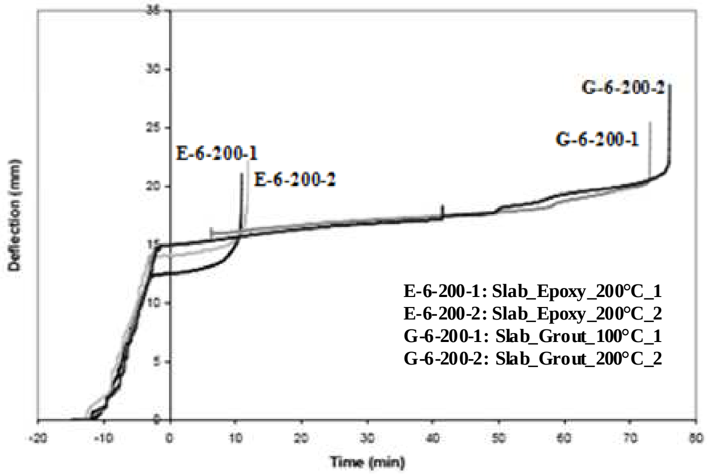

Figure 2.38 – Midspan deflection time curves specimens tested at 200°C [69]

The main conclusions were that specimens in which the NSM FRP strip was embedded with cementious grout performed considerably better than otherwise identical epoxy-bonded specimens. For instance epoxy-based specimens tested at 100°C (E-6-100-1) and at 200°C (E-6-200-1 and E-6-200-2) failed under the 20kN sustained load at 44 min, 11 min and 12 min of heating respectively. The grout specimen tested at 100°C (G-6-100-1) held the sustained load for more than 5 h of heating, at which time the load was increased to induce the failure (failure occurred at approximately 27 kN). Thus, the authors concluded that heating of 100°C has no considerably effect on the performance of the grout-based specimens. Grout-based specimens tested at 200°C (G-6-200-1 and G-6-200-2) failed under the applied load at 73 min and 76 min of heating respectively. Moreover the failure mode of the specimens embedded with epoxy resin was debonding at the interface resin/concrete with a smooth and distinct failure plane induced by the deterioration of the mechanical properties of the epoxy adhesive at elevated temperature (the failure mode of epoxy-based specimens tested at room temperature was bond failure 1 mm into the concrete substrate). Grout-based specimens failed by bond failure at the FRP strip-grout interface, again along a smooth, failure plane. The authors concluded that this type of failure was likely induced by loss of strength and stiffness in the polymer matrix resin, used to produce the preformed CFRP strips, at temperatures approaching its glass transition temperature.

In [72] a real compartment fire test was performed to study the performance of insulated FRP strengthened members under fire exposure. The investigation took place inside a compartment of a casted building with reinforced concrete floor slabs nominally 150 mm thick. Figure 2.39 shows the compartment prior of testing, with the FRP strengthening and insulated systems installed on the ceiling. The fire load consisted of office furnishings, arranged so that most of the fuel was towards the east, on the opposite side of the compartment to the window. More information about fire parameters can be found in [72].

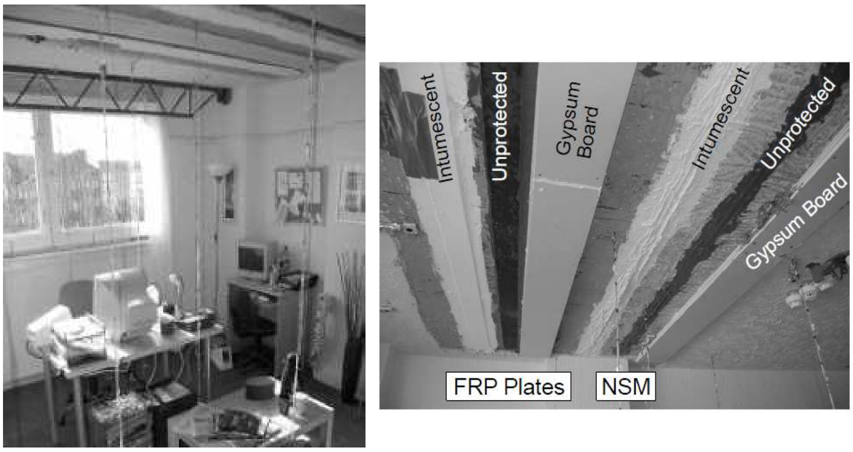

Figure 2.39 – Compartment prior to the fire test and FRP strengthening and insulated system [72]

In this study, externally bonded CFRP plates (100 x 1.4 mm) and near surface mounted CFRP bars (diameter 12 mm) were applied to the concrete ceiling (see Figure 2.39). Both FRP strengthening systems were embedded with an epoxy adhesive (T_g = 60°C, experimentally evaluated using dynamic mechanical thermal analysis, DMA, after 7 days of ambient curing) at the bottom of the concrete ceiling and into 15 mm deep grooves for the EBR and NSM strengthening technique respectively. The FRP was protected using either an intumescent coating or gypsum boards (12 mm thick), alongside FRP that was left unprotected as shown in Figure 2.39. The test demonstrated the vulnerability of FRP strengthening during a real compartment fire. The glass transition temperature was rapidly exceeded in the bonding adhesive for all samples. The unprotected and intumescent protected plate strengthening debonded from the ceiling around 10 minutes after the start of the fire. The test confirmed that the intumescent protection was ineffective due to an inappropriate activation temperature, as was expected by the authors prior to testing. The epoxy adhesive and the FRP matrix polymer had burnt away (FRP fibres forming the FRP EBR plate were exposed to fire). The authors concluded that the NSM strengthening system performed better than the EBR strengthening system.

For instance the NSM strengthening system stayed in position and there was less visible degradation of the bonding adhesive. The gypsum board protected the FRP strengthening from visible damage, but did not prevent the glass transition temperature from being exceeded, which may have affected its ability to strengthen the slab.

2.6.3 Conclusions fire endurance of FRP strengthened members

The literature review on fire endurance of FRP strengthened members has clearly demonstrated that fire insulation is generally needed to satisfy fire resistance requirements by providing additional protection to the concrete and longitudinal steel reinforcement. For instance the findings of different research projects showed that the beams strengthened in flexure with FRP can achieve a fire endurance of 2 and/or 4 h even after the adhesive temperature exceeds excessively the glass transition temperature, if the insulation system is able to keep the temperatures of the concrete in compression and the steel longitudinal reinforcement below critical levels. Moreover a numerical model for predicting the thermal and structural behavior of FRP strengthened and insulated members under fire behavior has been reviewed, focusing mainly in the calculation of the effect of adhesive bond degradation with increasing temperature.

The performance of FRP NSM flexural strengthening at elevated temperature (100°C and 200°C) has been also reviewed. The experimental tests were mainly based in comparing two different type of bonding adhesive: an epoxy and a grout adhesive. The findings of the reviewed research project showed that the grout-based specimens experienced a better performance at both 100°C and 200°C with respect to epoxy-based specimens. Finally, a research project on the performance of insulated FRP strengthened members under fire exposure has showed that NSM FRP strengthening system perform better than FRP EBR system, for a similar insulation adopted.

2.7 Summary

Based on the overview of previous research studies of FRP strengthened members at elevated temperature and under fire exposure, the following conclusions can be summarized.

Bond tests at elevated temperatures have shown that the bond behavior of FRP strengthening systems is clearly affected by temperatures close to the adhesive glass transition temperature; although no complete bond degradation was observed for all the reviewed research projects. The failure mode and transfer length are also affected by increasing temperature. Moreover for some of the reviewed tests an initial increase of load capacity is observed for temperatures below or/at the adhesive glass transition temperature. This behavior is attributed to the beneficial effect of induced thermal stresses, due to the difference in thermal expansion between the CFRP and the concrete and the reduction of adhesive Young's modulus. Both effects have been experimentally and analytically investigated in [11]. However, for temperatures higher than the glass transition temperature, the reduction of bond strength of the adhesive governed over the beneficial effect induced by the difference in thermal expansion and resulted in a reduction of failure loads and a change in failure mode. Finally, the residual CFRP to concrete bond properties after exposure to elevated temperature have shown the possibility to retain a high percentage of the room temperature bond strength up to an exposure to 140ºC (equal to $1.80T_g$ for the reviewed research). Increasing the temperature further a drastic reduction on bond strength in pure shear was observed. This behavior is attributed not only to the strength degradation of the adhesive but also to the influence of the moisture evaporation from the concrete substrate, which occur at temperatures above 100°C, causing damage to the adhesive layer.

The literature review on fire endurance of FRP strengthened members has clearly demonstrated that fire insulation is generally needed to satisfy fire resistance requirements by providing additional protection to the concrete and longitudinal steel reinforcement. For instance the findings of different research projects showed that beams strengthened in flexure with FRP can achieve a fire endurance of 2h and/or 4h even after the adhesive temperature exceeds excessively the glass transition temperature, if the insulation system is able to keep the temperatures of the concrete in compression and the steel longitudinal reinforcement below critical levels. Moreover a numerical model for predicting the thermal and structural behavior of FRP strengthened and insulated members under fire behavior has been reviewed, focusing mainly in the calculation of the effect of adhesive bond degradation with increasing temperature.

The performance of FRP NSM flexural strengthening at elevated temperature (100°C and 200°C) has also been reviewed. The experimental tests focused on comparing two different types of bonding adhesive: an epoxy and a grout adhesive. The findings of the reviewed research project showed that the grout-based specimens experienced a better performance at both 100°C and 200°C with respect to epoxy-based specimens. Finally, a research project on the performance of insulated FRP strengthened members under fire exposure has shown that NSM FRP strengthening systems perform better than FRP EBR systems, for a similar insulation adopted.

2.8 References

1. Clarke J.L. (1993). “Alternative materials for the reinforcement and prestressing of concrete”. *Chapman & Hall*, London, U.K., 204 pp.
2. Nanni A. (1993). “Fibre-Reinforced-Plastic (FRP) reinforcement for concrete structures: properties and applications”. *Developments in Civil Engineering 42*, Amsterdam, The Nederlands, 450 pp.
3. American Concrete Institute (ACI) (2007). “Report on Fiber-Reinforced Polymer (FRP) Reinforcement for Concrete Structures”. *ACI 440R-07*, Farmington Hills, MI, USA, 100 pp.
4. Neale K.W., Labossière P. (1991). “Material Properties of Fibre-Reinforced Plastics”. *In Advanced Composite Materials with Application to Bridges*. Edited by A.A. Mufti, M-A. Erki, and L.G. Jaeger. Canadian Society of Civil Engineering, Montreal, PQ, 21-69.
5. Matthys S. (2000). “Structural Behaviour and Design of Concrete Members Strengthened with Externally Bonded FRP Reinforcement”. *PhD-thesis*, Faculty of Engineering, Department of Structural Engineering, Ghent University, Belgium, 367 pp.
6. *fib* Task Group 9.3 (2001). “Externally bonded FRP reinforcement for RC structures”. *International Federation for Structural Concrete, fib* Bulletin 14.
7. Seberscu A., Palmieri A., Guadagnini M., Matthys S., Pilakoutas K. (2010). “Basalt FRP for strengthening of RC members”. *In Proc. of 5th Int. Conf. on FRP Composites in Civil Engineering*. Advances in FRP composites in civil engineering, 691-694.
8. American Concrete Institute (ACI) (2008). “Guide for the design and construction of externally bonded FRP systems for strengthening concrete structures”. *ACI 440.2R-08*, ACI Committee 440, 80 pp.
9. Taerwe L., Matthys S. (2011). “Use of FRP in concrete structures: trends and challenges”. *fib symposium*, Prague, 1071-1084.
10. NetComposites. (2006). "Guide to Composites". *NetComposites*, http://www.netcomposites.com/Education.asp.
11. Klamer E.L. (2009). “Influence of Temperature on Concrete Beams Strengthened in Flexure with CFRP”. *PhD thesis*, Department of architecture, building and planning, Eindhoven University of Technology, the Netherlands, 250 pp.

12. De Lorenzis L., Lundgren K., Rizzo A. (2004). “Anchorage length of near-surface mounted FRP bars for concrete strengthening – Experimental investigation and numerical modeling”. *ACI Structural Journal*, 101(2), 269-278.

13. De Lorenzis L., Nanni A. (2002). “Bond between NSM fiber-reinforced polymer rods and concrete in structural strengthening”. *ACI Structural Journal*, 99(2), 123-132.

14. De Lorenzis L., Teng J.G. (2007). “Near-surface mounted FRP reinforcement: an emerging technique for structural strengthening”. *Composite Part B: Eng*, 38, 119-143.

15. De Lorenzis L., Rizzo A., La Tegola A. (2002). “A modified pull-out test for bond of near surface mounted FRP rods in concrete”. *Composites Part B: Eng*, 33 (8), 589-603

16. Kotynia R. (2005). “Strain Efficiency of Near-Surface Mounted CFRP-strengthened Reinforced Concrete Beams”. *Proc. of International Conference on Composites in Construction*, Lyon, 35-42.

17. Palmieri A., Matthys S., Taerwe L. (2010). “Strengthening with Near Surface Mounted Reinforcement: Structural and Fire behavior”. *Proc. of 3rd fib International Congress (fib-2010)*, Washington DC.

18. Sena Cruz J.M. and Barros. J. (2004). “Bond between Near Surface Mounted Carbon-Fiber-Reinforced Polymer Laminate Strips and Concrete”. *J. Comp. Constr.*, ASCE, 8(6), 519-527.

19. Seracino R., Saifulnaz M.R.R., Oehlers D.J. (2007). “Generic Debonding Resistance of EB and NSM Plate-to-Concrete Joints”. *J. Comp. Constr.*, ASCE, 11(1), 62-70.

20. Teng J.G., De Lorenzis L., Wang Bo., Rong Li., Wong T.N., Lik Lam (2006). “Debonding failures of RC beams strengthened with near surface mounted CFRP strips”. *J Compos Constr*, ASCE, 10(2), 92-105.

21. Ceroni F., Pecce M., Bilotta A., Nigro M. (2012). “Bond behavior of FRP NSM systems in concrete elements”. *Composites Part B: Eng*, 43, 99-109.

22. Blaschko M. (2003). “Bond behaviour of CFRP strips glued into slits”. *Proc. of 6th Int. Symposium on FRP Reinforcement for Concrete Structures (FRPRCS-6)*, K. H. Tan, ed., World Scientific, Singapore, 205–214.

23. Raafat E.H., Rizkalla S.H. (2004). “Near-Surface-Mounted Fiber-Reinforced Polymer Reinforcement for Flexural Strengthening of Concrete Structures”. *ACI Structural Journal*, 101(5), 717-726.

24. Hassan T., Rizkalla S.H. (2003). "Investigation of Bond in Concrete Structures Strengthened with Near Surface Mounted Carbon Fiber Reinforced Polymer Strips". *J. Compos. Constr*, ASCE, 7(3), 248-257.

25. Barros J.A.O., Fortes A.S. (2004). "Flexural strengthening of concrete beams with CFRP laminates bonded into slits". *Cement & Concrete Composites*, Elsevier, 27 (1), 471-480.

26. Palmieri A., Matthys S., Taerwe L. (2012). "Bond Behaviour between NSM FRP Rods and Concrete: Experimental and Numerical Investigation". *Proc. in 12th International Conference on Recent Advances in Concrete Technology and Sustainability Issues*, Prague, 14 pp.

27. Bonaldo E., Barros J.A.O., Lourenço P.J.B. (2007). "Efficient strengthening technique to increase the flexural resistance of existing RC slabs". *J. Comp. Constr.*, ASCE, 12 (2), 149-159.

28. Barros J.A.O., Dias S.J.E., Lima J.L.T. (2007). "Efficacy of CFRP-based techniques for the flexural and shear strengthening of concrete beams". *Journal Cement and Concrete Composites*, 29(3), 203-217.

29. Costa I.G., Barros J.A.O. (2010). "Flexural and shear strengthening of RC beams with composites materials – the influence of cutting steel stirrups to install CFRP strips". *Cement and Concrete Composites Journal*, 32, 544-553.

30. Kotynia R., Abdel Baky H.M., Neale,K.W., Ebead U.A. (2008). "Flexural strengthening of RC beams with externally bonded CFRP systems: test results and 3-D nonlinear FE analysis". *J. Comp. Constr.*, ASCE, 12(2), 190-201.

31. Hughes Brothers (2011). "Aslan 500, Carbon Fiber Reinforced polymer (CFRP) tape". *http://aslanfrp.com/Aslan500/aslan500_applica.html*.

32. Asplund S.O. (1949). "Strengthening Bridge Slabs with Grouted Reinforcement". *Journal of the American Concrete Institute*, 20(6), 397-406.

33. Blontrock H., Taerwe L., Matthys S. (1999). "Properties of Fibre Reinforced Plastics at Elevated Temperatures with Regard to Fire Resistance of Reinforced Concrete Members". *ACI Structural Journal,* 188(5), 43-54.

34. Bisby L., Williams B., Kodur V.R., Green M. and Chowdhury E. (2005). "Fire Performance of FRP systems for Insfrastructure: A State-of-the-Art Report". *Research Report*, *Institute for Research in Construction*, National Research Council Canada, RR 179, IRC-IR-179.

35. Kodur V.K.R., Baingo D. (1998). "Fire Resistance of FRP Reinforced Concrete Slabs". *IRC Internal Report No. 758*, National Research Council of Canada, Ottawa.

36. Kodur V., Bisby L. and Green M.F. (2007). “Guidance for the design of FRP-strengthened concrete members exposed to fire”. *Journal of Fire Protection Engineering*, 17 (5), 5-16.
37. Wang Y.C., Wong P.M.H., Kodur V. (2007). “An experimental study of the mechanical properties of fibre reinforced polymer (FRP) and steel reinforcing bars at elevated temperatures”. *Composite Structures*, 80(1), 131-140.
38. Foster S.K., Bisby L.A. (2008) “Fire Survivability of Externally-Bonded FRP strengthening Systems” *J. Compos. Constr*, ASCE, 12(5), 553-561.
39. Sorathia U., Dapp T., Beck C. (1992). “Fire Performance of Composites”. *Materials Engineering*, September, 10-12.
40. Mouritz A.P., Mathys Z., Gibson A.G. (2006). “Heat release of polymer composite in fire”. *Composites: Part A*, 37 (7), 1040-1054.
41. Apicella F., Imbrogno M. (1999). “Fire performance of CFRP-composites used for repairing and strengthening concrete”. *In Proc. of Materials and Construction: Exploring the Connection. Proc. 5th ASCE Materials Engineering Congress*, Cincinnati, OH,, 260-266.
42. Tadeu A.J.B., Branco F.J.F.F. (2000). “Shear tests of steel plates epoxy bonded to concrete under temperature”, *Journal of Materials in Civil Engineering*, 12(1), 74–80.
43. Blontrock H. (2003). “Analyse en modellering van de brandweerstand van betonelementen uitwendig versterkt met opgelijmde composietlaminaten (in Dutch)”. *Ph-D Thesis*, Faculty of Engineering, Department of Structural Engineering, Ghent University, Belgium, 412 pp.
44. Leone M., Matthys S., Aiello M.A. (2009). “Effect of elevated service temperature on bond between FRP EBR system and concrete”. *Composites Part B: Eng*, Elsevier, 40, 85-93.
45. Wu Z.S., Iwashita K., Yagashiro S., Ishikawa T., Hamaguchi Y. (2004). “Temperature effect on bonding and debonding behavior between FRP sheets and concrete”. *In Proc. of FRP Composite in Civil Engineering- CICE 2004,* Adelaide, Australia, pp 905-912.
46. ISO 11359-2 (1999). “Plastics - Thermomechanical analysis (TMA) - Part 2 - Determination of linear thermal expansion coefficient and glass transition temperature”. *International Organization for Standardization*.
47. Di Tommaso A., Neubauer U., Pantuso A., Rostasy F.S. (2001). “Behaviour of adhesively bonded concrete CFRP joints at low and high temperatures”. *Mechanics of Composites Materials*, 37(4), 327-338.

48. Foster S.K., Bisby L.A. (2008). "Fire Survivability of Externally-Bonded FRP strengthening Systems". *J. Compos. Constr*, ASCE, 12(5), 553-561.

49. ASTM D3418 (2003). "Standard test method for transition temperatures of polymers by differential scanning calorimetry". *ASTM International*, West Conshohocken, Pa.

50. Bisby L.A., Stratford T.J. (2012). "Performance-based Structural Fire Resistance Design of FRP Strengthened Concrete". *In Proc. of 6th International Conference on Advanced Composite Materials in Bridge and Structures (ACMBS)*, Kingston, Canada, 8pp.

51. Deuring M., 1994, "Brandversuche an nachtralich verstarken Tragern aus Beton". *EMPA No. 148 795*, Eidgenössische Material prüfungs und Forschungs Anstalt, Dubendorf, Switzerland.

52. ISO 834 (1999). "Fire Resistance Tests – Elements of Buildings Construction – Part I – General Requirements". *International Organization for Standardization*.

53. EN 1992-1-1 (2004). "Eurocode 2- Design of concrete structures – Part 1-1: General rules and rules for buildings". *European Committee for Standardization.*

54. EN-1363-1 (1999). "Fire Resistance Tests – General Requirements – Part I". *European Committee for Standardization*.

55. Williams B, Kodur V., Green M.F., Bisby L. (2008). "Fire endurance of fiber-reinforced polymer strengthened concrete T-beams". *ACI Structural Journal*, 105 (1), 60-67.

56. Chowdhury E.U. (2005). "Performance in Fire of Reinforced Concrete T-Beams Strengthened with Externally Bonded Fibre-Reinforced Polymer Sheets". *M.Sc. thesis*, Department of Civil Engineering, Queen's University, Kingston, ON, Canada, 273 pp.

57. American Concrete Institute (ACI) (2002). "Guide for the Design and Construction of Externally Bonded FRP Systems for Strengthening Concrete Structures". *ACI 440.2R-02*, ACI Committee 440, Farmington Hills, MI, 2002, 113 pp.

58. Green M.F., Bénichou N., Kodur, V.K.R., Bisby, L.A., (2007). "Designed guidelines for fire resistance of FRP-strengthened concrete structures". *Proc. of the 8th International Symposium on Fiber Reinforced Polymer Reinforcement for Concrete Structures (FRPRCS-8)*, Patras, Greece.

59. ASTM E119 (2002). “Standard Test Methods for Fire Tests of Building Construction and Materials”. *ASTM International*, West Conshohocken, PA, 22 pp.
60. Chowdhury E.U., Bisby L.A., Green M.F., Kodur V.K.R. (2008). “Residual Behaviour of Fire-Exposed Reinforced concrete Beams Prestrengthened in Flexure with Fiber-Reinforced Polymer Sheets”. *J. Comp. Constr.*, 12 (1), 61-68.
61. Kodur V.K.R., Dwaikat M.B. (2008). “A numerical model for predicting the fire resistance of reinforced concrete beams”. *Cement and Concrete Composites*, 30, 431-443.
62. Kodur V.K.R., Ahmed, A. (2010). “Numerical Model for tracing the Response of FRP-Strengthened RC Beams Exposed to Fire” *J. Compos. Constr*, ASCE, 14(6), 730-742.
63. Ahmed A., Kodur V.K.R. (2011). “Effect of bond degradation on fire resistance of FRP-strengthened concrete beams”, *Composites Part B: Eng.*, 42(2), 226-237.
64. Harmathy T.Z.. (1967). “A comprehensive creep model”. *J Basic Eng*, 89(3), 496–502.
65. Harmathy T.Z. (1993). “Fire safety design and concrete”. *New York (NY): John Wiley & Sons*, Inc..
66. Anderberg Y., Thelandersson S. (1976) “Stress and deformation characteristics of concrete at high temperatures, 2-experimental investigation and material behaviour model”. *Lund, Sweden Bulletin 54*, Lund Institute of Technology.
67. Campbell T.I., Kodur V.K.R. (1990). “Deformation controlled nonlinear analysis of prestressed concrete continuous beams”. *PCI J*, 35(5), 42–90.
68. Ahmed A., Kodur V.K.R. (2010). “Performance of FRP-strengthened reinforced concrete beams under design fire exposure”. *In Proc. of sixth international conference on structures in fire*. East Lansing, Michigan;
69. Burke P.J., Bisby L.A., Green. M.F. (2008). “Structural Performance of NSM FRP Strengthened Concrete Slabs at Elevated Temperatures”. *Proc., Structural Faults and Repair*, Edinburgh, UK.
70. ASTM (2007). “ASTM E1356-03 Standard test method for the assignment of glass transition temperatures by differential scanning calorimetry”. *ASTM International*, p 4.

71. Kodur V.K.R., Bisby L.A., Green M.F., (2006). “FRP retrofitted concrete under fire conditions”. *Concrete International*, 28(12), 37-44.

72. Stratford T., Gillie M., Chen J. and Usmani A.S. (2006). “Bonded Fibre Reinforced Polymer Strengthening in Real fire”. *Advances in Structural Engineering*, 12 (6), 867-878.

Chapter 3
MATERIALS PROPERTIES AT ELEVATED TEMPERATURES

3.1 Introduction

The performance of FRP strengthened and insulated concrete structures under fire exposure is dependent on the fire load at which the structure is exposed and the thermal and mechanical properties of the constituents materials such as the concrete, the reinforcement steel, the FRP reinforcement, the adhesive and the insulation materials. In this chapter an overview of the different stages of a real fire and a comparison with the standard fire curve ISO 834 is given. Moreover the effects on the thermal and mechanical properties of the constituent materials of FRP strengthened RC members are discussed with reference to the literature review. The materials thermal and mechanical properties will be further used (see chapter 7) for the analytical simulations of the FRP strengthened and insulated beams and slabs under fire exposure.

3.2 Fire temperatures: specifications of fire testing

Figure 3.1 shows the idealized stages of the development of a real fire [1] as a temperature-time relationship. The distinct stages of fire are [2]: the ignition, the growth phase, the flashover, the fully developed burning phase (indicated in Figure 3.1 as heating) and the cooling phase.

Fire ignition is the period during which the fire begins. It is, usually, a localized phenomenon (e.g. can be piloted by a spark, match or other sources) and will cause local overheating of combustible materials. The combustion is restricted to local areas near the ignition source, temperatures of the combustion gases are low and the influence on the structural elements of the considered compartment is at this stage negligible. The ignition is always preceded by an incipient phase, which is when heating and gasification of a combustible is occurring. The incipient phase depends on the fuel, ambient conditions and many other variable factors required for ignition of a fuel. Smouldering type combustion may occur after ignition. This is a particularly slow fire development, in which energy release rates and temperatures are relative low. This type of combustion is synonymous with the production of high quantities of toxic gases and products of incomplete combustion, which present an extreme hazard to life.

Following ignition the fire initially grows (growth phase) by direct contact of the flames with combustible materials or by indirect contact though radiation to the nearby combustible materials. There are basically two possibilities: 1) if there is inadequate ventilation, the fire may self-extinguish or continue to burn at a very slow rate dictated by the availability of oxygen or 2) if there is sufficient fuel and ventilation the fire may progress to full room involvement in which all exposed combustible items are burning (flashover). During the growth period, the fire increases in size, to and beyond the point in which interaction with the compartment boundaries becomes significant. The transition to the fully developed fire is referred to as 'flashover' and involves a rapid spread from the area of localized burning to all combustible surfaces within the compartment. The transition is normally short in comparison with the duration of the main stages of fire (see Figure 3.1). During the fully developed stage of a fire, the temperatures and the rate of heat release reach a maximum and the threat to neighbouring compartments – and perhaps adjacent buildings- is the greatest. Flames may emerge from any ventilation opening, spreading fire to the rest of the building, either internally (through open doorways) or externally (through windows). It is during this stage, when temperature rises above 300 – 600 °C, that structural elements begin to weaken and deform due to the heating, perhaps leading to partial or total collapse of the building. Fully developed burning will continue as long as there are sufficient quantities of fuel and ventilation. The last stage is the cooling phase, often identified as the stage of the fire after the average temperature has fallen to 80% of its peak value. Decay will continue until fuel is consumed and/or the fire goes out.

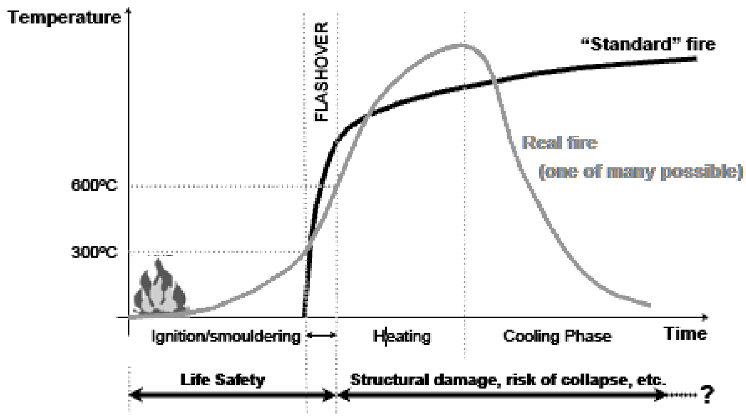

Figure 3.1 – Stages of real fire vs standard fire curve [1]

Simulating an exact fire event in an experimental investigation is very complicated due of the numerous variables involved such as: the geometrical characteristics of the compartment (length, width, height); thermal properties of the walls, floors, ceiling of the compartment; the ventilation conditions during the fire; the fuel load in the compartment. Although some parametric temperature time-curves have been widely accepted [3], it's clear that as more parameters are involved in the modeling of the fire, it corresponds better to a realistic situation but the complexity of the calculation will increase significantly. Existing knowledge on the various models for a compartment based real fire has been extensively reviewed previously in other research studies [4] and will not be presented herein.

Guidelines and standard fire tests have been developed all over the world to evaluate the capability of the structural elements to resist fire events. Although they may not represent a real fire event, standard fire tests can be regarded as a general procedure to conduct fire tests regardless of the tested material. Hereby, the fire event is simulated using a predetermined time-temperature curve. Figure 3.1 shows that a real fire differs in several important aspects with respect to the standard fires curves (e.g. ASTM E119 and ISO 834) that are generally assumed for structural fire resistance design. The most important difference is the presence of a cooling phase in a real fire, as opposite to the infinite heating of a standard fire which is physically unrealistic (though a conservative assumption). Though ISO 834 and ASTM E119 are generally used for fire testing in relation to buildings, it should be noted that these fire standard curves are considered as being too mild for fire scenario's such as petrochemical industries and tunnels for which more severe standard fire curves (eg. Hydrocarbon, RWS and RABT-curves) have become compulsory [5].

For the uniformity of assessment in the testing of structural elements, in the presented research program all the fire tested elements (beams and slabs) have been exposed to a EN 1363-1 [6] standard fire test and the temperature was controlled to follow the standard-time temperature curve according to ISO 834 [7]. The standard ISO 834 curve was also used for the thermal analysis simulation. This normalized time/temperature curve is the fire curve which is normally used for the test in accordance with the resistance function (criterion R), the separating function (criterion E) and/or the insulating function (criterion I) of structural elements in case of fire [8]. This standard curve is used as a model for representing a fully developed fire in a compartment and is given by the following equation:

$$T_{gas} = T_o + 345\log_{10}(8t+1) \tag{3.1}$$

Where: T_{gas} is the temperature of the combustion gases [°C]; T_o is the ambient temperature [20 °C]; t is the time in minutes [min]. Figure 3.2 shows the time-temperature curve of ISO 834.

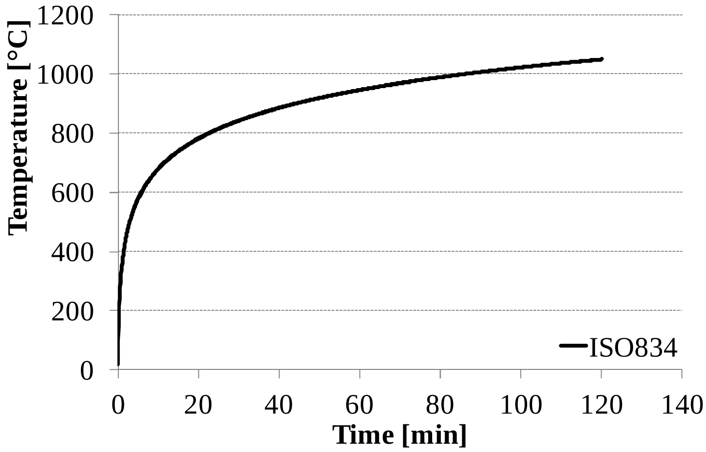

Figure 3.2 – Time-temperature curve ISO 834

3.3 Effect of temperature on material properties

The effect of temperature on the thermal and mechanical properties of concrete and steel has been investigated extensively [10-13] in the last century and is well explained in structural Eurocodes [8]. The thermal and physical properties (such as the thermal conductivity, the specific heat, the density, etc..) as well as the reduction of mechanical properties (such as the reduction of compressive strength, tensile strength and E-modulus) of concrete and steel as a function of the increasing temperatures have been extensively reviewed previously in other research studies [4;14-16]. A brief explanation of their thermal and mechanicals properties, further adopted in the analytical simulations (see chapter 7), is presented in the following.

3.3.1 Concrete

Concrete is composed of aggregates and hydrated cement paste, and contains free water as well as chemically and physically bound water. In [10] the influence of temperatures on material properties of concrete has been investigated. It was concluded that the effect of temperature on the concrete material properties is mainly related to the evaporation of water from the concrete and to changes in the chemical composition and physical structure of the concrete. These effects turned out to occur for the most part in the cement paste. At temperature of about 100°C water expulsion from hardened cement paste and aggregates occurs and at 180°C the first stage of dehydration in the form of the breakdown of calcium silicate hydrates (CSH) gel (release of chemically bound water with decomposition of hydrates) can be observed. The decomposition of calcium hydroxide takes place at 500 °C and the transformation of quartz at 570 °C. The complete decomposition of calcium silicate hydrates take place at 700 °C and the decarbonation of calcium carbonate in limestone aggregate concretes at 800 °C. The melting of cement paste and aggregates (in limestone aggregates concretes) starts at 1150-1200 °C. Other effects of an increase of temperature are the change in pore structure and the development of high-water vapor pressure in the concrete pores, which can result in thermal spalling of concrete. Also localized heating could result in spalling, especially when the thermal expansion is restricted by surrounding cool concrete which results in high compressive stresses in heated concrete.

3.3.1.1 Thermal properties of concrete

The thermal conductivity of concrete, λ_c, is the rate of heat transferred through a unit thickness of the material per unit temperature difference [W/m°C]. There are three principal factors influencing the thermal conductivity of concrete: 1) the aggregate type, 2) the aggregate volume (aggregate has a higher thermal conductivity than both cement and water) and 3) the moisture content – as concrete hydrates and dries, the space previously occupied by water empties and the conductivity reduces. In accordance to [8] the thermal conductivity, λ_c, of concrete may be determined between lower and upper limit values by using the equations 3.2 and 3.3 respectively.

$$\lambda_c(\theta) = 2 - 0.2451(\theta/100) + 0.0107(\theta/100)^2 \text{ for } 20°\text{C} \le \theta \le 1200°\text{C [W/m°C]} \quad (3.2)$$

$$\lambda_c(\theta) = 1.36 - 0.136(\theta/100) + 0.0057(\theta/100)^2 \text{ for } 20°\text{C} \le \theta \le 1200°\text{C [W/m°C]} \quad (3.3)$$

where θ is the concrete temperature.

The average value of the upper and lower limit, as proposed by Eurocode 2 [8], is adopted for the analytical simulations of beams and slabs under fire exposure:

$$\lambda_c(\theta) = 1.68 - 0.19055(\theta/100) + 0.0082(\theta/100)^2 \text{ for } 20°\text{C} \le \theta \le 1200°\text{C [W/m°C]} \quad (3.4)$$

The variation of the upper limit and lower limit of thermal conductivity with temperature, as well as the adopted curve are illustrated in Figure 3.3.

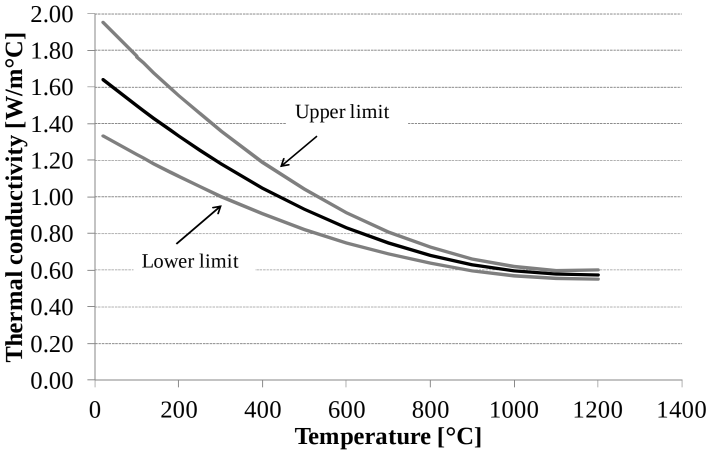

Figure 3.3 – Thermal conductivity – temperature curves concrete

In addition to the thermal conductivity of the concrete, it is important to define both the density, $\rho_c(\theta)$, and the specific heat, $c_p(\theta)$, of the material. The variation of the concrete density and specific heat are obtained in accordance to [8]. The product of the density and the specific heat is called volumetric heat capacity, $c_v(\theta)$, and it represents the ability of the material to store thermal energy:

$$c_v(\theta) = \rho_c(\theta)c_p(\theta) \qquad [\mathrm{J/m^3{}^\circ C}] \tag{3.5}$$

The variation of the volumetric heat capacity as a function of the temperature, adopted for the analytical simulations, is illustrated in Figure 3.4. Average moisture content in the range of 4-6 vol. % (obtained experimentally for each batch in accordance to [9], for beams tested in the first fire test a value of moisture content equal to 6% was obtained while for all the other fire tests a value of 4% was obtained) and a value of density at room temperature equal to 2400 kg/m^3 have been considered for the calculation of the volumetric heat capacity, $c_{v.}$ In order to take into account the moisture variation from the warmer zone to the coldest one, in accordance to [8] a variation of the concrete density as a function of the temperature has been considered according to [8]. Moreover the retarding influence of the moisture on the temperature increase is taken into account by a peak value in the volumetric heat capacity, situated between 100°C and 115°C with linear decrease between 115°C and 200°C (see Figure 3.4).

The thermal diffusivity indicates the rate at which temperature changes can take place in a material. Diffusivity can be calculated from equation 3.6:

$$a = \lambda_c(\theta) \big/ c_p(\theta)\rho_c(\theta) \qquad [m^2/s] \tag{3.6}$$

Where $\lambda_c(\theta)$ is the thermal conductivity, $c_p(\theta)$ is the specific heat and $\rho_c(\theta)$ is the density of the concrete as a function of the temperature [8]. It is a measure of the rate of temperature rise at a certain depth of the concrete with large diffusivities leading to faster temperature rises at a given depth. The thermal diffusivity decreases with increase in temperature due to the general decrease of thermal conductivity and increase in the specific heat at elevated temperatures.

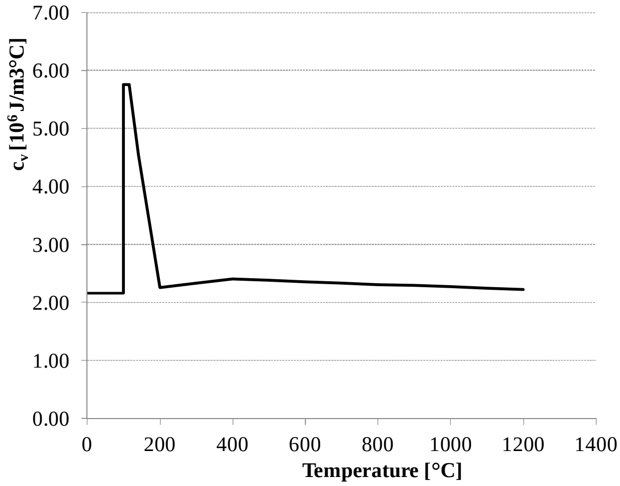

Figure 3.4 – Volumetric specific heat concrete as function of temperature

The free thermal expansion of the concrete is related to the free thermal expansion of the type of granulate and of the cement matrix. For the analytical simulations the thermal strain, $\varepsilon_{c,th}(\theta)$, has been calculated for the case of siliceous aggregates (as used in this research project) by using equation 3.7 [7]:

$$\varepsilon_{c,th}(\theta) = -1.8 \cdot 10^{-4} + 9 \cdot 10^{-6}\theta + 2.3 \cdot 10^{-11}\theta^3 \quad \text{for } 20°C \leq \theta \leq 700°C \tag{3.7}$$

$$\varepsilon_{c,th}(\theta) = 14 \cdot 10^{-3} \quad \text{for } 700°C \leq \theta \leq 1200°C$$

3.3.1.2 Mechanical properties of concrete

The behavior of concrete at elevated temperatures and for a given load level can be formulated with reference to several strains. Equation 3.8 presents the total strain, ε_{tot}, as the sum of the free thermal strain, ε_{th}, the instantaneous-stress-related strain ε_{σ}, the creep strain ε_{cr}, and the transient strain, ε_{tr}.

$$\varepsilon_{c,tot} = \varepsilon_{c,th}(\theta) + \varepsilon_{c,\sigma}(\sigma,\theta) + \varepsilon_{c,cr}(\sigma,\theta,t) + \varepsilon_{c,tr}(\sigma,\theta) \tag{3.8}$$

The different strains are a function of temperature θ, the stress σ, and the time t. The thermal strain, $\varepsilon_{c,th}$, is a simple function of the temperature, which makes it easy to model and is assumed in the analytical simulation by equation 3.7 (see section 3.3.1.1). The instantaneous-stress-related strains, $\varepsilon_{c,\sigma}$, are dependent on the temperature and on the stresses as defined by the stress-strain curve of Eurocode 2 [8]. This curve is given by equation 3.9 for the ascending branch and by equation 3.10 for the descending branch (a linear or non-linear descending branch is permitted by Eurocode 2 [8]).

$$\frac{\sigma_c}{f_c(20°C)} = \left(\frac{3\,\varepsilon_{c,\sigma} f_{c,\theta}}{2 + \left(\dfrac{\varepsilon_{c,\sigma}}{\varepsilon_{c1,\theta}} \right)^3} \right) \qquad 0 \le \varepsilon_{c,\sigma} \le \varepsilon_{c1,\theta}(\theta) \tag{3.9}$$

$$\frac{\sigma_c}{f_c(20°C)} = \frac{\varepsilon_{c,\sigma} - \varepsilon_{cu1,\theta}}{\varepsilon_{c1,\theta} - \varepsilon_{cu1,\theta}} \qquad \varepsilon_{c1,\theta} \le \varepsilon_{c,\sigma} \le \varepsilon_{cu1.\theta} \tag{3.10}$$

Where $f_{c,\theta}$ is the strength of concrete as a function of the temperature, $\varepsilon_{c1,\theta}$ is the peak strain corresponding to $f_{c,\theta}$ and $\varepsilon_{cu1,\theta}$ is the ultimate strain. Values of $\varepsilon_{c1,\theta}$ and $\varepsilon_{cu1,\theta}$ are taken in accordance to table 3.1 of Eurocode 2 [8]. Figure 3.5 illustrates the degradation of stress-strain curve as a function of temperature for a siliceous concrete [7].

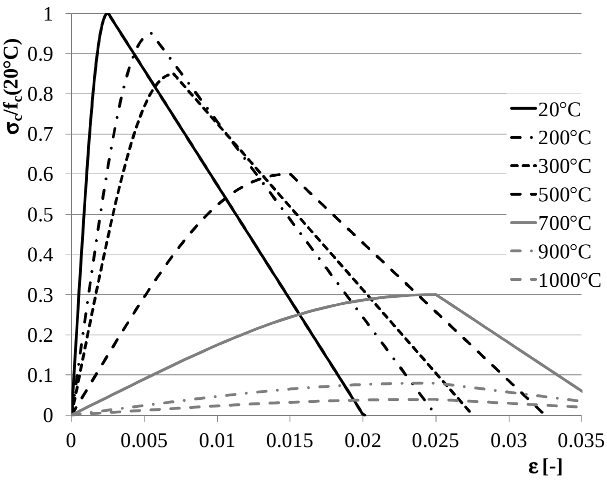

Figure 3.5 – Stress-strain relationship of ordinary siliceous concrete without external loading [EN 1992-1-2- Table 4.2]

The creep strain, ε_{cr}, depends on the concrete, the load, the temperature and the time. Equation 3.11 has been proposed in [11] to describe the creep for ordinary siliceous concrete at constant temperature and constant stress

$$\varepsilon_{c,cr} = -0.53 \cdot 10^{-3} \frac{\sigma_c}{f_{c,\theta}} \left(\frac{t}{t_r} \right)^{0.5} e^{0.00304\,(\theta-20)} \qquad (3.11)$$

Where t is the time, σ is the stress, $f_{c,\theta}$ is the concrete strength at the considered temperature and t_r is the reference loading duration time (180 minutes).

Anderberg [11] states that only above 400°C the creep may have some significance, as shown in Figure 3.6 where the creep vs time during 3 h is shown for a stress level equal to 22.5% as a function of different temperatures levels. Blontrock [4] has demonstrated that the stress-strain curve proposed in Eurocode 2 [8] takes implicitly into account the effect of the creep strain. This can be observed as follows. In Figure 3.7 the relation between the temperature and the Young's modulus of concrete with siliceous aggregates [8,10,13,17-20] is presented and compared to Eurocode 2 [8]. The Young's modulus according to Eurocode 2 [8] is calculated from the stress-strain relationship presented above (see Figure 3.5). From Figure 3.7 it can be observed that Eurocode 2 [8] indirectly takes the higher creep of concrete at elevated temperature into account, which results in lower values for the Young's modulus.

Therefore in the analysis of the beams and slabs under fire exposure the contribution of creep strain of equation 3.8 will be neglected (see chapter 7).

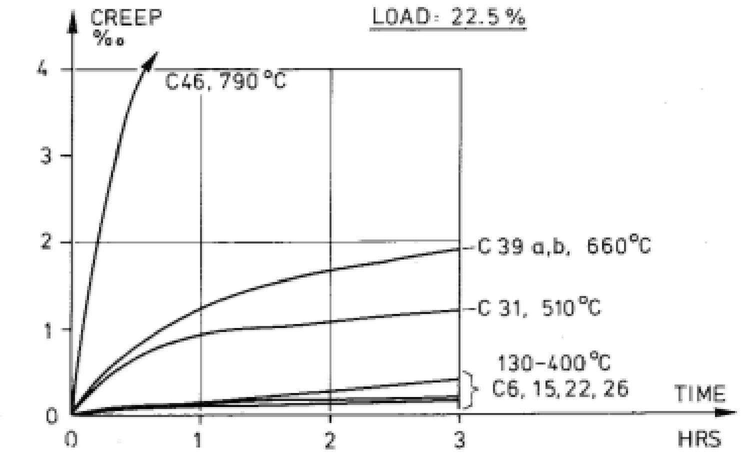

Figure 3.6 – Strain creep vs time for a stress level equal to 22.5% as a function of temperatures [11]

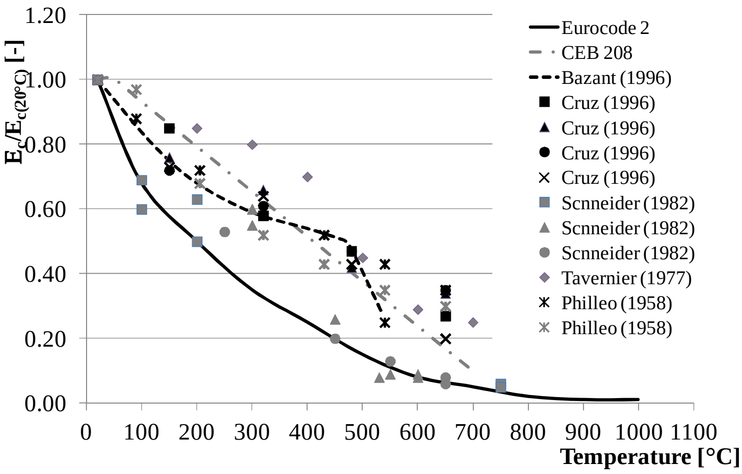

Figure 3.7 – Influence of temperature on the Young's modulus of concrete with siliceous aggregates [4]

The transient strain, $\varepsilon_{c,tr}$, is the hindered part of thermal expansion for loaded concrete structures exposed to heating. Anderberg [11] defines the transient creep as that part of the total strain obtained in stressed concrete under heating that cannot be accounted for otherwise. It accounts for the effect of temperature change, which will produce failure of the material and activate the reactions responsible for the decomposition. It is an irreversible process and occurs only during the first heating. Transient strains develop rapidly above 100°C when unsealed cement paste experiences considerable shrinkage and the aggregates continue to expand; it is assumed to be temperature-dependent (not time-dependent) and stress-dependent. The transient strain is found to be proportional to the thermal expansion and to the ratio between the compressive stress and strength at 20 °C [11] as shown in equation 3.12. However the relationship seems to be too conservative at temperatures above about 500°C. Therefore Anderberg [12] proposed a second equation for temperatures above 500°C (see equation 3.13).

$$\varepsilon_{c,tr} = -2.35\frac{\sigma}{f_{c,20^\circ C}}\varepsilon_{c,th} \qquad \text{for } \theta \leq 500°C \qquad (3.12)$$

$$\Delta\varepsilon_{c,tr} = -0.0001\Delta\theta\frac{\sigma}{f_{c,20^\circ C}} \qquad \text{for } 500°C < \theta \leq 800°C \qquad (3.13)$$

It has to be noted that, even though several models have been proposed in literature [11] the transient creep has been incorporated into the Eurocode model (value of $\varepsilon_{c1,\theta}$ in equation 3.9 and 3.10) in an implicit manner [4,21]. A limitation of considering the implicit model may be that the mechanical strain given by implicit models for a given stress-temperature state is the same, whether concrete has been heated and then loaded at control temperature or loaded and then heated under constant stress and this is known not to correspond to experimental evidence [13]. More information can be found in [4,16,21].

3.3.2 Steel

3.3.2.1 Thermal properties of steel

Steel reinforcement is not specifically considered in the thermal analysis because it does not significantly influence temperature distribution in the element cross-section unless a very dense reinforcement arrangement with several reinforcements and short spacing range between the bars is provided in the cross section. Measurements at various locations during fire testing showed that the difference in temperature in the rebars and related concrete sections are small [22-23]. Nevertheless the thermal properties of the steel as a function of the temperature will be briefly commented in this section.

The main thermal properties that influence the temperature rise in the steel are the thermal conductivity and the specific heat (often expressed as heat capacity). The thermal conductivity of steel, $\lambda_s(\theta)$, according to Eurocode 3 [24] can be calculated by the following equations:

$$\begin{aligned} &\lambda_s(\theta) = 54 - 3.33 \cdot 10^{-2}\theta && \text{for } 20°C \le \theta \le 800°C \quad [W/m°C] \\ &\lambda_s(\theta) = 27.3 && \text{for } 800°C \le \theta \le 1200°C \quad [W/m°C] \end{aligned} \qquad (3.14)$$

The variation of steel thermal conductivity with temperature is illustrated in Figure 3.8.

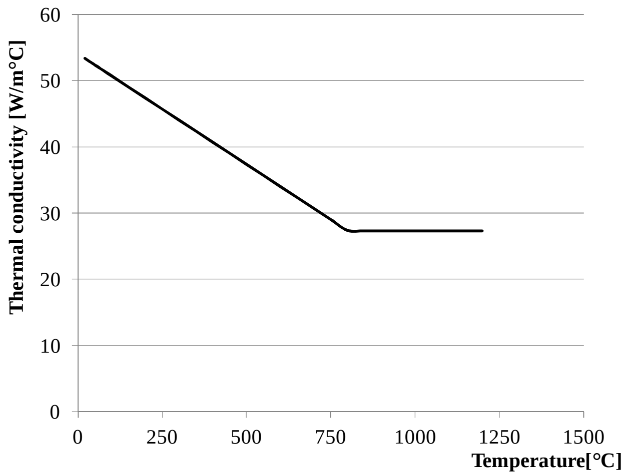

Figure 3.8 – Thermal conductivity – temperature curve steel

The specific heat of steel, $c_s(\theta)$, is independent of the composition of the steel. Its variation with temperature is shown in Figure 3.9. The steel specific heat increases with temperature, showing a peak at around 750 °C. This increase is due to individual atoms in steel moving further apart, thus achieving a higher energy state. This process absorbs considerable energy (heat), thus accounting for the peak at approximately 750 °C. The specific heat of steel, $c_s(\theta)$, according to Eurocode 3 [24] can be calculated according to equations 3.15:

$$
\begin{aligned}
c_s(\theta) &= 425 + 7.73\frac{\theta}{10} - 0.169\left(\frac{\theta}{10}\right)^2 + 2.22\cdot 10^{-3}\left(\frac{\theta}{10}\right)^3 && 0°C \le \theta \le 600°C \text{ [J/kg°C]} \\
c_s(\theta) &= 666 + \frac{13002}{738 - \theta} && 600°C \le \theta \le 735°C \text{ [J/kg°C]} \\
c_s(\theta) &= 545 + \frac{17820}{\theta - 731} && 735°C \le \theta \le 900°C \text{ [J/kg°C]} \\
c_s(\theta) &= 650 && 900°C \le \theta \le 1200°C \text{ [J/kg°C]}
\end{aligned}
\tag{3.15}
$$

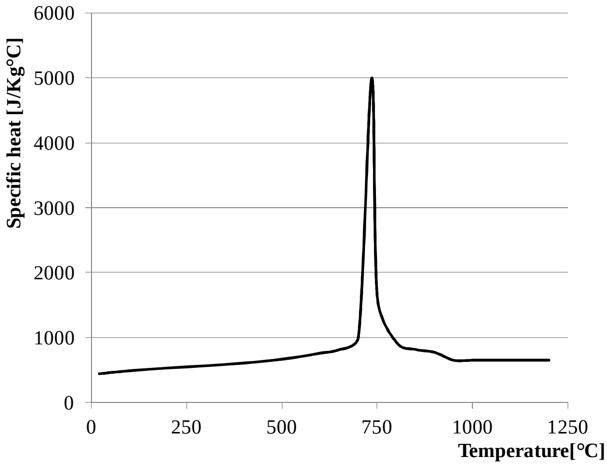

Figure 3.9 – Specific heat of steel as function of temperature

As shown in Figure 3.10 the free thermal strain of the steel increases with temperature up to nearly 750 °C, at which point a phase change takes place (as discussed above) and the thermal strain becomes nearly constant up to 860 °C, after which the thermal strain starts to increase again. For the analytical simulations, in accordance to [8] the thermal strain, $\varepsilon_{s,th}(\theta)$, has been calculated according to equation 3.16:

$$
\begin{aligned}
\varepsilon_{s,th}(\theta) &= -2.416\cdot 10^{-4} + 1.2\cdot 10^{-5}\,\theta + 0.4\cdot 10^{-8}\,\theta^2 && 20°C \le \theta \le 750°C \text{ [‰]} \\
\varepsilon_{s,th}(\theta) &= 11\cdot 10^{-3} && 750°C \le \theta \le 860°C \text{ [‰]} \\
\varepsilon_{s,th}(\theta) &= -6.2\cdot 10^{-3} + 2\cdot 10^{-5}\,\theta && 860°C \le \theta \le 1200°C \text{ [‰]}
\end{aligned}
\tag{3.16}
$$

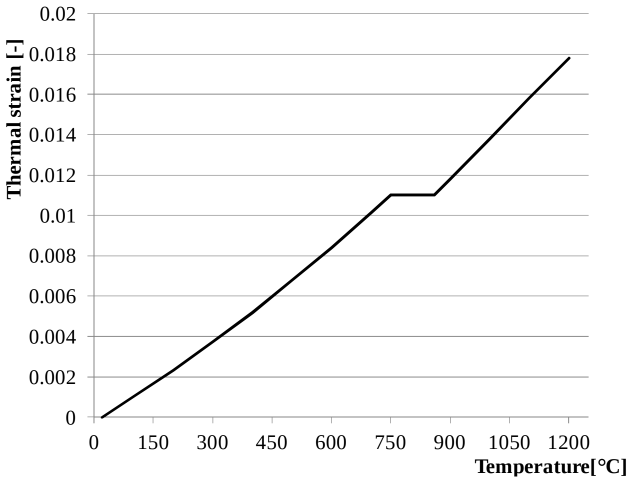

Figure 3.10 – Thermal strain steel as function of temperature

3.3.2.2 Mechanical properties of steel

A review of the literature indicated that there have been more studies on the high-temperature mechanical properties of steel than on thermal properties. Tests regarding the high temperature strength properties are conducted in mainly two ways: transient and steady-state tests [25]. In the transient-state tests the test specimen is subjected to a constant load and then exposed to uniformly increasing temperature, in the steady-state tests the test specimen is heated to a specific temperature and after that a tensile test is carried out. The variations in test methods resulted in variations in the reported mechanical properties, which in turn resulted in variations in the constitutive models specified in codes and standards. More information can be found in [4,25-26]. However, as for the concrete, the steel behavior at elevated temperature can be expressed as the sum of several strains. Equation 3.17 gives the total strain, $\varepsilon_{s,tot}$, as the sum of the free thermal strain, $\varepsilon_{s,th}$, the stress-related strain $\varepsilon_{s,\sigma}$ and the creep strain ε_{scr}.

$$\varepsilon_{s,tot} = \varepsilon_{s,th}(\theta) + \varepsilon_{s,\sigma}(\sigma,\theta) + \varepsilon_{s,cr}(\sigma,\theta,t) \tag{3.17}$$

The different strains are a function of temperature θ, the stress σ, and the time t. The thermal strain, $\varepsilon_{s,th}(\theta)$, is a simple function of the temperature, which makes it easy to model and can be obtained by using equation 3.16 described above. The stress-related strain $\varepsilon_{s,\sigma}(\theta)$, is function of the temperature and the acting stresses, σ_s. It is determined on the basis of transient tests under slow heating rates. Figure 3.11 shows schematically the stress-strain relationship according to [8]. In Table 3.1 the parameters of the stress-strain relationship are reported.

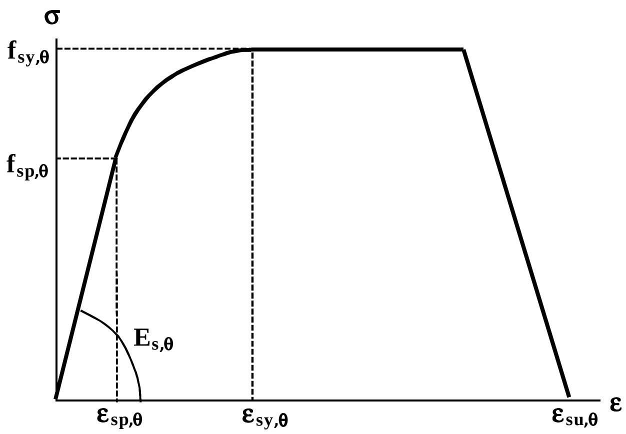

Figure 3.11 – Stress-strain relationship for steel [8]

Table 3.1 – Functions for the steel stress-strain relationship [8]

Range	Stress $\sigma(\theta)$
$0 \le \varepsilon < \varepsilon_{sp,\theta}$	$\varepsilon E_{s,\theta}$
$\varepsilon_{sp,\theta} \le \varepsilon < \varepsilon_{sy,\theta}$	$f_{sp,\theta} - c + (b/a)\left[a^2 - (\varepsilon_{sy,\theta} - \varepsilon)^2\right]^{0,5}$
$\varepsilon_{sy,\theta} \le \varepsilon < \varepsilon_{st,\theta}$	$f_{sy,\theta}$
$\varepsilon_{st,\theta} \le \varepsilon < \varepsilon_{su,\theta}$	$f_{sy,\theta}\left[1 - (\varepsilon - \varepsilon_{st,\theta})/(\varepsilon_{su,\theta} - \varepsilon_{st,\theta})\right]$
$\varepsilon > \varepsilon_{su,\theta}$	0.00
Parameter	$\varepsilon_{sp,\theta} = f_{sp,\theta} / E_{s,\theta}$ $\quad \varepsilon_{sy,\theta} = 0.02$ $\quad \varepsilon_{st,\theta} = 0.15$ $\quad \varepsilon_{su,\theta} = 0.20$
Functions	$a^2 = (\varepsilon_{sy,\theta} - \varepsilon_{sp,\theta})(\varepsilon_{sy,\theta} - \varepsilon_{sp,\theta} + c/E_{s,\theta})$ $b^2 = c(\varepsilon_{sy,\theta} - \varepsilon_{sp,\theta})E_{s,\theta} + c^2$ $c = \dfrac{(f_{sy,\theta} - f_{sp,\theta})^2}{(\varepsilon_{sy,\theta} - \varepsilon_{sp,\theta})E_{s,\theta} - 2(f_{sy,\theta} - f_{sp,\theta})}$

It can be seen that Eurocode 2 [8] distinguishes between two limits for the steel strength, f_s: the proportionality limit, $f_{sp,\theta}$, and the yield limit $f_{sy,\theta}$. The proportionality limit is the end of the linear portion of the stress-strain curve, after which point the stress-strain relation remains elastic but becomes nonlinear. The yield limit is the point after which the stress-strain behavior becomes both non-linear and inelastic. The concept of introducing proportionality limit in stress-strain curves at elevated temperatures is to capture the viscoelastic behavior that is partly due to the creep effect. The non-linearity after the proportionality limit indicates that stress causes more strain after this point than in the linear-elastic range. This simplification enables the stress-strain curves of Eurocode 2 [8] to partly account for creep strain at elevated temperature. Hence, the stress-strain relationship in accordance to Eurocode 2 can be defined by three parameters as a function of the steel temperature: the slope of the linear elastic range $E_{s,\theta}$, the proportional limit $f_{sp,\theta}$ and the yield limit (maximum stress level) $f_{sy,\theta}$. Figure 3.12 and Figure 3.13 show the strength and modulus of elasticity of steel as a function of temperature [8, 26-30]. Both the strength and elastic modulus decrease as temperature increases.

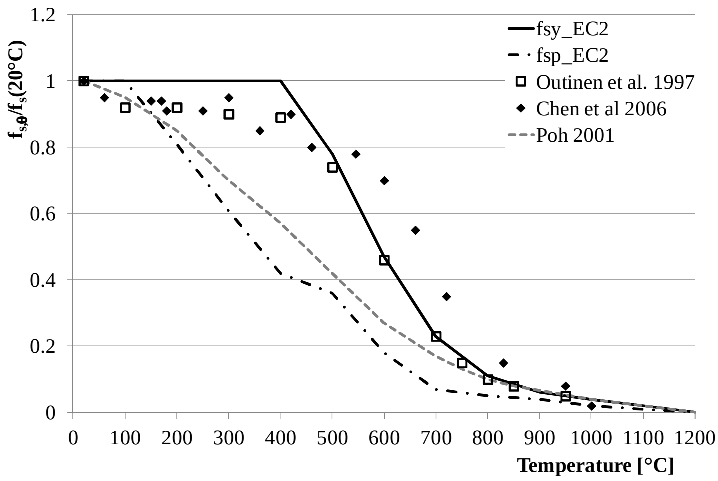

Figure 3.12 – Strength of steel as a function of the temperatures

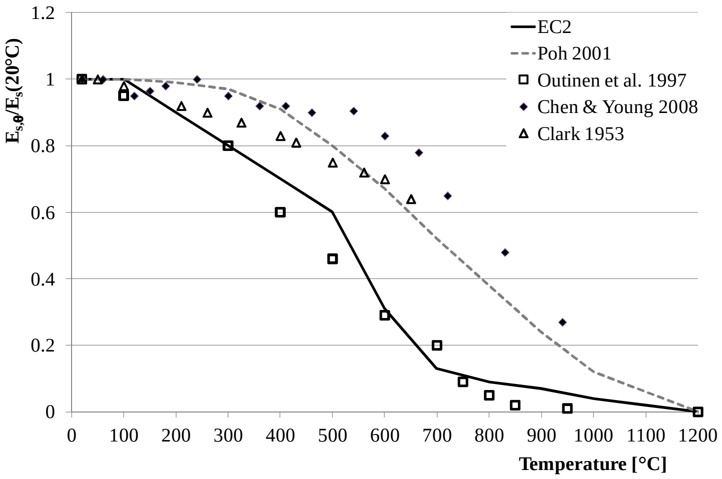

Figure 3.13 – Elastic modulus of steel as a function of the temperatures

Creep is defined as the time-dependent plastic strain under constant stress and temperature. At room temperature and under service load levels, creep deformations of steel are insignificant, however, at temperatures above 400°C creep deformations, $\varepsilon_{s,cr}$, become noticeable and may affect the global response of structures. More information about modeling the creep strain behavior as a function of temperature can be found in [31].

3.3.3 FRP

An understanding of FRP material behavior, in terms of thermal properties and deterioration of mechanical properties at high temperatures is essential to experimentally or/and analytically investigate the fire endurance of FRP strengthened structural members. The thermal and mechanical properties of FRPs depend on the type of fiber and the polymer resin matrix, the fiber volume ratio and the modulus of elasticity of both the fibers and the matrix materials. Based on literature review, the thermal and mechanical properties are discussed in the following sections in terms of fibers and polymer matrix materials followed by the effect of temperature on the material properties of the FRP reinforcement.

3.3.3.1 Fibre behaviour

As reported in [4, 32-33], studies have shown that carbon fibers experience little to no change to their tensile strength up to temperatures of more than 1000 °C [34-35], thus demonstrating more resistance to high temperature than glass fibers which (similar to steel reinforcement) lose 50% of their original tensile strength above 550 °C [36-37]. Figure 3.14 shows the variation in tensile strength of various fibers as a function of the temperature as reported in several studies.

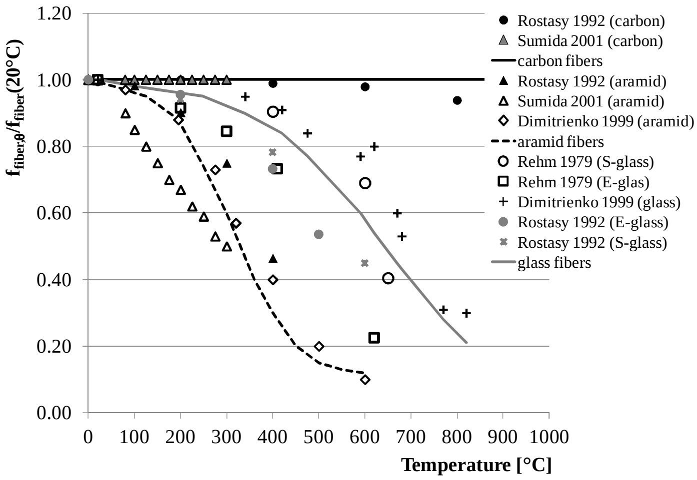

Figure 3.14 – Tensile strength FRP fibers as a function of temperature

Moreover, in [38] a series of tests on a variety of different glass fibers at high temperatures were performed. It was concluded, in accordance to other studies (see Figure 3.14), that the strength of glass fibers was reduced to about half of the room temperature value at about 550°C, and that the reduction of strength was independent of the type of glass fibers being used. In [35] the tensile strength of both carbon and aramid fibers at different temperatures was investigated (see Figure 3.14). It was concluded that while carbon fibers are unaffected by temperatures up to 300°C, aramid fibers experience an almost linear decrease in strength at temperatures above 50°C with a strength reduction of 50% at 300°C. More information about the decrease of tensile strength of different fibers can be found in [4,33]. In [33,39] it is stated that the type and quantity of the fiber will significantly influence the fire performance of an FRP composite. Glass and carbon FRPs generally smoke less, and give off less heat than those with organic fibers such as aramid fiber. The fiber type also significantly influences the thermal conductivity of FRP, with carbon FRPs having higher thermal conductivity than glass (particularly in the fiber direction). Finally Table 3.2 shows the coefficient of thermal expansion (CTE) of common FRP fibers [34]. It can be seen that glass fibers have an isotropic behavior in terms of thermal expansion while carbon and aramid fibers have an orthotropic behavior with a negative value for the coefficient of thermal expansion in longitudinal direction, which means that the fibers shorten with increasing temperature.

Table 3.2 – Coefficient of thermal expansion (CTE) fibers

Fibers	CTE Longitudinal [10^{-6}/°C]	CTE Transversal [10^{-6}/°C]
Glass	4 – 5.5	4 – 5.5
Carbon	–0.5	5.5
Aramid	–3.5	60

3.3.3.2 Polymer matrix behaviour

The main concerns related to the behaviour of the polymer matrix with elevated temperatures are related to the glass transition temperature, T_g. As the temperature of the polymer matrix approaches its glass transition temperature, the matrix transforms to a soft, rubbery material with reduced strength and stiffness. The glass transition temperature and the corresponding effect of temperature on the material properties is mainly related to the specific composition and the properties of the constituents [40] and is therefore different for each type of matrix material. A further discussion on the determination of T_g is given in section 3.3.3.2.1.

For epoxy resins, currently used as primer, adhesive and matrix for the FRP strengthening systems the degree of reduction of mechanical properties at temperatures close to their T_g (the T_g of ambient cured epoxies is usually in the range of 50-90 °C [4,33]) is of relevant importance for the strengthened structures, mostly in relation to the bond performance. As reported in [4, 33], a study conducted by Plecnik et al [41] investigated the fire behavior of epoxy resins commonly used for the FRP strengthening systems. A series of tests were performed (tensile, compressive and shear tests) to evaluate the high temperature mechanical properties of the resins. The results indicated that the strength of these materials dropped off very rapidly at temperatures near T_g, and that the strength was negligible at temperatures 100°C larger than T_g. The tensile strength reduction of the epoxy resin as a function of temperature, tested in [41], is reported in Figure 3.15. The other mechanical properties exhibit similar temperature dependence. In [37] a series of tests have been conducted in order to determine the thermo-mechanical properties of a variety of matrix materials. These testes on a specific epoxy material, which is not described in details, indicated a reduction in the elastic modulus of about 50% at 150°C and about 90% at about 300°C. Moreover it was found that the rates of reduction in strength depend on the heating rate, and was larger for higher rates of heating.

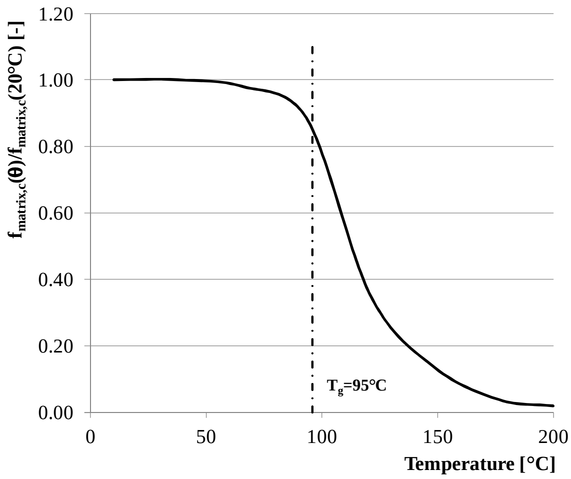

Figure 3.15– Influence of temperature on the tensile strength of epoxy resin [41]

In [42] flexural and compressive test at different temperatures have been performed on an epoxy resin (T_g= 62°C as reported by the manufacturer). The flexural tests indicated a reduction of the initial strength of about 80% at 80°C. The effect of an initial heating cycle was also investigated for the elastic modulus of the epoxy resin. Three compressive tests per temperature (up to 80 °C) were performed on prisms that were stored at 20°C and 60% R.H. for 14 days and which were then heated up to test temperature in 1 hour and subsequently tested in compression. Three other prisms per temperature were stored at 20 °C and 60% R.H. for 10 days, then stored at 80 °C for 2 days, and subsequently stored at 20 °C for another 2 days. Figure 3.16 shows the experimental results in terms of Young's modulus. Experimental outcomes of this study showed that the Young's modulus was significantly reduced at elevated temperatures. The reduction of the Young's modulus occurred at a higher temperature for the prisms that were stored at 80 °C for two days prior to testing. Heating the specimens for two days at 80 °C, did however not affect the Young's modulus at room temperature. The author concluded that the glass transition temperature, T_g, can be increased by applying a temperature cycle. This effect was also found in [43] demonstrating that the glass transition temperature could be increased from 62 °C to 81 °C by applying one heating cycle from -50°C to 200 °C before determining the glass transition temperature.

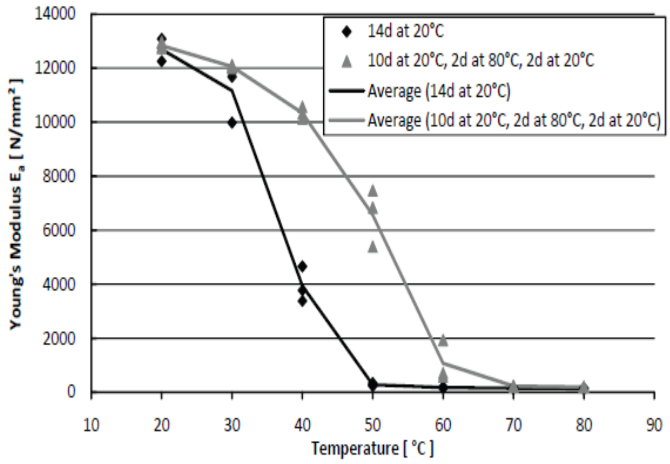

Figure 3.16 – Influence of temperature on the Young's modulus of epoxy resin [42]

3.3.3.2.1 Methods for determining the glass transition temperature

To investigate the thermal behavior of a polymer matrix and the T_g two techniques are often utilized: the differential scanning calorimetry (DSC) [44] and the dynamic mechanical analysis (DMA) [45-46]. DSC assigns the glass transition temperature on changes in specific heat capacity (DSC is a thermal, rather than physical, test method) while DMA assigns the glass transition temperature by measuring changes in the dynamic stress-strain behavior (physical test method). DMA tests can be used to determine not only the glass transition temperature but also the decrease of Young's modulus as a function of the temperature.

A third test that can be conducted on the polymer resin is the thermogravimetic analysis (TGA) [47-48] to observe the mass loss response with increasing temperature. The TGA allows determining temperatures at which thermal decomposition of the constituent materials occurs. More information about these tests can be found in Bakis 2008 [49], in which the various methods of assigning the glass transition temperature and the variability in the assigned value of T_g are discussed.

In [51] DSC and TGA tests have been performed for two different epoxy resins. The DSC tests determined the values of the glass transition temperature, that were equal to 78 °C and 85 °C for Epoxy 1 and Epoxy 2 respectively. The TGA tests showed that both epoxy resin systems lost 90% of their mass at 800 °C, 80-90% of this loss occurring between 300 and 400 °C. This mass loss was associated with thermal decomposition and volatilization of the polymers in this temperature range. Figure 3.17 shows the TGA curves for Epoxy 1 and Epoxy 2. Epoxy 1 experienced virtually zero mass loss before 300 °C, whereas Epoxy 2 (with a T_g value 7 °C higher than Epoxy 1) experienced a gradual mass loss of about 10% between 20°C and 300°C. The authors demonstrated that this difference in TGA behavior had a noticeably influence in retention of epoxy mechanichal property, as explained in the following.

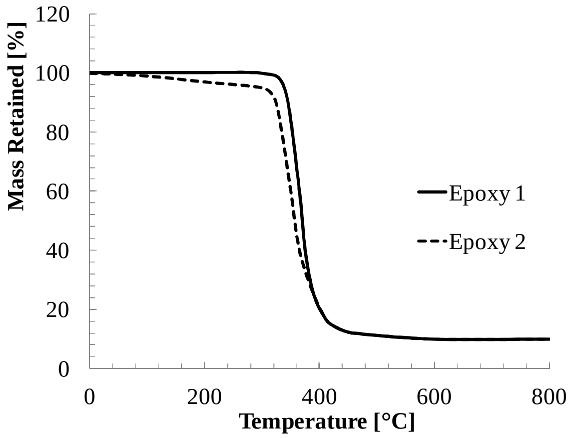

Figure 3.17 – Thermogravimetric (TGA) curves epoxy resins [51]

Moreover in [51] the residual performance of epoxy resin after high temperature exposure has been investigated. The specimens were heated to the desired temperatures at a rate of approximately 10°C/min and held constant for 3 h, after which the specimens were allowed to cool slowly to room temperature. Two different epoxy systems were investigated. Figure 3.18 and Figure 3.19 show the normalized tensile strength after exposure to elevated temperature. Experimental outcomes indicated that Epoxy 1 retained essentially all of its tensile strength up to exposure temperatures of at least 200 °C, but experienced major reduction (> 40%) in strength at 250 °C (at least 50 °C below the temperature at which it began to experience significant mass loss). Epoxy 2 appeared to increase in strength, by about 8% on average, up to exposure temperatures of 150 °C (likely resulting from a post-curing phenomenon of the epoxy at these temperatures) but subsequently lost 90% of its strength between 150 °C and 200 °C. The authors attributed this different behaviour to the different chemical formulations of the respective epoxies. They noticed that even small losses in mass (5%) can cause major reduction (90%) in the residual tensile strength of epoxy resins. Nevertheless, it has to be noted that the last conclusion should be related also to the different time dependent temperature effects (e.g. epoxy samples were heated at the same heating rate of the TGA test but the temperature has been held constant for 3h).

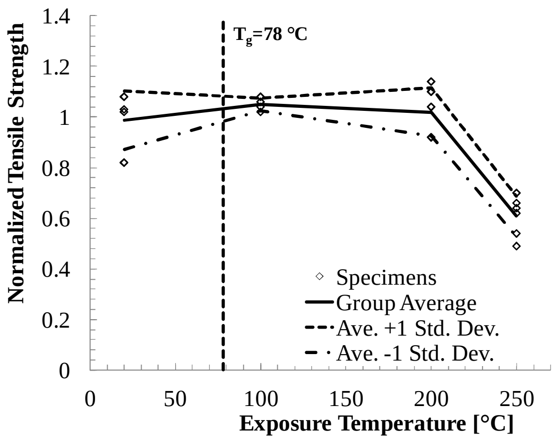

Figure 3.18 – Results direct tension tests on Epoxy 1 coupons after exposure to increasing elevated temperature [51]

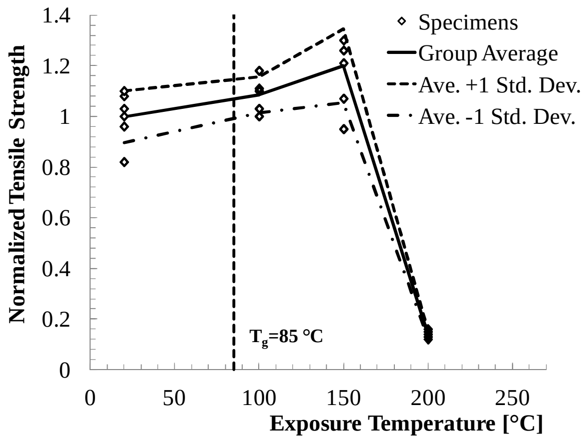

Figure 3.19 – Results direct tension tests on Epoxy 2 coupons after exposure to increasing elevated temperature [51]

In the current research study, in order to investigate the thermal decomposition and the glass transition temperature of the epoxy resins adopted to embed the FRP strengthening systems, thermogravimetric (TGA) and Differential scanning calorimetry (DSC) tests were performed. TGA and DSC tests were performed in accordance to ISO 11358 [47] and ISO 11357-2 [44] respectively for two adhesives (type Fortresin CFL, supplied by Fortius/Hughes Brother and type Sikadur-30, supplied by Sika). TGA tests have been performed on one sample of each epoxy resin, after curing for at least 7 days under ambient conditions. Each sample was heated in a helium atmosphere at a heating rate of 10°C/min in a temperature range from about room temperature (30°C) to 1000°C. Figure 3.20 shows the TGA curves for the two epoxy resin adhesives. From TGA, the epoxy resins began to lose their initial room temperature mass at approximately 242 °C and 122 °C for Sikadur-30 and Fortresin CFL respectively. Both resins lost about 26% and 40% of their mass at approximately 700 °C. The reason of the lower thermal decomposition of both epoxy resins with respect of that obtained in other studies [50-51] is not known but is suspected to be related to their different chemical composition.

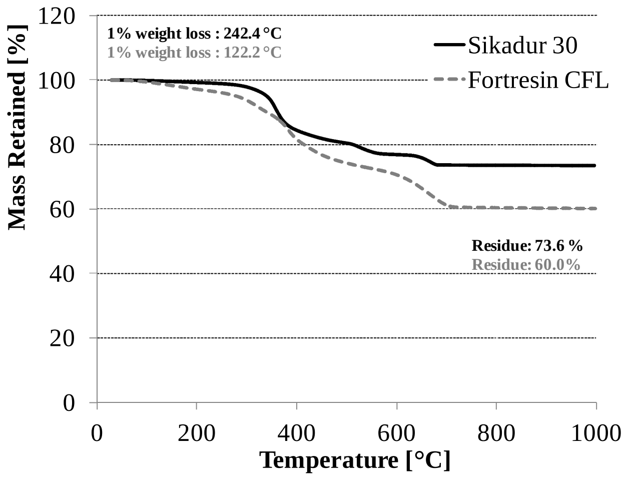

Figure 3.20 – Thermogravimetric (TGA) curves epoxy resins

The glass transition temperature, T_g, of the two utilized epoxy resins was analyzed using a Differential Scanning Calorimetry (DSC). The analysis has been performed on three samples of each epoxy resin, after curing of at least 7 days under ambient conditions. Each sample was held for 3 min at 0 °C and subsequently heated in a nitrogen atmosphere from 0°C to 120°C at 10°C/min. Two heating cycles have been performed. The glass transition temperature was determined on the 2nd heating cycle for both the specimens. Figure 3.21 and Figure 3.22 show the DSC curves of the second heating cycle for Sikadur-30 and Fortresin CFL respectively. The average glass transition temperature on three samples for each adhesive type is T_g=62.7°C for epoxy type Sikadur-30 and T_g= 66.3 °C for epoxy type Fortresin CFL.

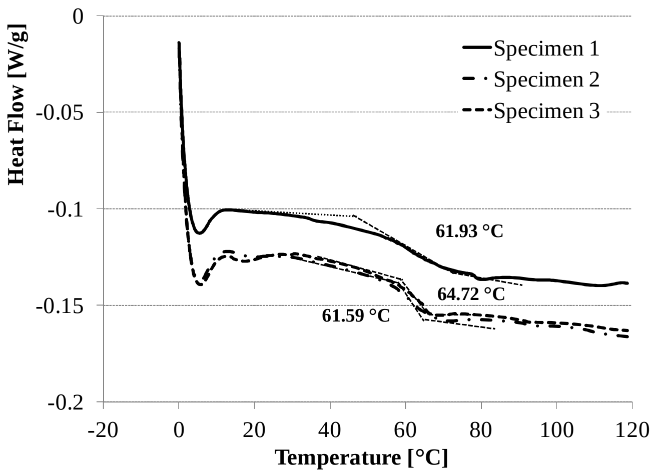

Figure 3.21– Heat flux–temperature curves Sikadur-30

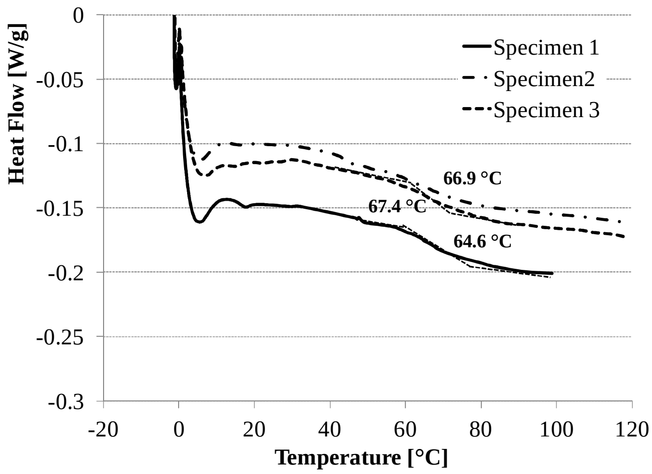

Figure 3.22– Heat flux–temperature curves Fortresin CFL

3.3.3.2.2 Conclusions polymer matrix behaviour at elevated temperatures

The most important property of the polymer matrix, as far as fire behavior in FRP strengthened concrete applications is concerned, is the glass transition temperature, T_g. Experimental tests at elevated temperatures have shown a reduction of strength and stiffness properties of the polymer matrix at temperatures close to T_g, although, no complete degradation of strength and stiffness was observed for all the reviewed research projects. Moreover it was found that the rates of reduction in strength and stiffness depend on the chemical composition as well as the heating rate (the reduction is larger for higher rates of heating) and that the adhesive T_g can be increased by applying a temperature cycle.

The residual performance of epoxy resin after exposure to elevated temperature have shown the possibility to retain a high percentage of the room temperature tensile strength up to an exposure to 150°C - 200°C. It was observed moreover that even small losses in mass (5%) can cause drastic reduction (up to 90%) in the residual tensile strength of the epoxy resins.

Finally it has to be noted that, in the presented research, thermal properties of epoxy resin are not a primary consideration because the amount of epoxy resin on the concrete member is small in comparison to the amount of concrete and will have a negligible influence in the thermal analysis. For the structural analysis the effect of degradation of the mechanical properties of the epoxy resin with elevated temperature is a main concern and was taken in account considering the bond degradation of the epoxy resin as a function of the temperature. This aspect will be extensively explained in chapter 7.

3.3.3.3 FRP behavior

As stated above, the thermal and mechanical properties of FRPs depend on the type of fibers and the polymer matrix, the fiber volume ratio and the way in which the FRP is loaded. For instance if the FRP is mainly loaded in tension the fiber thermo-mechanical properties will govern the FRP behavior at elevated temperature, while in case of flexural or shear strengthening, in which FRP requires to develop and transfer high shear stresses through the interface between the adhesive and the concrete substrate, the thermo-mechanical properties of the polymer matrix will govern the FRP bond interaction at elevated temperatures. The thermal behavior of FRP strengthening systems has been reviewed extensively in [33]. As for the epoxy resin, the thermal conductivity of FRPs is not a primary consideration because the amount of FRP in a concrete member will be small in comparison to the amount of concrete. Hence, the FRP's contribution to the overall heat transfer within the member will be negligible. Nevertheless, when used as external reinforcement, the effect of wrapping or plating may play a role given that the low transverse thermal conductivity of FRPs may act to insulate the substrate concrete from fire [33]. The thermal conductivity of an FRP depends on the resin type, the fiber type and orientation and the fiber volume fraction. Thermal conductivities of FRPs are generally low with the exception of CFRPs in the fiber direction (due to the high thermal conductivity of carbon fibers themselves). For unidirectional composites used in civil engineering applications, the fibres control the longitudinal thermal conductivity and the matrix controls the transverse thermal conductivity. Table 3.3 [33] shows typical thermal conductivity values at room temperature for various FRP materials in comparison steel reinforcement bars and concrete reported in [8].

Table 3.3 – Thermal conductivities of FRPs (based on [8,33]

Materials	Thermal conductivity [W/m°C]	
	Longitudinal	Transversal
Glass/Epoxy	3.46	0.35
Aramid/Epoxy	1.73	0.73
High Modulus Carbon/Epoxy	48.4-60.5	0.87
Steel	54	54
Concrete	1.36-2	1.36–2

Another important aspect is the significant difference in the coefficient of thermal expansion (CTE) between the concrete and the FRP when thermal action occurs. In the longitudinal direction of FRP the CTE is strongly dependent on fiber characteristics, but in transversal direction it is governed by the epoxy matrix. Table 3.4 shows typical CTEs for various FRP materials in comparison with that of steel reinforcement bars and concrete. Only GFRP, in longitudinal direction, has a nearly identical CTE to that of concrete. In transversal direction the CTE is higher than concrete for all the type of fibers. Therefore when high temperature variation takes place the large difference between transversal CTE can cause radial pressure on the surface of the FRP bars with possible cracking of surrounding concrete and longitudinal splitting of concrete cover. Moreover the difference in CTE in longitudinal direction can, also, induce thermal and shear stresses in the concrete-adhesive-FRP interface, which could affect their bond behavior and/or induce the bonding failure of the FRP strengthening system.

Table 3.4 – CTEs of various unidirectional FRPs and steel

Materials	CTE Longitudinal [10^{-6}/°C]	CTE Transversal [10^{-6}/°C]
Glass/Epoxy	6.0 to10.0	19.8 to 23.0
Aramid/Epoxy	-2 to -6	54.0 to 80.0
High Modulus Carbon/Epoxy	-1.44 to 0	22.0 to 50.0
Steel	10.8 to 18	10.8 to 18
Concrete	6 to 13	6 to 13

In [52] the coefficient of thermal expansion of two different glass/vinyl ester composite rods has been experimentally determined. It was found that the CTE, in the temperature range from 0°C and 60°C, was equal to 4.8×10^{-6}/°C and 8.2×10^{-6}/°C in the longitudinal direction and 38×10^{-6}/°C and 32×10^{-6}/°C in the transverse direction, highlighting the high directional dependence of the CTE. In [53] the effect of temperature variation on glass and aramid FRP-reinforced concrete elements was evaluated. Their study confirmed the influence of temperature variations on the state of thermal strain and stress within FRP-reinforced concrete, and the necessity of a minimum concrete cover to prevent cracking. More information about the coefficient of thermal expansion can be found in [33].

Bisby (2003) [32] and Williams (2004) [15] have performed finite difference heat transfer analyses of FRP strengthened structural members. They achieve satisfactory accurate temperature predictions using the mathematical relationships given in [22] for both concrete and steel and using the mathematical relationship given in [32] for the FRP. Further in [32] a mathematical model for thermal and physical properties of FRP based on limited research work presented in [54] has been presented. Figure 3.23 shows the thermal conductivity and thermal capacity of CFRP as a function of the temperature as modeled in [32]. Thermal conductivity of CFRP decreases with increasing temperature. The plateau in the high thermal capacity of CFRP in the range of 340 °C to 510°C is due to additional heat absorbed during decomposition of the resin matrix.

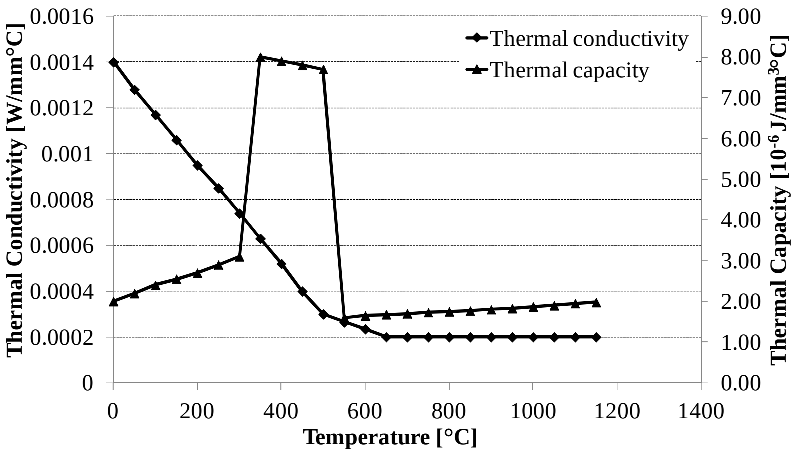

Figure 3.23 – Thermal properties of CFRP as a function of temperature [32]

As for the steel, the FRP mechanical behavior at elevated temperature can be expressed as the sum of several strains. Equation 3.18 presents the total strain, ε_{tot}, as the sum of the free thermal strain, ε_{th}, the stress-related strain ε_{σ}, and the creep strain ε_{cr}.

$$\varepsilon_{f,tot} = \varepsilon_{f,th}(\theta) + \varepsilon_{f,\sigma}(\sigma,\theta) + \varepsilon_{f,cr}(\sigma,\theta,t) \tag{3.18}$$

The different strains are a function of temperature θ, the acting stress σ, and the time t. The thermal strain, $\varepsilon_{f,th}(\theta)$, is directly dependent on the temperature in the element and can be obtained by knowing the temperature and the thermal expansion of the FRP by using equation 3.19.

$$\varepsilon_{f,th}(\theta) = \alpha_f \Delta\theta \tag{3.19}$$

where α_f is the longitudinal coefficient of thermal expansion and $\Delta\theta$ is the increase of temperature in the FRP bar. It has to be noted that for the analytical calculation only the effect of the longitudinal coefficient of thermal expansion has been taken into account.

The stress-related strain, $\varepsilon_{f,\sigma}$, is function of the temperature and the acting stresses, σ. An extensive literature review of test results on the strength and stiffness properties of various fiber and FRP types as a function of the temperature increase has been reported in [4,33]. The temperature dependant behavior of carbon and glass fiber FRPs strengthening systems is shown in Figure 3.24 and Figure 3.25 in terms of tensile strength and elastic modulus. For all the tested specimens a decrease of the mechanical properties with increasing temperature was observed, although, due to the different range of possible polymer matrix, fiber orientations, fiber volume fractions and surface configurations experimental results showed a large scatter.

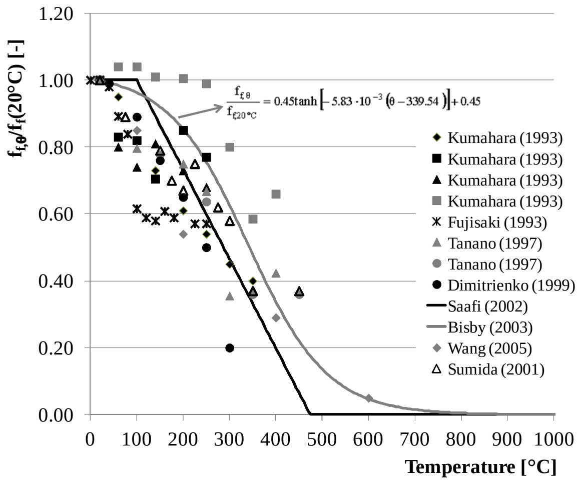

a)

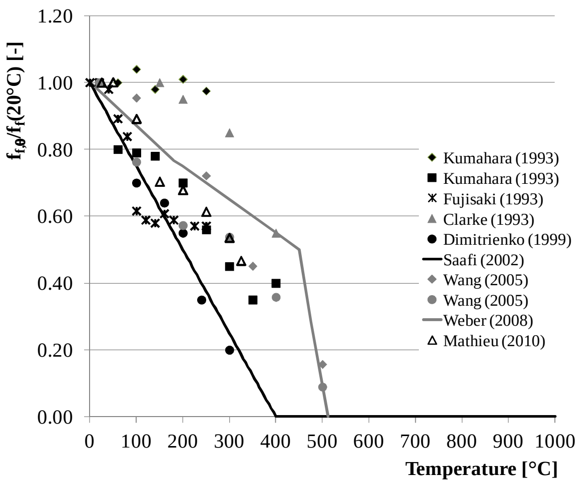

b)

Figure 3.24– Tensile strength as a function of temperature increase for a) CFRP and b) GFRP

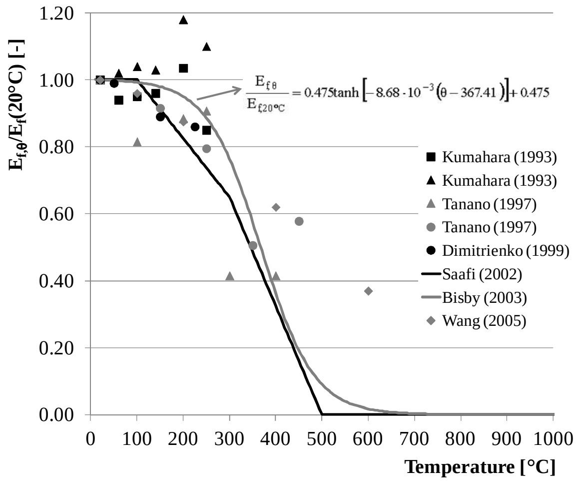

a)

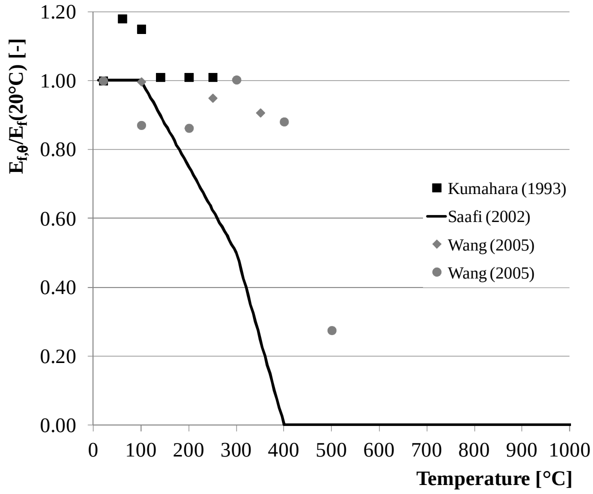

b)

Figure 3.25– Elastic modulus as a function of temperature increase for a) CFRP and b) GFRP

The effect of high temperature on the properties of FRP bars was also studied in [55]. In this test program, the fiber reinforcement consisted in carbon, glass and aramid fiber. The matrix materials consisted in epoxy resin, vinylester and polyphenylene sulfide (PPS). Also the surface configuration (smooth bars, ribbed bars and spirally wound bars) was investigated. They observed a tensile strength reduction of up to 25% at about 100 °C and 50% at 250 °C for carbon/epoxy reinforcing bars, and a tensile strength reduction of up to 20% at 100 °C and 40% at 250 °C for glass/vinylester FRP bars. No significant reduction in the elastic modulus was observed for the FRP bars up to a temperature of approximately 250°C. In [56] the influence of the geometric properties of the FRPs was investigated. The tested rods consisted of straight fibers, braided fibers and strands of fibers bundles. As for previous tests, the decrease of the modulus of elasticity was less pronounced than that observed for the tensile strength of the FRP bars. Moreover it was observed that the decrease of the modulus of elasticity follows the trend of other studies for bars with straight fibers, while a large dispersion of results was observed for rods with braided fibers and strands of fibers bundles. In [57] the temperature dependence of the tensile strength for a hybrid carbon/glass fiber grid during and after heating was investigated. Experimental results indicated a reduction of tensile strength of about 40 % at 100 °C and 60% at 250 °C. It has to be noted that the anchorages zones of the FRPs were insulated during testing. In [37] both CFRP and GFRP displayed strength and stiffness reductions of 20% at 200°C and about 40% at 250°C. Similar results in terms of tensile strength reduction were observed in [58] for CFRP. In [59] the reduction of mechanical properties of sand-coated GFRP reinforcing bars subjected to elevated temperatures (ranging from 25 °C to 315 °C) was investigated. They observed that the tensile strength starts to decrease at about 120 °C (the T_g of the polymer matrix). At high temperature (315°C) due to the thermal degradation of the polymer matrix a reduction of tensile strength of 60% was observed. As shown in Figure 3.24 b) the test results were in accordance to previous tests. In [32] an analytical model to predict the reduction of mechanical properties of CFRP materials at elevated temperatures has been presented (see Figure 3.24 and Figure 3.25). The following relationships for the tensile strength and modulus of elasticity have been proposed:

$$\frac{f_{f,\theta}}{f_{f,20°C}} = 0.45\tanh\left[-5.83\cdot 10^{-3}\left(\theta - 339.54\right)\right] + 0.45 \tag{3.20}$$

$$\frac{E_{f,\theta}}{E_{f,20°C}} = 0.475\tanh\left[-8.68\cdot 10^{-3}\left(\theta - 367.41\right)\right] + 0.475 \tag{3.21}$$

Where $f_{f,20°C}$ and $f_{f,\theta}$ are the tensile strength of FRP bars at 20°C and at different temperatures, θ, respectively, and $E_{f,20°C}$ and $E_{f,\theta}$ are the modulus of elasticity of FRP bars at 20°C and at different temperatures, θ, respectively.

Based on the experimental results collected in [4], Saafi (2002) [60] proposed the following temperature-dependant relationship for the tensile strength and modulus of elasticity of CFRP, GFRP and AFRP bars.

$$\frac{f_{f,\theta}}{f_{f,20°C}} = k_f \tag{3.22}$$

$$\frac{E_{f,\theta}}{E_{f,20°C}} = k_E \tag{3.23}$$

Where k_f and k_E are temperature reduction factors for the tensile strength and the modulus of elasticity. The proposed reduction factors as a function of the FRP temperature are shown in Figure 3.24- Figure 3.25 and are given by equations 3.24-3.27 for CFRP and GFRP respectively.

For CFRP bars:

$$\begin{aligned} &k_f = 1 && \text{for } 0°C \le \theta \le 100°C \\ &k_f = 1.267-0.00267\theta && \text{for } 100°C < \theta \le 475°C \\ &k_f = 0 && \text{for } \theta > 475°C \end{aligned} \tag{3.24}$$

$$\begin{aligned} &k_E = 1 && \text{for } 0°C \le \theta \le 100°C \\ &k_E = 1.175-0.00175\theta && \text{for } 100°C \le \theta \le 300°C \\ &k_E = 1.625-0.003325\theta && \text{for } 300°C \le \theta \le 500°C \\ &k_E = 0 && \text{for } \theta > 500°C \end{aligned} \tag{3.25}$$

For GFRP rebars:

$$\begin{aligned} &k_f = 1-0.0025\,\theta && \text{for } 0°C \le \theta \le 400°C \\ &k_f = 0 && \text{for } \theta > 400°C \end{aligned} \tag{3.26}$$

$$\begin{aligned} &k_E = 1 && \text{for } 0°C \le \theta \le 100°C \\ &k_E = 1.25-0.0025\,\theta && \text{for } 100°C < \theta \le 300°C \\ &k_E = 2-0.005\,\theta && \text{for } 300°C < \theta \le 400°C \\ &k_E = 0 && \text{for } \theta > 400°C \end{aligned} \tag{3.27}$$

According to these relations, the tensile strength of CFRP is unaffected up to 100°C, and decreases with increasing temperature, while the tensile strength of GFRP starts to decrease consistently with increase of temperature. The modulus of elasticity of both FRP bars is constant up to 100 °C, and then decreases with increasing temperature. The relations proposed by Saafi (2002) [60] have been used in the analytical simulations to determine the reduction of strength and stiffness of FRP bars materials at elevated temperature (see chapter 7).

Finally in [61] tension tests on CFRP and GFRP bars have been performed. Experimental results from the strength tests were used to show that temperatures of about 325°C and 250°C appear to be critical (based on a 50% strength reduction criterion) for GFRP and CFRP reinforcing bars, respectively. The modulus of elasticity of both FRP bars was constant up to 400 °C, at which point it decreased rapidly.

The third strain component $\varepsilon_{f,cr}(\sigma,\theta,t)$ in equation 3.16 is the creep effect. In general, the creep strain of FRPs increases with increasing temperature and is largely dependent on the matrix material. Fiber orientation greatly influences the temperature dependence of the creep characteristics of the FRP. The creep effects are minimal both at room and elevated temperatures for the direction of loading coinciding with the fiber direction since the fibers dominate the creep in the composites, and it has been observed that commercially available carbon and glass fibers do not creep significantly. Therefore creep strains, ε_{cr}, is negligible and is not accounted in the analysis since fiber direction coincides with loading direction [33]. Moreover it was demonstrated in [62] that the increase in creep strain is particularly large above 150 °C for an off-axis CFRP composites.

3.3.4 Insulation materials

Fire protection is crucial for structural elements with a low fire resistance rating. The applied protection extends the time before experiencing any major structural collapse during a fire event. Different type of fire insulations are tested in this research project: 3 board systems (type Promat-H and Promat-L500 supplied by Promatect and type Aestuver supplied by Xella) and 2 spry-applied insulation materials (type WR-APP type C supplied by Fyfe Co and type Hot Pipe Coating and Omega Fire supplied by Superior Product Europe). The insulation configurations were designed to limit the adhesive temperature during fire exposure, such to avoid significant dysfunction of the FRP during or after fire (see chapter 6). The thermal properties in terms of thermal conductivity and thermal capacity, used for the heat transfer analysis to determine the temperature distribution in the beams and slabs cross sections will be discussed in this section for the different insulation systems.

Promat H and Promat L 500 are medium and light density calcium silicate boards with a density at 20 °C of 870 kg/m^3 and 500 kg/m^3 respectively. Equations 3.28 and 3.29, proposed in [4] are used, for the heat transfer analysis, to determine the temperature distribution of Promat-H:

$$\lambda_{pr,H} = 0.196 - 0.207 \cdot 10^{-2} \frac{\theta}{100} + 0.131 \cdot 10^{-2} \left(\frac{\theta}{100} \right)^2 \quad [\mathrm{W/m°C}] \tag{3.28}$$

$$c_{pr,H} = 561 + 101.1 \frac{\theta}{100} - 22.4 \left(\frac{\theta}{100} \right)^2 + 2.5 \left(\frac{\theta}{100} \right)^3 \quad [\mathrm{J/kg°C}] \tag{3.29}$$

where $\lambda_{pr,H}$ is the thermal conductivity, $c_{pr,H}$ is the heat capacity and θ is the temperature during fire exposure. Equation 3.30 was used to model the variation of thermal conductivity of Promat-L500 as a function of temperature, while the same equation used for Promat-H (see equation 3.29) was used to model the variation of the specific heat with increasing temperature.

$$\lambda_{pr,L\text{-}500} = 0.0804 - 0.589 \cdot 10^{-3} \frac{\theta}{100} + 1.541 \cdot 10^{-3} \left(\frac{\theta}{100} \right)^2 \quad [\mathrm{W/m°C}] \tag{3.30}$$

Figure 3.26 and Figure 3.27 show the variation of thermal conductivity and volumetric heat capacity, $c_{v,}$ (given by the product of the density and the heat capacity) as a function of the temperature for the two insulation systems.

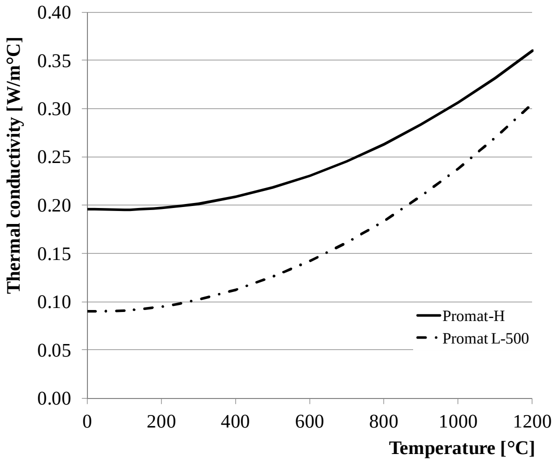

Figure 3.26 – Thermal conductivity of Promat-H and Promat L-500 as a function of temperature

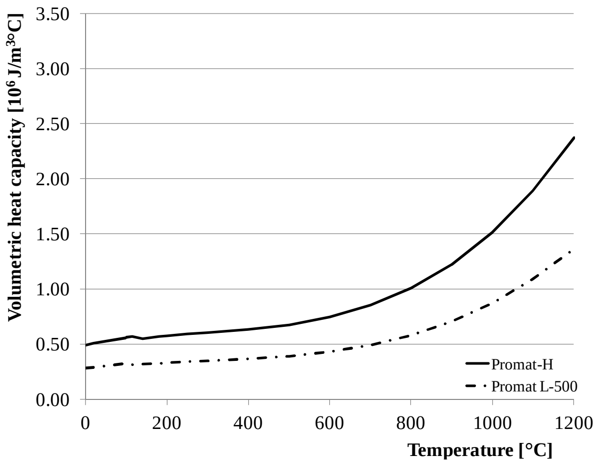

Figure 3.27 – Volumetric heat capacity of Promat-H and Promat L-500 as a function of temperature

Aestuver is a glass-fiber reinforced lightweight concrete board with a density at 20 °C equal to 680 kg/m^3. Figure 3.28 shows the variation of thermal conductivity, $\lambda_{aest.}$, and volumetric heat capacity, $c_{v,aest.}$(given by the product of the density and the heat capacity) as a function of the temperature, according to tests performed by the manufacturers. The thermal conductivity was obtained by the hotwire method in accordance to [63] and the specific heat by Differential Scanning calorimetry (DSC) in accordance to [64]. Equations 3.31 and 3.32 are used for the heat transfer analysis, to determine the temperature distribution of Aestuver:

$$\begin{aligned}
&\lambda_{aest.} = 2.21\cdot 10^{-1} - 8.0\cdot 10^{-3}\frac{\theta}{100} - 2.0\cdot 10^{-3}\left(\frac{\theta}{100}\right)^3 && 0°C < \theta \le 726°C \text{ [W/m°C]}\\
&\lambda_{aest.} = 4.2\cdot 10^{-1} - 2\cdot 10^{-2}\frac{\theta}{100} && 726°C < \theta \le 944°C \text{ [W/m°C]}\\
&\lambda_{aest.} = 6.1\cdot 10^{-1} - 9.1\cdot 10^{-2}\frac{\theta}{100} && 944°C < \theta \le 1000°C \text{ [W/m°C]}\\
&\lambda_{aest.} = 1.211 - 1.5\cdot 10^{-1}\frac{\theta}{100} && 1000°C < \theta \le 1200°C \text{ [W/m°C]}
\end{aligned} \tag{3.31}$$

$$\begin{aligned}
&c_{aest.} = 1740 && 0°C \le \theta \le 400°C \text{ [J/kg°C]}\\
&c_{aest.} = 1740 - \frac{(1740 - 1330)}{(401 - 400)}(401 - 400) && 400°C < \theta \le 401°C \text{ [J/kg°C]}\\
&c_{aest.} = 1330 && 401°C < \theta \le 700°C \text{ [J/kg°C]}\\
&c_{aest.} = 1330 - \frac{(1330 - 470)}{(701 - 700)}(701 - 700) && 700°C < \theta \le 701°C \text{ [J/kg°C]}\\
&c_{aest.} = 1470 && 701°C < \theta \le 900°C \text{ [J/kg°C]}\\
&c_{aest.} = 1470 - \frac{(1470 - 625)}{(901 - 900)}(901 - 900) && 900°C < \theta \le 901°C \text{ [J/kg°C]}\\
&c_{aest.} = 625 && 901°C < \theta \le 1100°C \text{ [J/kg°C]}\\
&c_{aest.} = 625 - \frac{(625 - 1101)}{(1101 - 1100)}(1101 - 1100) && 1100°C \le \theta \le 1101°C \text{ [J/kg°C]}
\end{aligned} \tag{3.32}$$

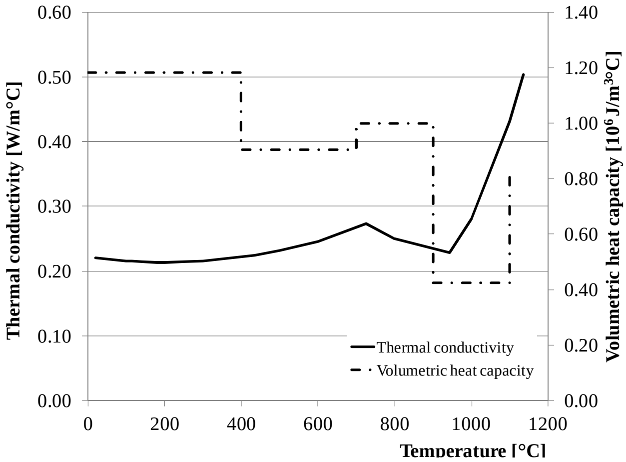

Figure 3.28 –Thermal conductivity and volumetric heat capacity as a function of temperature for Aestuver

Experimental tests showed (see Figure 3.28) that the thermal conductivity of the Aestuver board increases up to 726 °C, after which it decreases till approximately 926 °C and then continued increasing with increase temperature. The volumetric heat capacity remained nearly constant up to 400 °C, at which point a decrease of thermal capacity was observed likely due to chemicals reaction in the insulation material. A second drop in the volumetric heat capacity was observed at approximately 900 °C. At that point the volumetric heat capacity remained nearly constant up to 1100 °C, at which point it started to increase again. This behavior is related to several chemical reactions inside the insulation materials that have not been investigated in details in the present research program.

WR-type C is a vermiculite/gypsum fire resistant lightweight cementious plaster with a density at 20 °C of 269 kg/m^3. The thermal properties in terms of thermal conductivity and volumetric heat capacity based on a semi-empirical relationship suggested in [32] (see equation 3.5, 3.33 and 3.34) have been incorporated into the thermal analysis. Figure 3.29 shows the thermal conductivity and the volumetric heat capacity of WR-type C as a function of the temperature. According to [32] the thermal conductivity decreased up to 200°C, remained nearly constant till 500°C and then increased with temperature. The peak for the volumetric heat capacity was at about 100°C and was due to evaporation of entrapped water that consumed most of the heat energy.

$$
\begin{aligned}
&\lambda_{WR} = 0.12 && 0°C \le \theta \le 50°C \quad [W/m°C] \\
&\lambda_{WR} = 0.12 + \frac{(0.07-0.12)}{(101-50)}(\theta - 50) && 50°C < \theta \le 101°C \ [W/m°C] \\
&\lambda_{WR} = 0.07 && 101°C < \theta \le 500°C \ [W/m°C] \\
&\lambda_{WR} = 0.07 + \frac{(0.09-0.07)}{(550-500)}(\theta - 500) && 500°C < \theta \le 550°C \ [W/m°C] \\
&\lambda_{WR} = 0.09 && 550°C < \theta \le 650°C \ [W/m°C] \\
&\lambda_{WR} = 0.09 + \frac{(0.11-0.09)}{(700-650)}(\theta - 650) && 650°C < \theta \le 700°C \ [W/m°C] \\
&\lambda_{WR} = 0.11 && 700°C < \theta \le 800°C \ [W/m°C] \\
&\lambda_{WR} = 0.12 + \frac{(0.2-0.12)}{(1000-800)}(\theta - 800) && 800°C < \theta \le 1200°C \ [W/m°C]
\end{aligned}
\tag{3.33}
$$

$$
\begin{aligned}
&c_{p,WR} = 854.7 + \frac{(854.7-1139.6)}{(50-20)}(\theta - 50) && 0°C \le \theta \le 50°C \quad [J/kg°C] \\
&c_{p,WR} = 854.7 + \frac{(4045.58-854.7)}{(100-50)}(\theta - 50) && 50°C < \theta \le 100°C \ [J/kg°C] \\
&c_{p,WR} = 4045.58 + \frac{(854.7-4045.58)}{(150-100)}(\theta - 100) && 100°C \le \theta \le 150°C \ [J/kg°C] \\
&c_{p,WR} = 854.67 + \frac{(968.66-854.67)}{(600-150)}(\theta - 150) && 150°C \le \theta \le 600°C \ [J/kg°C] \\
&c_{p,WR} = 968.66 + \frac{(1255.07-968.66)}{(650-600)}(\theta - 600) && 600°C \le \theta \le 650°C \ [J/kg°C] \\
&c_{p,WR} = 1255.07 + \frac{(712.25-1255.07)}{(712-650)}(\theta - 650) && 650°C \le \theta \le 712°C \ [J/kg°C] \\
&c_{p,WR} = 712 && 712°C \le \theta \le 1200°C \ [J/kg°C]
\end{aligned}
\tag{3.34}
$$

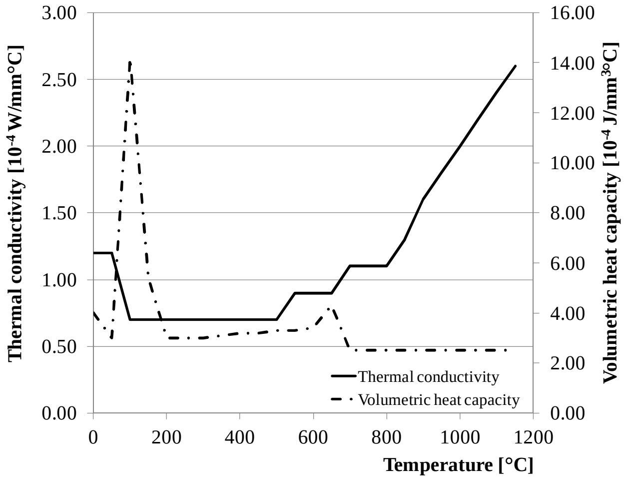

Figure 3.29 –Thermal conductivity and volumetric heat capacity as a function of temperature WR-type C

The second spry-applied fire protection system consists in two ceramic based materials: Hot Pipe Coating (HPC) and Omega Fire [65]. Hot pipe coating is designed to control heat transfer on surface temperatures. It is a unique combination of a specially designed resin blend with specific ceramic compounds (seven different ceramic compounds) added to provide a non-conductive block against heat transfer. It is water-borne and lightweight in appearance; the density at 20 °C is 599 kg/m^3. This coating will dry slowly by evaporation and can be aided in the dry down by adding heat to the environment. The Omega Fire contains eight different ceramics mixed with glazing materials and will glaze and harden to stop flame, smoke and gas penetration. Its density at 20°C is equal to 1138.5 kg/m^3.

Figure 3.30 shows the thermal conductivity and the volumetric heat capacity (obtained multiplying the density with the heat capacity) of the HPC insulation system as a function of the temperature. The thermal conductivity was obtained experimentally, by manufacturers, according to [63], in which the thermal conductivity of the HPC at different temperature up to 500°C was experimentally tested. Based on experimental outcomes the equation 3.36 was proposed by the manufacturers.

$$\lambda_{HPC} = 0.059 + 0.000115\theta \qquad [W/m°C] \qquad (3.35)$$

Where λ_{HPC} is the thermal conductivity of HPC and θ is the temperature.

The heat capacity of the Hot Pipe Coating was obtained experimentally by Modulated Differential Scanning Calorimetry (MDSC). Tests were carried out at Ghent University. MDSC measurements were carried out using a Q2000 Modulated DSC equipped with a refrigerated cooling system. Dry nitrogen at a flow rate of 50 ml/min was used to purge the DSC cell. The amplitude of the temperature was 0.5 °C, the period was 100s and the underlying heating rate was 2°C/min. Three samples were tested. The heat capacity was evaluated from 0°C to 380°C. Experimental outcomes showed a peak of the heat capacity at about 100 °C, at which point the heat capacity stayed approximately constant up to 270°C, then a decrease was observed. For temperatures higher than 380°C, a constant value of heat capacity was considered. Based on the experimentally outcomes equation 3.36 is proposed for the heat capacity as a function of temperature:

$$
\begin{aligned}
c_{p,HPC} &= 1890 && 0°C \le \theta \le 100°C \quad [J/kg°C] \\
c_{p,HPC} &= 1890 + \frac{(5510 - 1890)}{(110 - 100)}(\theta - 100) && 100°C < \theta \le 110°C \quad [J/kg°C] \\
c_{p,HPC} &= 5510 + \frac{(4500 - 1890)}{(120 - 110)}(\theta - 110) && 110°C < \theta \le 120°C \quad [J/kg°C] \\
c_{p,HPC} &= 4500 + \frac{(4610 - 4550)}{(170 - 120)}(\theta - 120) && 120°C < \theta \le 170°C \quad [J/kg°C] \\
c_{p,HPC} &= 4610 && 170°C < \theta \le 240°C \quad [J/kg°C] \\
c_{p,HPC} &= 4610 + \frac{(1890 - 4610)}{(260 - 240)}(\theta - 240) && 240°C < \theta \le 260°C \quad [J/kg°C] \\
c_{p,HPC} &= 1890 && 260°C < \theta \le 1200°C \quad [J/kg°C]
\end{aligned}
\qquad (3.36)
$$

The volumetric heat capacity, $c_{v,HPC}$, used in the heat transfer analysis, was obtained according to equation 3.5.

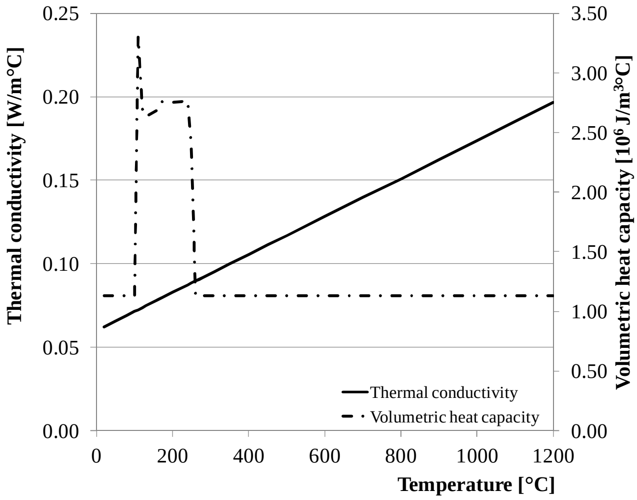

Figure 3.30 –Thermal conductivity and volumetric heat capacity as a function of temperature HPC

The thermal conductivity of Omega Fire was obtained by the hotwire method in accordance to [67]. Experimental tests were carried out at the Department of flow, heat and combustion mechanics of university of Ghent. The sample was positioned in an oven to measure the thermal conductivity at room temperature, 100°C, 200°C, 300°C, 400 °C, 500°C and 600°C. However, between 200°C and 300°C the sample expanded and the test had to be stopped. Consequently, only results for the first three measurements were available. It has to be noted that a similar behavior (expansion of Omega Fire with considerably cracks) was observed also during the fire tests (see chapter 6). No further tests were conducted on the Omega fire for investigating its thermal conductivity. The average thermal conductivity up to 200°C was equal to $\lambda_{OmegaFire}$= 0.24 W/m°C.

The heat capacity of the Omega fire was experimentally tested following the same procedure adopted for the thermal capacity of the HPC coating. As stated before, for temperature higher than 380°C the heat capacity was assumed constant with increasing temperature. Based on the experimental results equation 3.37 is proposed for the heat capacity as a function of temperature:

$$
\begin{aligned}
&c_{p,OM} = 1120 && 0°C \le \theta \le 90°C \quad [J/kg°C]\\
&c_{p,OM} = 1120 + \frac{(1270-1120)}{(110\text{-}90)}(\theta - 90) && 90°C \le \theta \le 110°C \quad [J/kg°C]\\
&c_{p,OM} = 1270 + \frac{(5510-1270)}{(250-110)}(\theta - 110) && 110°C \le \theta \le 250°C \quad [J/kg°C]\\
&c_{p,OM} = 5510 + \frac{(1410-5510)}{(330-250)}(\theta - 250) && 250°C \le \theta \le 330°C \quad [J/kg°C]\\
&c_{p,OM} = 1410 && 330°C \le \theta \le 1200°C\ [J/kg°C]
\end{aligned}
\tag{3.37}
$$

The volumetric heat capacity, $c_{v,OM}$, used in the heat transfer analysis, was obtained according to equation 3.5. In Figure 3.31 the volumetric heat capacity of Omega Fire as a function of the temperature is shown.

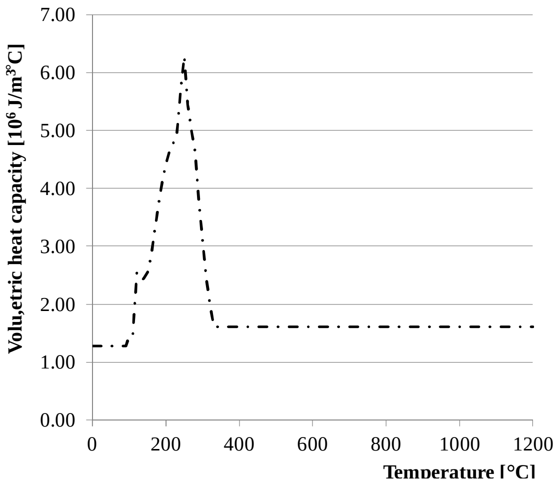

Figure 3.31–Volumetric heat capacity as a function of temperature Omega Fire

3.4 Conclusions

In this chapter an overview on the effect of temperature on the thermal and mechanical properties of concrete, steel reinforcement, adhesive, FRP and insulation materials has been given. It has been shown that, for all the constituent materials of an FRP strengthened member, the mechanical properties degrade with increasing temperature. There are many available studies on the fire behavior of conventional concrete and steel structural members. These studies demonstrated that the behavior of constituent materials at elevated temperature and for a given load level can be formulated with reference to several strains as a function of the temperature (θ), the acting stresses (σ) and the time of exposure (t). Also an understanding of FRP and polymer matrix behavior, in terms of thermal properties and deterioration of mechanical properties at elevated temperatures is essential to experimentally or/and analytically investigate the fire endurance of FRP strengthened structural members. Fibers exhibit a good resistance to elevated temperature, while for FRP composites, the rate of degradation of strength and stiffness properties is faster than concrete and steel due to the low tolerance of the polymer matrix to elevated temperatures.

The most important property of the polymer matrix, as far as fire behavior in reinforced concrete applications is concerned, is the glass transition temperature, T_g. Reduction of strength and stiffness properties of the polymer matrix have been observed, in several research studies, at temperatures close to T_g. In the reviewed literature, strength of epoxy is completely lost for values of temperatures higher than 2-2.5 T_g. At 1.5 T_g strength and stiffness are reduced; yet limited stress transfer remains possible as ~15% of the original strength and ~3% of the original stiffness remain available. Although the reduced stiffness of the adhesive at elevated temperature can have a positive influence on a FRP strengthened member (the reduced stiffness of the adhesive can reduce the shear stresses at the FRP/concrete interface), as will be discussed further in the following chapters (see chapter 4, section 4.5 and chapter 7 section 7.4).

Moreover it was found that the rates of reduction in strength and stiffness depend on the heating rate (the reduction of mechanical properties is larger for higher rates of heating) and that the adhesive T_g can be increased by applying a temperature cycle. The residual performance of epoxy resin after exposure to elevated temperature have shown the possibility to retain essentially all its strength up to exposure of 150°C (~2T_g). From experimental results on tensile tests and TGA results it looks that considerable reductions of epoxy resin tensile strength are observed at temperatures close to that at which epoxy resins have experienced significant mass lost. For instance even small losses in mass (5%) can cause drastic reduction (up to 90%) in the residual tensile strength of the epoxy resins.

The thermal and mechanical properties as a function of the temperature of concrete, steel reinforcement, FRP strengthened system and insulation materials, described in this chapter, will be used in chapter 7 for the heat transfer and structural analysis of the tested beams and slabs under fire exposure.

3.5 References

1. Bisby L.A., Stratford T.J. (2012) “Performance-based Structural Fire Resistance Design of FRP Strengthened Concrete”. *In Proc of 6th International Conference on Advanced Composite Materials in Bridge and Structures (ACMBS)*, Kingston, Canada, 8 pp.
2. Drysdale D. (2011) “An Introduction to fire dynamics”. John *Wiley and Sons*. eds, 551 pp.
3. EN 1991-1-2 (2002). “Eurocode 1- Actions on Structures – Part 1-2: General actions - Actions on structures exposed to fire”. *European Committee for Standardization.*
4. Blontrock H. (2003). “Analyse en Modellering Van De Brandweerstand Van betonelementen Uitwendig Versterkt Met Opgelijmde Composietlaminaten”. *Ph-D Thesis*, Faculty of Engineering, Department of Structural Engineering, Ghent University, Belgium, 412 pp.
5. *fib* Task Group 4.3 (2007). “Fire design of concrete structures – materials, structures and modeling”. *International Federation for Structural Concrete*, *fib* Bulletin 38.
6. EN-1363-1 (1999). “Fire Resistance Tests – General Requirements – Part I” *European Committee for Standardization*.
7. ISO 834 (1999). “Fire Resistance Tests – Elements of Buildings Construction – Part I – General Requirements”. *International Organization for Standardization.*
8. EN 1992-1-2 (2004). “Eurocode 2 – Design of concrete structures – Part 1-2: General rules – Structural fire design”. *European Committee for Standardization.*
9. EN 13369 (2004). “Common rules for precast concrete products”. *European Committee for Standardization.*
10. Bazant Z.P., Kaplan M.F. (1996). “Concrete at high temperature: Materials properties and mathematical models”. *Concrete design and constructions series*, Essex, Longman Group Limited.
11. Anderberg Y., Thelandersson S. (1976). “Stress and deformation characteristic of concrete at high temperatures:2. Experimental investigation and material behavior model”. *Bulletin 54*, Lund Institute of Technology, Lund.

12. Anderberg Y. (1976). “Fire – exposed hyperstatic concrete structures – an experimental and theoretical study”. *Bulletin 55*, Lund Institute of Technology, Lund.
13. Schneider U. (1976). “Behaviour of concrete under thermal steady state and no steady state conditions” *Fire Materials*, 1, 103-115.
14. Lie T.T. (1992). “Structural fire protection”. *American Society of Civil Engineers manual and reports on engineering practice no 78*, New York, NY, USA. ASCE.
15. Williams B.K. (2004). “Fire performance of FRP-strengthened reinforced concrete flexural members”. *Ph-D thesis*, Department of Civil Engineering, Queen’s University, Kingston Ontario, Canada.
16. Annerel E. (2010). “Assesment of the Residual Strength of Concrete Structures after Fire Exposure”. *Ph-D Thesis*, Faculty of Engineering, Department of Structural Engineering, Ghent University, Belgium, 291 pp.
17. CEB (1991). “Fire design of concrete structures”. *CEB Bulletin d’information nr. 208*, Lausanne, Switzerland.
18. Cruz C. (1966). “Elastic Properties of Concrete at High Temperatures”. *Journal of the PCA Research and Development Laboratories*, 37-45.
19. Philleo R. (1958). “Some Physical Properties of Concrete at high Temperatures”. *Journal of the American Concrete Institute*, 29(10), 857-864.
20. Tavernier E., Collet Y. (1977). “Studie van de eigenschappen van beton onderworpen aan hoge temperature”. *Raport RR OCCN 45-n-1977*, Nationaal centrum voor wetenschappelijk en technisch onderzoek der cementnijverheid, 32 pp.
21. Gernay T., Fransseen J.M. (2011). “A Comparison Between Explicit and Implicit Modelling of transient Creep strain in Concrete Uniaxial Constitutive Relationship”. *Proc. of the Fire and Materials 2011 Conference*, San Francisco, California, 405-416.
22. Lie T.T., Irwin R.J. (1993). “Method to calculate the fire resistance of reinforced concrete colums with rectangular cross section”. *ACI Strtruct. Journal*, Am. Constr. Inst., 90(1), 52-60.
23. Dwaikat M.B., Kodur V.K.R. (2008). “A numerical approach for modeling the fire induced restraint effects in reinforced concrete beams”. *Fire Safety Journal*, 43(4), 291-307.

24. EN 1993-1-2 (2005). "Eurocode 3 – Design of steel structures – Part 1-2: General rules – Structural fire design". *European Committee for Standardization*.
25. Kodur V., ASCE F., Dwaikat M. and Fike R. (2010) "High-Temperature Properties of Steel for Fire Resistance Modelling of Structures". *Journals of Materials in Civil Engineering*, ASCE, 22 (5), 423-434.
26. Poh K. (2001). "Stress-Strain-Temperature Relationship for Structural Steel". *Journal of Materials in Civil Engineering*, 13(5), 371-379.
27. Outinen, J., Kesti, J., Mäkeläinen, P. (1997). "Fire design model for structural steel S355 based upon transient state tensile test results." *J. Constr. Steel Res.*, 42(3), 161–169.
28. Chen, J., Young, B., Uy, B. (2006). "Behavior of high strength structural steel at elevated temperatures". *J. Struct. Eng.*, 132 (12), 1948–1954.
29. Chen, J., Young, B. (2008). "Design of high strength steel columns at elevated temperatures". *J. Construct. Steel Res.*, 64 (6), 689–703.
30. Clark, C. L. (1953). High-temperature alloys, Pitman, New York.
31. Dorn J. (1954). "Some fundamental experiments on high temperature creep". *Journal of the Mechanics and Physics of solids*, 3(12), 85-88.
32. Bisby L.A. (2003). "Fire behaviour of fibre-reinforced polymer (FRP) reinforced or confined concrete". *PhD thesis*, Department of Civil Engineering, Queen's University, Kingston, Canada.
33. Bisby L., Williams B., Kodur V.R., Green M., Chowdhury E. (2005). "Fire Performance of FRP systems for Insfrastructure: A State-of-the-Art Report", *Research Report*, Institute for Research in Construction, National Research Council Canada, RR 179, IRC-IR-179.
34. Rostasy F. (1992). "Fibre Composite Elements and Techniques as Non-Metallic Reinforcement of Concrete". Brite-Euram Project 4142/BREU – CT 91 0515, Evaluation of Potentials and Production Technologies of FRP, Technical Report Task 1, 95 pp.
35. Sumida A., Fujisaki T., Watanabe K., Kato T. (2001). "Heat Resistance of Continuous Fiber Reinforced Plastic Rods". *In The Fifth Annual Symposium on Fibre-Reinforced-Plastic Reinforcement for Concrete Structures (FRPRCS-5)*, Edited by C. Burgoyne, Thomas Telford, London, 557-565.
36. Rehm G., Franke L. (1974). "Kunstharzgebundene Glasfäserstabe als Bewehrung im Betonbau". *Die Bautechnik*, Heft 4, 115-120.

37. Dimitrienko Y.I. (1999). "Thermomechanics of Composites under High Temperatures". *Klewer Academic Publishers*, London, 347 pp.
38. Sen R., Mariscal D., Shahawy M. (1993). "Durability of Fiberglass Prestensioned Beams". *ACI Structural Journal*, 90(5), 525-533.
39. Sorathia U., Dapp T., Beck C. (1992). "Fire Performance of Composites". *Materials Engineering*, September, 10-12.
40. Saafi M. (2002). "Effect of fire on FRP reinforced concrete members". *Composite Structures*, 58(1), 11-20.
41. Plecnik J., Bresler B., Cunnigham D., Iding R. (1980). "Temperature effects on epoxy adhesives". *Journal of Structural Engineering*, ASCE, 106(1), 99-113.
42. Klamer E.L. (2009) "Influence of Temperature on Concrete Beams Strengthened in Flexure with CFRP". *PhD thesis*, Department of architecture, building and planning, Eindhoven University of Technology, the Netherlands, 250 pp.
43. Leone M., Matthys S., Aiello M.A. (2009). "Effect of elevated service temperature on bond between FRP EBR system and concrete". *Composite Part B: Eng*, 40, 85-93.
44. ISO 11357-2 (1999). "Plastics – Differential scanning calorimetry (DSC)- Part 2: Determination of glass transition temperature". *International Organization for Standardization*.
45. ISO/CD 6721–11 (2008). "Plastics – Determination of Dynamic Mechanical Properties – Determination of glass transition temperature". *International Organization for Standardization*.
46. ASTM Standard E1640 (2004). "Standard Test Method for Assignment of the Glass Transition Temperature by Dynamic Mechanical Analysis". *ASTM International*, West Conshohocken, PA.
47. ISO 11358 (1997). "Plastics – Thermogravimetry (TG) of polymers – General principles". *International Organization for Standardization*.
48. ASTM E1131-08 (2008). "Standard Test Method for Compositional Analysis by Thermogravimetry". *ASTM International*, West Conshohocken, PA.
49. Bakis C.E. (2008). "Elevated Temperature Capability of Epoxy Resins: Issues and Developments". *Proc. US-South America Workshop on Innovative Materials for Civil Infrastructure*, Research and Education, M.M. Lopez, Ed., National Science Foundation, Chile, 4 p. (CDROM).

50. Chowdhury E.U. (2009). “Behaviour of Fibre Reinforced Polymer Confined Reinforced Concrete Columns Under Fire condition”. *PhD thesis*, Department of Civil Engineering, Queen’s University, Kingston, Canada, 235 pp.

51. Foster S.K., Bisby L.A. (2008). “Fire Survivability of Externally-Bonded FRP strengthening Systems”. *J. Compos. Constr*, ASCE, 12(5), 553-561.

52. Gentry T.R., Hudak C.E. (1996). “Thermal Compatibility of Plastic Composite Reinforcement and Concrete”. *In Advanced Composite Materials for Bridges and Structures*. Edited by M. El- Badry. Avantage Inc., Montreal, PQ, 149-156.

53. Aiello M.A., Focacci F., Huang P.C., Nanni, A. (1999). “Cracking in Fibre Reinforced Polymer Reinforced Concrete under Thermal Loads”. *In Fibre Reinforced Polymer Reinforcement for Reinforced Concrete Structures*, edited by A. Nanni, C.W. Dolan, and S.H. Rizkalla. American Concrete Institute, Detroit, Michigan, 233-243.

54. Griffis C.A., Masmura R.A., Chang C.I. (1984). “Thermal response of graphite epoxy composite subjected to rapid heating”. *Environmental Effects on Composite Materials*, Vol. 2, Technomic Publishing Company, Lancaster, Pennsylvania, 245-260.

55. Kumahara S., Masuda Y., Tanano H., Shimizu A. (1993), “Tensile Strength of Continuous Fibre Bar under High Temperature”. *In Proc. of the International Symposium on Fibre-Reinforced-Plastic Reinforcement for Concrete Structures*, Eds. Nanni A. en Dolan C., ACI SP-138, 731-742.

56. Tanano H., Masuda Y., Sakashita M., Oono Y., Nonomura K., Satake K. (1997). “Tensile Properties at High Temperature of Continuous Fibre Bars and Deflections of Continuous Fibre Reinforced Concrete Beams under High-Temperature Loading”. *Non-Metallic (FRP) Reinforcement for Concrete Structures*, Japan Concrete Institute, Vol. 2, 43-50.

57. Fujisaki T., Nakatsuji T., Sugita M. (1993), “Research and Development of Grid Shaped FRP Reinforcemen”, *In Proc of the international symposium on Fibre-Reinforced-Plastic Reinforcement for Concrete Structures*, Eds. Nanni A. en Dolan C., ACI SP-138, 177-192.

58. Sumida A., Fujisaki T., Watanabe K., Kato, T. (2001). “Heat Resistance of Continuous Fiber Reinforced Plastic Rods”. *The Fifth Annual Symposium on Fibre-Reinforced-Plastic Reinforcement for Concrete Structures (FRPRCS-5)*, Edited by C. Burgoyne, Thomas Telford, London, 557-565.

59. Mathieu R., Brahim B. (2010). “Behaviour of GFRP Reinforcing Bars Subjected to Extreme Temperatures”. *J. Compos. Constr*, ASCE, 14(4), 353-360.

60. Saafi M. (2002). “Effect of fire on FRP reinforced concrete members”. *Journal of Composite Structures*, 58, 11–20.

61. Wang Y.C., Kodur V.K.R. (2005). “Variation of strength and stiffness of fiber reinforced polymer reinforcing bars with temperature”. *Cement & Concrete Composites*, 27, 864-874.

62. Gates T.S. (1991). "Effects of elevated temperature on the viscoelastic modeling of GraphiteIPolymeric composites," *NASA Technical Memorandum* 1041 60, National Aeronautics and Space Administration, Langley Research Center, 29 pp.

63. ISO 8894-1 (2010). “Refractory Materials- Determination of Thermal Conductivity- Part 1 – Hot wire methods”. *International Organization for Standardization*.

64. ISO 11357-4 (2005). “Differential Scanning Calorimetry (DSC) – Part 4 – Determination of specific heat capacity”. *International Organization for Standardization*.

65. Superior Product Europe. http://www.specoatings.com.

66. Hens H. (2007). “Thermal conductivity Hot Pipe Coating”. *Research Report*, Faculty of Engineering Department of Civil Engineering Laboratory Buildings and Physics, Catholic University of Leuven.

67. NBN B 62-202 (1978) “Bepaling van de thermische geleidbaardheid van de bouwmaterialen met de parallelsonde”. 1-12 pp.

Chapter 4

BOND OF NSM FRP BARS UNDER ELEVATED SERVICE TEMPERATURE: EXPERIMENTAL AND ANALYTICAL INVESTIGATION

4.1 Introduction

The deterioration of mechanical properties in individual materials is not the only concern related to FRP strengthened elements under elevated temperature and/or fire exposure. Indeed a temperature rise also affects the bond behaviour between the FRP-adhesive and adhesive-concrete interface. Experimental results, from literature review (see chapter 2), have shown a decrease of bond behaviour at the FRP-adhesive or the adhesive-concrete interface for EBR strengthening systems at elevated temperatures. Temperatures, at or beyond the glass transition temperature, significantly influence the stress transfer mechanism, especially in terms of maximum bond stress, transfer length and bond failures modes.

While the bond behavior of NSM FRP strengthening systems, at ambient temperature, has been investigated quite extensively [1-5] focusing on the effects of various system parameters (e.g. groove characteristics, adhesive type, FRP shape, FRP surface configuration, bond length, etc..), to the knowledge of the author, no information is apparently available in literature on the influence of elevated service temperatures on the debonding behaviour of near surface mounted FRP strengthening systems.

Therefore, to investigate the effect of service temperature in terms of failure load, strain distribution, bond strength and failure aspect, 20 double bond shear tests at different temperatures (up to 100°C) have been executed [6-7]. A comparison between un-conditioned (20°C) and conditioned specimens was performed to evaluate the degradation due to thermal exposure.

4.2 Description of specimens and test matrix

The double bond test is schematically represented in Figure 4.1. The specimen (nominal dimensions 150 mm x 150 mm x 800 mm) is composed of two concrete blocks (150 mm x 150 mm x 400 mm) with a square/rectangular groove in the middle at both sides for embedment of the NSM rods/strips. A thin metal plate separates the two concrete blocks. The height of this plate is taken 135 mm (15 mm less than the height of the prisms) so that both prisms remain aligned during hardening of the adhesive, specimen manipulation and FRP application. Two steel rebars, with a diameter of 16 mm, are embedded in each prism. These internal steel bars do not connect the two concrete parts, which means that the two blocks are only joined through the NSM FRP bars. The FRP reinforcement is left un-bonded over a central zone of 100 mm (where the two concrete blocks connect to each other). Only one block is the test region, and for which a bond length of 300 mm has been applied for all the test specimens. To prevent bond failure in the second concrete block a bond length of 350 mm and an extra clamp anchorage are used.

The influence of the FRP reinforcement shape (rods versus strips), the type of fibers (carbon and glass fibers) as well as the type of surface configuration (sand coated and spirally wound bars) are evaluated. The NSM FRP reinforcement comprises CFRP rods and strips, and GFRP rods. The material properties are given in section 4.3. Four different levels of temperature have been used: 50, 65, 80 and 100 °C. The temperature level was chosen in relation to the glass transition temperature (T_g) of the utilized epoxy resin which equals 66°C. The glass transition temperature of the epoxy resins was experimentally determined on the basis of DSC (differential scanning calorimetry), according to ISO 11357-2 [8] as specified in chapter 3. The tests conducted at elevated temperatures are compared with those at room temperature (20 °C).

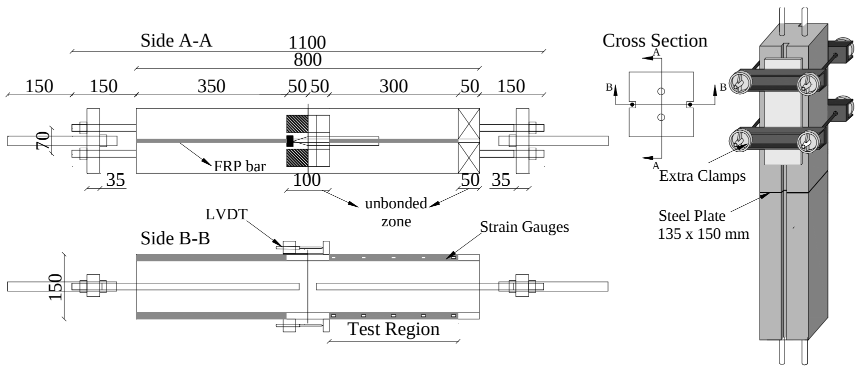

Figure 4.1- Double face bond shear test set up (dimensions in mm)

An overview of the different test specimens and the main test parameters (type of fiber, surface configuration, bar/strip dimensions, groove dimension, temperature and batch number) are given in Table 4.1**.** The specimens are listed using the following designation: the first letter C or G indicates carbon fibers or glass fibers, respectively; the second notation, SC, SW and STR indicates the type of reinforcement: sand coated rods, spirally wound bars or smooth strips; the third notation indicates the test temperature: 20, 50, 65, 80 and 100 °C. The last letter indicates the test sequence of the two similar specimens tested for each analyzed parameter.

Table 4.1 – NSM FRP properties

Specimens	Fiber	Surface	Dimen. [mm]	Groove dimension [mm]	Temp. [°C]	Batch no
C_SC_20_a C_SC_20_b	Carbon	Sand coated	9.53	15 x15	20	2
C_SC_50_a C_SC_50_b	Carbon	Sand coated	9.53	15 x 15	50	2
C_SC_65_a C_SC_65_b	Carbon	Sand coated	9.53	15 x 15	65	2
C_SC_80_a C_SC_80_b	Carbon	Sand coated	9.53	15 x 15	80	3
C_SC_100_a C_SC_100_b	Carbon	Sand coated	9.53	15 x 15	100	3
G_SW_20_a G_SW_20_b	Glass	Spirally Wound	10.0	15 x 15	20	1
G_SW_65_a G_SW_65_b	Glass	Spirally Wound	10.0	15 x 15	65	1
G_SW_100_a G_SW_100_b	Glass	Spirally Wound	10.0	15 x 15	100	1
C_STR_20_a C_STR_20_b	Carbon	Smooth	2 x 16	8 x 25	20	3
C_STR_100_a C_STR_100_b	Carbon	Smooth	2 x 16	8 x 25	100	3

4.3 Material properties

Three different concrete batches with the same concrete composition were used. The concrete composition (per m^3) is given in Table 4.2. The maximum size of aggregates was 16 mm. For each batch extra specimens have been cast, to determine the properties of the hardened concrete: three cylinders (height 300 mm and diameter 150 mm) for compressive strength testing and three prisms 150 mm x 150 mm x 600 mm for the bending tensile strength testing. These tests have been conducted according to Belgium standard [9-10]. The mean cylinder compressive strength, f_c, at 28 days equals 43.7 N/mm^2, 45.1 N/mm^2 and 45.5 N/mm^2 respectively and the tensile strength, f_{ct} (the tensile strength was determined by splitting tests on the remaining halves of the prisms for the bending test) equals 3.2 N/mm^2, 3.2 N/mm^2 and 3.3 N/mm^2 respectively.

Table 4.2 – Concrete composition

Material	Composition
Fine sand 0/4	655.0 Kg
Fine aggregate 2/8	190.0 Kg
Coarse aggregate 8/16	1120.0 Kg
Cement CEM I 52.5	300.0 Kg
Water	165.0 Kg

The FRP reinforcement consisted of: CFRP rods and strips (type Aslan 200 and Aslan 500, supplied by Fortius/Hughes Brothers) with a nominal diameter of 9.53 mm and dimension of 2 mm x 16 mm respectively, and GFRP rods (type Aslan 100 supplied by Fortius/ Hughes Brothers) with a nominal diameter of 10 mm. The CFRP rods, as reported by manufactures, have 1900 MPa tensile strength and 126 GPa Young's modulus, the CFRP strips 2068 MPa tensile strength and 124 GPa Young's modulus and the GFRP rods 760 MPa tensile strength and 40.8 GPa Young's modulus. An overview of the FRP reinforcement properties is also given in Table 4.3.

Table 4.3 – Properties FRP reinforcements

FRP	Type	Dim. [mm]	f_f [MPa]	E_f [10^3MPa]	ε_{fu} [%]
Aslan 200	CFRP	9.53	1900	126	1.6
Aslan 100	GFRP	10.0	760	40.8	1.8
Aslan 500	CFRP	2 x 16	2068	124	1.7

All the NSM FRP reinforcements were embedded into the grooves by means of an epoxy resin (type Fortresin CFL supplied by Fortius). The epoxy resin had a direct tensile strength of 27 MPa, an elastic modulus of approximately 4000 MPa, evaluated according to EN ISO 527-2 [11], and a glass transition temperature equal to 66 °C evaluated according to ISO 11357-2 [8].

4.4 Specimen preparation and test procedure

The FRP NSM rods/strips were applied according to the procedures specified by the manufacturers. After hardening of the concrete, the grooves were saw-cut and then air-blasted to remove the powdered concrete produced by the cutting. The dimensions of the grooves (Table 4.1) were defined in order to be at least 1.5 times the diameter, d_f, of the NSM FRP bars and at least 3 times the width and 1.5 times the height of the NSM FRP strips. The grooves were filled half way with epoxy resin and the bars were then positioned and lightly pressed. More material was applied if needed and the surface was leveled. Curing of the FRP NSM was allowed for at least 7 days under laboratory environment. No pressing devices were applied during curing.

Specimens were equipped with five strain gauges on each NSM FRP rod/strip to measure the strains along the bonded length. The gauges were applied at 10, 80, 150, 220 and 290 mm from the loaded end of the bonded rod/strip (see Figure 4.2). The spacing (70 mm) between each strain gauge has been considered as a compromise in order to limit the influence on the bond mechanism [12] and to have a local measure of the bond shear stress. The relative displacement between the FRP reinforcement and the concrete, at the loaded end, was recorded with two linear variable differential transducers (LVDTs), one per side face of the monitored prism. LVDTs are fixed to the concrete by means of a metal holder and are directly connected to the reinforcement (see Figure 4.1).

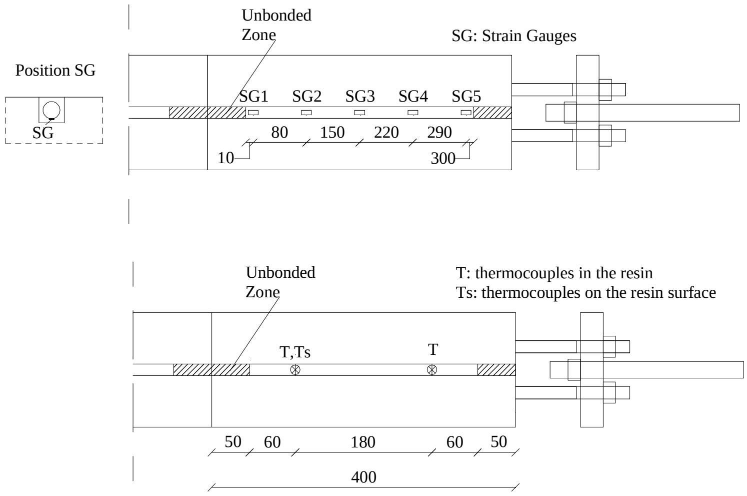

Figure 4.2– Position of strain gauges and thermocouples

For the tests at elevated temperatures an electrical hollow furnace was used. The oven was placed around the specimen in the zone without clamps (monitored side). All gaps between the furnace and the specimen were filled with mineral wool. The temperature in the furnace (by measuring the air temperature inside the furnace) and the temperature within the test region of the specimen were controlled by thermocouples (type K). Two thermocouples were placed inside the epoxy resin at respectively 60 and 240 mm from the end of the rod/strip (see Figure 4.2). The specimens were heated in the oven for at least 18 hours before testing. Hereby, the defined testing temperature (Table 4.1) is obtained at the measuring locations. The temperature was kept constant during testing. All the specimens were axially loaded up to failure in a 1000kN universal axial testing machine. Testing was conducted in displacement control mode with a 1 mm/min cross-head displacement rate. In Figure 4.3 a view of the test set up with and without the oven is given.

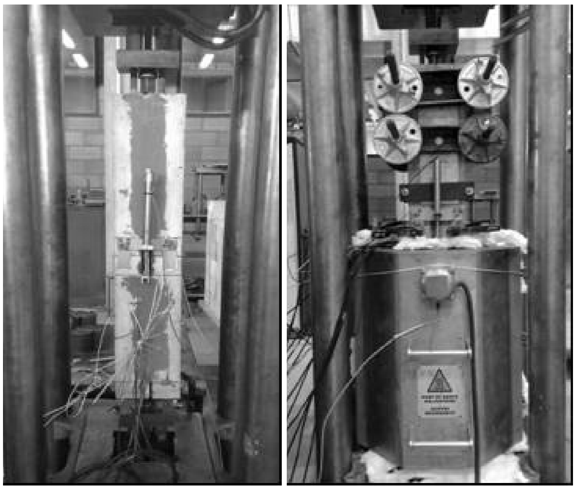

Figure 4.3 – Position of strain gauges and thermocouples

4.5 Test results

4.5.1 Behavior at ultimate load

The main tests results are reported in Table 4.4 where F_u is the ultimate load of one bar/strip (half of the load applied on the specimen) at bond failure; $F_{u,T}/F_{u,20}$ the ratio between the ultimate load at different temperatures and the ultimate load at ambient temperature (20 ^oC), $\tau_{av}=F_u/u_f l_b$ is the average bond shear stress obtained as the ratio between the ultimate load of one bar/strip and the product of the perimeter of the bar and the bond length, l_b, τ_{max} is the peak values of the local shear stress evaluated by the strains recorded by gauges 1 and 2 (see Figure 4.2) and $\tau_{max,T}$ /$\tau_{max,20}$ is the ratio between the maximum local shear stress at temperature T and that at ambient temperature. In Table 4.4 also the observed failure mode is reported, using the following abbreviation: DB R/C is the debonding at resin/concrete interface, and PO is the pull out of the bar.

Bond stresses have been evaluated by utilizing experimentally recorded strains along the FRP. The equilibrium of an infinitesimal length dx of an FRP reinforcement bar/strip (Figure 4.4) can be expressed by equation 4.1:

$$\sigma_f A_f + \tau_f u_f dx = (\sigma_f + d\sigma_f)A_f \tag{4.1}$$

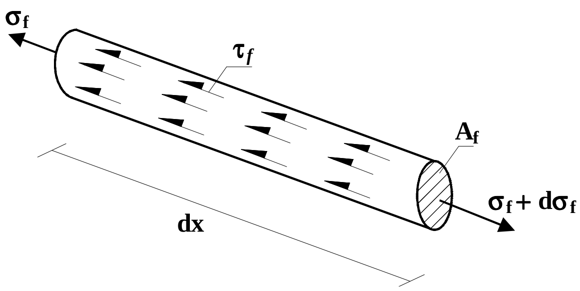

Figure 4.4 – Equilibrium FRP bar

Therefore referring to two consecutive strain gauges, ranging Δx_i= 70 mm, the equilibrium equation, assuming uniform distribution of the bond stress in the analyzed discrete interval gives equation 4.2:

$$\tau_x = E_f \frac{A_f}{u_f} \frac{\Delta \varepsilon_i}{\Delta x_i} \tag{4.2}$$

With τ_x the bond stress in the FRP reinforcement between two consecutive strain gauges, E_f the elastic modulus of the FRP reinforcement, A_f the cross-section area, u_f the perimeter of the FRP reinforcement and $\Delta\varepsilon_i$ the measured strain difference between the two considered strain gauges. In Table 4.4 reference is made (unless stated otherwise) to the average test results obtained by the two equivalent specimens tested for each parameter combination. The standard deviation for each parameter is shown in brackets.

From experimental outcomes, an increase of load capacity equal to 21% was observed by heating the specimen C_SC to a temperature equal to 50°C. Further increases of temperature (65°C, 80°C and 100°C) resulted in a decrease of failure load for all the type of specimens tested, though the extent of reduction of failure load differs significantly. As demonstrated in [13-14] for EBR strengthening, the tendency of an increasing failure load with increasing temperatures up to 50°C (specimen C_SC_50) can be related to the difference in coefficient of thermal expansion between concrete and CFRP and/or the reduced Young's modulus of the adhesive.

Table 4.4 –Test results

Specimens	F_u [kN]	$F_{u,T}/F_{u,20}$ [-]	τ_{av} [MPa]	τ_{max} [MPa]	$\tau_{max,T}/\tau_{max,20}$ [-]	Failure mode
C_SC_20	57.8 (0.2)	1.00	6.4	12.8 (0.2)	1.00	DB C/R
C_SC_50	70.2 (2.9)	1.21	7.8	14.2 (1.7)	1.11	DB C/R
C_SC_65	52.0 (3.9)	0.90	5.8	9.9 (0.8)	0.77	PO
C_SC_80	31.9 (5.2)	0.55	3.5	7.5 (1.98)	0.58	PO
C_SC_100	24.0 (0.6)	0.42	2.7	4.45 (-)	0.34	PO
G_SW_20	50.6 (2.2)	1.00	5.6	8.5 (0.81)	1.00	DB C/R
G_SW_65	41.0 (1.2)	0.81	4.6	6.4 (0.3)	0.75	PO
G_SW_100	14.7 (0.2)	0.29	1.6	2.6 (-)	0.31	PO
C_STR_20	46.5 (6.7)	1.00	5.2	7.8 (0.0)	1.00	DB C/R
C_STR_100	22.3 (6.5)	0.48	2.4	3.8 (0.13)	0.49	PO

(-) data of one specimen

Moreover it was observed that, considering that all the NSM FRP rods/strips were embedded with the same adhesive, specimens strengthened with CFRP rods/strips show a lower decrease of failure load with respect to GFRP rods with increasing temperature (e.g. the decrease of load at 100°C equals respectively 58% and 52% for NSM FRP carbon rods and strips with respect to NSM FRP glass rods that was equal to 71%). This difference disappears when the maximum bond shear stresses are compared. This can be justified considering the decreasing of bond strength of the concrete/adhesive interface with increasing temperature and the change of type of bond failure by increasing the temperature (see section 4.5.2). The smaller decrease of ultimate load found for specimens strengthened with CFRP strips compared to specimens strengthened with CFRP rods can be related to several aspects: the smaller width of the groove (see table 4.1) in which the NSM strip is embedded, the higher confinement effect of the concrete on NSM strips (induced by a larger bond surface), the different stress distribution, the bond stiffness and the surface configuration. It was, also, observed that specimens strengthened with NSM FRP strips have a higher standard deviation than the others specimens.

Increasing the temperature at and beyond the glass transition temperature, T_g, of the adhesive results in a reduction of the maximum bond stress, τ_{max}, (caused mainly by the decreasing of bond strength of the concrete/adhesive interface with increasing temperature) and in a change of the type of bond failure (see section 4.5.2). The reduction of peak bond stress as function of temperatures is also plotted in Figure 4.5. The small impact on peak bond stress at elevated temperature (100°C) of the NSM strip ($\tau_{max,T}/\tau_{max,20}$=0.49) is mainly related to its relatively low cross sectional area/perimeter ratio with respect to round bars ($\tau_{max,T}/\tau_{max,20}$=0.34 and $\tau_{max,T}/\tau_{max,20}$=0.31 for CFRP and GFRP rods respectively), whereas the temperature influence mainly acts on the bond interface.

No complete bond degradation at the FRP-concrete interface is observed by increasing the temperature up to $1.5T_g$.

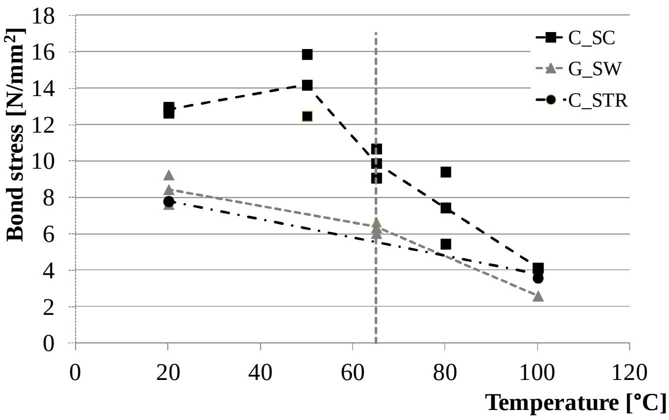

Figure 4.5 – Bond shear stresses as a function of temperature

4.5.2 Failure modes

Two different types of failure modes were observed. Debonding at the concrete/epoxy interface (DB C/R) with varying degrees of concrete damage, depending on the bar/strip surface configuration, was the predominant failure mode observed for specimen tested at 20°C and 50°C (the failure of specimen C_SC_20 and G_SW_20 is reported in Figure 4.6 a-b as reference). For GFRP specimens the higher deformed area of spirally wound rods let to a more brittle failure with respect of that observed in specimens strengthened with sand coated rods and smooth strips. Indeed for specimens strengthened with GFRP rods, once the longitudinal cracks had developed along the bond length, the epoxy cover spalled together with a layer of concrete surrounding the grooves (see Figure 4.6b).

Increasing the temperature at or beyond the adhesive transition temperature leads to a change in failure mode. Indeed at temperatures higher than 50°C the failure mode changes from debonding at the concrete/epoxy interface to debonding at the FRP/epoxy interface (PO) with a pull out of the FRP rod/strip (see Figure 4.6c). This type of failure mode occurs as a pure interfacial failure and is identified by the absence of adhesive attached to the bar surface after failure. This change in failure mode is a clear indication of deterioration of mechanical properties of the epoxy adhesive at elevated temperatures; indeed at temperatures higher than 50°C the failure aspect becomes similar for all the specimens, no matter which was the bar surface configuration, as in this condition the decrease of the adhesive's mechanical property is always governing.

a) b) c)

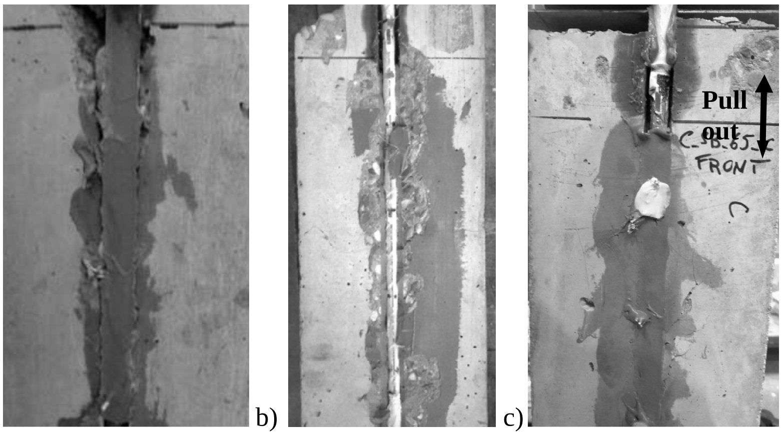

Figure 4.6 – Debonding concrete/epoxy interface at 20 °C for specimen C_SC (a) and G_SW (b) and pull out of bar at 65 °C for specimen C_SC (c)

4.5.3 Strain distribution

The bond behavior along the bond length is reflected by the strain readings at different load levels. Figures 4.7- 4.9 show the strain distribution (average strain of two sides) along the bar bonded length for specimens tested at 20°C. Each curve is corresponding to a specific load represented as a percentage of the ultimate load (it has to be noted that for some of the specimens the strain gauges get damaged before reaching the failure load). The x-axis starts from the loaded end of the FRP rod/strip and ends at the end of the concrete block (free end). The first point for each load level is the theoretical strain, ε_t, computed as equation 4.3

$$\varepsilon_t = \frac{F_u}{E_f A_f} \tag{4.3}$$

Where F_u is the load of one FRP bar/strip, E_f is the elastic modulus of the FRP bar/strip and A_f is the cross section area.

The strain measurements were connected with straight lines to visualize the tendency of the strain distribution. It should however be realized that the actual strain distribution is not necessarily linear distributed between two points. From the strain distribution diagrams the load transfer mechanism can be observed. The strain distribution along the bond length is characterized by an almost exponential trend of strains at lower load levels and the strain gauges far from the loaded end do not read strains. The distance required for the strain to reach almost zero (the strain value is defined negligible at 1% of the strain measured at the loaded end for each load level, %F_u) in the stage of linear elastic material behavior is the so-called transfer length.

At lower load levels (a load value equal to 20kN, equal to almost 40% of the ultimate load of specimens tested at room temperature, was chosen for all the specimens) and at ambient temperature (20°C) the strains are concentrated respectively in the first 150 mm from the loaded end of the FRP reinforcement for specimens strengthened with carbon bars (C_SC) and glass bars (G_SW) and 100 mm for specimens strengthened with carbon strips (C_STR). This means that the FRP shear and normal stresses are mainly transferred in this area. Once debonding starts at the loaded end, a further increase in load gradually displaces the transfer region towards the unloaded end and the strain distribution gradually approaches a linear shape (see Figure 4.7-4.9). It has to be noted that specimens strengthened with glass bars evidenced a more concentrated strain distribution along the bond length (around 220 mm at 80% of failure load, as shown in Figure 4.8) with respect to specimens strengthened with carbon bars and strips in which, at loads close to failure, the full available bond length of 300 mm is developed. Considering that, at

20°C, the glass bars achieved a failure load comparable with that achieved by the carbon bar/strips, the different behavior in strain distribution may be related to the surface configuration of the glass bar as well as to the different Young's modulus (126 GPa for CFRP rods, 124 GPa for CFRP strips and 40.8 GPa for GFRP rods) whereas smaller transfer length is expected for stiffer material behaviour.

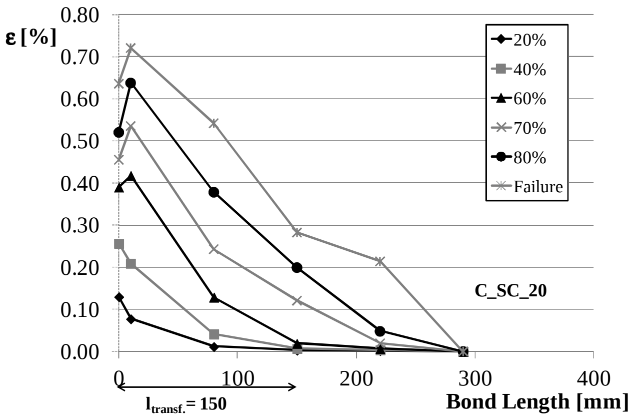

Figure 4.7 – Strain distribution specimen C_SC_20

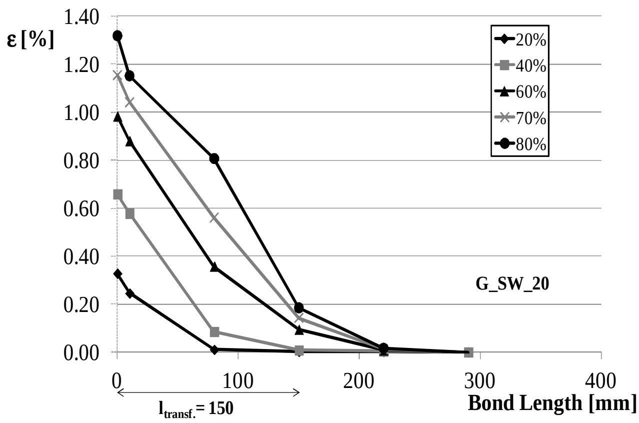

Figure 4.8 – Strain distribution specimen G_SW_20

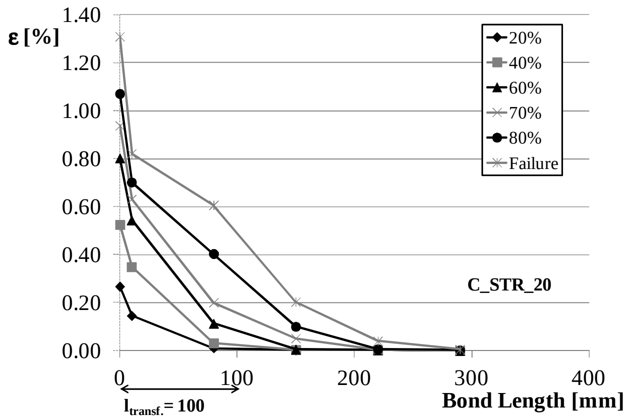

Figure 4.9 – Strain distribution specimen C_STR_20

In Figure 4.10- 4.13 the mechanical strain distribution (strain average values of two specimens) of specimens strengthened with carbon bars (C_SC) tested at different service temperatures are reported. The strain measurement just before applying the load was taken as reference, to make a clear distinction between the mechanical and thermal strain. The transfer length was evaluated for a chosen load level equal to 20 kN (equal to almost 40% of the ultimate load of specimens tested at room temperature), which belongs to the elastic stage of specimens tested at room temperature. It has to be noted that for specimen tested at 80°C and 100°C the load level of 20 kN is no longer corresponding to the elastic stage of the specimens.

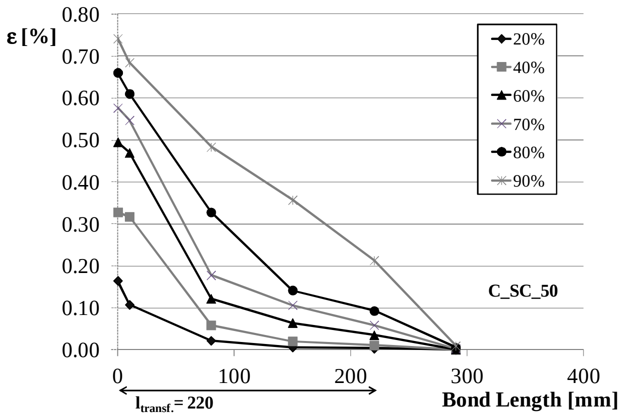

Figure 4.10 – Strain distribution of specimen C_SC_50

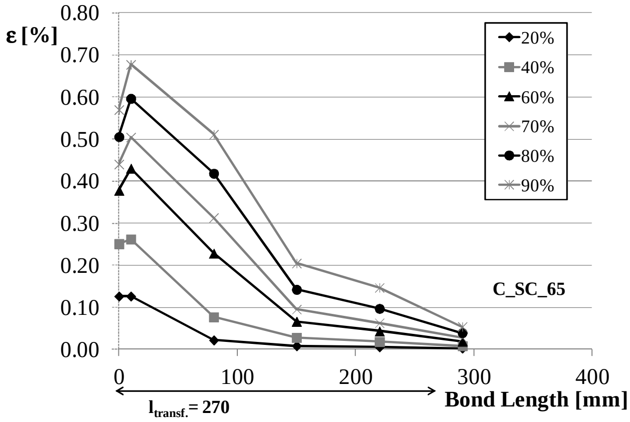

Figure 4.11– Strain distribution of specimen C_SC_65

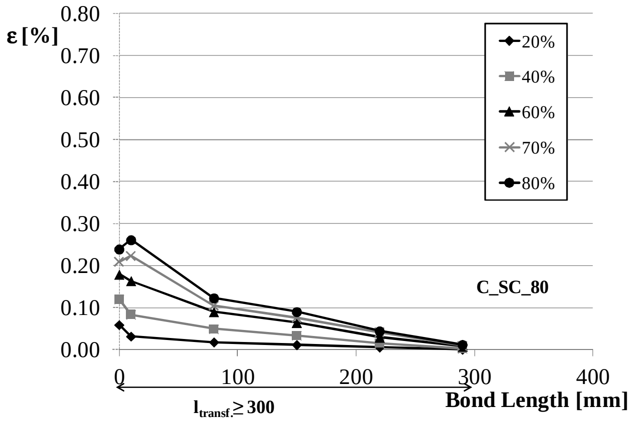

Figure 4.12 – Strain distribution of specimen C_SC_80

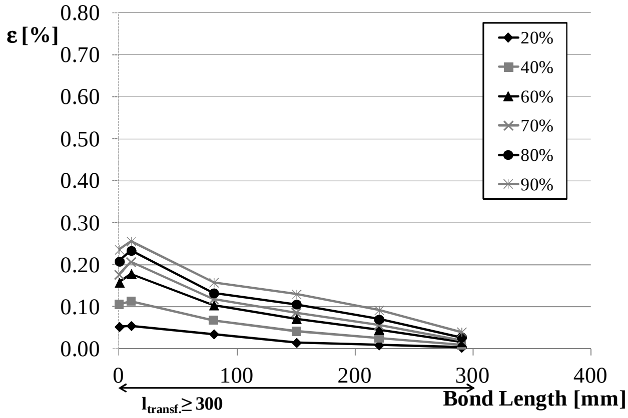

Figure 4.13 – Strain distribution of specimen C_SC_100

It was observed that the transfer length at room temperature increased by increasing the temperature, with a consequent more linear distribution of strains over the FRP bond length. In particular for specimens tested at 80°C and 100°C the transfer length increased with a factor of 2.0 with respect to 20°C. Similar behavior was observed for specimens strengthened with GFRP rods and CFRP strips. The strain distributions at different temperatures for all specimens are reported in Appendix A (section A.3). An overview of the increase of transfer length with increasing temperature is given in Table 4.5.

Table 4.5 –Evaluated transfer length at 20 kN as a function of the temperature

	20°C	50°C	65°C	80°C	100°C
L_t C_SC [mm]	150	220	270	≥ 300	≥ 300
L_t G_SW [mm]	150	-	270	-	≥ 300
L_t C_STR [mm]	100	-	-	-	≥ 300

4.5.4 Shear Stresses

The double bond shear tests were carried out in two different steps: (1) heating of the specimens and (2) loading of the specimens at constant temperature. During both steps shear stresses are transferred from the FRP NSM strengthened systems to the concrete. Applying a load to the NSM FRP strengthened bars will result in mechanical shear stresses at the concrete/FRP interface. Moreover it has to be noted that, during the heating of the specimen, the difference in coefficient of thermal expansion between the concrete (α_c=10x10^{-6}/°C) and the FRP (e.g. α_f= -1 to 0 x10^{-6}/°C in the fiber direction for CFRP) will, also, result in the development of shear thermal stresses at the concrete/FRP interface and corresponding normal thermal stresses in the FRP with increasing temperature.

The shear thermal stresses at the concrete/FRP interface were determined analytically according to a kinematic model developed in [15]. The model only takes linear elastic material behavior of the concrete and FRP into account as thermal stresses can be expected to be small. The model, in accordance to previous studies [14] was modified considering also the shear stiffness of the adhesive layer, which was not included in [15], in order to take into account the effect of the reduced Young’s modulus of the adhesive at elevated temperature. The model is described in details in Appendix A (section A.1). The shear thermal stresses are determined by equations 4.4 and 4.5 for round bars and strips respectively:

$$\tau_c(x) = E_f \frac{d_b}{4} \omega \frac{\varepsilon_{\Delta T}}{\cosh\left(\omega \, l/2\right)} \sinh(\omega x) \tag{4.4}$$

$$\tau_c(x) = E_f t_f \omega \frac{\varepsilon_{\Delta T}}{\cosh\left(\omega \, l/2\right)} \sinh(\omega x) \tag{4.5}$$

where:

- E_f is the Young’s modulus of the FRP reinforcement
- $\varepsilon_{\Delta T} = \alpha_c \Delta T$ is the thermal strain of the concrete
- α_c is the coefficient of thermal expansion of concrete
- $\omega^2 = \frac{4k_G}{E_f d_b}$ for round bars and $\omega^2 = \frac{2k_G}{E_f t_f}$ for strips
- $\frac{1}{k_G} = \frac{1}{k_{Gc}} + \frac{1}{k_{Ga}}$

- $k_{Gc} = \dfrac{E_c(T)}{2 \cdot (1+\nu_c) \cdot h_{c,ef}}$ is the stiffness of the concrete
- $k_{Ga} = \dfrac{E_a(T)}{2 \cdot (1+\nu_a) \cdot t_a}$ is the stiffness of the adhesive
- $E_c(T)$ is the young modulus of the concrete at temperature T
- $h_{c,ef}$ is the effective height equal to 50 mm or two times the maximum aggregate size
- $E_a(T)$ is the Young modulus of the adhesive at temperature T
- t_a is the thickness of the adhesive layer
- d_b is the diameter of the FRP bar
- t_f is the thickness of the FRP strip
- ν_c and ν_a are the Poisson ratio of the concrete and the adhesive assumed equal to ν_c=0.2 and ν_a= 0.3 respectively
- *l* is the bonded length
- x is the distance from the middle of the bonded length

The analytical shear stresses for specimen C_SC at different temperatures are given in Figure 4.14.

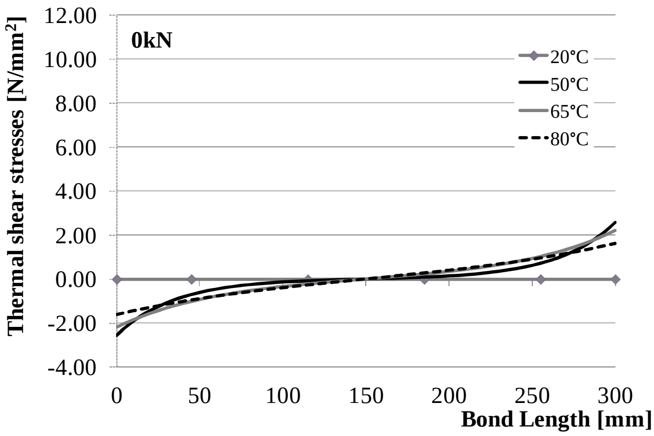

Figure 4.14 – Thermal shear stresses specimen C_SC at different temperatures and at 0kN

The mechanical shear stresses, induced by loading of the FRP strengthened systems were determined from experimental data by using equation 4.2 (see section 4.5.1). The shear stress distributions are plotted in Figure 4.15 - 4.17 for specimen

C_SC_20, C_SC_50, C_SC_65 and C_SC_80 at different failure load. Note that shear stresses are calculated in the midpoint between two strain gauges and considering the strain at the loaded end (see section 4.5.3 and equation 4.3). Shear stresses build up from zero at bond length 0 mm (free surface of the adhesive at the loaded end), as can be observed from Figure 4.16 and 4.17. This is also the case for low load levels (Figure 4.15), yet not visible from the calculated points, as in this case the peak shear stress is located very close to the loaded end.

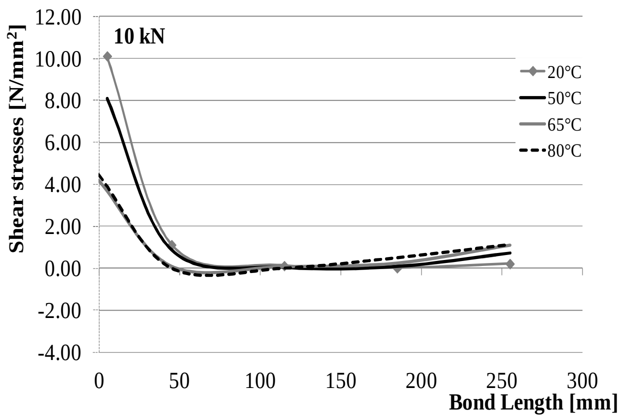

Figure 4.15 – Total shear stresses specimen C_SC at different temperatures and at 10kN

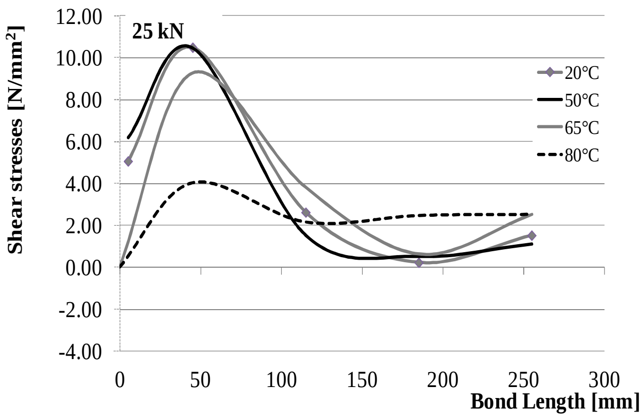

Figure 4.16 – Total shear stresses specimen C_SC at different temperatures and at 25kN

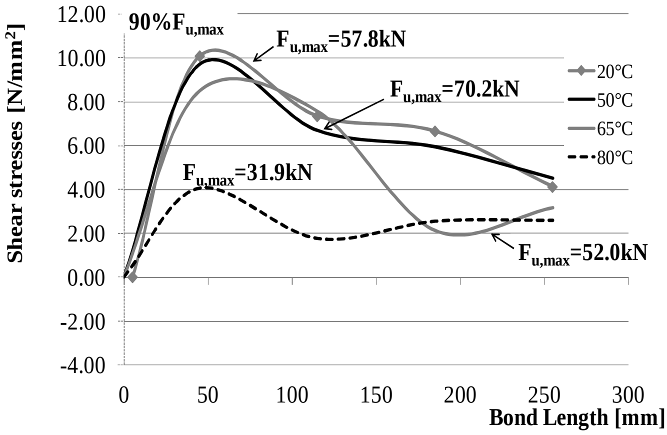

Figure 4.17 – Total shear stresses specimen C_SC at different temperatures and at 90% of the failure load

It was observed that the shear thermal stresses are developed at the ends of the bonded length, where the FRP force is transferred to the concrete (see Figure 4.14). Increasing the temperature from 50°C to 65°C and 80°C a reduction of the peak thermal shear stress is observed, mainly due to the reduced Young modulus of the adhesive. Moreover, in accordance to previous studies [13-14], it is observed that at the loaded end of the FRP bar (0 mm), the direction of thermal shear stresses (Figure 4.14) is opposite to the direction of the shear stress induced by the loading (Figure 4.15). Therefore shear stresses due to the loading will first have to compensate the thermal shear stresses at the loaded end, resulting in a lower shear stress peak with increasing temperature (see Figure 4.15 - 4.16) which can explain the increasing failure load with increasing temperature up to 50°C (see Figure 4.17). Nevertheless, increasing the temperature to and/or beyond the glass transition temperature (T_g= 66°C for the adopted epoxy resin) a reduction of the bond strength of the adhesive governed over a possible positive influence induced by the shear thermal stresses. Indeed, as shown in Figure 4.16 - 4.17, increasing the temperature to 65°C and 80°C resulted in a more uniform distribution of stresses but in a significantly lower failure load.

4.5.5 Local bond stress – slip behaviour

The effect of bond strength degradation with increasing temperatures can be better understood by comparing the bond shear stress-slip curves with increasing temperatures. The slip, s(x), corresponding to the shear stress, τ(x), is calculated by integrating the experimental strain along the FRP bar/strip. In the discrete field one obtains:

$$s(x) = \sum_{i=1}^{n} \varepsilon_i \Delta_{xi} \tag{4.6}$$

It has to be noted that the slip between the FRP reinforcement and the concrete can be also directly measured by the LVDT's during the test. However as observed by other researchers, due to the poor accuracy of the experimental measurement of the slip in particular with increasing temperature, it was preferred to derive the slip from experimental strain readings rather than using low accuracy slip readings. The experimental slip measurements were used as a general measure to evaluate possible eccentricities in loading during the test. In Figure 4.18 - 4.20 the bond stress-slip relationships of all the tested specimens at different temperature are reported. In these curves the bond shear stresses and the slip were evaluated considering the distance between the first and the second strain gauges as dx; therefore the shear bond stresses as well as the slip were evaluated at a distance equal to x= 45 mm from the loaded end. It has been observed, as discussed above, that increasing the temperature the stiffness of the adhesive is reduced. For temperatures up to 50°C (see Figure 4.18) the stiffness of the adhesive was not significantly reduced so that the beneficial effect of the thermal stresses yielded the higher bond stresses and failure load. Further increasing the temperature (up to 100 °C for this testing program) resulted in a decrease of shear stresses and ultimate load mainly governed by the softening of the adhesive.

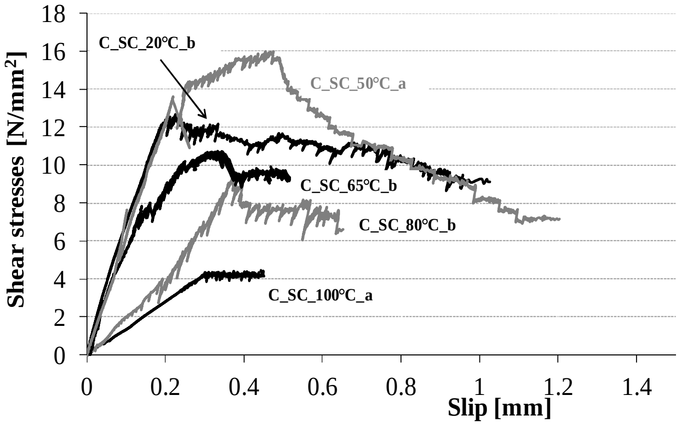

Figure 4.18 – Bond stress-slip curves specimen C_SC at different temperatures

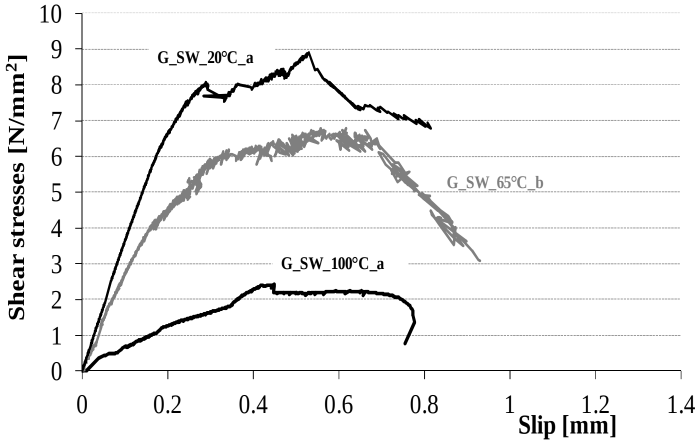

Figure 4.19 – Bond stress-slip curves specimen G_SW at different temperatures

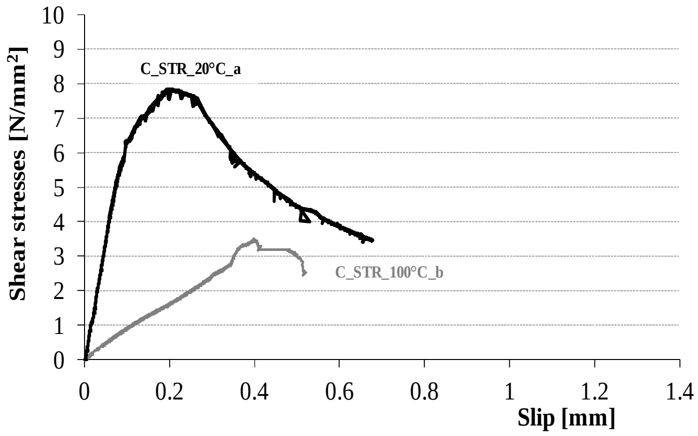

Figure 4.20 – Bond stress-slip curves specimen C_STR at different temperatures

For a temperature at/or beyond the glass transition temperature, a change in the bond shear-slip relationship is observed. For instance, for temperatures equal to 80°C and 100°C, the bond shear-slip relationship is characterized by an ascending branch followed by an almost horizontal plateau (with a sudden drop in shear stress at the end of this plateau). This different behavior with respect to that of specimens tested at temperature below the T_g can be, once again, related to the softening and strength reduction of the adhesive, also resulting in a change in failure mode.

4.6 Conclusions

A series of 20 double bond shear tests at different temperatures (up to 100 °C) have been conducted in order to investigate the influence of temperature on the bond behavior of the FRP-adhesive-concrete interface for the NSM FRP strengthening technique. Based on the experimental outcomes it is observed that increasing the temperature up to 50°C resulted in an increase of failure load and bond stresses, while further increase of temperature (up to 100°C for the presented test program) resulted in a decrease of failure load and change of failure mode. This is in accordance with previous studies [13-14]. For temperatures below the glass transition temperature the failure mode is characterized by debonding at the concrete/resin interface with varying degrees of concrete damage, as a function of the FRP bar surface configuration, while increasing the temperature at/or beyond the adhesive T_g resulted in a debonding of the FRP NSM bars at the adhesive/bar interface (pull-out of the bar). However the decrease of the failure load at an elevated temperature equal to T_g is equal to approximately 10% and 18% for specimens strengthened with CFRP (C_SC) and GFRP bars (G_SW) respectively and no complete degradation of bond strength is observed for temperatures up to $1.5T_g$ for all the tested specimens. It is, moreover, observed that the transfer length increased by increasing the temperature, with a consequent more linear distribution of strains over the FRP bond length. In particular for specimens tested at a temperature higher than T_g the initial transfer length increased with a factor 2 to 3 with respect to the transfer length at 20°C.

Based on the analysis of the shear stresses it can be concluded that the increasing failure load at 50°C is mainly due to thermal shear stresses, induced by the difference of coefficient of thermal expansion between the FRP and the concrete. Above this temperature the softening and strength reduction of the adhesive are governing over a possible positive effect of thermal stresses induced by heating of the specimens.

Based on the tests, the local bond stress-slip behavior could be characterized experimentally. At elevated temperatures beyond T_g the bond stress-slip behavior becomes elasto-plastic.

4.7 References

1. De Lorenzis L., Lundgren K., Rizzo A. (2004). “Anchorage length of near-surface mounted FRP bars for concrete strengthening – Experimental investigation and numerical modeling”. *ACI Structural Journal*, 101(2), 269-278.

2. De Lorenzis L., Teng J.G. (2007). “Near-surface mounted FRP reinforcement: an emerging technique for structural strengthening”. *Composite Part B: Eng*, 38, 119-143.
3. Ceroni F., Pecce M., Bilotta A, Nigro E., (2012). “Bond behavior of FRP NSM systems in concrete elements”. *Composites Part B: Eng*, 43, 99-109.
4. Sena Cruz J.M. and Barros. J. (2004). “Modeling of bond between near surface mounted CFRP laminate strips and concrete”. *Computers and Structures*, Vol 82, Issues 17-19, 1513-1521.
5. Seracino R., Saifulnaz M.R.R., Oehlers D.J. (2007). “Generic Debonding Resistance of EB and NSM Plate-to-Concrete Joints”. *J. Comp. Constr.*, ASCE, 11(1), 62-70.
6. Palmieri A., Matthys S., Taerwe L., (2011). “Influence of high temperature on bond between NSM FRP bars/strips and concrete”. *In Proc. of the 10th International Symposium on FRP Reinforcement for Reinforced Concrete Structures (FRPCS-10)*, Tampa, Florida, 12 pp.
7. Palmieri A., Matthys S., Taerwe L. (2011). “Bond behavior of NSM FRP bars at elevated temperatures”. *In Proc. of SMAR 2011 First Middle East Conference on Smart Monitoring, Assessment and Rehabilitation of Civil Structures*, Dubai, UAE, 8 pp.
8. ISO 11357-2 (1999). “Plastics – Differential scanning calorimetry (DSC)- Part 2: Determination of glass transition temperature”. *International Organization for Standardization*.
9. NBN-B15-220 (1990). “Proeven op beton- Bepaling van de druksterke”.
10. NBN-B15-214 (1990). “Proven op beton-buigproef op betonprisma’s”.
11. EN ISO 527-2 (1993) “Plastics – Determination of tensile properties- Part 2: Test conditions for moulding and extrusion plastics”. *International Organization for Standardization*.
12. Seracino R., Jones N.M., Page M.W., Ali M.S.S., Oehlers D.J. (2007). “Bond strength of near surface mounted FRP-to concrete joints”. *J. Comp. Constr.* ,ASCE, 11(4), 401-409.
13. Blontrock H. (2003). “Analyse en modellering van de brandweerstand van betonelementen uitwendig versterkt met opgelijmde composietlaminaten (in Dutch)”. *Ph-D Thesis*, Faculty of Engineering, Department of Structural Engineering, Ghent University, Belgium, 412 pp.

14. Klamer E.L. (2009). “Influence of temperature on concrete beams strengthened in flexure with CFRP”. *PhD thesis*, Department of architecture, building and planning, Eindhoven University of Technology, the Netherlands, 250 pp.

15. Di Tommaso A., Neubauer U., Pantuso A., Rostasy F.S. (2001). “Behaviour of adhesively bonded concrete CFRP joints at low and high temperatures”. *Mechanicsof Composites Materials*, 37(4), 327-338.

Chapter 5
STRUCTURAL BEHAVIOUR OF RC MEMBERS STRENGTHENED IN FLEXURE WITH NSM FRP

5.1 Introduction

Before studying the behaviour of NSM FRP strengthened elements under fire exposure, their behaviour at ambient temperature has been investigated. Five beams (one unstrengthened and four beams strengthened in flexure with different NSM FRP systems and/or bonding adhesives) and three slabs (one unstrengthened and two slabs strengthened with different types of NSM FRP) are tested in four-point bending at room temperature. This study of the behaviour at ambient conditions forms the basis for studying the behaviour at and after fire exposure (see chapter 6). The experimental tests aim to investigate the structural performance of the NSM FRP strengthened beams and slabs. In this chapter the increase of flexural load carrying capacity, failure mode, load-deflection response and cracking of the tested specimens is presented and discussed. Moreover experimental results have been, also, analytically verified based on existing models for the structural behaviour of FRP strengthened RC members. Analytical models are used to predict the failure load, failure mode, load-strain behaviour of the constituent materials (concrete, steel and FRP), load deflection-curve and service load. A good correspondence between the experimental and analytical results is observed.

5.2 Description of specimens and material properties

Tests specimens comprised 5 steel reinforced concrete beams with rectangular cross section (width 200 mm and height 300 mm), one of which was the reference specimen and the others were strengthened in flexure with different NSM FRP systems. Furthermore, 3 steel reinforced concrete slabs with rectangular cross section (width 400 mm and height 150 mm), one of which was the reference specimen and the others were strengthened in flexure. The dimensions of the beams and slabs are given in Figure 5.1-Figure 5.2. For the beams internal reinforcement deformed steel bars S500 were used; two steel rebars with diameter 16 mm and two steel rebars with diameter 10 mm were used as lower and upper longitudinal reinforcement respectively. The beams shear reinforcement consisted of steel stirrups with 8 mm diameter, spaced every 100 mm in the shear span and every 150 mm in the constant moment region. The concrete cover was 30 mm. For the internal reinforcement of the slabs 4 deformed steel bars S500 with a diameter 8 mm in the longitudinal direction and deformed steel bars S500 with diameter 6 mm, spaced at a distance of 200 mm, in the transversal direction were used. The reinforcing bars were tied together at their junction points with steel binders. The concrete cover was 25 mm. The FRP reinforcement of the NSM FRP strengthened beams consisted of CFRP sand-coated rods (type Aslan 200, supplied by Fortius/Hughes Brother), GFRP ribbed rods (type Combar supplied by Schöek) and CFRP smooth strips (type Aslan 500 supplied by Hughes Brothers). The FRP reinforcement of the NSM FRP strengthened slabs consisted of GFRP spirally wound rods (type Aslan 100, supplied by Fortius/Hughes Brothers) and BFRP sand coated rods (type Rockbar supplied by Magmatech). The length of the FRP NSM was taken, for all the specimens, as 2800 mm. Two commercial epoxy resins (type Sikadur-30, supplied by Sika and Fortresin CFL, supplied by Fortius/Hughes Brothers) were used as embedding adhesive, as a function of the type of FRP bar/strip as requested by the manufacturers. For beam B4 the embedding adhesive consisted in an expansive cementious mortar (type Sikagrout-212, supplied by Sika). Figure 5.1 and Figure 5.2 show the strengthening scheme of the beams and slabs and the detailed configuration of the strengthened section. Specimen details are also indicated in Table 5.5.

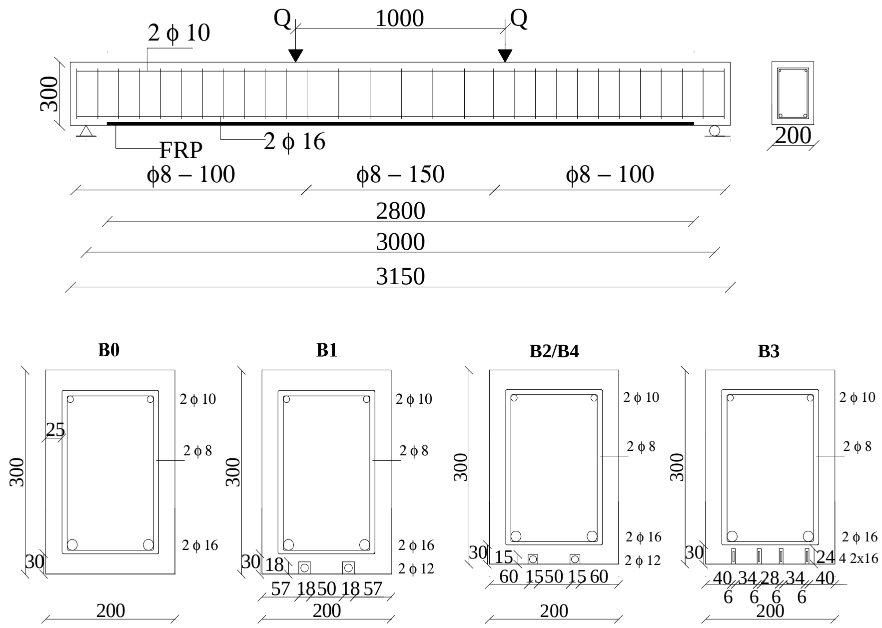

Figure 5.1 – Beam specimens

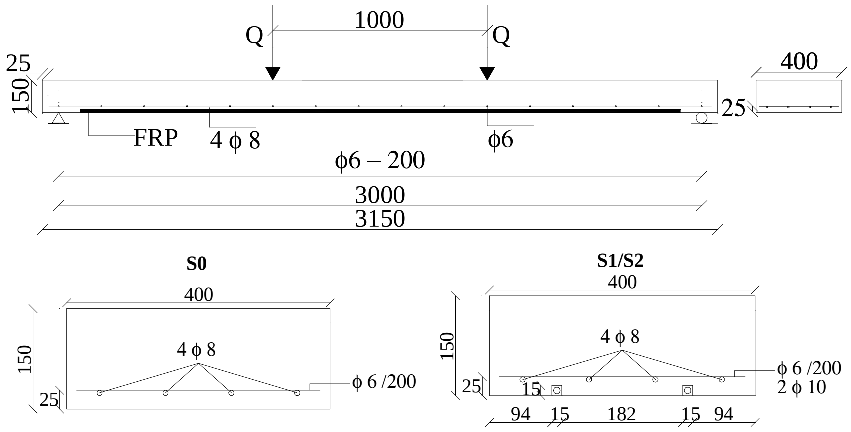

Figure 5.2 – Slab specimens

The concrete mix design was identical for all the elements (beams and slabs) and incorporates siliceous aggregates with a maximum diameter of 16 mm. The concrete composition (per m^3) is given in Table 5.1. Three different batches were manufactured in the laboratory. Tested properties of the fresh concrete included slump, flow test and density (see Table 5.2). At an age of 28 days and at the age of testing the beams and slabs, the properties of the hardened concrete are determined by means of Belgium standard tests [1-2]. The mean cylinder compression strength, f_c, determined on cylinders with a diameter of 150 mm and a height of 300 mm (at an age of 28 days and at the age of testing of the beams/slabs), the mean compression strength, $f_{c,cub}$, determined on cubes with side length 150 mm (at age of testing), the flexural tensile strength, $f_{ctb,}$ determined by means of 3-point bending tests on prisms 150 mm x 150 mm x 600 mm and a span of 500 mm (at age of testing), the splitting tensile strength, f_{cts}, determined by splitting tests on the remaining halves of the prisms for the bending test (at age of testing) and the Young modulus, E_c, determined on cylinders with a diameter of 150 mm and a height of 300 mm (at age of testing) are given in Table 5.3.

Table 5.1 – Concrete composition beams and slabs tested at room temperature

Material	Composition
Fine sand 0/4	655.0 kg
Fine aggregate 2/8	190.0 kg
Coarse aggregate 8/16	1120.0 kg
Cement CEM I 52.5	300.0 kg
Water	165.0 kg

Table 5.2– Properties fresh concrete

Batch	Slump [mm]	Flow test	Density [kg/m^3]
RT_1	45	2.22	2350
RT_2	50	1.67	2388
RT_3	55	1.74	2394

Table 5.3–Properties hardened concrete

Batch	At 28 days	At age of testing				
	f_c [N/mm^2]	f_c [N/mm^2]	$f_{c,cub}$ [N/mm^2]	$f_{c,tb}$ [N/mm^2]	$f_{c,ts}$ [N/mm^2]	E_c [N/mm^2]
RT_1	41.5	42.1	48.6	5.8	3.8	30653
RT_2	44.2	45.1	51.6	5.1	3.7	36309
RT_3	44.2	46.2	52.5	4.8	3.6	33801

For the internal steel reinforcement, deformed bars S500 were used with guaranteed characteristic yield strength of 500 N/mm^2. Properties of the steel were determined by means of tensile tests according to [3]. The properties are given in Table 5.4.

Properties of the FRP NSM strengthening systems, as reported by the manufacturers, in terms of type of material, FRP bar dimension, tensile strength, f_f, ultimate strain, ε_{fu}, and elastic modulus, E_f, are given in Table 5.5. An overview of the test matrix in terms of specimen designation, batch number and age of testing is also given in Table 5.5.

Table 5.4–Properties steel reinforcements

Steel	Diameter [mm]	$f_{s,y}$ [N/mm^2]	$f_{s,u}$ [N/mm^2]	$\varepsilon_{s,u}$ [%]	E_s [N/mm^2]
ϕ16	16	570	660	10.5	205000
ϕ10	10	575	650	10.9	205330
ϕ8	8	560	639	11.2	208000

Table 5.5–Test matrix of beams and slabs tested at room temperature

Spec	FRP	Dim. [mm]	f_f [MPa]	E_f [GPa]	ε_{fu} [%]	Adhesive	Batch no.	Age at test [days]
B0	-	-	-	-	-	-	RT_1	109
B1	Combar GFRP	12.0	1350	60	1.8	Sikadur 30	RT_1	110
B2	Aslan200 CFRP	9.53	1900	126	1.6	Fortresin CFL	RT_2	120
B3	Aslan500 CFRP	2 x 16	2068	124	1.7	Fortresin CFL	RT_2	121
B4	Aslan200 CFRP	9.53	1900	126	1.6	Sikagrout 212	RT_3	120
S0	-	-	-	-	-	-	RT_1	111
S1	Aslan100 GFRP	10.0	760	40.8	1.8	Fortresin CFL	RT_3	121
S2	Rockbar BFRP	10.0	1170	59.0	2.0	Sikadur 30	RT_3	122

5.3 Specimens preparation and test procedure

During the first 7 days after casting the specimens remained covered with a plastic foil. The formwork (side faces) was removed after 1 day. At an age of 7 days, the beams were placed on supports and stored (uncovered) in the laboratory until testing. The NSM FRP reinforcement was applied to the beams at least 14 days before testing, according to the following procedure. Installation of the NSM FRP reinforcing bars/strips begins by making the specified grooves in the concrete cover on the tension surface of the beams/slabs with a special concrete saw with a diamond blade (see Figure 5.3 a). The dimensions of the grooves (see Figure 5.1 and Figure 5.2) were defined in order to be at least 1.5 times the diameter, d_f, of the NSM FRP bars and at least 3 times the width and 1.5 times the height of the NSM FRP strips. Each of the strengthened beams and slabs was turned upside-down during the groove cutting operations to allow the groove to be easily and precisely cut into the concrete cover. After cutting, the grooves were air-blasted to remove debris and fine particles to ensure proper bond between the epoxy adhesive and the concrete. The grooves were filled over half way with the adhesive (epoxy or mortar) as shown in Figure 5.3b (in between the grooves for ease of cleaning, the soffit of the element was temporarily covered with tape). The NSM FRP bars/strips were inserted into the grooves and lightly pressed to allow the adhesive to flow around the bars/strips (see Figure 5.3c). Finally more adhesive was applied if needed and the surface was leveled (see Figure 5.3d). 7 days after installation of the FRP NSM bars/strip the specimens were turned upside-down to the original position and stored in the laboratory until testing.

Figure 5.3 – Specimens preparation (a) cutting of the grooves (b) filling of the grooves with epoxy (c) installation FRP bars and (d) final view bottom side.

The specimens were tested in 4-point bending as shown in Figure 5.1 and Figure 5.2. The load was applied by means of two hydraulic jacks with a capacity of 500 kN. The load was increased stepwise (to allow for manual measurements) until yielding of the internal steel, after which the load was gradually increased until failure. Point load increments of 3kN and 2kN were used until first cracking for beams and slabs respectively, while thereafter increments of 10kN and 4kN were applied. An unloading-reloading cycle was incorporated in the loading scheme of the unstrengthened beam B0 ad unstrengthened slab S0 at 30kN and 8kN respectively and at 40kN and 10kN for the strengthened beams and strengthened slabs respectively. During the tests, both manual and electronic measurements were taken (see Figure 5.4 and Figure 5.5).

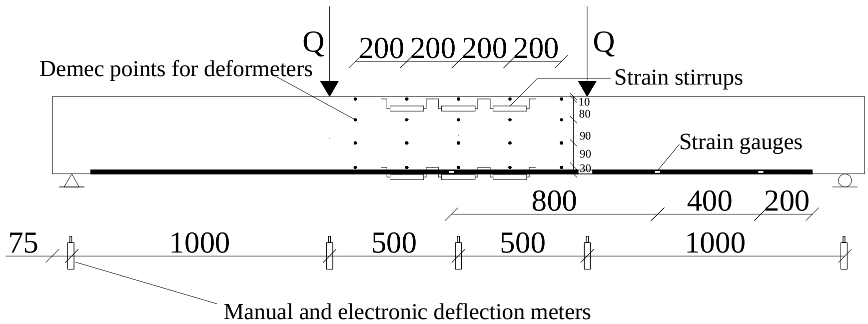

Figure 5.4– Measurement equipment beams tested at room temperature

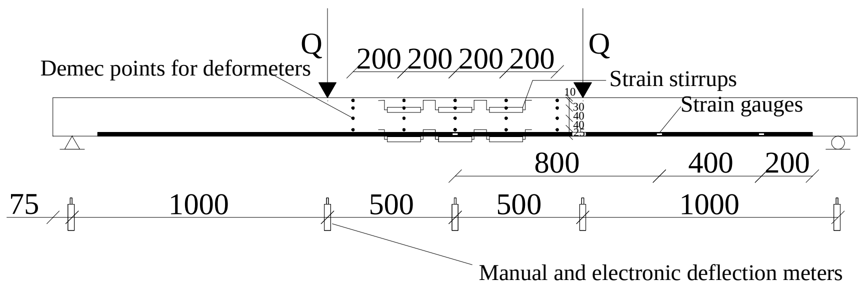

Figure 5.5 – Measurement equipment slabs tested at room temperature

The deflection of the specimens was measured at midspan, under the point loads and at the supports, using dial gauges (manual measurements) and linear variable displacement transducers, LVDTs (electronic measurements). Mechanical deformeters with a gauge length of 200 mm were used to measure manually concrete deformations in the central zone of the specimens, according to the arrangement shown in Figure 5.4 and Figure 5.5. This arrangement allows to take an average of ten measurements (two side faces) at several levels over the specimen depth. The strains were also measured electronically by means of strain stirrups (U-shaped stirrups instrumented with strain gauges). Six strain stirrups were applied on one side of the specimen. Three of them are measuring the strain of the concrete as close as possible to the level of the fibre with the maximum compressive strain and the other three were applied on a side face of the specimen to record the concrete strain at the level of the internal steel reinforcement. Strains of the FRP were recorded by means of strain gauges positioned at three different locations (at midspan, at 800 mm and 1200 mm from the midspan on one FRP bar). The limited number of strain gauges was considered in order to limit their influence on the bond mechanism. Moreover, at each load interval, the appearance and development of cracks were indicated after visual inspection and crack widths were recorded by means of a crack microscope.

5.4 Experimental results

5.4.1 Failure mode

The reference beam and slab failed by yielding of the steel followed by concrete crushing. Beams B1 and B3 failed by FRP debonding with detached concrete cover below the steel rebars as shown in Figure 5.6 and Figure 5.7. The debonding of the NSM bars/strips was preceded by a typical for flexure vertical cracking of the beam in the pure bending region. The debonding was, moreover, preceded by a cracking noise indicating the internal cracking of the epoxy followed by the formation of inclined and longitudinal cracks in the concrete surrounding the grooves. These splitting longitudinal cracks led to the loss of bond of the NSM FRP reinforcement followed by a loss of the concrete cover likely starting in the maximum moment region and moving to one of the supports. The NSM bars/strips debonded from the beam with the concrete remaining attached to the surface of the reinforcement over the whole depth of the groove. Failure of beam B2 and B4, strengthened with sand coated CFRP bars embedded with epoxy resin (beam B2) and grout mortar (beam B4), was due to splitting of the epoxy cover in the groove followed by complete debonding of the FRP reinforcing bars at the CFRP-adhesive interface as shown in Figure 5.8. Initiation of the cracking in the epoxy was accompanied by a distinct noise followed by progressive cracking of the epoxy paste. Longitudinal splitting cracks, which developed in the epoxy cover, led to the loss of bond of the NSM CFRP reinforcing bars. The steel yielding/FRP bond failure was, except for beam B4, directly followed by concrete crushing. This indicates that the premature debonding occurred (for most of the beams) close to the expected failure assuming full composite action between FRP and concrete.

a)

b)

Figure 5.6 – Failure mode beam B1 (a) side view (b) bottom view

Figure 5.7 – Failure mode beam B3

a) b)
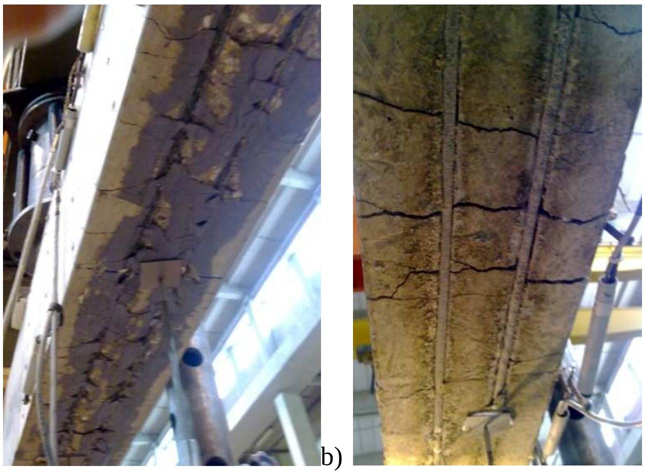

Figure 5.8 – Failure mode beam (a) B1 and (b) B4

Failure of slab S1 was due to steel yielding followed by concrete crushing and debonding of the FRP reinforcing bars due to the splitting of the epoxy cover in the groove as shown in Figure 5.9 a. Failure of slab S2 was governed by flexure failure mode with yielding of the steel reinforcement followed by concrete crushing. No debonding of the FRP basalt bars were observed up to failure.

a) b)
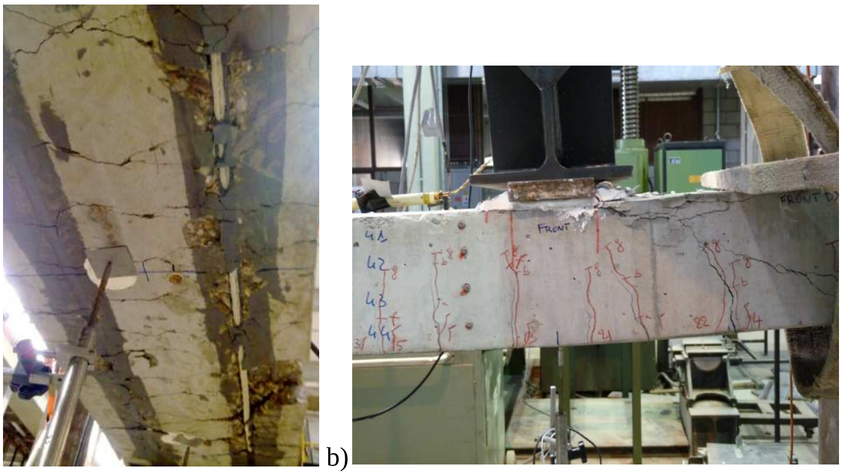

Figure 5.9 – Failure mode slab (a) S1 and (b) S2

5.4.2 Behavior at ultimate load

The main tests results are reported in Table 5.6 where Q_u is the ultimate load, $Q_u/Q_{u,ref}$ the ratio between the ultimate load of the strengthened beam/slab and the ultimate load of the unstrengthened beam/slab, Δ_u is the ultimate deflection at midspan, Δ_u/Δ_{ref} is the ratio between the ultimate deflection at midspan of the strengthened beam/slab and that of the unstrengthened beam/slab, ε_{fQu} the FRP strain recorded at the ultimate load, $\varepsilon_{fQu}/\varepsilon_{fu}$ the ratio between the strain recorded at ultimate load and the ultimate tensile strain of the FRP bar/strip. In Table 5.6 also the observed failure aspect is repeated, using the following designation: YS/CC is yielding of steel followed by concrete crushing, DB A/C is debonding at the adhesive/concrete interface and DB FRP/A is debonding at the FRP/adhesive interface.

Table 5.6 – Test results at ultimate load

Spec.	Q_u [kN]	Q_u/Q_{ref} [-]	Δ_u [mm]	Δ_u/Δ_{ref} [-]	ε_{fQu} [%]	$\varepsilon_{fQu}/\varepsilon_{fu}$ [-]	Failure mode [-]
B0	57.3	1.00	85.8	1.00	-		YS/CC
B1	96.9	1.69	64.6	0.75	1.30	0.73	DB A/C
B2	101.5	1.77	48.7	0.56	1.07	0.67	DB FRP/A
B3	102.2	1.78	63.3	0.74	1.18	0.69	DB A/C
B4	73.3	1.27	27.8	0.32	0.36	0.25	DB FRP/A
S0	14.6	1.00	117.4	1.00	-	-	YS/CC
S1	28.6	1.95	127.0	1.08	1.30	0.72	YS/CC - DB FRP/A
S2	31.0	2.12	124.0	1.05	1.42	0.71	YS/CC

Strength increases between 1.7 and 1.8 were obtained for the NSM FRP strengthened beams in which the FRP bars/strips were embedded with epoxy adhesive. The lower strength increase of the grout adhesive NSM FRP strengthened beams (strength increase equal to 1.27 with respect to the unstrengthened beam) is thought to have resulted from the lower tensile and shear strength of the grout adhesive as compared to that of the epoxy adhesive. Whereas the strengthened beams show a considerable increase of failure load, this corresponds to a decrease in ductility. Decrease of deflections, Δ_u, between 25% and 68% were obtained for the NSM FRP strengthened beams. Table 5.6 provides also the maximum tensile strain recorded in the NSM FRP bar/strip and its ratio to the ultimate tensile strain which indicates the efficiency of utilization of the strengthening system. The efficiency of the NSM FRP bar/strip ranged between 69% - 73% for the beams in which the NSM FRP bars/strip are embedded with epoxy resin and was equal to 25% for beam B4 in which the CFRP bars are embedded with grout adhesive, mainly due to the premature debonding of the NSM FRP strengthening system, as discussed above. Remark that full utilization of the NSM FRP reinforcement (i.e. failure by tensile rupture of the FRP) was not expected for any of the beams as the design concept of the beams was steel/yielding and concrete crushing even if the possibility of debonding is excluded.

The strengthened slabs experienced a strength increase equal to 1.95 and 2.12. Due to the significant increase of the slab load carrying capacity, provided by the NSM strengthening technique, the slabs failed in a flexural mode with steel yielding/concrete crushing followed, in the case of slab S1, by NSM FRP debonding but for a deflection that was higher than that observed for the unstrengthened slab. As observed previously for the strengthened beam, an elevated efficiency of utilization of the NSM FRP reinforcing bars is observed with FRP strains values equal to 72% and 71% for slab S1 and S2 respectively.

For all the specimens, the level of strengthening achieved for the NSM strengthened specimens is larger than the levels generally applicable for design of real FRP strengthening applications, which would normally be in the range of 50% for realistic live to dead ratios [4-5]. This unrealistic level of strengthening was intentional, however, in order to obtain a considerable increase of the service load of the strengthened member, at which the specimens will be loaded during the fire tests. The increase of service load is in the range of 20%-35% with respect to the unstrengthened element.

A comparison of the load-midspan deflection behavior of the strengthened beams and slabs with that of the unstrengthened specimens is shown in Figure 5.10 and Figure 5.11. Prior to cracking, the load-deflection behavior for all the strengthened specimens is similar to that of the respective unstrengthened element. This behavior indicates that using NSM FRP reinforcement did not contribute to increasing the stiffness and strength of the RC members in the elastic range. After cracking, however, the flexural stiffness and strength of the strengthened beams and slabs were significantly improved with respect to that of the unstrengthened beams and slabs. As a result of the FRP strengthening the yielding load increased appreciably (an increase of yielding load equal to ~25% with respect to that of the unstrengthened specimen was observed for both the strengthened beams and slabs). Moreover, after cracking, a nonlinear behavior of all the strengthened specimens was observed up to failure, indeed yielding of the steel rebars led to a reduction in slope, but the NSM FRP bars/strips allowed the specimens to take additional load up to failure. Comparing the grout adhesive NSM FRP strengthened beam with respect to the epoxy resin NSM FRP strengthened beams, e.g. by means of load-midspan deflection of beams B1 and B4 (see Figure 5.10), a premature debonding of the

NSM FRP bars is observed for beam B4, after which the load dropped to a load equivalent to that of an unstrengthened beam and the deflection increased until failure occurred due to concrete crushing. It has to be noted that the test on beam B4 was stopped as soon as first indications of concrete crushing were appearing in order to avoid any possible damage to the instrumentation at the beam soffit.

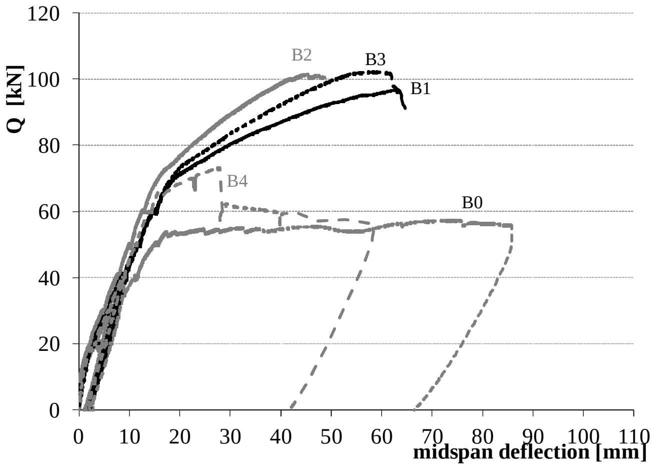

Figure 5.10 – Load-midspan deflection beams

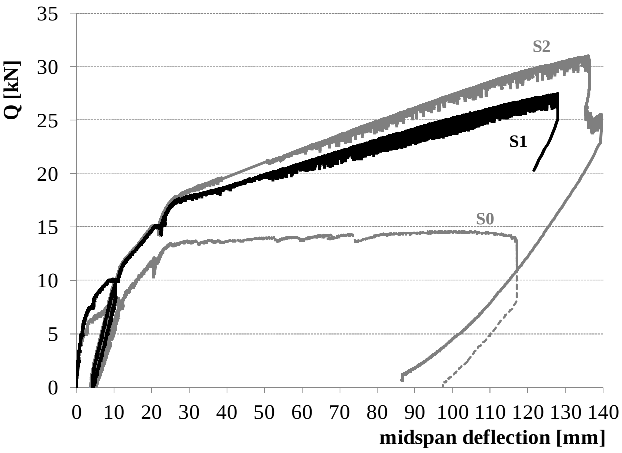

Figure 5.11 – Load-midspan deflection slabs

5.4.3 Cracking behaviour

All the beams started cracking at about the same load level $Q_{cr}\approx$ 11.0 kN and all the slabs around $Q_{cr}\approx$ 5.0 kN. The recorded mean crack width of the beams and slabs are compared in Figure 5.12 and Figure 5.13 respectively. From these figures, the restraining effect of the FRP strengthening on the crack width is noted.

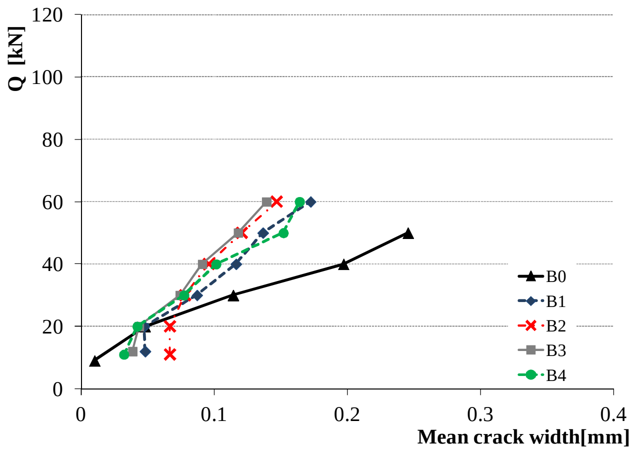

Figure 5.12 – Mean crack width of tested beams

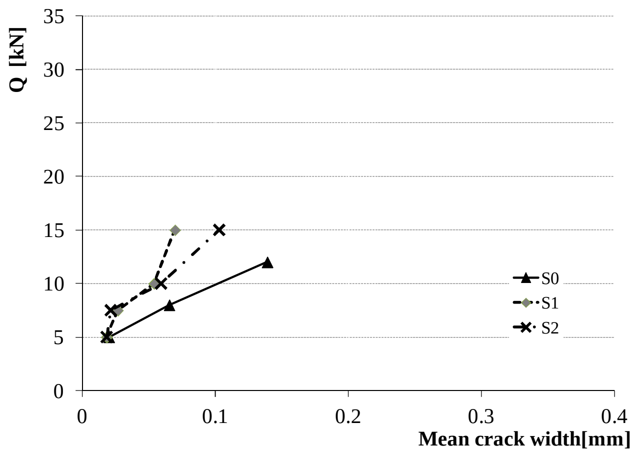

Figure 5.13 – Mean crack width of tested slabs

5.5 Analytical verifications

The behavior of the RC members (beams and slabs) under increasing load was evaluated based on strain compatibility and equilibrium of forces following well-established procedures for RC concrete structures [6] providing the contribution of the FRP strengthening system. Figure 5.14 shows the principle of calculation.

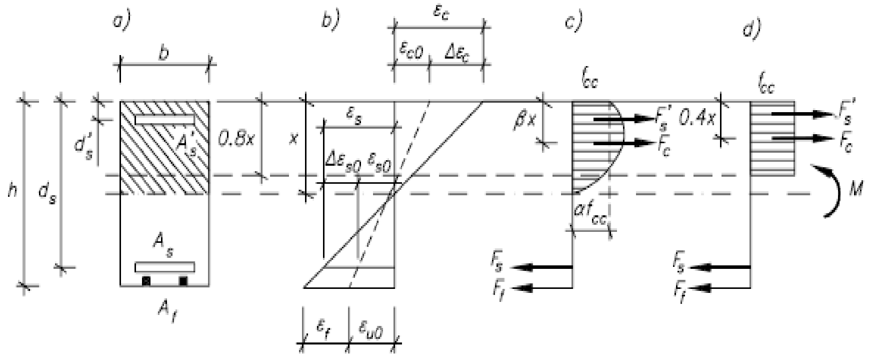

Figure 5.14 – Principle of calculation

The stress-strain relationship of the constitutive materials (concrete, steel and FRP) are modeled as shown in Figure 5.15. For the stress-strain relation of concrete in compression, the parabola-rectangle diagram was assumed [6-7]. The maximum strain of ε_{cu}= 3.5‰ was chosen based on the strain limit for concrete crushing in design of reinforced concrete structures [6]. Cracking is assumed to occur when the concrete reached the tensile strength $f_{ct}=0.9f_{c,ts}$ (values of $f_{c,ts}$ for each concrete batch are reported in Table 5.3). The steel rebars and the FRP bars/strips were modeled as elastic-plastic and linearly elastic up to failure respectively.

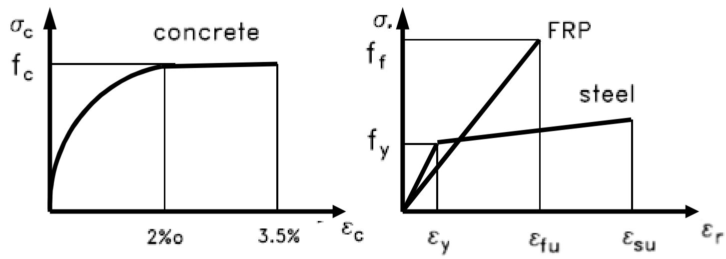

Figure 5.15 – Stress strain model of constituent materials

The following assumptions are made:

- Bernoulli's hypothesis applies, i.e. strains across the cross section vary rectilinearly. This implies that linear strain in the concrete, steel and FRP reinforcement that occur at the same level is of the same size. No slip between the longitudinal reinforcement and the concrete is assumed to occur.
- The contribution of concrete in tension is neglected.
- The epoxy in the grooves is neglected and all computations are made as if the NSM bars are embedded in the concrete.

Taking the concrete strain ε_c at the top fibre as parameter, the strain in the longitudinal bottom and upper steel, ε_s and $\varepsilon_s^{'}$, the strain in the FRP ε_f and the moment M, were derived as follows. Defining the parameter λ, equal to:

$$\lambda = \frac{0.002}{\varepsilon_c} \tag{5.1}$$

The following coefficients related to the concrete stress block can be defined [7]:

$$\begin{aligned} \lambda \geq 1: \quad \psi &= \frac{3\lambda - 1}{3\lambda^2} \quad \delta_G = \frac{4\lambda - 1}{4(3\lambda - 1)} \\ \lambda \leq 1: \quad \psi &= 1 - \frac{\lambda}{3} \quad \delta_G = \frac{\lambda^2 - 4\lambda + 6}{4(3 - \lambda)} \end{aligned} \tag{5.2}$$

with ψ the ratio of the average over the maximum concrete compressive stress (stress block area coefficient) and δ_G the distance from the compression face to the compression force divided by the depth of the compression zone (stress block centroid coefficient).

The neutral axis depth x and the strains ε_s, $\varepsilon_s^{'}$ and ε_f are evaluated based on the equilibrium of forces ($\Sigma F=0$) and strain compatibility:

$$\psi b x f_c + A_s^{'} E_s \varepsilon_s^{'} = A_s E_s \varepsilon_s + A_f E_f \varepsilon_f \tag{5.3}$$

where:

$$\varepsilon_s = \varepsilon_c \frac{d_s - x}{x} \quad \text{with } \varepsilon_s \leq \frac{f_y}{E_s} \tag{5.4}$$

$$\varepsilon_s' = \varepsilon_c \frac{x - d_s'}{x} \quad (E_s\varepsilon_s' \text{ not to exceed } f_y) \tag{5.5}$$

$$\varepsilon_f = \varepsilon_c \frac{h - x}{x} - \varepsilon_0 \tag{5.6}$$

And with ε_0 the initial strain at the extreme tension fibre before strengthening. From the equilibrium of moments ($\Sigma M=0$), the bending moment is obtained as:

$$M = \psi b x f_c (d_s - \delta_G x) + A_s' E_s \varepsilon_s' (d_s - d_s') + A_f E_f \varepsilon_f (h - d_s) \tag{5.7}$$

The effect of initial load prior to strengthening (dead load) should be considered in the calculation of the strengthened member. Before strengthening equations 5.3 and 5.7 were applied with $A_f=0$. When reaching the moment M_0 at which the FRP was applied, the strain ε_0 follows from:

$$\varepsilon_0 = \varepsilon_{c0} \frac{h - x}{x} \tag{5.8}$$

with $\varepsilon_c=\varepsilon_{c0}$ the concrete strain at the top fibre corresponding to M_0.

According to the above equations the behavior of the beams and slabs was verified analytically. The concrete strain ε_c (and hence M) was increased step wise until reaching the failure load. It was assumed that, considering full composite action between the FRP and concrete, failure occurred when either the concrete strain reached the maximum strain value assumed equal to ε_{cu}= 3.5‰ (steel yielding followed by concrete crushing) or the FRP bars/strips attained their ultimate strain, ε_{fu} (steel yielding followed by FRP rupture).

Moreover, considering that there is still limited understanding of the mechanism of debonding in members strengthened in flexure with NSM systems and that the likeliness of a debonding failure in a RC member strengthened in bending with NSM reinforcement depends on several parameters (among which the internal steel reinforcement ratio, the external NSM FRP reinforcement ratio, the cross-sectional shape, the surface configuration of the NSM reinforcement and the tensile strength of both the epoxy and the concrete), the failure of the RC members is modeled also by limiting the NSM FRP ultimate strain in order to take into account failure mode governed by debonding. Based on the experimental results and on design guidelines [4-5] the strain of the FRP was limited as follows:

$$\varepsilon_{f,lim} = 0.7\varepsilon_{fu} \tag{5.9}$$

Analytical results of the above mentioned calculations in terms of failure load for the tested elements are reported in Table 5.7. As first verification the failure load, Q_{u1}, was obtained assuming full composite action between the FRP and the concrete. For the calculations all the material safety factor were taken equal to one. As second verification the failure load, Q_{u2}, was obtained by limiting the ultimate strain of the NSM FRP by using equation 5.9. Considering that, for all the specimens, the NSM FRP reinforcement was extended as close as practically possible to the support and that no anchorage failure was experimentally observed in any of the test specimens, the anchorage failure was not analytically verified further.

Table 5.7– Analytical failure load

	Experimental		Analytical full composite action			Analytical NSM FRP strain limitation		
Spec.	Q_u [kN]	Failure mode [-]	Q_{u1} [kN]	Q_u/Q_{u1} [-]	Failure mode [-]	Q_{u2} [kN]	Q_u/Q_{u2} [-]	Failure mode [-]
B0	57.3	YS/CC	57.9	1.01	YS/CC	-	-	YS/CC
B1	96.9	DB A/C	109.3	0.89	YS/CC	100.1	0.97	DB FRP
B2	101.5	DB FRP/A	118.0	0.86	YS/CC	103.6	0.98	DB FRP
B3	102.2	DB A/C	116.7	0.88	YS/CC	107.5	0.95	DB FRP
B4	73.3	DB FRP/A	118.0	0.62	YS/CC	103.6	0.71	DB FRP
S0	14.6	YS/CC	14.3	1.02	YS/CC	-	-	YS/CC
S1	28.6	YS/CC - DB FRP/A	29.6	0.96	YS/FF	25.5	1.12	DB FRP
S2	31.0	YS/CC	38.1	0.82	YS/FF	30.9	1.00	DB FRP

From this table it is noted that the FRP bond failure, experimentally obtained, happened close to the expected failure load assuming full composite action, (except for beam B4). Results of the analytical verification considering the FRP strain limitation equal to $0.7\varepsilon_{fu}$ and experimental failure loads are also in good correlation. For beam B4, for which the NSM rods are embedded with a grout adhesive, a large difference of results between analytical and experimental loads is observed, due mainly to the fact that assuming an FRP strain limitation equal to $0.7\varepsilon_{fu}$ seems to give poor agreement in predicting debonding at the grout interface. A refined calculation in which the reduced tensile strength of the grout mortar with respect to that of the adhesive is taken into account would give a better prediction.

Results of the calculation in terms of predicted load-strain curves in the concrete, steel reinforcement and FRP bars/strips, compared with the measured strains, are given in Appendix B as well as in Figure 5.16 and Figure 5.17 for beam B0 and B1. Comparing the measured and predicted load-strain curves a good agreement is noticed.

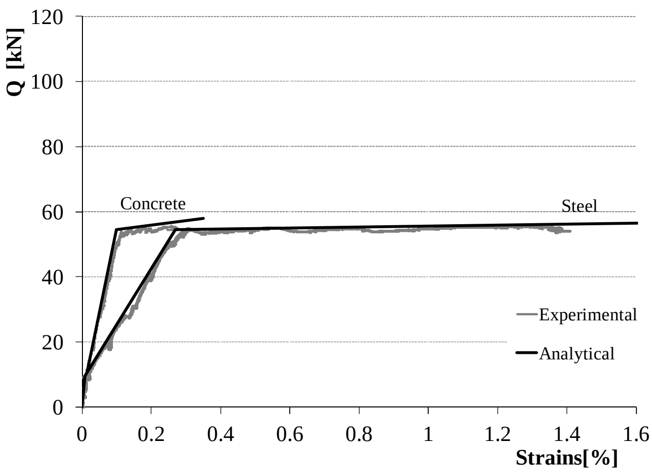

Figure 5.16 – Load-strains curves beam B0

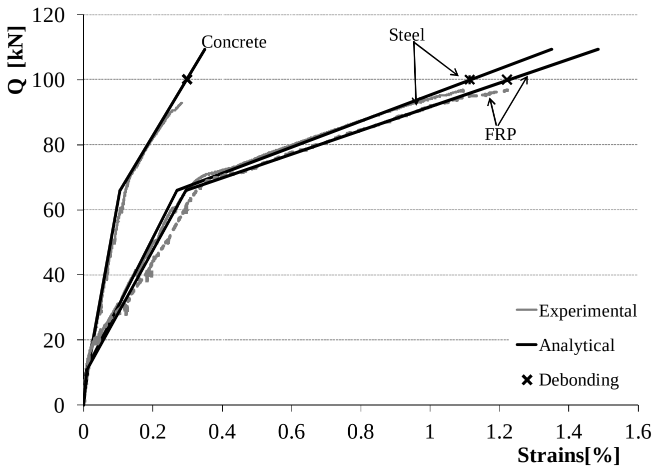

Figure 5.17 – Load-strains curves beam B1

5.5.1 Load- deflection

The load-deflection behavior has been predicted using a virtual work approach. The deflection at midspan of the beam was calculated by:

$$a = \int (1/r)\overline{M}dx \tag{5.10}$$

With, $\overline{M}$ the moment line of a beam with a point load Q=1 at midspan and 1/r is the curvature along the length of the beam. In the cross section analysis, the moment and corresponding curvature has been determined at cracking ($f_{c,t}$= $0.9f_{c,ts}$), steel yielding and failure (concrete or FRP failure). The curvature was obtained as:

$$\frac{1}{r_i} = \frac{\varepsilon_c + \varepsilon_f}{h} \tag{5.11}$$

Where $1/r_i$ is the curvature at cracking, steel yielding and failure; ε_c is the concrete strain at the top fiber; ε_f is the FRP strain (for the unstrengthened beam and slab the steel strain ε_s was used). Results of the load-deflection predictions are given in Figure 5.18 and Figure 5.19 for the beams and slabs respectively. Analytical and experimental curves (except for beam B4) are in good agreement up to the point in which debonding start, at which moment the experimental curves becomes less stiff than the predicted ones. This can be explained due to the bond degradation at the interface between the adhesive and the FRP, which was not accounted for in the model.

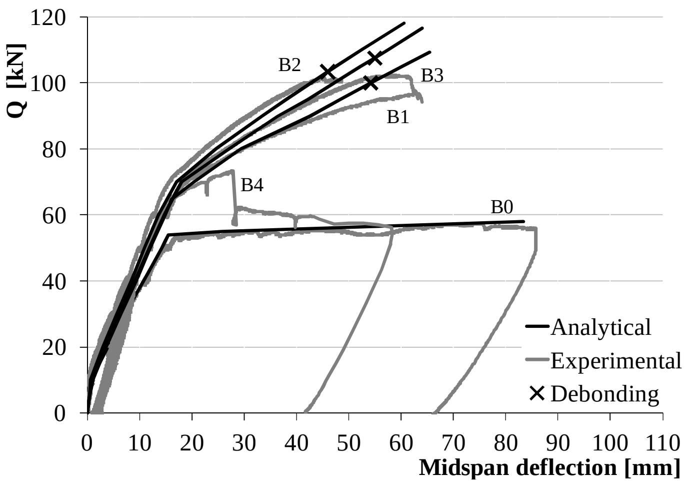

Figure 5.18 – Load-midspan deflection beams

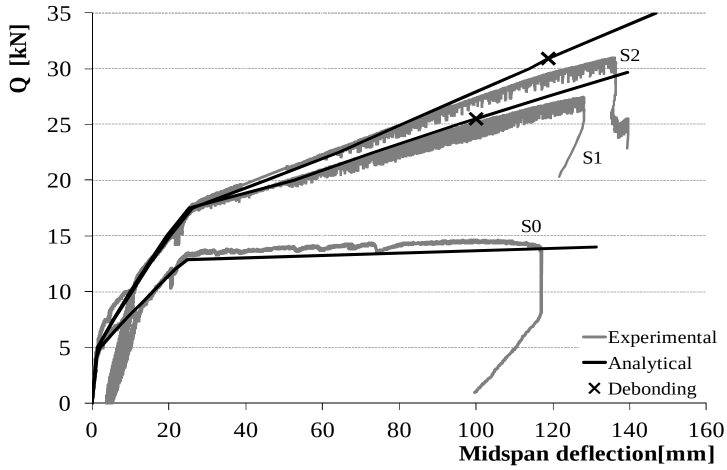

Figure 5.19 – Load-midspan deflection slabs

5.6 Serviceability limit state

5.6.1 Basis of calculation

Calculations to verify the serviceability limit states were carried out considering all materials having a linear-elastic behavior for both un-cracked and cracked transformed sections conditions. As reported in [4-7], assuming linear elastic material behavior and that the concrete does not sustain tension, the cracked section analysis can be based on Figure 5.20.

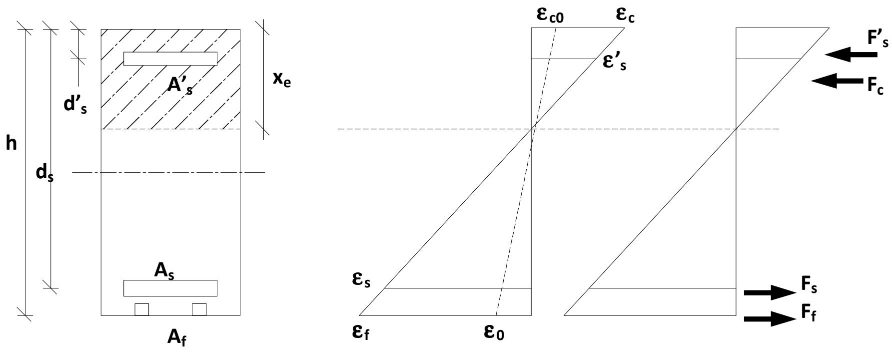

Figure 5.20 – Linear elastic analysis of cracked section

From the equilibrium of forces and strain compatibility the depth of the neutral axis x_e is given as:

$$1/2bx_e^{\,2} + (\alpha_s - 1)A_s^{'}(x_e - d_s^{'}) = \alpha_s A_s (d_s - x_e) + \alpha_f A_f \left(h - \left(1 + \frac{\varepsilon_0}{\varepsilon_c} \right) x_e \right) \qquad (5.12)$$

where, ε_0 is the initial concrete strain at the extreme tension fibre determined according to equation 5.8; α_s=E_s/E_c and α_f=E_f/E_c the modular ratios with E_c, E_s and E_f the modulus of elasticity of the concrete, the steel and the FRP respectively. For small values of ε_0, the term (1+ε_0/ε_c) equals about 1, so that equation 5.12 can be directly solved. For large values of ε_0 compared to the acting concrete strain ε_c at the extreme compression fibre, the neutral axis depth x_e should be solved from equations 5.8, 5.12 and 5.13:

$$E_c\varepsilon_c = \frac{M_k}{1/2bx_e\left(h-\frac{x_e}{3}\right)+(\alpha_s-1)A_s^{'}\frac{x_e-d_s^{'}}{x_e}(h-d_s^{'})-\alpha_s A_s\frac{d_s-x_e}{x_e}(h-d_s)} \quad (5.13)$$

Once the depth of the neutral axis is obtained, the moment of inertia of the cracked section can be determined as given by equation 5.14:

$$I_2 = bx_e^3/3+(\alpha_s-1)A_s^{'}(x_e-d_s^{'})^2+\alpha_s A_s(d_s-x_e)^2+\alpha_f A_f(h-x_e)^2 \quad (5.14)$$

and depends, similar as for x_e, on the acting moment M_k.

The un-cracked section analysis can be performed in a similar way as the above mentioned cracked section analysis. However, as M_0 is mostly larger than the cracking moment M_{cr} and as the influence of the FRP reinforcement is limited anyway, the geometrical characteristics of the un-cracked section before strengthening apply. Neglecting also the contribution of the steel reinforcement, the moment of inertia can be approximated as:

$$I_1 \approx \frac{bh^3}{12} \quad (5.15)$$

And the cracking moment M_{cr} as:

$$M_{cr} \approx f_{ctm}\frac{bh^2}{6} \quad (5.16)$$

where according to [6], reference is made to the mean concrete tensile strength f_{ctm}.

5.6.2 Service load

In Table 5.8 the service load of the tested specimens (beams and slabs) is given based on verification in the ultimate limit state (ULS) and the serviceability limit states (SLS). The service load Q_{serv} equals the smallest value of:

- Q_{k1}, ULS calculation. The calculation is based on equilibrium of forces and strain compatibility as described in section 5.5, taking into account appropriate partial safety factors [4, 6].
- Q_{k2}, SLS calculation with respect to the stress limitations. The calculation is carried out for the rare load combination by limiting the tensile stresses of concrete, steel and FRP as following:

$$\sigma_c \leq 0.6 f_{ck} \;;\; \sigma_s \leq 0.8 f_{yk} \;;\; \sigma_f \leq \eta f_{fk} \qquad (5.17)$$

where the stress limitation coefficient η was assumed to be equal to η= 0.8 for carbon bars and strips and to η= 0.3 for glass and basalt bars.

- Q_{k3}, SLS calculation with respect to an allowable crack width w_{lim}= 0.3 mm. As also noted from section 5.4.3, w_{lim} is not reached for $Q < Q_y$.
- Q_{k4}, SLS calculation with respect to an allowable deflection a_{lim} = l/250 [6]. The calculation was carried out as described in section 5.5.1

Table 5.8 – Service load tested specimens

Spec.	Q_u [kN]	Q_{k1} [kN]	Q_{k2} [kN]	Q_{k3} [kN]	Q_{k4} [kN]	Q_{serv} [kN]	Q_u/Q_{serv} [kN]	$Q_{u,ref}/Q_{serv}$ [kN]
B0	57.3	30.7	39.5	> 54.5	42.3	30.7	1.86	1.86
B1	96.9	54.0	36.0	> 64.8	50.3	36.0	2.69	1.59
B2	101.5	56.2	40.5	> 67.1	58.2	40.5	2.50	1.41
B3	102.2	55.1	41.0	> 66.9	50.3	41.0	2.49	1.40
B4	73.3	56.2	40.5	> 67.1	58.2	40.5	1.80	1.41
S0	14.6	7.5	9.1	> 12.9	8.5	7.5	1.94	1.94
S1	28.6	17.6	11.2	> 15.5	10.1	10.1	2.91	1.49
S2	31.0	17.8	12.4	> 16.9	10.2	10.2	3.16	1.49

Results of calculations (see Table 5.8) showed that the service load, Q_{serv}, of the reference specimens (beams and slabs) was governed by the ULS. For the strengthened beams the service load was restricted by the allowable concrete compressive stress in the SLS. For the strengthened slabs the service load Q_{serv}, was restricted by the allowable deflection a_{lim} = l/250.

In Table 5.8 the safety of the specimens against an overloading situation is reported by means of the ratio of the ultimate to the service load. A ratio Q_u/Q_{serv} between 1.8 and 2.69 is found for all the beams and between 1.94 and 3.16 for all the slabs. Furthermore, it can be noted (see Table 5.8) that the service loads of the strengthened specimens in this test program remain smaller than the ultimate load of the reference beam and slab. Hence in case of accidental loss of the NSM FRP reinforcement under service load, the specimens will not collapse. The safety against overloading in case of accidental situation is given by the ratio between the ultimate load of the reference specimens, $Q_{u,ref}$, and the service load of the strengthened specimens, Q_{serv}.

5.7 Conclusions

Based on the experimental and analytically study on NSM FRP strengthened beams and slabs presented herein the following conclusions can be made.

Experimental results demonstrate that using NSM FRP reinforcing bars and strips significantly improves the stiffness and increase the flexural capacity of the strengthened members.

For the beams tested in this test program, a strength increase between 1.7 and 1.8 has been obtained for beams in which the FRP was embedded into the grooves with epoxy adhesive. Beam B4 experienced a strength increase equal to 1.27 mainly due to the lower tensile and shear strength of the grout adhesive as compared to that of epoxy resin. Two different types of failure mode were observed. Beams B1 and B4 strengthened with ribbed GFRP bars and CFRP strips respectively failed by FRP debonding with detached concrete cover below the longitudinal steel reinforcement. Beams B2 and B4 strengthened with sand coated CFRP bars failed by splitting of the adhesive. This different trend of failure suggests an influence of the FRP surface configuration on the failure mode. Debonding of the NSM FRP rods/strips occurred at tensile strains ranging between 69% - 73% of the ultimate tensile strain of the FRP bars/strips, confirming the higher efficiency of the NSM strengthening technique compared to FRP EBR strengthening systems. With similar axial stiffness the latter usually has tensile stresses which ranges between 35% - 45% (e.g. see [7]). The ductility of the strengthened beams decreased between 25% - 68%.

For the slabs tested in this test program, a strength increase between 1.95 and 2.12 has been obtained. Due to the considerable increase of failure load both slabs failed by concrete crushing, although for slab S1 debonding of the FRP bars was observed as well. Similar as for the strengthened beams, an elevated efficiency of utilization of the NSM FRP reinforcing bars is observed with increased strain values equal to 72% and 71% for slab S1 and S2 respectively.

As the FRP NSM increases the stiffness of the specimens and as a denser crack pattern with smaller crack widths is obtained, also the service load was increased for all the specimens. An increase of service load in the range of 20%-36% depending of the type of the FRP strengthening systems was obtained for all the specimens.

The structural behavior of the specimens in terms of ultimate load, failure type, strains and deflection could be predicted in an accurate way. An exception is the beam B4 in which the FRP is embedded with cementious grout, and poor agreement between the experimental and analytical results is observed by using the FRP limitation equal to $0.7\varepsilon_{fu}$. Finally the service load of strengthened beams appeared to be governed by the allowable concrete compressive stress in the SLS. For the strengthened slabs the service load Q_{serv}, was restricted by the allowable deflection $a_{lim} = l/250$.

5.8 References

1. NBN-B15-220 (1990). "Proeven op beton- Bepaling van de druksterke".
2. NBN-B15-214 (1990). "Proven op beton-buigproef op betonprisma's".
3. NBN EN 10002-1 (2002). "Metallic Materials – Tensile Tests-Part 1: Method of Test At Ambient Temperature".
4. *fib* Task Group 9.3 (2001). "Externally bonded FRP reinforcement for RC structures". *International Federation for Structural Concrete*, *fib* Bulletin 14.
5. American Concrete Institute (ACI) (2008). "Guide for the design and construction of externally bonded FRP systems for strengthening concrete structures". *ACI 440.2R-08*, ACI Committee 440, 80 pp.
6. EN 1992-1-1 (2004). "Eurocode 2- Design of concrete structures – Part 1-1: General rules and rules for buildings". *European Committee for Standardization.*
7. Matthys S. (2000). "Structural Behaviour and Design of Concrete Members Strengthened with Externally Bonded FRP Reinforcement". *PhD-thesis*, Faculty of Engineering, Department of Structural Engineering, Ghent University, Belgium, pp. 367.

Chapter 6

FIRE ENDURANCE OF INSULATED NSM STRENGTHNED CONCRETE MEMBERS: EXPERIMENTAL INVESTIGATION

6.1 Introduction

In this chapter, experimental results on 4 fire tests series conducted on 20 full-scale NSM FRP strengthened and insulated beams and 4 full-scale NSM FRP strengthened and insulated slabs subjected to their service load and under standard fire exposure are reported.

In the first two fire test series [1] 12 full-scale beams, including two unstrengthened and unprotected reference beams, were exposed to 2 h of fire exposure. These two fire test series aim to carefully document the performance of NSM FRP strengthened and insulated beams under fire exposure, testing different material aspects and examining and optimizing the insulation configuration, the insulation material type and dimensions in order to develop practical methods for protecting FRP during fire exposure. Hereafter structural testing to failure at room temperature of the fire tested beams has been carried out in order to evaluate their residual strength after 2 h of fire exposure.

In the third fire test series [2] 6 additional concrete beams, with the same configuration and mechanical properties and using the insulation materials which gave the best results in the preceding fire test, were tested under fire in order to: (1) investigate the reliability of the previous tests results; (2) investigate if the NSM FRP strengthened system is active during fire by testing one of the beams till failure at 1 hour of fire exposure; (3) investigate the adhesive bond degradation at temperatures moderately higher than the adhesive glass transition temperature (in order to do this, different insulation thickness have been investigated in order to achieve different temperatures into the adhesive and a time of 1 h of fire exposure was choose to avoid loss of composite action due to an excessive heating of the adhesive); (4) investigate the influence of using an expansive mortar, alternative to the epoxy based adhesive. In view of point (3) structural testing to failure at room temperature of the fire tested beams was carried out to evaluate their residual strength after fire exposure.

In the fourth fire test series 2 NSM FRP strengthened beams and 4 NSM FRP strengthened slabs have been tested for 2 h of fire exposure. The parameters investigated in the two additionally tested beams were the effectiveness of a partial insulation along the length of the beam and the influence of using an expansive mortar as alternative to an epoxy based adhesive for 2 h of fire exposure. The performance of the NSM FRP strengthened systems under fire exposure was, moreover, investigated for 4 additional NSM FRP strengthened and insulated RC slabs. As for the previous fire test series structural testing at room temperature of the fire tested beams and slabs was carried out to evaluate their residual strength after fire exposure.

6.2 Description of specimens and material properties

The complete fire testing program consists of 4 fire test series and involved the design and fabrication of 20 steel reinforced concrete beams with rectangular cross section (width 200 mm and height 300 mm) and 4 steel reinforced concrete slabs with rectangular cross section (width 400 mm and height 150 mm). The beam and slab overall dimensions equal those given in Chapter 5 and are given in Figure 6.1 a-b. The experimental investigation involved standard fire tests (see section 6.4) on simply supported beams and slabs tested in four point bending. The dimensions of the specimens were chosen based on the dimensions of the floor furnace, which is a chamber of 6000 mm long and 3000 mm wide, in order to maximize the number of tests for each fire test series as shown in section 6.4. The amount and position of internal steel reinforcement as well as the concrete cover equals that given in chapter 5.

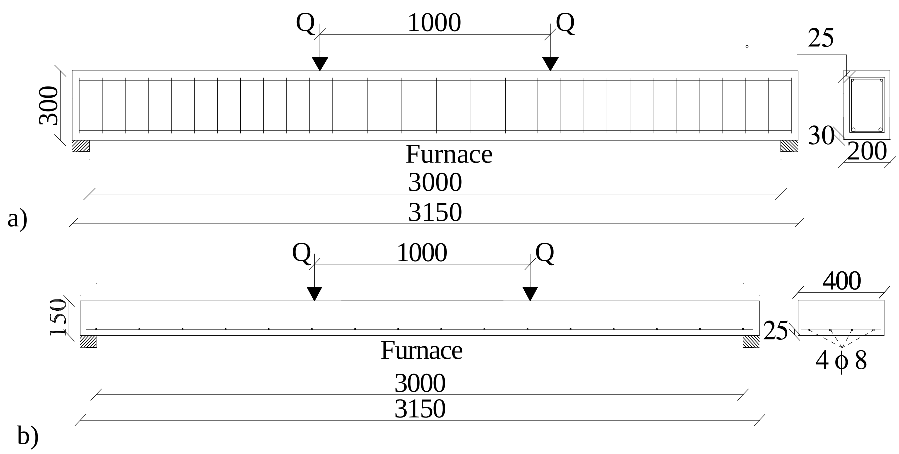

Figure 6.1 – Specimens dimensions a) beams b) slabs (dimensions in mm)

The concrete composition (per m^3) is given in Table 6.1. Nine different batches were manufactured in the laboratory. The average cylinder compressive strength, f_c, at time of testing was respectively 48.0 N/mm^2, 50.0 N/mm^2, 49.0 N/mm^2, 42.0 N/mm^2, 44.0 N/mm^2, 41.3 N/mm^2, 42.0 N/mm^2, 44.3 N/mm^2 and 43.4 N/mm^2 for concrete batch 1 to 9 respectively. Detailed information on materials properties of fresh and hardened concrete can be found in Appendix C.

The FRP reinforcement of the NSM FRP strengthened beams consisted of: CFRP sand-coated rods and smooth strips (type Aslan 200 and Aslan 500, supplied by Fortius/Hughes Brothers) with a nominal diameter of 9.53 mm and dimension of 2x 16 mm respectively and GFRP rods (type Combar supplied by Schöek) with a nominal diameter of 12 mm. The FRP reinforcement of the NSM FRP strengthened slabs consisted of GFRP spirally wound rods (type Aslan 100 supplied by Fortius/ Hughes Brothers) with a nominal diameter of 10 mm and BFRP sand coated rods (type Rockbar supplied by Magmatech) with a nominal diameter of 10 mm. The main characteristics of the NSM FRP reinforcements, as reported by the manufacturer, are summarized in Table 6.2. Given the lack of data of mechanical properties of BFRP rods, tensile tests in accordance to ISO 10406-1 2008 [3] have been performed.

Table 6.1 – Concrete composition

Material	Composition
Fine sand 0/4	655.0 kg
Fine aggregate 2/8	190.0 kg
Coarse aggregate 8/16	1120.0 kg
Cement CEM I 52.5	300.0 kg
Water	165.0 kg

Table 6.2 – Properties NSM FRP reinforcement

FRP	Type	Dim. [mm]	f_f [N/mm^2]	E_f [10^3 N/mm^2]	ε_{fu} [%]
Aslan 200	CFRP	9.53	1900	126	1.6
Combar	GFRP	12.0	1350	60	1.8
Aslan 500	CFRP	2 x 16	2068	124	1.7
Aslan 100	GFRP	10.0	760	40.8	1.8
Rockbar	BFRP	10.0	1170	59	1.9

Four different adhesives were used to embed the bars/strips into the elements. For most of the elements two commercial epoxy resins (type Sikadur-30, supplied by Sika and Fortersin CFL, supplied by Fortius/Hughes Brothers) were used as embedding adhesive, as a function of the type of FRP bars/strips as requested by the manufacturer (see Table 6.4). These two epoxy adhesives have a glass transition temperature equal to 62 °C (epoxy type Sikadur 30) and 66 °C (epoxy type Fortresin CFL) as has been experimentally evaluated by Differential Scanning Calorimetry, DSC, according to ISO 11357-2 [4]. In Table 6.3 the epoxy adhesive mechanical properties (experimentally evaluated according to EN ISO 527-2 [5]) in terms of tensile strength, f_a, and Young's modulus, E_a, are reported. The influence of the adhesive on the performance of the NSM FRP strengthened beams under fire exposure was evaluated by using also an epoxy resin (type High T_g supplied by Fyfe) with a high glass transition temperature (T_g equal to 82 °C as reported by the manufacturer) and an expansive cementious mortar (type Sikagrout-212 supplied by Sika). The mechanical properties of the last two adhesives are also given in Table 6.3, as reported by the manufacturers.

Table 6.3 – Adhesive properties

Adhesive	Type	f_a [N/mm^2]	E_a [10^3 N/mm^2]
Sikadur-30	Epoxy	27.0	3.78
Fortresin CFL	Epoxy	26.5	3.65
High T_g	Epoxy	30.0	3.18
Sikagrout 212	Mortar	4.1	-

An overview of the test matrix in terms of fire test series, specimen designation, FRP reinforcement, FRP bars/strips dimension, adhesive type, batch number, and age of testing is given in Table 6.4. The mentioned specimen designation refers to the following parameters: reference beam – fire test series – test sequence of specimen with similar NSM FRP strengthening system tested. As an example B1-F1-1 refers to: the strengthened beam that is strengthened such as the reference beam B1 - the first fire test - first specimen of F1 strengthened as reference beam B1.

Table 6.4 – Test matrix fire tests

Fire series	Specimen	FRP	Dim. FRP [mm]	Adhesive	Batch no	Age of testing [days]
First series (2 h exposure)	B0-F1	-	-	-	1	111
	B1-F1-1	GFRP	12.0	Sikadur 30	2	109
	B1-F1-2	GFRP	12.0	Sikadur 30	2	109
	B2-F1-1	CFRP	9.5	Fortresin CFL	1	111
	B2-F1-2	CFRP	9.5	Fortresin CFL	3	105
	B3-F1-1	CFRP	2x16	Fortresin CFL	3	105
Second series (2 h exposure)	B0-F2	-	-	-	4	186
	B1-F2-1	GFRP	12.0	Sikadur 30	5	192
	B1-F2-2	GFRP	12.0	Sikadur 30	5	192
	B1-F2-3	GFRP	12.0	Sikadur 30	5	192
	B2-F2-1	CFRP	9.5	High T_g	4	186
	B2-F2-2	CFRP	9.5	High T_g	4	186
Third series (1 h exposure)	B1-F3-1	GFRP	12.0	Sikadur 30	6	186
	B1-F3-2	GFRP	12.0	Sikadur 30	6	186
	B1-F3-3	GFRP	12.0	Sikadur 30	6	186
	B1-F3-4	GFRP	12.0	Sikadur 30	7	192
	B2-F3-1	CFRP	9.5	Fortresin CFL	7	192
	B4-F3-1	CFRP	9.5	Sikagrout	7	192
Fourth series (2 h exposure)	B2-F4-1	CFRP	9.5	Fortresin CFL	8	186
	B4-F4-1	CFRP	9.5	Sikagrout	8	186
	S0-F4	-	-	-	8	186
	S1-F4-1	GFRP	10.0	Fortresin CFL	9	192
	S2-F4-1	BFRP	10.0	Sikadur 30	9	192
	S2-F4-2	BFRP	10.0	Sikadur 30	9	192

All the specimens were casted in the Magnel Laboratory for Concrete Research. During the first 7 days after casting the specimens remained covered with a plastic foil. The formwork (side faces) was removed after 1 day. At an age of 7 days, the beams were placed on supports and stored (uncovered) in the laboratory. The NSM FRP reinforcement was applied to the beams at least 14 days before testing over a length of 2800 mm with the same grooves size, according to the procedures specified in Chapter 5 for the reference beams.

6.3 Insulation materials

Five fire insulation systems were investigated: a glass-fiber cement fire protection board (type Aestuver supplied by Xella), two types of calcium silicate protection board (type Promatect- H and Promatect L-500 supplied by Promat), a two component system under development (type WR-APP C supplied by Fyfe Co) and one insulation system composed of two ceramic based coatings (type Hot Pipe Coating and Omega Fire supplied by Superior Product Europe). The fire insulation systems were applied to the beams over a total length of 2900 mm in order to avoid any damages of the fire protection by touching the furnace wall during the increase of beams deflection. The small gap (approximately 50 mm) between the furnace walls and the insulation was filled with ceramic wool attached to the concrete and the surface wall with silicate glue (Promakol – K84 supplied by Promat). Figure 6.2 shows, as reference, the layout of one of the adopted insulation systems along the beam length. Table 6.5 shows the thermal properties of the different fire protection systems in terms of density and thermal conductivity as discussed in chapter 3.

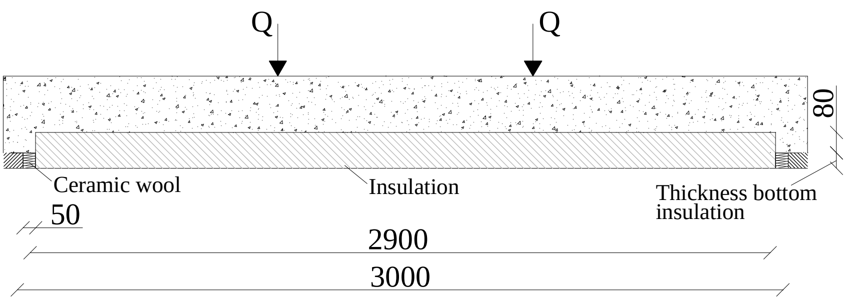

Figure 6.2 – Layout insulation along the specimen's length

Table 6.5 – Thermal properties insulation materials

Insulation	Density [Kg/m^3]	Thermal Conductivity [W/mK]
Aestuver	680	0.22
Promatect H	870	0.19
Promatect L-500	500	0.08
WR-APP type C	269	0.12
Hot Pipe Coating	599	0.06
Omega Fire	1138	0.25

In the following sections (6.3.1-6.3.4) a detailed description of the fire insulation systems, applied for each specimen, will be made grouped per fire test series performed (see Table 6.4). The layout of the insulation system over the length of the specimens is also reported in Appendix C.

6.3.1 Insulation details of first fire test series

Figure 6.3 till Figure 6.7 show the layout of the different fire protection systems applied to the beams for the first fire test. Beam B0-F1 was unprotected and unstrengthened.

Beam B1-F1-1 (see Figure 6.3) was protected with Promatect H fixed in a U shaped form. The width of the bottom plates was equal to the width of the beam (200 mm), the total thickness was equal to 40 mm (composed of two plates Promatect H with respectively thickness 25 and 15 mm, stapled together) and the length equal to 2900 mm. The bottom protection was not directly connected to the bottom side of the beam. The side plates consist of Promatect-H with a width equal to 120 mm and a thickness equal to 15 mm. Staples, to create the U-shaped insulation form, are provided each 200 mm for the connection between the side plates and the bottom plates. Screws, each 250 mm, were provided to mechanically fix the side plates to the concrete beam.

WR-APP type C was manually applied (toweled) on beam B1-F1-2 (see Figure 6.4) with a thickness of 30 mm on the bottom and 15 mm to the sides. A topcoat material consisting of a fire-resistant sandstone texture coating was applied in a thin layer of a nominal thickness of 0.1 mm.

Beam B2-F1-1 was protected with Aestuver fixed in a U shaped form (see Figure 6.5). The width of the bottom plate was equal to 200 mm and the thickness was equal to 30 mm. The bottom protection was composed by two boards of 1400 mm length joined by an extra board of 100 mm length in the middle to cover the desired length of 2900 mm of fire protection. The joints were closed by an intumescent strip (type Aestuver band BSD). The sides plates consist of Aestuver with a width equal to 110 mm and a thickness equal to 15 mm. Screws, to create the U-shaped insulation form, are provided each 250 mm for the connection between the side plates and the bottom plates as well as to mechanically fix the side plates to the concrete beam (Figure 6.5).

The bottom fire insulation system of beam B2-F1-2 consists of a plate, type Aestuver, with a width of 200 mm and a thickness of 40 mm. Screws, each 250 mm, were mechanically fixed to the bottom of the beam (see Figure 6.6). As for beam

B2-F1-1, the insulation system was composed by two boards of 1400 mm length joined by an extra board of 100 mm length in the middle. The joints in between the three boards were closed by an extra board with a width equal to 200 mm, thickness of 15 mm and a length of 300 mm.

Beam B3-F1-1 has the same fire insulation system of beam B2-F1-1 but the thickness of the bottom protection was increased from 30 mm to 40 mm (see Figure 6.7).

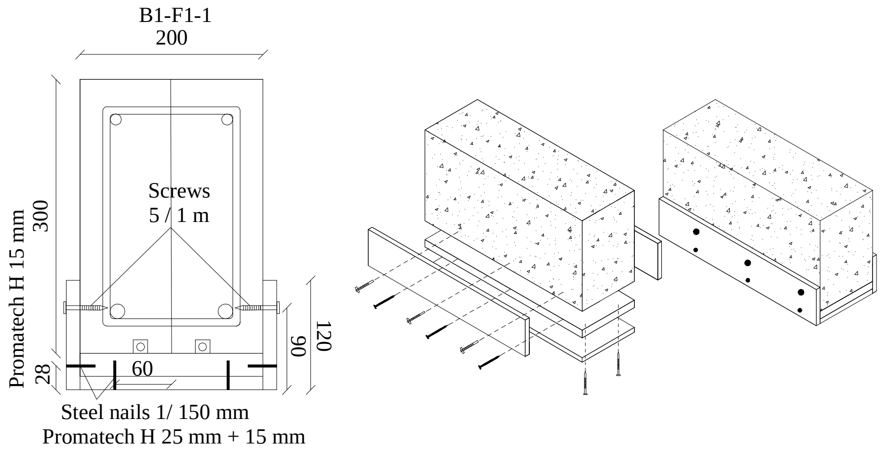

Figure 6.3 – Insulation layout beam B1-F1-1

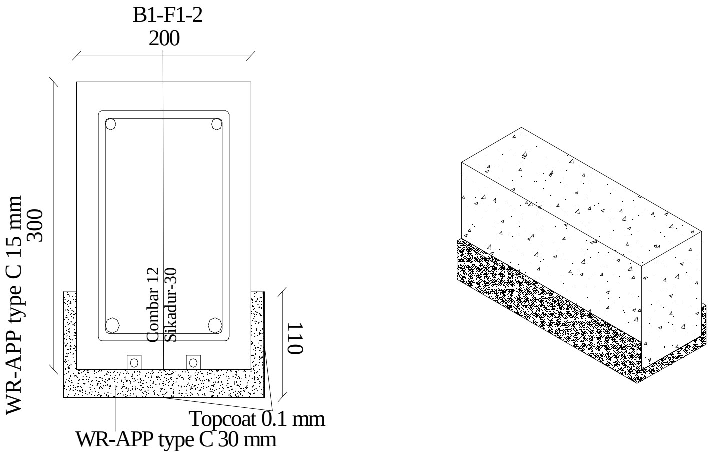

Figure 6.4 – Insulation layout beam B1-F1-2

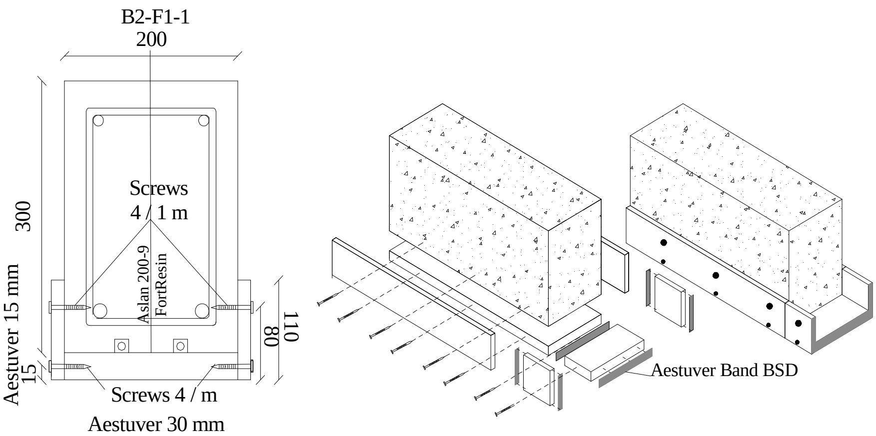

Figure 6.5 – Insulation layout beam B2-F1-1

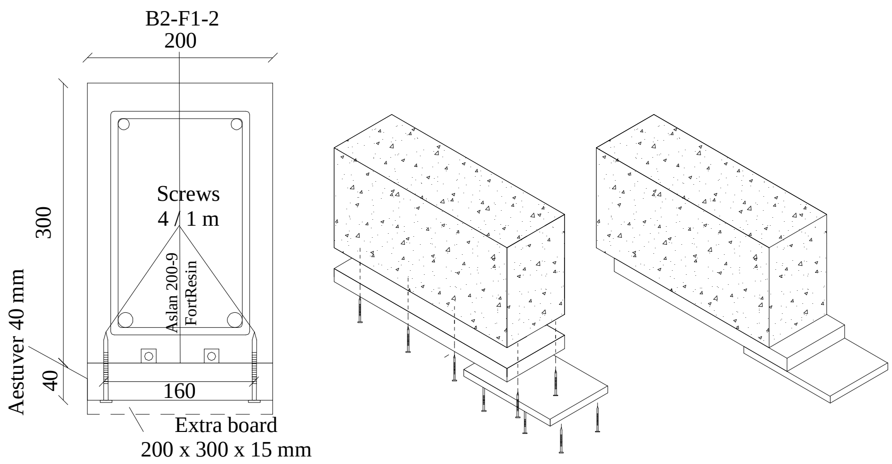

Figure 6.6 – Insulation layout beam B2-F1-2

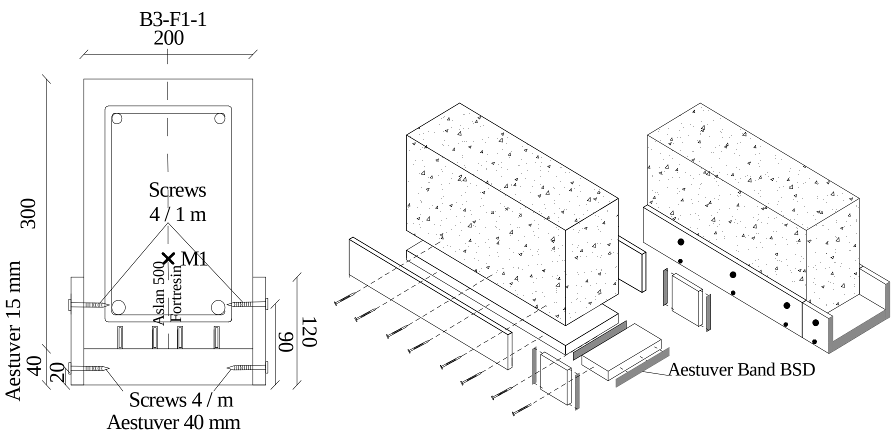

Figure 6.7 – Insulation layout beam B3-F1-1

6.3.2 Insulation details of second fire test series

Figure 6.8 till Figure 6.14 show the layout of the different fire protection systems applied to the beams for the second fire test. Beam B0-F2 was unprotected and unstrengthened. Beam B1-F2-1 (see Figure 6.8) was protected with Promatect L-500 fixed in a U shaped form. The thickness of the plate at the bottom was 100 mm, composed of Promat L-500 200 mm wide plates with a thickness of 50 mm, as indicated in Figure 6.8**.** The first 50 mm length of protection has been composed of two plates with a length of 1450 mm joint together in the longitudinal direction by means of silicate glue (type Promacol k84 supplied by Promat), so to achieve a total length of 2900 mm. These two plates have been attached to the beam soffit by means of silicate glue. At the bottom of the first layer, two additionally plates with the same geometry have been mechanically fixed with screw placed at a distance of 200 mm in longitudinal direction (silicate glue was also added in between the plates). The insulation at the side faces has been composed of Promat L-500 180 mm wide with a thickness of 20 mm (the first fire test series has shown that a side thickness of 20 mm was enough to delay the increase of temperature in the longitudinal steel reinforcement and FRP bars). A layer of silicate glue has been also provided at the inner surface of the side plates as shown in Figure 6.8. Screws, to create the U-shaped insulation form, are provided each 150 mm for the connection between the side plates and bottom plates and each 200 mm for the connection of the side plates to the beam. The screws were additionally protected with silicate glue in order to minimize the effect of screws on heat transfer.

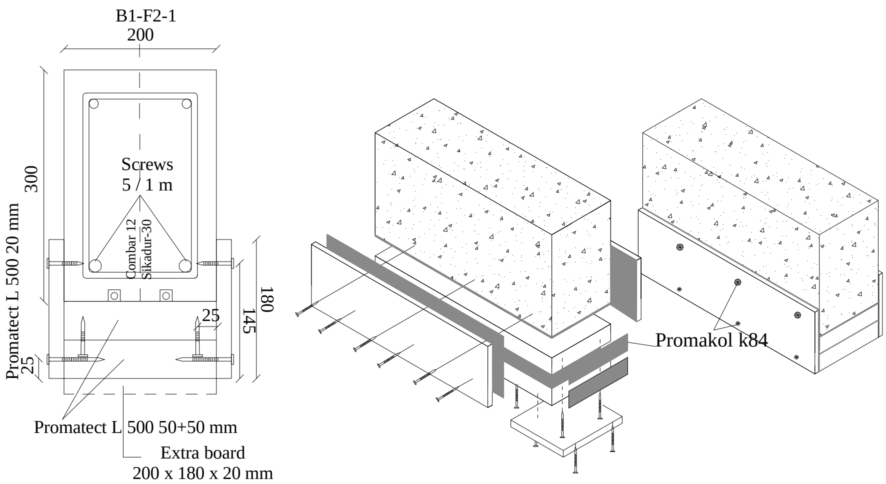

Figure 6.8 – Insulation layout beam B1-F2-1

Beams B1-F2-2 and B1-F2-3 were insulated with Hot Pipe Coating (HPC), which has been spray applied with a thickness of 25mm (beam B1-F2-2) and 40 mm (beam B1-F2-2) to the bottom, and 20 mm to the sides (see Figure 6.9 and Figure 6.10). The total thickness is built up in different layers in a range of 0.2-1 mm each (Figure

6.11 shows the application of the fire protection system). On top of the HPC a layer of Omega Fire has been spray applied with a thickness of 20 mm for both beams.

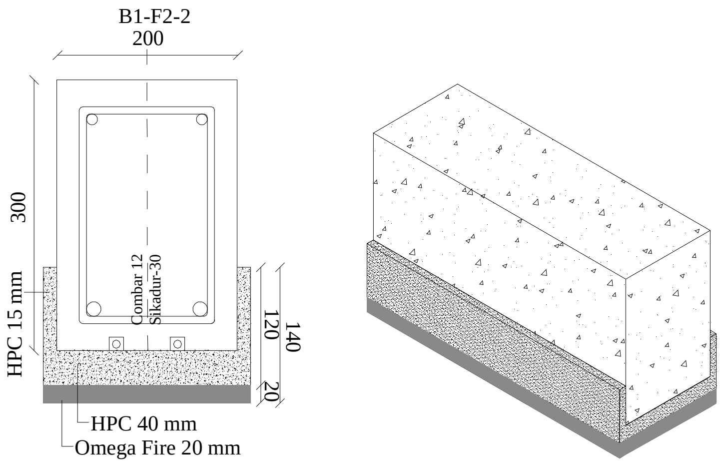

Figure 6.9 – Insulation layout beam B1-F2-2

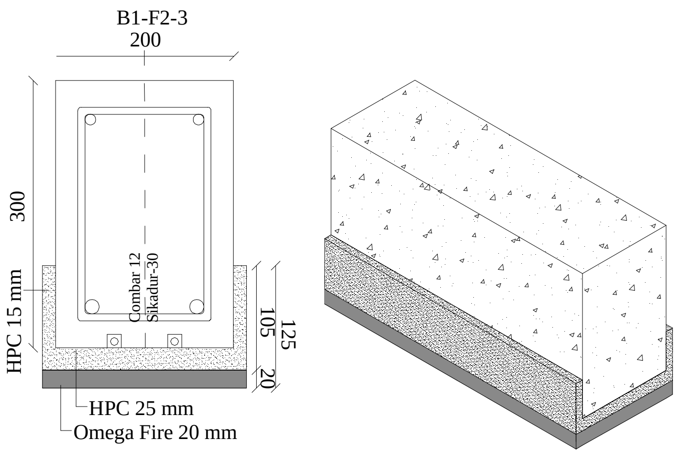

Figure 6.10 – Insulation layout beam B1-F2-3

Figure 6.11 – Application HPC + Omega Fire

Beams B2-F2-1 and B2-F2-2 were insulated with WR-APP type C, which has been spray applied with a thickness of 30 mm (beam B2-F2-1), and 40 mm (beam B2-F2-2) to the bottom, and 20 mm to the sides for both beams (see Figure 6.12 and Figure 6.13). The total thickness is built up in different layers in a range of 5 mm each (Figure 6.12 shows the application of the fire protection system).

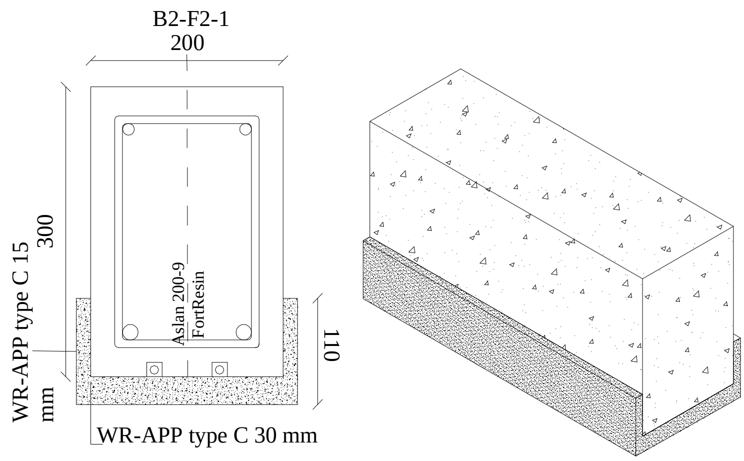

Figure 6.12 – Insulation layout beam B2-F2-1

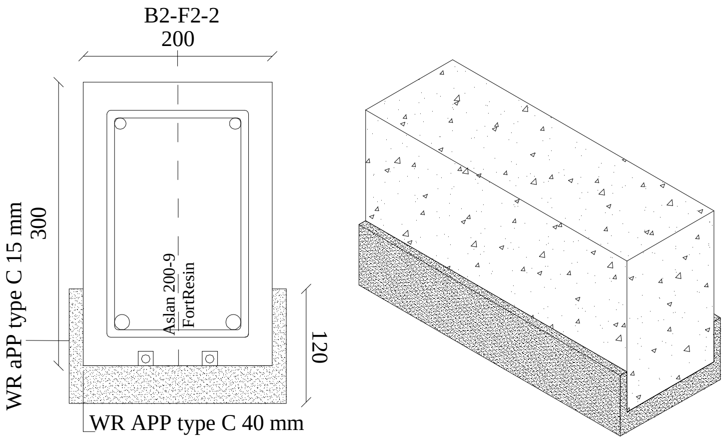

Figure 6.13 – Insulation layout beam B2-F2-2

Figure 6.14 – Application WR-APP type C

6.3.3 Insulation details of third fire test series

Figure 6.15 till Figure 6.20 show the layout of the different fire protection systems applied to the beams for the third fire test. Beam B1-F3-1 and B2-F3-1 (see Figure 6.15 and Figure 6.16) were protected with Promatect L-500 fixed in a U shaped form. The thickness of the plate at the bottom is 100 mm for beam B1-F3-1, composed of Promat L- 500 200 mm wide plates with a thickness of 50 mm, as indicated in Figure 6.15**.** The first 50 mm layer of insulation has been composed of two plates with a length of 1450 mm joint together in the longitudinal direction by means of silicate glue (type Promacol k84 supplied by Promat), so to achieve a total length of 2900 mm. These two plates have been attached to the beam soffit by means of silicate glue. At the bottom of the first layer, two additionally plates with the same geometry were mechanically fixed with screws placed at a distance of 200 mm in longitudinal direction. In between the two layers of 50 mm an extra layer of silicate glue has been also provided (Figure 6.15). The configuration of the bottom protection of beam B2-F3-1 was taken the same as for beam B1-F3-1, but plates with a thickness of 30 mm were used (see Figure 6.16). The insulation at the side faces has been composed of Promat L-500 180 mm wide (beam B1-F3-1) and 140 mm wide (beam B2-F3-1) with a thickness of 20 mm. Screws, to create the U-shaped insulation form, are provided each 150 mm for the connection between the side plates and bottom plates and each 200 mm for the connection of the side plates to the beam. An extra layer of silicate glue has been provided at the inner surface of the side plates. The screws were additionally protected with silicate glue in order to minimize the effect of screws on heat transfer.

Beams B1-F3-2, B1-F3-3 and B1-F3-4 were insulated with Hot Pipe Coating (HPC), which has been spray applied with a thickness of 25mm (beam B1-F3-2), 35 mm (beam B1-F3-3) and 20 mm (beam B1-F3-4) to the bottom, and 10 mm to the sides. The total thickness is built up in different layers in a range of 0.2-1 mm each. On top of the HPC a layer of Omega Fire has been spray applied with a thickness of 20 mm (beams B1-F3-2 and B1-F3-3) and 15 mm (beam B1-F3-4) to the bottom, and 10 mm to the sides (see Figure 6.17 till Figure 6.19).

For beam B4-F3-1, in which the NSM FRP bars were embedded with an expansive mortar, a layer of HPC and Omega Fire (10 mm + 10 mm at the bottom and the sides) was provided for the insulation (see Figure 6.20).

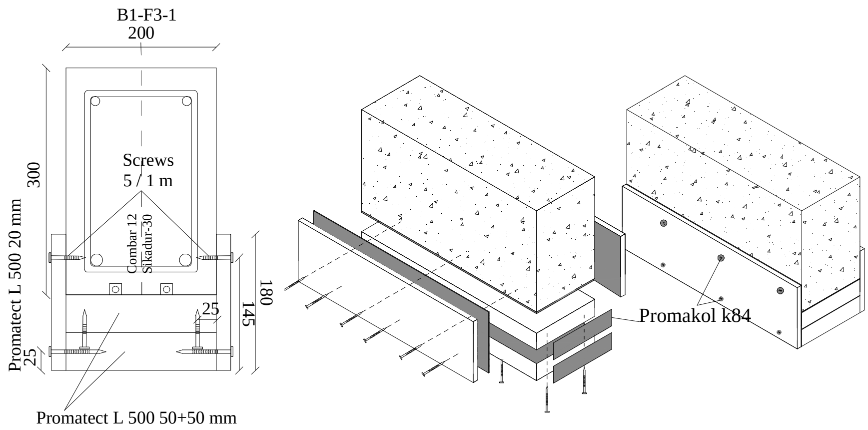

Figure 6.15 – Insulation layout beam B1-F3-1

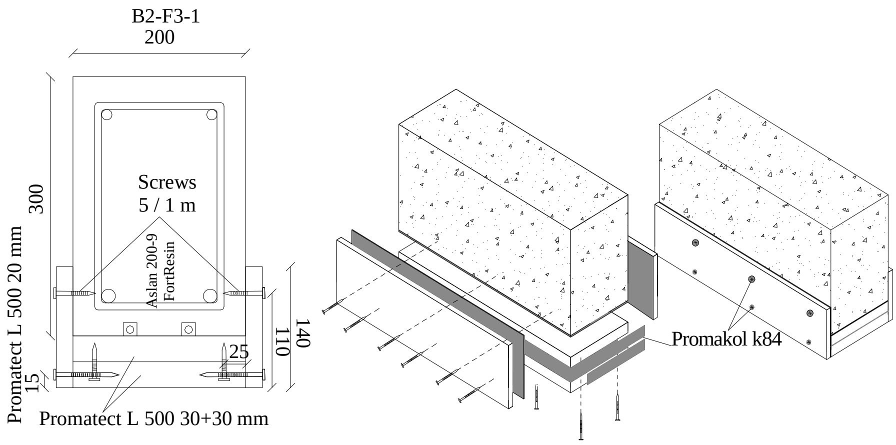

Figure 6.16 – Insulation layout beam B2-F3-1

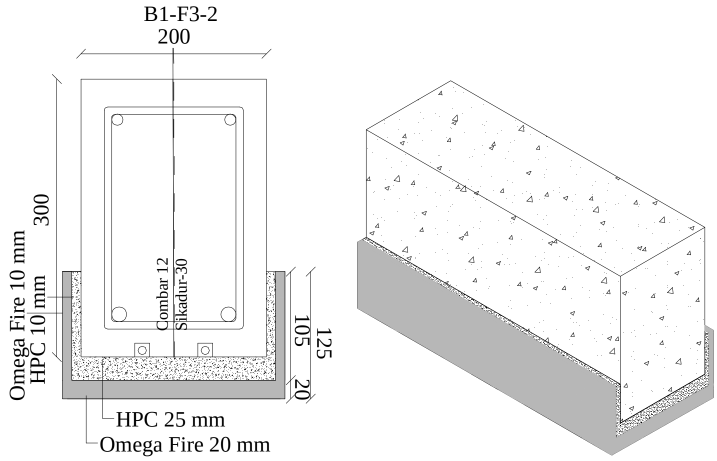

Figure 6.17 – Insulation layout beam B1-F3-2

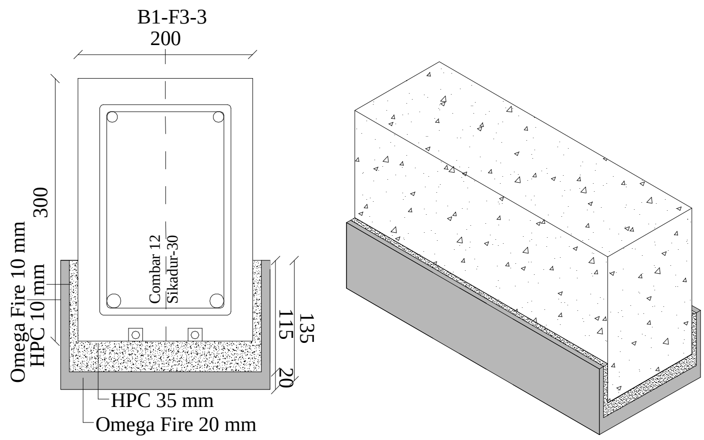

Figure 6.18 – Insulation layout beam B1-F3-3

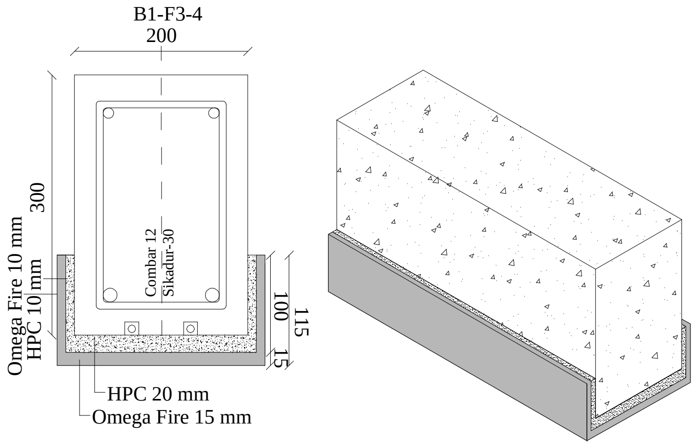

Figure 6.19 – Insulation layout beam B1-F3-4

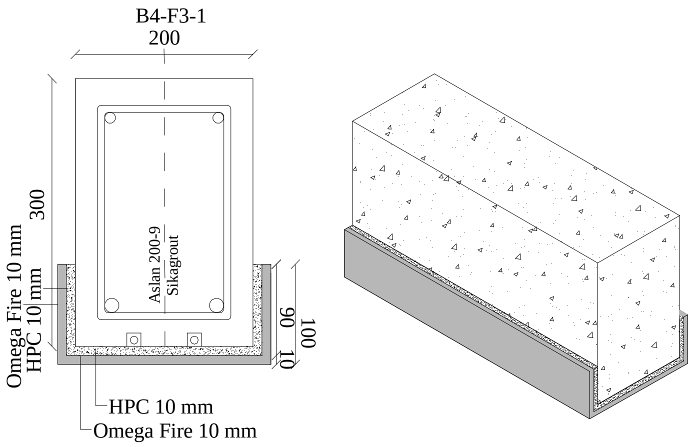

Figure 6.20 – Insulation layout beam B4-F3-1

6.3.4 Insulation details of fourth fire test series

Figure 6.21 till Figure 6.25 show the layout of the different fire protection systems applied to the beams/slabs for the fourth fire test. Beam B2-F4-1 (see Figure 6.21), in which the NSM FRP bars were embedded into the grooves for a length equal to 500 mm from the free end of the FRP at both sides (see Appendix C), has been insulated with Hot Pipe Coating (HPC) and Omega Fire. The insulation system has been applied only at the bonded length of the FRP NSM, keeping the unbounded side unprotected. HPC fire insulation system has been spry-applied with a thickness of 25 mm to the bottom and 10 mm to the side. On the top of HPC a layer of Omega Fire has been spry-applied with a thickness of 20 mm to the bottom and 10 mm to the side.

For beam B4-F4-1, in which the NSM FRP bars were embedded with an expansive mortar, a layer of HPC and Omega Fire (20 mm + 10 mm) has been provided at the bottom for the insulation (see Figure 6.22). The insulation thickness at the side was equal to 10 mm for both HPC and Omega Fire.

One slab (specimen S0) was tested under fire exposure unprotected and unstrengthened as reference. All the insulated slabs were exposed to fire only at the soffit, therefore the fire insulation was provided only at the soffit of the slabs. Slab S1-F4-1 has been insulated with Hot Pipe coating with a thickness of 25 mm. On the top of the HPC insulation a layer of Omega fire with a thickness of 20 mm has been provided (see Figure 6.23). As for the beams, the total thickness is built up in different layers in a range of 0.2-1 mm each.

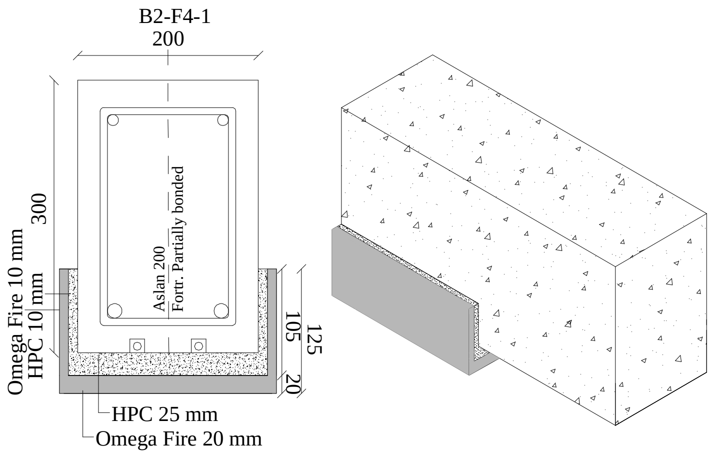

Figure 6.21 – Insulation layout beam B2-F4-1

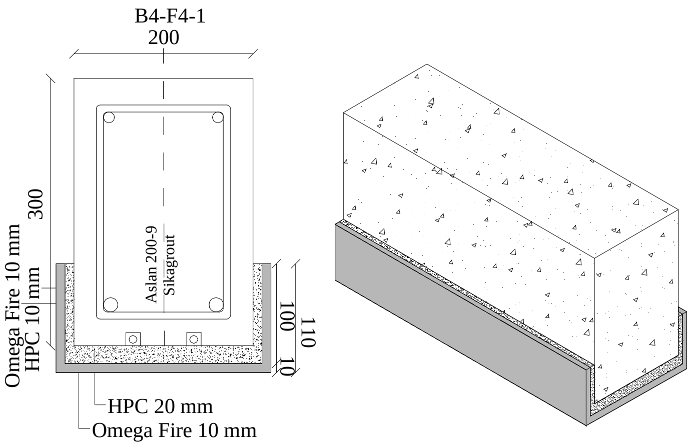

Figure 6.22 – Insulation layout beam B4-F4-1

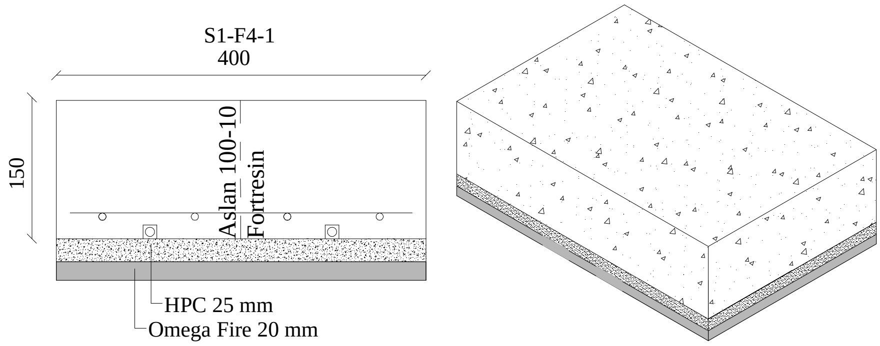

Figure 6.23 – Insulation layout beam S1-F4-1

Slabs S2-F4-1 and S2-F4-2 (see Figure 6.24 and Figure 6.25) have been protected with Promatect L-500. The thickness of the plate at the bottom was taken 80 mm for slab S2-F4-1, composed of Promat L- 500 400 mm wide plates with a thickness of 50 mm and 30 mm, as indicated in Figure 6.24**.** The first 50 mm layer of protection was composed of two plates with a length of 1450 mm joint together in the longitudinal direction by means of silicate glue (type Promacol k84 supplied by Promat), so to achieve a total length of 2900 mm. A layer of silicate glue at the beam soffit has been also provided. Additionally, these two plates were mechanical fixed to the bottom surface by mean of screws with a distance of 250 mm. At the bottom of the first layer, two additional plates with a thickness of 30 mm were mechanically fixed with screws placed at a distance of 200 mm in longitudinal direction. In order to fill any possible gap in between the board layers, silicate glue has been also provided at the inner surface of the fire insulation plates of 30 mm (see Figure 6.24). The configuration of the bottom protection of slab S2-F4-2 was the same adopted in slab S2-F4-1, but plates with a thickness of 30 mm were used (see Figure 6.25). The screws were additionally protected with silicate glue in order to minimize the effect of screws on heat transfer.

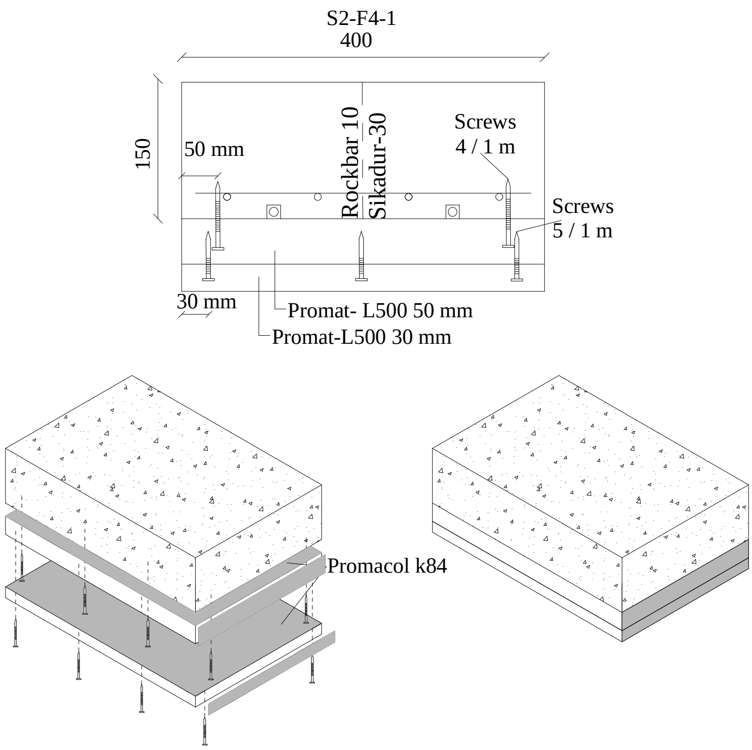

Figure 6.24 – Insulation layout beam S2-F4-1

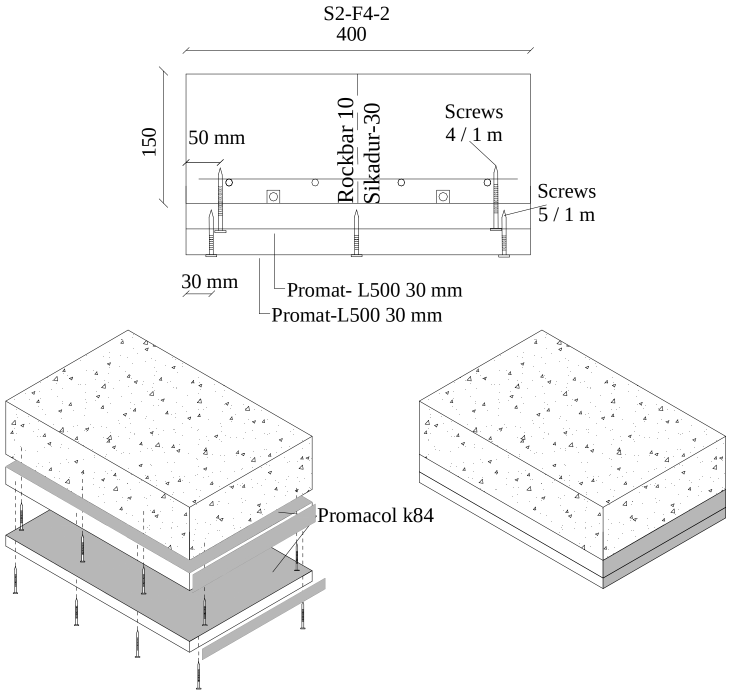

Figure 6.25 – Insulation layout beam S2-F4-2

6.4 Test setup and test procedure

The specimens were tested simultaneously in a horizontal furnace of 6000 mm long by 3000 mm wide. The specimens were lifted and placed on the top of a steel ring frame that is placed on the top of the furnace chamber (see Figure 6.26). No axial restraints were provided during the fire tests. The specimens are placed in the transverse direction of the furnace (the clear span of the specimens being 3000 mm). The openings on both sides of the test specimens have been closed with 150 mm thick aerated concrete slabs. In between the aerated concrete slabs and the test specimens, ceramic wool (20 mm thick) has been placed. Thereafter, the beams were exposed to fire from three sides (bottom of the beams and lateral sides for a height equal to 150 mm) and the top surface was exposed to ambient temperature as shown in Figure 6.27. The tested slabs were exposed to fire only from the soffit and the top surface was exposed to ambient temperature as shown in Figure 6.28. Figure 6.27 shows the test set-up of fire test series one till three, in which 6 beams are placed on the top of the furnace. Figure 6.28 shows in a similar way the fourth fire test series with a combination of beams and slabs. The test set-up of all the fire test series is shown more into detail in Appendix C.

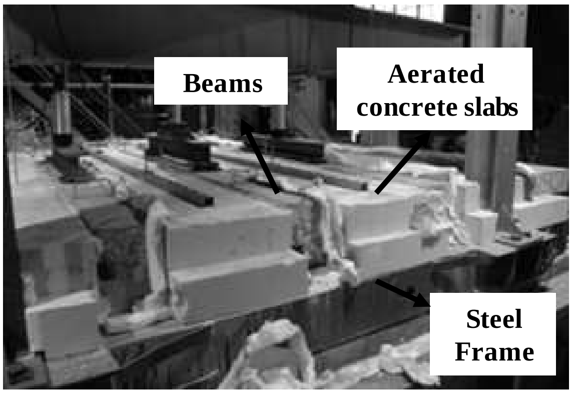

Figure 6.26 – Furnace chamber

Fire testing standards [9,11] require that structural elements need to resist the service loads during the fire test. Thus, before starting the fire test all the test specimens were loaded to their service load (as calculated in Chapter 5, section 5.6.2). The applied service loads (at each point load) Q_{serv}, the percentage of the ultimate capacity of the reference NSM FRP strengthened beam/slab, $Q_{serv}/Q_{u,str.}$ and the percentage of the ultimate capacity of the reference unstrengthened beam/slab, $Q_{serv}/Q_{u,unst}$ is given in Table 6.6.

Table 6.6 – Applied service loads during fire exposure

Fire Series	Specimens	Q_{serv} [kN]	$Q_{serv}/Q_{u,str.}$ [%]	$Q_{serv}/Q_{u,unst}$ [%]
First fire test series	B0-F1	30.5	-	54.0
	B1-F1-1, B1-F1-2	36.0	37.0	63.0
	B2-F1-2, B2-F1-2, B3-F1-1	40.5	40.0	71.0
Second fire test series	B0-F2	30.5	-	54.0
	B1-F2-1, B1-F2-2, B1-F2-3	36.0	37.0	63.0
	B2-F2-1, B2-F2-2	40.5	40.0	71.0
Third fire test series	B1-F3-1, B1-F3-2 B1-F3-3, B1-F3-4	36.0	37.0	63.0
	B2-F3-1, B4-F3-1	40.5	40.0	71.0
Fourth fire test series	B2-F4-1, B4-F4-1	40.5	40.0	71.0
	S0-F4	7.5	-	52.0
	S1-F4-1, S2-F4-1, S2-F4-2	10.0	30.0	68.0

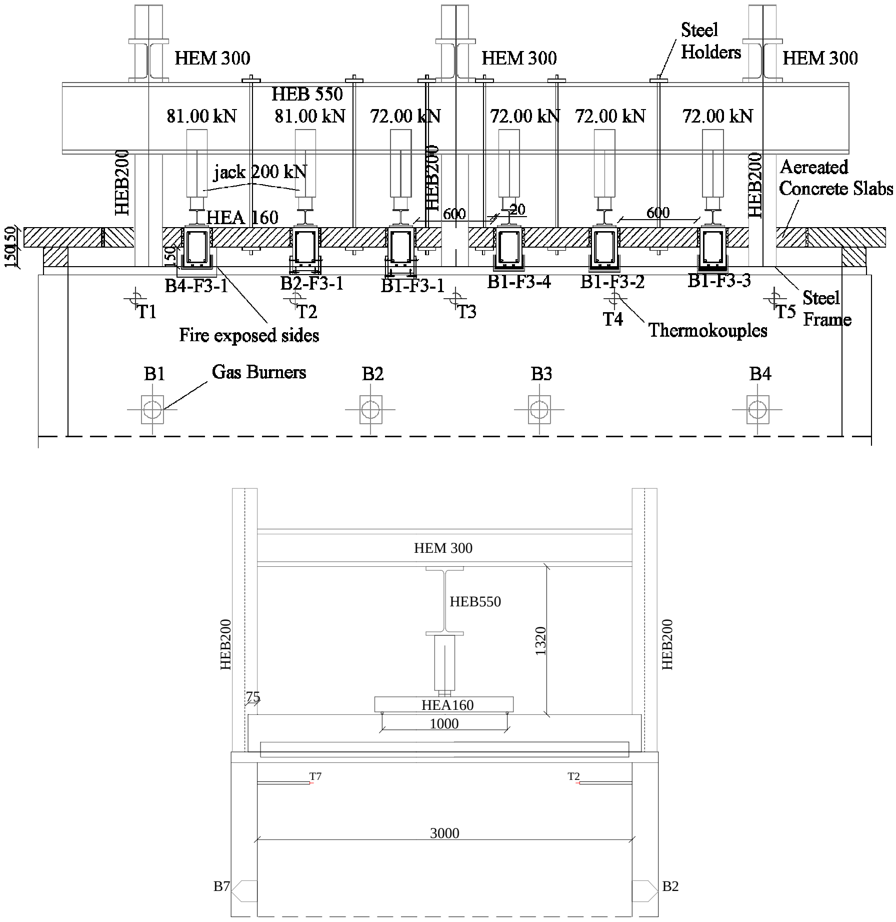

Figure 6.27 – Test setup first till third fire test series (6 beams per fire test, figure shows beams of third fire test series)

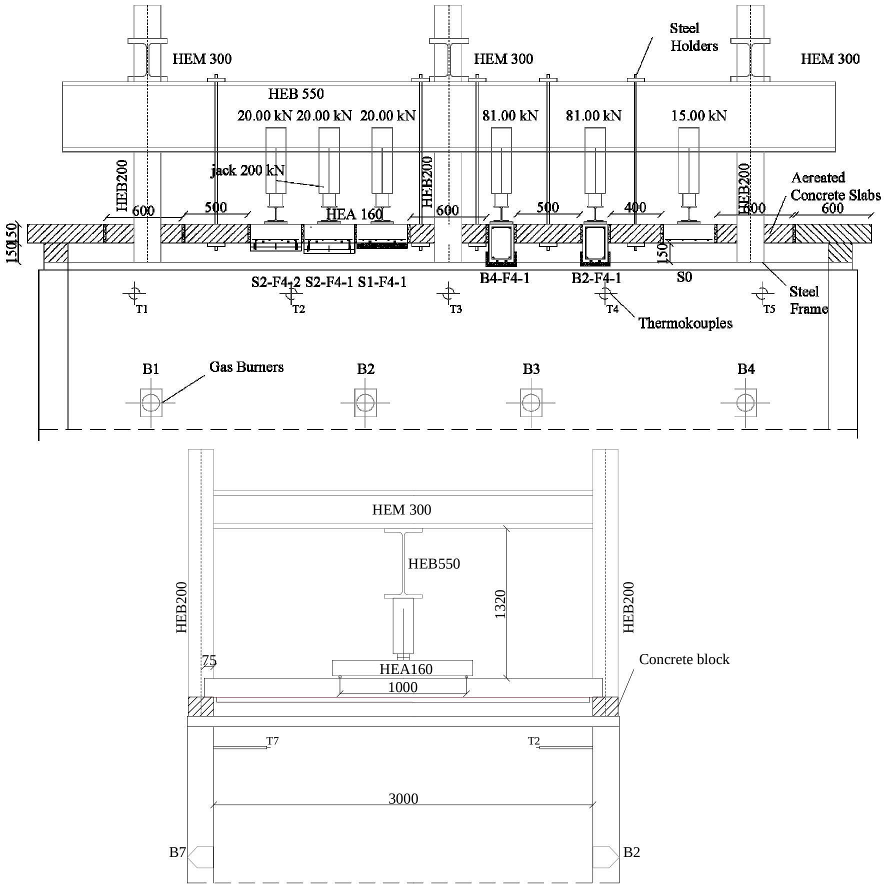

Figure 6.28 – Test setup fourth fire test series (2 beams and 4 slabs)

The service load has been applied by a separate hydraulic unit as a function of the required load, so that specimens with the same FRP strengthened reinforcement system where loaded in groups. During the fire test all the specimens were loaded in 4 point bending in a purpose built loading frame as shown in Figure 6.29. The load was applied by means of a hydraulic jack, with a maximum capacity of 200 kN, controlled by a load cell. The load was applied approximately 30 min prior to the start of the fire, so that a steady condition (no increase in deflection with time) is reached. The load is kept constant during the fire test. A maximum of 2 h fire exposure was chosen for fire test series one, two and four while a maximum of 1 h of fire exposure was chosen for fire test series three. After reaching the desired time of fire exposure the tests were stopped and specimens remained on top of the furnace during an ambient cooling (with open furnace, by removing the aereated concrete slabs) of about 48 hours.

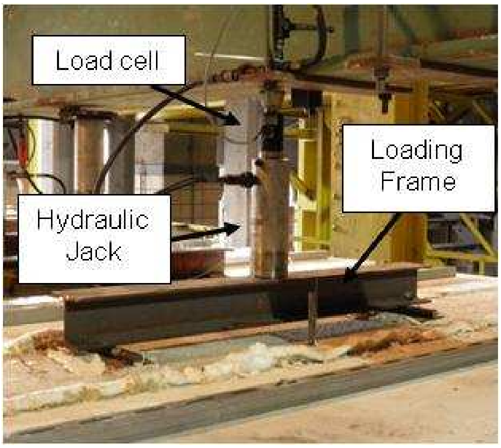

Figure 6.29 – Loading equipment during fire

All the beams and slabs were exposed to a EN 1363-1 [9] standard fire. This means that the furnace temperature is controlled to follow the standard time-temperature curve according to ISO 834 [10]. This standard prescribes the heating by the combustion gases as function of time and is given by equation 6.1:

$$T_{gs} = T_0 + 345\log_{10}(8t + 1) \tag{6.1}$$

Where T_{gs} = the temperature of the combustion gases [°C], T_0 = the initial temperature [°C] and t = the time [min]. The temperatures recorded in the furnace for the 4 test series are shown in Appendix C.

6.5 Instrumentations

The specimens were instrumented to measure temperature distributions throughout the cross section. Twenty thermocouples, type K, were placed inside the concrete at two different cross-sections of the member (each at a distance equal to 375 mm from the middle of the specimen). For the beams, in each measurement section ten thermocouples are placed as indicated in Figure 6.30: one is placed at the soffit of the concrete, one at the interface between the adhesive and the FRP reinforcement, two at the lower steel reinforcement, one at the unexposed upper concrete surface and the remaining thermocouples in the concrete section. For the slabs in each concrete section nine thermocouples per measuring section are placed in a similar way as for the beams. This is illustrated in Figure 6.31.

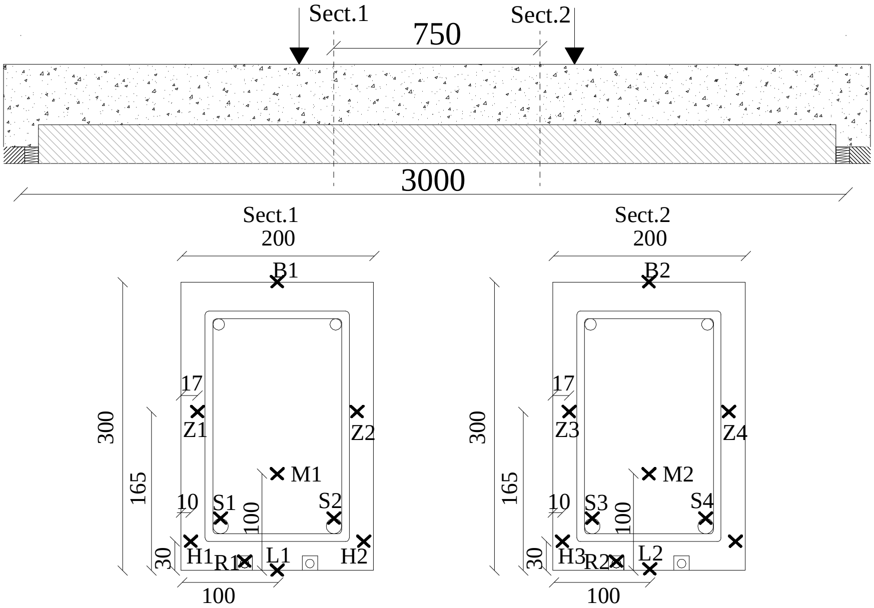

Figure 6.30 – Location thermocouples into the beams

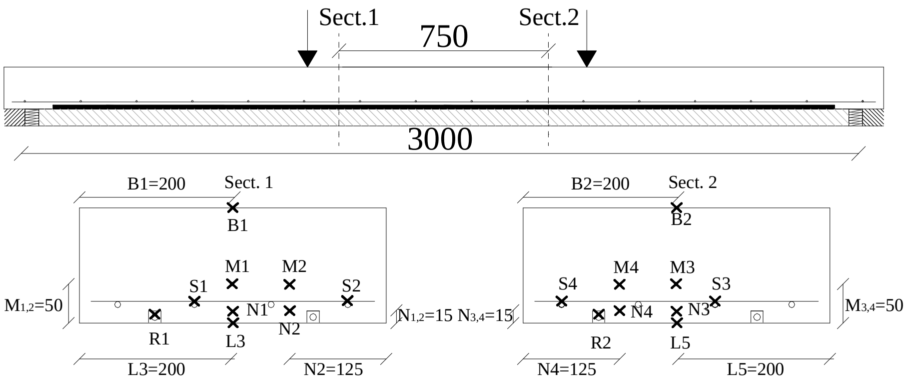

Figure 6.31 – Location thermocouples into the slabs

In addition a displacement transducer (LVDT) was connected to the unexposed surface of each specimen to measure the deflection at midspan in the pre-load phase and during fire testing. To avoid any damage of the displacement transducers, it was decided to place the LVDTs outside the furnace and connect them to the midspan of the elements through a system of wires and rollers, as shown in Figure 6.32. The midspan deflection of the specimens was also recorded manually by means of a ruler against a reference wire, as shown in Figure 6.33. During the fire tests, also visual observations were made trough view ports in the furnace to record the progression of possible cracks or/and localized burning in the insulation as well as possible delamination of the insulation or/and FRP reinforcement system.

Figure 6.32 – LVDTs midspan deflection measurement system

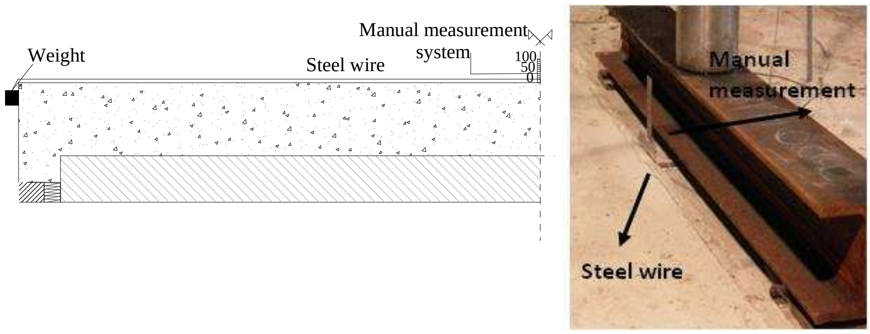

Figure 6.33 – Midspan deflection manual measurement system

6.6 Test results in terms of main observations

The overall performance of the different insulation systems under standard fire exposure, in terms of time at which a detachment of the fire insulation system was observed (t_{detach}) is given in Table 6.7. A summary of the visual observations during each fire test series is presented and discussed in detail in the following sections.

Table 6.7 – Performance of fire insulation system

Fire series	Specimen	Insulation system	Thickness bottom [mm]	Thickness side [mm]	t_{detach} [min]
First series	B0-F1	-			-
	B1-F1-1	Promat H	25+15	15	N.D.
	B1-F1-2	WR-APP type C	30	15	-*
	B2-F1-1	Aestuver	30	15	70
	B2-F1-2	Aestuver	40	-	34
	B3-F1-1	Aestuver	40	15	105
Second series	B0-F2	-			-
	B1-F2-1	Promatect L-500	50+50	20	N.D.
	B1-F2-2	HPC/Omega Fire	25 / 20	15 / -	N.D. / 20
	B1-F2-3	HPC/Omega Fire	25 / 20	15	N.D. / 20
	B2-F2-1	WR-APP type C	30	15	N.D.
	B2-F2-2	WR-APP type C	40	15	100
Third series	B1-F3-1	Promatect L-500	50+50	20	N.D.
	B1-F3-2	HPC/Omega Fire	25 / 20	10 / 10	N.D. / 18
	B1-F3-3	HPC/Omega Fire	35 / 20	10 / 10	N.D. / 18
	B1-F3-4	HPC/Omega Fire	20 / 15	10 / 10	N.D. /18
	B2-F3-1	Promatect L-500	30+30	20	N.D.
	B4-F3-1	HPC/Omega Fire	10 / 10	10 /10	N.D. / N.D.
Fourth series	B2-F4-1	HPC/Omega Fire	25 / 20	10 / 10	N.D. / 30
	B4-F4-1	HPC/Omega Fire	20 / 10	10 / 10	N.D. / 30
	S0-F4	-			-
	S1-F4-1	HPC/Omega Fire	25 / 20	-	N.D./75
	S2-F4-1	Promatect L-500	50+30	-	N.D.
	S2-F4-2	Promatect L-500	30+30	-	N.D.

N.D.: No detachment
** improper application of the insulation material*

6.6.1 First fire test

At 65 min of fire exposure a sudden increase of deflection was observed for reference beam B0-F1. The load was removed at approximately 105 min of fire exposure to avoid collapse of the beam into the furnace.

Except for some discoloration and small cracks in the lower bottom protection board of beam B1-F1-1 insulated with Promat-H, the fire insulation board system was intact and few signs of deterioration were observed (see Figure 6.34a). After fire exposure the boards were carefully removed and no signs of damage were observed to the adhesive.

The fire protection of board B1-F1-2 delaminated prematurely within 5 minutes of fire exposure for the entire length of the beam. This unexpected behaviour was diagnosed to improper application of the insulation material. It is likely that during application the insulation did not bond well with the soffit of the beam resulting in debonding of the insulation off of the substrate concrete prematurely during fire exposure. For this reason test results of beam B1-F1-2 will not be discussed further.

At approximately 70 minutes into the test, for beam B2-F1-1, a partial detachment of one of the two insulation boards was observed (see Figure 6.34b), allowing heat to be transferred more rapidly into the beam section. At the end of the 2 h of fire exposure the epoxy resin was partially burned off.

At 34 min. of fire exposure the protection plate of beam B2-F1-2 started to detach from the underside of the beam. Within 10 min. the insulation system felt completely into the test furnace. This resulted in burning of the bonding agent. At the end of the 2h of fire exposure the NSM FRP reinforcement stayed into the grooves, although the adhesive had extensively burnt off (see Figure 6.34c).

Also for beam B3-F1-1 one of the two bottom plate detach completely from the beam at approximately 105 min into the test. Indeed at around 90 min into the test a detachment of the intumescent strip, in between the board joint, was observed followed by progressive cracks around the screws, as shown in Figure 6.34d.

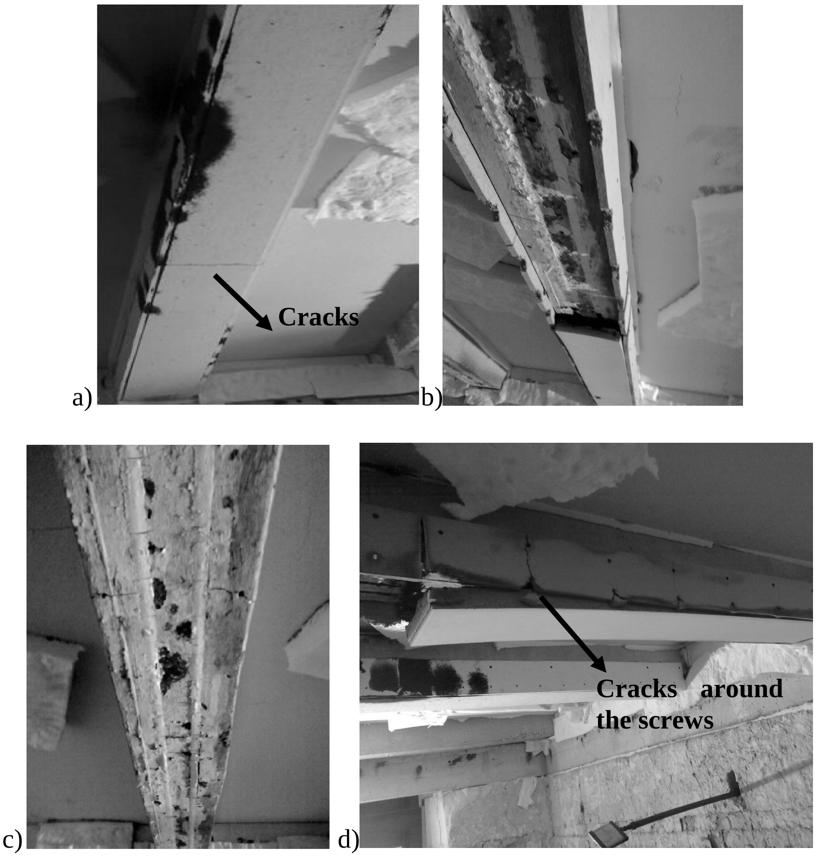

Figure 6.34 – Beams a) B1-F1-1, b) B2-F1-1, c) B2-F1-2 and d) B3-F1-1 after fire exposure

6.6.2 Second fire test

Despite the different insulation types and/or thickness all the insulated beams of the second fire test series could withstand the 2 hours fire test, while submitted to their service load. It should be observed that, while for the first fire test series the sides of the beams were exposed directly to the fire for an height equal to 70 mm (free space between the fire protection system and the aerated concrete slabs) in the second fire test series the ceramic wool (utilized to insulate the joints between the aerated concrete slabs and the specimens), was accidentally not removed from the surface of the beams as for the first fire test series, allowing a beneficial effect due to the additional insulation (see Figure 6.35a).

At 100 min of fire exposure, as observed during the first fire test series, a sudden increase of the deflection was observed for the reference beam B0-F2 and continued increasing till 110 min into the test, when the load was removed to avoid the collapse of the beam into the furnace. Several cracks and discoloration of the concrete surface were observed (see Figure 6.35a).

The fire insulation of beam B1-F2-1 (insulated with Promat –L 500) showed a single crack, for the lower bottom insulation board as shown in Figure 6.35b. The top bottom protection board was fully intact after the test. After fire exposure the boards were carefully removed and no signs of damage were observed to the adhesive.

Within 3 min of initiation of the fire test, surface flaming of the Omega fire coating of beams B1-F2-2 and B1-F2-3 was observed and lasted for approximately 7 min. At approximately 20 min into the tests, for both beams, the layer of Omega Fire detached from the layer of HPC. At 40 min flaming was observed at the outer few millimetres of the layer of HPC for both beams and lasted for approximately 20 min into the test. For Beam B1-F2-2, after detachment of the Omega layer (20 min. into the test), the layer of HPC was consumed in portions of the exposed face, presenting several cracks in proximity of the FRP anchorage zone (although the precise consumption of a certain amount of insulation or possible cracks could not be observed). These cracks widen as test progressed, and at almost 110 min. of fire exposure, for beam B1-F2-2, part of the HPC coating (for a length approximately equal to 500 mm) clearly detached from the bottom surface of the beam with consequently an increase of recorded temperature inside the adhesive. Due to the direct fire exposure, flaming of the bonding agent was observed. Observation after fire exposure revealed that the HPC protection coating was consumed (the outer few millimetres of the layer burned away) in portions of the exposed face for beam B1-F2-3 as shown in Figure 6.35c. After fire exposure the HPC layer was carefully removed and no signs of damage were observed to the adhesive for beam B1-F2-3. For beam B1-F2-2, after visual inspection, the portion of adhesive directly exposed to the fire was obviously burned away as shown in Figure 6.35d.

At 20 min into the fire tests, for both beams B2-F2-1 and B2-F2-2, transversal cracks on the surface of the insulation were observed (see Figure 6.36a-b) with consequently flaming of the surface. The crack opening gradually increased as the test progressed, likely due to thermally-induced shrinkage of the insulation. The flaming was thought to be associated with localized burning of the epoxy adhesive/matrix beneath the insulation at the location of cracks. Despite the large amount of cracks, the insulation system of beam B2-F2-1 remained attached to the beam for the complete fire exposure time (see Figure 6.36a). For beam B2-F2-2 the insulation system detached locally (for a length approximately equal to 500 mm) near 100 min. into the fire test with consequently burning of the epoxy adhesive (see Figure 6.36f). After fire exposure the insulation system of beam B2-F2-1 was carefully removed and it was observed that the epoxy adhesive was locally burnt off.

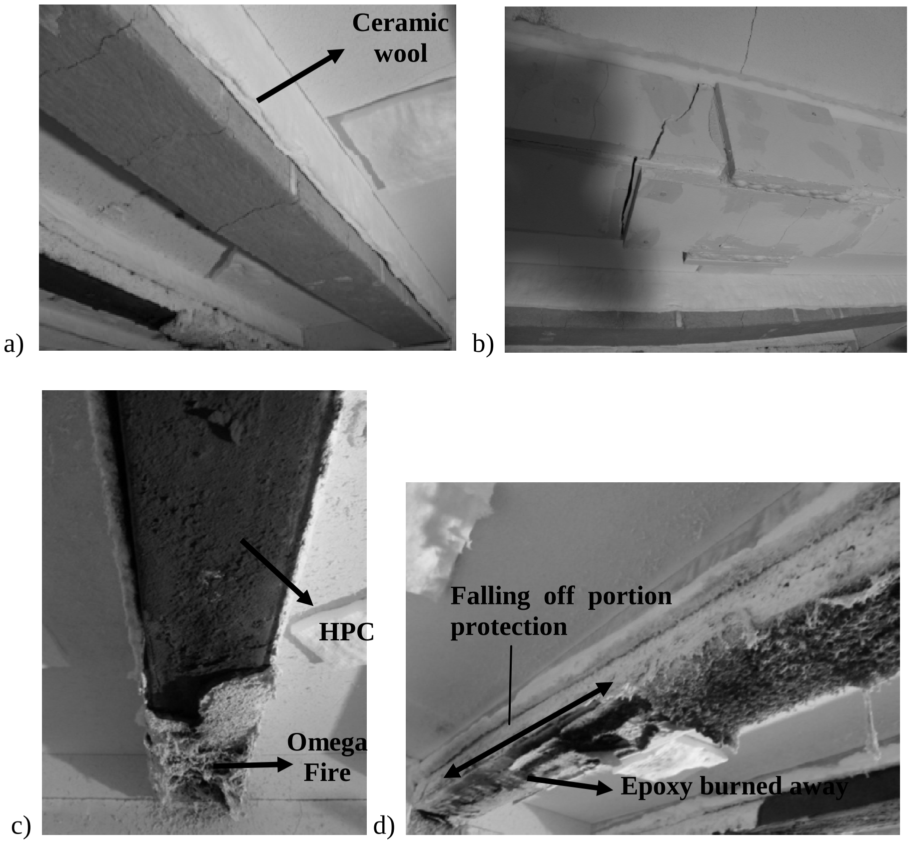

Figure 6.35 – Beams a) B0-F2, b) B1-F2-1, c) B1-F2-3 and d) B1-F2-2 after fire exposure

a) b)

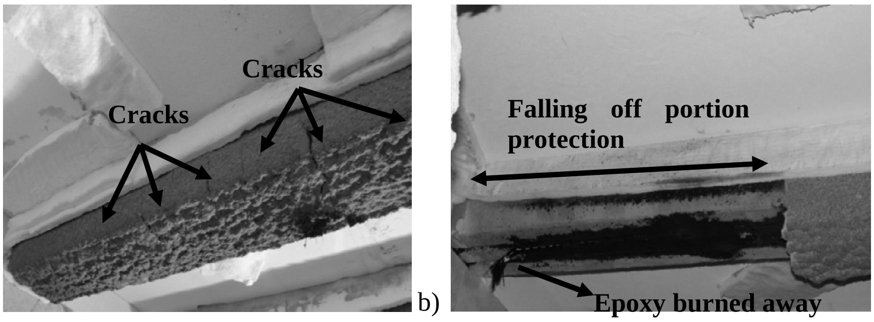

Figure 6.36 – Beams a) B2-F2-1 and b) B2-F2-2 after fire exposure

6.6.3 Third fire test

For the third fire test, all the beams were exposed to one hour of fire exposure. As for the first fire test series, the beams were exposed to the fire from three sides: the bottom side and the two lateral sides for a height equal to 150 mm. For the latter, 80 mm was insulated with different insulation systems (see section 6.3.3) and 70 mm was without any insulation.

Except for some discoloration and small cracks in the lower bottom protection board of beams insulated with Promatect L-500 (beams B1-F3-1 and B2-F3-2), the fire insulation board system was intact and few signs of deterioration were observed, as shown in Figure 6.37a-b. After fire exposure the boards were carefully removed and no signs of damage were observed to the adhesive.

At approximately 18 min into the tests for beams B1-F3-2, B1-F3-3 and B1-F3-4, insulated with HPC and Omega fire system, several cracks were observed for the outer layer of Omega Fire (the temperature in the furnace was approximately equal to 770 °C at that time) with surface flaming of the product. These cracks appear to rapidly widen as the test progressed. At approximately 30 min into the test, in the two lateral sides of the beams, the Omega Fire insulation started to detach (see Figure 6.37c-d and Figure 6.38a). At the same time cracks, at the bottom appeared to widen as the test progressed. Considering the considerable cracks observed and the partial detachment, it is likely that Omega fire was ineffective at approximately 30 min into the fire exposure. At 50 min into the test the layer of Omega Fire detached from the HPC layer at the bottom of the beams (temperature in the furnace was approximately 900°C). By observation, the HPC fire insulation system performed well for all the duration of fire exposure. Observations after fire exposure revealed that the HPC protection coating was consumed (the outer few millimetres of the layer burned away) in portions of the exposed face, presenting cracks for some of the beams in the outer layers (although the precise consumption of a certain amount of insulation or possible cracks could not be observed; see Figure 6.37c-d and Figure 6.38a).

Different behaviour was observed for beam B4-F3-1, for which, due maybe to the less thickness of the insulation with respect to the others beams insulated with the same material, no cracks were observed during the fire exposure. Observation after fire exposure revealed that Omega fire was consumed in portions of the exposed face (see Figure 6.38b). More investigations are needed for clearly understand the behaviour of Omega fire at fire exposure. After fire exposure, for all the beams insulated with HPC and Omega fire, the fire insulation system was carefully removed and no signs of damage were observed to the adhesive (resin or mortar).

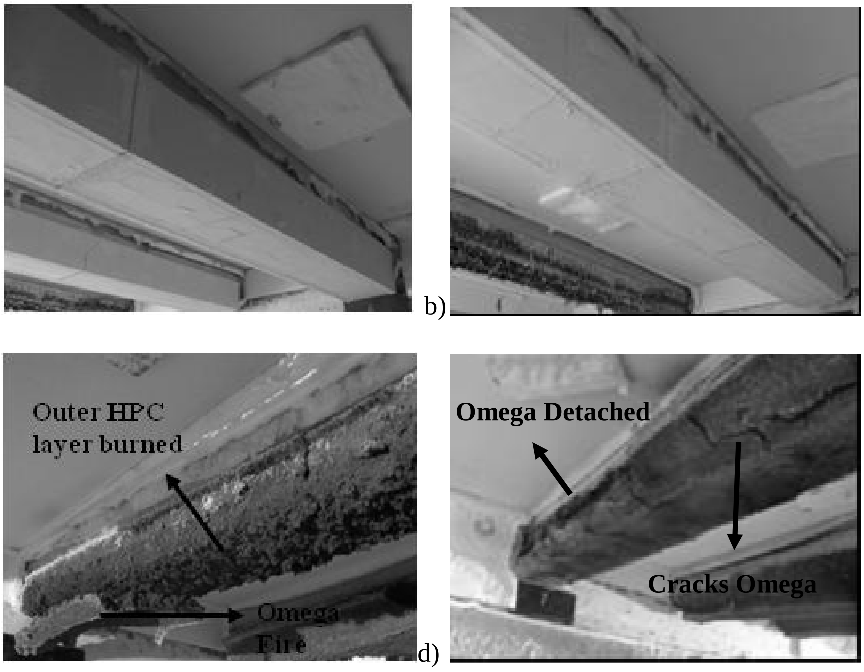

a) b) c) d)

Figure 6.37 – Beams a) B1-F3-1, b) B2-F3-2, c) B1-F3-2 and d) B1-F3-3 after fire exposure

a) b)

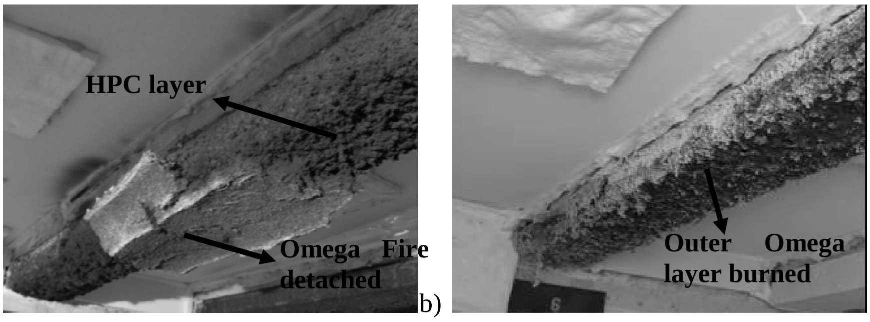

Figure 6.38 – Beams a) B1-F3-4 and b) B4-F3-1 after fire exposure

6.6.4 Fourth fire test

For beam B2-F4-1, for which the FRP was partially bonded and partially insulated, the fast increase of temperatures into the unprotected area led to a fast increase of temperature into the longitudinal steel (the concrete cover was around 15 mm close to the grooves) with consequently failure of the beam under the applied load. The beam felt into the oven around approximately 118 min of fire exposure. At that time for security reason the fire test was halted. Visual observations during fire show an early detachment of Omega fire at around 30 min into the tests with flaming of the product, as shown in Figure 6.39a.

At approximately 15 min into the test several cracks were observed for the outer layer of Omega Fire for beam B4-F4-1 with surface flaming of the product. The flaming lasted for approximately 30 min into the test and crack width increased as the test progressed. At 64 min into the test the outer layer of Omega fire was consumed in portion due to the flaming of the product (although the precise description of consumption of a certain amount of insulation could not be observed). By observations after fire exposure, the Omega fire layer was completely consumed and the HPC fire insulation was still intact along the length of the beam showing some cracks in the outer layer, as shown in Figure 6.39b. After fire exposure the insulation was carefully removed and no significant signs of damage were observed to the adhesive.

At 34 min of fire exposure, several cracks were observed at the concrete bottom surface of slab S0. A fast increase of deflection as the test progressed was observed. At approximately 50 min into the test the increase of deflection was around 70 mm, and the load was removed to avoid the collapse of the slab into the furnace. By observations, after fire exposure, several cracks, concrete cover spalling and discoloration of the concrete surface have been observed (see Figure 6.40a).

At approximately 15 min into the test several cracks were observed for the outer layer of Omega Fire of slab S1-F4-1 with surface flaming of the product. The flaming lasted for approximately 40 min into the test and cracks widen as test progressed. At 75 min into the tests the Omega Fire detached from the bottom of the beam and only the HPC layer stayed attached all along the length of the beam, as shown in Figure 6.40b. At that time a slightly increase of the FRP temperature as well as deflection was observed. After fire exposure the HPC layer was carefully removed and no signs of damage were observed to the adhesive.

Except for some discoloration and some cracks in the lower bottom protection board of slabs insulated with Promatect L-500 (slabs S2-F4-1 and S2-F4-2), the fire insulation board system was intact and few signs of deteriorations were observed, as shown in Figure 6.40c-d. After fire exposure the boards were carefully removed and no signs of damage were observed to the adhesive.

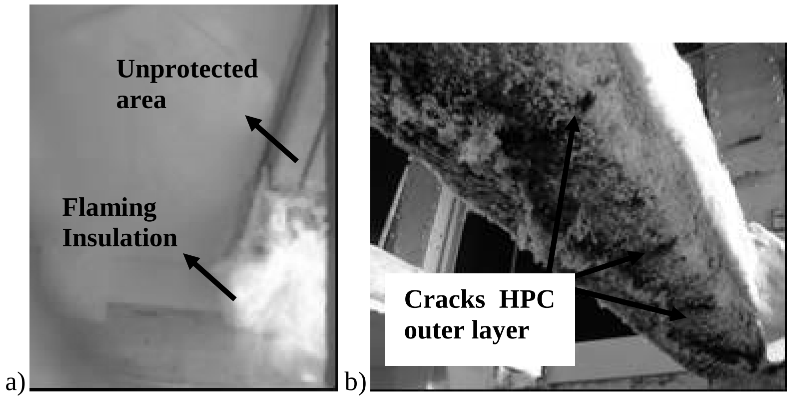

Figure 6.39 – Specimens a) B3-F4-1 and b) B4-F4-1 after fire exposure

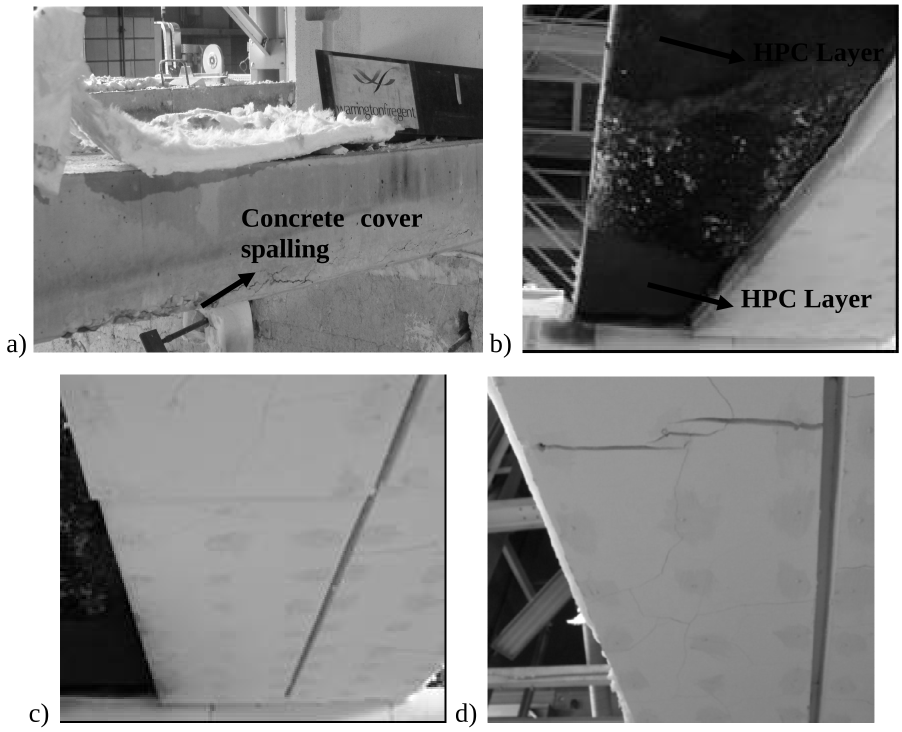

Figure 6.40 – Specimens a) S0-F4, b) S1-F4-1, c) S2-F4-1 and d) S2-F4-2 after fire exposure

6.7 Thermal performance of the FRP strengthened members under fire exposure

The thermal response of the FRP strengthened members (beams and slabs) under fire exposure can be studied by comparing the temperature increase into the monitored sections. The performance of the insulation played a key role in limiting the temperatures in the concrete, steel rebars, FRP reinforcement and adhesive (epoxy or mortar). The fire endurance (with respect to the 2 h or/and 1 h fire duration of this research program) was defined as the amount of time that: (1) the structural members must sustain the applied load without structural failure (according to the EN 1363-1 [9]), (2) the unexposed average temperatures of the concrete should not increase the initial average temperature by more than 140 °C or the temperature at any location of the unexposed concrete part should not increase above the initial average temperature by more than 180°C (if the specimen should fulfil a separating function during fire, in accordance to EN 1363-1 [9]) and (3) the temperature in the reinforcing steel should not increase more than a critical temperature assumed equal to 593 °C (this critical temperature, according to table 3.2a of Eurocode 2 [7], ASTM E119 [11] and as reported in previous work of Kodur et al. 2010 [12], can be assumed as the temperature where the steel has lost approximately 50% of its yield strength at room temperature).

It has to be noted that the fire resistance of typical FRP-strengthened flexural members is mainly influenced by the strength and stiffness properties of the adhesive and longitudinal steel reinforcement, since the temperatures in concrete, for insulated beams and slabs, remain low for most of the fire duration (see Table 6.8). Indeed, as the rate of degradation of the adhesive is expected to be faster with respect to the steel due to its lower tolerance to high temperatures, the temperatures in the longitudinal steel reinforcements, in particular in case of FRP loss of composite action due to high temperature at the adhesive/FRP interface, become an important indicator of the fire performance of the FRP-strengthened RC elements. For this reason comments about the increase of temperatures of longitudinal steel reinforcement and at the FRP/adhesive will be discussed in the following sections for each fire test series. A summary of temperatures recorded at the bottom longitudinal steel reinforcement and at the FRP/adhesive interface is given in Table 6.8 section 6.8. A complete overview of the temperature increase in the beams/slabs sections is given in Appendix C.

6.7.1 First fire test

Figure 6.41 shows the increase of temperature recorded by the thermocouples (average values of four thermocouples) at the longitudinal steel reinforcements. As expected, the test results show that supplemental insulation influences the temperature increase at the longitudinal steel reinforcement. Beam B0-F1 did not satisfy the thermal criteria, described in the section above, for which the steel temperature should be lower than 593 °C.

The bottom longitudinal steel rebars in beams B1-F1-1, B2-F1-1 and B3-F1-1 experienced a steady rise in temperature for the entire test duration. This is due to the presence of insulation, which played a key role in limiting the temperature of the longitudinal steel reinforcement for the entire duration of the fire test. For beam B2-F1-1 a change in the slope of the time-temperature curve was observed at around 70 min into the test. At that time part of the insulation detached from the beam.

The recorded rebars temperatures of beam B2-F1-2 are higher than recorded for the three others insulated beams since the beam was insulated only at the bottom surface. Moreover, due to the detachment of the insulation at approximately 34 min of fire exposure, the increase of temperature is mainly equal to the unprotected beam (the average longitudinal steel temperature after 2 h of fire exposure was approximately 570 °C).

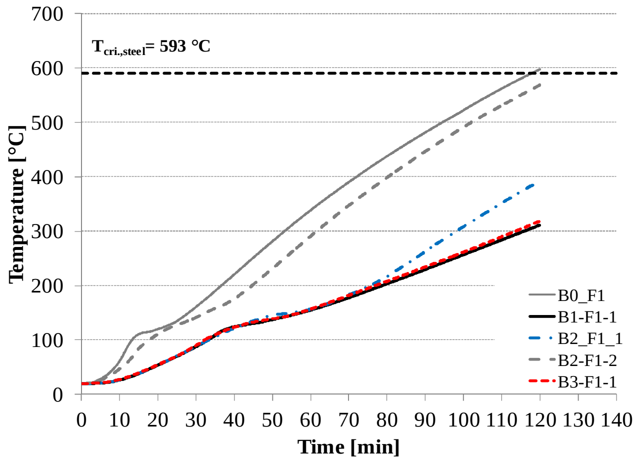

Figure 6.41 – Increase of temperatures longitudinal steel reinforcement first fire test

The temperature increase at FRP/epoxy interface is given in Figure 6.42. For most beams, temperatures recorded at the two measurement sections (see Figure 6.30) were very similar. Hence, the average value is shown. For beams B2-F1-1 and B3-F1-1, due to the partial detachment of the fire protection, temperature measurements in the 2 sections differs significantly and individual curves are given.

For beam B1-F1-1, the temperature increased to 100°C within 30 min., followed by a constant plateau lasting until approximately 55 min, caused by the evaporation of the free water into the concrete and the insulation material. Thereby the temperature increases slightly with fire exposure time. The maximum recorded temperature at the FRP/epoxy interface after 2 h of fire exposure was approximately 300°C. The epoxy resin started to lose strength and stiffness when the glass transition temperature was exceeded and can be ineffective by the end of the fire test.

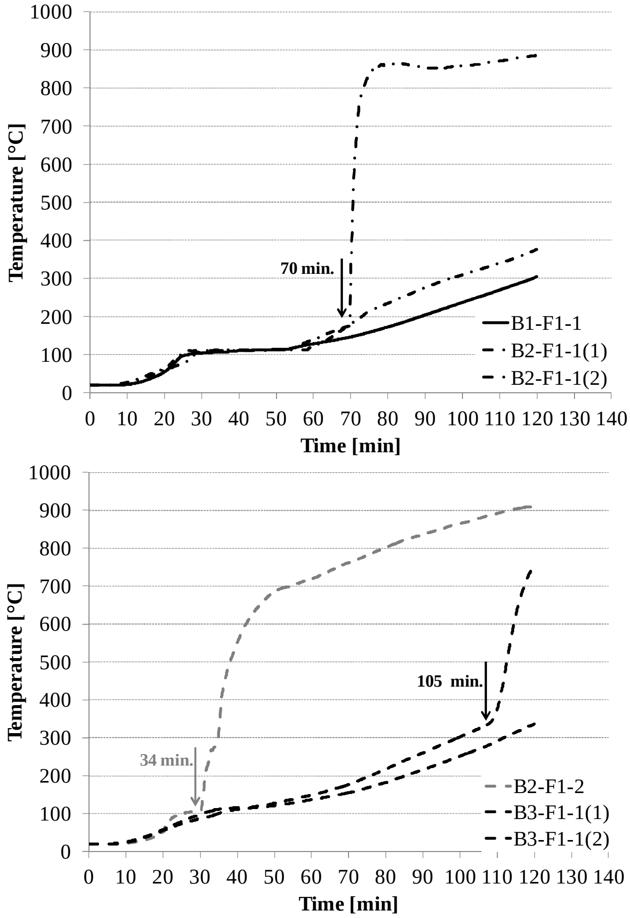

Figure 6.42 – Increase of temperatures at FRP/epoxy interface of first fire test

For beam B2-F1-1, due to the partial detachment of the insulation material, a sudden increase of temperature was recorded in one of the two monitored sections. This sudden increase of temperature is attributed to the burning of the adhesive and FRP bars matrix. In a similar way, at 34 min into the fire test the detachment of fire protection system was the cause of the sudden increase of temperature recorded at the interface between the adhesive and the FRP for beam B2-F1-2. At the end of the fire exposure the epoxy adhesive was completely glazed and ineffective. The fire board protection of beam B3-F1-1 is the same as for beam B2-F1-2 but additional boards with a thickness of 15 mm were provided at both sides along the entire length of the beam. The temperature at the FRP/epoxy interface increased to 100 °C within approximately 35 min, followed by a constant plateau lasting until 60 min, after that the temperature continued to increase with fire exposure. The intumescent strip, used to close the joints between the boards, performed well for a time equal to 105 min of fire exposure. At that time a sudden increase of temperature was observed in one of the two monitored sections due to the partially detachment of the fire protection. After 2 h of fire exposure, the maximum recorded temperature (on the side where the fire protection board was still in place) was approximately 330 °C while for the un-protected side approximately 700 °C. The epoxy adhesive was burned and no strength contribution of the bonded FRP was expected.

6.7.2 Second fire test

Figure 6.43 shows the increase of temperature recorded by the thermocouples (average values of four thermocouples) at the longitudinal steel reinforcements of the second fire test. It can be seen that the longitudinal steel reinforcement in the control beam reaches a high temperature value of approximately 590 °C in 120 min of fire exposure. The bottom longitudinal steel rebars in the insulated beams experience a steady rise in temperature for the entire test duration. For all the insulated beams the steel temperature remained well below 593 °C. This temperature trend can be attributed to the low thermal conductivity of the different insulation materials applied, that helps to keep the longitudinal steel reinforcement temperatures low.

Despite the higher insulation thickness, the recorded longitudinal steel reinforcement temperatures of beam B1-F2-2 are higher as compared to beam B1-F2-3. This can be related to the early development of cracks in the insulation, as discussed in section 6.6.2 or/and can be explained considering that part of the HPC layer was detached with the Omega fire layer (although the precise description of detachment of a certain amount of insulation could not be observed).

It has to be noted that for beam B2-F2-2 no sudden increase of longitudinal steel temperature was observed during fire exposure. This can be related to the fact that, as discussed in the above section, the cracks in the insulation mainly developed close to the FRP anchorage zone; therefore far from the two monitored sections.

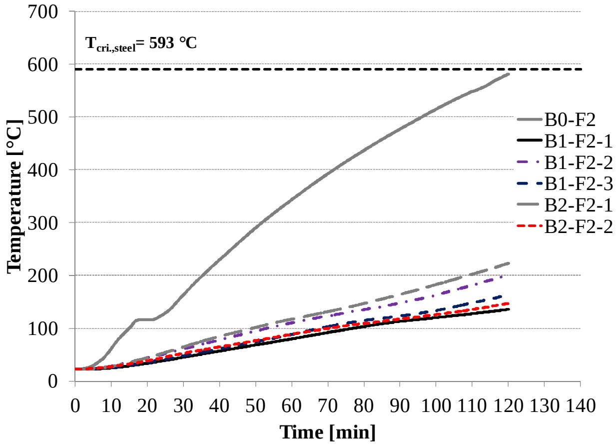

Figure 6.43 – Increase of temperatures longitudinal steel reinforcement second fire test

The temperature increase at the FRP/adhesive interface (average values of two thermocouples) for the second fire test is given in Figure 6.44. For beam B1-F2-1 the temperature increased slightly with fire exposure time. The temperature reached the epoxy glass transition temperature (T_g = 62°C) at approximately 60 min of fire exposure and the rate of increase of temperature remained steady during the fire exposure time without showing any abrupt increase. After 2 h of fire exposure the maximum recorded temperature at the FRP/epoxy interface was equal to 115°C (1.85 T_g).

Also for beam B1-F2-2 and B1-F2-3 the temperature increases slightly with increasing fire temperature exposure time. As observed for the longitudinal steel, despite the higher insulation thickness the development of cracks at the bottom surface of the insulation layer results in a higher temperature for beam B1-F2-2 with respect to beam B1-F2-3. It has to be noted that the temperatures of beam B1-F2-2 are higher than recorded in beam B1-F2-3 starting from 20 min into the test. At that time the Omega Fire detached from the layer of HPC and several cracks were observed close to the FRP anchorage zone. The glass transition temperature of the epoxy adhesive was reached at about 50 min into the fire test. An abrupt increase of temperature was recorded at almost 110 min into the fire test for beam B1-F2-2, due to the partial detachment of the insulation material from the bottom surface of the beam. After 2 h of fire exposure the maximum recorded temperature at the FRP/adhesive interface was equal to 281°C (4.5 T_g) and 160°C (2.6 T_g) respectively for beam B1-F2-2 and B1-F2-3.

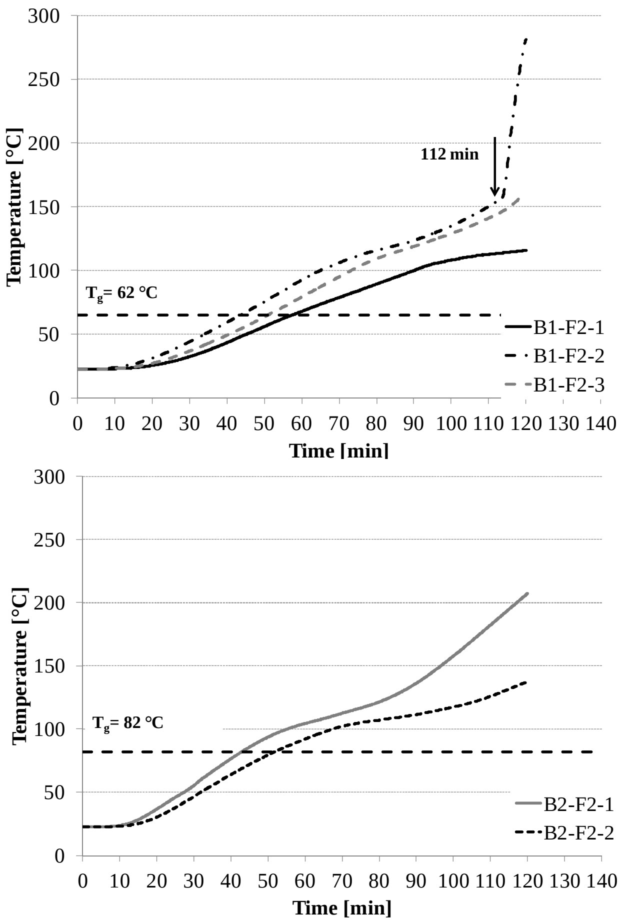

Figure 6.44 – Increase of temperatures at FRP/epoxy interface second fire test series

The data in Figure 6.44 shows a slightly higher increase of temperature at the adhesive/FRP interface for beam B2-F2-1 and beam B2-F2-2 with respect to the other insulated beams. This increase can be attributed to widening cracks in the insulation. For beam B2-F2-1 the glass transition temperature (T_g = 82°C) is reached at around 44 min of exposure and the rate of increase of temperature remained steady until 78 min after which point a change in the slope of the time-temperature curve was observed. This can be related to the development of cracks within the insulation. The final recorded temperature was approximately 210°C (2.52 T_g). For beam B2-F2-2 the adhesive glass transition temperature (T_g = 82°C) was reached at approximately 58 min of exposure and no abrupt increase of temperature was recorded during fire exposure (it has to be noted that the position of the thermocouples were far from the portion of insulation that detached and were therefore not able to record the increase of temperature due to the burning of the adhesive and FRP matrix). The final recorded temperature in the protected portion of adhesive was approximately 140 °C (1.70 T_g). The recorded temperatures within beam B2-F2-1 are higher than that recorded within beam B2-F2-2. This difference of temperatures is likely due to the 10 mm difference in thickness of fire protection.

6.7.3 Third fire test

Figure 6.45 shows the increase of temperature recorded by the thermocouples (average values of four thermocouples) at the longitudinal steel reinforcements of the third fire test. For all the beams the recorded temperatures of the longitudinal bottom steel reinforcement, after 1 hour of fire exposure remained well below the critical temperatures of 593°C. This can be expected (as verified in previous reference fire tests), given the 30 mm concrete cover and the beam geometry. The insulation only limited the temperatures even more below the critical temperature.

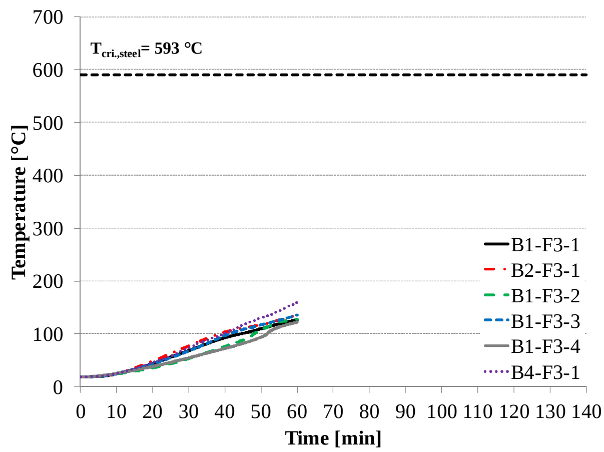

Figure 6.45 – Increase of temperatures longitudinal steel reinforcement third fire test

The temperature increase at the FRP/adhesive interface (average values of two thermocouples) for the third fire test series is given in Figure 6.46.

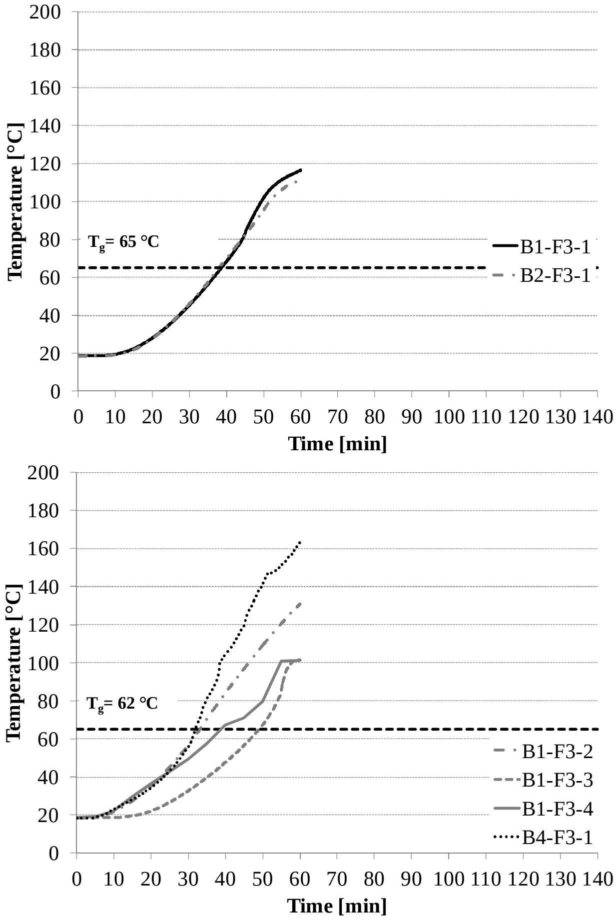

Figure 6.46 – Increase of temperatures at FRP/adhesive interface third fire test

The experimental data demonstrates that, for beams B1-F3-1 and B2-F3-1 insulated with Promatect L-500, despite the different thickness, both beams performed similarly (more investigations are needed to clarify this aspect). For both beams the temperature increased slightly with fire exposure time. The temperature in the adhesive reached its glass transition temperature (T_g= 62 ºC and T_g= 65 ºC for beam B1-F3-1 and B2-F3-1 respectively) at around 39 min of exposure and the rate of increase of temperature remained steady during the fire exposure time without showing any abrupt increase. After 1 h of fire exposure the maximum recorded temperature into the adhesive was equal to 116.5 °C for beam B1-F3-1 and 111.0 °C for beam B2-F3-1 corresponding to 1.87 T_g and 1.70 T_g respectively.

A different behaviour was observed for the beams insulated with HPC and Omega fire, in which the thermal performance of the insulation depends heavily on its overall thickness. For instance for beams B1-F3-2, B1-F3-3 and B1-F3-4 for which the FRP bars were embedded with the same adhesive and were insulated with the same material, increasing the thickness from 20 mm of HPC and 15 mm of Omega fire to 35 mm of HPC and 20 mm of Omega fire resulted in an increasing of reaching the glass transition temperature from about 33 min to 49 min. The temperature increase for beams B1-F3-2 and B1-F3-4 was equal up to approximately 30 min into the fire. At that moment the increase of temperature into the adhesive of beam B1-F3-4, despite the lower thickness of insulation, became lower than that of beam B1-F3-2. This can be related to a different deterioration or crack propagation of the inner layer of HPC along the beams. After 1 hour of fire exposure the maximum recorded temperature into the adhesive for beams B1-F3-2, B1-F3-3 and B1-F3-4 was 131 °C (2.1 T_g), 101.5 °C (1.63 T_g) and 101.0 °C (1.63 T_g) respectively. Beam B4-F3-1 with an insulation thickness of 10 mm of HPC and 10 mm of Omega fire, obtained the highest recorded increase of temperature into the bonding agent. After 1 h of fire exposure the temperature into the expansive mortar was about 163 °C.

6.7.4 Fourth fire test

Figure 6.47 shows the increase of temperature recorded by the thermocouples (average values of four thermocouples) at the longitudinal steel reinforcements for the two beams tested in the fourth fire test series, including the reference beam B0-F1 tested in the first fire test series. It has to be noted that for the partially bonded and partially insulated beam B2-F4-1 the recorded temperatures at the bottom longitudinal steel refers to the unprotected area. Beam B2-F4-1 did not satisfy the thermal criteria for which the steel temperature should be lower than 593 °C; the recorded temperature reached a high temperature value of approximately 630 °C in 118 min of fire exposure.

In beam B2-F4-1, the longitudinal steel reinforcement displayed higher temperatures as compared to the reference beam B0-F1, due to the smaller concrete cover in proximity of the grooves where the CFRP are inserted, allowing heat to be transferred more rapidly into the beam section. The bottom longitudinal steel rebars in the beam B4-F4-1 experienced a steady rise in temperature for the entire test duration; the steel rebars temperature was approximately 300 °C after 2 h of fire exposure.

The temperature increase at the FRP/adhesive interface (average values of two thermocouples) for the beams tested in the fourth fire test is given in Figure 6.48.

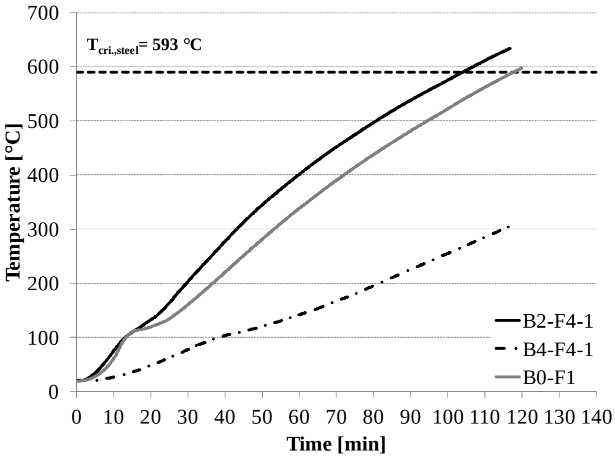

Figure 6.47 – Increase of temperatures longitudinal steel reinforcement beams fourth fire test

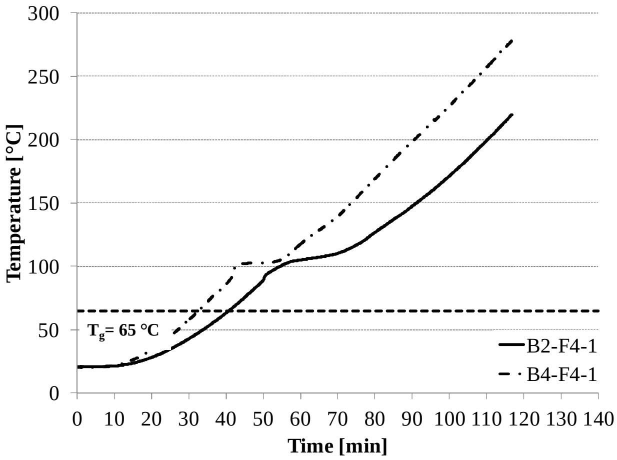

Figure 6.48 – Increase of temperatures at FRP/adhesive interface beams fourth fire test

For beam B2-F4-1, the recorded temperatures at the FRP/adhesive interface refers to the insulated area (see Appendix C). The temperature increased to 100°C within 50 min, followed by an almost constant plateau lasting until approximately 65 min. Thereby the temperature increased slightly with fire exposure time. The temperature reached the epoxy glass transition temperature (T_g = 65 °C) at approximately 40 min of fire exposure. After 2 h of fire exposure the maximum recorded temperature at the FRP/epoxy interface was equal to 220 °C (3.4 T_g). Beam B4-F4-1 with an insulation thickness of 20 mm of HPC and 10 mm of Omega Fire, presented a higher recorded increase of temperature at the FRP/adhesive interface with respect of beam B2-F4-1. After 2 h of fire exposure the temperature into the expansive mortar was about 280 °C. The cementious mortar likely started to lose strength and stiffness, considering the high temperatures recorded, and was possibly ineffective by the end of the fire test.

Figure 6.49 shows the increase of temperature recorded by the thermocouples at the longitudinal steel reinforcements for the four slabs tested in the fourth fire test. For the insulated slabs temperature measurements of the internal and external steel rebars differs significantly and individual curves (average of two thermocouples) are given.

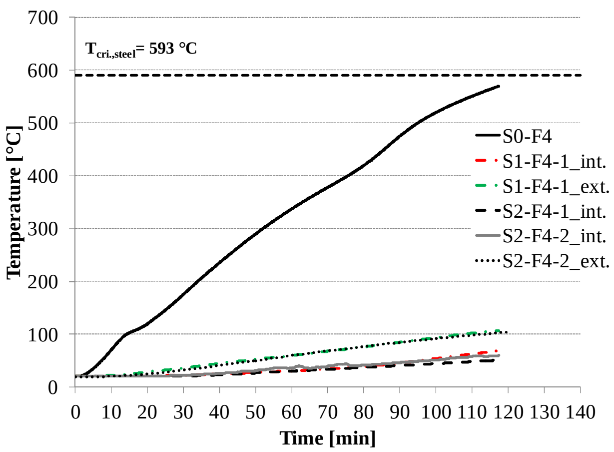

Figure 6.49 – Increase of temperatures longitudinal steel reinforcement slabs fourth fire test

It can be seen that the longitudinal steel reinforcement (average temperature of 4 thermocouples) in the control slab reached a high temperature value of approximately 580 °C in 120 min of fire exposure. It has to be noted that at approximately 50 min into the fire test the slab S0-F4 was unloaded to avoid any collapse into the furnace. The bottom longitudinal steel rebars in the insulated slabs experience a steady rise in temperature for the entire test duration. For all the insulated slabs the steel temperature remained well below 593 °C.

The temperature increase at the FRP/adhesive interface (average values of two thermocouples) for the third fire test series is given in Figure 6.50.

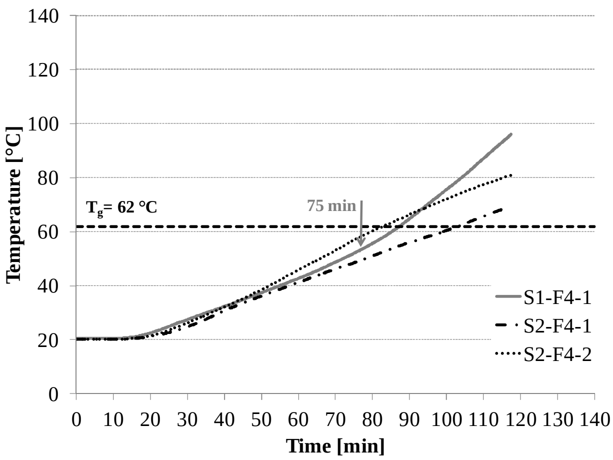

Figure 6.50 – Increase of temperatures at FRP/adhesive interface slabs fourth fire test

The experimental data demonstrates that, for slab S1-F4-1, the temperature at adhesive/FRP interface increased slightly with fire exposure time. At approximately 75 min into the fire test a change in the slope of the time-temperature curve was observed, maybe induced by local cracks of the HPC protection layer combined with the complete detachment of Omega fire from the bottom of the slab. The temperature in the adhesive reached its glass transition temperature (T_g = 62 °C) at approximately 90 min of fire exposure. After 2 h of fire exposure the maximum recorded temperature at the FRP/adhesive interface was equal to 96 °C corresponding to 1.54 T_g. For the two slabs S2-F4-1 and S2-F4-2 insulated with Promatect L-500, the thermal performance of the insulation depends on the overall thickness. For instance increasing the thickness from 60 mm (slab S2-F4-2) to 80 mm (slab S2-F4-1) resulted in an increasing of reaching the glass transition temperature from approximately 83 min to 105 min. For both slabs the temperature increased slightly with fire exposure time without showing any abrupt increase. After 2 h of fire exposure the maximum recorded temperature into the adhesive was equal to 70 °C for slab S2-F4-1 and 80 °C for slab S2-F4-2 corresponding to 1.11 T_g and 1.30 T_g respectively.

6.8 Fire endurance of the FRP strengthened members under fire exposure

The failure criteria adopted to determine the fire endurance with respect to 2h or/and 1h fire duration of this research program were outlined in section 6.7. The experimental data, discussed in the above sections, demonstrated that all the insulated beams and slabs, excluding beam B2-F4-1 obtained the fire endurance ratings of 2h or/and 1h by satisfying both thermal and load bearing criteria described in section 6.7. A summary of the temperatures recorded at the unexposed concrete surface, at the bottom longitudinal steel reinforcement and at the adhesive/FRP (epoxy or mortar) interface is reported in Table 6.8. The time when the adhesive reached the T_g, for the beams and slabs strengthened with FRP bars/strips embedded with the epoxy resin, is also reported in Table 6.8. The unstrengthened and un-protected beams did not achieve a 2h fire endurance rating because they failed to satisfy the thermal criterion for the longitudinal steel reinforcement. The reference slab (slab S0-F4) achieved the 2 h fire endurance since the average temperature at the bottom longitudinal steel reinforcement was approximately 580 °C after 2 hours of fire exposure. Nevertheless it has to be noted that around 50 min into the test, the slab was unloaded and the fire test was continued on the reference slab without any load applied. For all the insulated beams and slabs, excluding beam B1-F4-2, the longitudinal steel bottom reinforcement is well insulated. Therefore the recorded temperatures remained, after 2 h and/or 1 h of fire, well below the before mentioned critical temperature of 593 °C. This can be attributed to the low thermal conductivity of the insulation materials that play a key role in keeping low the temperature of the steel rebars for the entire duration of the fire exposure. It has to be noted that the geometry of the beams and slabs are designed in order that the average temperature of the unexposed concrete side is, for all the specimens, below the critical temperature of 140 °C. The thermal criterion for the FRP or adhesive temperature during fire exposure, is currently limited in design guidance documents (*fib* bulletin 14 [8] and ACI 440.2R-2008 [13]) by considering T_g as limiting value. The obtained experimental results demonstrate that even if the recorded temperature of the epoxy resin, exceed the glass transition temperature in a time range between 20 min and 60 min for the insulated beams and 80 min and 105 min for the insulated slabs, depending on the type of fire insulation and thickness, no impending failure of the insulated beams and slabs was observed during fire test, and all the insulated beams (excluding beam B2-F4-1) and slabs were able to withstand the acting service load of the strengthened beams and slabs for the entire duration of fire exposure.

Considering that for most of the beams and slabs the concrete temperature at the unexposed side and the bottom longitudinal steel temperatures are well below their respective critical temperatures, it has to be clarified that the presented research program focuses on the aspect of critical FRP bond adhesive temperature in relation to the adhesive glass transition temperature and the insulations were designed to limit the adhesive temperature, such to avoid significant dysfunctions in terms of strength compatibilities between the FRP and the RC members during or after fire. Therefore to know if the FRP strengthening is still active in some degree during or after fire exposure, deflection curves during fire were observed (next section) and residual strength testing has been performed as discussed in section 6.10.

Table 6.8 – Recorded temperatures

Fire series	Specimen	T_{concr} [°C]	T_{steel} [°C]	$T_{adh.}$ [°C]	$t_{Tadh=Tg.}$ [min]
First series (2 h exposure)	B0_F1	100.0	597.0	-	-
	B1-F1-1	72.0	310.0	305.0	22
	B2-F1-1	88.0	392.0	631.0	20
	B2-F1-2	94.0	570.0	644.0	20
	B3-F1-1	77.0	318.0	546.0	22
Second series (2 h exposure)	B0-F2	81.0	590.0	-	-
	B1-F2-1	48.0	135.8	115.7	60
	B1-F2-2	60.0	201.0	282.0	45
	B1-F2-3	51.0	163.0	158.0	50
	B2-F2-1	54.0	223.0	207.0	44
	B2-F2-2	53.0	147.0	137.0	58
Third series (1 h exposure)	B1-F3-1	34.6	126.4	116.5	39
	B1-F3-2	33.9	127.4	131.0	33
	B1-F3-3	33.8	135.4	101.5	49
	B1-F3-4	34.6	122.0	101.0	37
	B2-F3-1	39.2	135.1	111.0	38
	B4-F3-1	45.0	160.0	163.0	-
Fourth series (2 h exposure)	B2-F4-1	167.0	630.0	220.0	40
	B4-F4-1	77.0	310.0	278.0	-
	S0-F4	108.0	580.0	-	-
	S1-F4-1	35.0	88.0	96.0	87
	S2-F4-1	32.0	77.0	69.0	105
	S2-F4-2	35.0	85.0	80.0	83

6.9 Structural performance at fire exposure

All the specimens were loaded to their service load and this load was kept constant during the entire fire exposure time. The structural response of the beams and slabs can be observed through deflection progression with fire exposure time. A sudden increase in deflection during fire exposure can be considered as the loss of bond at FRP/concrete interface due to the weakening of the epoxy adhesive. An overview of the time at which the loss of bond at FRP/concrete interface was observed, t_{deb}, is given in Table 6.9. The deflections of each specimen were measured in the pre-load phase and during fire testing. The time-increase midspan deflections during fire exposure will be discussed in the following sections for each fire test series.

Table 6.9 – Loss of composite action FRP/concrete interface

Fire series	Specimen	Insulation system	$t_{deb,exp}$ [min]
First series	B0-F1	--	-
	B1-F1-1	Promat H	90
	B2-F1-1	Aestuver	70
	B2-F1-2	Aestuver	34
	B3-F1-1	Aestuver	90
Second series	B0-F2	-	-
	B1-F2-1	Promatect L-500	> 120
	B1-F2-2	HPC/Omega Fire	100
	B1-F2-3	HPC/Omega Fire	> 120
	B2-F2-1	WR-APP type C	25
	B2-F2-2	WR-APP type C	30
Third series	B1-F3-1	Promatect L-500	> 60
	B1-F3-2	HPC/Omega Fire	> 60
	B1-F3-3	HPC/Omega Fire	> 60
	B1-F3-4	HPC/Omega Fire	> 60
	B2-F3-1	Promatect L-500	> 60
	B4-F3-1	HPC/Omega Fire	> 60
Fourth series	B2-F4-1	HPC/Omega Fire	50
	B4-F4-1	HPC/Omega Fire	> 120
	S0-F4	-	-
	S1-F4-1	HPC/Omega Fire	> 120
	S2-F4-1	Promatect L-500	> 120
	S2-F4-2	Promatect L-500	> 120

6.9.1 First fire test

Figure 6.51 shows the increase of midspan deflections as function of time for the beams of the first fire test series (the initial deflection at the start of the fire test is not shown in the graphs).

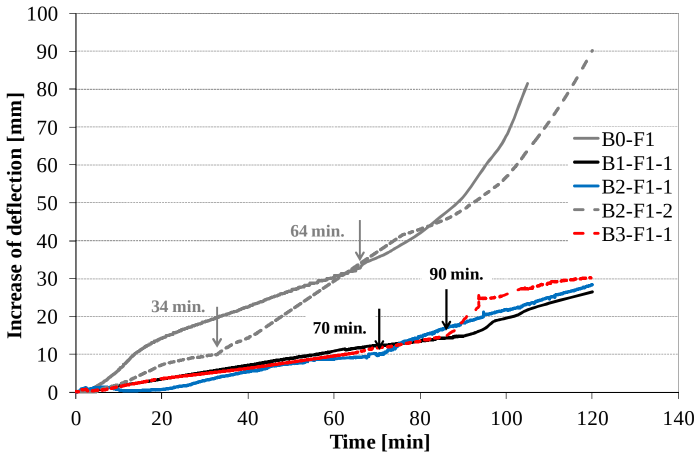

Figure 6.51 – Increase of midspan deflections as function of time first fire test

Beam B0-F1 was unloaded at approximately 105 min of fire exposure due to the rapid increase of deflection observed. Under fire, the midspan deflection increased gradually for the entire fire exposure time for beam B1-F1-1. A slight change in the slope of the curve was observed at approximately 90 min into the test due to the high temperature reached at the FRP/epoxy interface at that time.

For beam B2-F1-1, the midspan deflection increased gradually with fire exposure time till 70 min into the test. At that time, due to the partial detachment of the fire protection, the adhesive lost strength and its bond to the concrete, resulting in a sharp increase of deflection.

For beam B2-F1-2 a sudden increase of deflection was observed at 34 min of fire exposure. At that time the insulation system detached completely from the soffit of the beam and it may be assumed that the interaction between the FRP reinforcement and the concrete is lost due to the weakening of the epoxy adhesive. From 34 min into the fire test the beam behave as an unstrengthened and unprotected beam. Moreover, due to the higher applied service load, the final recorded increase of deflection was higher than the unstrengthened beam B0-F1. A sudden increase of deflection was observed also at approximately 90 min of fire exposure for beam B3-F1-1. However, it is interesting to note that deflections in beams B1-F1-1, B2-F1-1 and B3-F1-1 are lower as compared to the unstrengthened and unprotected beam B0-F1. This is because the different insulations, for the time in which it remained attached to the beams, contributed effectively to control the rise of temperature in the adhesive and in the longitudinal reinforcement (FRP bars and steel) and thus the loss of strength with temperature is gradual.

6.9.2 Second fire test

Figure 6.52 shows the increase of midspan deflections as function of time for the beams of the second fire test series. Beam B0-F2 was unloaded at approximately 110 min of fire exposure due to the sharp increase of deflection observed.

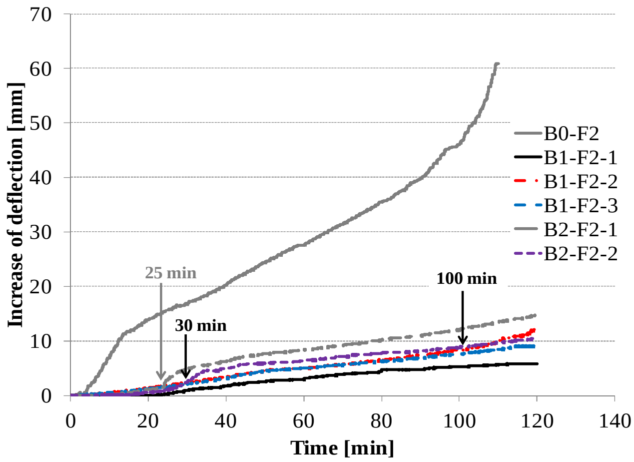

Figure 6.52 – Increase of midspan deflections as function of time second fire test

Under fire exposure, the midspan deflection increased gradually for the entire fire exposure time for beam B1-F2-1 and B1-F2-3. No significant changes, in terms of sudden increase of deflection or rate of deflection, in the slope of the time deflection curves were observed for both beams.

For beam B1-F2-3, the midspan deflection increased gradually with fire exposure time till approximately 100 min. into the test. At that time, due to the progressive cracks, the insulation partially detached from the bottom of the beam resulting in a sharp increase of deflection.

The midspan deflection increased gradually with fire exposure time till approximately 25 min and 30 min for respectively beam B2-F2-1 and B2-F2-2. At that time the measured deflection showed a sudden increase, due to the bond loss at the FRP/concrete interface with temperature in the area were cracks were mainly located (it has to be noted that the thermocouples were far from the anchorage zone and therefore not able to record the rise of adhesive temperatures due to the opening of cracks with fire exposure). This sudden increase of deflection at respectively 25 min (beam B2-F2-1) and 30 min (beam B2-F2-2) will be confirmed through deflection calculations discussed in chapter 7.

6.9.3 Third fire test

Figure 6.53 shows the increase of midspan deflections as function of time for the beams of the third fire test series.

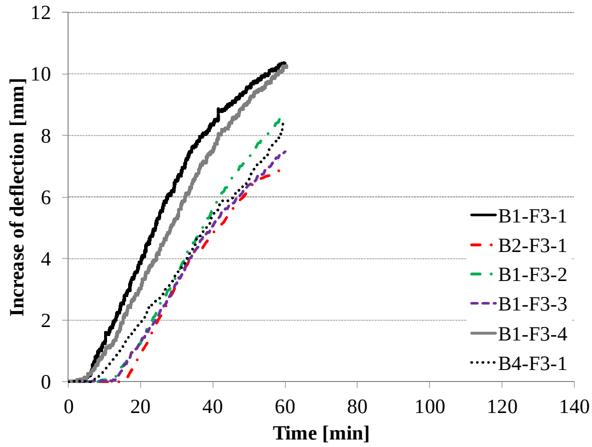

Figure 6.53 – Increase of midspan deflections as function of time third fire test

From experimental outcomes it is clear that all the insulated beams were able to support the service load of the strengthened beam throughout the 1 hour fire tests without any signs of impending failure. No significant changes, in terms of sudden increase of deflection or rate of deflection, in the slope of the time deflection curves were observed for all of the tested beams.

At the end of the 60 min, the fire was halted and all the beams were unloaded except for beam B1-F3-2, for which the applied load was increased up to failure. At that moment the temperature at the adhesive/FRP interface was about $T_{adhesive}$= 130 °C equal to 2.1 T_g and was constant during the increase of the load (the increase of load took approximately 10 min up to the point of beam failure). Figure 6.54 shows the load deflection curve of beam B1-F3-2 in the three phases of pre-loading up to its service load (curve A-B), fire exposure (curve B-C) and increase of loading after fire exposure (curve C-D). A comparison with the FRP strengthened reference beam B1 and the unstrengthened beam B0 tested at ambient temperature is also reported in Figure 6.54.

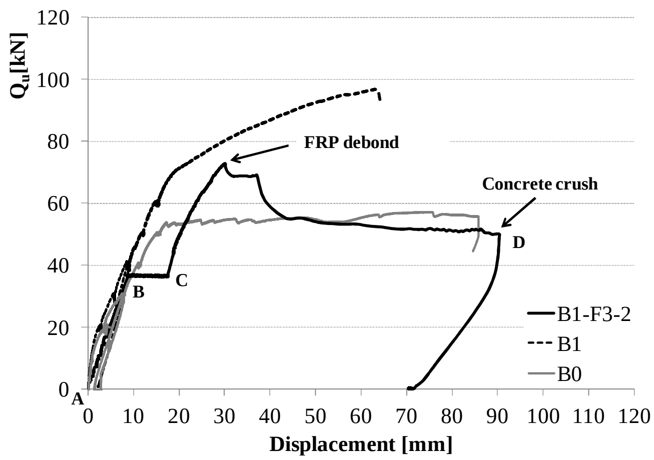

Figure 6.54 – Load - deflection curve beam B1-F3-2

When the load was increased, at 60 min of fire exposure (point C of Figure 6.54), the deflection increased accordingly up to the point at which debonding of the bars occurred (at that moment the load was about Q_u=75.2 kN); after debonding the load dropped to approximately that of the corresponding unstrengthened beam (Q_u=55.0 kN) and the deflection increased until the concrete crushed. The failure of the beam was preceded by extended flexural vertical cracking of the beam in the pure bending region that led to the yielding of steel and loss of bond of the NSM FRP bars followed by concrete crushing. This test clearly demonstrates that the adhesive likely started to lose strength and stiffness and its bond to the concrete when the glass transition temperature was reached, but it was still effective to some degree and therefore able to transfer stresses from the FRP to the concrete surface. For instance, the recorded failure load Q_u=75.2 kN was equal to 131% of that of the unstrengthened beam ($Q_{u,unstr.}$= 57.3 kN) and equal to 77% of that of the same strengthened beam tested at ambient condition up to failure ($Q_{u,strength.}$= 96.9 kN).

6.9.4 Fourth fire test

Figure 6.54 shows the increase of midspan deflections as function of time for the two beams tested in the fourth fire test series, including the reference beam B0-F1 tested in the first fire test.

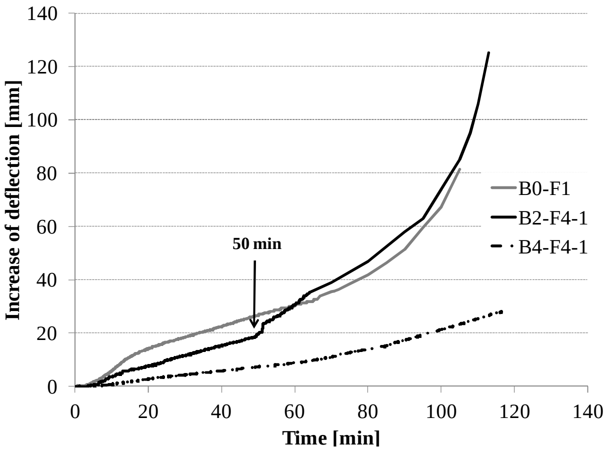

Figure 6.55 – Increase of midspan deflections as function of time beams B2-F4-1, B4-F4-1 and B0-F1.

For beam B2-F4-1 (partially bonded and partially insulated) the midspan deflection increased gradually with fire exposure time till approximately 50 min into the test and was lower than that observed for the unprotected and unstrengthened beam. This is because, up to 50 min into the test, the insulation at the anchorage zone (length equal to 500 mm) contributed effectively to control the rise of temperature at the FRP/adhesive interface along the protected anchorage zone. After 50 min of fire exposure the interaction between the FRP reinforcement and the concrete was lost resulting in a fast increase of deflection with fire exposure time. At that time the temperature into the oven was approximately 915 °C and therefore in the unprotected area the FRP matrix was already completely melted and only the carbon fibers were contributing to flexural strength of the beam. The temperature at the insulated area was approximately 100 °C. Therefore the weakening of the epoxy resin at the insulated area and/or the possible FRP bars slip, due to the melting of the epoxy resin at the transition point between the insulated and unprotected area of the beam (more investigations are needed to clarify this aspect) resulted in a fast increase of deflection with increasing fire exposure. The beam failed under the service load at approximately 118 min into the test, due to the loss of strength and stiffness of the longitudinal steel reinforcement, in addition to almost zero contribution of the FRP towards the capacity of the beam.

For beam B4-F4-1, the midspan deflection increased accordingly with the rise of temperature at the longitudinal steel reinforcement and FRP bars. No significant changes in the slope of the time – increase of deflection curve were observed for the duration of fire exposure. Figure 6.56 shows the increase of midspan deflections as function of time for the four slabs tested in the fourth fire test series.

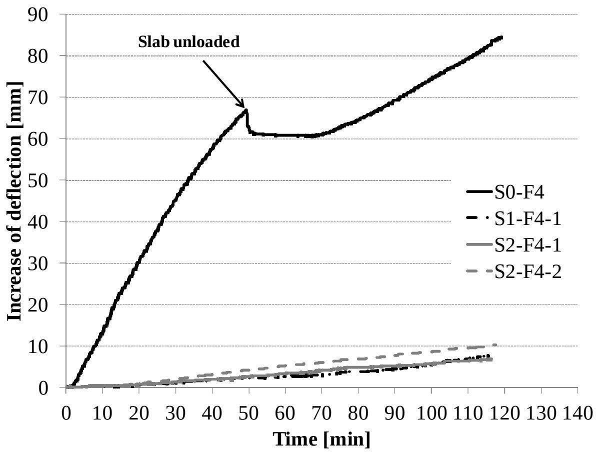

Figure 6.56 – Increase of midspan deflections as function of time for slabs tested in the fourth fire test

Due to the fast increase of deflection observed at approximately 50 min into the test, slab S0-F4 was unloaded and the test was continued for this reference slab without any load applied. From experimental outcomes it is clear that all the insulated slabs were able to support the service load of the strengthened slab throughout the 2 hour fire tests without any signs of impending failure. No significant changes, in terms of sudden increase of deflection or rate of deflection, in the slope of the time deflection curves were observed for all of the insulated slabs.

6.10 Specimens' residual strength

Another potentially important aspect of fire performance of FRP strengthened concrete structures is their residual behaviour after fire exposure. The post-fire residual behavior of RC members depends on the internal temperatures attained in fire, the load experienced by the members in fire, the cooling method (air cooled method for this test program) and the strength recovering time following the cooling period. The fire damaged beams and slabs were stored for approximately one month at laboratory ambient temperature and then tested up to failure to determine their residual strength. The test set-up was the same adopted for the fire test and to test the reference beams at ambient temperature (see chapter 5).

The fire damaged beams and slabs were all tested to failure in 4 point bending, and were instrumented with LVDTs and dial gauges in order to measure electronically and manually the deflection at midspan, under the point loads and at both supports. The experimental results in terms of residual strength capacity of the tests elements and load – midspan deflection for the residual strength tests will be discussed in the following sections for each fire test series. Because the beams were pre-cracked from the service load applied during the fire endurance tests, none of the curves for the residual strength testing demonstrate a cracking load.

6.10.1 First fire test

Experimental load - midspan deflections curves for the residual strength tests of beam tested in the first fire test series are shown in Figure 6.57-6.59, in which each fire damaged beam is compared with the respective reference strengthened and unstrengthened beam tested at ambient condition. Beam B2-F1-2 was not tested for the residual strength due to the large amount of damages observed after the fire test. As expected beam B0-F1 experienced a 15% decrease of the flexural strength and stiffness due to the increase of temperature in the compressive concrete and longitudinal bottom steel reinforcement during the fire test (see Figure 6.57).

The experimental load-midspan deflection curve of beam B1-F1-1 (see Figure 6.58) is initially in close agreement with that of the strengthened beam B1 until the reinforcement started yielding. The observed stiffness and yield load was higher than that of the unstrengthened beam B0 tested in ambient condition. After yielding of the steel no more contribution of the FRP was observed and failure was due to steel yielding followed by concrete crushing. This behaviour can be explained considering that after 2 h of fire exposure the insulation board was effectively able to maintain relatively low temperatures in the compressive concrete zone and the longitudinal steel reinforcement but the recorded temperature of the adhesive ($T_{adhesive}$= 305 °C) was well beyond its glass transition temperature value (T_g= 62 °C).

The experimental load-midspan deflection curves of beams B2-F1-1 and B3-F1-1 (see Figure 6.59-Figure 6.60), in which the fire protection detached at 70 min and 90 min respectively, clearly showed no residual strength of the adhesive after 2 h of fire exposure. Indeed the load-midspan deflection curves perfectly match the unstrengthened beam B0. This is because the different insulations, for the time during which they remained attached to the beams, contributed effectively to control the rise of temperature in the compressive concrete zone and in the longitudinal reinforcement. Thus they retained almost fully their unstrengthened flexural strength. Both beams failed by steel yielding followed by concrete crushing.

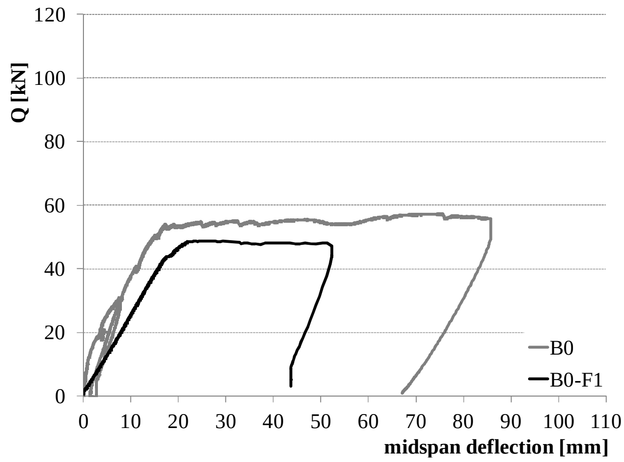

Figure 6.57 – Load – midspan deflection curve residual strength test beam B0-F1 vs reference beam

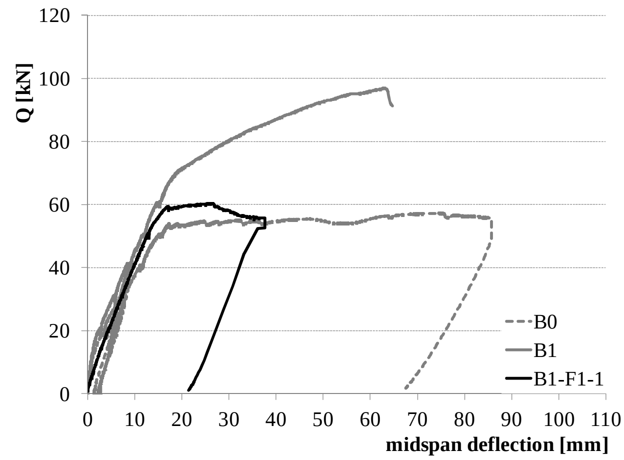

Figure 6.58 – Load – midspan deflection curve residual strength test beam B1-F1-1 vs reference beams

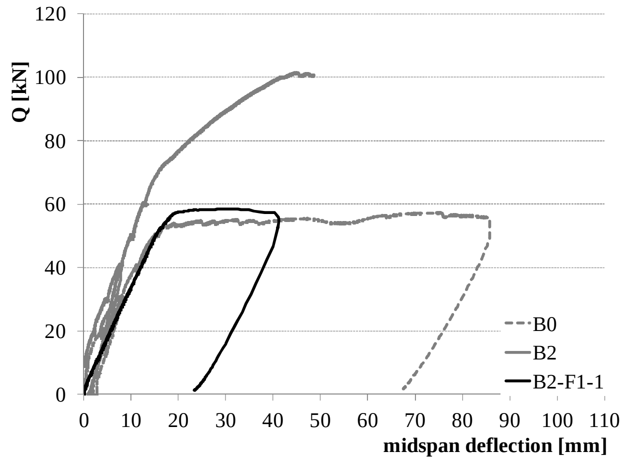

Figure 6.59 – Load – midspan deflection curve residual strength test beam B2-F1-1 vs reference beams

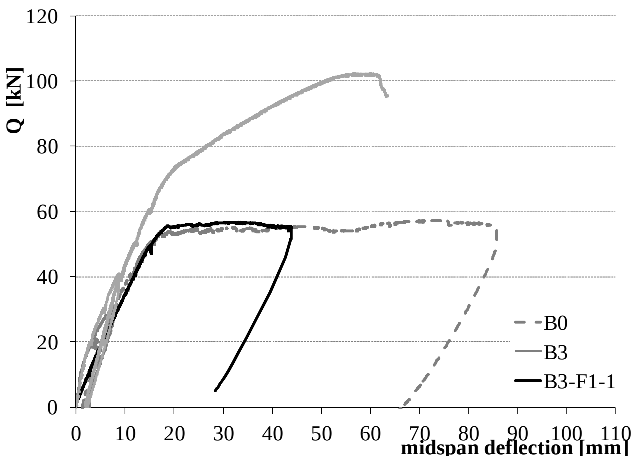

Figure 6.60 – Load – midspan deflection curve residual strength test beam B3-F1-1 vs reference beams

6.10.2 Second fire test

Beam B0-F2 experienced a 15% decrease of the flexural strength and stiffness due to the increase of temperature in the compressive concrete and longitudinal bottom steel reinforcement during the fire test (see Figure 6.61). The failure mode was steel yielding followed by concrete crushing.

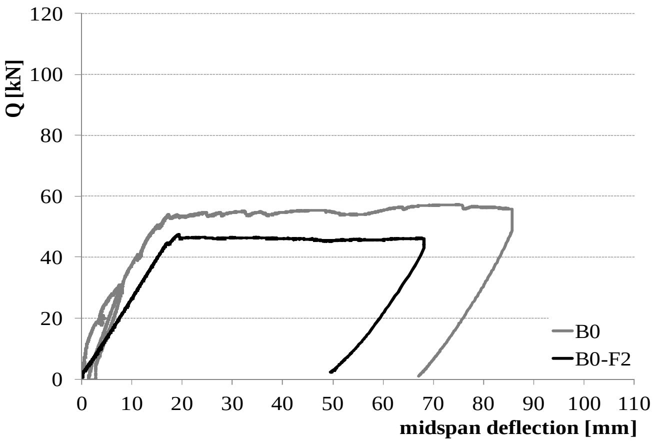

Figure 6.61 – Load – midspan deflection curve residual strength test beam B0-F2 vs reference beam

The experimental load-midspan deflection curves of beams B1-F2-1 and B1-F2-3 were in close agreement with that of the FRP strengthened beam B1 tested at ambient condition until they start failing under the applied loads (see Figure 6.62). The two insulation systems were able to keep, during the fire exposure, the adhesive at relatively low temperature ($T_{adhesive}$= 115 °C and $T_{adhesive}$= 159 °C respectively for beam B1-F2-1 and B1-F2-3) so that they retained a significant part of their original strength at room temperature. Despite the higher value of the adhesive temperature ($T_{adhesive}$= 1.86 T_g and $T_{adhesive}$= 2.56 T_g, respectively for beam B2-F2-1 and B1-F2-3) with respect to the glass transition temperature (T_g = 62 °C), the adhesive was still able to transfer stresses from the FRP to the concrete surface; clearly its strength and stiffness was reduced. For instance, even after 2 h of fire exposure, beams B1-F2-1 and B1-F2-3 were able to increase their flexural strength up to 41% (failure load equal to $Q_{u,residual}$= 81 kN) and to 34 % (failure load equal to $Q_{u,residual}$= 77 kN) in comparison to that of the unstrengthened beam B0 (failure load value equal to Q_u = 57.3 kN). Their residual strength was equal to 84% and 79% in comparison to the FRP strengthened beam tested at ambient temperature (failure load equal to Q_u= 96.8 kN). The failure of both beams (see Figure 6.63) was yielding of the steel followed by debonding of the NSM FRP bars. The debonding failure was characterized by lost of the concrete cover for beam B1-F2-1 and debonding at the FRP/adhesive interface without any concrete rip-off for beam B1-F2-3. This demonstrated that the different temperatures reached during the fire test of these two beams lead to a different failure mode, mainly due to the higher epoxy weakening of strength and stiffness for beam B1-F2-3.

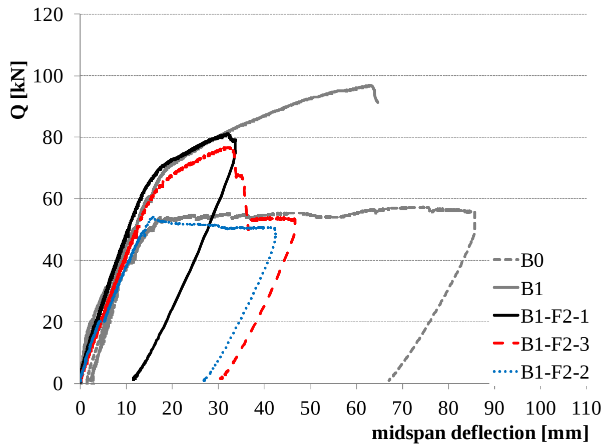

Figure 6.62– Load – midspan deflection curve residual strength test beam B1-F2-1, B1-F2-2 and B1-F2-3 vs reference beams

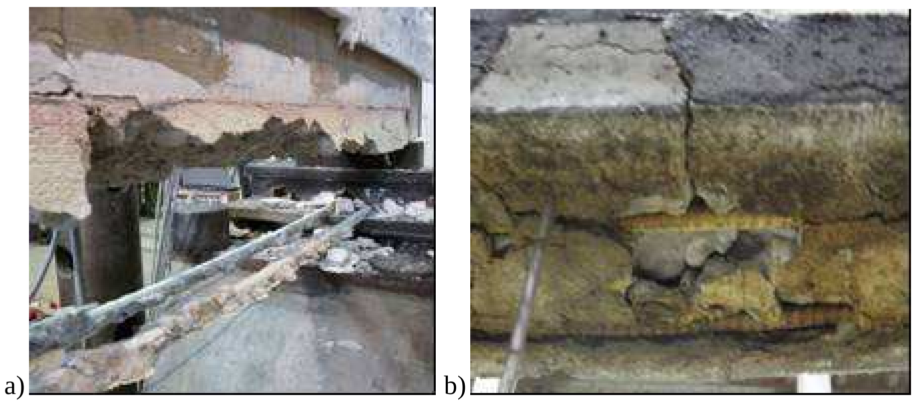

Figure 6.63 – Failure mode beams a) B1-F2-1 and b) B1-F2-3

Due to the partial detachment of the HPC insulation system and the local burning of the epoxy during fire test no residual strength was observed for the adhesive of beam B1-F2-2. Nevertheless, the beam was able to retain the original strength of the unstrengthened beam tested at ambient condition (see Figure 6.62). The failure mode was yielding of the steel followed by concrete crushing.

In the same way the experimental load- midspan deflection curves of beams B2-F2-1 and B2-F2-2 clearly showed no residual strength of the adhesive after 2 h of fire exposure. Indeed whereas relatively low temperature increases of the adhesive were recorded (at the two measurement sections), respectively $T_{adhesive}$= 207 °C and $T_{adhesive}$= 138 °C for beam B2-F2-1 and B2-F2-2, the tendency of the insulation layer to crack during fire exposure allow rapid heat ingress at localized areas (close to the FRP anchorage zone) resulting in local burning of the epoxy adhesive. Despite this cracking of the insulation the system was able to keep the temperatures low of the longitudinal steel reinforcement and they were able to retain the strength of the unstrengthened beam tested at ambient condition (see Figure 6.64). For both beams the failure mode was due to steel yielding followed by concrete crushing.

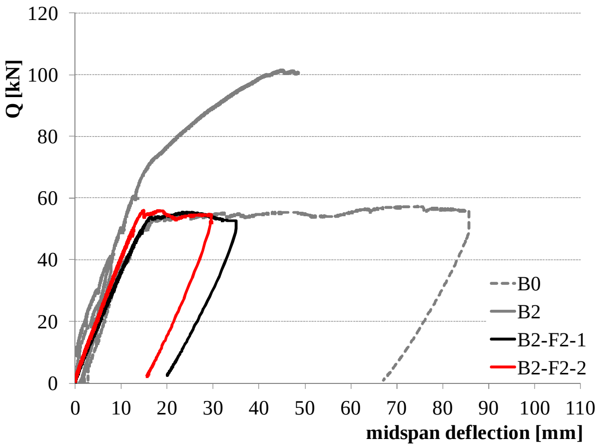

Figure 6.64 – Load – midspan deflection curve residual strength test beam B2-F2-1, and B2-F2-2 vs reference beams

6.10.3 Third fire test

For the third fire test the internal temperatures of the concrete compression zone and tension steel were well below the critical temperature of 140 °C and 593 °C respectively. The beams were expected to recover at least all of their unstrengthened flexural strength after the recovery time. This was indeed observed for all the tested beams. Moreover, for all the beams in which the FRP bars were embedded with an epoxy adhesive, the insulation systems were able to keep the adhesive temperature at relatively low temperatures (in the range between 100 °C and 130 °C) so that they retained almost completely their original strength at room temperature. For instance, even after 1h of fire exposure, all the tested beams were able to increase their flexural strength up to 56% in comparison to that of the unstrengthened beam B0. Their residual strength was in a range between 86% and 92% in comparison to the FRP strengthened beams tested at ambient temperatures.

Table 6.10 summarizes the experimental results, including that of the beams tested at room temperature, in terms of ultimate load capacity, $Q_{u,residual}$, increase of flexural strength with respect to that of the unstrengthened beams at room temperature, $Q_{u,residual}/Q_{u,unstr.}$, percentage of residual strength with respect of the strengthened beam tested at room temperature, $Q_{u,residual}/Q_{u,str,}$, failure mode (YY/CC for yielding of steel reinforcement followed by concrete crushing, DB for debonding at the adhesive/concrete interface) and temperature of the adhesive after 1h fire exposure as a function of the adhesive glass transition temperature, for the beams in which the FRP reinforcement was embedded with epoxy resin.

Table 6.10 – Experimental results residual strength test of third fire test

Specimen	$Q_{u,residual}$ [kN]	$Q_{u,residual}/Q_{u,unstr}$ [-]	$Q_{u,residual}/Q_{u,str.}$ [kN]	$T_{adhesive}$ [-]	Failure mode
B0	57.3	1.00	-	-	YY/CC
B1	96.9	1.69	-	-	DB
B2	101.5	1.77	-	-	DB
B4	73.3	1.27	-	-	DB
B1-F3-1	85.0	1.48	0.87	$1.87T_g$	DB
*B1-F3-2	75.2	1.31	0.77	$2.10T_g$	DB
B1-F3-3	89.7	1.56	0.92	$1.63T_g$	DB
B1-F3-4	88.7	1.54	0.91	$1.63T_g$	DB
B2-F3-1	87.7	1.53	0.86	$1.78T_g$	DB
B4-F3-1	67.3	1.17	0.91	-	YY/CC

* *Tested immediately after fire exposure without cooling*

Also beam B4-F3-1, for which the FRP bars were embedded with an expansive mortar, retained a great portion (91%) of its original strength. The primary beneficial effect of using expansive mortar as bond adhesive, instead of using epoxy resin, is that the mortar does not experience significant loss of mechanical and bond properties in the range of the epoxy glass transition temperature (usually in the range between 50-90 °C for ambient cured epoxies) [12]. Indeed experimental results demonstrated that despite the lower insulation thickness of beam B4-F3-1 with respect to that of all the other beams and consequently the relatively higher adhesive temperature value ($T_{adhesive}$= 167°C) recorded after 1h of fire exposure, beam B4-F3-1 was able to increase the flexural strength up to 17% in comparison to that of the unstrengthened beam B0 showing a residual strength equal to 91% of the FRP strengthened beam tested at room temperature. Therefore, with respect to the adhesive temperature reached during the 1 h of fire exposure for this test program, using expansive mortar as bond adhesive can be considered a good alternative to the epoxy resin for strengthening concrete structures in which moderate flexural strength increase is needed, and this is in agreement with the findings of previous research [12].

The recorded load-midspan deflection curves of the residual strength tests of the beams of the third fire test series are shown in Figure 6.65 till Figure 6.68. The experimental curves were in close agreement with that of the FRP strengthened beams tested at ambient condition until they started failing under the applied loads. In the final stage the midspan deflection indicates a limited reduction in the bond adhesive (epoxy or mortar) strength and stiffness.

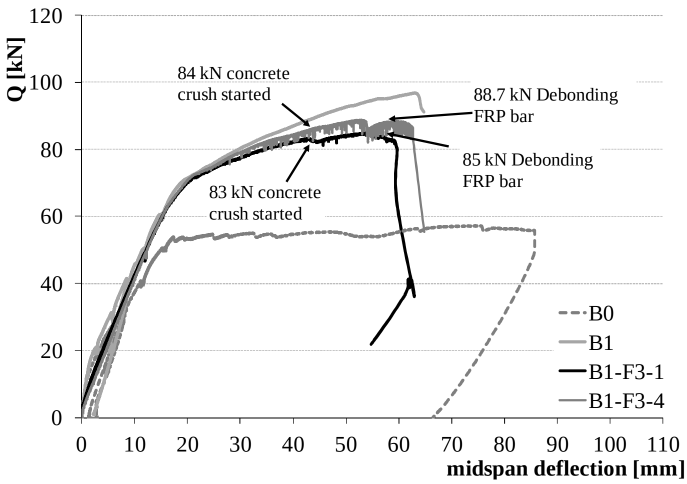

Figure 6.65 – Load – midspan deflection curve residual strength test beam B1-F3-1, and B1-F3-4 vs reference beams

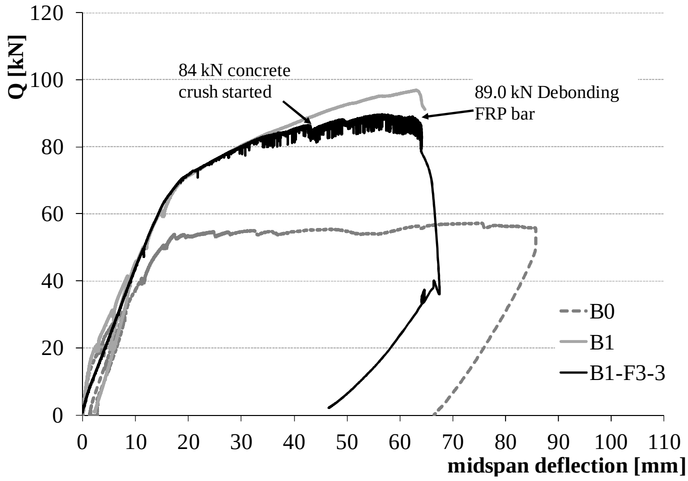

Figure 6.66 – Load – midspan deflection curve residual strength test beam B1-F3-3, and B1-F3-4 vs reference beams

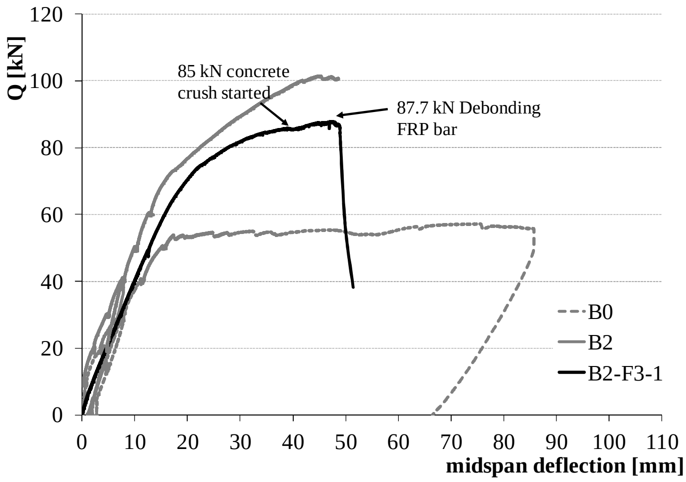

Figure 6.67 – Load – midspan deflection curve residual strength test beam B2-F3-1, vs reference beams

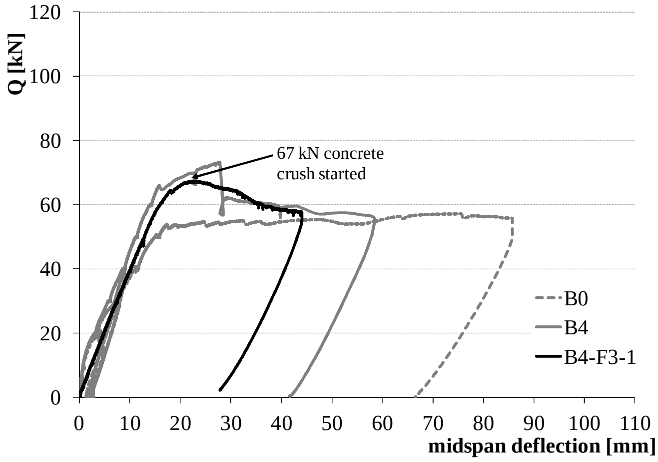

Figure 6.68 – Load – midspan deflection curve residual strength test beam B4-F3-1 vs reference beams

Figure 6.69 and Figure 6.70 show the failure mode of the beams tested in the third fire test series. It has to be noted that all the beams in which the NSM FRP was embedded with epoxy resin failed by FRP debonding with loss of concrete cover. For beam B4-F3-1, in which the FRP bars were embedded with cementitious mortar, the failure of the beam was preceded by extended flexural cracking of the beam in the pure bending region that led to the yielding of the steel followed by concrete crushing. This behaviour can be explained considering a possible slip of the bar due to the extensive flexural cracks in combination with lower strength and stiffness of the expansive mortar.

a)  b) 

Figure 6.69 – Failure mode beams a) B1-F3-1 and b) B1-F3-4

Figure 6.70 – Failure mode beams a) B1-F3-3 b) B2-F3-1 and c-d) B4-F3-1 residual strength tests

6.10.4 Fourth fire test

Figure 6.71 shows the load-midspan deflection curve of the residual strength test of beam B4-F4-1 tested in the fourth fire test series. During the 2 h of fire exposure the beam, under the service applied load, did not experience any abrupt increase of deflection. Despite this observation, the residual strength test revealed no residual strength of the mortar after the recovery time. This can be explained considering the moderate capacity of flexural strength increase of the expansive mortar in addition to the high temperature recorded into the mortar during the two hours of fire exposure ($T_{adhesive}$= 278.0 °C). At this temperature the cementious mortar is expected to loose a considerable part of its strength and stiffness (more investigations are needed to clarify this aspect) as well as the NSM CFRP bars. The failure mode (see figure 6.70) indeed was preceded by extended flexural cracking of the beam in the pure bending region that led to the yielding of the steel followed by concrete crushing. This behaviour can be explained considering slip of the bar due to the extensive flexural cracks in combination with the lower strength and stiffness of the expansive mortar after fire.

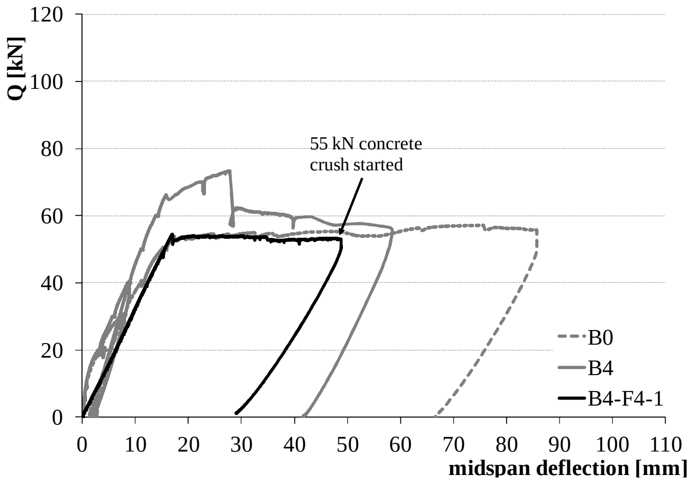

Figure 6.71 – Load–midspan deflection curve residual strength test beam B4-F4-1 vs reference beams.

Figure 6.72 – Failure mode beams B4-F4-1 residual strength test

The unprotected and unstrengthened slab S0-F4 experienced a decrease of the flexural strength and stiffness due to the increase of temperature in the compressive concrete and longitudinal bottom steel reinforcement during the fire test (see Figure 6.71). The residual strength of the fire damaged slab S0-F4 was 73% of that of the reference slab tested at ambient condition. The failure mode was steel yielding followed by concrete crushing.

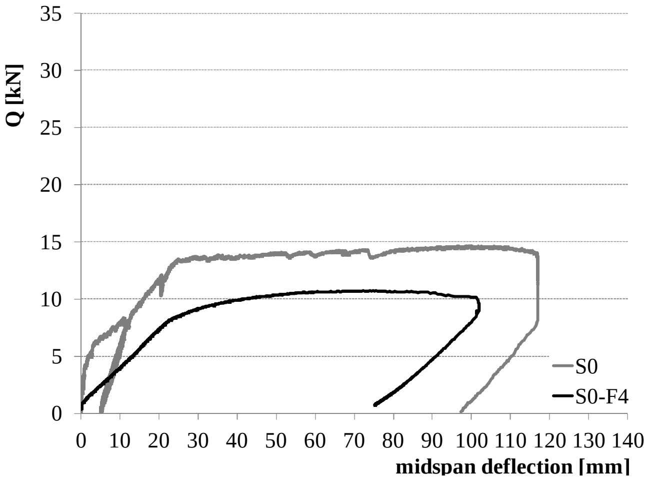

Figure 6.73 – Load–midspan deflection curve residual strength test slab S0-F4 vs reference slabs

For the insulated slabs tested in the fourth fire test, the insulation systems were able to keep the adhesive temperature at relatively low temperatures (in a range between 70 °C and 96 °C) so they retained essentially their original strength at room temperature. For instance, even after 2 h of fire exposure, all the insulated slabs were able to increase their flexural strength with up to 102% in comparison to the unstrengthened slab S0. Their residual strength was in a range between 88% and 95% in comparison to the FRP strengthened slabs tested at ambient temperatures. Table 6.11 summarizes the experimental results, including the slabs tested at room temperature, in terms of ultimate load capacity, $Q_{u,residual}$, increase of flexural strength with respect to that of the unstrengthened slabs at room temperature, $Q_{u,residual}/Q_{u,unstr.}$, percentage of residual strength with respect of the strengthened beam tested at room temperature, $Q_{u,residual}/Q_{u,str,}$, failure mode (YY/CC for yielding of steel reinforcement followed by concrete crushing, DB for debonding at adhesive/concrete interface) and temperature of the adhesive after 2h fire exposure as a function of the adhesive glass transition temperature.

Table 6.11– Experimental results residual strength test slabs fourth fire test

Specimen	$Q_{u,residual}$ [kN]	$Q_{u,residual}/Q_{u,unstr}$ [-]	$Q_{u,residual}/Q_{u,str.}$ [kN]	$T_{adhesive}$ [-]	Failure mode
S0	14.6	1.00	-	-	YY/CC
S1	28.6	1.95	-	-	DB
S2	31.0	2.12	-	-	YY/CC
S0-F4	10.7	0.73	-	-	-
S1-F4-1	25.3	1.73	0.88	$1.54T_g$	DB
S2-F4-1	29.5	2.02	0.95	$1.11T_g$	YY/CC
S2-F4-2	29.6	2.02	0.91	$1.29T_g$	YY/CC

The recorded load-midspan deflection curves of the residual strength tests of the insulated slabs tested in the fourth fire test series are shown in Figure 6.74 and Figure 6.75. The experimental curves were in close agreement with that of the FRP strengthened beams tested at ambient condition until they started failing under the applied loads. Given the relatively low values of temperature recorded at the adhesive/FRP interface the midspan deflection indicates a small reduction in the bond adhesive stiffness.

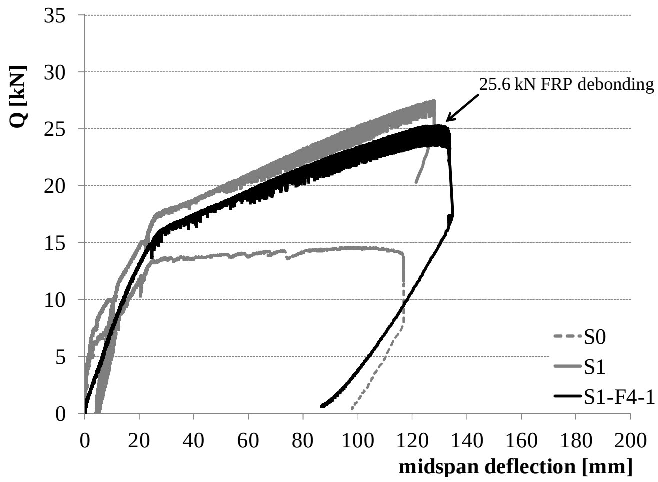

Figure 6.74 – Load–midspan deflection curve residual strength test slab S1-F4-1 vs reference slabs

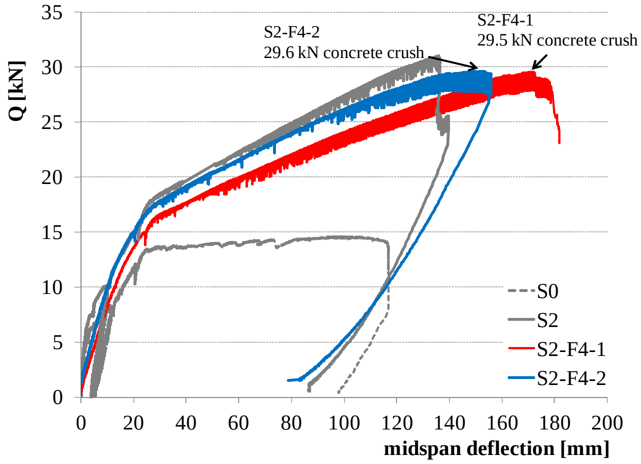

Figure 6.75 – Load–midspan deflection curve residual strength test slabs S2-F4-1 and S2-F4-2 vs reference slabs

Figure 6.76 shows the failure mode of slab S1-F4-1. The slab failed by FRP debonding with rupture of the FRP GFRP bars for a load of 25.6 kN.

Figure 6.76 – Failure mode slab S1-F4-1 residual strength test

Due to the significant increase of the slab load carrying capacity and slab deflections, provided by the NSM strengthening bars, both slabs S2-F4-1 and S2-F4-2 failed in flexural failure mode (see Figure 6.77) with a deflection that was higher than that of the unstrengthened slab tested at ambient condition. At the time of failure cracking observations (see Figure 6.77 b-c) at the soffit of the slabs indicate a significant improvement in the cracking behaviour of RC slabs, in the pure bending region. No debonding of the basalt FRP bars was observed.


a) b) c)

Figure 6.77 – Failure mode slabs a) S2-F4-1 b-c) S2-F4-2 residual strength test

6.11 Conclusions

Based on the results of large-scale fire endurance tests on NSM FRP strengthened and insulated beams and slabs presented herein the following conclusions can be made.

In line with previous works the findings of the first and second fire test series showed that the beams can achieve 2h of fire endurance ratings even after the adhesive temperature exceeds excessively the glass transition temperature, although FRP loss of composite action after 20-110 min, depending on the applied insulation scheme and its thermal performance, was observed for some of the beams. This relates to the fact that, considering the higher acting service load than for an unstrengthened beam, in case of loss of FRP composite actions the low thermal conductivity of the insulation materials play a key role in keeping the temperature of the longitudinal steel reinforcement well below the critical temperatures of 593 °C for the entire duration of fire exposure. As the temperature of the concrete (at the compression side) and the longitudinal bottom steel reinforcement were below the critical temperatures, even in case of accidental drop out of FRP, the beams will not collapse for the acting service load. However, residual flexural strength tests on these fire tested beams have demonstrated that in some cases the FRP seems to be able to retain bond strength to the concrete for the beams where the adhesive temperature remained less than about 2.5 times T_g and the the beams are still able to retain considerably part of their strength (up to 84% for 2h of fire exposure in this test program). The experimental research presented herein focuses in this aspect of critical FRP bond adhesive temperature in relation to the glass transition temperature and the insulation materials were designed to limit the adhesive temperature, such to avoid significant dysfunctions in terms of strength compatibilities between the FRP and the RC members during or after fire.

For the third fire test series, despite the higher service load applied to the fire tested beams, the experimental results have clearly demonstrated the feasibility of providing 1h fire endurance rating under service load of the strengthened beams, without significant loss of bond integrity of the FRP during or after fire, if adequate protection against fire is provided. For none of the strengthened beams FRP NSM detached visibly. The insulation systems evaluated appear to have effectively protected the NSM FRP strengthened beams from heat penetration during 1 hour of fire exposure. The adhesive temperature was maintained to low temperatures ($T_{adhesive}$=130 °C and $T_{adhesive}$=167 °C for epoxy resin and expansive mortar) and no impending failure was observed during the 1h fire exposure. The fire resistance effectiveness of the FRP strengthening system after fire exposure was evaluated in two different ways. For one of the tested beam (B1-F3-2) the load was increased immediately after the 1h of fire exposure, keeping the high temperature constant. This beam B1-F3-2 achieved a residual strength capacity equal to 77% with respect to that tested at room temperature, yet 127% of the unstrengthened beam. All the other fire damaged beams were tested up to failure after been air cooled and stored in the laboratory for approximately one month. These residual strength tests demonstrate that, if the insulation is able to maintain the adhesive temperature at relatively low temperature ($T_{adhesive}$=100 °C to 130 °C and $T_{adhesive}$=167 °C for epoxy resin and expansive mortar) the FRP is able to retain bond strength to the concrete (in agreement with previous work on double bond shear test by Foster and Bisby 2008) and the beam is still able to retain considerably part (in this test program up to 92% for 1h of fire exposure) of the flexural capacity of the FRP strengthened beam at ambient condition.

In the fourth fire test the experimental outcomes have shown that the partial insulation of the NSM FRP strengthened system (for a length equal to 500 mm for this test program) was effective for a fire endurance of approximately 50 min into the fire test. At that time loss of composite action between the FRP and concrete was observed. The influence of the adhesive used to embed the NSM FRP bars in the grooves was also investigated for 2h of fire exposure time. Experimental outcomes showed that the expansive mortar, despite the higher temperature reached into the adhesive, was able to withstand the applied service load during the 2 h of fire exposure. Nevertheless residual strength test experienced no contribution of the NSM FRP strengthened system after the recovering time. This can be related to the decreased strength of the expansive mortar at relative high temperature ($T_{adhesive}$= 280 °C) experienced during the 2 h of fire exposure.

For all the strengthened and insulated slabs, tested in the fourth fire test, experimental results have demonstrated the feasibility of providing 2h of fire endurance ratings under the applied service load, if adequate protection against fire is provided. The insulation systems appear to have effectively protected the NSM FRP strengthened slabs from heat penetration during the 2h of fire exposure, keeping the adhesive temperature really low (in a range between 70 °C and 96 °C). Residual strength tests demonstrated that, if the insulation is able to keep the adhesive at relatively low temperature ($T_{adhesive}$= 70 °C to 96°C) the FRP strengthened slab is able to retain almost its full flexure capacity of the FRP strengthened slab at ambient condition (in this test program up to 95% for 2h of fire exposure).

6.12 References

1. Palmieri A., Matthys S., Taerwe L. (2012). "Experimental investigation on fire endurance of insulated beams strengthened with near surface mounted FRP bar reinforcement". *Composites part B: Eng*, 43 (3), 885-895.
2. Palmieri A., Matthys S., Taerwe L. (2012). "Fire endurance and residual strength of insulated concrete beams strengthened with Near Surface Mounted reinforcement". *J. Comp. Const.*, (DOI information 10.1061/(ASCE)CC.1943-5614.0000338).
3. ISO 10406-1 (2008). "Fibre-reinforced polymer (FRP) reinforcement of concrete – Tests methods – Part 1: FRP bars and grids. *International Organization for Standardization.*
4. ISO 11357-2 (1999). "Plastics – Differential scanning calorimetry (DSC)- Part 2: Determination of glass transition temperature. *International Organization for Standardization.*

5. EN ISO 527-2 (1993). “Plastics – Determination of tensile properties- Part 2: Test conditions for moulding and extrusion plastics”.
6. NBN B 62-202 (1978) “Bepaling van de thermische geleidbaardheid van de bouwmaterialen met de parallelsonde”. 1-12.
7. EN 1992-1-1 (2004). “Eurocode 2- Design of concrete structures – Part 1-1: General rules and rules for buildings”. *European Committee for Standardization.*
8. *fib* Task Group 9.3 (2001). “Externally bonded FRP reinforcement for RC structures”. *International Federation for Structural Concrete*, *fib* Bulletin 14.
9. EN-1363-1 (1999). “Fire Resistance Tests – General Requirements – Part I”. *European Committee for Standardization*.
10. ISO 834 (1999). “Fire Resistance Tests – Elements of Buildings Construction – Part I – General Requirements”. *International Organization for Standardization*.
11. ASTM E119. “Standard Test Methods for Fire Tests of Building Construction and Materials”. *ASTM International*, West Conshohocken, PA, 2002, 22 pp.
12. Kodur V., Ahmed A. (2010). “Numerical Model for tracing the Response of FRP-Strengthened RC Beams Exposed to Fire”. *J. Compos. Constr*, ASCE, 14(6), 730-742.
13. American Concrete Institute (ACI). (2008). “Guide for the design and construction of externally bonded FRP systems for strengthening concrete structures.” *ACI 440.2R-08*, ACI Committee 440, Farmington Hills, MI, USA.
14. Burke P.J., Bisby L.A. and Green M.F. (2008). “Structural Performance of NSM FRP Strengthened Concrete Slabs at Elevated Temperatures.” *Proc. of Structural Faults and Repair*, Edinburgh, UK.
15. Foster S.K. and Bisby L.A. (2008). “Fire Survivability of Externally-Bonded FRP strengthening Systems”. *J. Compos. Constr*, ASCE, 12(5), 553-561.

Chapter 7

THERMAL AND STRUCTURAL ANALYSIS OF NSM FRP STRENGTHENED AND INSULATED RC MEMBERS UNDER FIRE EXPOSURE

7.1 Introduction

In this chapter a numerical model, for evaluating the behavior of NSM FRP strengthened and insulated beams and slabs exposed to fire, is presented. A heat transfer model and a structural response model are applied using a finite element program (Diana TNO 9.4.3) and a two dimensional cross-section layered model (excel visual basic) respectively, to investigate the thermal and structural behavior of NSM FRP strengthened and insulated beams and slabs under fire exposure. The predicted behavior is compared with experimental data discussed in chapter 6. The model accounts for temperature dependent thermal and mechanical constituent's materials properties (concrete, steel, FRP and insulation system). The spalling of concrete is not specifically considered in the model, since, given the appropriate fire insulation systems provided to all the specimens, no concrete spalling was observed for all the insulated specimens. Moreover the analytical model incorporates an elastic analysis for predicting the NSM FRP bond shear stresses along the FRP bonded length with increasing temperature, assuming a condition of pure shear. By modeling the combined effects of temperature dependent adhesive strength and stiffness reduction with the distribution of shear stresses at the FRP/adhesive interface the analysis tentatively predicts the time of FRP loss of composite action (bond failure) during fire exposure. Loss of composite action at the FRP/adhesive interface is assumed if, given the applied load, the predicted shear stresses exceed the temperature dependent bond strength resistance at the FRP/adhesive interface.

7.2 Analytical model

7.2.1 Thermal analysis

The fire temperatures were calculated by assuming that the exposed sides of the specimens (three sides for the beams and bottom side for the slabs as reported in chapter 6) are exposed to heat of fire, whose temperature follows the standard time-temperature curves according to [1] (see chapter 3 equation 3.1). Once the temperature-time relationship of the fire is determined, the next step is to calculate the temperatures within the beam cross section. These temperatures are calculated by means of a 2D heat flow analysis with the finite element package DIANA. The specimens are idealized in the longitudinal direction by dividing the member into a number of segments along its length. The midsection of each segment is assumed to represent the overall behavior of the segment. Assuming that the temperature is uniform along the length of the segment, the cross sectional area of each segment is divided in a number of elements as illustrated in Figure 7.1. Due to the symmetry of the materials and boundary conditions half of the cross section was modeled. As explained in chapter 3, only the concrete and the insulation system are modeled for the thermal analysis. Element types Q4HT (four-node quadrilateral isoparametric element for general potential flow analysis) were used for the concrete and the insulation systems. Element types B2HT (two nodes isoparametric boundary element for general potential flow analysis) were used for the heat transfer at the boundaries. A mesh size of 10x10 mm and 5x10 mm has been used for predicting temperatures inside the concrete of the beams and slabs respectively. A finer mesh, as a function of the geometry, was used for predicting the temperatures within the insulation system. The temperature at the center of the steel reinforcement and the FRP reinforcement is approximated by the temperature at the location of the center of the bar cross-section (in the concrete).

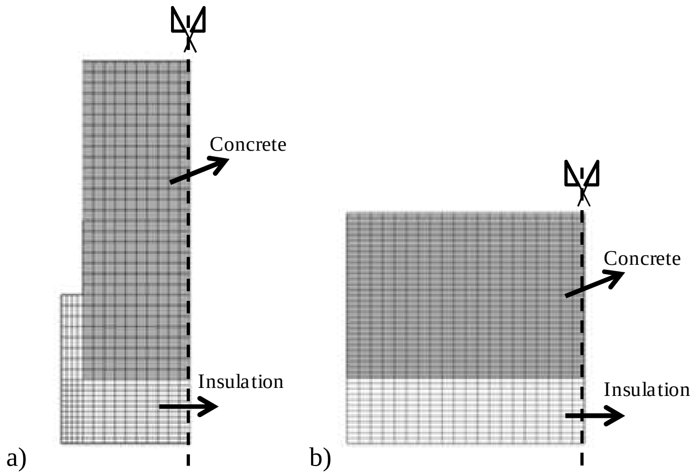

Figure 7.1 – Discretization of the cross sectional area: a) beams b) slabs

Calculating temperatures in a structural member exposed to fire involves heat transfer analysis. There are three basic mechanisms of heat transfer: conduction, convection and radiation. In conduction, energy of heat is exchanged within the solid body. Convection refers to heat transfer at the interface between a fluid and a solid surface, while radiation is the exchange of energy by electromagnetic waves, like visible light, which can be absorbed, transmitted or reflected at a surface. In the context of structural fire exposure, the heat conduction describes the heat transfer process inside the structural member (e.g. within the concrete or from insulation to concrete) and heat transfer from fire to the boundary elements (either the exposed side, or unexposed side) is through convection and radiation. In the following a brief introduction of the governing equation of the heat transfer analysis and how it is considered into the finite element model is given. More information about the solution of transfer heat analysis can be found in [3].

The governing equation for transient heat conduction within the specimen cross section, based on the law of conservation of energy, for an element dV (see Figure 7.2) is given by equation 7.1:

$$\frac{\partial}{\partial x}\left(\lambda\frac{\partial\theta}{\partial x}\right)+\frac{\partial}{\partial y}\left(\lambda\frac{\partial\theta}{\partial y}\right)+\frac{\partial}{\partial z}\left(\lambda\frac{\partial\theta}{\partial z}\right)=\rho c\frac{\partial\theta}{\partial t} \tag{7.1}$$

where:

- x,y,z are the coordinates [m]
- θ is the temperature [°C]
- λ is the thermal conductivity [W/m°C]
- c is the thermal capacity [J/kg°C]
- ρ is the density [kg/m^3]
- t is the time [s]

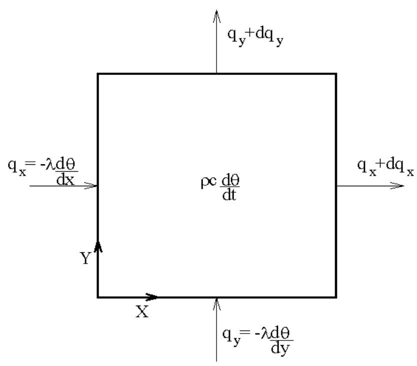

Figure 7.2 – Draft of heat transfer equation [3]

If no thermal gradient occurs in the longitudinal direction z of an exposed element, this term may be omitted in the above equation.

Temperature dependent thermal properties of the modeled materials (concrete and fire insulations) were applied into the finite element program as described in chapter 3. These properties account for the variation of density, volumetric heat capacity and thermal conductivity as a function of the temperature. It has to be noted that the model does not consider the transport of moisture through the concrete during heating. The retarding influence of the moisture on the temperature increase was only taken into account by means of a peak in the specific heat curve (see chapter 3 section 3.3.1.1).

The governing equation of heat transfer by convection is given by equation 7.2:

$$q_c = h(T_{gas} - T_s) \qquad [W/m^2] \qquad (7.2)$$

where:

- h is the convection coefficient [$W/m^2°C$]
- T_{gas} is the compartment gas temperature [°C]
- T_s is the surface temperature of the element [°C]

In the analysis a convection coefficient equal to 25 $W/m^2°C$ and 9 $W/m^2°C$ was assumed for the exposed surfaces and unexposed top surface of the elements respectively.

The heat transfer by radiation describes the energy exchange that takes place between the solid and its environment by thermal radiation or, in other words, the exchange of radiant energy between the test element and the combustion gases (radiation from the flame and the combustion gases) as well as the exchange of radiant energy between the test element and the inner walls of the furnace. The governing equation of the heat transfer by radiation is given in equation 7.3:

$$q_r = k\varepsilon\, F\left(T_{gas}^4 - T_s^4\right) \qquad [W/m^2] \qquad (7.3)$$

where:

- k is the constant of Stefan-Boltzman: 5.67×10^{-8} [$W/m^2°C^4$]
- ε is the relative emissivity [-]
- F is a geometrical parameter, depending on the dimensions and relative positions of the objects [-]
- T_{gas} is the compartment gas temperature [°C]
- T_s is the surface temperature of the element [°C]

In the analysis a constant value of relative emissivity equal to 0.56 (product of emissivity of 0.8 for compartments and 0.7 for concrete surfaces) was adopted. The geometrical parameter, F, was assumed equal to 1 for the lower side of the specimens. For the irradiated side surfaces of the specimens a smaller value of F, equal to 0.8 [3], was adopted. These side faces are indeed also irradiated by the other cover plates of the oven that are at a lower temperature than the furnace walls.

It has to be noted that the finite element package DIANA, for the heat transfer from fire to the boundary, works only with convection (in DIANA: CONVEC, CONVTT) [2]. However, in order to take into account both the convection and radiation effect, a fictitious convection coefficient was adopted as described in the following equations:

$$q = q_c + q_r = h(T_{gas} - T_s) + k\varepsilon F\left(T_{gas}^4 - T_s^4\right) = h_{fictitious}\left(T_{gas} - T_s\right) \qquad [\mathrm{W/m^2}] \qquad (7.4)$$

where:

$$h_{fictitious} = h + k\varepsilon F \frac{\left(T_{gas}^4 - T_s^4\right)}{\left(T_{gas} - T_s\right)} \qquad (7.5)$$

A comparison between the predicted temperature into the specimens and experimental values is given in section 7.3. The thermal model gives a fairly accurate prediction of the measured temperatures (average error ΔT=±5-10°C). Figure 7.3 shows, as an example, the temperature distribution in the cross section of beam B1-F2-1 after 2h of fire exposure.

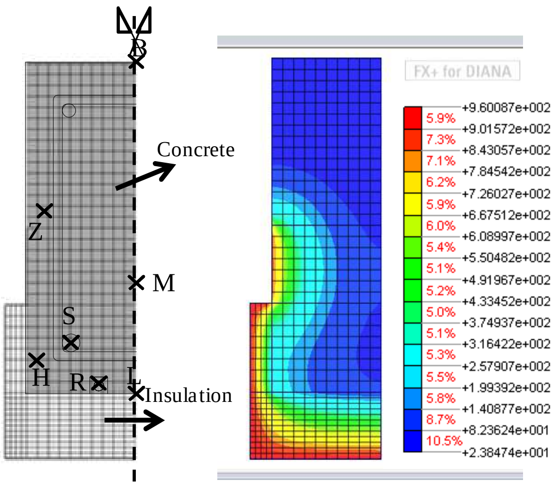

Figure 7.3 – Cross section temperature distribution (numbers in °C)

7.2.2 Structural analysis

The computed cross sectional temperatures generated from the thermal analysis are used to develop moment-curvature relationships at various time steps. For the generations of moment-curvature relationships, the following assumptions are made:

- plane sections remain plane;
- the total strain in the reinforcement is equal to the total strain in the concrete at the same location (i.e. quasi perfect bond between the concrete and steel reinforcement);
- the tensile strength of the concrete is negligible and can be ignored;
- the FRP has a linear stress-strain relationship.

The strength calculations, at elevated temperatures, are carried out using the same mesh as used for the thermal analysis. Each node of the element used for the thermal calculation, is considered the center of a square with area a_i (to simulate the experimental results, the cross section of beams and slabs is divided into squares or rectangles with sides 10 x 10 mm and 10 x 5 mm respectively). Therefore the deformations and stresses in each element are represented by the corresponding values at the center of the element.

As already discussed in chapter 3 section 3.3.1.2, the total strain of the concrete for a member exposed to elevated temperatures and for a given load level can be formulated as the sum of different strains. For the current research project, the concrete total strain, $\varepsilon_{c,tot}$, is expressed as the sum of the thermal strains, $\varepsilon_{c,thermal}$, and the strains induced by the external loads, $\varepsilon_{c,load}$.

$$\varepsilon_{c,tot} = \varepsilon_{c,thermal} + \varepsilon_{c,load} \tag{7.6}$$

Considering the temperature gradient over the cross section of the concrete element exposed to elevated temperature, the thermal strains can be divided in two more components:

- the free thermal strain, $\varepsilon_{c,th}$, which is a simple function of the temperature (see equation 3.7) and which is the thermal elongation if no restraining effect would occur.
- the restraint thermal strain, $\varepsilon_{c,th,rest}$, which is induced because, given plain sections remain plain, the thermal elongation can not occur in a completely free way.

Therefore equation 7.6 can be re-written as follow (Figure 7.4):

$$\varepsilon_{c,tot} = \varepsilon_{c,th} + \varepsilon_{c,th,rest} + \varepsilon_{c,load} \tag{7.7}$$

Considering the mechanical strains, $\varepsilon_{c,\sigma}$, as the sum of the internally thermal restraint strain, $\varepsilon_{c,th,rest}$, and the strains induced by the external load, $\varepsilon_{c,load}$, the total strain, $\varepsilon_{c,tot}$, can be expressed as follow (Figure 7.4):

$$\varepsilon_{c,tot} = \varepsilon_{c,th} + \varepsilon_{c,\sigma} \tag{7.8}$$

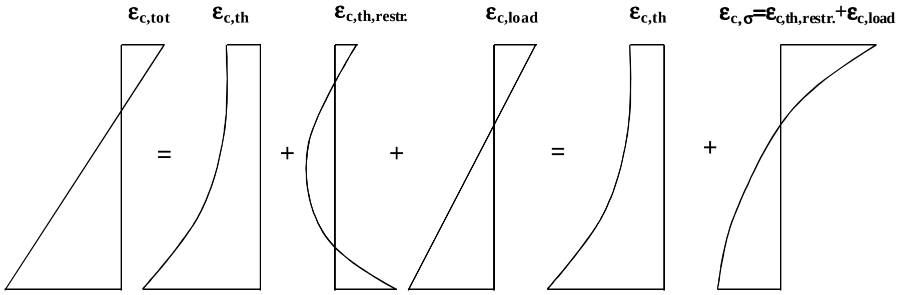

Figure 7.4 – Graphical representation of strain components within concrete

Based on the same assumptions the total strain of the steel and the FRP reinforcements can be expressed as follow:

$$\varepsilon_{s,tot} = \varepsilon_{s,th} + \varepsilon_{s,\sigma} \tag{7.9}$$

$$\varepsilon_{f,tot} = \varepsilon_{f,th} + \varepsilon_{f,\sigma} \tag{7.10}$$

In equations 7.8, 7.9 and 7.10 the thermal strains in each element of concrete, steel reinforcement and FRP reinforcement are computed as discussed in chapter 3. Moreover, at any fire exposure time, the total strain ($\varepsilon_{i,tot}$) in each element of concrete, steel reinforcement and FRP reinforcement can be expressed as a function of the concrete strain at top most fiber, $\varepsilon_{c,top}$, and the curvature (1/r) by the following expression:

$$\varepsilon_{i,tot} = \varepsilon_{c,top} + \frac{1}{r} y_i \tag{7.11}$$

where y_i is the distance from the uppermost concrete fiber to the center of the considered element with area a_i (see Figure 7.5).

With this approach all strain components in equations 7.8, 7.9 and 7.10 except mechanical strains, ε_σ, are known and thus the mechanical strains in each element is computed by rearranging equations 7.8, 7.9 and 7.10 as follows:

$$\varepsilon_{c,\sigma} = \varepsilon_{c,tot} - \varepsilon_{c,th} \tag{7.12}$$

$$\varepsilon_{s,\sigma} = \varepsilon_{s,tot} - \varepsilon_{s,th} \tag{7.13}$$

$$\varepsilon_{f,\sigma} = \varepsilon_{f,tot} - \varepsilon_{f,th} \tag{7.14}$$

Once the mechanical strains are calculated, stresses in each of the concrete, steel and FRP elements are obtained through temperature dependent stress-strain relationships (see chapter 3) and thereafter also the respective forces can be computed. As shown in Figure 7.5 at each time step the computed forces are used to check the force equilibrium. For instance, for an assumed total strain at the uppermost concrete fibre, $\varepsilon_{c,top}$, the curvature is iterated until force equilibrium is satisfied. Once this condition is satisfied, the moment-curvature corresponding to that strain $\varepsilon_{c,top}$ is computed. Through this approach various points of the moment-curvature curve are generated for each segment in longitudinal direction of the member (beam or slab) and for each time step with given temperature distribution.

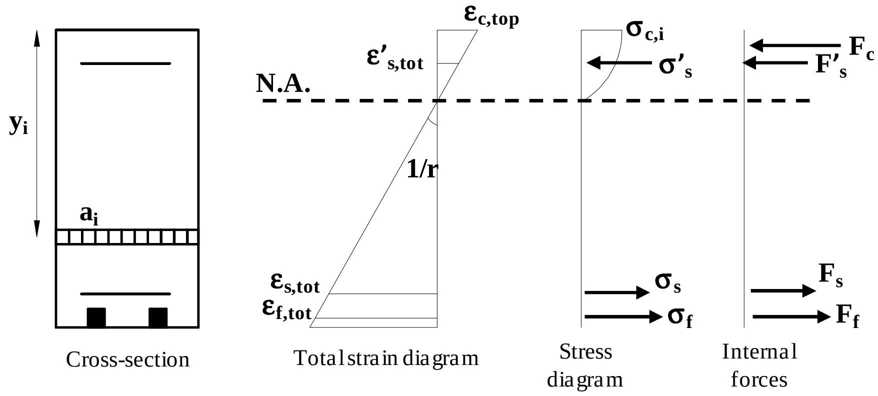

Figure 7.5 – Variations of strains, stresses and internal forces in a beam cross section exposed to fire

It has to be noted that, based on equations 7.12, 7.13 and 7.14, the overall behavior of the beam/slab under fire exposure will primarily depend on the properties of the concrete, steel reinforcement and FRP reinforcement at elevated temperature neglecting the reduction in the adhesive strength and stiffness through the increase of temperature. As already demonstrated in chapter 4, experimental and analytical results have shown a decrease of bond interaction at the FRP/adhesive or adhesive/concrete interface with increasing temperature. Temperatures at or beyond the glass transition temperature significantly influence the stress transfer mechanism; especially in terms of maximum bond stress at the FRP/adhesive/concrete interface. Thus, bond degradation with increasing temperature is to be properly accounted for reliable assessment of the fire resistance in FRP strengthened RC members. In this study the effect of bond degradation with increasing temperature is taken into account considering the decrease of shear strength and stiffness of the adhesive with increasing temperature as described in the following section.

7.2.2.1 Effect of adhesive bond degradation

Bond failure occurs if the bond stresses exceed a critical value (related to the temperature dependent bond shear strength of the materials). Given the high shear strength of the structural adhesives, at ambient temperature debonding will normally occur in the concrete. However with increasing the temperature, failure in the adhesive is governing.

The beams and slabs are (as for the structural analysis) idealized into a number of segments along their length (see Figure 7.6a). For each beam segment i, considering two cross-sections at a distance Δ_x subjected to a moment M and M+ΔM respectively (see Figure 7.6d), the average shear stresses, τ_f, along the FRP NSM bond length can be expressed as:

$$\tau_f = \frac{\Delta N_f}{u_f \Delta_x} \qquad [\mathrm{N/mm^2}] \qquad (7.15)$$

where:

- ΔN_f is the difference in FRP axial forces, over the length Δ_x, computed given the FRP mechanical strains obtained by equation 7.14.
- u_f is the perimeter of the NSM FRP bar/strip

The FRP reinforcement is generally ended at some distance from the support. At the end of the FRP reinforcement, the theoretical FRP force N_{f1} in Figure 7.6b (value as if the FRP would be ended at the support) is actually equal to zero. This is achieved by transferring the force from the FRP to the concrete (and subsequently to the tensile reinforcement) by means of additional shear stresses along the anchorage length. In other words, starting from the free end, the force in the NSM has to be built up. Hereby, extra bond shear stresses, $\Delta\tau_f$, are introduced at the FRP/concrete interface (Figure 7.6c).

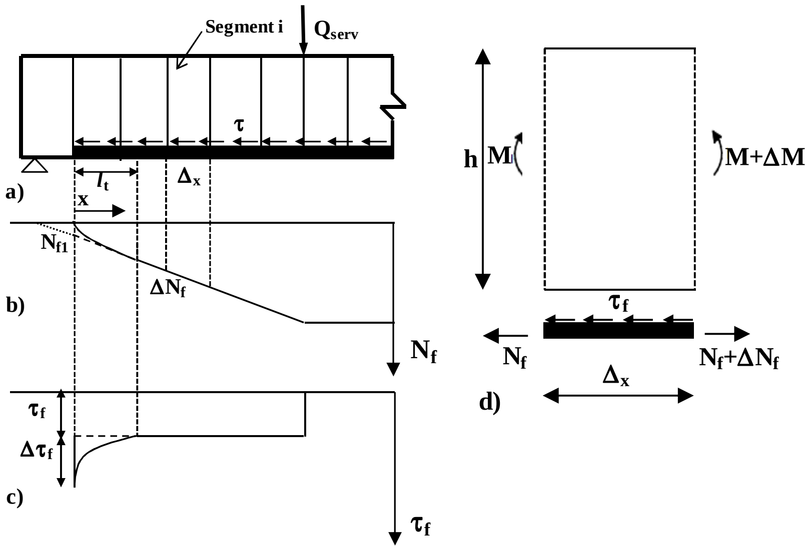

Figure 7.6 – NSM FRP forces and shear stress distribution in a NSM FRP strengthened beam

Assuming that the NSM FRP bar is subjected to pure shear and considering only the ascending branch of a bi-linear τ-slip relation of the NSM FRP bar/strip, the following relationship for the extra bond shear stresses, $\Delta\tau_f$, has been derived by several authors [4-6] (the model is described in details in Appendix D):

$$\Delta\tau_f = \alpha \frac{N_{f1}}{u_f} \frac{\cosh[\alpha(l_t - x)]}{\sinh(\alpha l_t)} \qquad [\mathrm{N/mm^2}] \quad (7.16)$$

where:

- $\alpha = \sqrt{\dfrac{k_{el} u_f}{A_f E_f}}$ with k_{el} the stiffness of the NSM FRP τ-slip relationship; u_f is the bar/strip perimeter, A_f is the cross-sectional area and E_f is the Young's modulus of the FRP bar/strip reinforcement. The adhesive stiffness, k_{el}, reduces with temperature and is determined from the experimental bond shear stress-slip relationship of the double bond shear tests at elevated service temperature discussed in chapter 4. This is further elaborated in section 7.2.2.2.

- N_{f1} is the theoretical FRP force at the end of the NSM FRP bar/strip reinforcement.
- x is the distance along the NSM FRP bar/strip (with x=0 the free end of the FRP)
- l_t is the transfer length

For a given transfer length, l_t, the peak shear stress $\Delta\tau_f = \Delta\tau_{max}$ is obtained for x=0 in equation 7.16:

$$N_{f1} = \frac{\Delta\tau_{max} u_f}{\alpha} \tanh(\alpha l_t) \qquad (7.17)$$

Equation 7.17 is maximized for large values of the transfer length l_t:

$$N_{f1} = \frac{\Delta\tau_{max} u_f}{\alpha} \qquad (7.18)$$

From equation 7.18 the peak shear stress $\Delta\tau_{,max}$ can be derived as follow:

$$\Delta\tau_{max} = \frac{\alpha N_{f1}}{u_f} \qquad (7.19)$$

The transfer length l_t according to equation 7.16 corresponds to $\Delta\tau_f$=0, which is theoretically obtained for $l_t=\infty$. For practical calculations $\Delta\tau_f(0) = 2\xi_l \approx 0$ can be assumed, or based on equations 7.16 and 7.18, with $\sinh(\alpha l_t) \approx e^{\alpha lt} / 2$:

$$l_t \approx \frac{1}{\alpha} \ln\left(\frac{\Delta\tau_{max}}{\xi_l}\right) \qquad (7.20)$$

where a boundary condition ξ_l equal to 0.005 N/mm^2 is proposed.

Once the transfer length l_t is determined the extra bond shear stresses $\Delta\tau_f$ can be determined with equation 7.16. From equation 7.15 and 7.16 the shear stresses along the NSM FRP bond length are calculated with the following equation:

$$\tau_f^* = \tau_f + \Delta\tau_f \qquad [\text{N/mm}^2] \quad (7.21)$$

where τ_f^* depends on (1) the adhesive stiffness, which decreases with temperature and (2) the force in the FRP which in turn depends on the temperature and curvature.

From the bond shear stresses, τ_f^*, the mechanical FRP strains were calculated as follows. Equation 7.15, with the assumption of linearly elastic behavior of the bar/strip, can be expressed as follows:

$$\tau_x = E_f \frac{A_f}{u_f} \frac{\Delta\varepsilon_i}{\Delta x_i} \tag{7.22}$$

where, assuming $\tau_x = \tau_f^*$, the increase of strains, $\Delta\varepsilon_i$, along the NSM FRP bond length can be obtained as follows:

$$\Delta\varepsilon_i = \frac{\tau^*_{f,i} u_f}{E_f A_f} \Delta x_i \tag{7.22}$$

Once $\Delta\varepsilon_i$ is obtained the mechanical strains along the transfer length can be obtained as:

$$\varepsilon^*_{fi,\sigma} = \varepsilon_i + \Delta\varepsilon_i \tag{7.23}$$

where at the end of the NSM FRP bar/strip (x=0) the FRP strain, $\boldsymbol{\varepsilon^*_{fi,\sigma}}$, is zero. Figure 7.7 shows the distribution of the mechanical strain along the NSM FRP bond length.

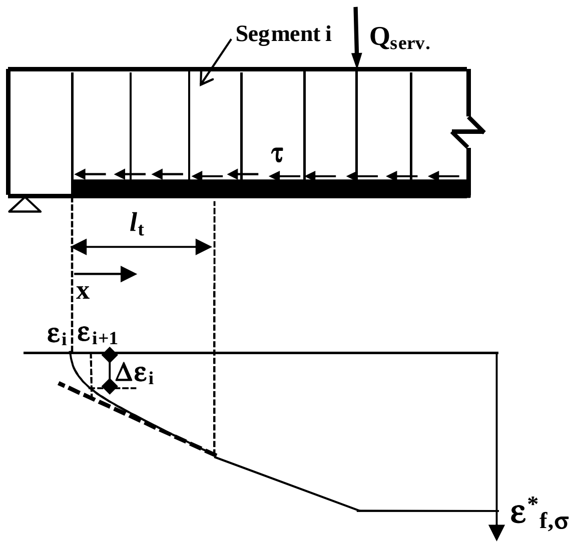

Figure 7.7 – NSM FRP strains and shear stress distribution in a NSM FRP strengthened beam

These effective mechanical strains, $\varepsilon^*_{fi,\sigma}$, which also take into consideration the bond degradation can be used to calculate stresses and tensile forces in the FRP bar/strip reinforcement. Therefore considering equation 7.12 and 7.13 for concrete and steel respectively and equation 7.23 for the FRP reinforcement a new curvature is iterated until force equilibrium is satisfied and the moment-curvature corresponding to these strains is computed for each beam segment and at each time step.

7.2.2.2 Prediction of deflection

Following the generation of the moment curvature relationship, the increase of deflection at midspan with increasing temperature for each time step, $\Delta_{a,}$ is obtained with the following equation:

$$\Delta_{a,t} = a_{\theta,t} - a_{20°C} \tag{7.24}$$

where:

- $a_{\theta,t} = \int_0^L \left(\frac{1}{r}\right)_\theta \overline{M}dx$ is the deflection at midspan at each time step t as a function of the temperature increase, θ. Where $(1/r)_\theta$ is the curvature as a function of the temperature obtained by the equilibrium of forces for each beam segment and $\overline{M}$ is the bending moment due to a unit load applied at midspan.
- $a_{20°C} = \int_0^L \left(\frac{1}{r}\right)\overline{M}dx$ is the deflection at midspan before starting the fire test.

7.2.2.3 Failure criteria

The following failure criteria have been adopted into the model to determine the failure of the NSM FRP strengthened and insulated RC members exposed to fire:

- Strength limit state, defined as the time when the structural member cannot resist the applied load due to the failure of one of the constituent materials (concrete, steel and FRP).
- The temperature of the bottom steel reinforcement and/or the average temperature of the unexposed concrete exceed critical temperature values (see chapter 6 section 6.7).
- The deflection of the beam exceeds L/20, where L is the length of the RC member.

- The rate of deflection exceeds the limit $L^2/9000d$ (mm/min) where L is the length of the RC member and d the effective depth of the RC member
- The calculated bond shear stress, τ_f^*, exceeds the decreasing bond shear strength capacity with increasing temperature. In this case debonding of the NSM FRP strengthening system is assumed.

Regarding the last point, the reduction of bond shear strength with increasing temperature is obtained from the experimental results of the double bond shear tests at elevated temperature discussed in chapter 4. The variation of stiffness of the adhesive and the bond shear strength with increasing temperature is shown in Figure 7.8-Figure 7.11 for each type of NSM FRP bar/strip used to strengthen the tested beams and slabs. It has to be noted that for obtaining these values extra double bond shear tests have been carried out for NSM GFRP type Combar 12. More information about the test results are reported in Appendix B.

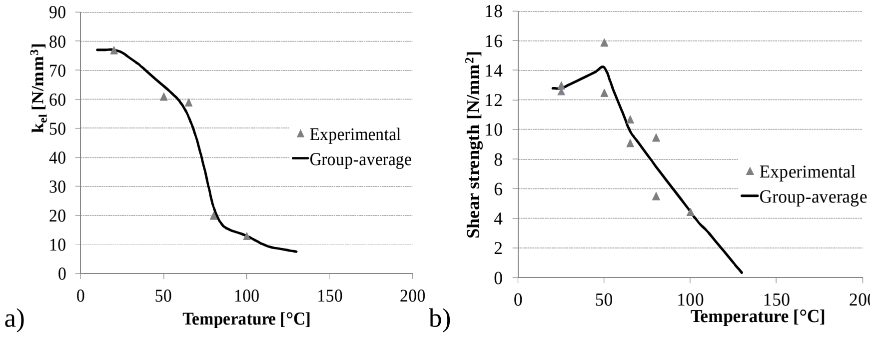

Figure 7.8 – a) Adhesive stiffness and b) bond strength of specimen strengthened with NSM CFRP rods type Aslan 200 adopted for beams type B2

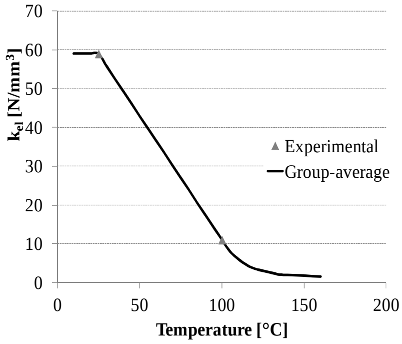

a)

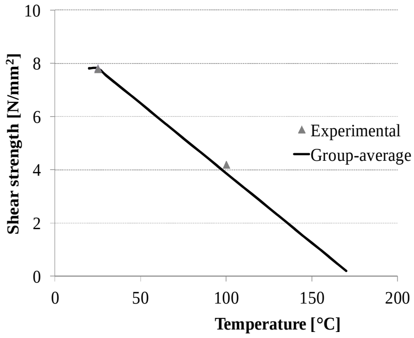

b)

Figure 7.9 – a) Adhesive stiffness and b) bond strength of specimen strengthened with NSM CFRP rods type Aslan 500 adopted for beams type B3

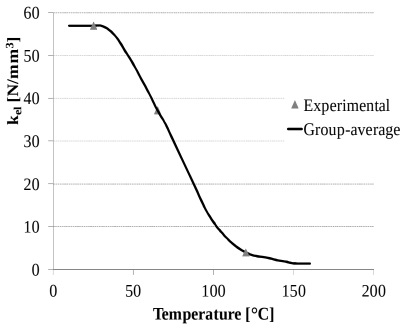

a)

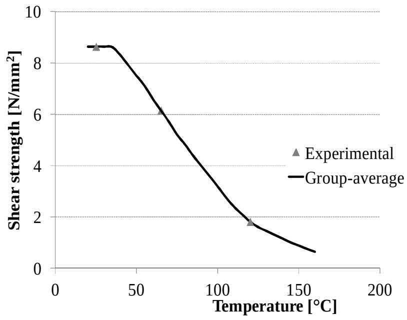

b)

Figure 7.10 – a) Adhesive stiffness and b) bond strength of specimen strengthened with NSM GFRP rods type Combar adopted for beams type B1

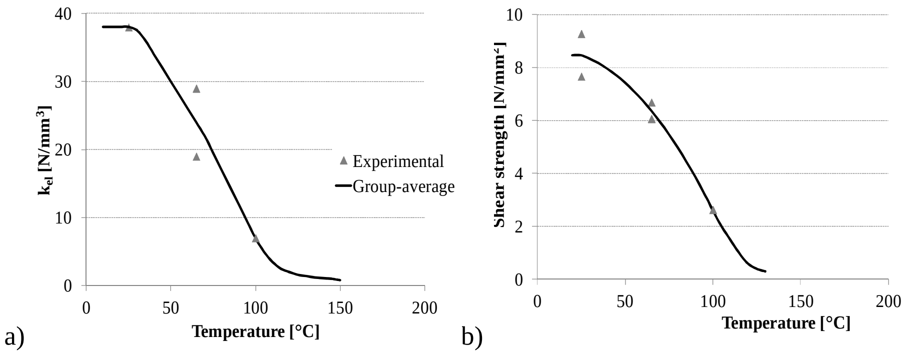

Figure 7.11 **–** a) Adhesive stiffness and b) bond strength of specimen strengthened with NSM GFRP rods type Aslan 100 adopted for slabs type S1-S2

It has to be noted that, for adhesive temperature values higher than tested with the double bond shear tests, the adhesive stiffness and bond strength were calibrated by best fitting through comparison between experimental and predicted results of midspan deflection of beams and slabs exposed to fire.

7.3 Temperature predictions

The thermal analysis described in section 7.2.1 is verified by comparing temperature predictions from the model with measured test data on beams and slabs exposed to fire.

As already mentioned in chapter 6, the fire resistance of typical FRP-strengthened flexural members is mainly influenced by the strength and stiffness properties of the adhesive and by the longitudinal steel reinforcement, since the temperatures in the concrete for insulated beams and slabs remain low for most of the fire duration (see chapter 6). For this reason, in the following the measured (test data) and predicted (from thermal analysis) temperatures in the longitudinal steel reinforcement and in the adhesive will be discussed. A complete overview of predicted temperatures vs experimental one in the beams/slabs cross sections is given in Appendix C.

7.3.1 First fire test

A comparison between the predicted vs experimental (average of four thermocouples) temperatures of the bottom steel reinforcement are shown in Figure 7.12. An analogous comparison of temperatures at the adhesive/FRP reinforcement interface (average value of two thermocouples) is shown in Figure 7.13 and Figure 7.14. The thermal analysis of beams B2-F1-1, B2-F1-2 and B3-F1-1 has been carried out in two parts. In a first part the predicted temperatures are calculated considering the fire protection system attached to the beams up to the moment in which a complete or partial detachment was observed. Thereafter, in a second part, the predicted increase of temperature was calculated on an un-protected beam under fire exposure. The moment at which the fire protection system detached was derived on the basis of experimental results (temperature on thermocouples attached to the soffit of the beams). For the prediction of the temperatures at the adhesive/FRP reinforcement interface both calculations, considering the fire protection attached to the beams for the entire fire exposure time and considering the detachment of the fire protection system are shown (see Figure 7.13 and Figure 7.14).

The heat transfer model is able to predict the temperatures increase in the bottom longitudinal steel reinforcement and at the adhesive/FRP interface with reasonable accuracy with a scatter between predicted and experimental values between ±15-20°C. This limited deviation between the predicted and experimental results may be mostly due to the fact that the thermal induced moisture migration within the concrete is not taken into account in the thermal analysis. The experimental increase of temperature of the longitudinal bottom steel reinforcement, for example, increases faster in the first 30 min than the predicted one due to the moisture migration (see Figure 7.12) followed by an almost horizontal threshold due to evaporation of water at approximately 100°C. In the thermal analysis, as specified in section 7.2 only the evaporation of water into the concrete was taken into account by considering a peak value in the specific heat. Therefore the model tends to under-predict the increase of temperature within the first 30 min of fire exposure with closer agreement at later stages.

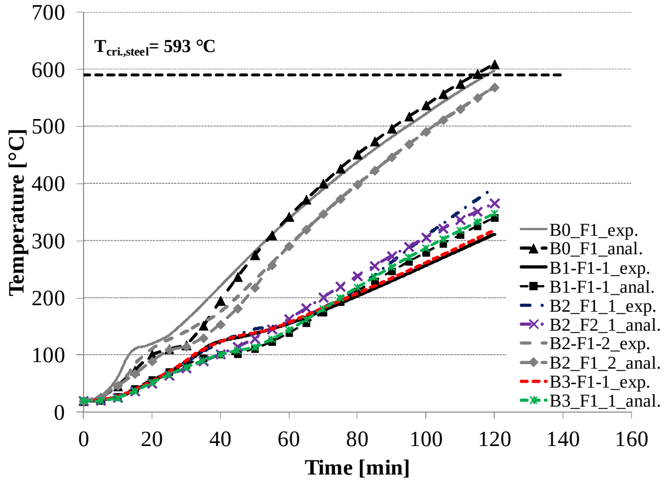

Figure 7.12 – Predicted vs experimental temperatures at longitudinal steel reinforcement of beams of first fire test

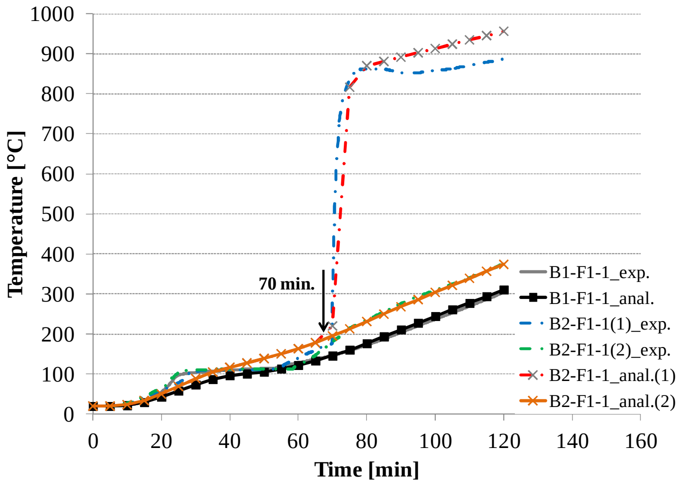

Figure 7.13 – Predicted vs experimental temperatures at adhesive/FRP interface of beams B1-F1-1 and B2-F1-1 of first fire test

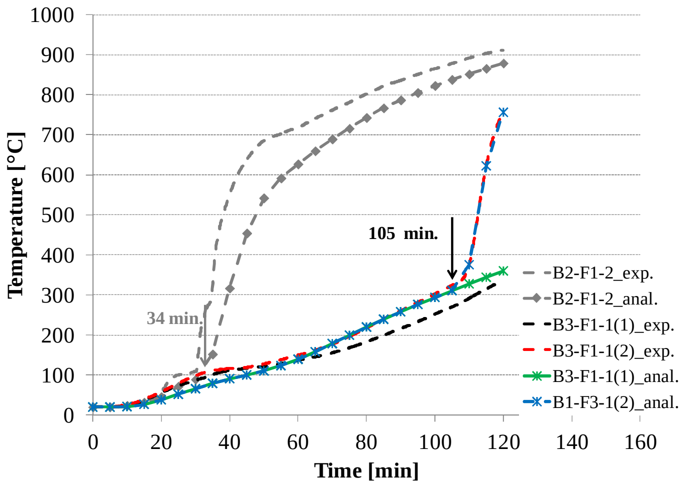

Figure 7.14 – Predicted vs experimental temperatures at adhesive/FRP interface of beams B2-F1-2 and B3-F1-1of first fire test

7.3.2 Second fire test

A comparison between the predicted vs experimental (average of four thermocouples) temperatures of the bottom steel reinforcement is shown in Figure 7.15 and Figure 7.16. An analogous comparison of temperatures at the adhesive/FRP reinforcement interface (average value of two thermocouples) is shown in Figure 7.17 and Figure 7.18.

As discussed in the previous section, for the beam B0-F2 the predicted temperatures of the bottom steel reinforcement are lower than the experimental ones for the first 40 min of fire exposure with closer agreement at later stages (see Figure 7.16). The heat transfer model was able to predict the temperature increase at the bottom longitudinal steel reinforcement and at adhesive/FRP interface with good accuracy for beam B1-F2-1 for all the duration of fire exposure (see Figure 7.15 and Figure 7.17).

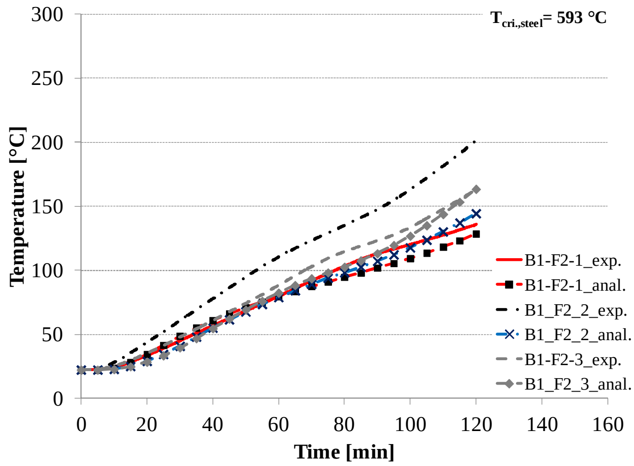

Figure 7.15 – Predicted vs experimental temperature at longitudinal steel reinforcement of beams B1-F2-1; B1-F2-2 and B1-F2-3 of second fire test

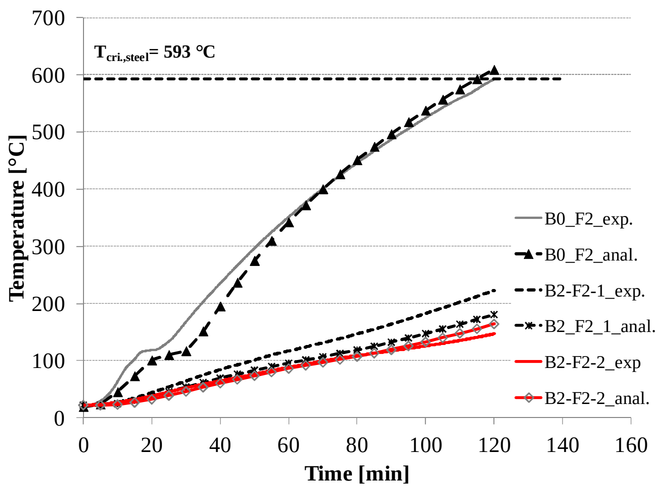

Figure 7.16 – Predicted vs experimental temperature at longitudinal steel reinforcement of beams B0-F2; B2-F2-1 and B2-F2-2 of second fire test

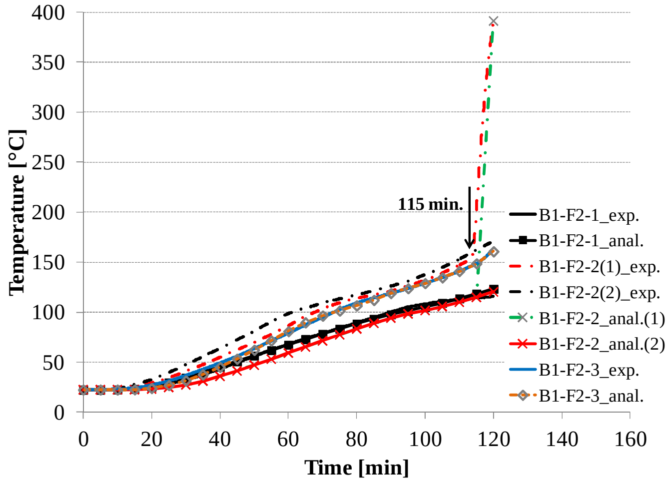

Figure 7.17 – Predicted vs experimental temperatures at adhesive/FRP interface of beams B1-F2-1; B1-F2-2 and B1-F2-3 of second fire test

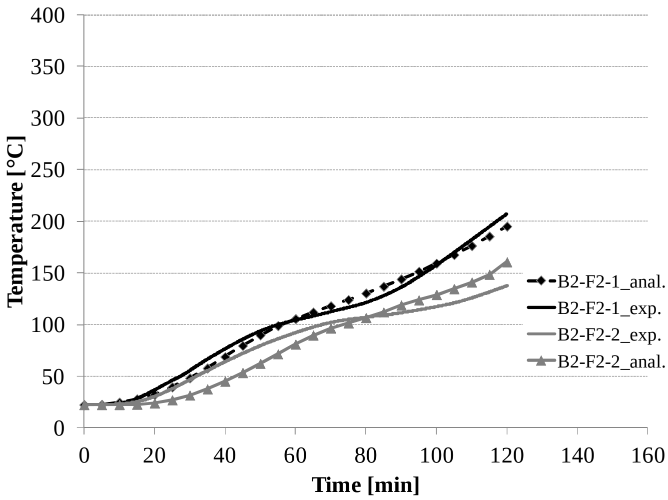

Figure 7.18 – Predicted vs experimental temperatures at adhesive/FRP interface of beams B2-F2-1 and B2-F2-2 of second fire test

Considering that, within 3 min of initiation of the fire test, surface flaming of the Omega fire coating of beam B1-F2-2 and B1-F2-3 was observed and that it detached within 20 min into the tests it was decided to model both beams considering only the HPC insulation system. Comparison between experimental and predicted temperatures (see Figure 7.15 and Figure 7.17) shows a good agreement for both temperatures at the bottom steel reinforcement and at the adhesive/FRP interface for beam B1-F2-3. However the model tends to under-predict the temperatures of beam B1-F2-2. This can be explained considering the formation of cracks and/or partial detachment of the HPC layer of beam B1-F2-2 during fire exposure. It has to be noted that, in the model, no cracks in the fire insulation system were taken into account. This can leads to an underestimation of the temperature increase in the beam cross section. While this result shows that cracking of the insulation may be important for predicting the heat transfer in insulated FRP strengthened beams, such detailed modeling of the insulation material is beyond the scope of the current project.

Although, as discussed previously in chapter 6, transversal cracks on the surface of the insulation system of beam B2-F2-2 were observed within 20 min into the fire test with consequently partial detachment of the insulation system at around 100 min into the test the analytical model (in which no cracks are taken into account) was able to predict with good accuracy the temperature at the bottom steel reinforcement and at adhesive/FRP interface (see Figure 7.16 and Figure 7.18). This may be related to the fact that cracks in the insulation mainly developed far from the two monitored sections. In the following section this is confirmed further by comparing the experimental and analytical increase of deflection during fire exposure.

Different behaviour was observed for beam B2-F2-1, for which a variation between the predicted and experimental temperatures is observed at the bottom steel reinforcement. It has to be noted that, oppositely to beam B2-F2-2, in beam B2-F2-1 the cracks formation on the surface of the insulation system has influenced the experimentally recorded steel temperatures during fire exposure. Indeed a significant variability is observed in the experimental data at the monitored sections, likely due to the formation of cracks. For a better understanding in Figure 7.19 the experimental temperature-time curves of the four thermocouples attached to the steel and the average value is compared to the predicted time-temperature curve at the bottom steel reinforcement. It can be noted that the predicted temperatures are in good agreement with experimental values for sections in which cracks might not have been developed during fire exposure (temperatures recorded by thermocouples 3 and 4).

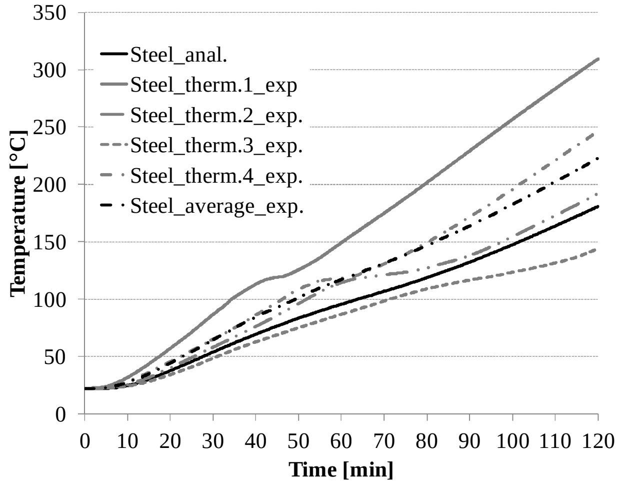

Figure 7.19– Predicted vs experimental temperatures at bottom steel reinforcement of beam B2-F2-1

7.3.3 Third fire test

A comparison between the predicted vs experimental (average of four thermocouples) temperatures of the bottom steel reinforcement are shown in Figure 7.19, Figure 7.20 and Figure 7.21. An analogous comparison of temperatures at the adhesive/FRP reinforcement interface (average value of two thermocouples) is shown in Figure 7.23 and Figure 7.24.

The numerical model was able to predict the temperatures at the bottom longitudinal steel reinforcement of beams B1-F3-1 and B2-F3-2 close to the temperatures observed during the fire tests (see Figure 7.20). This result shows that, given the geometry of the fire insulation (same thickness at the beam sides and different thickness at the bottom of the beam), the steel temperature increase seems to be governed more by the insulation system applied to the side of the beam rather than the one at the bottom of the beam. Regarding the increase of temperature at the adhesive/FRP interface (see Figure 7.23), the numerical model, while predicting with good accuracy the temperature increase of beam B2-F3-1, it tends to under-predict the temperature increase at FRP/adhesive interface of beam B1-F3-1, given the higher thickness of the fire protection boards with respect to beam B2-F3-1. The unexpected experimental behavior of beam B1-F3-1 can be related to possible cracks formation at the bottom of the fire protection or a possible gap between the fire insulation boards that were not taken into account into the model.

Based on experimental observation (see chapter 6), it was decided to model the beams B1-F3-2, B1-F3-3 and B1-F3-4 considering only the HPC insulation system. Overall it is clear from Figure 7.21, Figure 7.22 and Figure 7.24 that there is a good agreement between the experimental and predicted temperatures for all the beams protected with HPC fire insulation system. Although, based on the hypothesis of considering only the HPC fire insulation material, the numerical model slightly overpredicts the temperatures at the steel reinforcements for some of the beams.

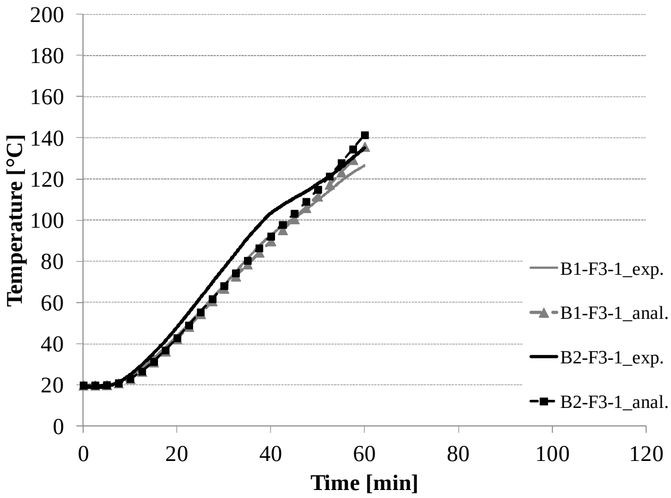

Figure 7.20 – Predicted vs experimental temperature at longitudinal steel reinforcement of beams B1-F3-1and B2-F3-1 of third fire test

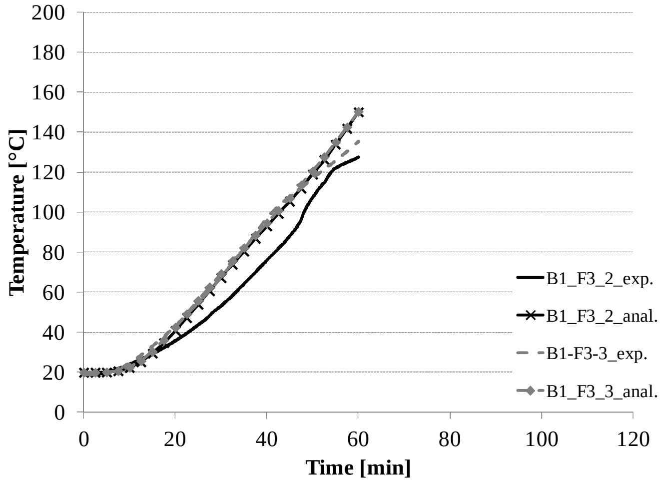

Figure 7.21 – Predicted vs experimental temperature at longitudinal steel reinforcement of beams B1-F3-2and B1-F3-2 of third fire test

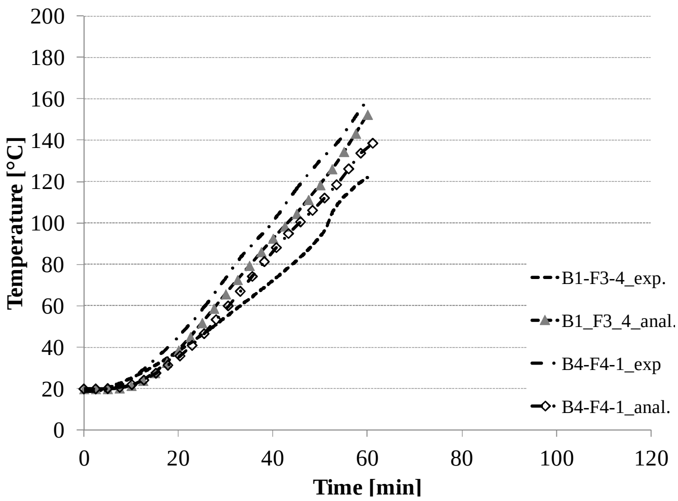

Figure 7.22 – Predicted vs experimental temperature at longitudinal steel reinforcement of beams B1-F3-4and B4-F4-1 of third fire test

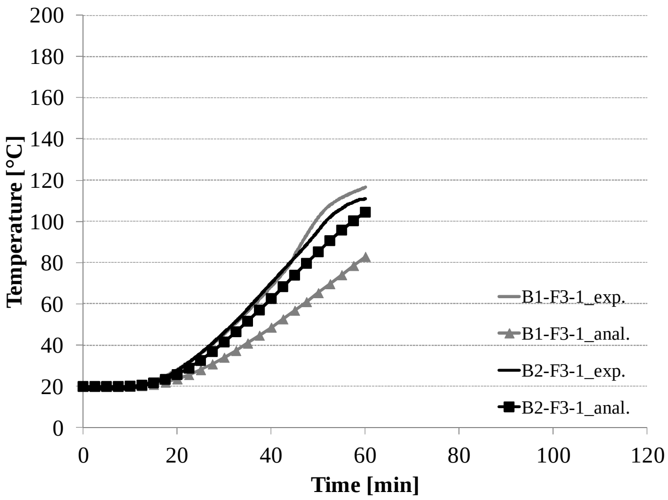

Figure 7.23 – Predicted vs experimental temperatures at adhesive/FRP interface of beams B1-F3-1 and B2-F3-1 of third fire test

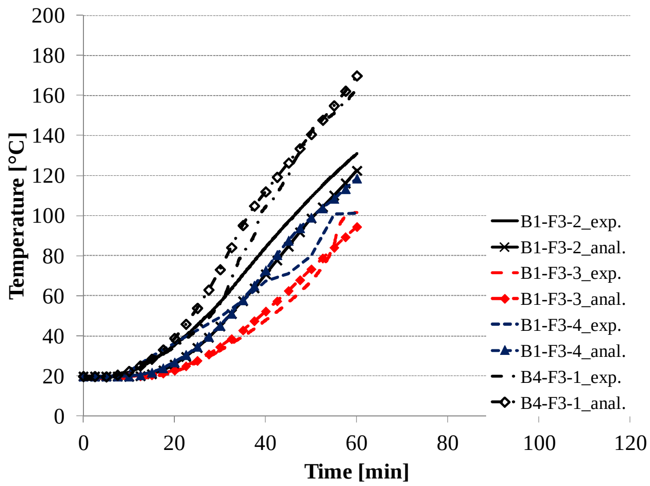

Figure 7.24 – Predicted vs experimental temperatures at adhesive/FRP interface of beams B1-F3-2, B1-F3-3, B1-F3-4 and B4-F3-1 of third fire test

7.3.4 Fourth fire test

A comparison between the predicted vs experimental (average of four thermocouples) temperatures of the bottom steel reinforcement is shown in Figure 7.25 and Figure 7.26. An analogous comparison of temperatures at the adhesive/FRP reinforcement interface (average value of two thermocouples) is shown in Figure 7.27 and Figure 7.28. For the insulated slabs, temperature measurements of the steel rebars at the corners (indicated with number 1 in Figure 7.26) and at the inner steel rebars (indicated with number 2 in Figure 7.26) differs significantly and individual curves (average of two thermocouples) are given for both experimental and analytical results.

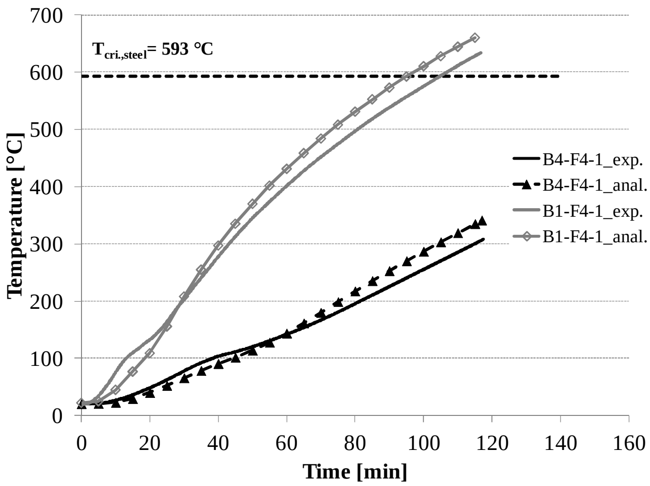

Figure 7.25 – Predicted vs experimental temperature at longitudinal steel reinforcement of beams B4-F4-1and B1-F4-1 of fourth fire test

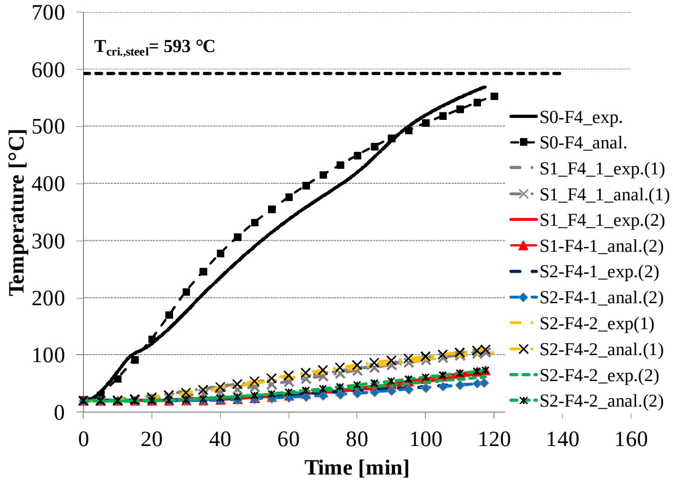

Figure 7.26 – Predicted vs experimental temperature at longitudinal steel reinforcement of slabs S0-F4, S1-F4-1, S2-F4-1 and S2-F4-2 of fourth fire test

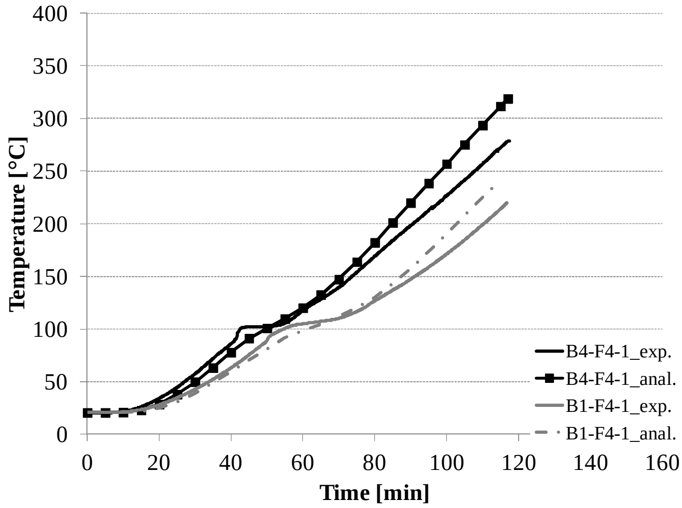

Figure 7.27 – Predicted vs experimental temperatures at adhesive/FRP interface of beams B4-F4-1 and B1-F4-1of fourth fire test

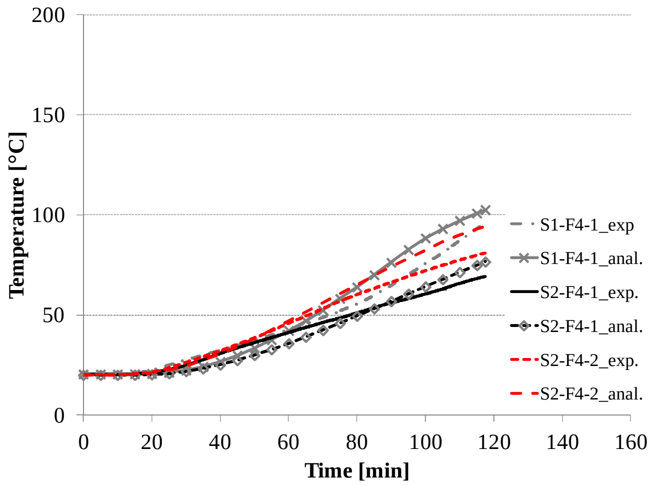

Figure 7.28 – Predicted vs experimental temperatures at adhesive/FRP interface of slabs S1-F4-1, S2-F4-2 and S2-F4-2of fourth fire test

The heat transfer model is able to predict the temperatures increase in the bottom steel longitudinal reinforcement and at adhesive/FRP interface with reasonably accuracy for both beams B1-F4-1 and B4-F4-1 although it tends to overpredict the temperature increase at the later stage of fire exposure. A good agreement between the predicted and experimental temperatures increase for the longitudinal reinforcement and at FRP/adhesive interface was also obtained for all the slabs for the entire duration of fire exposure.

7.4 Predicted increase of deflection and bond failure

The structural analysis described in section 7.2.2 is verified by comparing predictions of the increase of midspan deflection from the model with measured test data for each fire test series. Moreover the analysis incorporates an elastic analysis for predicting the FRP bond shear stresses along the FRP bonded length with increasing temperature. By modeling the combined effects of adhesive strength and stiffness reduction with increasing temperature, as discussed in section 7.2, the analysis yields bond failure if the shear stresses exceed a critical bond strength value (see section 7.2.2.2). The predicted bond failure is compared with experimental data, in which a sudden increase of deflection during fire exposure was considered as loss of bond at the FRP/concrete interface. A comparison between predicted and experimental increase of deflection at midspan is also shown in Appendix C for all the tested beams and slabs under fire exposure.

7.4.1 First fire test

A comparison between the predicted and experimental increase of midspan deflection is shown in Figure 7.29 and Figure 7.30. For the control beam (B0-F1) the predicted increase of midspan deflection is slightly underestimated with respect to the experimental one (see Figure 7.29). This difference can be attributed to the discrepancy between the predicted and measured temperatures of the bottom steel reinforcement, as discussed in section 7.3.1. The analytical model predicts the failure at 110 min into the fire test (based on the strength limit state) as compared to 105 min measured during the test. The strength limit state is defined as the time when the structural member cannot resist the applied service load.

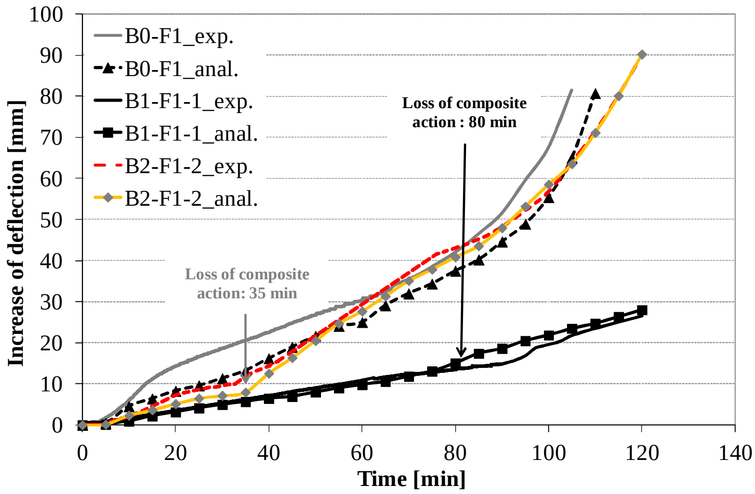

Figure 7.29 – Predicted vs experimental increase of deflection at midspan of beams B0-F1, B1-F1-1 and B2-F1-2 of first fire test

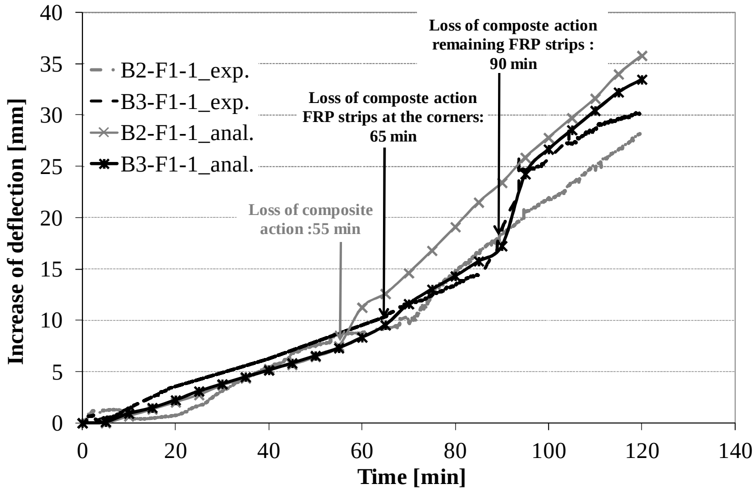

Figure 7.30 – Predicted vs experimental increase of deflection at midspan of beams B2-F1-1 and B3-F1-1of first fire test

A good agreement between the measured and predicted increase of deflection at midspan is observed for beams B1-F1-1, B2-F1-2 and B3-F1-1 for all the duration of fire exposure. For beam B2-F1-1 a close agreement between predicted and experimental results is observed in the first 55 minutes into the fire test, after which point the predicted deflection overestimates the increase of deflection at midspan. It has to be noted that for beam B2-F1-1, at the moment of the partial detachment of the fire insulation system, the deflection was modeled considering an un-protected beam under fire exposure for the complete length of the specimen. This assumption can lead to an overestimation of the increase of deflection at midspan.

To illustrate the effect of bond degradation at the FRP/adhesive interface on the fire response, the variation of the bond shear stress distribution over a distance from the NSM FRP bar/strip end up to the loading point (x=900 mm), for different fire exposure times, is shown in Figure 7.31 for beam B1-F1-1 and in Figure 7.32 (bond shear stresses of the strips at the corner) and Figure 7.33 (bond shear stresses of the inner strips) for beam B3-F1-1. The calculated variation of bond shear stress distribution for all the specimens of the first fire test series is given in Appendix D.

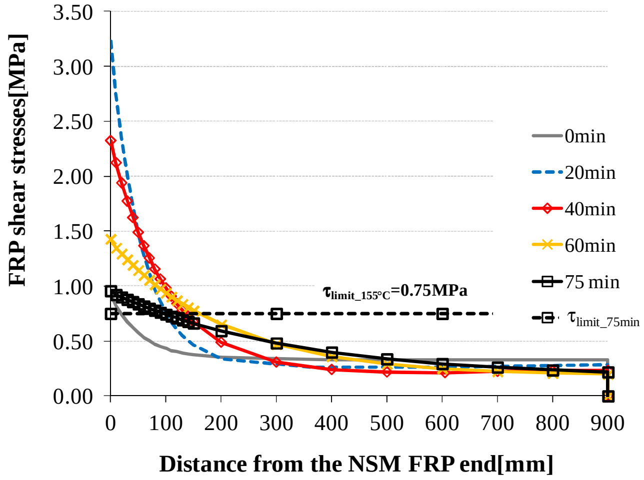

Figure 7.31 – Variation of shear stress distribution as a function of the fire exposure time of beam B1-F1-1

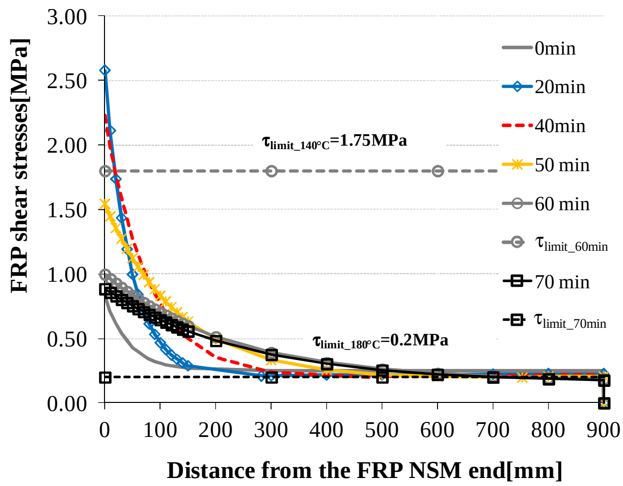

Figure 7.32 – Variation of shear stress distribution strips at corners as a function of the fire exposure time of beam B3-F1-1

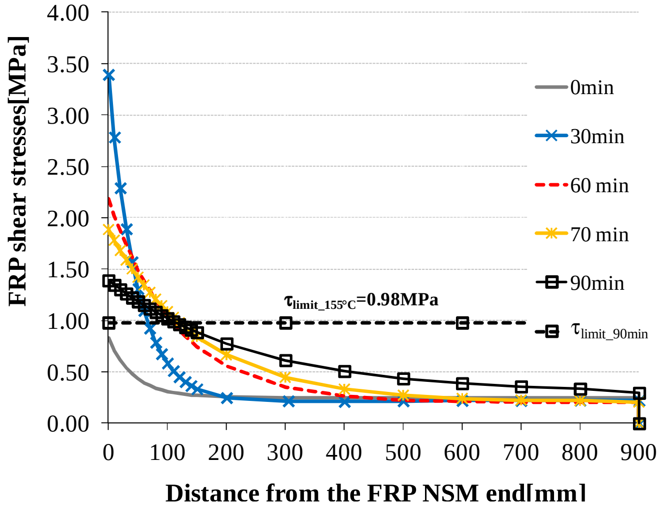

Figure 7.33 – Variation of shear stress distribution inner strips as a function of the fire exposure time of beam B3-F1-1

At low temperatures the shear stresses are concentrated at the end of the FRP bar/strip. Away from the FRP bar/strip end, the shear stresses distribution is predicted by simply beam theory, with a peak in shear stress at the loading point (x= 900 mm). Increasing the temperature at and beyond the glass transition temperature resulted in an increase of the transfer length, l_t, with a consequent reduction of the peak shear stresses and a more uniform distribution of shear stresses over the FRP bond length. This effect can be attributed to the reduction in stiffness of the adhesive with temperature increasing. These results are in line with experimental results obtained for double bond shear tests at elevated temperature (see chapter 4). On the other hand increasing the temperature, at and beyond T_g, results in a reduction of the bond strength at the FRP/adhesive interface, τ_{limit} (see section 7.2.2.2). When the calculated shear stresses exceed the decreasing shear capacity at the FRP/adhesive interface, loss of composite action at the NSM FRP/concrete interface is assumed. The model is able to predict the experimental observed time in which FRP debonding occurs, although a premature prediction of failure is observed for some of the beams. A summary of the time of loss of composite action observed experimentally, $t_{deb,exp}$, the analytical assumed time of loss of composite action, $t_{deb,anal}$, the calculated bond shear stresses $\boldsymbol{\tau_f^*}$ (at time of loss of composite action at the NSM FRP/concrete interface) and the bond strength at the FRP/adhesive interface τ_{limit} (at the analytical assumed time of loss of composite action at NSM FRP/concrete interface) is reported in Table 7.1.

Table 7.1 – Results of structural analysis for beams of the first fire test

Specimen	$t_{deb,exp}$ [min]	$t_{deb,anal}$ [min]	τ_f^* [N/mm^2]	τ_{limit} [N/mm^2]
B1-F1-1	90	75	0.95	0.75
B2-F1-1	70	55	3.00	1.70
B2-F1-2	34	35	4.58*	5.20*
B3-F1-1	90	90	1.34	0.98

* *Values prior to detachment of fire insulation system*

It has to be noted that given the nature of the analysis of bond shear stresses along the NSM FRP bond length (elastic analysis), the model tends to calculate a concentration of high shear stresses at the NSM FRP end. In reality although these shear stresses exceed the bond strength at the FRP/adhesive interface, they will not cause an immediate debonding of the NSM FRP bars but lead to an increase of slip at the FRP/adhesive interface that occurs prior to failure (FRP debonding). It is likely possible that, under the acting load, an elastoplastic model of the adhesive behavior will lead to a plateau in the shear stresses at the NSM FRP end (plastic zones at the NSM FRP end) that spread along the adhesive joint as temperature increase allowing load transfer over a larger transfer length. However, a bond model that incorporates the complexities of elastoplastic adhesive behavior, given the lack of data of the adhesive behavior at elevated temperatures attained during the fire tests, is beyond the scope of the current project. Instead the aim is to use a simplified elastic model to explore the influence of elevated temperature beyond the adhesive T_g of the adhesive, for NSM FRP strengthened RC members. With this scope in mind the failure criteria was considered conservatively to be reached as soon the shear stresses exceeds the bond shear strength at the FRP/adhesive interface.

For instance, it is interesting to note that for all of the tested beams the debonding failure was obtained for a temperature value higher than the adhesive glass transition temperature. This is because, at a temperature equal to T_g, the shear stresses at the FRP/concrete interface induced by the applied loads (service loads) are lower than the bond shear strength. In other words at a temperature equal to the glass transition temperature the adhesive still has enough strength and stiffness to transfer the shear stresses, induced by the applied loads, from the FRP to the concrete.

7.4.2 Second fire test

A comparison between the predicted and experimental increase of midspan deflection of the beams tested in the second fire test series is shown in Figure 7.34 and Figure 7.35. For the control beam (B0-F2) the predicted increase of midspan deflection is slightly underestimated with respect to the experimental one for the first 40 min of fire exposure and slightly overestimated in the later stages. However, overall increase of deflection prediction is in good agreement with experimental results. The deviation can be attributed to the discrepancy between the predicted and measured temperatures of the bottom steel reinforcement, as discussed in section 7.3.2. The analytical model predicts the beam failure (110 min into the fire test) with good accuracy, based on the strength limit state.

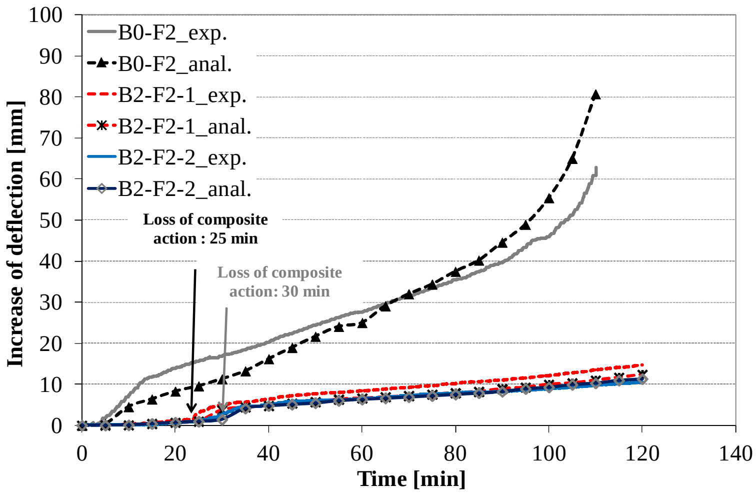

Figure 7.34 – Predicted vs experimental increase of deflection at midspan of beams B0-F2, B2-F2-1 and B2-F2-2 of second fire test

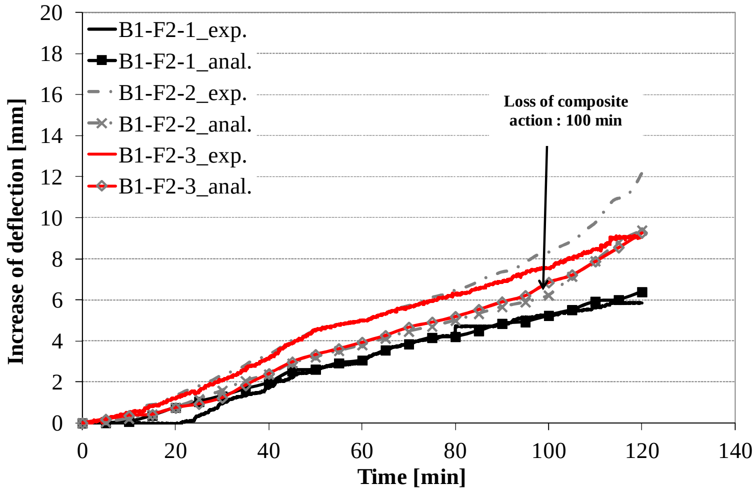

Figure 7.35 – Predicted vs experimental increase of deflection at midspan of beams B1-F2-1, B1-F2-2 and B1-F2-3 of second fire test series

It has to be noted that for beams B2-F2-1 and B2-F2-2 the time at which loss of composite action is achieved was determined based on experimental observation, as discussed in section 7.3.2. Therefore at a time equal to 25 min and 30 min for beams B2-F2-1 and B2-F2-2 respectively, the beams were modelled as an unstrengthened beam with fire protection all along the length of the beam. A good agreement between the measured and predicted increase of deflection at midspan is observed for beam B2-F2-2, while a slightly underestimation of predicted deflection is observed for beam B2-F2-1 due to the variation between predicted and recorded temperature at the bottom steel reinforcement (see section 7.3.2).

Good agreement between the measured and predicted increase of deflection at midspan is also observed for beams B1-F2-1 and B1-F2-3 for all the duration of fire exposure. A slight underestimation of predicted deflection was observed for beam B2-F2-2. The deviation in prediction can be explained from the variation in predicted and measured temperatures of the steel and FRP reinforcement related to the formation of cracks in the insulation layer that was not taken into account in the analytical model (see section 7.3.2).

The variation of bond shear stress distribution over a distance from the NSM FRP bar/strip end up to the loading point (x=900 mm), for different fire exposure time, is shown in Figure 7.36 and Figure 7.37 for beam B1-F2-1 and beam B1-F2-3 respectively. The calculated variation of bond shear stress distribution for all the specimens of the second fire test series is given in Appendix D.

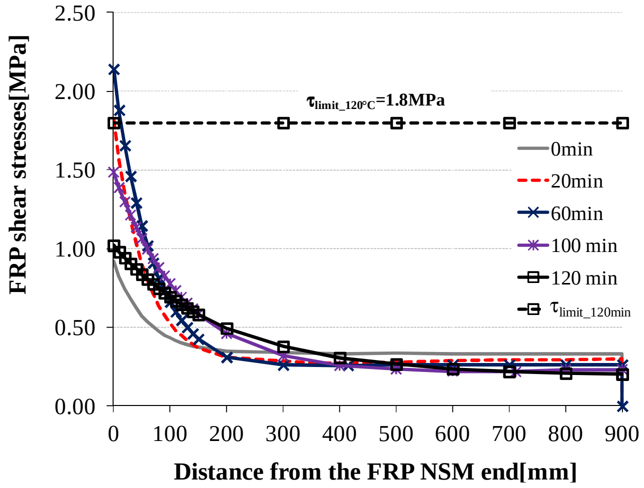

Figure 7.36 – Variation of shear stress distribution as a function of the fire exposure time of beam B1-F2-1

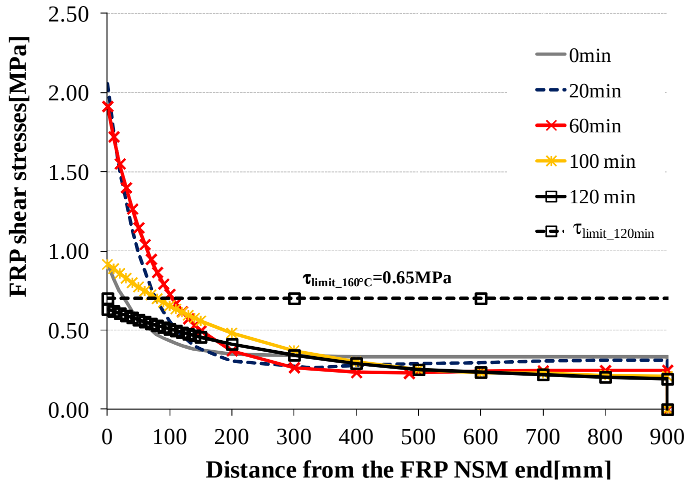

Figure 7.37 – Variation of shear stress distribution as a function of the fire exposure time of beam B1-F2-3

As previously observed for the first fire test series, at low temperatures the shear stresses are concentrated at the end of the FRP bar. Increasing the temperature at and beyond the glass transition temperature resulted in an increase of the transfer length, l_t, with a consequent reduction of the peak shear stresses and a more uniform distribution of shear stresses over the FRP bond length. For both beams the shear stresses remain in the elastic region of the bond shear stress-slip relationship and moreover the predicted shear stress distribution is below the reduced bond strength at the FRP/adhesive interface for all the duration of fire exposure. The model closely follows the experimental observation for which no sign of debonding failure was observed for both beams, although the adhesive temperature was well beyond its glass transition temperature. Again, given the insulation system and the acting loading level during fire exposure, the adhesive was still stiff enough to withstand the FRP shear stresses. A summary of the time of loss of composite action observed experimentally, $t_{deb,exp}$, the analytical assumed time of loss of composite action, $t_{deb,anal}$, the calculated bond shear stresses $\boldsymbol{\tau}_f^*$ (at time of loss of composite action at the NSM FRP/concrete interface) and the bond strength at the FRP/adhesive interface τ_{limit} (at the analytical assumed time of loss of composite action at NSM FRP/concrete interface) is reported in Table 7.2.

Table 7.2 – Results of structural analysis for beams of the second fire test

Specimen	$t_{deb,exp}$ [min]	$t_{deb,anal}$ [min]	$\tau_{f.}^*$ [N/mm^2]	τ_{limit} [N/mm^2]
B1-F2-1	>120	>120	1.00	1.82
B1-F2-2	100	100*	1.77	3.15
B1-F2-3	>120	>120	0.60	0.65
B2-F2-1	25	25*	3.62	13.10
B2-F2-2	30	30*	4.02	13.10

* *Values assumed based on experimental observation*

7.4.3 Third fire test

A comparison between the predicted and experimental increase of midspan deflection of the beams tested in the third fire test series is shown in Figure 7.38, Figure 7.39 and Figure 7.40.

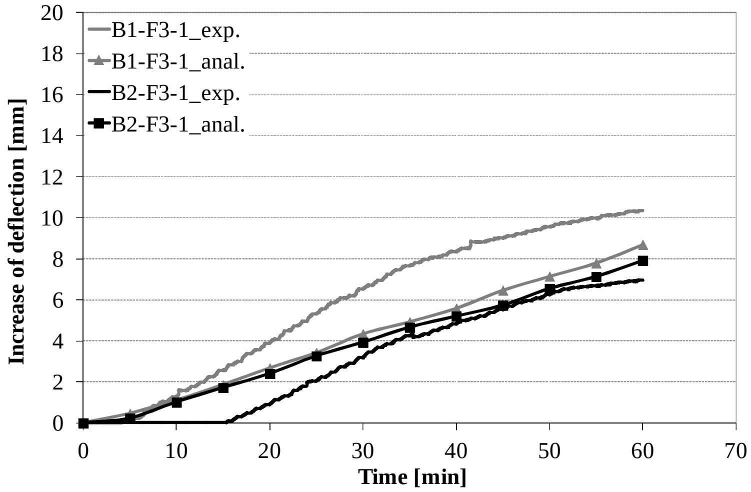

Figure 7.38 – Predicted vs experimental increase of deflection at midspan of beams B1-F3-1 and B2-F3-1 of third fire test

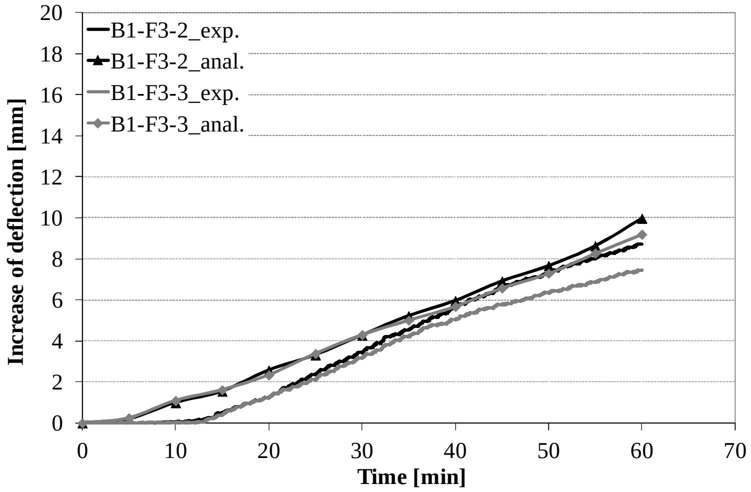

Figure 7.39 – Predicted vs experimental increase of deflection at midspan of beams B1-F3-2 and B1-F3-3 of third fire test

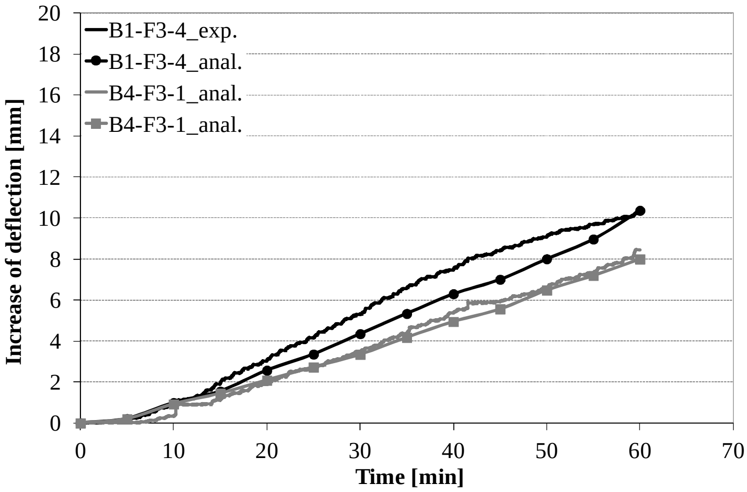

Figure 7.40 – Predicted vs experimental increase of deflection at midspan of beams B1-F3-4 and B4-F3-1 of third fire test

The model is able to predict with reasonable accuracy the increase of deflection of beam B2-F3-1 while it underestimates the increase of deflection at midspan for beam B1-F3-1. This deviation is due to the differences between the predicted and measured temperature of the adhesive as discussed in section 7.3.3. From Figure 7.39 and Figure 7.40 it is clear that the model predicts the increase of deflection at midspan with good accuracy for all the beams insulated with HPC fire insulation system, although it tends to slightly overpredict the increase of deflection in the early stages of fire exposure. However it has to be noted that for almost all the beams insulated with HPC fire insulation system the recorded increase of deflection at midspan was almost zero in the first 10-15 minutes into the fire test. It is possible that the adopted measuring system was not accurate enough to measure the low values of increase of deflection in the early stage of fire exposure.

For beam B4-F3-1 the effect of bond degradation was not taken into account due to lack of data related to the reduction of adhesive (cementious mortar) stiffness and strength with increasing temperature of the NSM FRP strengthening system embedded in cementious mortar. Therefore full composite action between FRP and mortar was considered for all the duration of fire exposure.

In order to validate the analytical model and the assumed failure criteria the variation of bond shear stress distribution over a distance from the NSM FRP bar end up to the loading point (x=900mm) of beam B1-F3-2 is shown in Figure 7.41 for different fire exposure times and in Figure 7.42 as a function of the increased load immediately after fire exposure. It can be noted that the shear stresses do not exceed the bond strength at the FRP/adhesive interface for the duration of fire exposure.

For beam B1-F3-2, after fire exposure the analytical structural analysis was conducted considering the materials temperatures constant for the duration of increased load. It is noted that (see Figure 7.42), FRP shear stresses significantly increases after yielding of the internal steel (in Figure 7.42 Q= 50kN is just before yielding of steel). Indeed once the yield stress in the steel is reached a further increase of tensile force (and hence bending moment) is mainly related to the NSM FRP. A shear stress concentration is noted at the FRP end and after yielding of the steel also near the point load. Beam B1-F3-2 is able to resist the increasing load up to the point in which the shear stresses exceed the adhesive bond strength, after which point debonding of the FRP occurs.

Moreover Figure 7.43 shows the predicted and experimental load-deflection curves of beam B1-F3-2 in the three phases of pre-loading up to its service load (curve A-B), fire exposure (curve B-C) and increase of loading after fire exposure (curve C-D). It can be noted that the analytical model is able to predict with good accuracy the experimental load-deflection curves in all the three stages and the residual strength capacity of the beam.

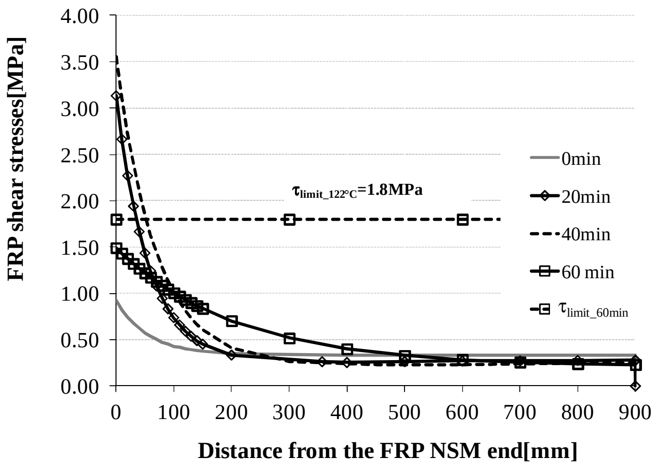

Figure 7.41 – Variation of shear stress distribution as a function of the fire exposure time of beam B1-F3-2

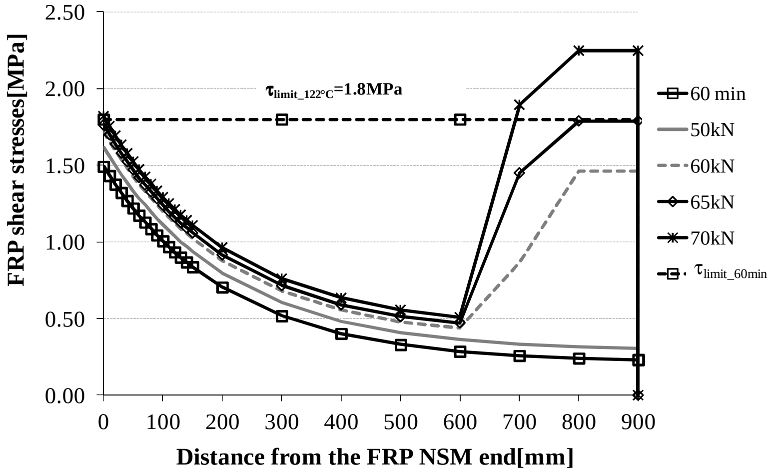

Figure 7.42 – Variation of shear stress distribution with increasing load after fire exposure of beam B1-F3-2

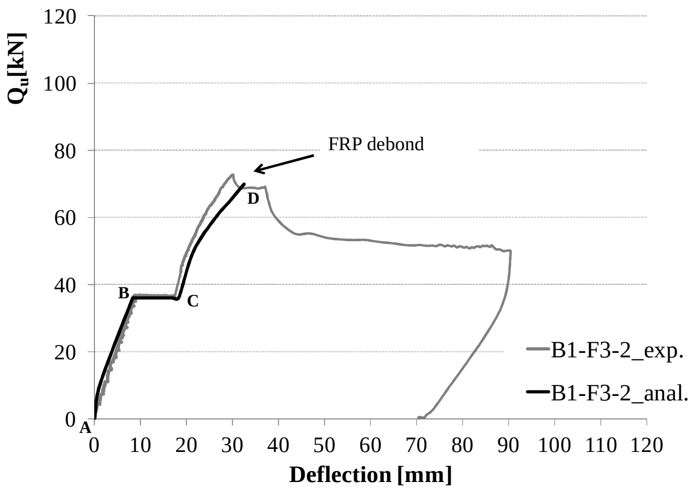

Figure 7.43 – Predicted vs experimental load-deflection curves of beam B1-F3-2

A summary of the time of loss of composite action observed experimentally, $t_{deb,exp}$, the analytical assumed time of loss of composite action, $t_{deb,anal}$, the calculated bond shear stresses $\boldsymbol{\tau_f^*}$ (at time of loss of composite action at the NSM FRP/concrete interface) and the bond strength at the FRP/adhesive interface τ_{limit} (at the analytical assumed time of loss of composite action at NSM FRP/concrete interface) is reported in Table 7.3.

Table 7.3 – Results of structural analysis for beams of the third fire test

Specimen	$t_{deb,exp}$ [min]	$t_{deb,anal}$ [min]	τ_f^* [N/mm^2]	τ_{limit} [N/mm^2]
B1-F3-1	>60	>60	3.80	4.75
B1-F3-2	>60	>60	1.50	1.80
B1-F3-3	>60	>60	2.82	3.15
B1-F3-4	>60	>60	1.48	1.82
B2-F3-1	>60	>60	4.48	4.52
B4-F3-1	>60	>60	-	-

7.4.4 Fourth fire test

A comparison between the predicted and experimental increase of midspan deflection of the beams and slabs tested in the fourth fire test series is shown in Figure 7.44 and Figure 7.45. As previously discussed, beam B4-F4-1 with mortar instead of epoxy as adhesive is modeled considering full composite action between the FRP and the adhesive. From Figure 7.44 it is observed that, although a slight overestimation of temperature at the bottom steel reinforcement and the FRP/adhesive interface is obtained (see section 7.3.4), the predicted increase of deflection at midspan for beam B4-F4-1 at later stages of fire exposure is stiffer than the experimental one. This is because in the model is not taking into account the bond degradation at the FRP/adhesive interface and the overall behavior of the temperature primarily depends on the high temperature proprerties of the FRP bar reinforcement.

For beam B2-F4-1 the NSM FRP bars are partially bonded and behave as a single element placed in tension and anchored at the two ends of the beam. An analytical model that incorporates the complexities of unbounded tensile members combined with fire exposure is beyond the scope of the developed model and has not been further incorporated in the framework of the current research program.

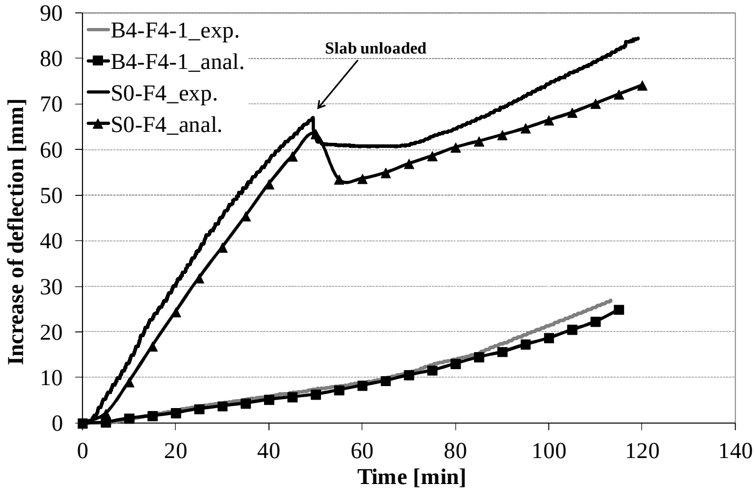

Figure 7.44 – Predicted vs experimental increase of deflection at midspan of beam B4-F4-1 and slab S0-F4 of fourth fire test

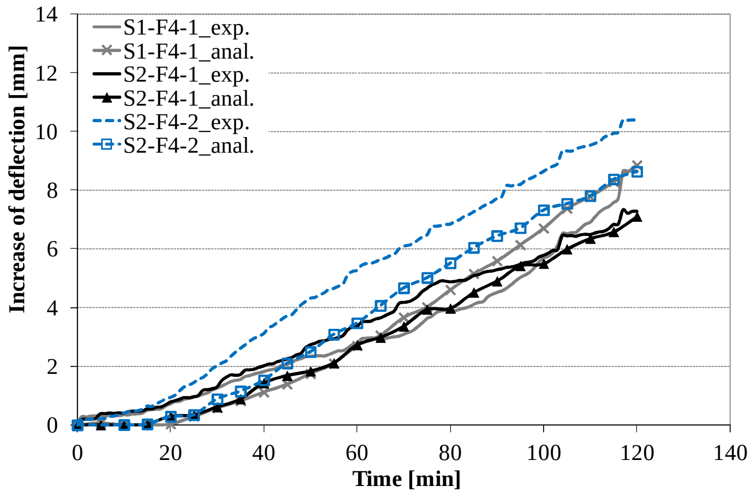

Figure 7.45 – Predicted vs experimental increase of deflection at midspan of slabs S1-F4-1, S2-F4-1 and S2-F4-2 of fourth fire test

For the control slab (S0-F4) the predicted increase of midspan deflection is slightly underestimating the experimental results (see Figure 7.44) for the entire duration of the fire test exposure. This deviation can be attributed to the discrepancy between the predicted and measured temperatures of the bottom steel reinforcement. The behavior of NSM FRP strengthened and insulated slabs are predicted with reasonably accuracy. The deviation between predicted and experimental increase of midspan deflection of slab S2-F4-2 can be related to uncertainty of temperature dependent mechanical properties of the basalt bars and at FRP/adhesive interface (given the lack of data the bond degradation at the FRP/adhesive interface of slabs S2-F4-1 and S2-F4-2 has been modeled based on data of GFRP bars similar as applied for slab S1-F4-1).

The variation of bond shear stress distribution over a distance from the NSM FRP bar/strip end up to the loading point (x=900 mm), for different fire exposure times, is shown in Figure 7.46 for slab S1-F4-1. The calculated variation of bond shear stresses distribution for all the specimens of the fourth fire test series is given in Appendix D.

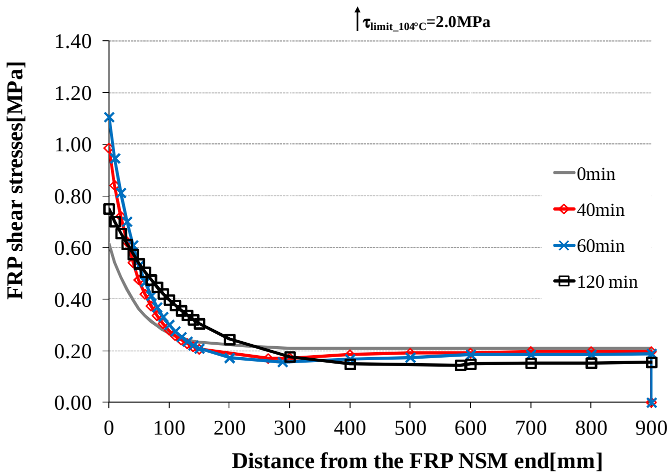

Figure 7.46 – Variation of shear stres distribution as a function of the fire exposure time of beam S1-F4-1

From Figure 7.46 is clear that, at low temperatures, the shear stresses are concentrated at the end of the FRP bar. Increasing the temperature at and beyond the glass transition temperature, results in an increase of the transfer length, l_t, with a consequent reduction of the peak shear stresses and a more uniform distribution of shear stresses over the FRP bond length. The shear stresses remain in the elastic region of the bond shear stress-slip relationship and the predicted shear stress distribution was below the reduced bond strength at FRP/adhesive interface for all the duration of fire exposure. The model closely follows the experimental observation for which no sign of debonding failure was observed during fire exposure, although the adhesive temperature was beyond its glass transition temperature ($T_{adhesive}$=1.6T_g).

A summary of the time of loss of composite action observed experimentally, $t_{deb,exp}$, the analytical assumed time of loss of composite action, $t_{deb,anal}$, the calculated bond shear stresses $\boldsymbol{\tau_f^*}$ (at time of loss of composite action at the NSM FRP/concrete interface) and the bond strength at the FRP/adhesive interface τ_{limit} (at the analytical assumed time of loss of composite action at NSM FRP/concrete interface) is reported in Table 7.3.

Table 7.4 – Results of structural analysis for specimen of the fourth fire test

Specimen	$t_{deb,exp}$ [min]	$t_{deb,anal}$ [min]	$\tau_{f.}^*$ [N/mm^2]	τ_{limit} [N/mm^2]
B4-F4-1	>120	>120	-	-
S1-F4-1	>120	>120	0.75	2.00
S2-F4-1	>120	>120	1.47	4.98
S2-F4-2	>120	>120	1.06	3.25

7.5 Conclusions

In this chapter an analytical model has been introduced to simulate the heat transfer within the NSM FRP strengthened and insulated beams and slabs using a finite element program (DIANA TNO 9.4.3) and to simulate their structural behavior under fire exposure using a two dimensional cross-section layered model. The model accounts for temperature dependent thermal and mechanical materials properties (concrete, steel, FRP and insulation materials). Comparing the results from the analytical model against the experimental results discussed in chapter 6, the numerical model can predict the temperatures within the NSM FRP strengthened and insulated beams and slabs and their structural behavior under fire exposure with reasonably accuracy (with a deviation in a range between ±5-10%).

Moreover the analytical model incorporates an elastic analysis to predict, given the applied load, the distribution of NSM FRP bond shear stresses along the FRP bond length with increasing temperature. By modeling the combined effect of temperature dependent adhesive strength and stiffness reduction with the shear stress distribution at the FRP/adhesive interface, the analysis tentatively predicts the time at which the loss of composite action occurs. This type of failure is assumed if, given the applied load, the predicted shear stresses exceed the bond shear strength at the FRP/adhesive interface.

Comparing the results from the analytical model against the experimental results of the first fire test series (in which the loss of composite action at the FRP/adhesive interface was considered based on a sudden increase of experimental time-deflection curves), the analytical model is able to predict with good accuracy the loss of composite action at the FRP/adhesive interface, although these predictions seem to be conservative for some of the tested beams.

Moreover comparing the results from the analytical model against the experimental results for all the fire test series, the analytical model has confirmed the experimental findings, for which no failure at the FRP/adhesive interface is observed even after the adhesive temperature exceeds moderately the glass transition temperature. This is valid since the bond shear stresses along the FRP bond length, given the applied load and the fire insulation protection, are below the temperature dependent adhesive bond strength. For instance it was analytically demonstrated that, for all the tested beams and slabs in which the FRP loss of composite action was not observed experimentally, the shear stresses remained well below the adhesive bond strength for all the duration of fire exposure. Moreover for beam B2-F3-2, it was analytically demonstrated that, keeping the temperature attained after 60 min of fire exposure constant, a further increase of load leads to an increase of bond shear stresses at the FRP/adhesive interface. Bond failure is obtained as soon as the predicted shear stresses exceed the adhesive bond strength.

7.6 References

1. ISO 834 (1999). "Fire Resistance Tests – Elements of Buildings Construction – Part I – General Requirements". *International Organization for Standardization.*

2. Manie, J., Kikstra, W.P. (2010). "DIANA finite element analysis". *User's manual release 9.4.3*, Element library, TNO DIANA, Delft.

3. Blontrock H. (2003). "Analyse en modellering van de brandweerstand van betonelementen uitwendig versterkt met opgelijmde composietlaminaten (in Dutch)". *Ph-D Thesis*, Faculty of Engineering, Department of Structural Engineering, Ghent University, Belgium, 412 pp.

4. Kaiser H. (1989). "Bewehren von Stahlbeton mit kohlenstoffaserverstarkten Epoxidharzen". (in German), *Ph-D thesis*, Thechnical University of Zurich, Switzerland, 224 pp.

5. Taljsten B. (1994). “Plate Bonding –Strengthening of Existing Concrete Structures with Epoxy Bonded Plates of Steel or Fibre Reinforced Plastics”. *Ph-D thesis*, Lulea University of Technology, Sweden, 281 pp.

6. Faella C., Martinelli E., Nigro E. (2005). “Interface behaviour in FRP plates bonded to concrete: experimental tests and theoretical analyses”. *In Proc. of 2003 ECI conference on advanced materials for construction of bridges, buildings, and other structures III*, vol. P5. Davos, Switzerland.

Chapter 8

CONCLUSIONS AND FUTURE RESEARCH

8.1 General

In recent years, strengthening technologies for reinforced concrete (RC) structures using fiber reinforced polymer (FRP) composites have been gaining widespread interest and growing acceptance in the civil engineering industry. Given the importance of repair and strengthening of concrete structures, the commercial and research interest in this strengthening technique is considerable. During the last decade one of the developments, to strengthen existing concrete structures, is the use of FRP bars/strips as near surface mounted (NSM) reinforcement, which consists in grooving the surface of the member and embedding the FRP bars/strips into the grooves with a high strength adhesive.

Despite the increasing success in applying the FRP strengthening system in reinforced concrete structures, the weak performance of this strengthening technique under elevated temperatures, as might be experienced in a fire, has hindered their application in buildings and infrastructures. A temperature increase is affecting the behaviour of FRP in different ways, as a temperature increase has different effects, like a change in the mechanical properties of the FRPs and reduction of the bond strength at the FRP/adhesive/concrete interface. Both effects are primarily related to the deterioration of the polymer matrix (used as primer, adhesive and matrix) for increasing temperature at or beyond its glass transition temperature.

A limited number of research projects around the world have investigated the influence of elevated temperature on the bond between externally bonded FRP reinforcement (FRP EBR) and concrete. Furthermore, existing researches suggest that concrete structures strengthened with FRPs can achieve a satisfactory fire endurance rating, though contribution of the FRP is generally assumed as lost during fire exposure, by providing an adequate fire insulation system in order to keep the concrete and internal reinforcing steel temperatures below critical temperatures, which are regulated by fire standards.

This PhD thesis has contributed to obtain a better insight in the bond behaviour of NSM FRP strengthening systems at elevated temperatures and fire endurance of NSM strengthened and insulated reinforced concrete members under fire exposure. Moreover, a valuable contribution to the knowledge on the degree of FRP bond loss or/and adhesive bond degradation at temperatures higher than the adhesive glass transition temperature is provided.

8.2 Bond behaviour under elevated service temperature

The bond behaviour at the FRP/adhesive and the adhesive/concrete interface for the NSM FRP strengthening technique was investigated with double bond shear tests. The tests were carried out within the temperature range between 20°C till 100°C. The temperature level was chosen in relation to the glass transition temperature (T_g) of the utilized epoxy resin which equals $T_g \approx 65$°C. The glass transition temperature of the epoxy resin was experimentally determined on the basis of DSC (differential scanning calorimetry), as specified in chapter 3. The tests conducted at elevated temperatures were compared with those at room temperature.

From the conducted experimental work, it follows that increasing the temperature up to 50°C resulted in an increase of failure load and bond shear stresses, while further increase of temperature resulted in a decrease of failure load and change of failure mode. For temperatures below the glass transition temperature the failure mode was characterized by debonding at the concrete/resin interface with varying degrees of concrete damage, as a function of the FRP bar surface configuration. Increasing the temperature at/or beyond the adhesive T_g resulted in a debonding of the FRP NSM bars at the adhesive/bar interface (pull-out of the bar). However the decrease of the failure load at an elevated temperature equal to T_g was equal to approximately 10% and 18% for specimens strengthened with CFRP and GFRP bars respectively and no complete degradation of bond strength was observed for temperatures up to $1.5T_g$ for all the tested specimen. It is, moreover, observed that the transfer length increased by increasing the temperature, with a consequent more linear distribution of strains over the FRP bond length. In particular for specimens tested at a temperature higher than T_g the transfer length increased with a factor 2 to 3 with respect to the transfer length at 20°C.

Based on the analysis of the bond shear stresses it can be concluded that the increasing failure load at 50°C is mainly due to thermal shear stresses, induced by the difference of coefficient of thermal expansion between the FRP and the concrete. In accordance with previous studies, it was observed that the shear thermal stresses mainly develop at the ends of the FRP bond length, where the FRP force is transferred to the concrete (Figure 4.14 Chapter 4) and that the direction of these thermal shear stresses is opposite to the direction of the shear stress induced by the loading (Figure 4.15 Chapter 4). Therefore, shear stresses due to the loading will first have to compensate the thermal shear stresses at the loaded end, resulting in a lower shear stress peak with increasing temperature which can explain the increasing failure load with increasing temperature up to 50°C. Nevertheless, increasing the temperature to and/or beyond the glass transition temperature the softening and strength reduction of the adhesive are governing over a possible positive effect of thermal stresses induced by the heating of the specimens. Indeed increasing the temperature resulted in a more uniform distribution of stresses but in significantly lower failure load.

Finally based on the tests, the local bond-stress slip behaviour could be characterized experimentally. At elevated temperature beyond T_g the bond stress-slip behaviour becomes elasto-platic. Strength and stiffness reduction functions of the adhesive at increasing temperature have been derived.

8.3 Structural behaviour of RC members strengthened in flexure with NSM FRP

Before studying the behaviour of NSM FRP strengthened elements under fire exposure, their behaviour at ambient temperature has been investigated. The influence of the type of FRP bars (carbon and glass fibers), the FRP's shape (rods versus strips), the surface configuration (sand coated, ribbed and spirally wound bars) as well as the type of adhesive used to embed the FRPs into the grooves (epoxy resin versus grout adhesive) were investigated. This study forms the basis for studying the behaviour at and after fire exposure.

From the conducted experimental work, it follows that strengthening of existing concrete members by means of near surface mounted FRP reinforcement is a feasible and efficient technique, which allows the enhancement of the flexural capacity of RC beams and slabs. Results have shown that beams in which the FRP was embedded into the grooves with epoxy adhesive experienced a higher strength increase values with respect to beam in which a grout adhesive was used. Among the beams with epoxy resin as adhesive, the different trend of failure suggests an influence of the FRP surface configuration on the failure mode. Debonding of the NSM FRP rods/strips occurred at tensile strains ranging between 69% - 73% of the ultimate tensile strain of the FRP bars/strips, confirming the higher efficiency of the NSM strengthening technique compared to FRP EBR strengthening systems. With similar axial stiffness the latter usually has tensile strains which ranges between 35% - 45%. The ductility of the strengthened beams decreased between 25% - 68%.

Due to the considerable increase of failure load both NSM FRP slabs failed by concrete crushing, although debonding of the FRP bars was observed as well. Similar as for the strengthened beams, an elevated efficiency of utilization of the NSM FRP reinforcing bars is observed with strain values equal to approximately 72%.

From the analytical verifications, it appears that the structural behaviour of the strengthened concrete members can be predicted in an accurate way. For flexural strengthening of RC beams, classical calculation methods still apply as long as full composite action between the FRP and the concrete may be assumed. Considering that there is still limited understanding of the mechanism of loss of this composite action (debonding) for members strengthened with FRP NSM and that this mechanism can be influenced by several parameters (among which the internal steel reinforcement ratio, the NSM FRP reinforcement ratio, the shape and surface configuration of the NSM FRP reinforcement and the tensile strength of both epoxy and concrete), the debonding of the NSM FRP strengthening system was modeled by limiting the NSM FRP ultimate strain. This method gives good prediction except for the beam in which the FRP bars were embedded with grout adhesive, for which the adopted method was not able to accurately predict the failure mechanism of the beam.

8.4 Fire behaviour of NSM FRP strengthened and insulated members under fire exposure

The fire behaviour of NSM FRP strengthened and insulated members (beams and sabs) has been experimentally studied by means of 4 full-scale fire test series. These full-scale fire tests involved the design and fabrication of 20 NSM FRP strengthened and insulated beams and 4 NSM FRP strengthened and insulated slabs. All the specimens have been pre-loaded to the service load and subsequently exposed to a standard fire, while the load was kept constant during fire exposure. The fire endurance of the NSM FRP strengthened and insulated beams and slabs has been investigated varying several parameters with respect to insulation materials type and thickness, insulation configuration and type of adhesive for embedding the FRP bars/strips into the grooves. The effect of bond degradation at temperatures higher than the adhesive glass transition temperature has been also investigated (in order to do so a time of 1 h of fire exposure was choose to avoid loss of composite action due to an excessive heating of the adhesive). Furthermore the fire resistance effectiveness of the NSM FRP strengthening system after fire exposure has been investigated by structural testing up to failure.

Based on the results of fire endurance tests presented in Chapter 6, it can be concluded that NSM FRPs can be used in buildings to strengthen reinforced concrete beams and slabs if supplemental fire protection system is provided over the FRP strengthening system. By providing appropriate fire insulation, the reinforced concrete beams and slabs that have been strengthened in flexure with NSM FRP can endure the elevated temperatures of the standard fire under the acting service loads for 2h even after the adhesive temperature exceeds extensively the glass transition temperature and loss of the FPR reinforcement can be assumed. No obvious dysfunction of the FRP in terms of strength compatibilities between the FRP and the RC members during and after fire was observed if adequate fire insulation system was provided. The insulation systems evaluated in this research project appear to have effectively protected the NSM FRP strengthened beams from heat penetration during the fire exposure, although FRP loss of composite action after 20-110 min, depending on the applied fire insulation scheme and its thermal performance, was observed for some of the beams. In the latter case experiments have demonstrated that as the temperature of the concrete (at compression side) and the longitudinal bottom steel reinforcement were below critical temperatures, even in case of accidental drop out of FRP, the beams will not collapse immediately under the acting service load.

Based on residual strength tests , it was observed that if the fire insulation system is able to maintain the adhesive temperature at relatively low temperature ($T_{adhesive}$=100 °C to 130 °C and $T_{adhesive}$=167 °C for epoxy resin and grout mortar respectively) the FRP is able to retain bond strength to the concrete and the beams and slabs are still able to retain considerably part (up to 84% and up to 92% for 2h and 1h of fire exposure respectively) of the flexural capacity of the FRP strengthened beam at room condition.

Finally a numerical model, for simulating the behaviour of NSM FRP strengthened and insulated members under fire exposure, was developed. A heat transfer model and structural response model are applied using a finite element program (Diana TNO 9.4.3) and a two dimensional cross-section layered model (excel visual basic) respectively, to investigate the thermal and structural behavior of NSM FRP strengthened and insulated beams and slabs under fire exposure. The model accounts for temperature dependent thermal and mechanical properties of the constituent materials (concrete, steel FRP and insulation system) as well as for the effect of bond degradation at the FRP/adhesive interface with increasing temperature. For instance based on experimental results of Chapter 4, the temperature dependent reduction of both the adhesive stiffness and the bond strength at the FRP/adhesive interface were introduced into the model. By combining the above described temperature effects with the acting load, the shear stress distribution along the FRP bond length were calculated.

The heat transfer model was able to make reasonable predictions of the temperature within both un-strengthened and un-insulated and NSM FRP strengthened and insulated beams and slabs under fire exposure.

Based on the structural analytical results, it was observed that a temperature increase results in an increase of bond shear stress at the NSM FRP end, but, with further increase of temperature, these stresses are partially redistributed due to the reduced adhesive stiffness. For instance, temperatures at and beyond the glass transition temperature resulted in an increase of the transfer length with a consequent reduction of the peak shear stresses as well as a more uniform distribution of these shear stresses along the FRP bond length. On the other hand a temperature increase is accompanied by a significant reduction of the bond strength at the FRP/adhesive interface. The overall capacity of the FRP strengthened members depends on which effect is the most governing. For instance the structural analysis confirm the experimental results, demonstrating that if stresses at the FRP/adhesive interface are low (as is generally the case for service load levels) during fire exposure, no debonding is experienced at the FRP/adhesive interface even if the glass transition temperature is moderately exceeded (up to $1.6T_g$). This is valid since these bond shear stresses, given the applied load and the fire insulation system, are below the temperature dependent adhesive bond strength.

Therefore the effectiveness of the FRP strengthening system under fire exposure should be defined in terms of time that the strengthening system is still active during fire exposure, rather than the time it takes for the temperature to exceed the glass transition temperature of the adhesive.

8.5 Future research

The research work performed within this thesis, has contributed to obtain a better understanding regarding the behaviour of NSM FRP strengthening systems at elevated temperatures and under fire exposure. Clearly not all aspects were covered and further research in this field is needed.

Concerning the bond behaviour at elevated temperature further research should focus on the following aspects:

- Repeatability of the obtained tests results should be verified by performing additional tests per test condition (in the current research program only two specimens for test condition have been tested).
- Additional tests on different types of FRP reinforcement, surface configuration and type of embedding adhesive (grout adhesive and/or epoxies with elevated glass transition temperature) are required in order to have a better understanding on the effect of temperature increase on the bond behaviour at the FRP/adhesive interface.
- Other test set-ups that allow for a longer embedded length should be considered for the characterization of the bond behaviour at elevated temperature in order to achieve a better understanding on the increase of

transfer length, strain and bond shear stress distribution with increasing temperature.

Concerning the fire behaviour further research should focus on the following aspects:

- Additional full scale fire tests on NSM FRP strengthening systems embedded with grout mortar or/and different type of epoxy resins with an higher glass transition temperature with respect to that used in this research program. Moreover it should be interesting to investigate concrete members that are strengthened with different types of FRPs, although similar results can be expected.
- The type of fire exposure. All the tests in this research program have been carried out for standard fire tests. In Chapter 3 it was shown that a 'real' fire differs in several aspects from the standard fires. The most important difference being the presence of a cooling phase in a real fire. The use of real fire that accounts for fuel load and ventilation conditions for the compartment can, of course, have a high influence on the fire resistance of a NSM FRP strengthened member and on the design of the fire insulation system.
- Loading configuration. It would be interesting to investigate also an uniformly loaded configuration, as this configuration occurs more frequently in practice.
- Structural analysis under fire exposure. Despite the obtained model is giving good results, several simplifications have been introduced in this model. In order to refine the model, among the possible improvements, it would be interesting to introduce the elasto-plastic behaviour of the adhesive with increasing temperature as well as the adhesive creep effect as they will affect the stress distributions in the anchorage zone of the NSM FRP bar/strip, and hence the stress concentration at the NSM FRP bar end. Although the creep effect is generally a positive effect for full scale beams and slabs, as it reduces the shear stress concentration in the end of the anchorage zone, further research is recommended.
- Develop design values of critical temperatures, e.g. up to $1.5T_g$, in relation to the load level during fire and the required residual strength level.

To conclude the NSM FRPs strengthening systems can be used in buildings with fire endurance requirements to strengthen reinforced concrete beams and slabs, if an appropriate fire protection system is provided over the FRP strengthening system. If stresses at the FRP/adhesive interface are low (as is generally the case for service load levels) during fire exposure, no debonding is experienced at the FRP/adhesive interface even if the glass transition temperature is moderately exceeded. This is valid since these stresses, given the applied load and the fire insulation system, are below the temperature dependent adhesive bond strength. This research line is to be continued in the future to be able to generalize the obtained results.

APPENDIX A
DOUBLE BOND SHEAR TESTS AT ELEVATED TEMPERATURES

A.1 Thermal shear stresses model

Based on a kinematic model developed by Di Tommaso et al. (2001) and considering the reduction of the adhesive Young's modulus in accordance to Klamer (2009), the shear thermal stresses of the NSM FRP strengthening bars can be calculated as follows. Considering the FRP NSM rebar as a linear element restrained along its length by springs with an elastic constant k_G (see Figure A.1), the equilibrium of an infinitesimal length dx of an FRP reinforcement bar (see Figure A.2) can be expressed as:

$$\frac{dN}{u_f dx} = \tau(x) = k_G u(x) \tag{A.1}$$

Where N is the normal force in the FRP bar, u_f is the perimeter of the FRP bar, $\tau(x)$ is the shear stress, and u(x) is the elastic bond slip.

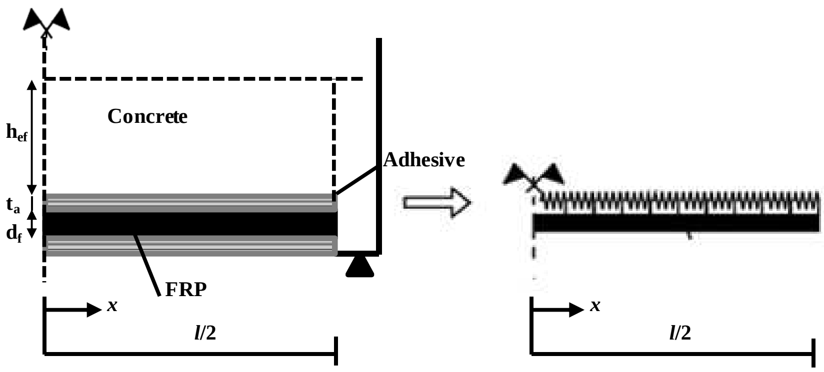

Figure A.1 – Theoretical beam model (Di Tommaso et al. 2001)

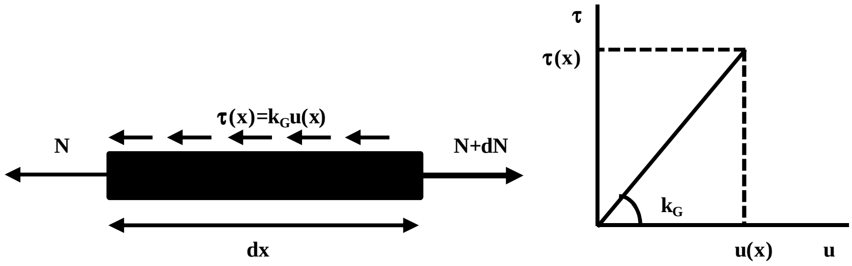

Figure A.2 – Equilibrium of an infinitesimal element and idealized bond slip law

The strain in the FRP bar, ε_f, can be divided into two parts, the strain due to the expansion of the concrete due to temperature variation, $\varepsilon_{\Delta T}=\alpha\Delta T$, and the strain in the FRP itself, due to the (corresponding) FRP force (strain induced by the internal restrained effect), $\varepsilon_{f,ext}$:

$$\varepsilon_f = \frac{du}{dx} = \varepsilon_{\Delta T} + \varepsilon_{f,ext} \qquad \text{(A.2)}$$

where:

- $\varepsilon_{\Delta T}=\alpha_c\Delta T$
- α_c is the coefficient of thermal expansion of concrete
- ΔT is the variation in temperature

The FRP bar force, N, can be expressed as:

$$N = \sigma_f \cdot A_f = E_f \cdot \varepsilon_{f,ext} \cdot A_f = E_f \cdot \frac{\pi d_f^2}{4}\left(\frac{du}{dx} - \varepsilon_{\Delta T}\right) \qquad \text{(A.3)}$$

where:

- E_f is the Young modulus of the FRP bar
- d_f is the diameter of the FRP bar

Differentiating equation A.3 with respect to dx and rewriting equation A1 gives two expressions for dN/dx:

$$\frac{dN}{dx} = E_f \frac{\pi d_f^2}{4} \frac{d^2u(x)}{dx^2} \qquad (A.4)$$

$$\frac{dN}{dx} = k_G \cdot u(x) \cdot \pi d \qquad (A.5)$$

Substituting equation A.4 into equation A.5 gives:

$$\frac{d^2u(x)}{dx^2} - \omega^2 \cdot u(x) = 0 \qquad (A.6)$$

where:

- $\omega^2 = \frac{4k_G}{E_f d_f}$
- $\frac{1}{k_G} = \frac{1}{k_{Gc}} + \frac{1}{k_{Ga}}$
- $k_{Gc} = \frac{E_c(T)}{2 \cdot (1+\nu_c) \cdot h_{c,ef}}$ is the stiffness of the concrete
- $k_{Ga} = \frac{E_a(T)}{2 \cdot (1+\nu_a) \cdot t_a}$ is the stiffness of the adhesive
- $E_c(T)$ is the young modulus of the concrete at temperature T
- $h_{c,ef}$ is the effective height equal to 50 mm or two times the maximum aggregate size [Di Tommaso et al. 2011]
- $E_a(T)$ is the Young modulus of the adhesive at temperature T
- t_a is the thickness of the adhesive layer
- d_f is the diameter of the FRP bar
- t_f is the thickness of the FRP strip
- ν_c and ν_a are the Poisson ratio of the concrete and the adhesive assumed equal to ν_c=0.2 and ν_a= 0.3 respectively
- *l* is the bonded length
- x is the distance from the middle of the bonded length [$-l/2 < x < l/2$]

The general solution of equation A.6 is:

$$u(x) = C\cosh(\omega x) + D\sinh(\omega x) \qquad (A.7)$$

C and D can be determined by using the boundary conditions, assuming that the displacement at midspan is zero and the FRP force at the end of the bar is zero:

$$x = 0 \Rightarrow u(0) = 0 \Rightarrow C = 0 \tag{A.8}$$

$$x = \frac{l}{2} \Rightarrow N(\frac{l}{2}) = 0 \Rightarrow \varepsilon_{f,ext} = 0 \Rightarrow \frac{du(l/2)}{dx} = \varepsilon_{\Delta T} \tag{A.9}$$

D can be determined by substituting equation A.9 in equation A.7

$$u(\frac{l}{2}) = D\sinh(\omega \cdot \frac{l}{2}) \Rightarrow \frac{du(l/2)}{dx} = \omega \cdot D\cosh(\omega \cdot \frac{l}{2}) = \varepsilon_{\Delta T} \Rightarrow D = \frac{\varepsilon_{\Delta T}}{\omega \cdot \cosh(\omega \cdot \frac{l}{2})} \tag{A.10}$$

u(x), σ_f(x) and τ(x) can then be expressed as:

$$u(x) = \frac{\varepsilon_{\Delta T}}{\omega \cdot \cosh(\omega \cdot \frac{l}{2})} \sinh(\omega \cdot x) \tag{A.11}$$

$$\sigma_f(x) = \frac{N(x)}{A_f} = E_f(\frac{du}{dx} - \varepsilon_{\Delta T}) = E_f[\frac{\varepsilon_{\Delta T}}{\cosh(\omega \frac{l}{2})} \cdot \cosh(\omega \cdot x) - \varepsilon_{\Delta T}] \tag{A.12}$$

$$\tau(x) = \frac{dN(x)}{dxu_f} = E_f \frac{\pi d^2}{4} \frac{1}{\pi d} \frac{d^2u(x)}{dx^2} = E_f \frac{d}{4} \omega \frac{\varepsilon_{\Delta T}}{\cosh(\omega \cdot \frac{l}{2})} \sinh(\omega \cdot x) \tag{A.13}$$

Figure A.3 – A.5 show the shear stress at the FRP/concrete interface, the FRP normal stresses and the slip at the FRP/concrete interface after an increase in temperature from 20 °C to 50 °C. A positive value of σ_f in equation A.12 and Figure A.4 corresponds to tension.

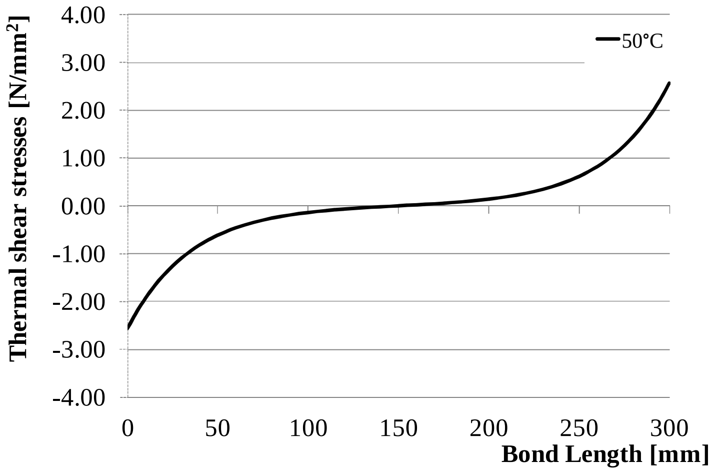

Figure A.3 - Thermal shear stresses specimen C_SC at 50 °C and at 0kN

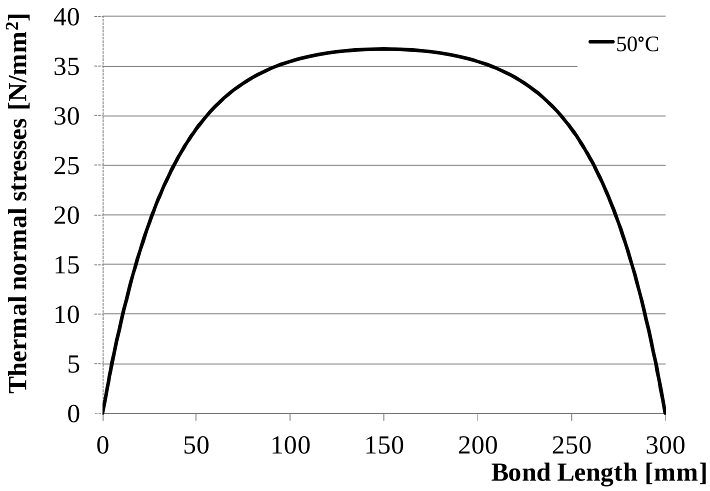

Figure A.4 - Thermal normal stresses specimen C_SC at 50 °C and at 0kN

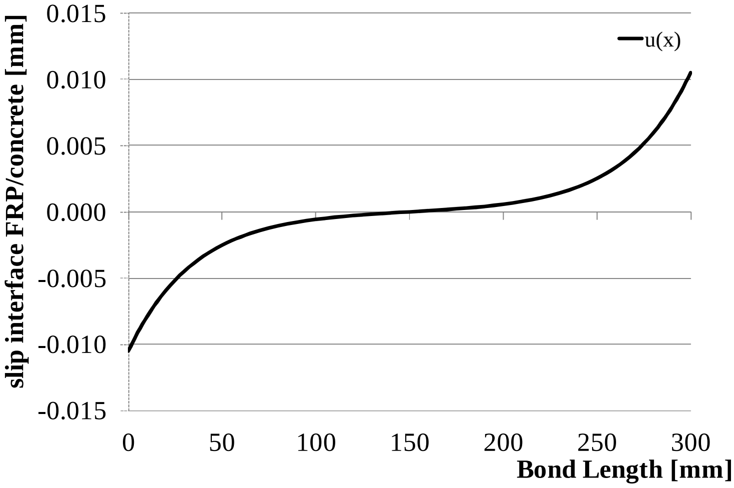

Figure A.5 – Slip interface FRP/concrete specimen C_SC at 50 °C and at 0kN

A.2 Load – LVDTs slip curves

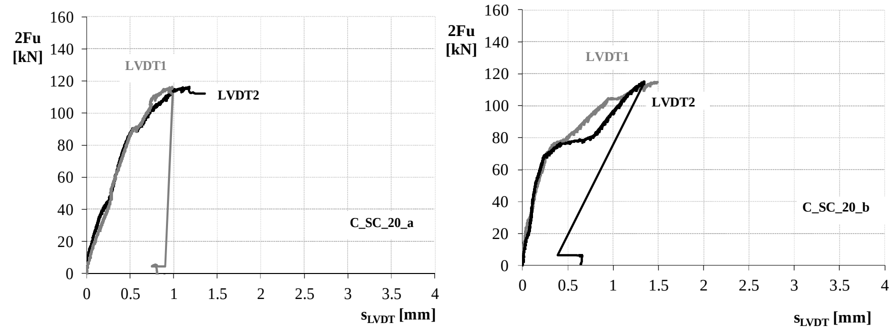

Figure A.6 – Load-LVDTs slip curves specimens C_SC_20

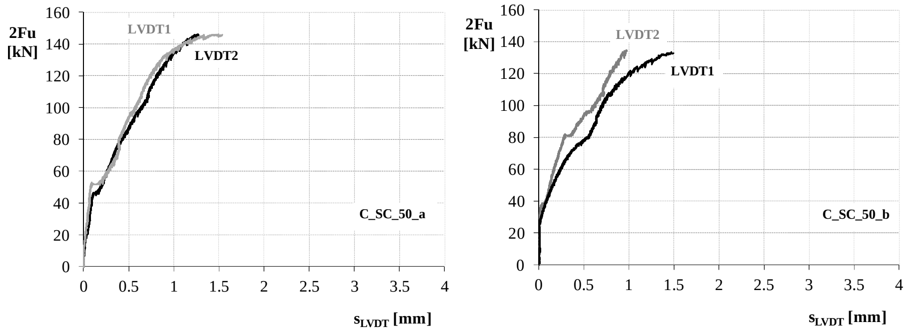

Figure A.7 – Load-LVDTs slip curves specimens C_SC_50

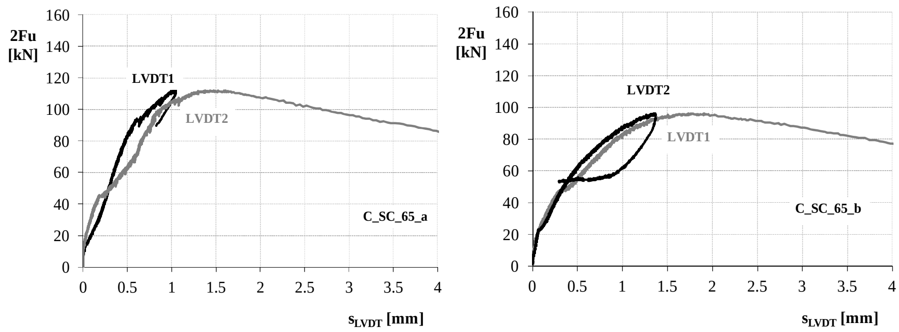

Figure A.8 – Load-LVDTs slip curves specimens C_SC_65

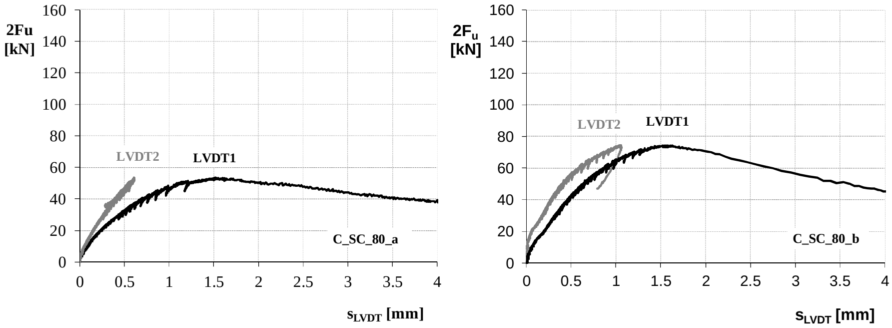

Figure A.9 – Load-LVDTs slip curves specimens C_SC_80

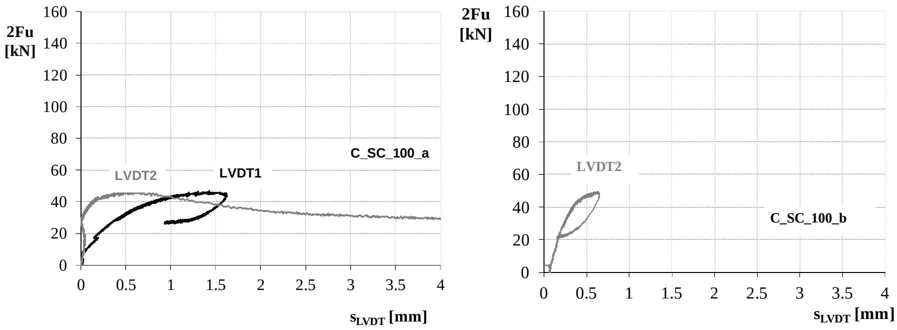

Figure A.10 – Load-LVDTs slip curves specimens C_SC_100

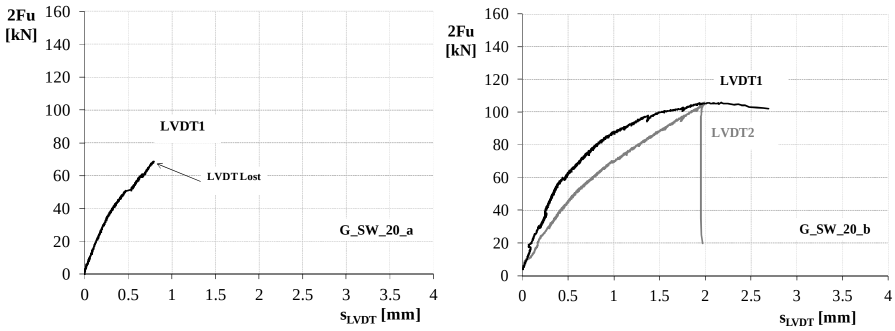

Figure A.11 – Load-LVDTs slip curves specimens G_SW_20

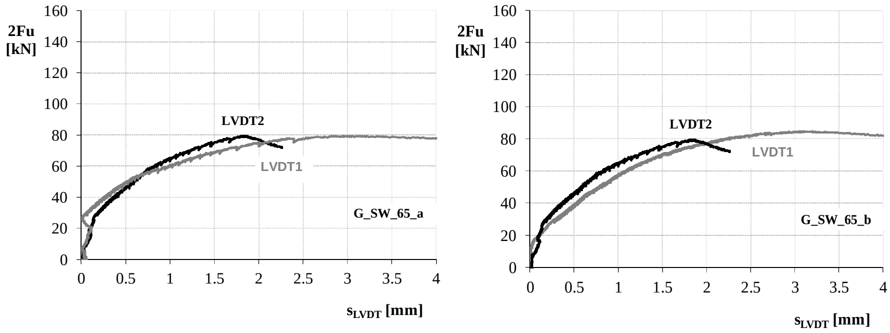

Figure A.12 – Load-LVDTs slip curves specimens G_SW_65

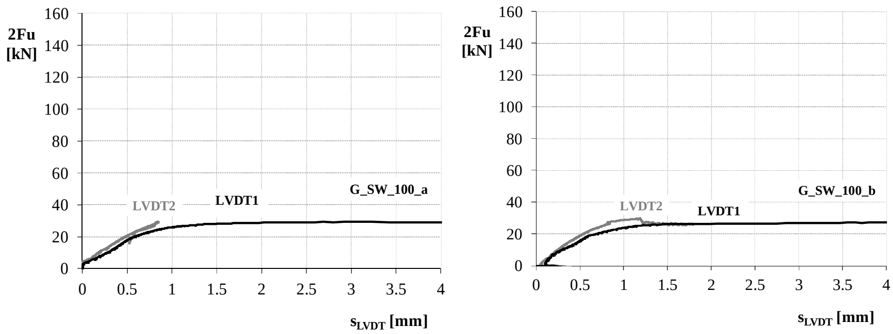

Figure A.13 – Load-LVDTs slip curves specimens G_SW_100

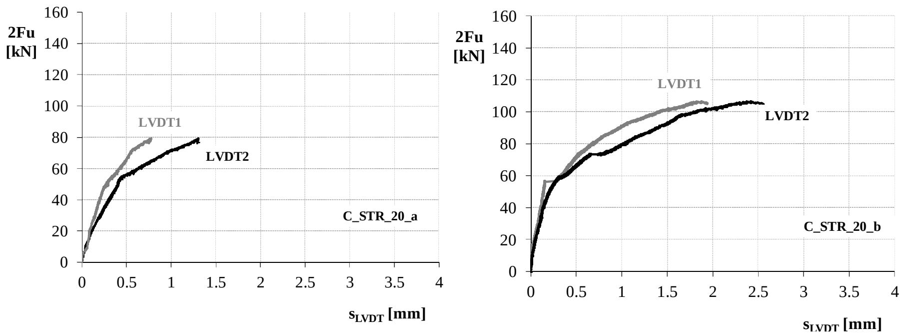

Figure A.14 – Load-LVDTs slip curves specimens C_STR_20

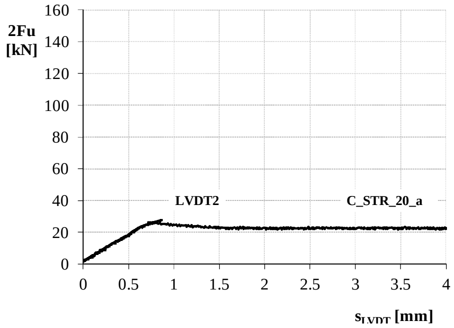

Figure A.15 – Load-LVDTs slip curves specimens C_STR_100

A.3 Mechanical strains along the bonded length

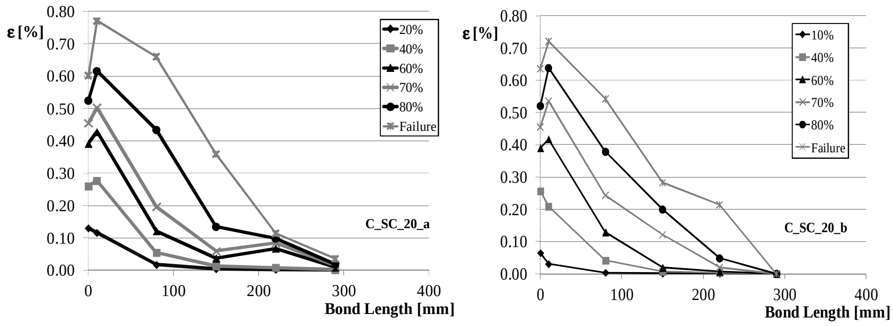

Figure A.16 – Strain distribution specimens C_SC_20

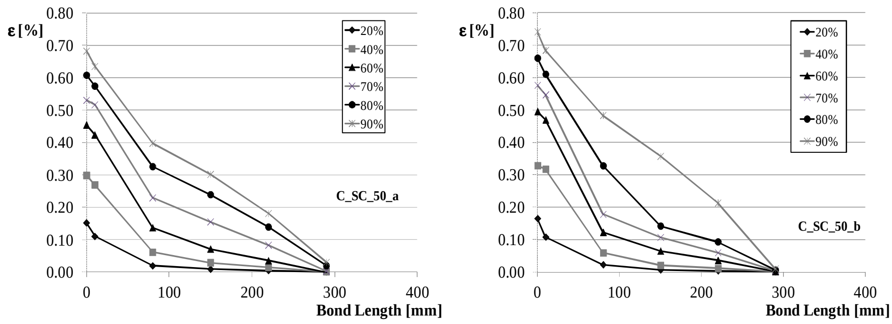

Figure A.17 – Strain distribution specimens C_SC_50

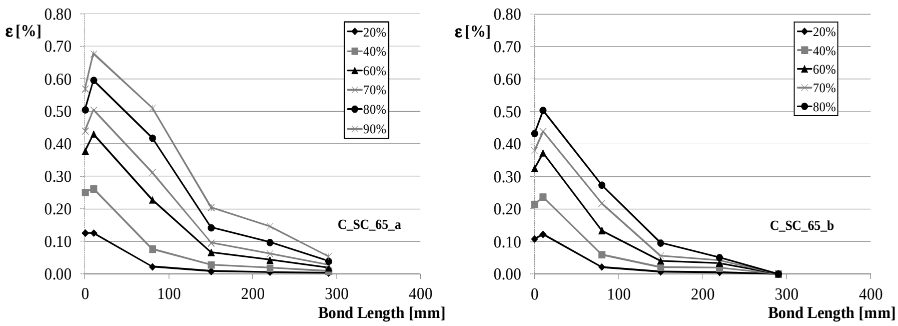

Figure A.18 – Strain distribution specimens C_SC_65

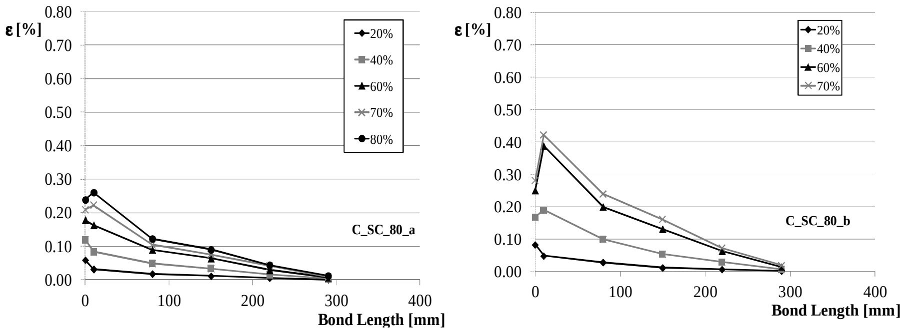

Figure A.19– Strain distribution specimens C_SC_80

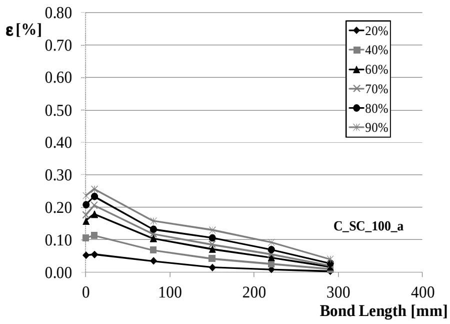

Figure A.20– Strain distribution specimen C_SC_100

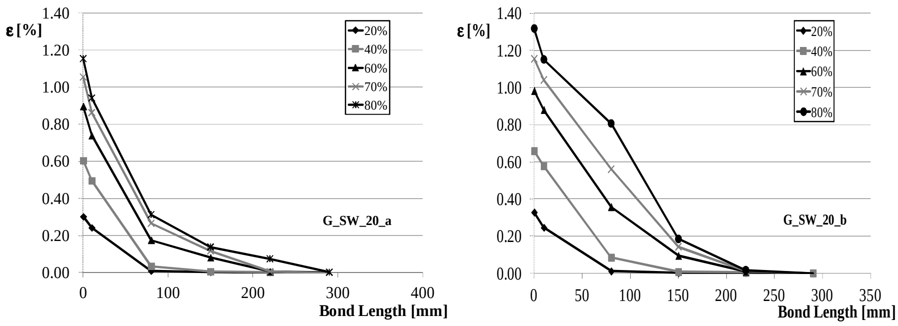

Figure A.21– Strain distribution specimens G_SW_20

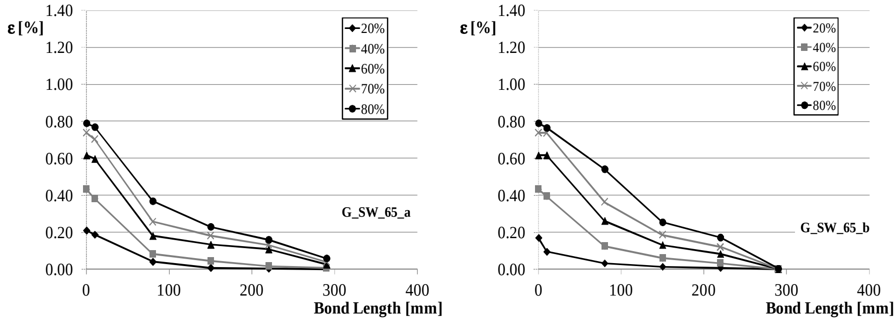

Figure A.22 – Strain distribution specimens G_SW_65

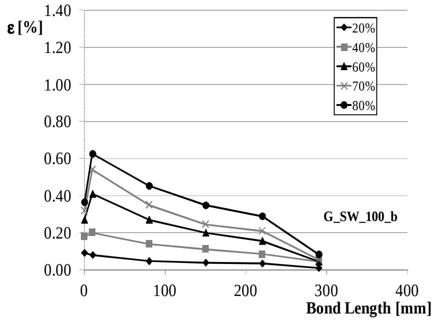

Figure A.23– Strain distribution specimen G_SW_100

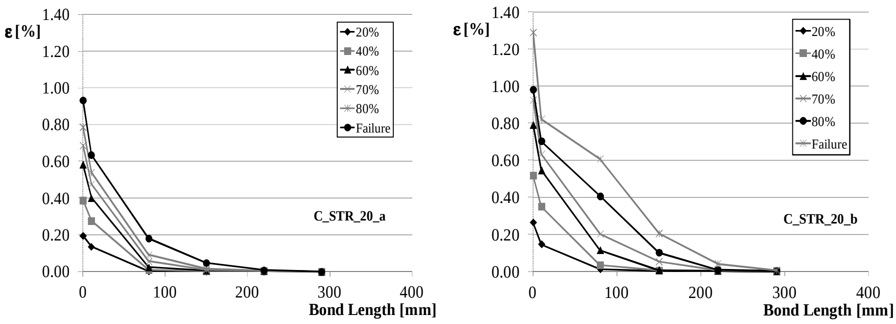

Figure A.24– Strain distribution specimens C_STR_20

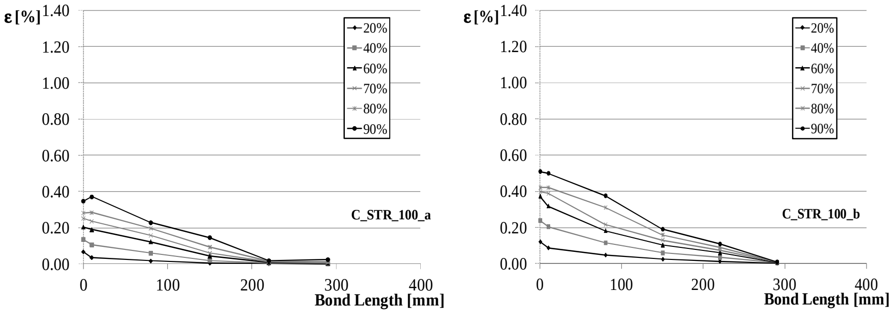

Figure A.25– Strain distribution specimens C_STR_100

A.4 Experimental results specimens strengthened with GFRP ribbed bars

In Figure A.26 the mechanical strain distribution of specimens strengthened with glass bars with ribbed surface configuration (G_RB) tested at different service temperatures are reported.

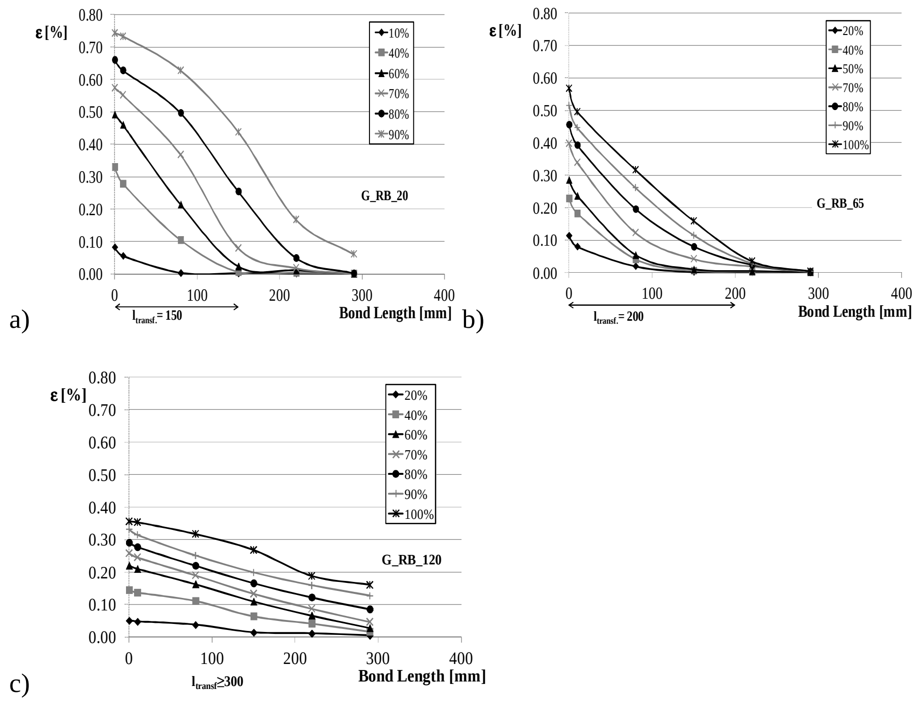

Figure A.26 – Strain distribution specimens a) G_RB_20, b) G_RB_65 and c) G_RB_120

In Figure A.27 the bond stress-slip relationships at different temperature are given. In these curves the bond shear stresses and the slip are evaluated considering the distance between the first and the second strain gauges as dx; therefore the shear bond stresses as well as the slip were evaluated at a distance equal to x= 45 mm from the loaded end.

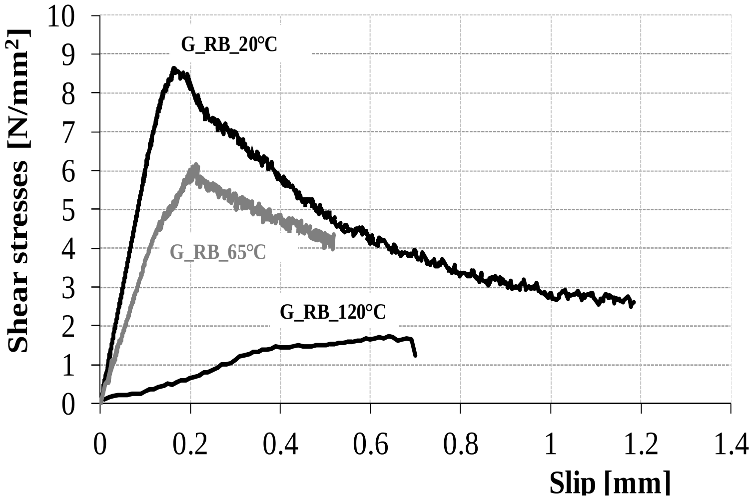

Figure A.27 – Bond stress-slip curves specimen G_RB at different temperatures

APPENDIX B
STRAIN VARIATION AS FUNCTION OF THE LOAD OF MEMBERS TESTED AT AMBIENT TEMPERATURE

B.1 Strain along the FRP NSM strengthening system

In the following the strain distribution along the length of the FRP is shown for the tested elements described in Chapter 5. The experimental strains are those recorded by the strain gauges up to failure. Considering that only three strain gauges are used to record the FRP strains, it was assumed that the FRP strains were constant in the pure moment region. In this way the strain distribution is given along half of the specimen length. Note that the measuring points (symbols in figures) are connected with straight lines, though this is not necessary an exact representation of the distribution between the measured data.

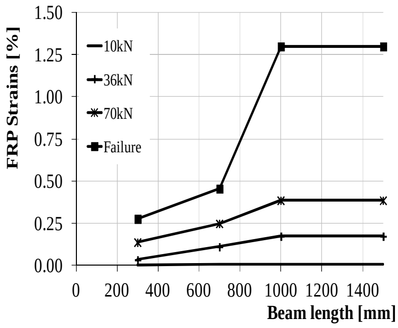

a)

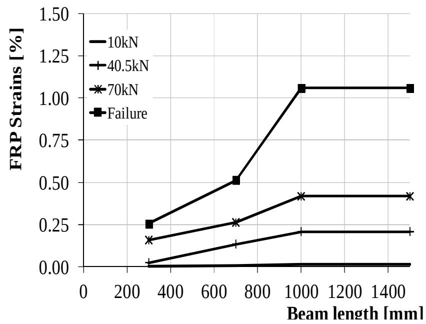

b)

Figure B.1– Strain distribution beams (a) B1 and (b) B2

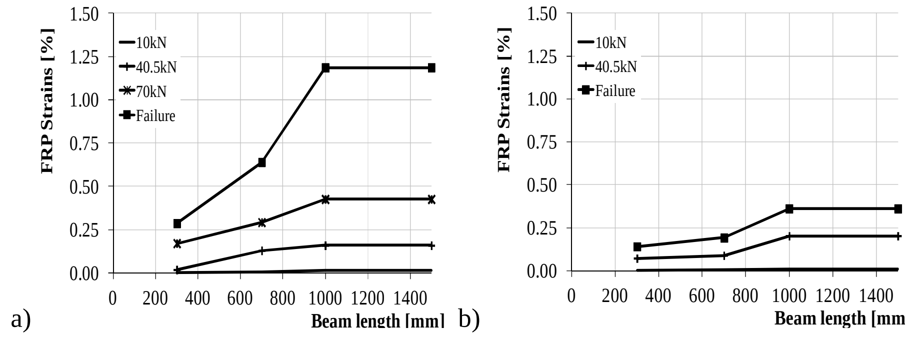

Figure B.2– Strain distribution beams (a) B3 and (b) B4

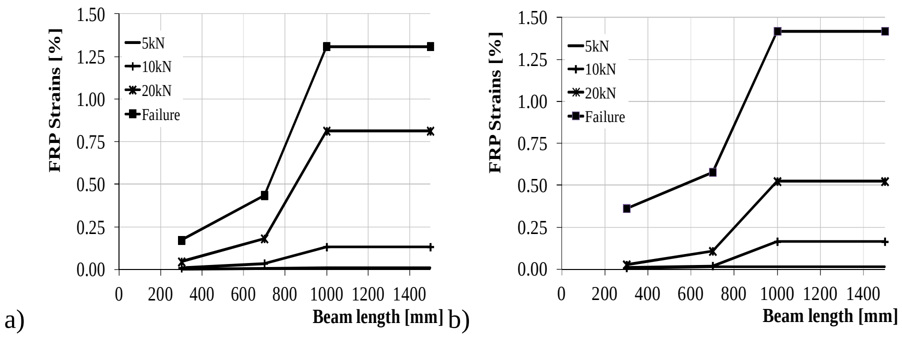

Figure B.3– Strain distribution slabs (a) S1 and (b) S2

B.2 Load –strains curves

In the following the measured strains are given as a function of the applied load (Q represents one point load not the total load), and compared with analytical strain prediction (see Chapter 5).

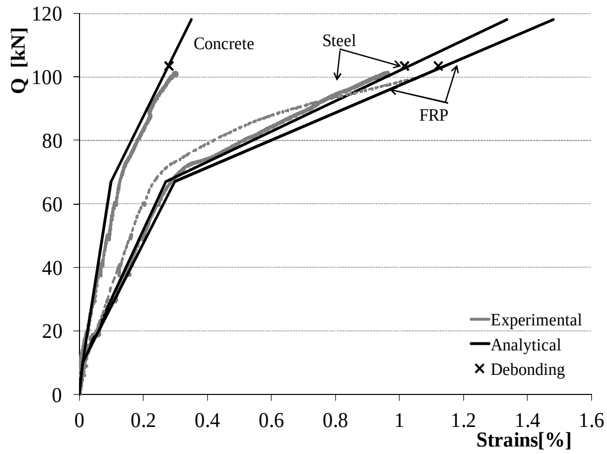

Figure B.4 – Load- strains curves concrete, steel and FRP beam B2

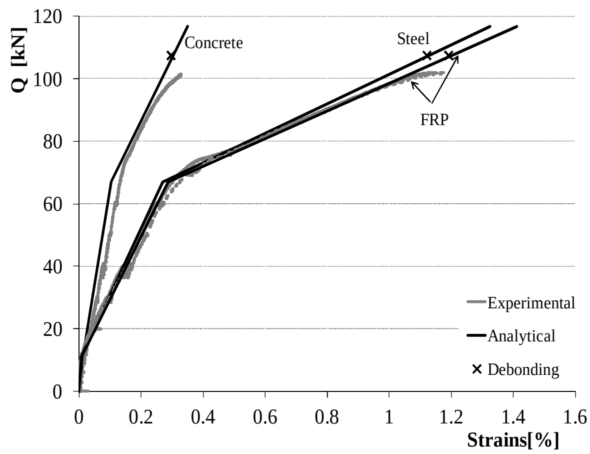

Figure B.5 – Load- strains curves concrete, steel and FRP beam B3

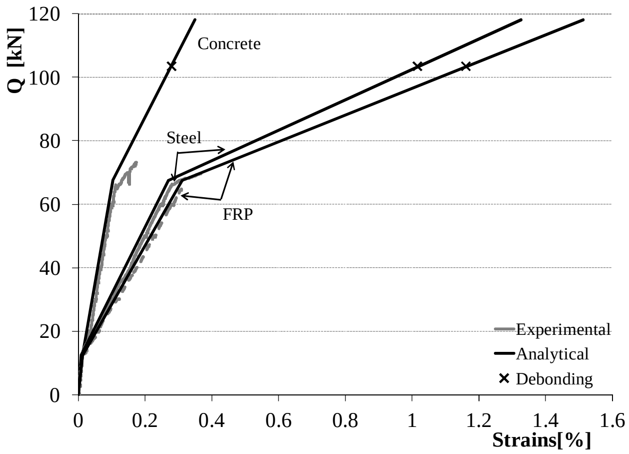

Figure B.6 – Load- strains curves concrete, steel and FRP beam B4

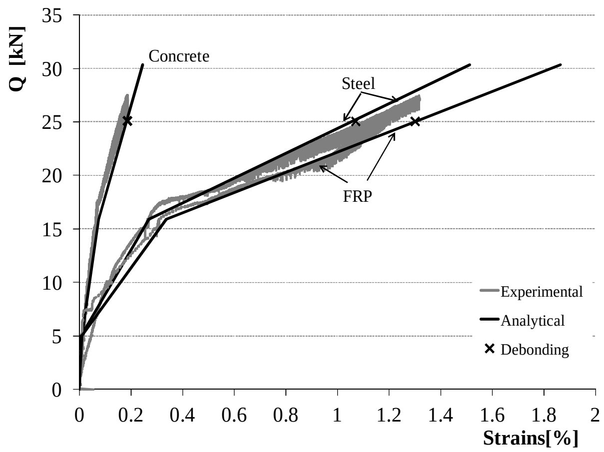

Figure B.7 – Load- strains curves concrete, steel and FRP slab S1

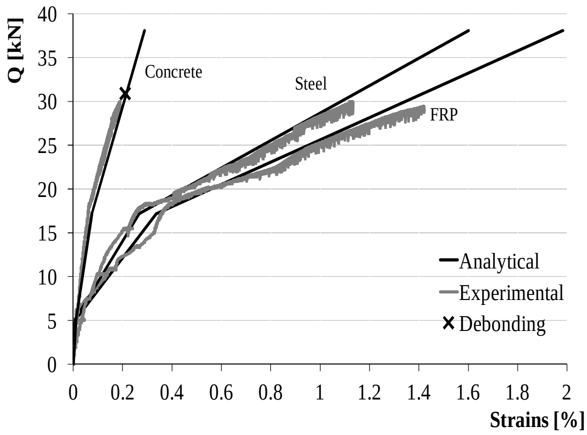

Figure B.8 – Load- strains curves concrete, steel and FRP slab S2

APPENDIX C
EXPERIMENTAL AND ANALYTICAL RESULTS FIRE TESTS OF FRP STRENGTHENED AND INSULATED RC MEMBERS

C.1 Concrete properties

For each concrete batch quality control tests were performed. Tested properties of the fresh concrete include slump, flow test and density (see Table C.1). At an age of 28 days and at the age of testing the beams and the slabs, the properties of the hardened concrete are determined by means of standard tests [1-2]. For the hardened concrete (see Table C.2) some or all of the following properties were determined:

- Compressive cylinder strength f_c on cylinders with a diameter of 150 mm and a height of 300 mm.
- Compressive strength $f_{c,cub}$ on cubes with side length 150 mm.
- Flexural tensile strength f_{ctb} by means of 3-point bending tests on prisms 150 mm x 150 mm x 600 mm and a span of 500 mm.
- Splitting tensile strength f_{cts} by splitting tests on the remaining halves of the prisms of the bending test.
- Young modulus, E_c, by axial compression tests on a cylinder with a diameter of 150 mm and a height of 300 mm

Table C.1 – Properties fresh concrete

Batch	Slump [mm]	Flow test	Density [kg/m^3]
1	55	1.75	2387
2	60	1.76	2368
3	55	1.76	2368
4	70	1.87	2406
5	70	1.92	2400
6	95	2.07	2418
7	65	1.85	2400
8	80	1.93	2406
9	40	1.83	2393

Tests on the hardened concrete were performed on 3 specimens, except for the modulus of elasticity which involved one specimen.

Table C.2 – Properties hardened concrete

Batch	At 28 days	At age of tests				
	f_c [N/mm^2]	f_c [N/mm^2]	$f_{c,cub}$ [N/mm^2]	$f_{c,tb}$ [N/mm^2]	$f_{c,ts}$ [N/mm^2]	E_c [N/mm^2]
1	44.5	48.0	51.4	5.5	3.8	34520
2	47.1	50.0	53.6	5.8	4.1	34893
3	45.7	49.0	53.9	5.5	3.9	34449
4	41.5	42.0	48.0	5.2	3.6	35083
5	43.2	44.0	47.8	5.4	3.6	34573
6	39.3	41.3	46.9	5.2	3.6	34217
7	41.3	42.0	48.0	5.2	3.6	34322
8	43.1	44.3	51.6	5.5	3.9	34672
9	42.2	43.4	49.8	5.7	3.9	34898

C.2 Test set-up fire test series

The tests set-up of the four fire test series are shown in Figure C.1–C8. The horizontal furnace has a top opening 6.0 m long and 3.0 m wide. Heat in the furnace is supplied by 8 gas burners in the longitudinal walls of the furnace chamber (4 for each side). For each fire test series, 6 specimens were tested simultaneously. The specimens were lifted and placed on the top of a steel ring frame that was placed on the top of the furnace chamber. The specimens were placed in the transverse direction of the furnace (the clear span of the specimens being 3 m). The gap between two adjacent specimens and between the specimen and the furnace walls were closed with aerated concrete slabs. These slabs are 150 mm deep and are insulated on their sides with 20 mm thick ceramic wool. Thereafter, the beams were exposed to fire from three sides (bottom of the beams and lateral sides for a height equal to 150 mm) and the top surface was exposed to ambient temperature. The slabs were exposed to fire only from the bottom side and the top surface was exposed to ambient temperature.

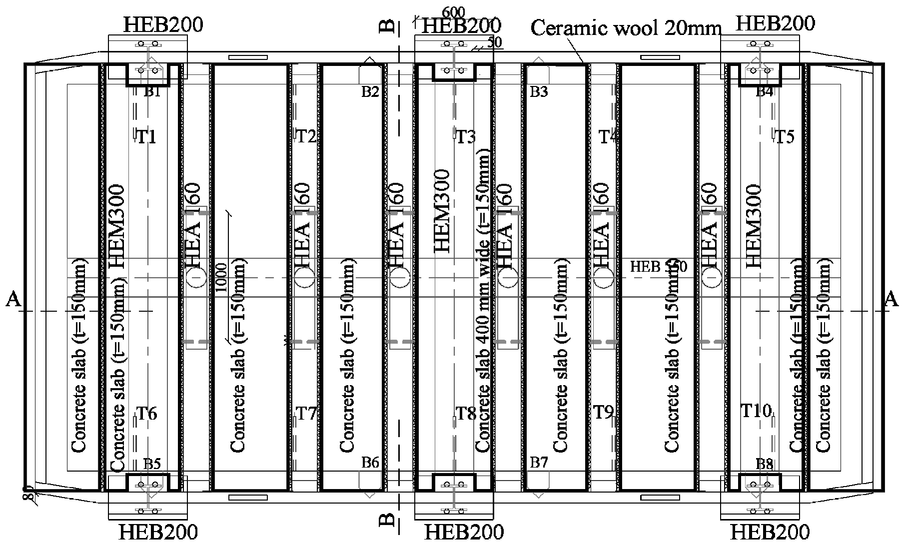

Figure C.1 – Top-view test set-up of the first, second and third fire test series

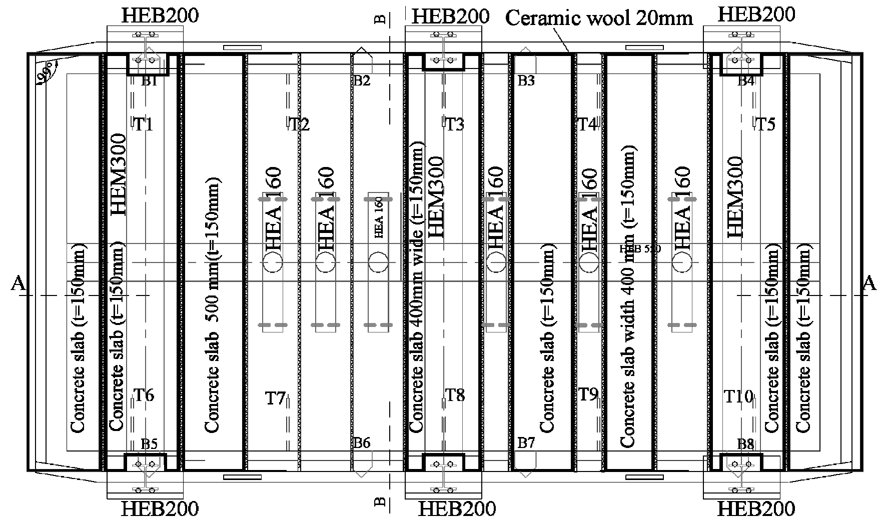

Figure C.2 – Top-view test set-up of the fourth fire test series

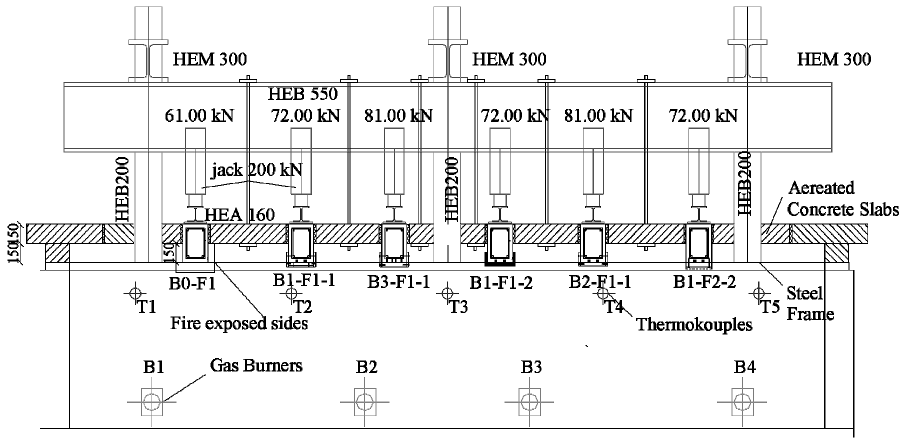

Figure C.3 – Longitudinal view test set-up of the first fire test series

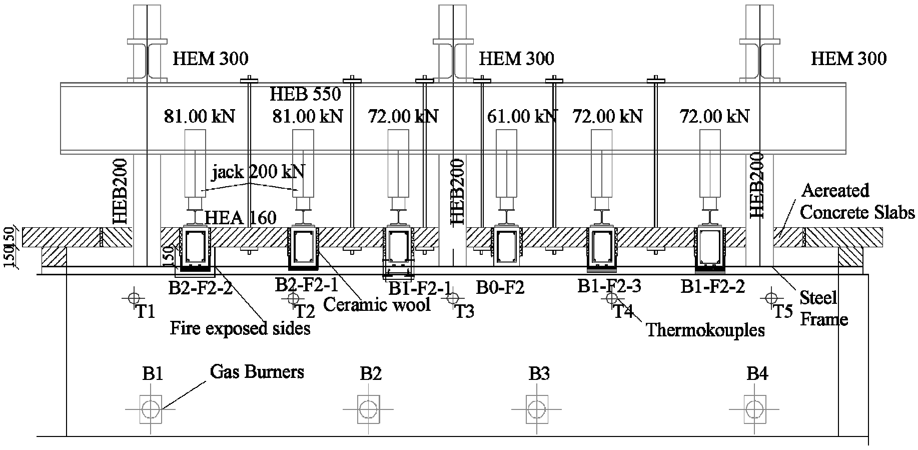

Figure C.4 – Longitudinal view test set-up of the second fire test series

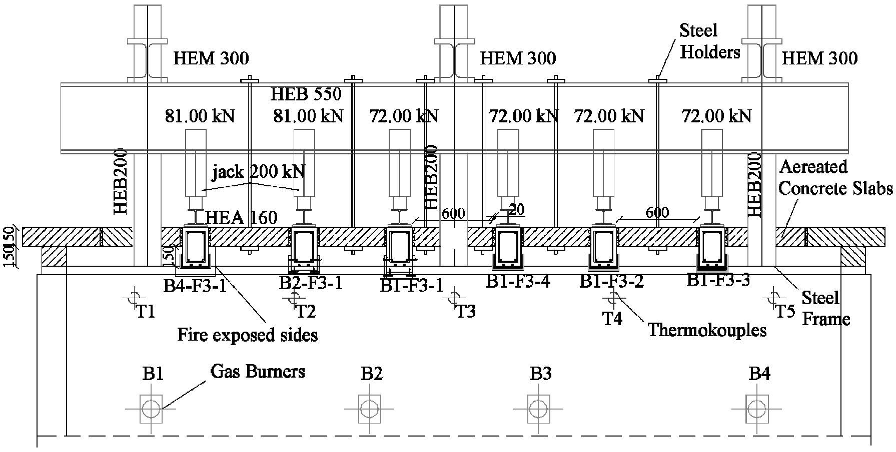

Figure C.5 – Longitudinal view test set-up of the third fire test series

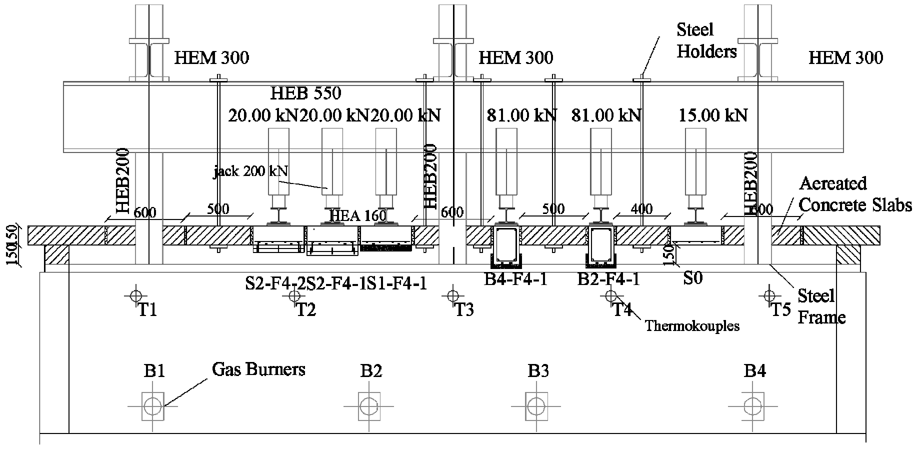

Figure C.6 – Longitudinal view test set-up of the second fire test series

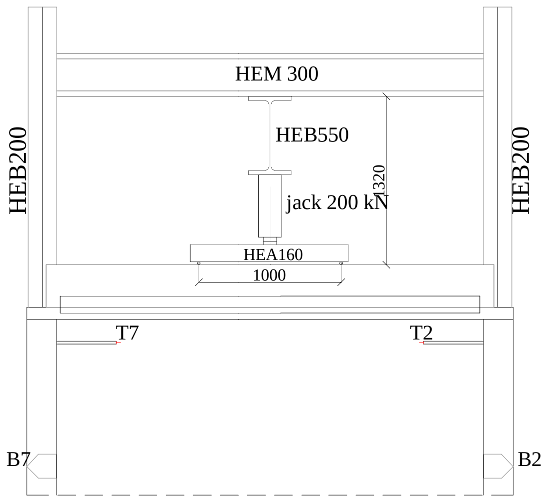

Figure C.7 – Transversal view test set-up for the beams tested in the first, second, third and fourth fire test series

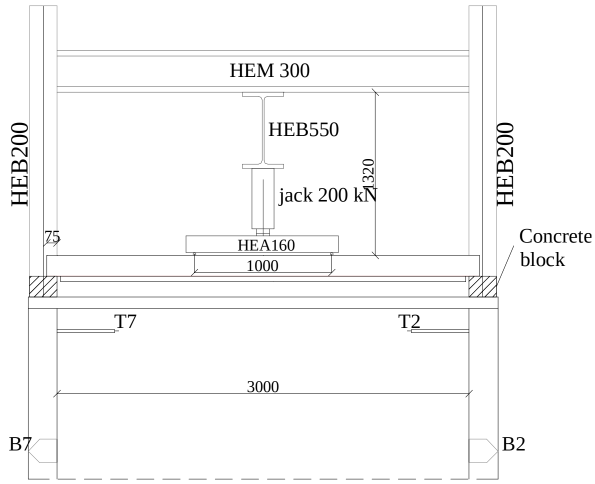

Figure C.8 – Transversal view test set-up for the slabs tested in the fourth fire test series

C.3 Time-Temperature curves furnace

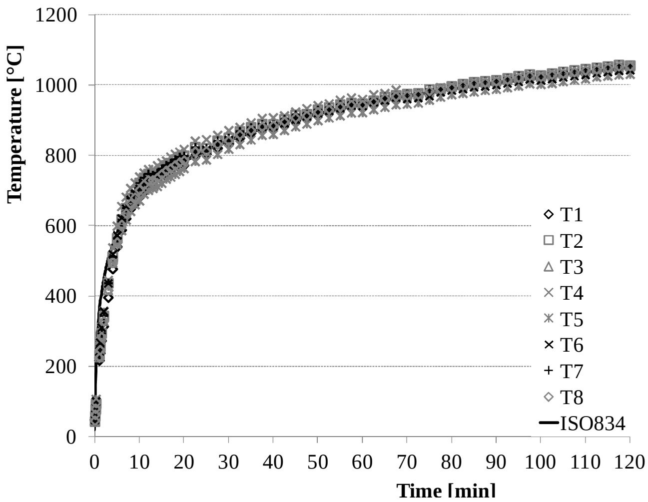

Figure C.9 – Time – temperature curves furnace of first fire test series

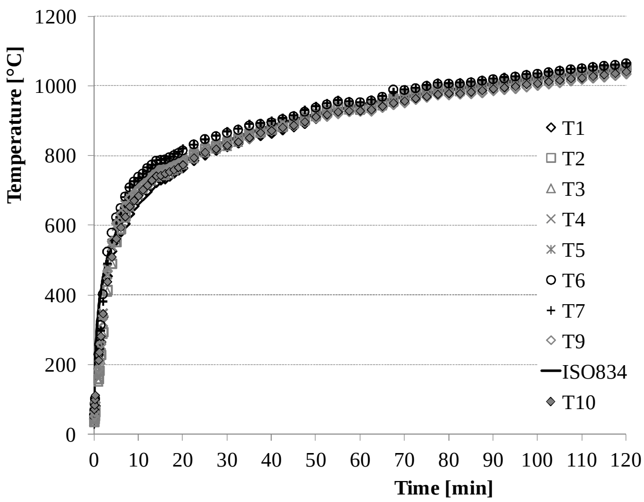

Figure C.10 – Time – temperature curves furnace of second fire test series

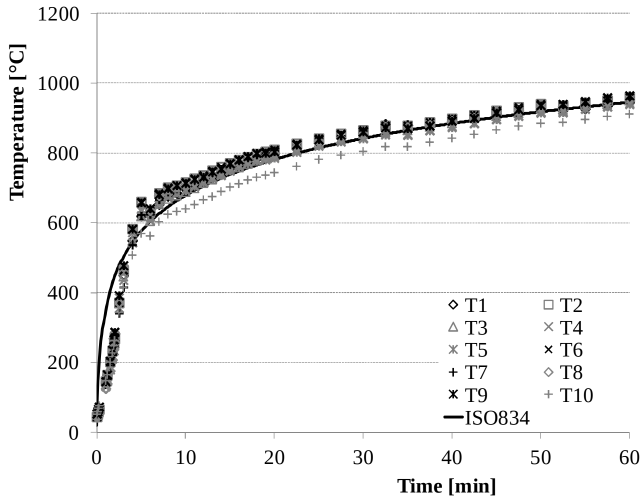

Figure C.11 – Time – temperature curves furnace of third fire test series

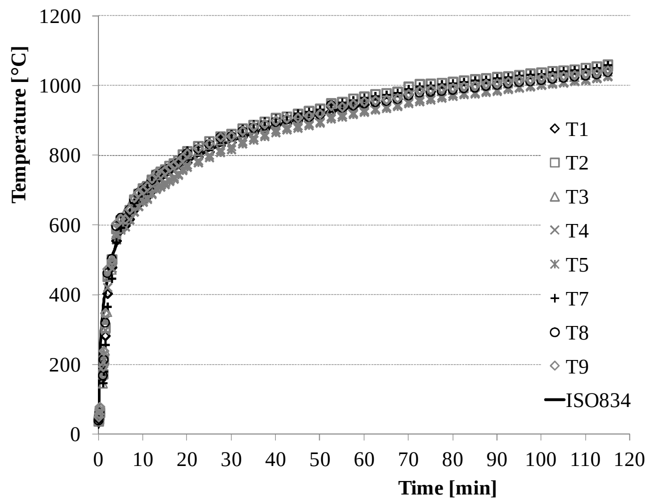

Figure C.12 – Time – temperature curves furnace of fourth fire test series

C.4 Experimental and analytical results specimens exposed to fire

In the following sections an overview of the test set-up, the position of the thermocouples, the experimental and analytical temperatures within the cross section and the experimental and analytical deflections for each beam and slab tested under fire exposure is given.

C.4.1 Beam B0-F1

C.4.1.1 Geometry of the specimen

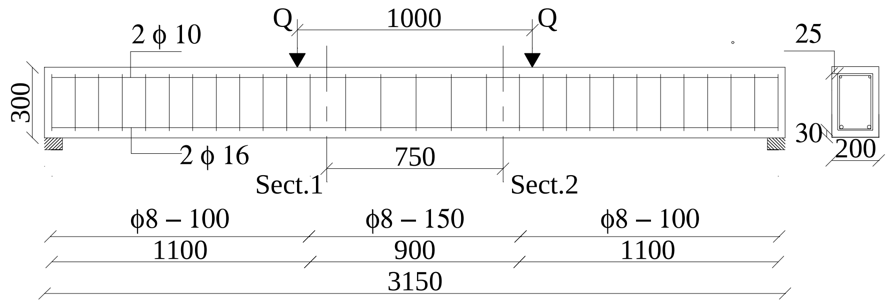

Figure C.13 – Geometry beam B0-F1

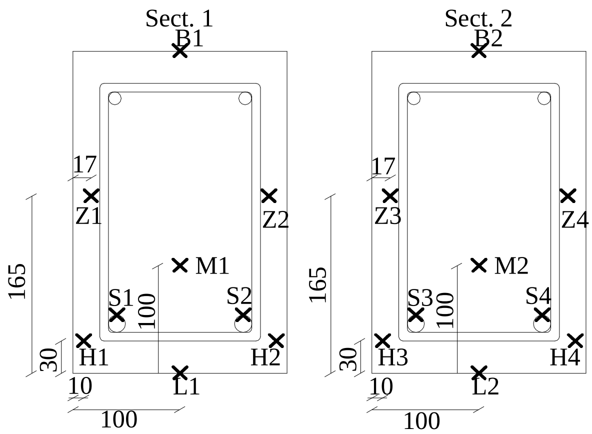

Figure C.14 – Position thermocouples specimen B0-F1

C.4.1.2 Time-temperatures and time- increase of deflection curves

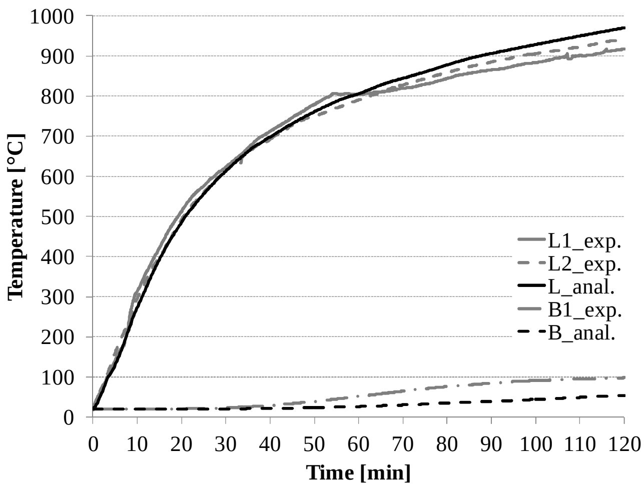

Figure C.15 – Experimental and analytical temperature-time curves thermocouples L and B

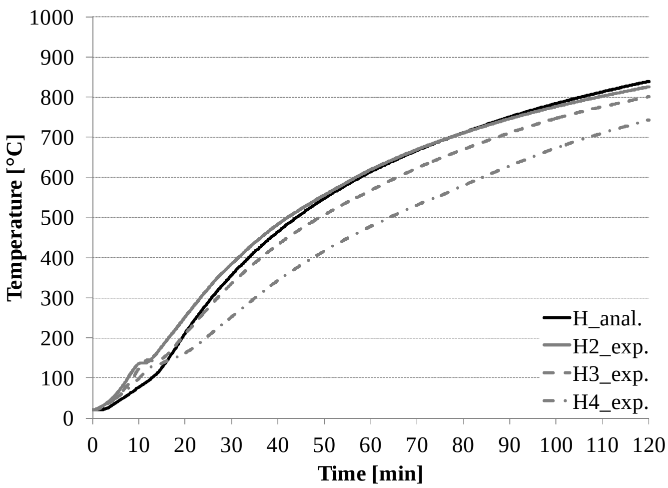

Figure C.16 – Experimental and analytical temperature-time curves thermocouples H

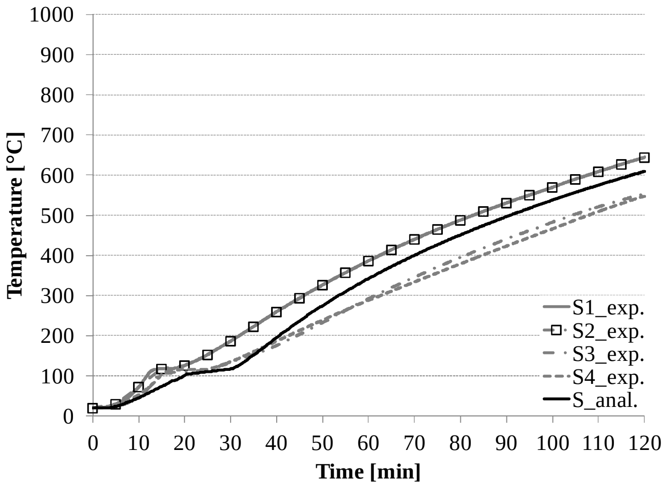

Figure C.17 – Experimental and analytical temperature-time curves thermocouples S

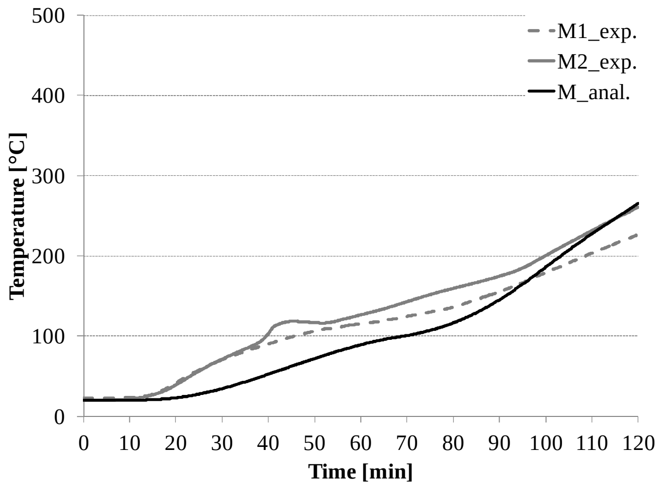

Figure C.18 – Experimental and analytical temperature-time curves thermocouples M

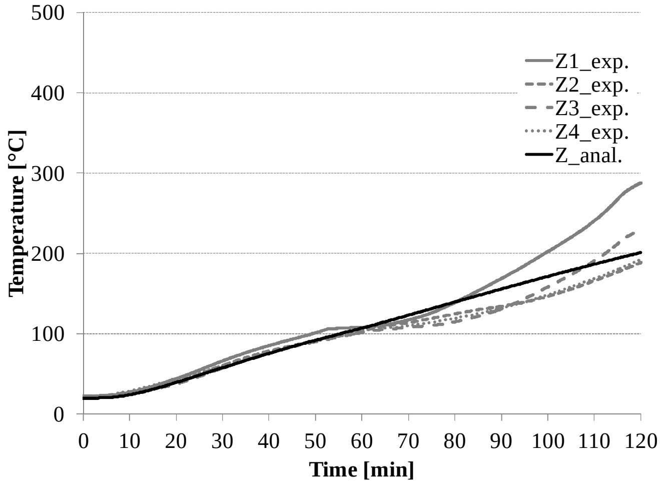

Figure C.19 – Experimental and analytical temperature-time curves thermocouples Z

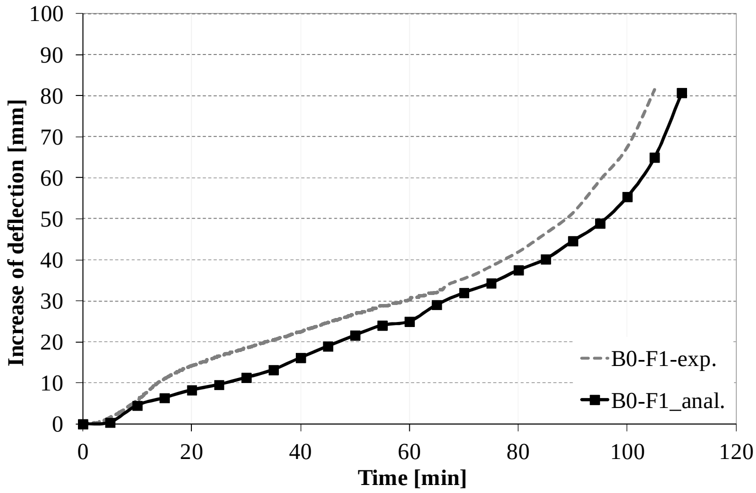

Figure C.20 – Experimental and analytical increase of midspan deflections as a function of time beam B0-F1

C.4.2 Beam B1-F1-1

C.4.2.1 Geometry of the specimen

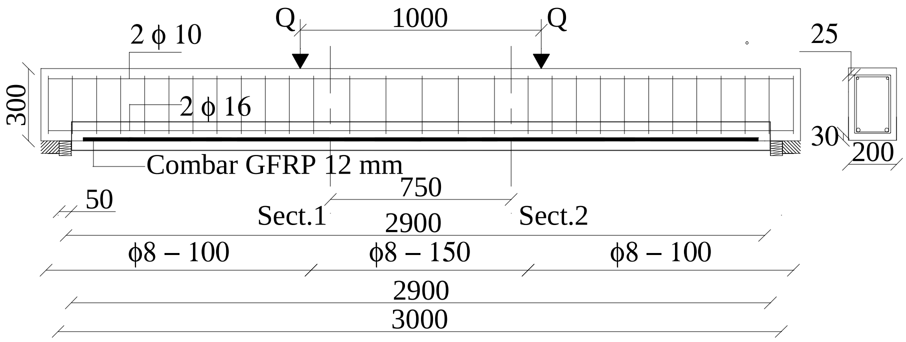

Figure C.21 – Geometry beam B1-F1-1

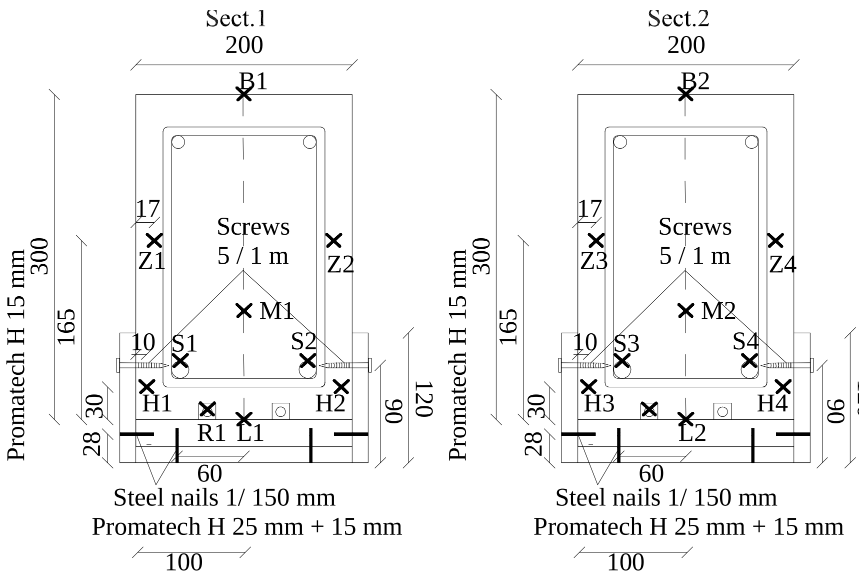

Figure C.22 – Insulation details and position thermocouples beam B1-F1-1

C.4.2.2 Time-temperatures and time- increase of deflection curves

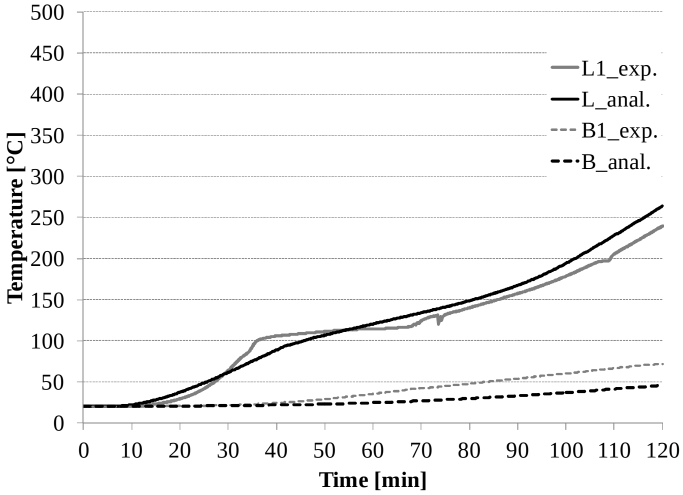

Figure C.23 - Experimental and analytical temperature-time curves thermocouples L and B

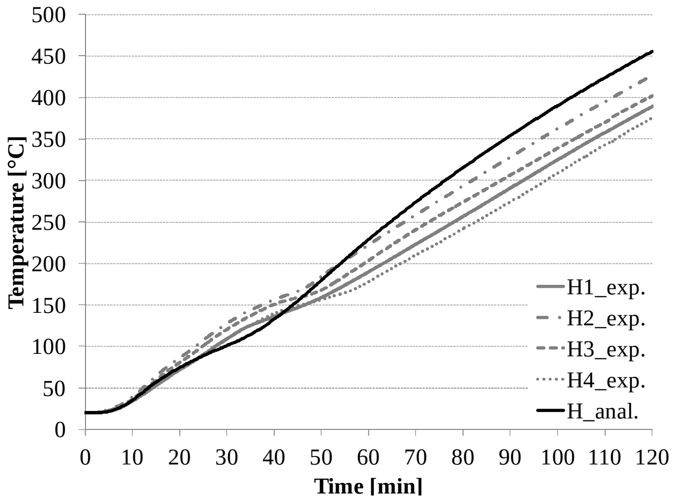

Figure C.24 – Experimental and analytical temperature-time curves thermocouples H

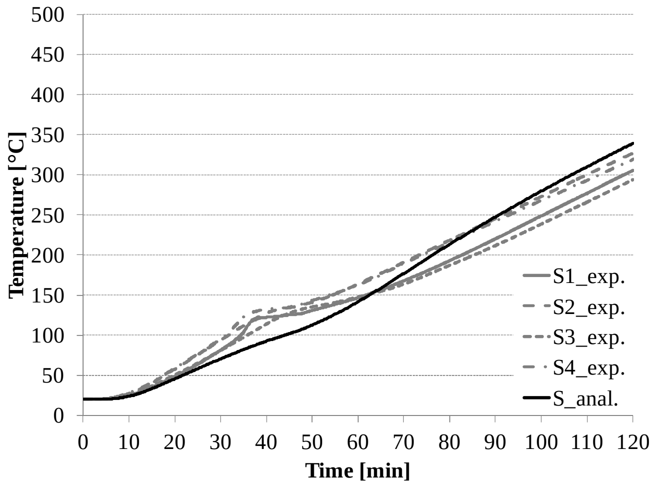

Figure C.25 – Experimental and analytical temperature-time curves thermocouples S

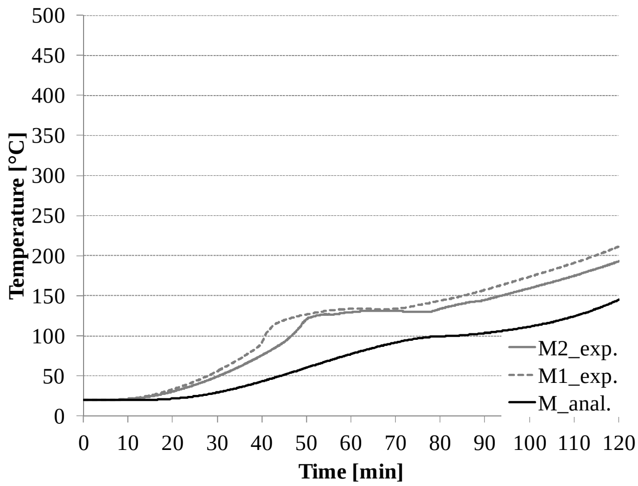

Figure C.26 – Experimental and analytical temperature-time curves thermocouples M

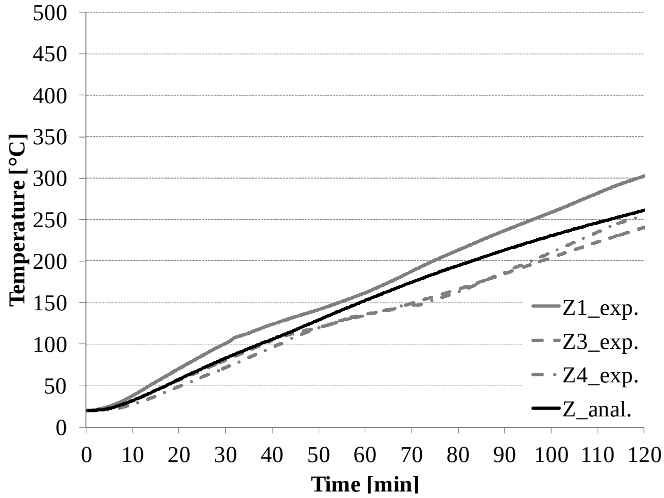

Figure C.27 – Experimental and analytical temperature-time curves thermocouples Z

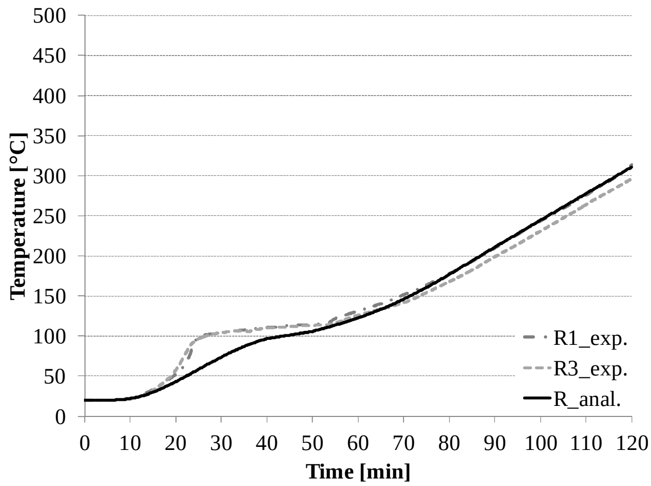

Figure C.28 – Experimental and analytical temperature-time curves thermocouples R

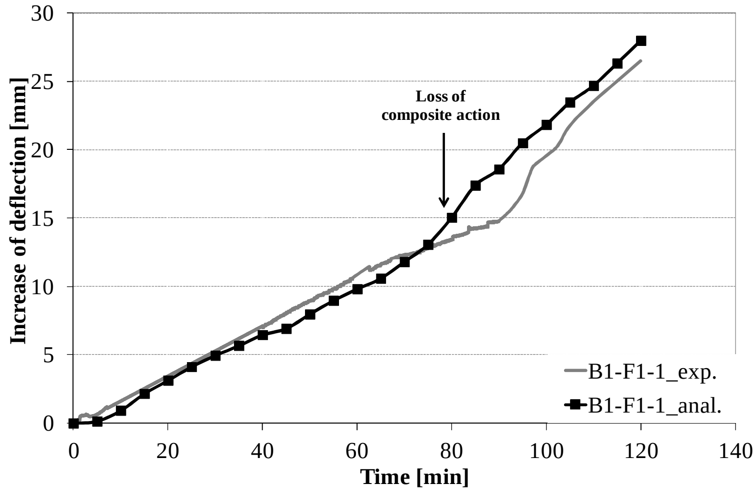

Figure C.29 – Experimental and analytical increase of midspan deflections as a function of time beam B1-F1-1

C.4.3 Beam B2-F1-1

C.4.3.1 Geometry of the specimen

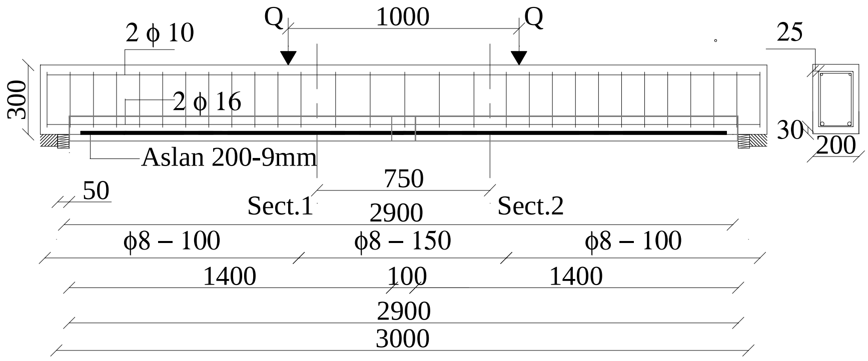

Figure C.30 - Geometry beam B2-F1-1

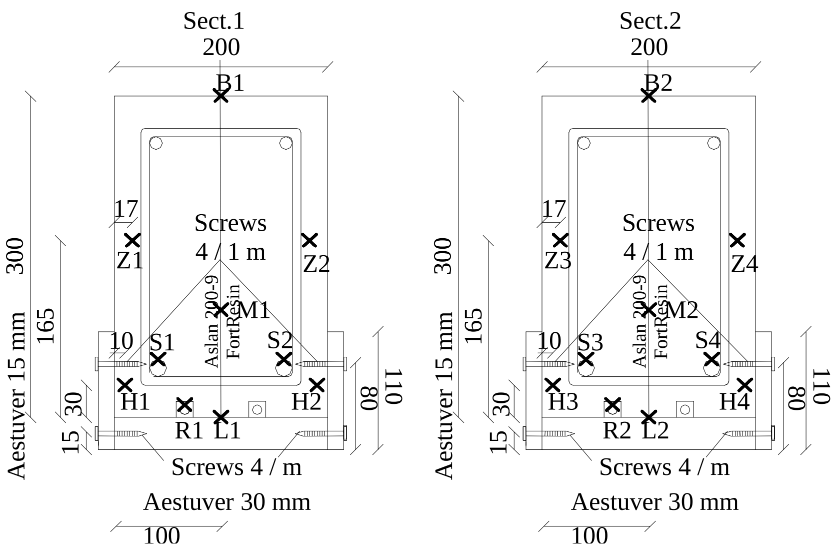

Figure C.31 – Insulation details and position thermocouples beam B2-F1-1

C.4.3.2 Time-temperatures and time- increase of deflection curves

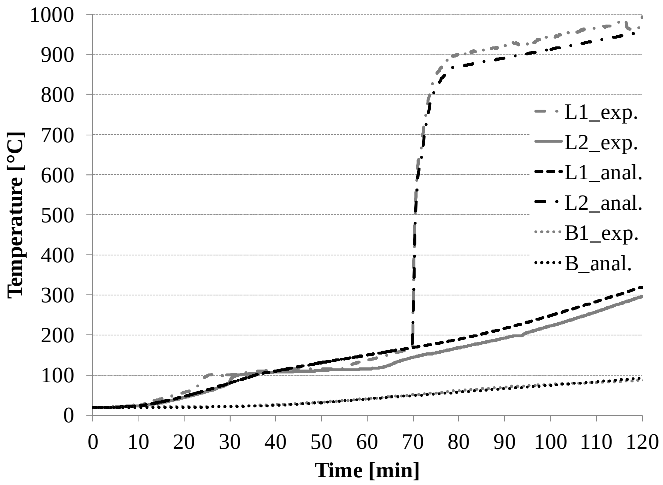

Figure C.32 - Experimental and analytical temperature-time curves thermocouples L and B

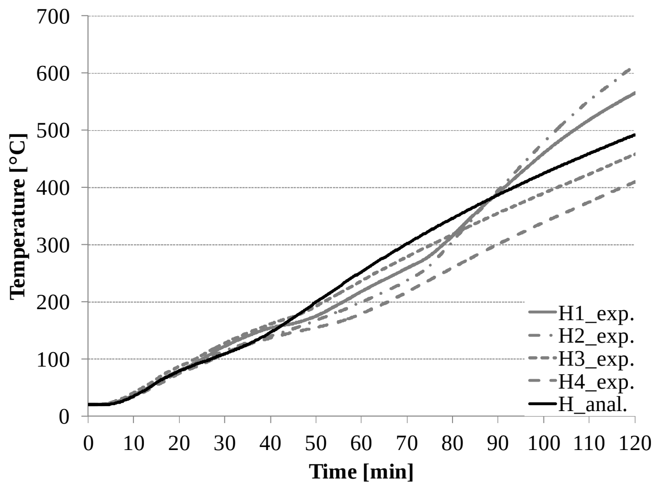

Figure C.33 – Experimental and analytical temperature-time curves thermocouples H

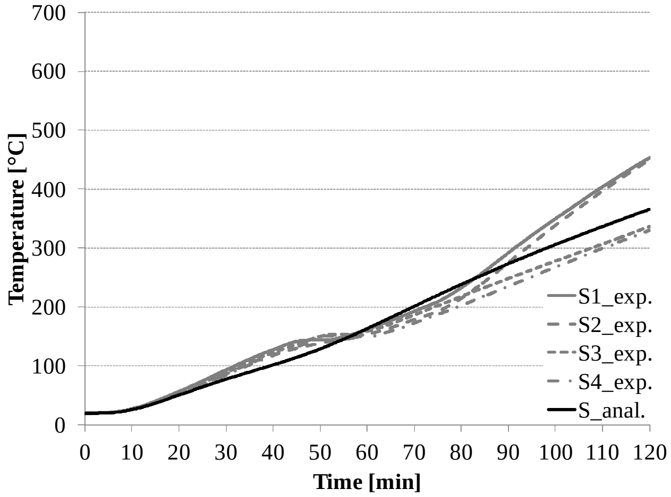

Figure C.34 – Experimental and analytical temperature-time curves thermocouples S

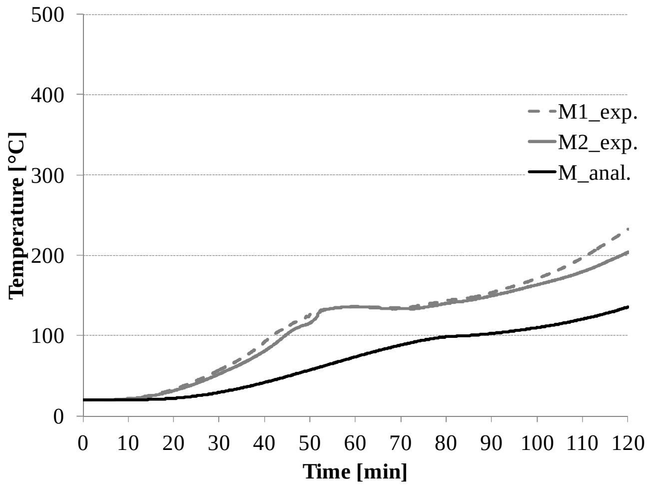

Figure C.35 – Experimental and analytical temperature-time curves thermocouples M

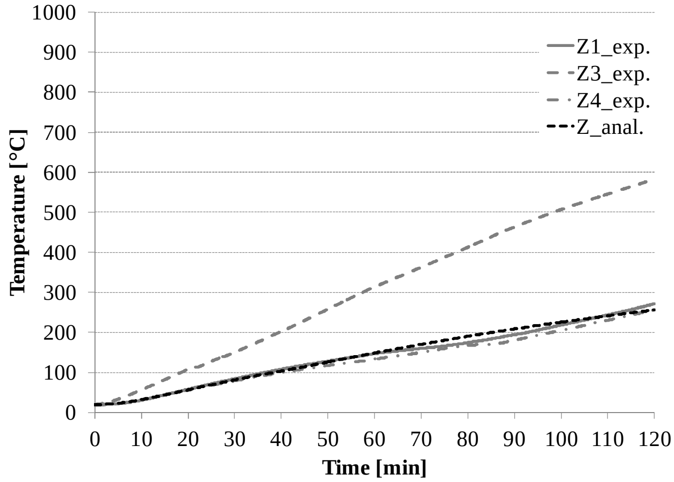

Figure C.36 – Experimental and analytical temperature-time curves thermocouples Z

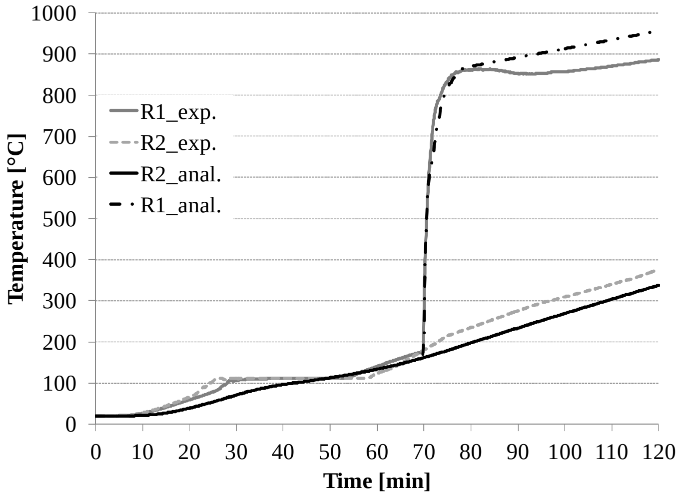

Figure C.37 – Experimental and analytical temperature-time curves thermocouples R

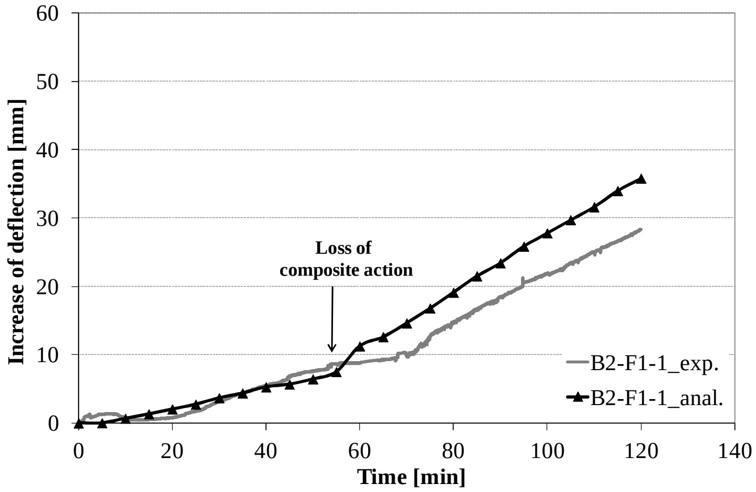

Figure C.38 – Experimental and analytical increase of midspan deflections as a function of time beam B2-F1-1

C.4.4 Beam B2-F1-2

C.4.4.1 Geometry of the specimen

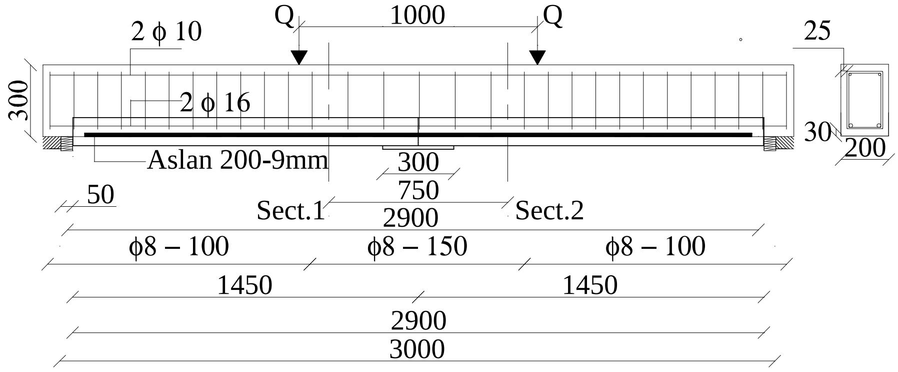

Figure C.39 - Geometry beam B2-F1-2

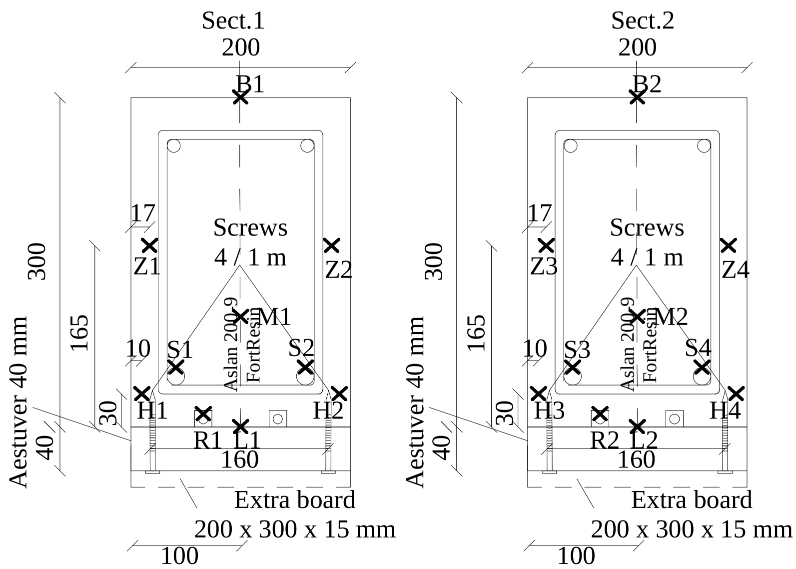

Figure C.40 – Insulation details and position thermocouples beam B2-F1-2

C.4.4.2 Time-temperatures and time- increase of deflection curves

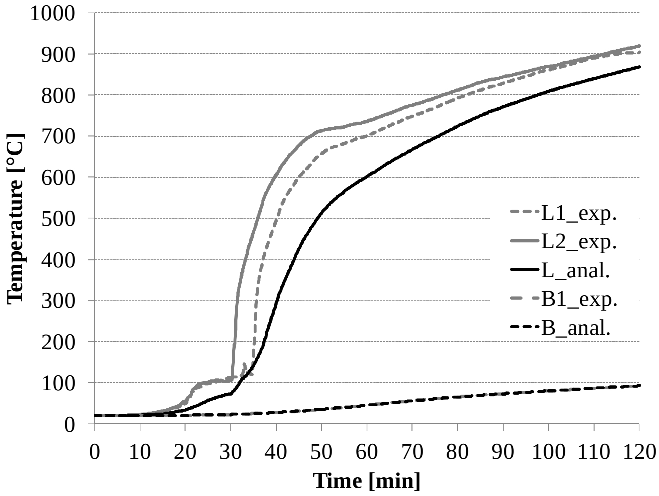

Figure C.41 - Experimental and analytical temperature-time curves thermocouples L and B

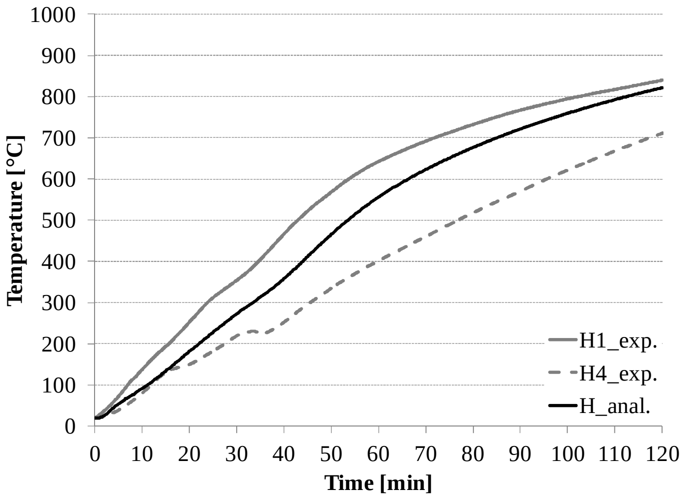

Figure C.42 – Experimental and analytical temperature-time curves thermocouples H

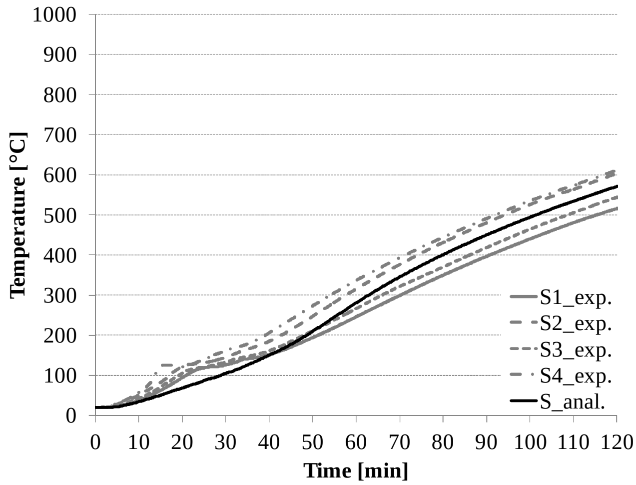

Figure C.43 – Experimental and analytical temperature-time curves thermocouples S

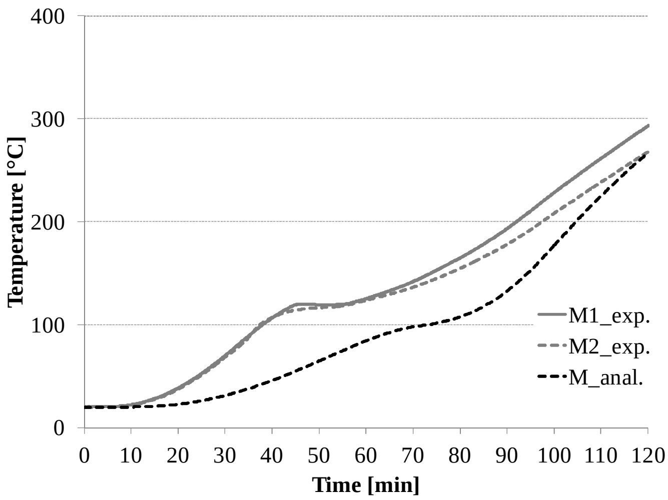

Figure C.44 – Experimental and analytical temperature-time curves thermocouples M

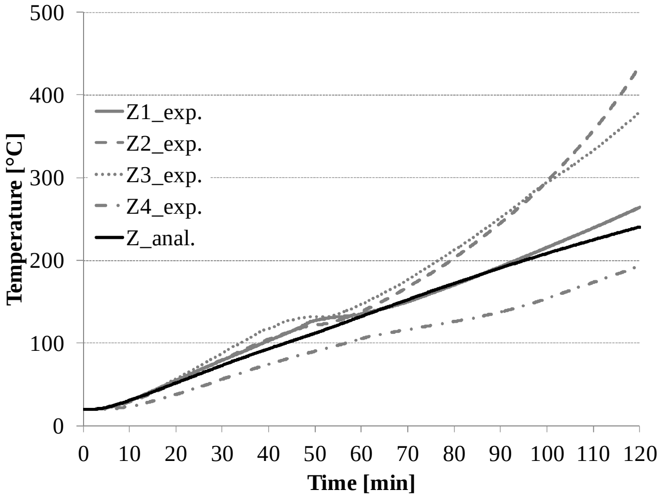

Figure C.45 – Experimental and analytical temperature-time curves thermocouples Z

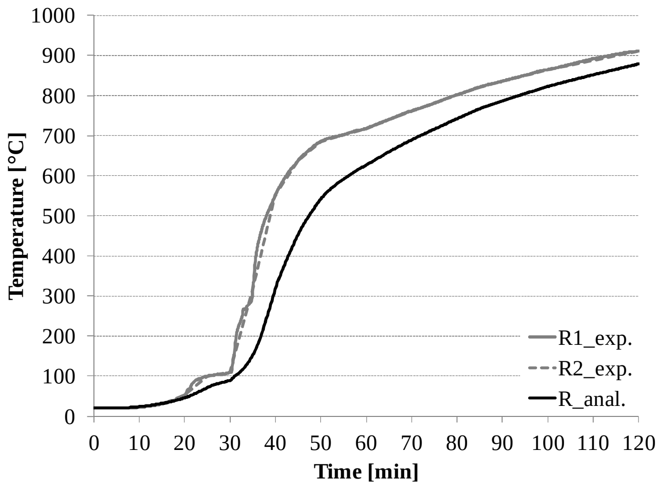

Figure C.46 – Experimental and analytical temperature-time curves thermocouples R

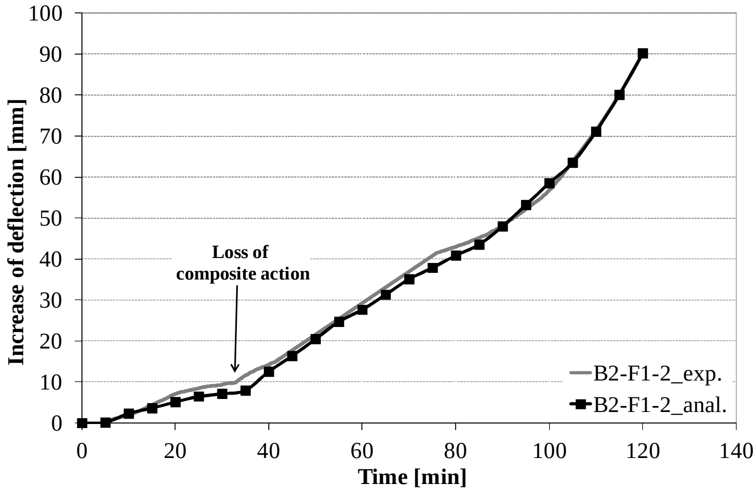

Figure C.47 – Experimental and analytical increase of midspan deflections as a function of time beam B2-F1-2

C.4.5 Beam B3-F1-1

C.4.5.1 Geometry of the specimen

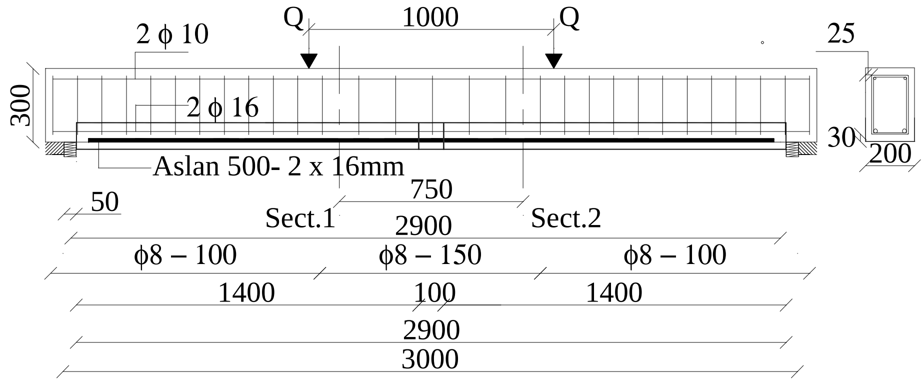

Figure C.48 – Geometry beam B3-F1-1

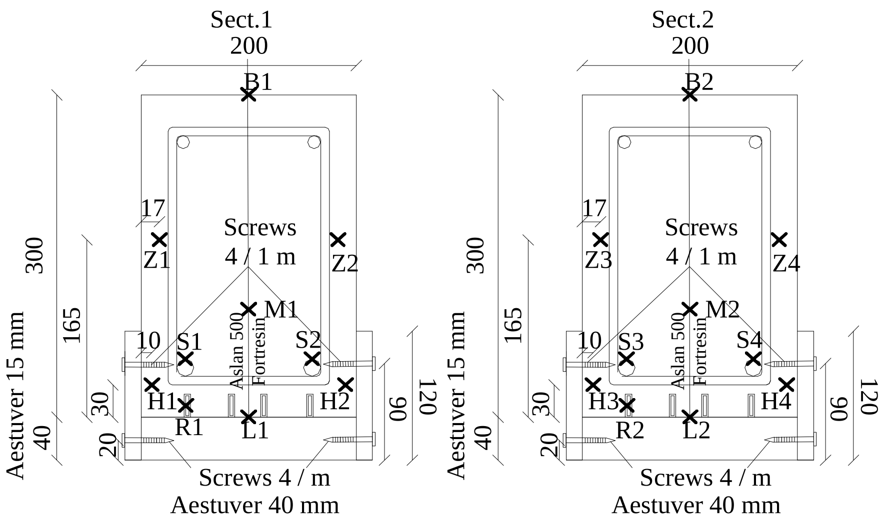

Figure C.49 – Insulation details and position thermocouples beam B3-F1-1

C.4.5.2 Time-temperatures and time- increase of deflection curves

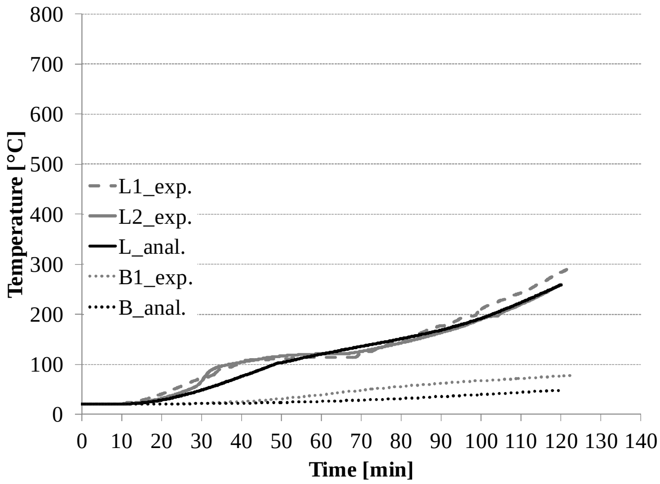

Figure C.50 – Experimental and analytical temperature-time curves thermocouples L and B

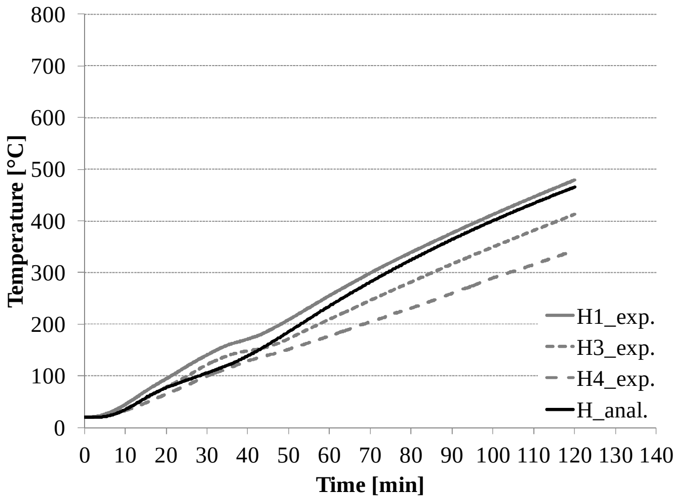

Figure C.51 – Experimental and analytical temperature-time curves thermocouples H

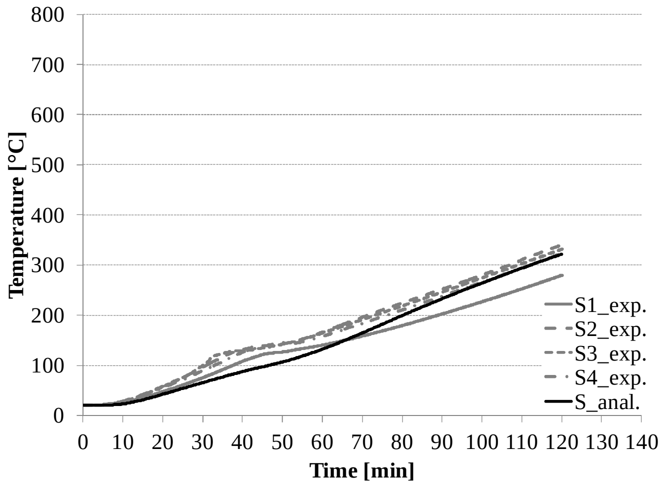

Figure C.52 – Experimental and analytical temperature-time curves thermocouples S

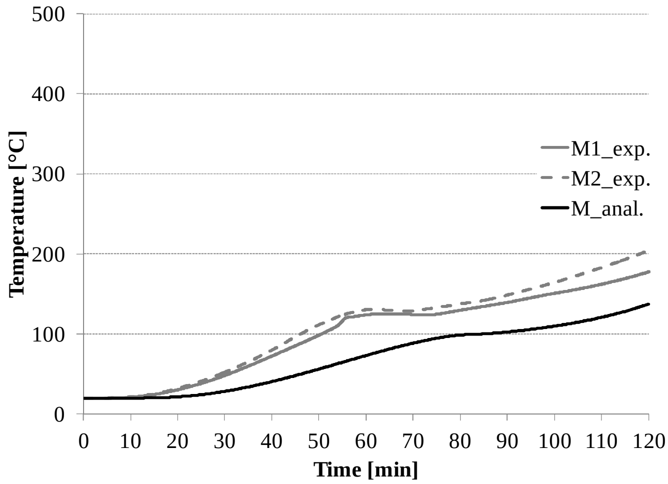

Figure C.53 – Experimental and analytical temperature-time curves thermocouples M

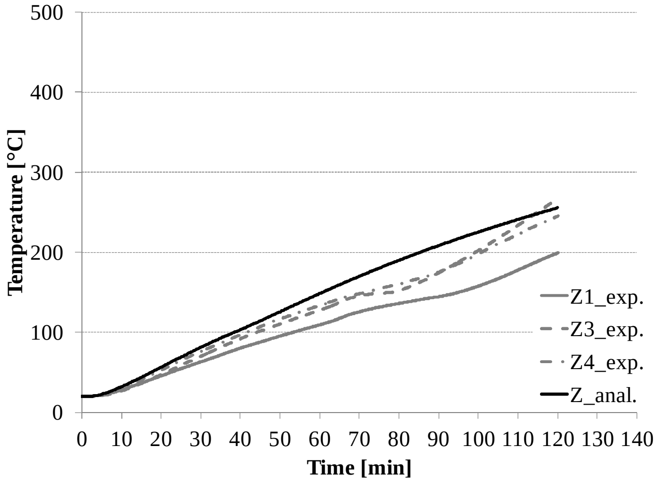

Figure C.54 – Experimental and analytical temperature-time curves thermocouples Z

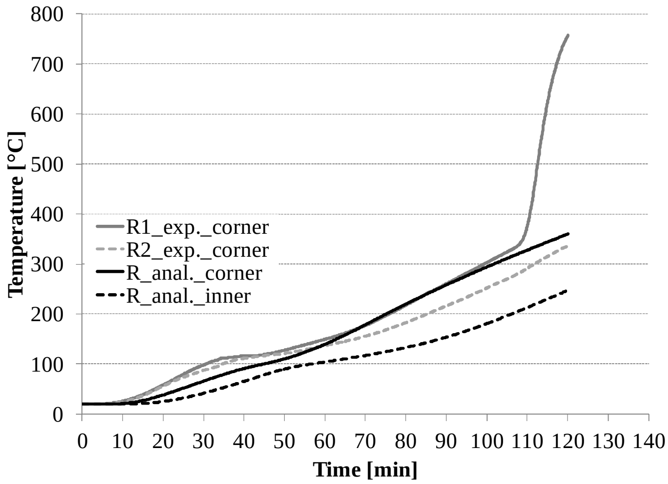

Figure C.55 – Experimental and analytical temperature-time curves thermocouples R

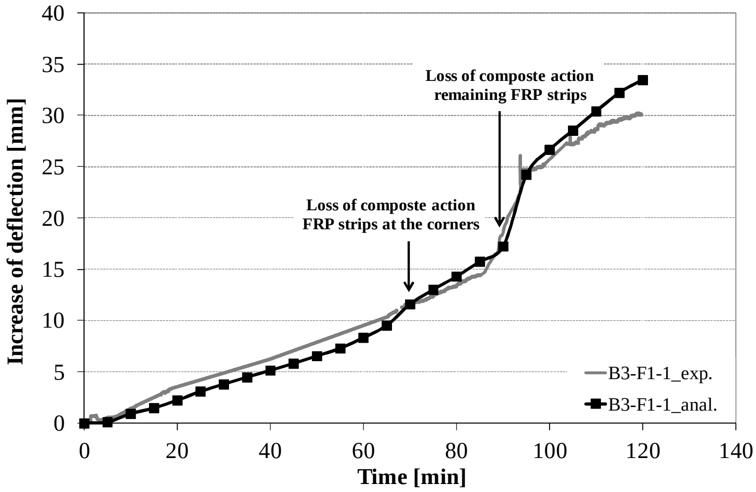

Figure C.56 – Experimental and analytical increase of midspan deflections as a function of time beam B3-F1-1

C.4.6 Beam B0-F2

C.4.6.1 Geometry of the specimen

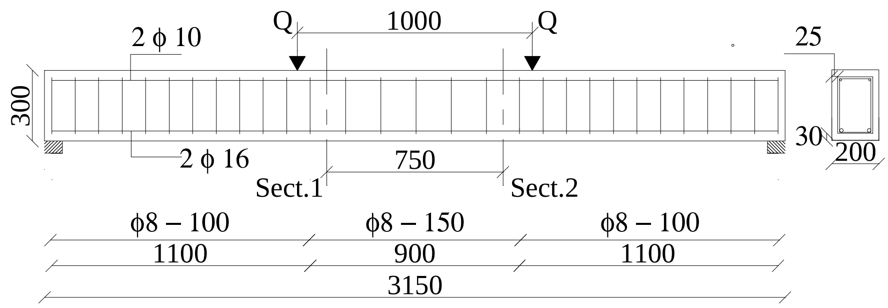

Figure C.57 – Geometry beam B0-F2

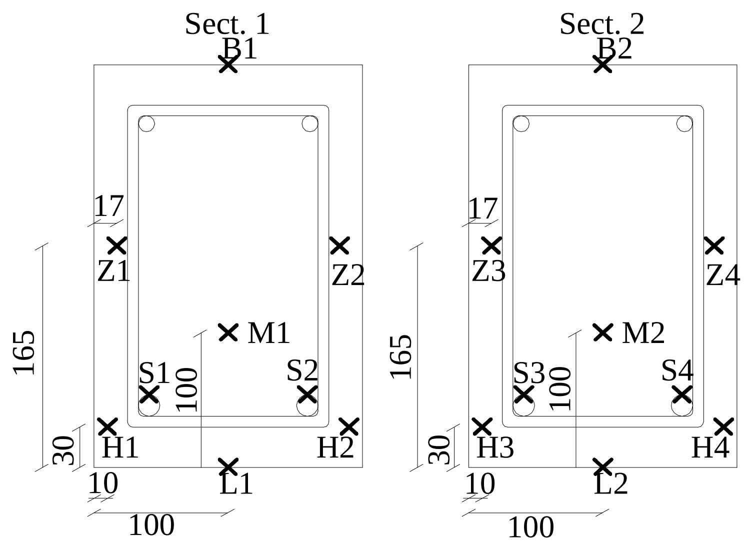

Figure C.58 – Insulation details and position thermocouples beam B0-F2

C.4.6.2 Time-temperatures and time- increase of deflection curves

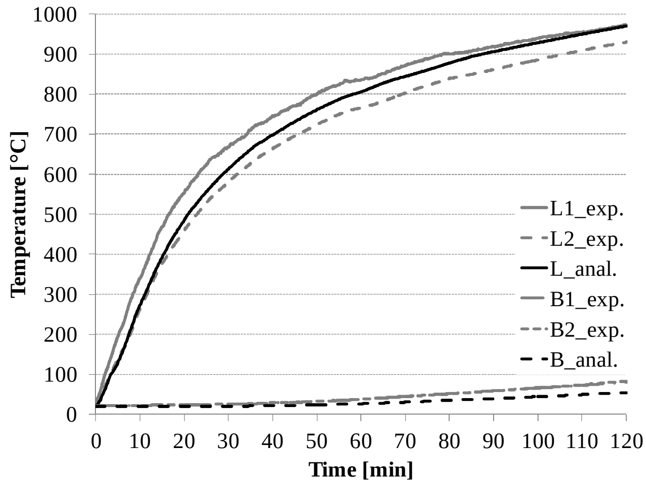

Figure C.59 – Experimental and analytical temperature-time curves thermocouples L and B

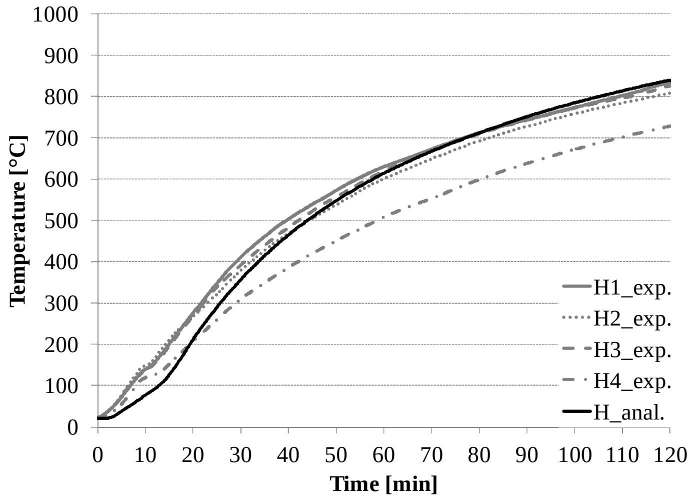

Figure C.60 – Experimental and analytical temperature-time curves thermocouples H

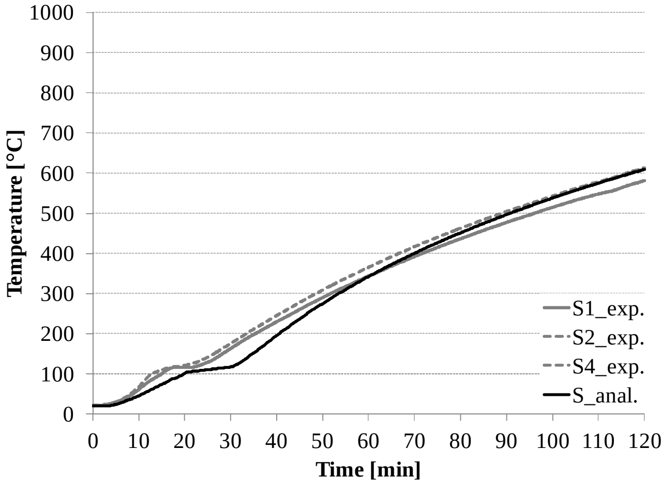

Figure C.61 – Experimental and analytical temperature-time curves thermocouples S

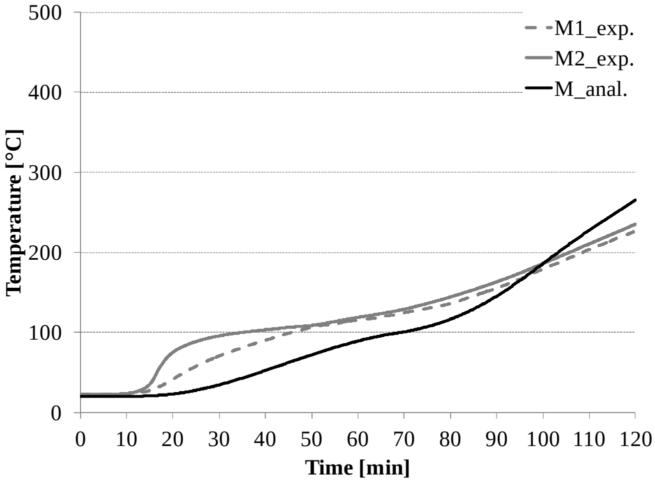

Figure C.62 – Experimental and analytical temperature-time curves thermocouples M

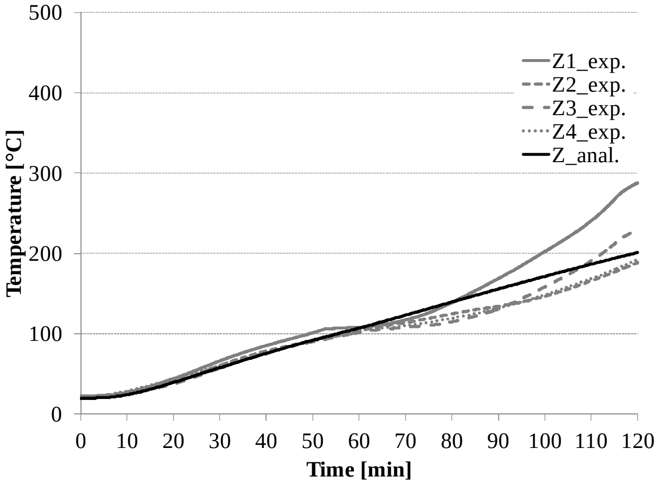

Figure C.63 – Experimental and analytical temperature-time curves thermocouples Z

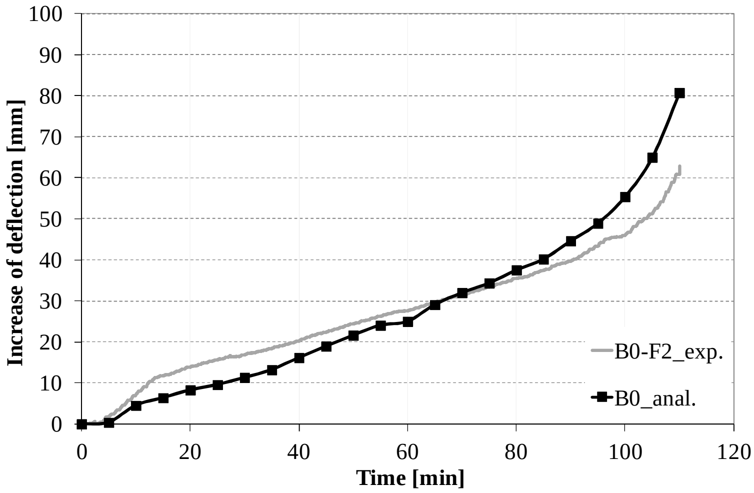

Figure C.64 – Experimental and analytical increase of midspan deflections as a function of time beam B0-F2

C.4.7 Beam B1-F2-1

C.4.7.1 Geometry of the specimen

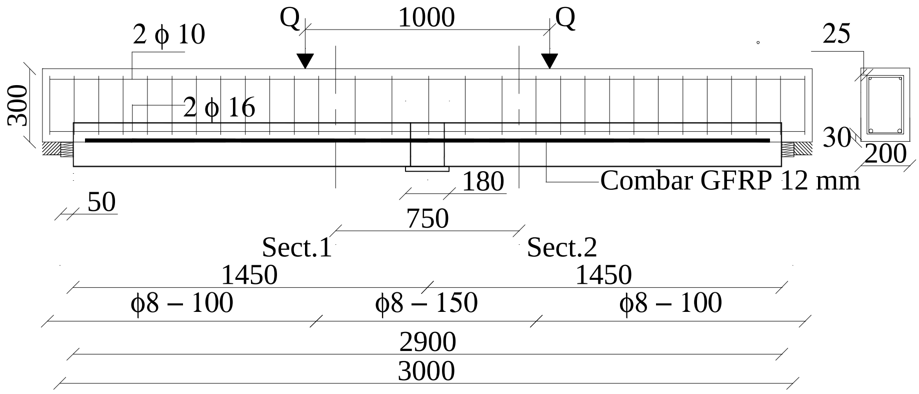

Figure C.65 – Geometry beam B1-F2-1

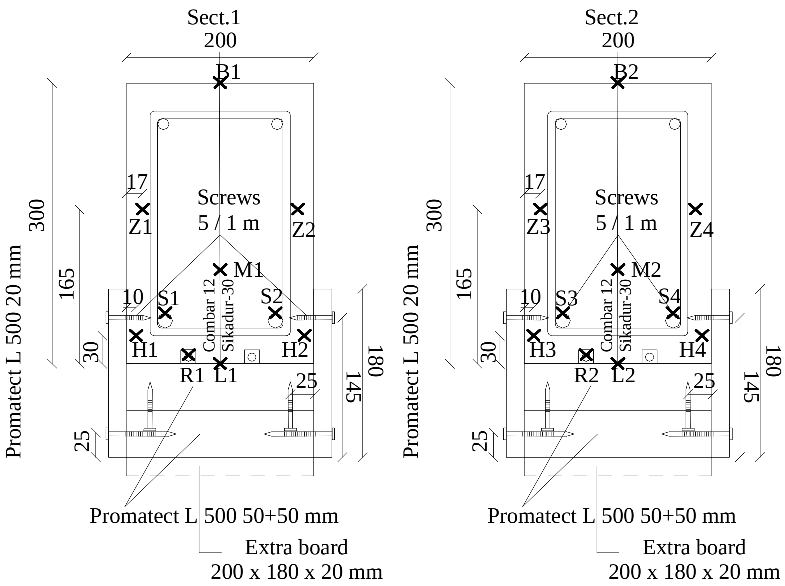

Figure C.66 – Insulation details and position thermocouples beam B1-F2-1

C.4.7.2 Time-temperatures and time- increase of deflection curves

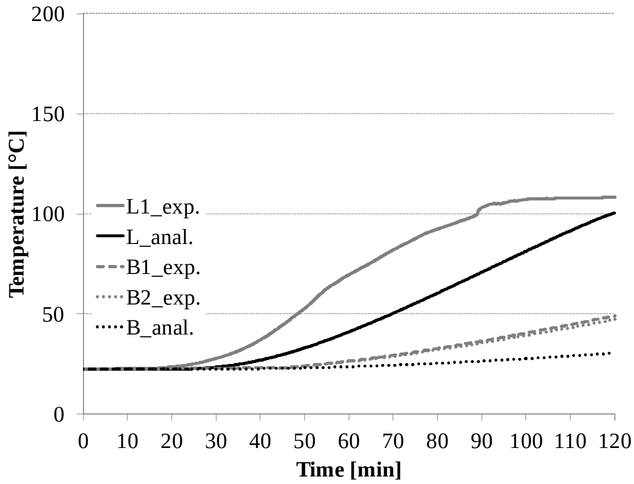

Figure C.67 – Experimental and analytical temperature-time curves thermocouples L and B

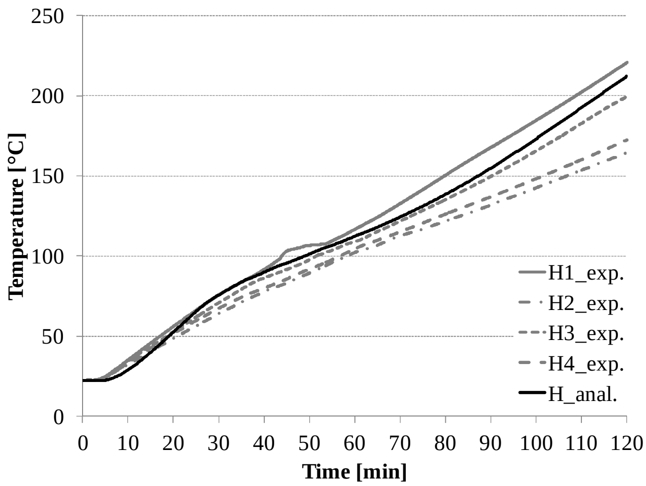

Figure C.68 – Experimental and analytical temperature-time curves thermocouples H

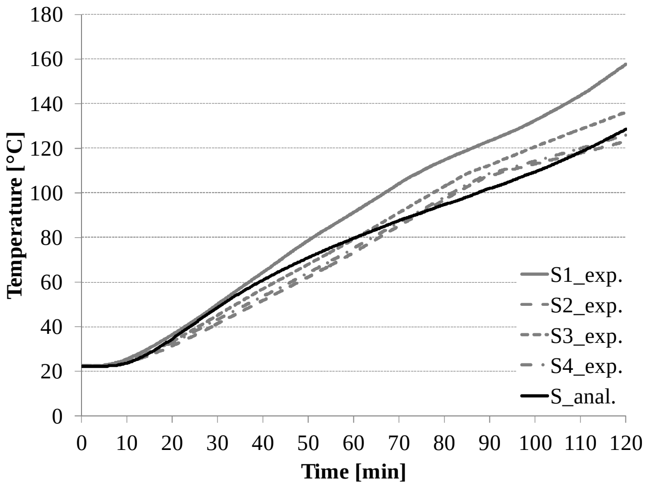

Figure C.69 – Experimental and analytical temperature-time curves thermocouples S

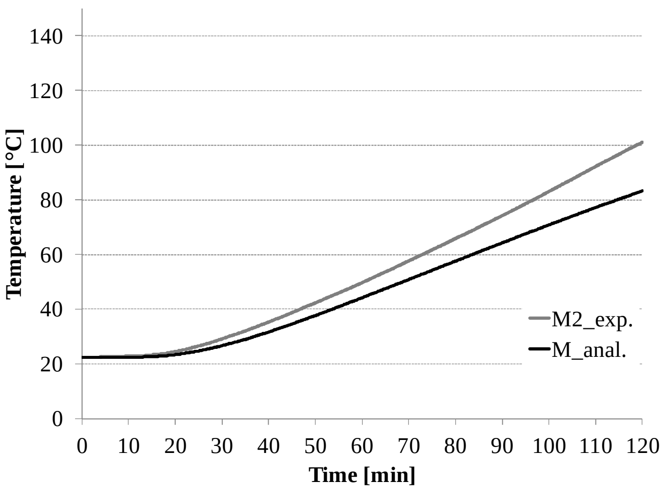

Figure C.70 – Experimental and analytical temperature-time curves thermocouples M

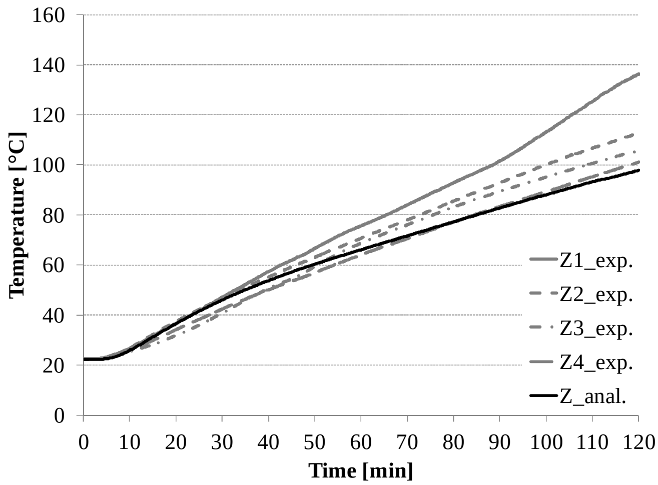

Figure C.71 – Experimental and analytical temperature-time curves thermocouples Z

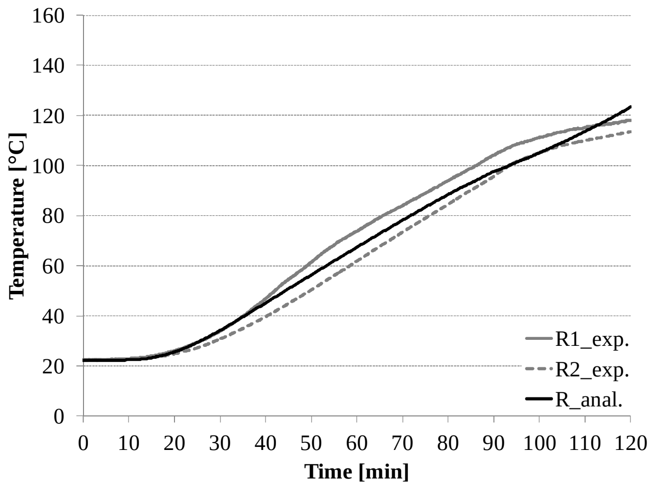

Figure C.72 – Experimental and analytical temperature-time curves thermocouples R

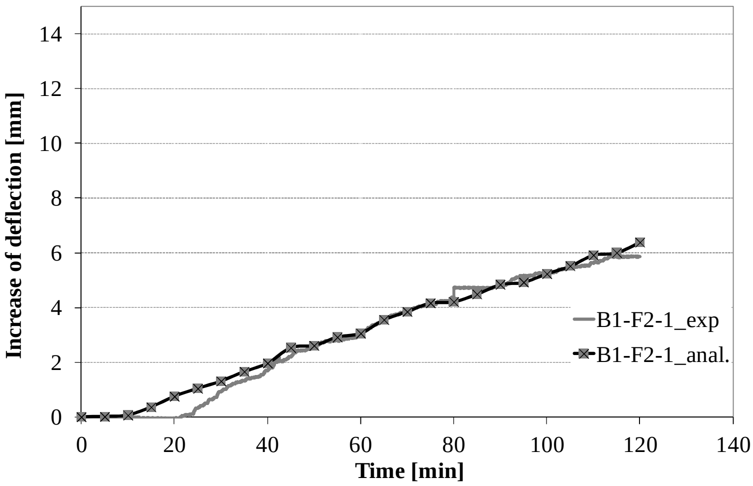

Figure C.73 – Experimental and analytical increase of midspan deflections as a function of time beam B1-F2-1

C.4.8 Beam B1-F2-2

C.4.8.1 Geometry of the specimen

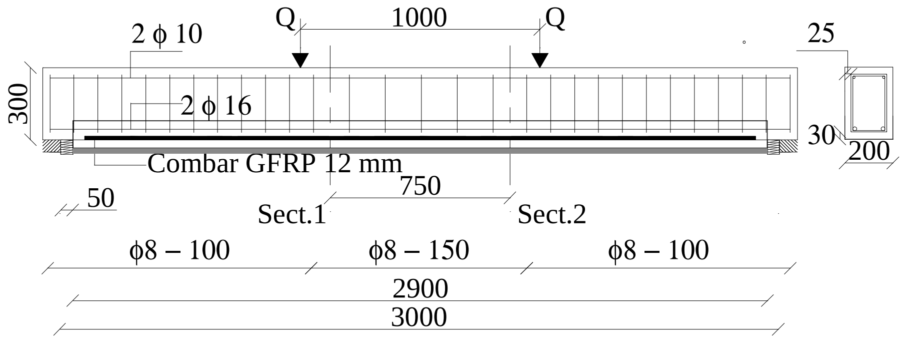

Figure C.74 – Geometry beam B1-F2-2

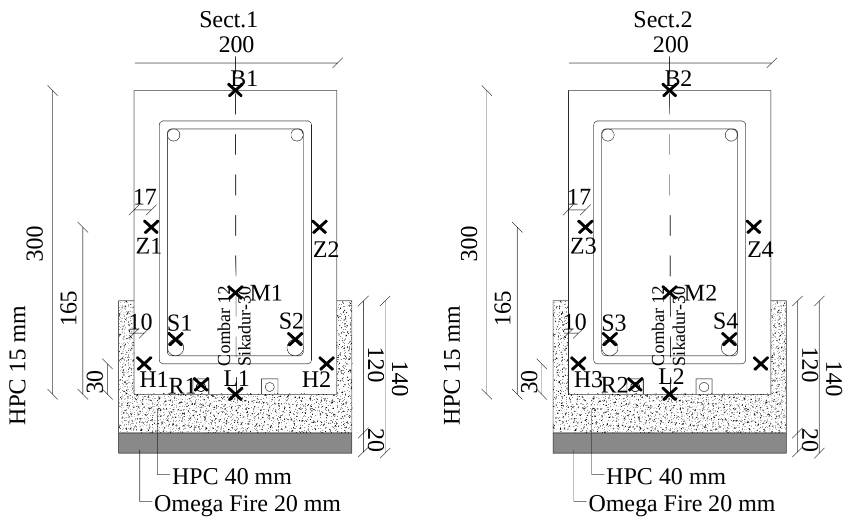

Figure C. 75 – Insulation details and position thermocouples beam B1-F2-2

C.4.8.2 Time-temperatures and time- increase of deflection curves

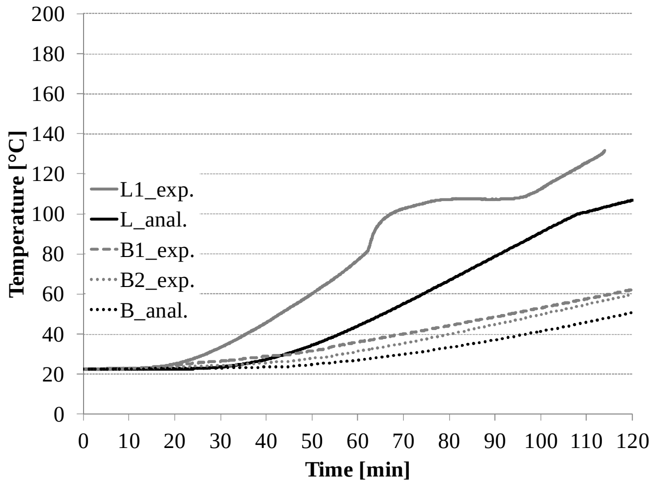

Figure C.76 – Experimental and analytical temperature-time curves thermocouples L and B

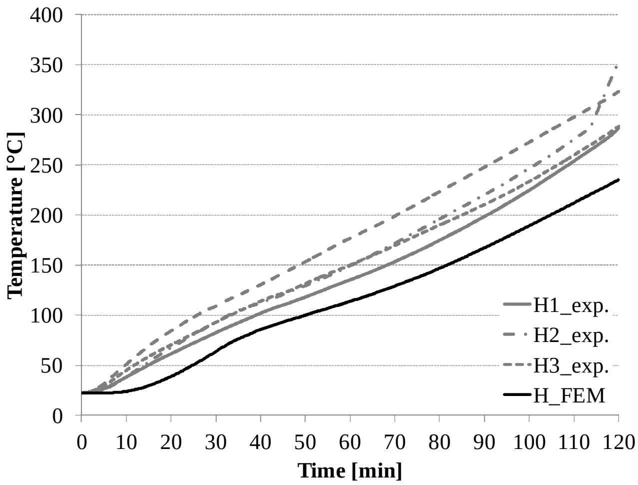

Figure C.77 – Experimental and analytical temperature-time curves thermocouples H

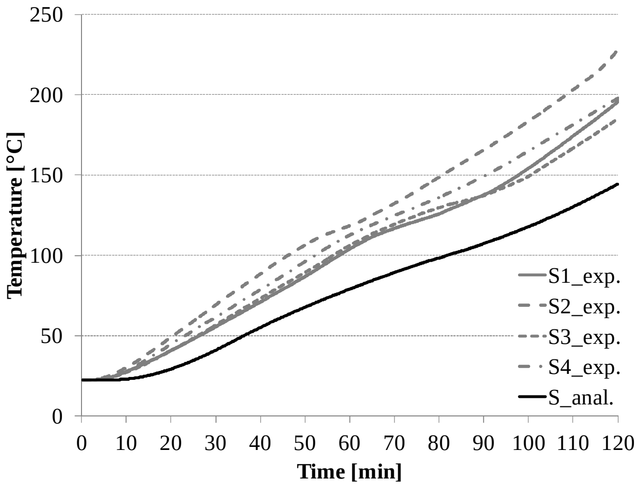

Figure C.78 – Experimental and analytical temperature-time curves thermocouples S

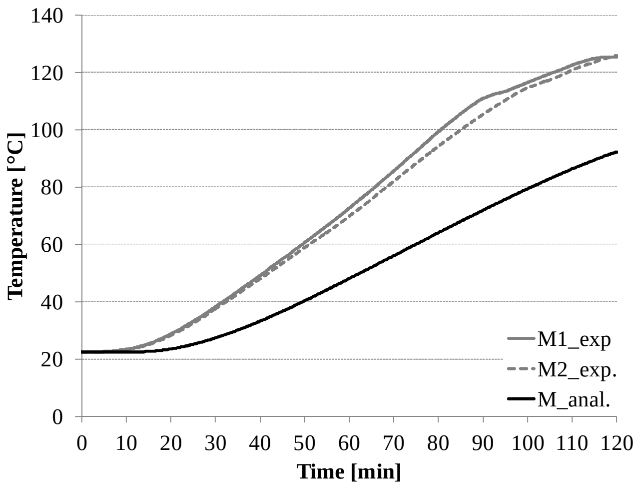

Figure C.79 – Experimental and analytical temperature-time curves thermocouples M

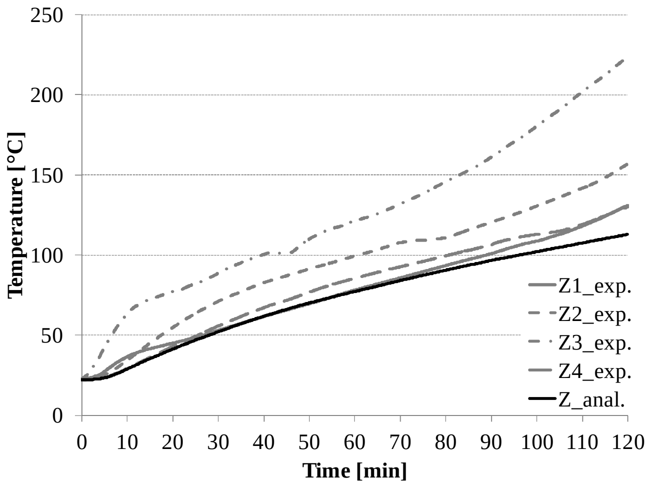

Figure C.80 – Experimental and analytical temperature-time curves thermocouples Z

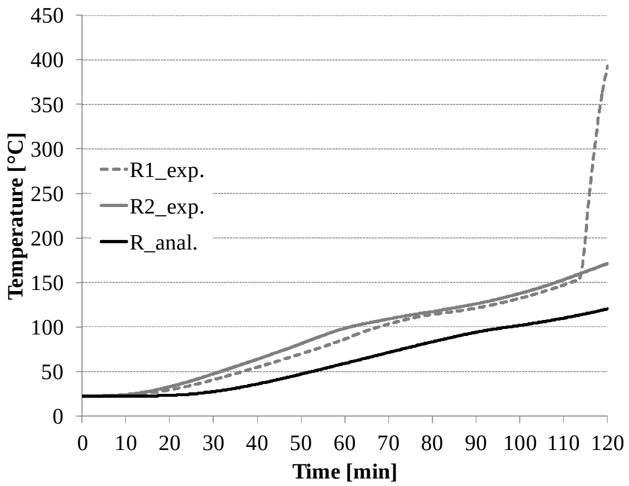

Figure C.81 – Experimental and analytical temperature-time curves thermocouples R

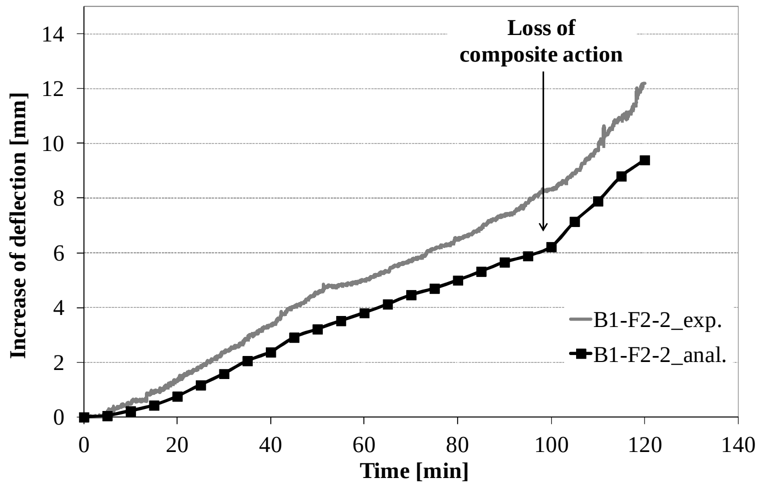

Figure C.82 – Experimental and analytical increase of midspan deflections as a function of time beam B1-F2-2

C.4.9 Beam B1-F2-3

C.4.9.1 Geometry of the specimen

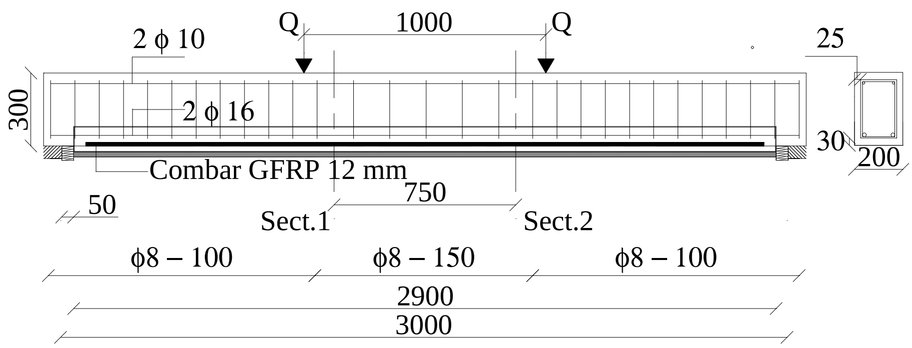

Figure C.83 – Geometry beam B1-F2-3

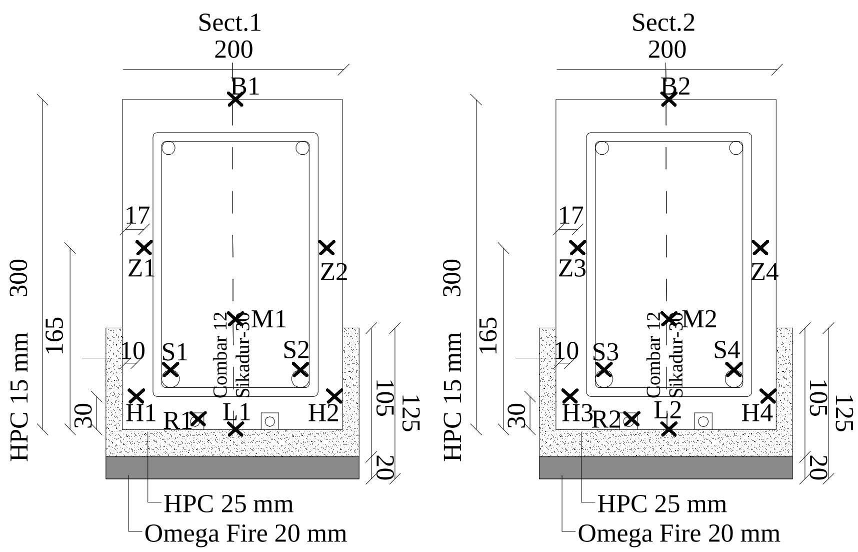

Figure C.84 – Insulation details and position thermocouples beam B1-F2-3

C.4.9.2 Time-temperatures and time- increase of deflection curves

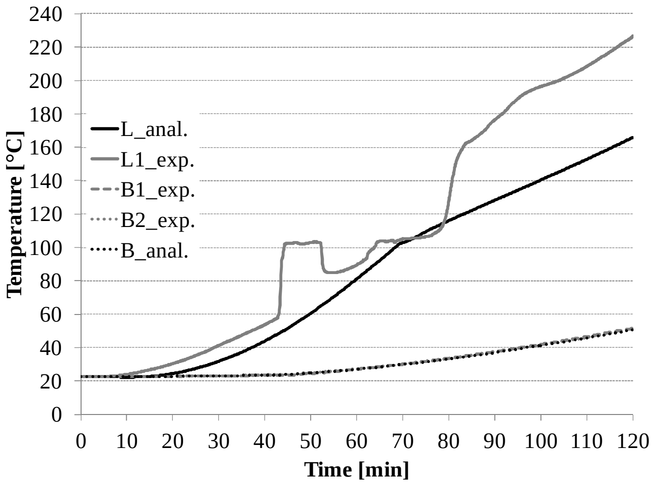

Figure C.85 – Experimental and analytical temperature-time curves thermocouples L and B

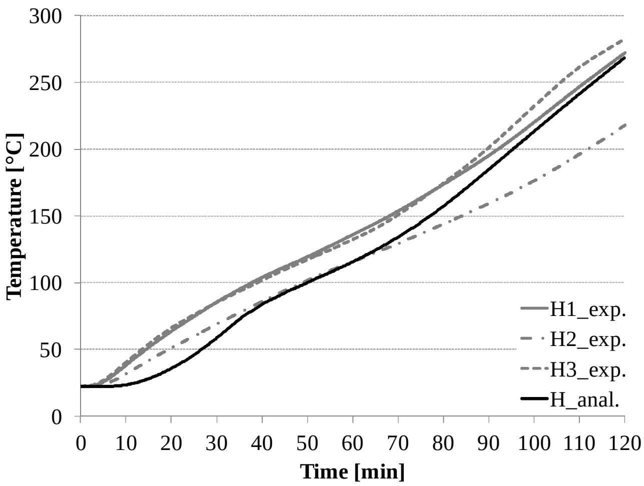

Figure C.86 – Experimental and analytical temperature-time curves thermocouples H

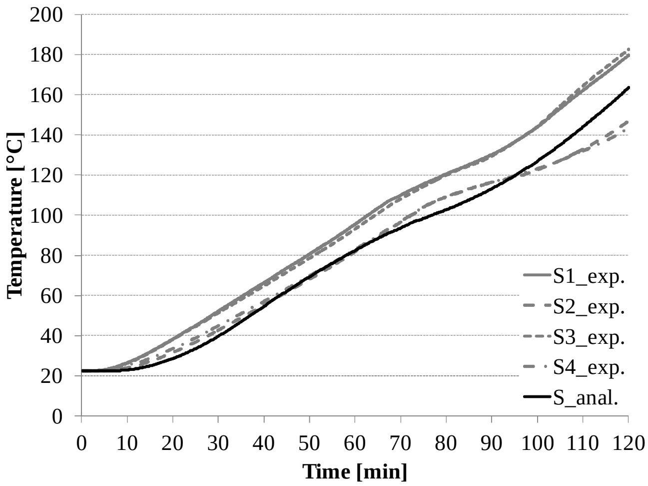

Figure C.87 – Experimental and analytical temperature-time curves thermocouples S

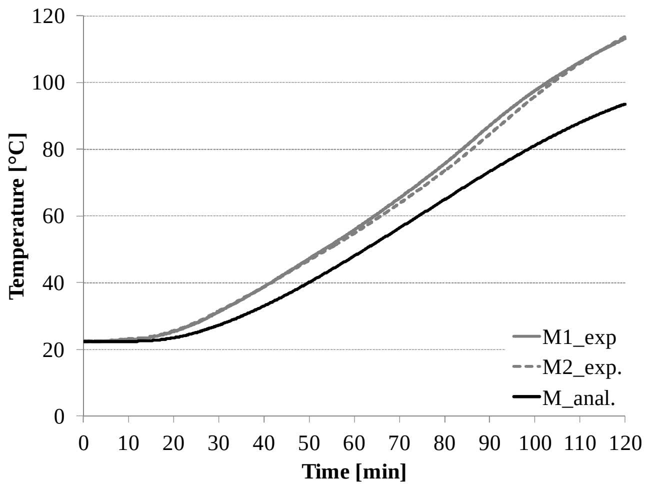

Figure C.88 – Experimental and analytical temperature-time curves thermocouples M

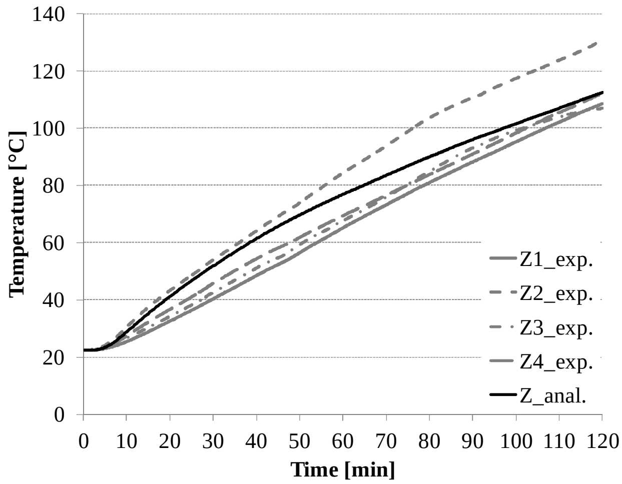

Figure C.89 – Experimental and analytical temperature-time curves thermocouples Z

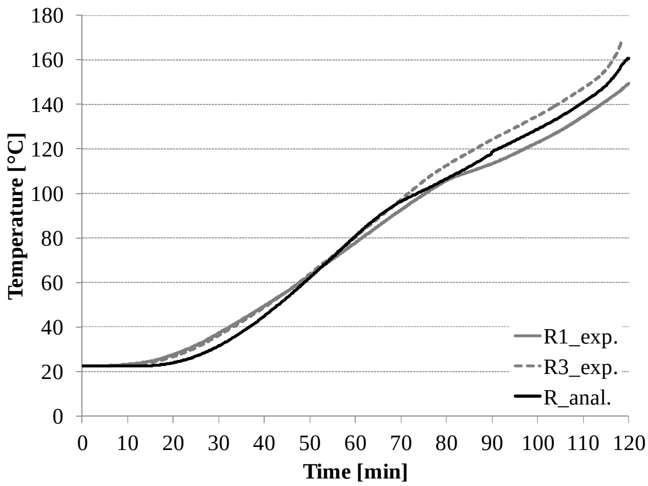

Figure C.90 – Experimental and analytical temperature-time curves thermocouples R

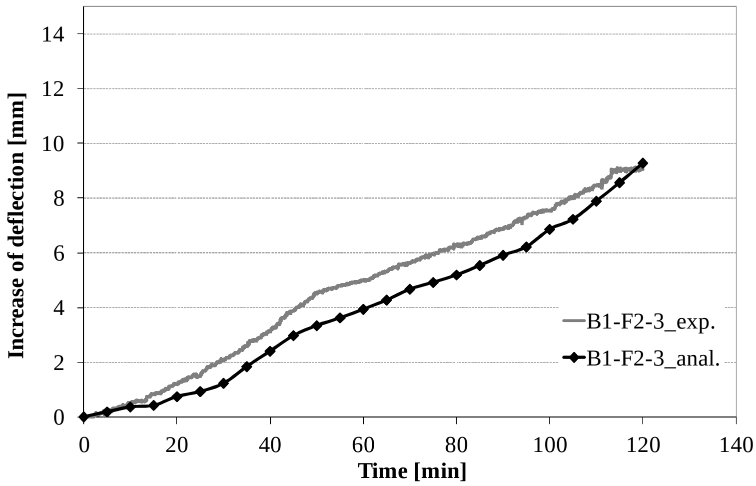

Figure C.91 – Experimental and analytical increase of midspan deflections as a function of time beam B1-F2-3

C.4.10 Beam B2-F2-1

C.4.10.1 Geometry of the specimen

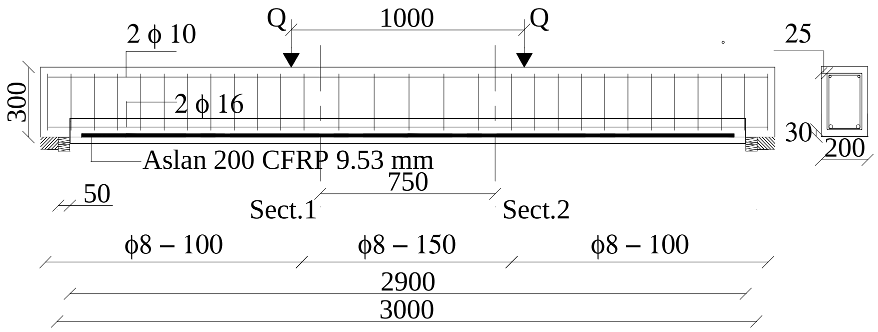

Figure C.92 – Geometry beam B2-F2-1

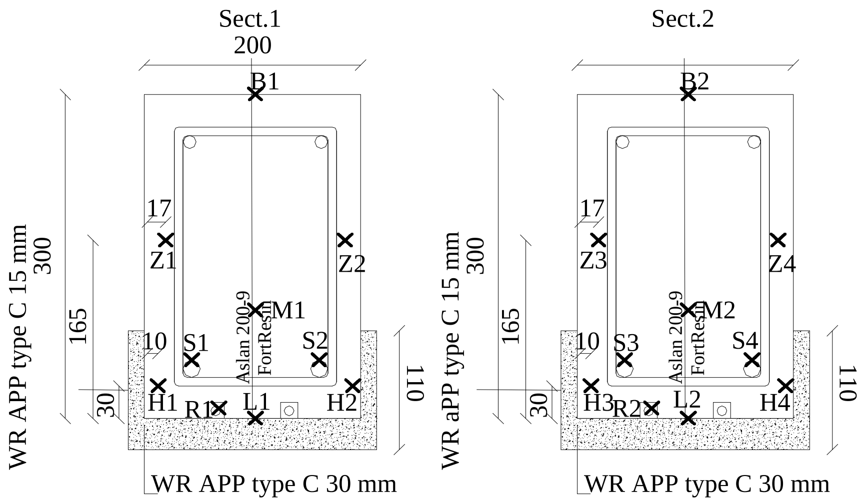

Figure C.93 – Insulation details and position thermocouples beam B2-F2-1

C.4.10.2 Time-temperatures and time- increase of deflection curves

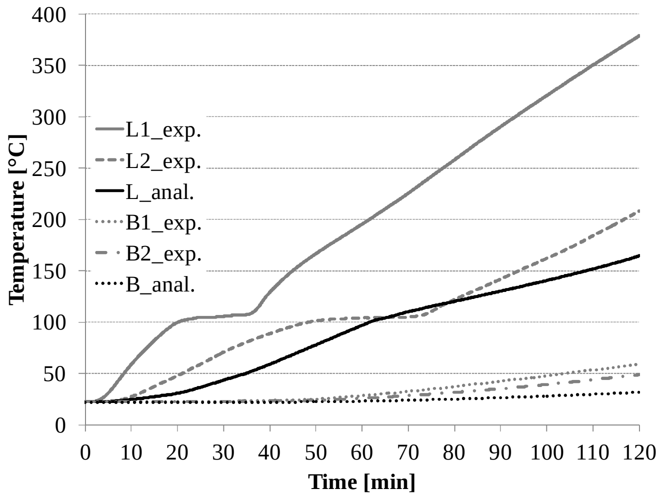

Figure C.94 – Experimental and analytical temperature-time curves thermocouples L and B

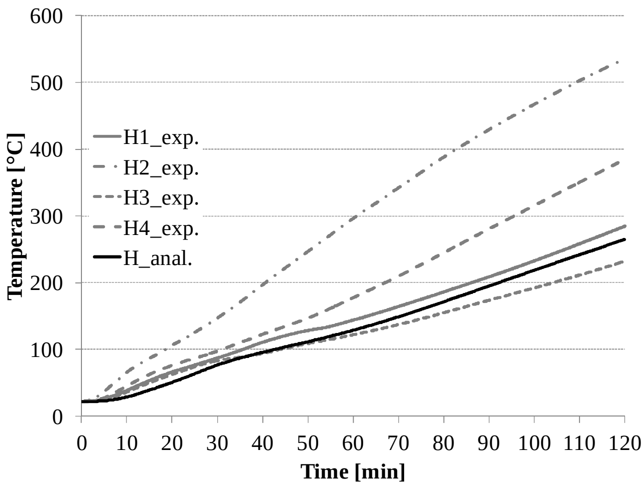

Figure C.95 – Experimental and analytical temperature-time curves thermocouples H

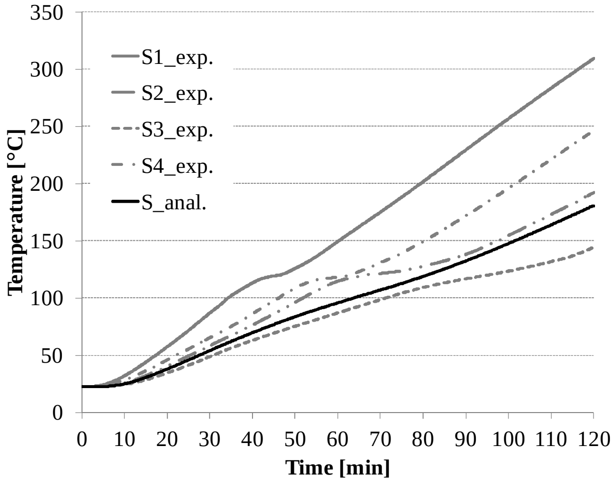

Figure C.96 – Experimental and analytical temperature-time curves thermocouples S

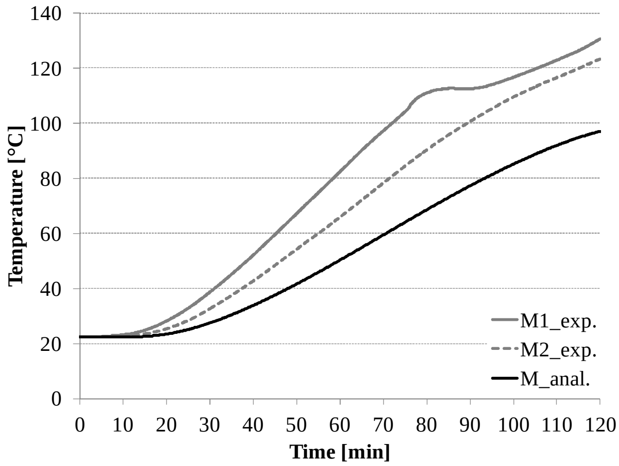

Figure C.97 – Experimental and analytical temperature-time curves thermocouples M

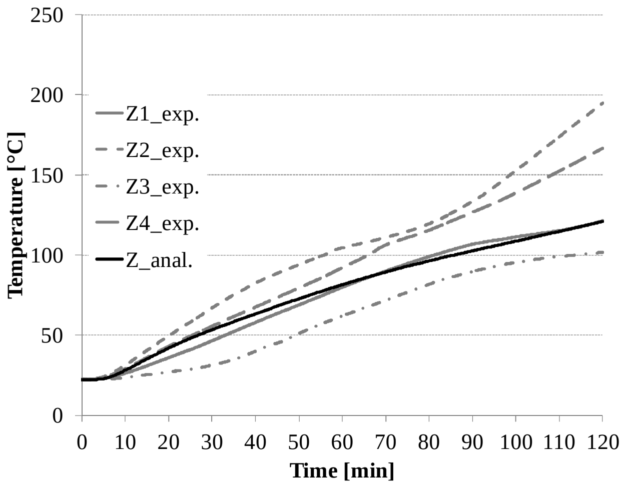

Figure C.98 – Experimental and analytical temperature-time curves thermocouples Z

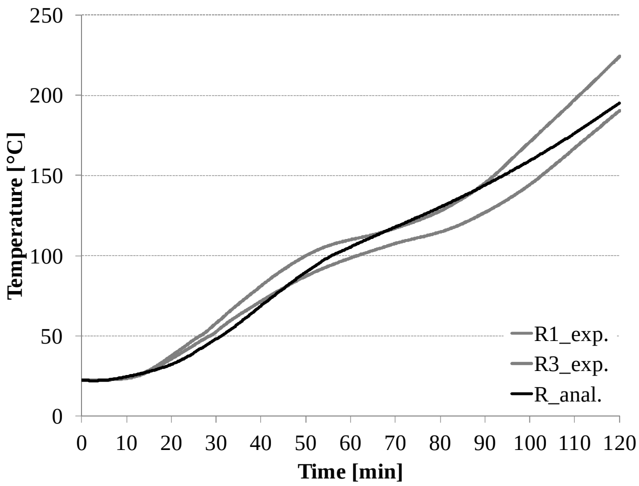

Figure C.99 – Experimental and analytical temperature-time curves thermocouples R

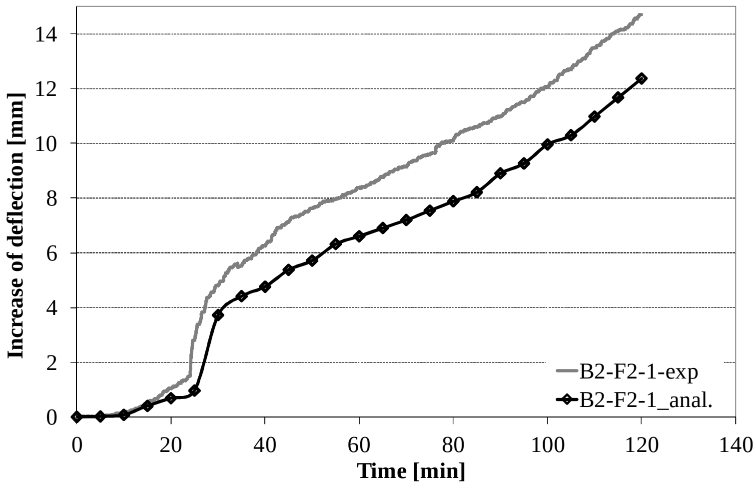

Figure C.100 – Experimental and analytical increase of midspan deflections as a function of time beam B2-F2-1

C.4.11 Beam B2-F2-2

C.4.11.1 Geometry of the specimen

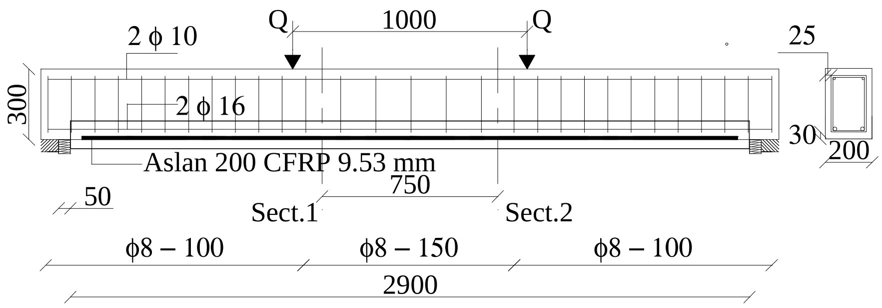

Figure C.101 – Geometry beam B2-F2-2

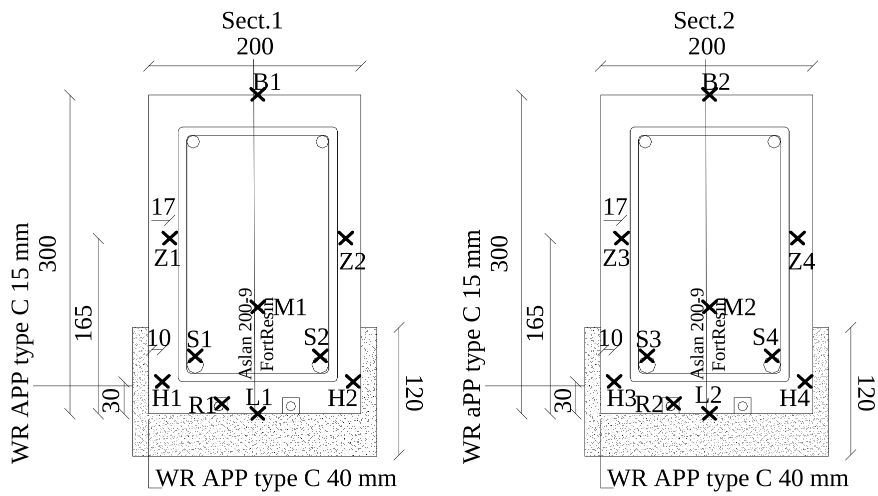

Figure C.102 – Insulation details and position thermocouples beam B2-F2-2

C.4.11.2 Time-temperatures and time- increase of deflection curves

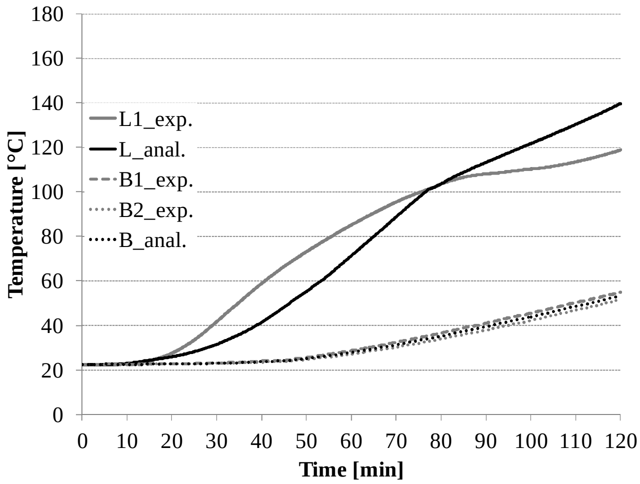

Figure C.103 – Experimental and analytical temperature-time curves thermocouples L and B

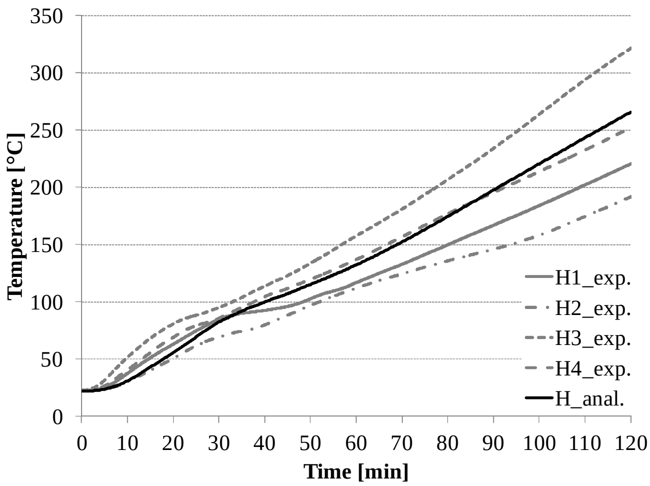

Figure C.104 – Experimental and analytical temperature-time curves thermocouples H

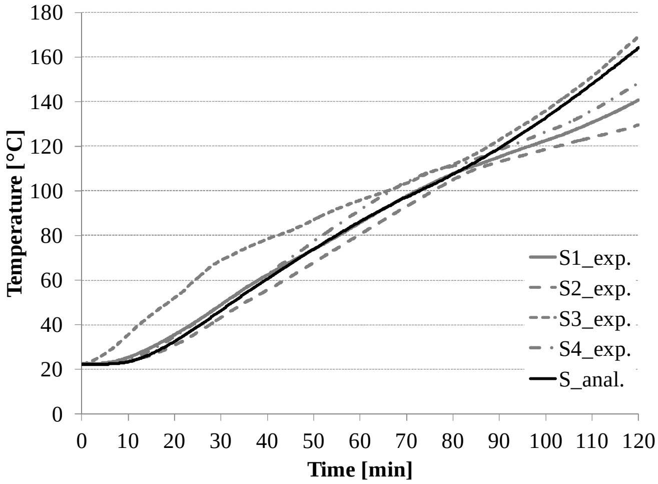

Figure C.105 – Experimental and analytical temperature-time curves thermocouples S

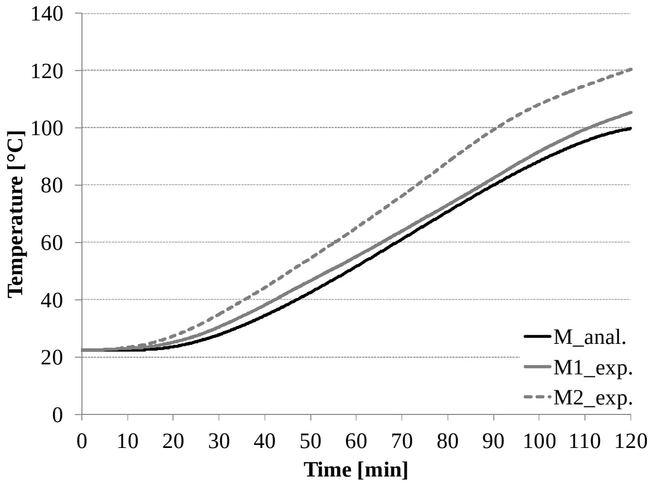

Figure C.106 – Experimental and analytical temperature-time curves thermocouples M

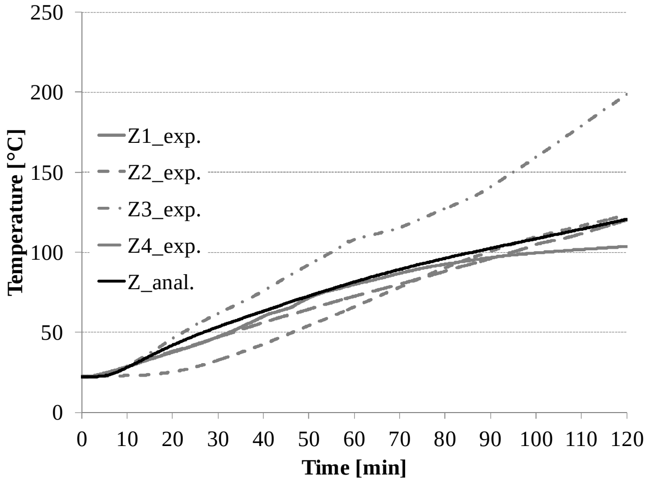

Figure C.107 – Experimental and analytical temperature-time curves thermocouples Z

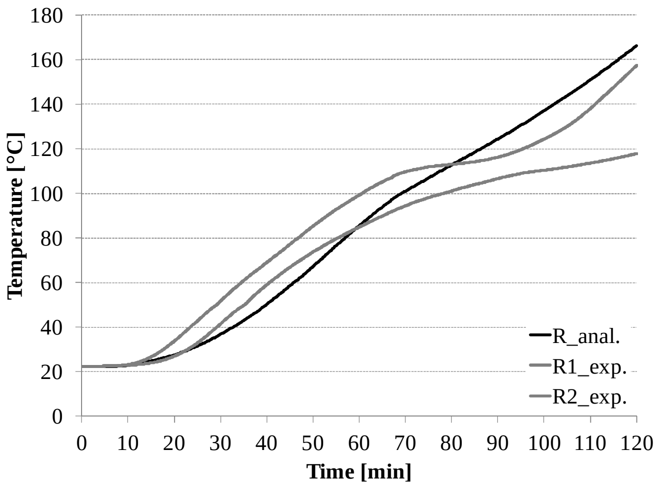

Figure C.108 – Experimental and analytical temperature-time curves thermocouples R

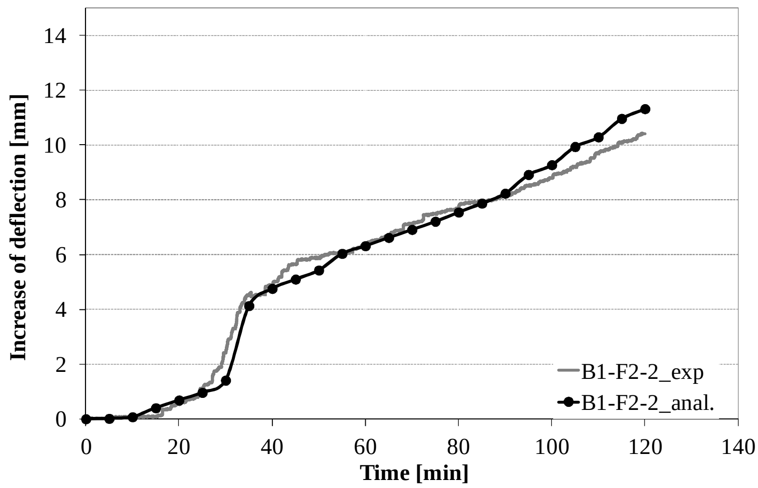

Figure C.109 – Experimental and analytical increase of midspan deflections as a function of time beam B2-F2-2

C.4.12 Beam B1-F3-1

C.4.12.1 Geometry of the specimen

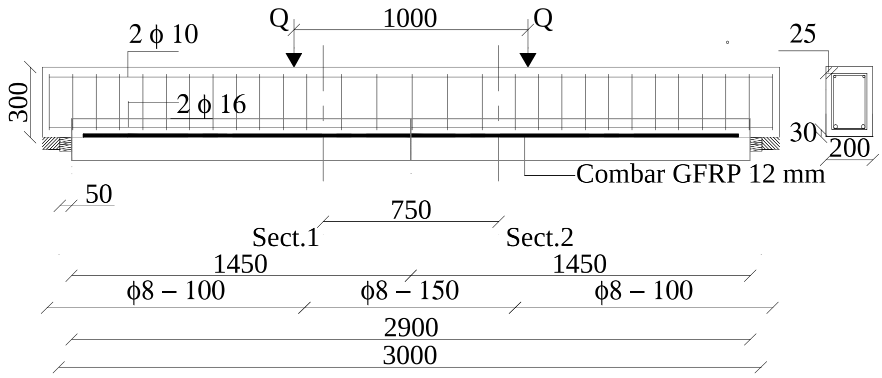

Figure C.110 – Geometry beam B1-F3-1

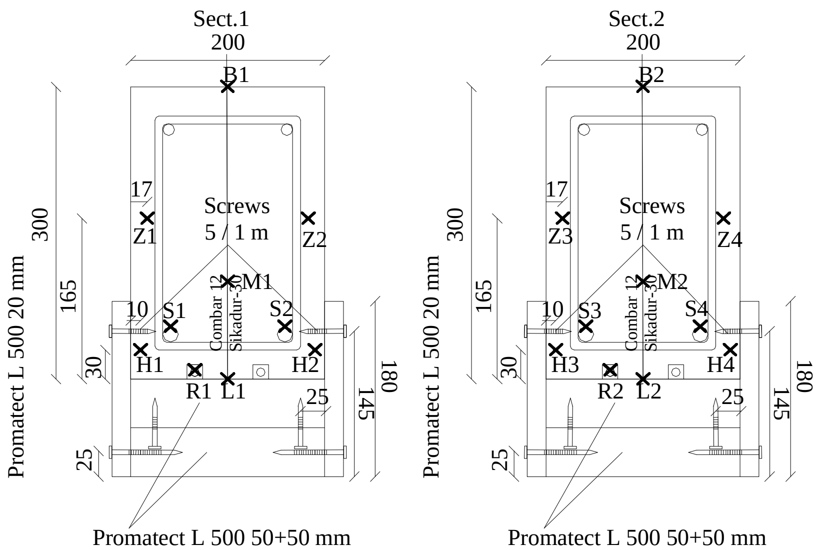

Figure C.111 – Insulation details and position thermocouples beam B1-F3-1

C.4.12.2 Time-temperatures and time- increase of deflection curves

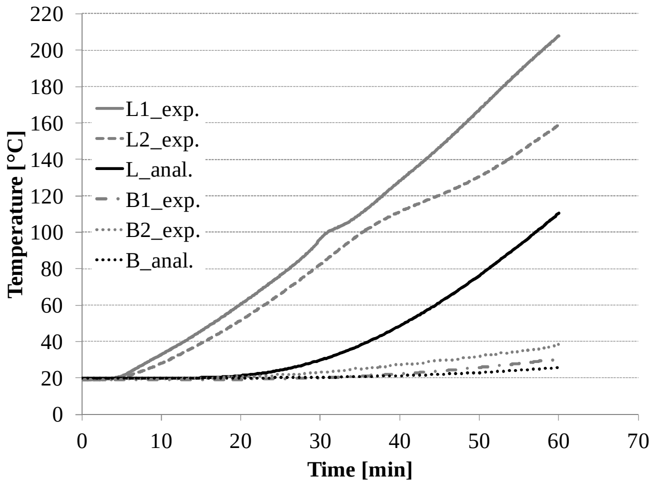

Figure C.112 – Experimental and analytical temperature-time curves thermocouples L and B

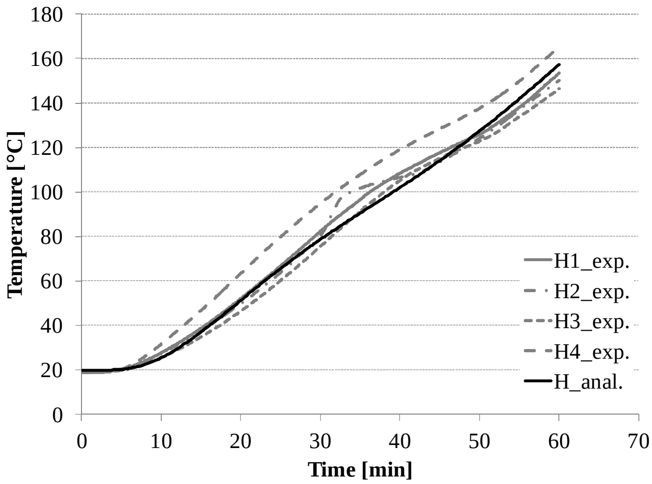

Figure C.113 – Experimental and analytical temperature-time curves thermocouples H

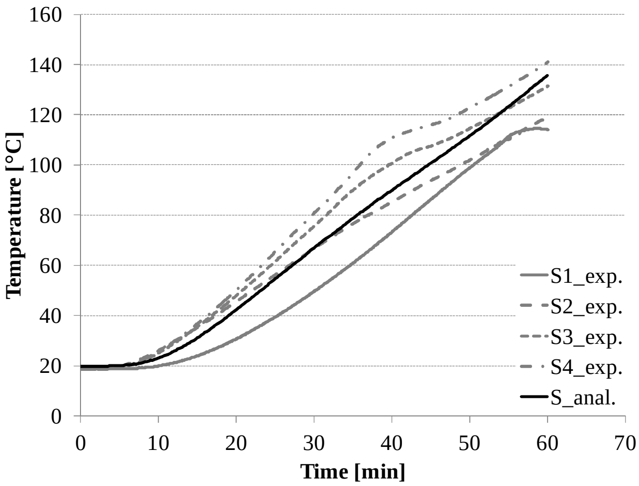

Figure C.114 – Experimental and analytical temperature-time curves thermocouples S

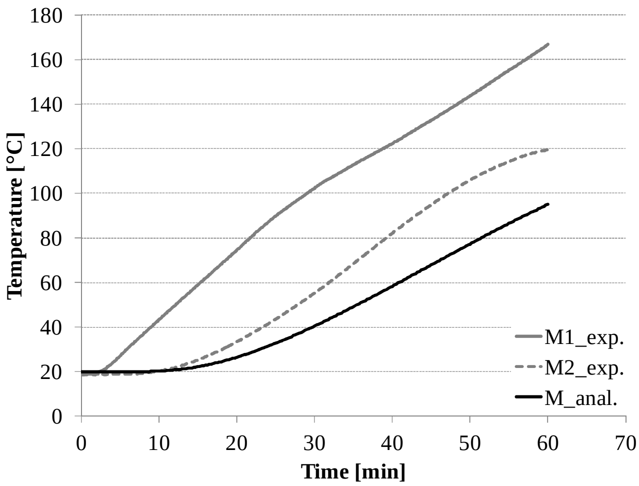

Figure C.115 – Experimental and analytical temperature-time curves thermocouples M

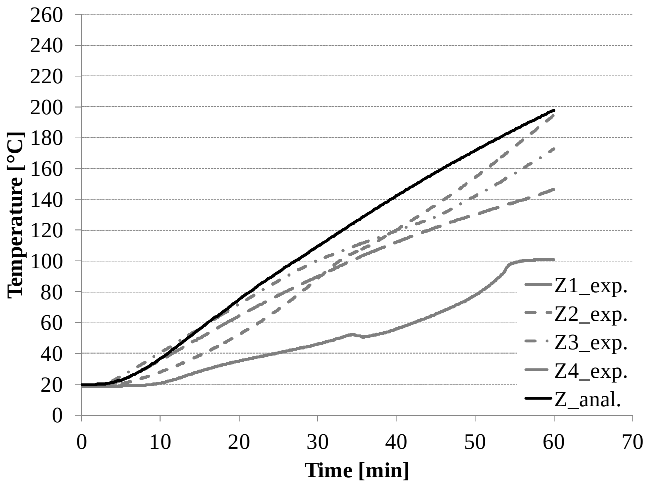

Figure C.116 – Experimental and analytical temperature-time curves thermocouples Z

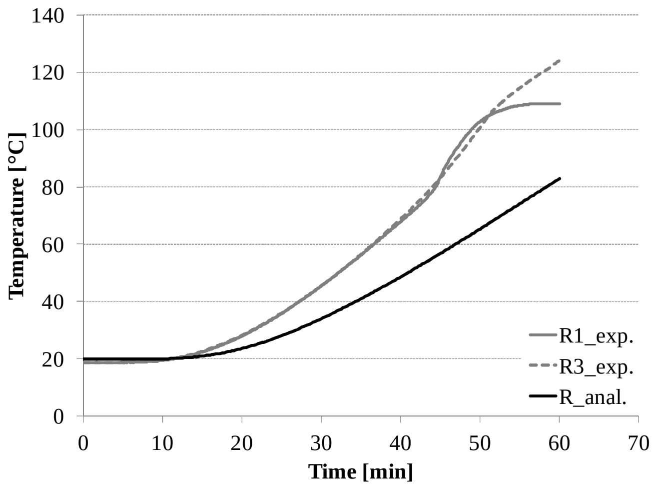

Figure C.117 – Experimental and analytical temperature-time curves thermocouples R

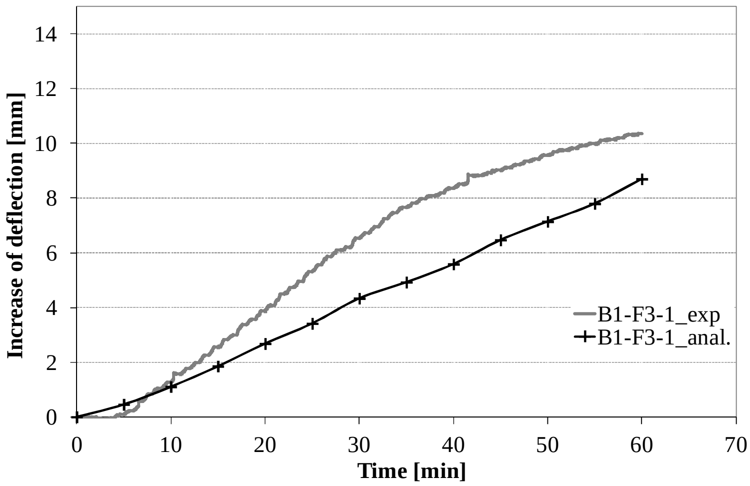

Figure C.118 – Experimental and analytical increase of midspan deflections as a function of time beam B1-F3-1

C.4.13 Beam B2-F3-1

C.4.13.1 Geometry of the specimen

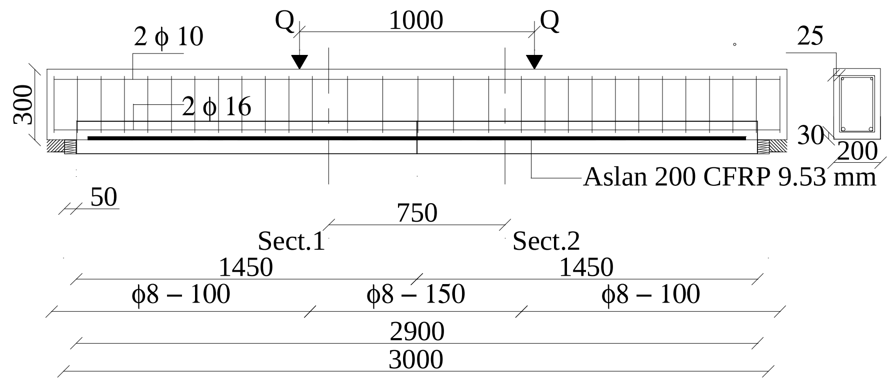

Figure C.119 – Geometry beam B2-F3-1

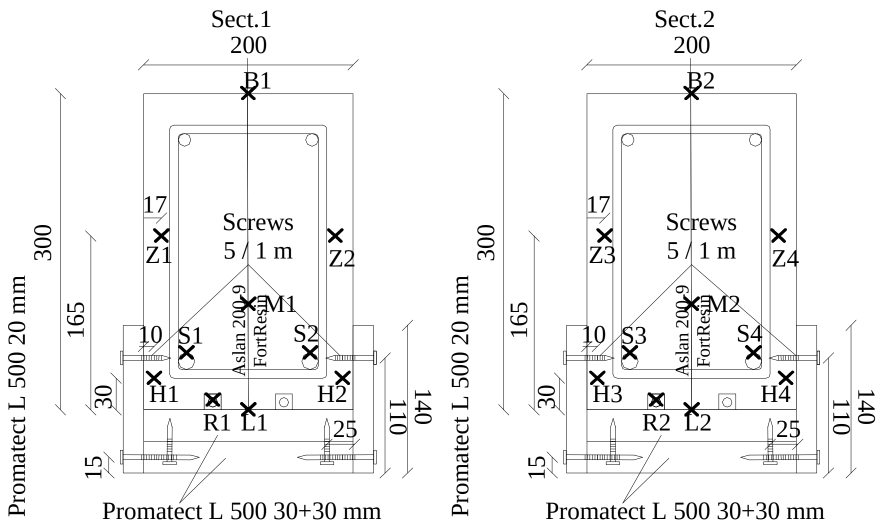

Figure C.120 – Insulation details and position thermocouples beam B2-F3-1

C.4.13.2 Time-temperatures and time- increase of deflection curves

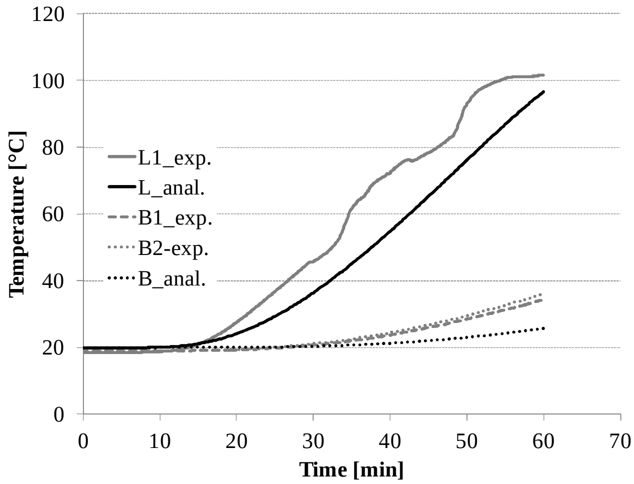

Figure C.121 – Experimental and analytical temperature-time curves thermocouples L and B

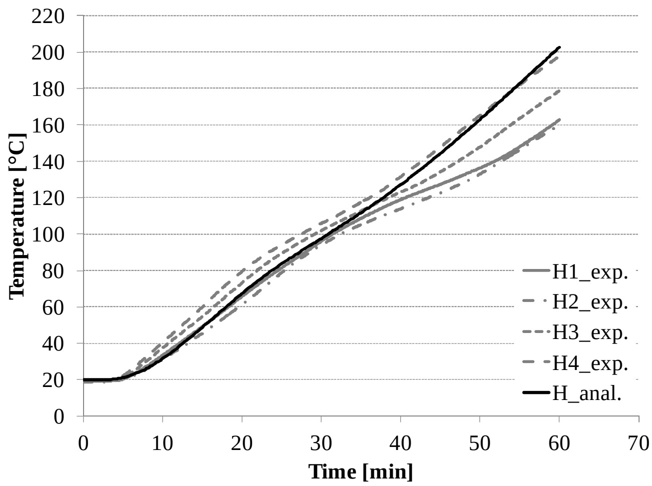

Figure C.122 – Experimental and analytical temperature-time curves thermocouples H

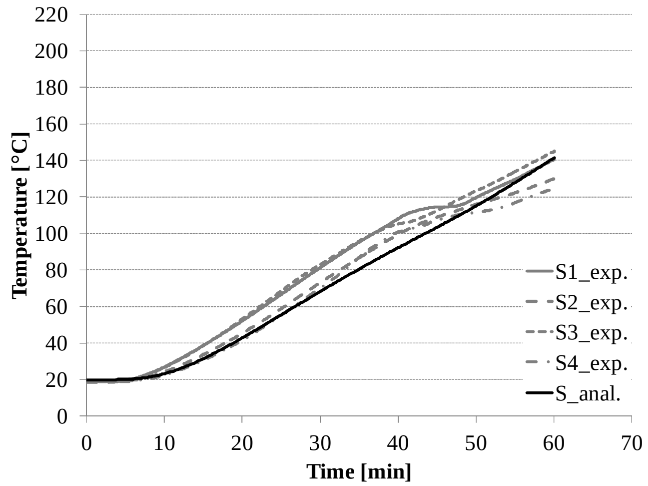

Figure C.123 – Experimental and analytical temperature-time curves thermocouples S

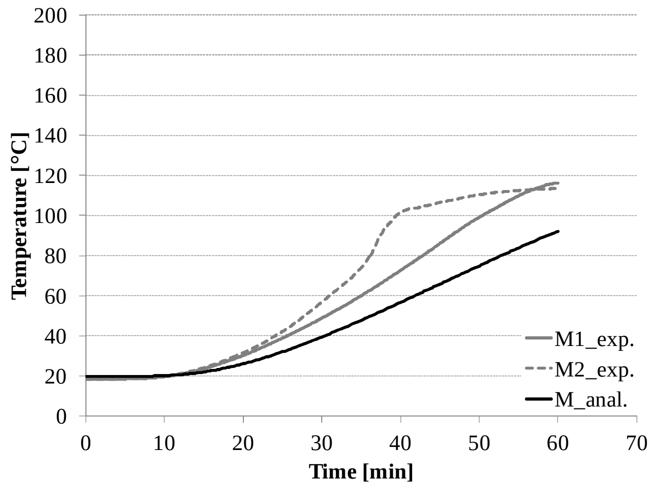

Figure C.124 – Experimental and analytical temperature-time curves thermocouples M

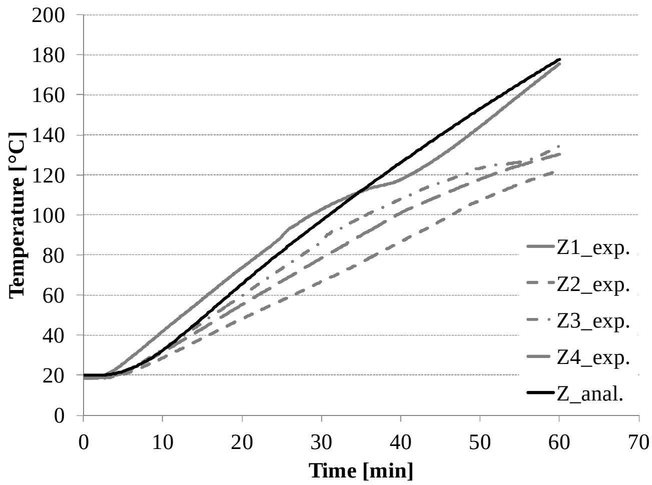

Figure C.125 – Experimental and analytical temperature-time curves thermocouples Z

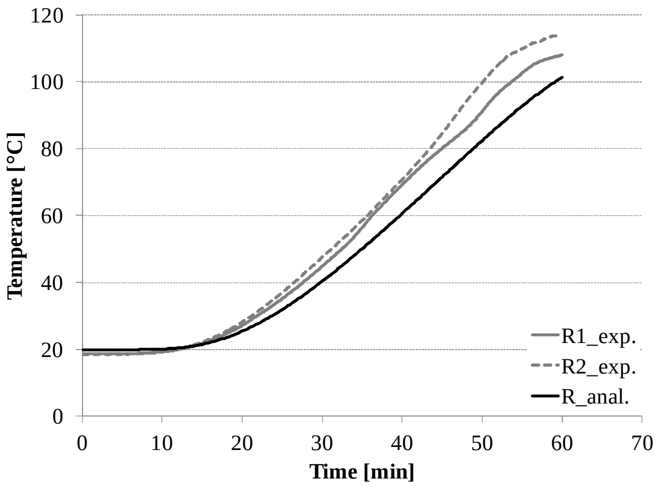

Figure C.126 – Experimental and analytical temperature-time curves thermocouples R

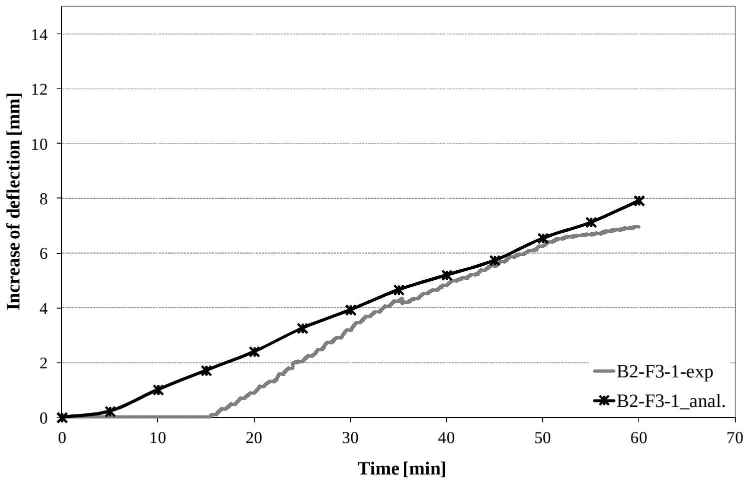

Figure C.127 – Experimental and analytical increase of midspan deflections as a function of time beam B2-F3-1

C.4.14 Beam B1-F3-2

C.4.14.1 Geometry of the specimen

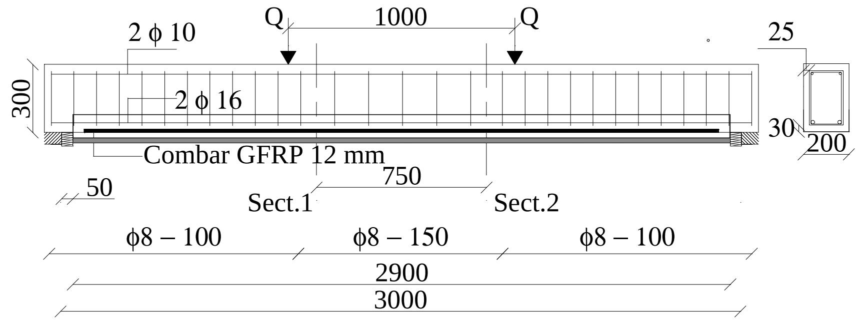

Figure C.128 – Geometry beam B1-F3-2

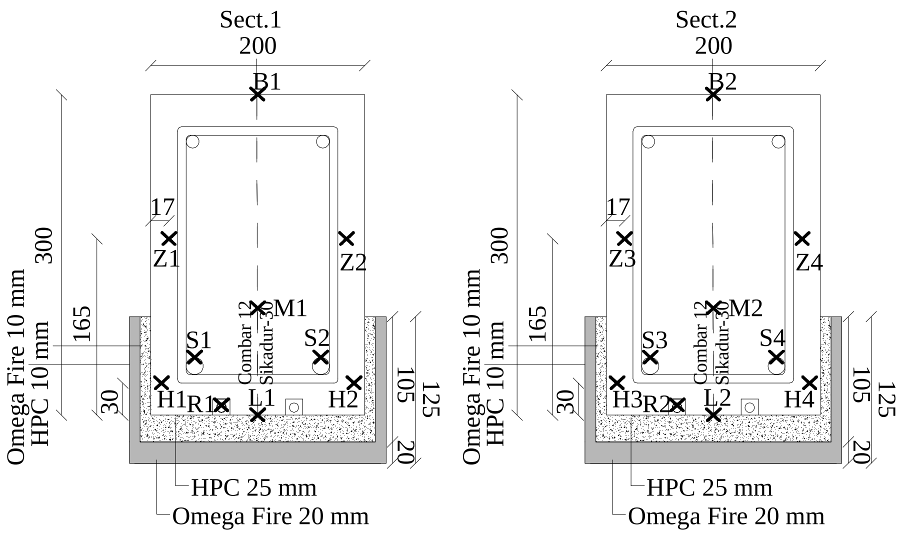

Figure C.129 – Insulation details and position thermocouples beam B1-F3-2

C.4.14.2 Time-temperatures and time- increase of deflection curves

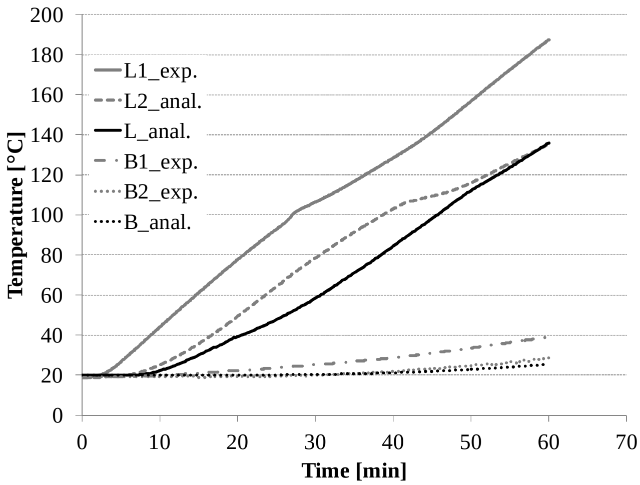

Figure C.130 – Experimental and analytical temperature-time curves thermocouples L and B

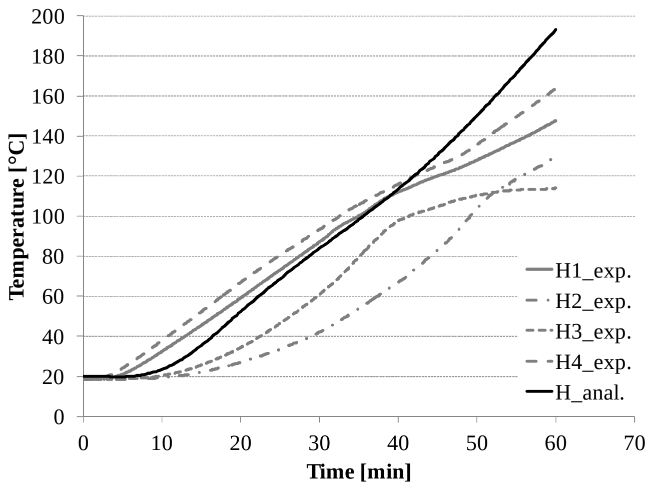

Figure C.131 – Experimental and analytical temperature-time curves thermocouples H

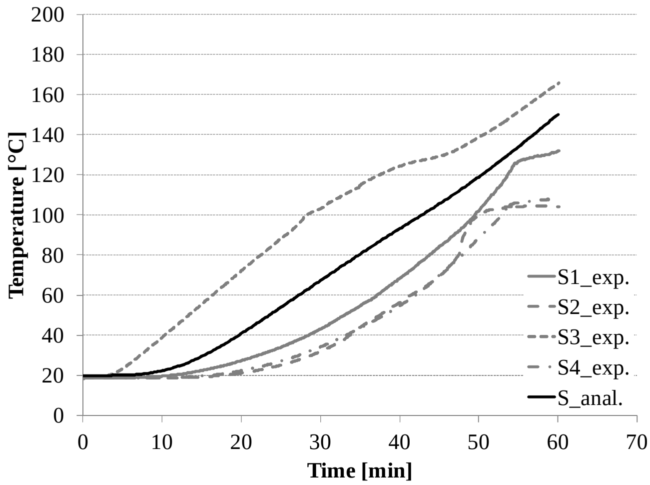

Figure C.132 – Experimental and analytical temperature-time curves thermocouples S

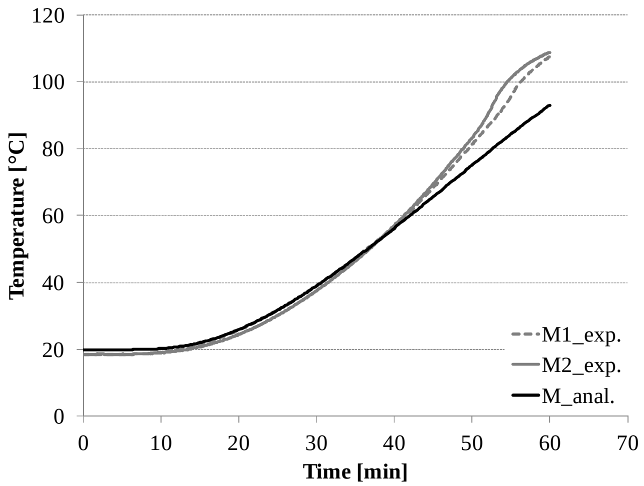

Figure C.133 – Experimental and analytical temperature-time curves thermocouples M

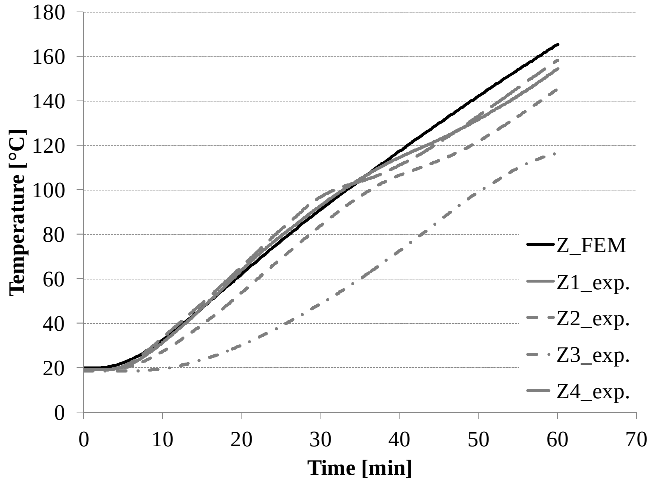

Figure C.134 – Experimental and analytical temperature-time curves thermocouples Z

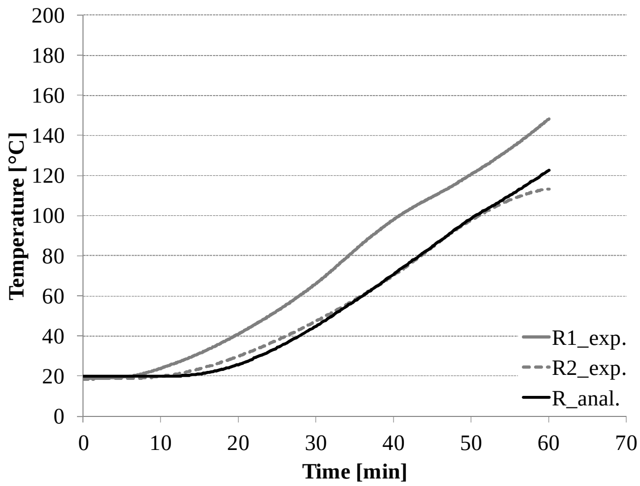

Figure C.135 – Experimental and analytical temperature-time curves thermocouples R

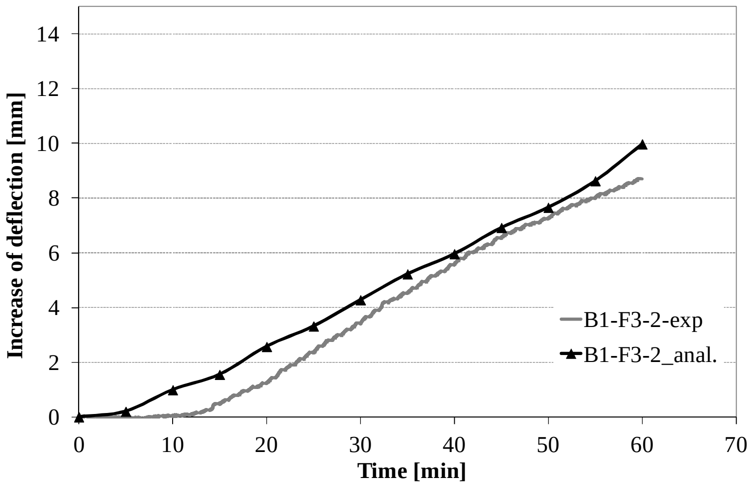

Figure C.136 – Experimental and analytical increase of midspan deflections as a function of time beam B1-F3-2

C.4.15 Beam B1-F3-3

C.4.15.1 Geometry of the specimen

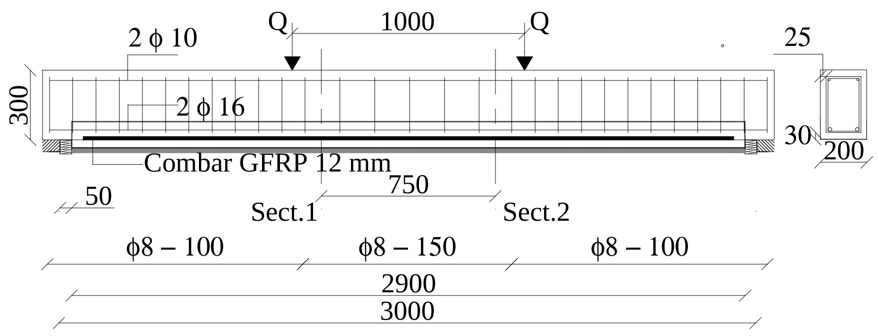

Figure C.137 – Geometry beam B1-F3-3

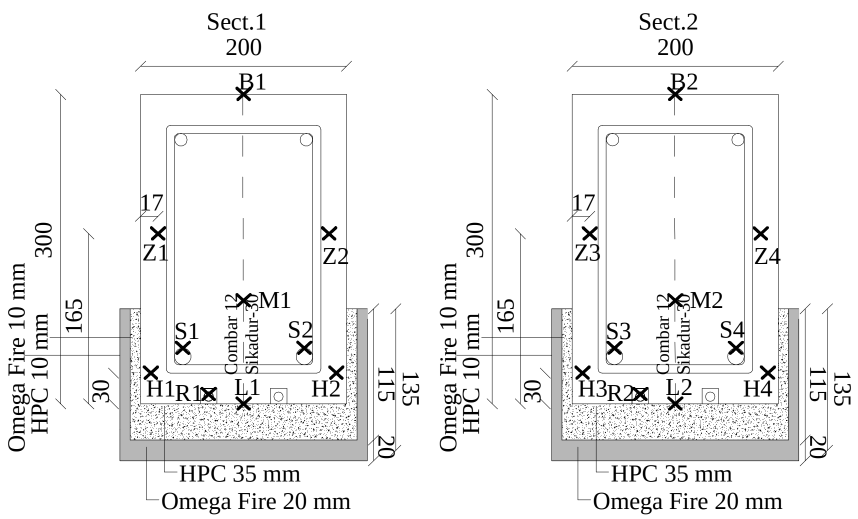

Figure C.138 – Insulation details and position thermocouples beam B1-F3-3

C.4.15.2 Time-temperatures and time- increase of deflection curves

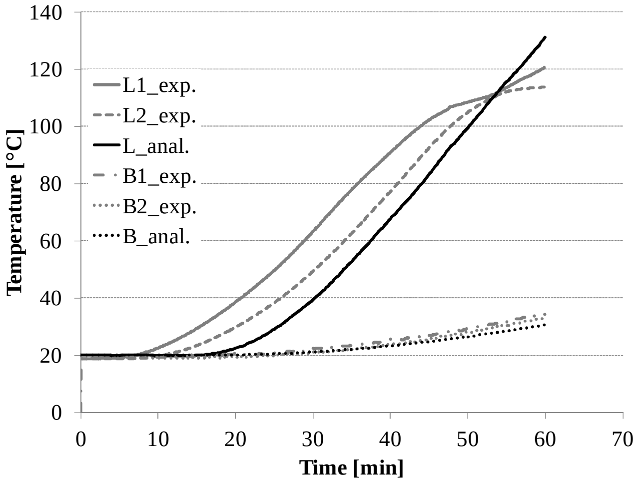

Figure C.139 – Experimental and analytical temperature-time curves thermocouples L and B

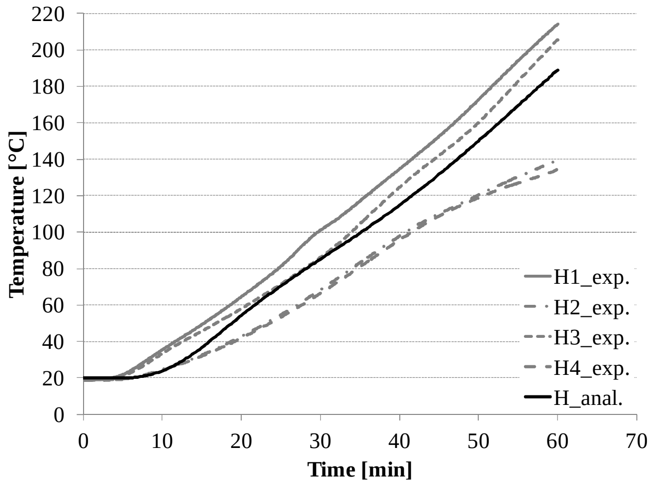

Figure C.140 – Experimental and analytical temperature-time curves thermocouples H

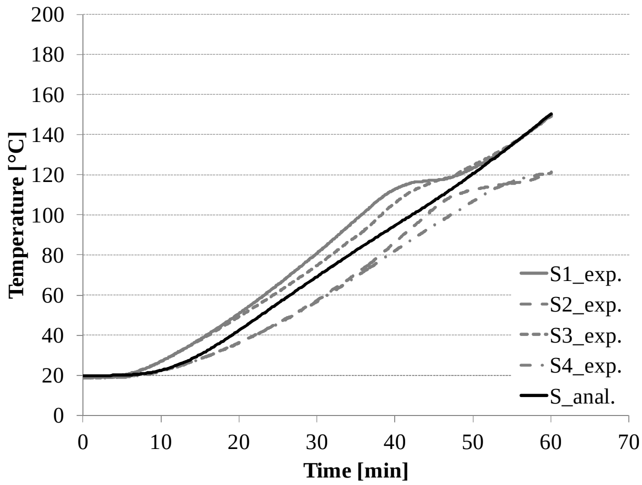

Figure C.141 – Experimental and analytical temperature-time curves thermocouples S

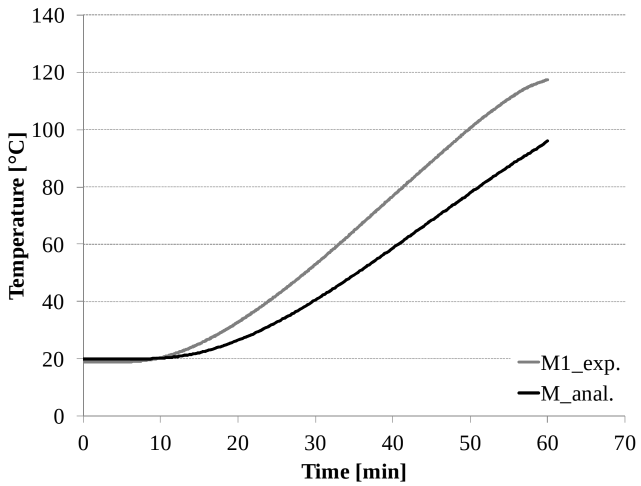

Figure C.142 – Experimental and analytical temperature-time curves thermocouples M

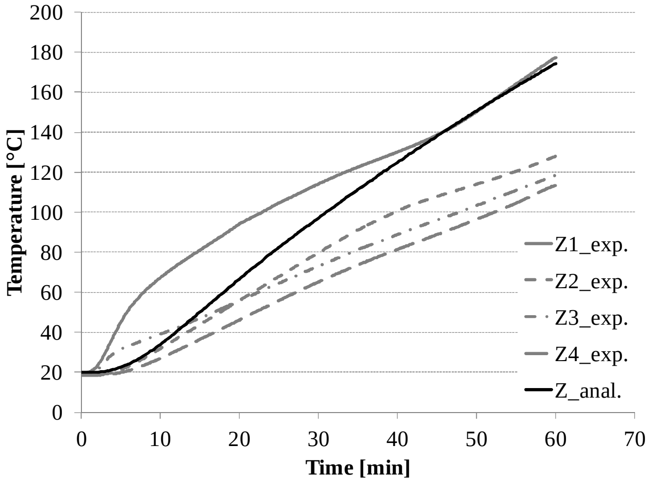

Figure C.143 – Experimental and analytical temperature-time curves thermocouples Z

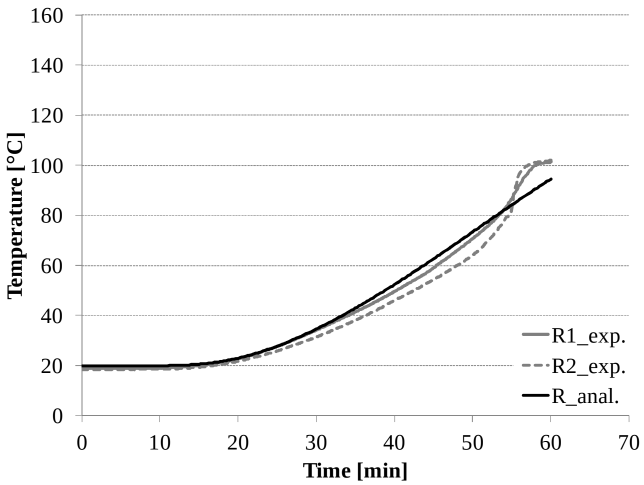

Figure C.144 – Experimental and analytical temperature-time curves thermocouples R

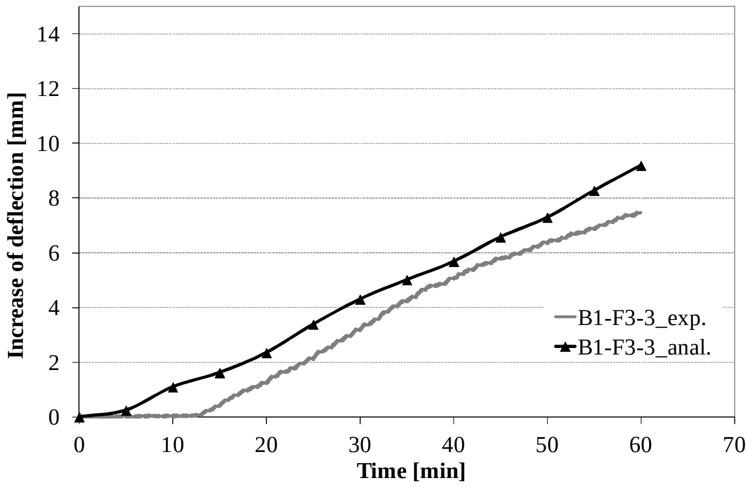

Figure C.145 – Experimental and analytical increase of midspan deflections as a function of time beam B1-F3-3

C.4.16 Beam B1-F3-4

C.4.16.1 Geometry of the specimen

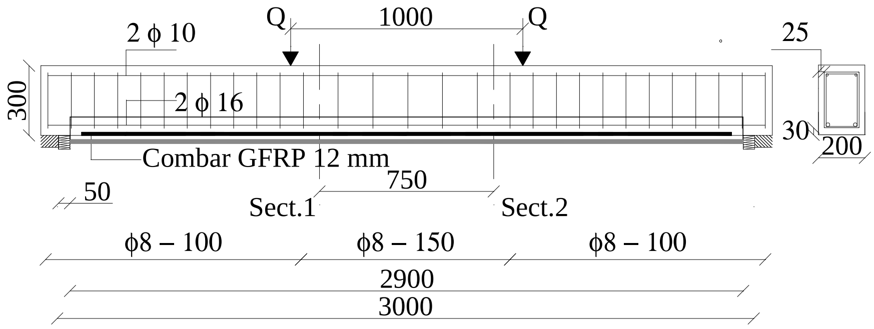

Figure C.146 – Geometry beam B1-F3-4

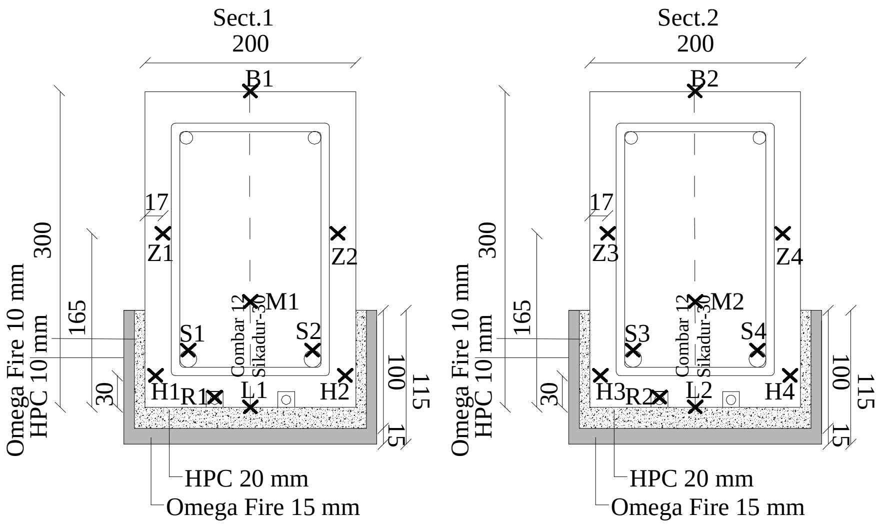

Figure C.147 – Insulation details and position thermocouples beam B1-F3-4

C.4.16.2 Time-temperatures and time- increase of deflection curves

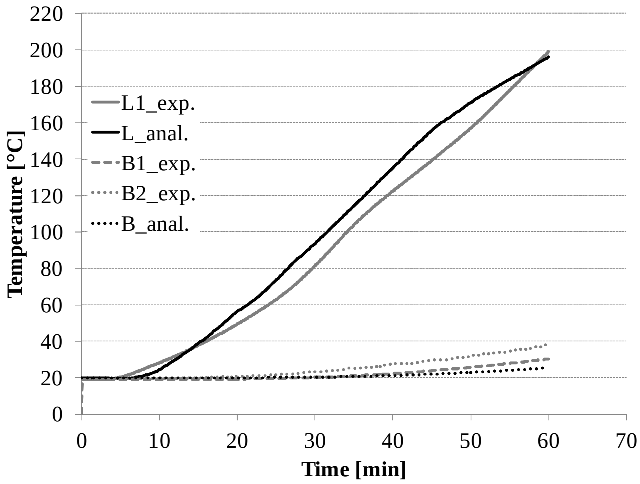

Figure C.148 – Experimental and analytical temperature-time curves thermocouples L and B

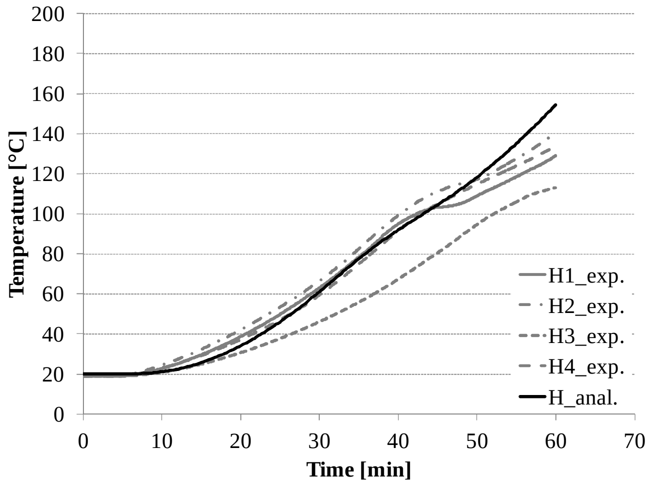

Figure C.149 – Experimental and analytical temperature-time curves thermocouples H

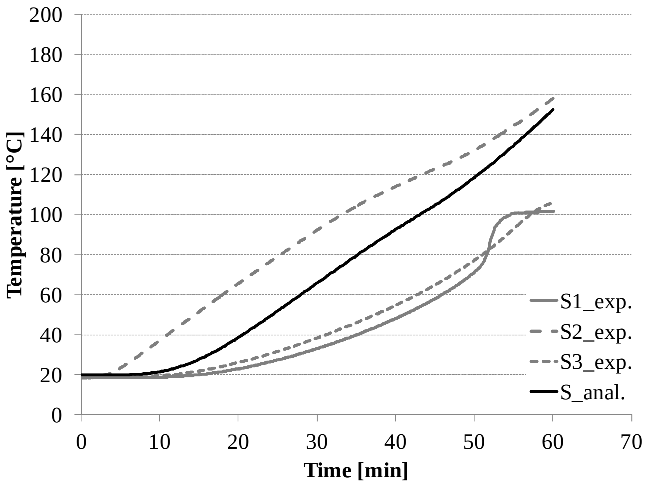

Figure C.150 – Experimental and analytical temperature-time curves thermocouples S

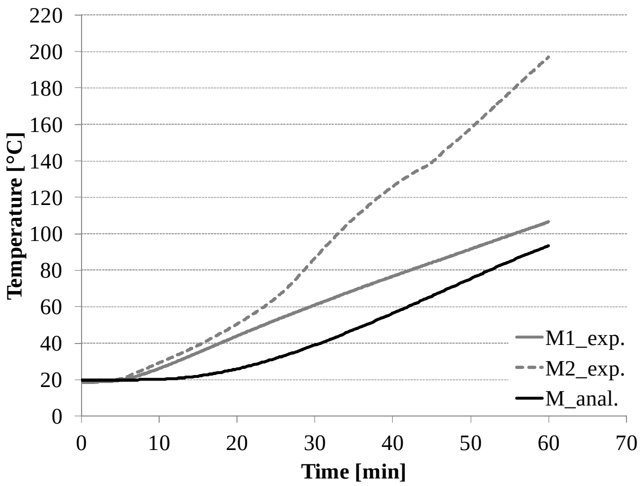

Figure C.151 – Experimental and analytical temperature-time curves thermocouples M

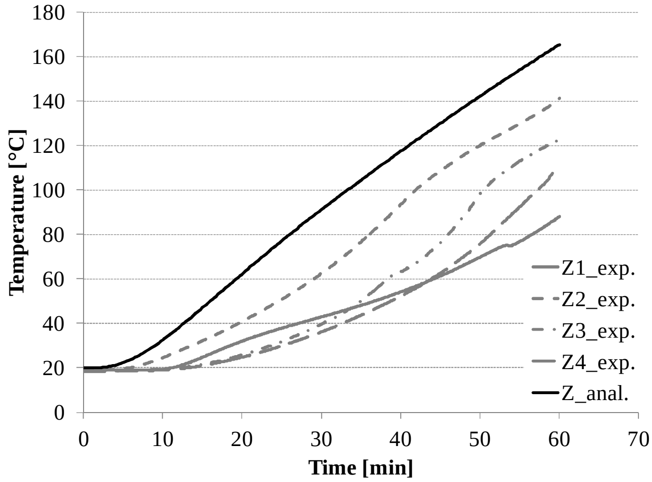

Figure C.152 – Experimental and analytical temperature-time curves thermocouples Z

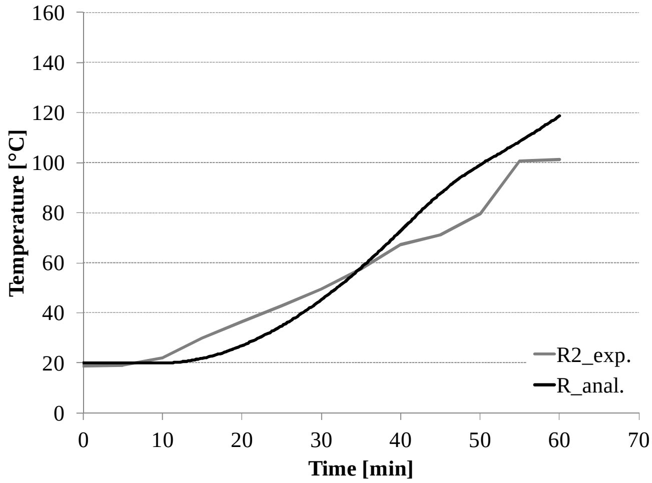

Figure C.153 – Experimental and analytical temperature-time curves thermocouples R

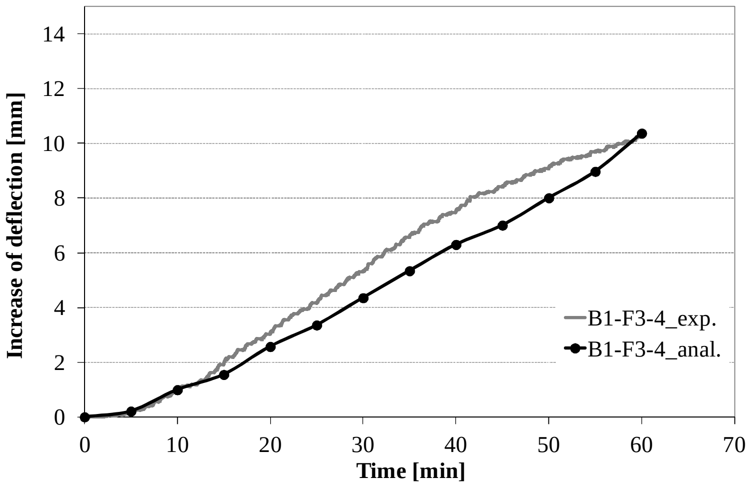

Figure C.154 – Experimental and analytical increase of midspan deflections as a function of time beam B1-F3-4

C.4.17 Beam B4-F3-1

C.4.17.1 Geometry of the specimen

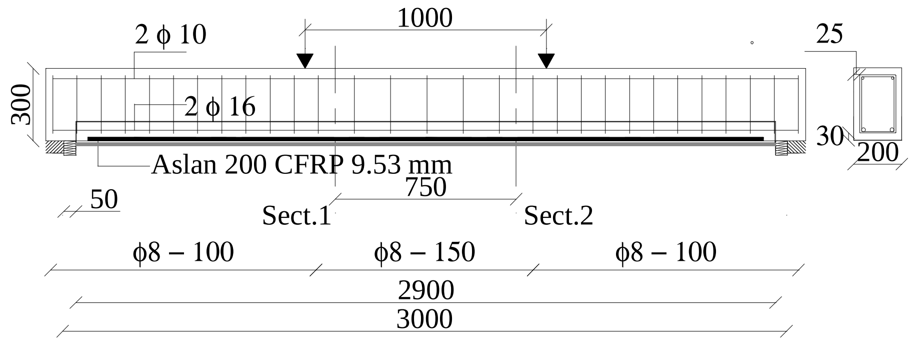

Figure C.155 – Geometry beam B4-F3-1

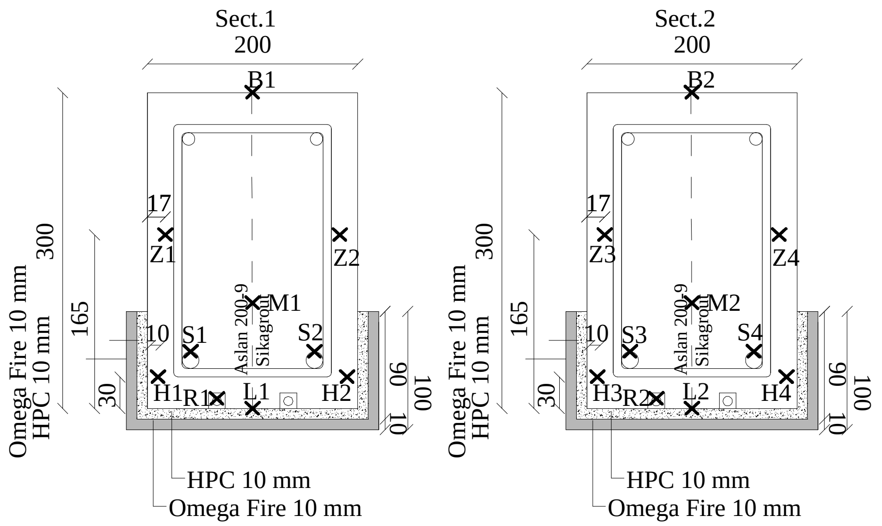

Figure C.156 – Insulation details and position thermocouples beam B4-F3-1

C.4.17.2 Time-temperatures and time- increase of deflection curves

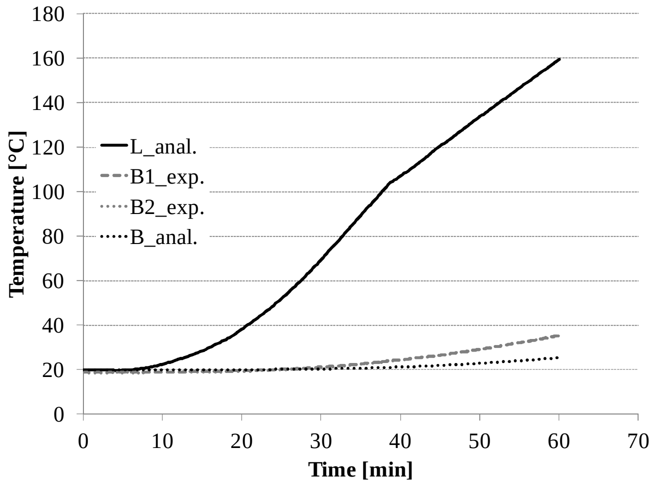

Figure C.157 – Experimental and analytical temperature-time curves thermocouples L and B

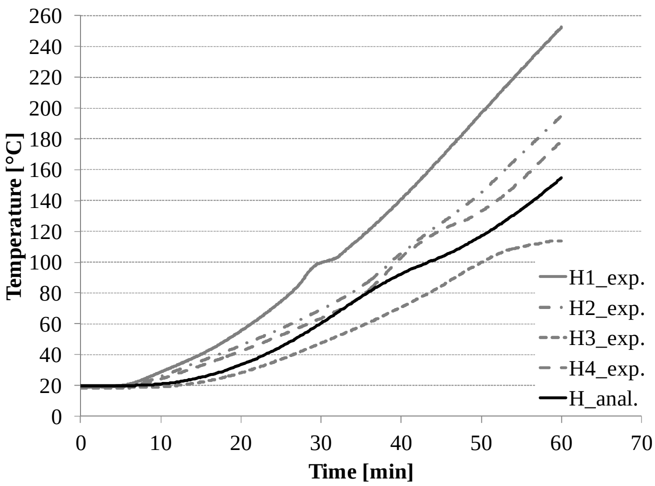

Figure C.158 – Experimental and analytical temperature-time curves thermocouples H

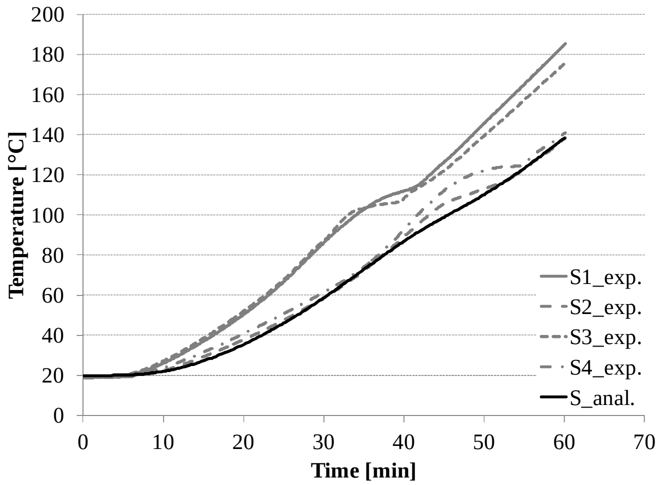

Figure C.159 – Experimental and analytical temperature-time curves thermocouples S

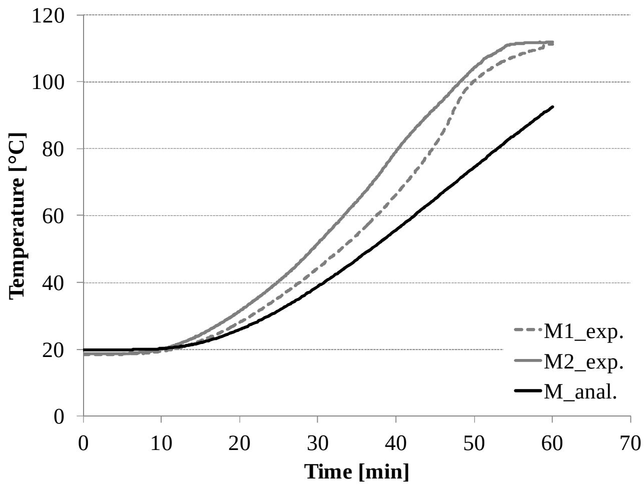

Figure C.160 – Experimental and analytical temperature-time curves thermocouples M

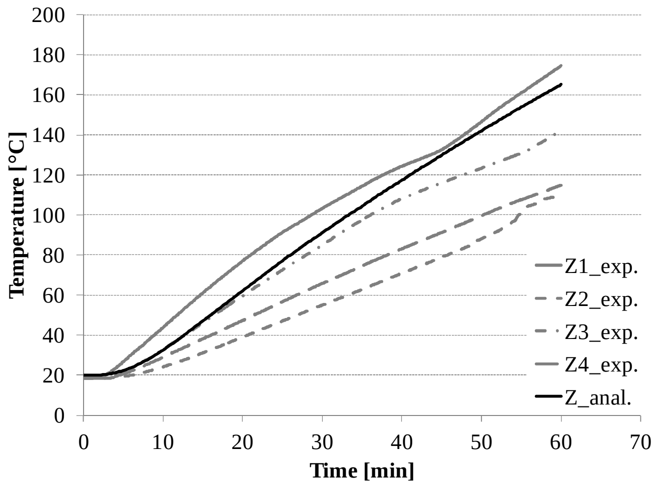

Figure C.161 – Experimental and analytical temperature-time curves thermocouples Z

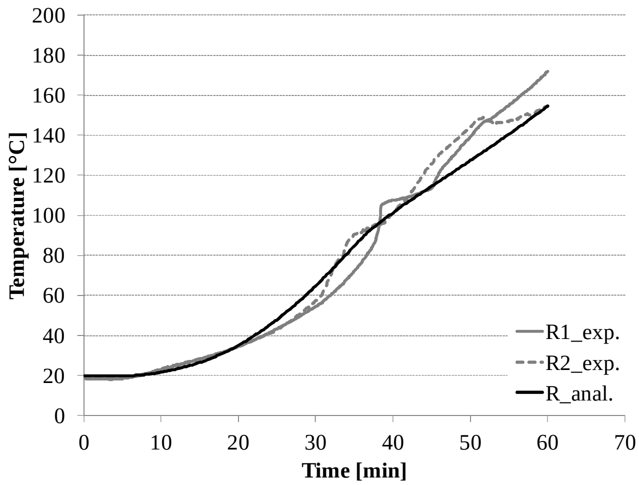

Figure C.162 – Experimental and analytical temperature-time curves thermocouples R

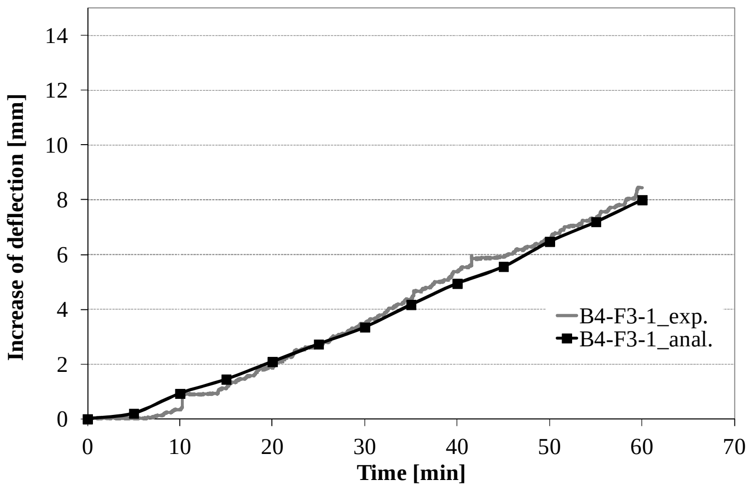

Figure C.163 – Experimental and analytical increase of midspan deflections as a function of time beam B4-F3-1

C.4.18 Beam B2-F4-1

C.4.18.1 Geometry of the specimen

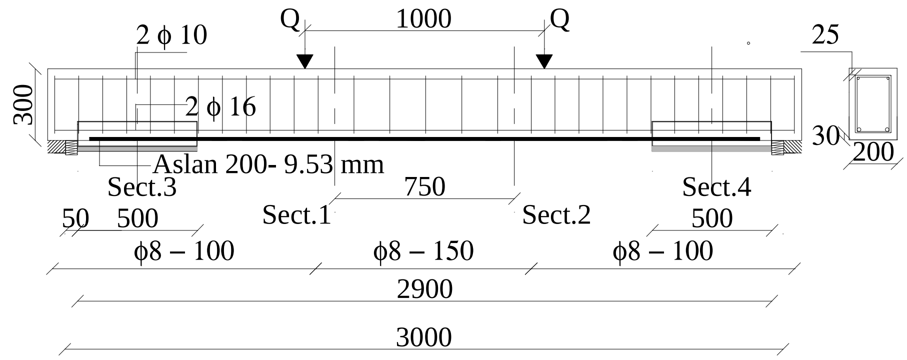

Figure C.164 – Geometry beam B2-F4-1

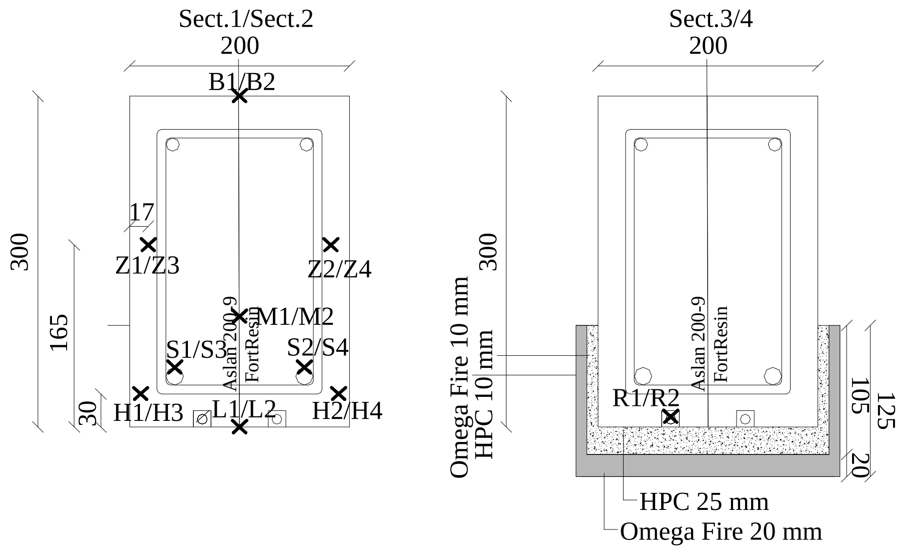

Figure C.165 – Insulation details and position thermocouples beam B2-F4-1

C.4.18.2 Geometry of the specimen

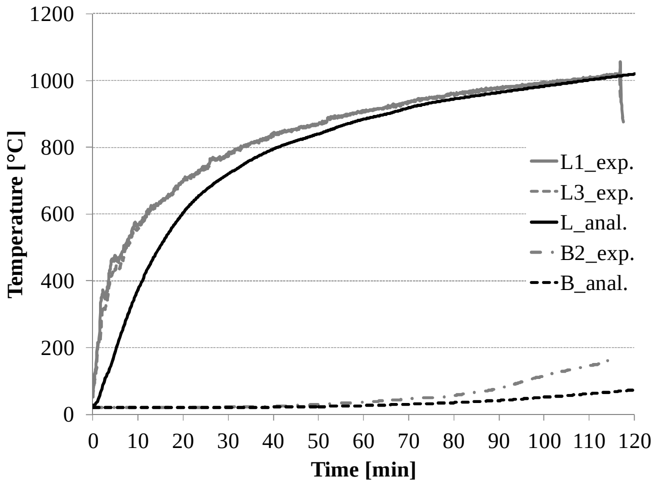

Figure C.166 – Experimental and analytical temperature-time curves thermocouples L and B

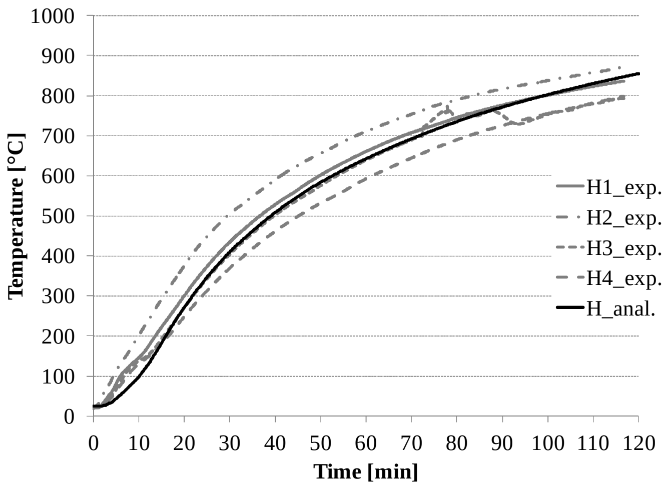

Figure C.167 – Experimental and analytical temperature-time curves thermocouples H

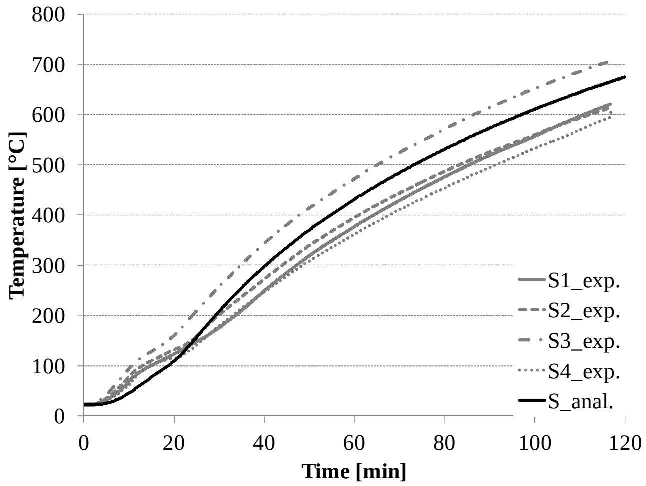

Figure C.168 – Experimental and analytical temperature-time curves thermocouples S

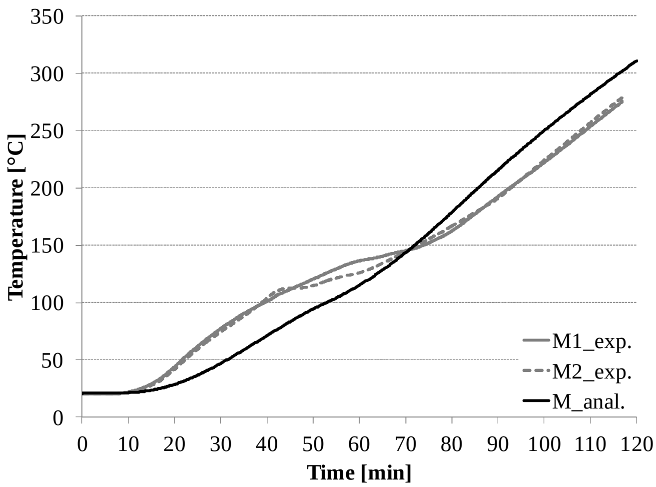

Figure C.169 – Experimental and analytical temperature-time curves thermocouples M

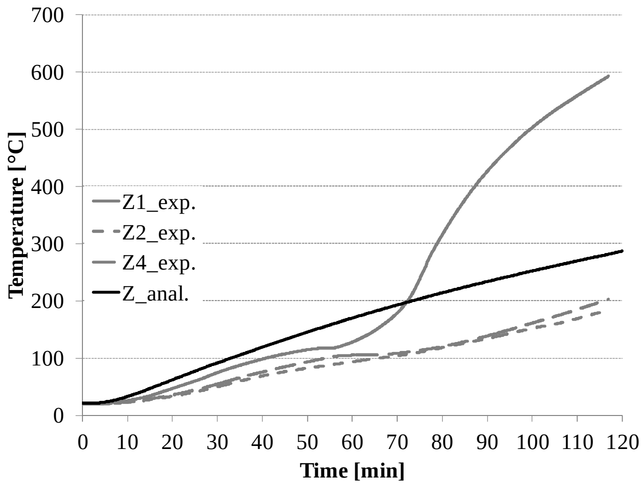

Figure C.170 – Experimental and analytical temperature-time curves thermocouples Z

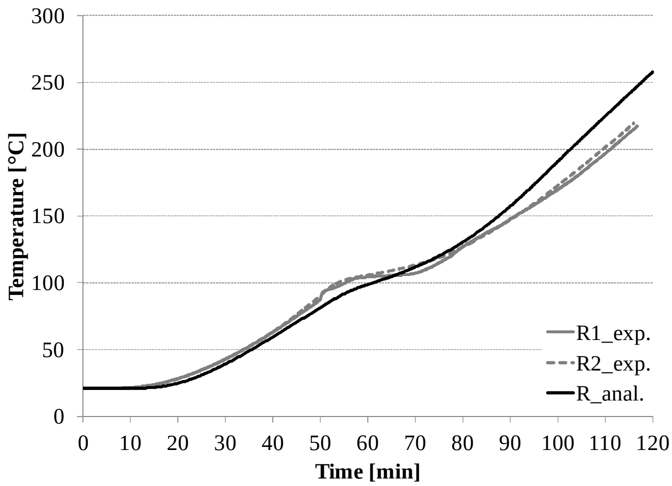

Figure C.171 – Experimental and analytical temperature-time curves thermocouples R

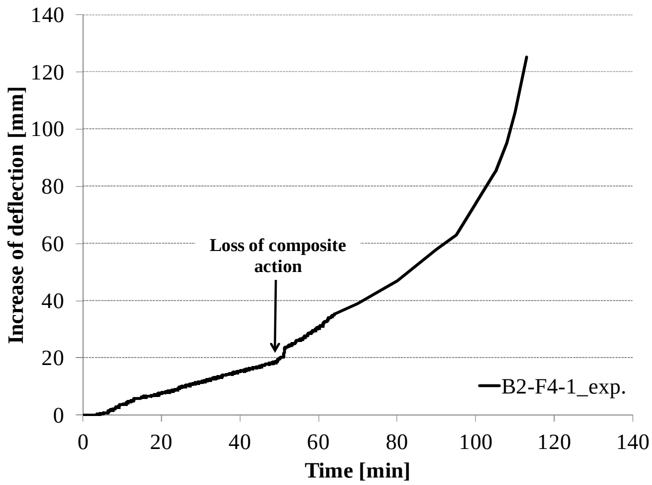

Figure C.172 – Experimental increase of midspan deflection as a function of time beam B2-F4-1

C.4.19 Beam B4-F4-1

C.4.19.1 Geometry of the specimen

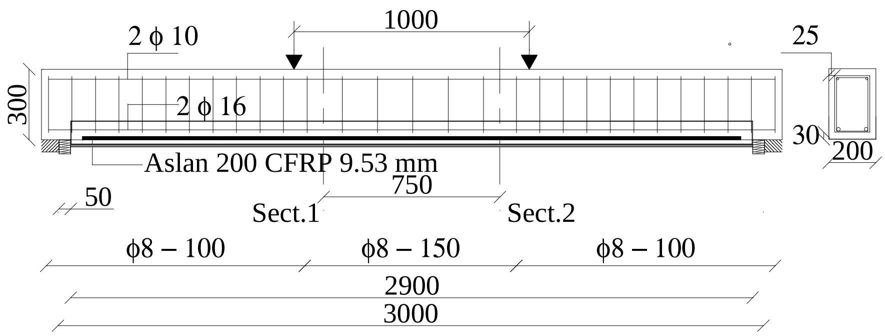

Figure C.173 – Geometry beam B4-F4-1

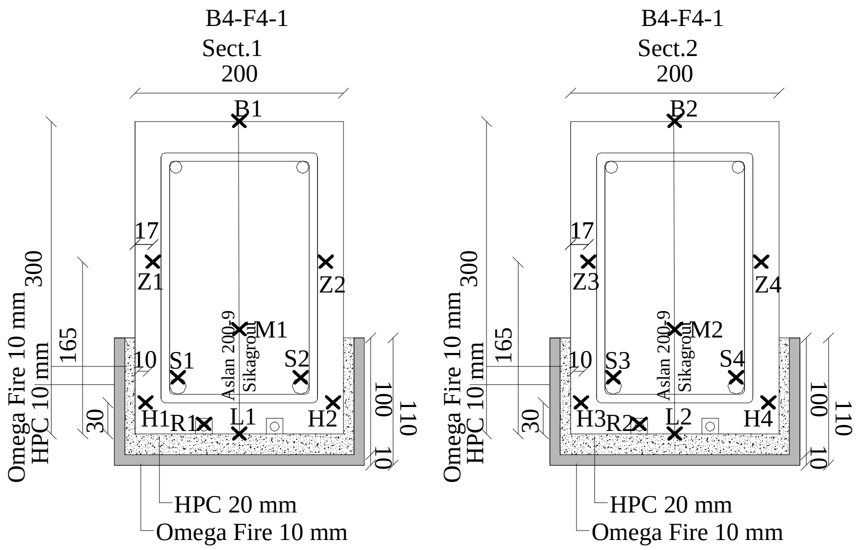

Figure C.174 – Insulation details and position thermocouples beam B4-F4-1

C.4.19.2 Time-temperatures and time- increase of deflection curves

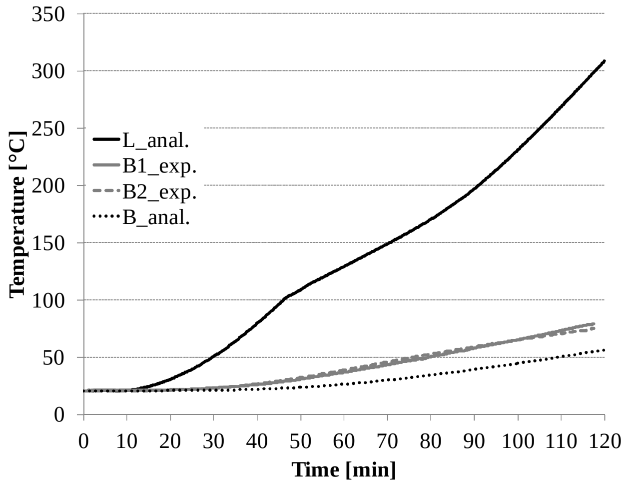

Figure C.175 – Experimental and analytical temperature-time curves thermocouples L and B

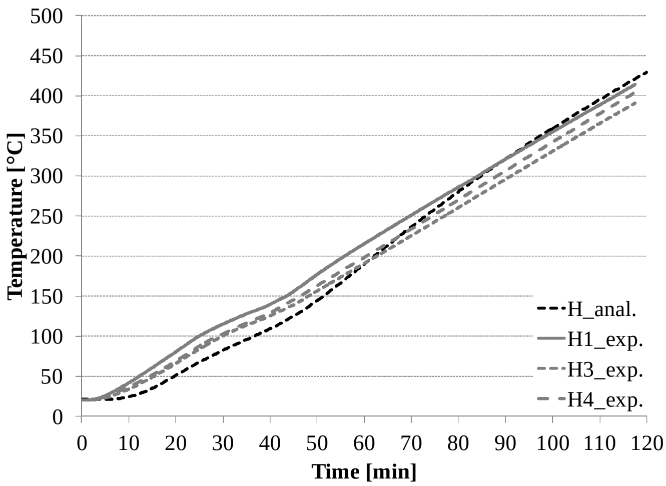

Figure C.176 – Experimental and analytical temperature-time curves thermocouples H

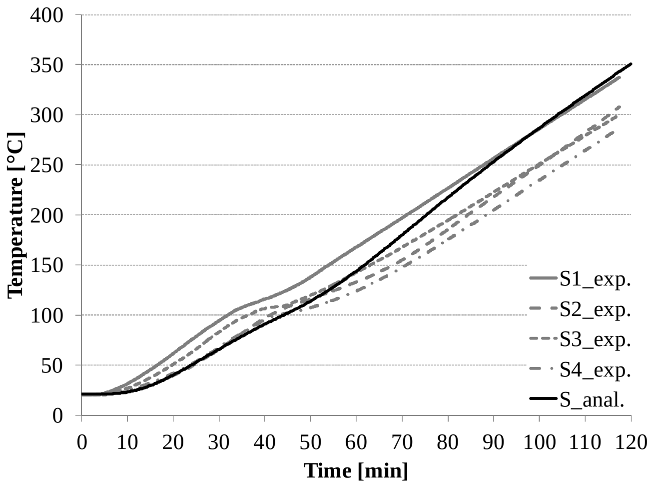

Figure C.177 – Experimental and analytical temperature-time curves thermocouples S

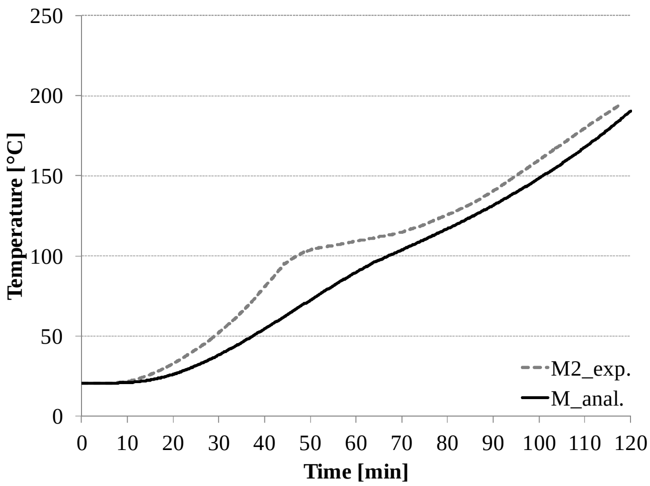

Figure C.178 – Experimental and analytical temperature-time curves thermocouples M

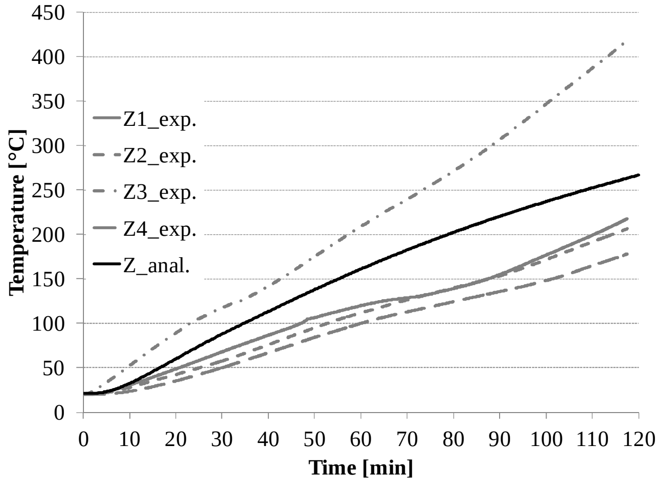

Figure C.179 – Experimental and analytical temperature-time curves thermocouples Z

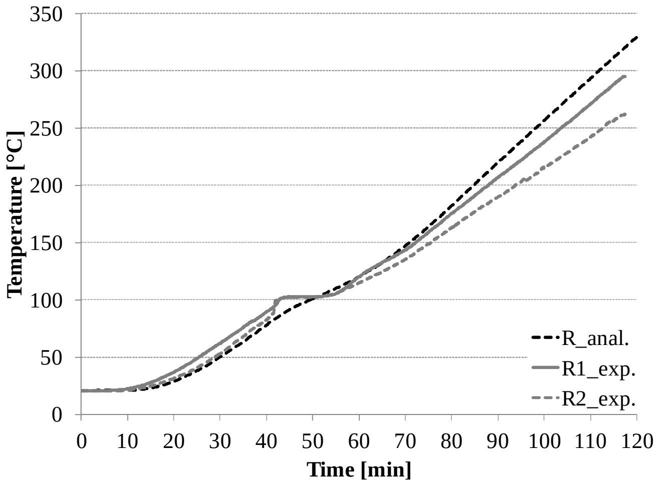

Figure C.180 – Experimental and analytical temperature-time curves thermocouples R

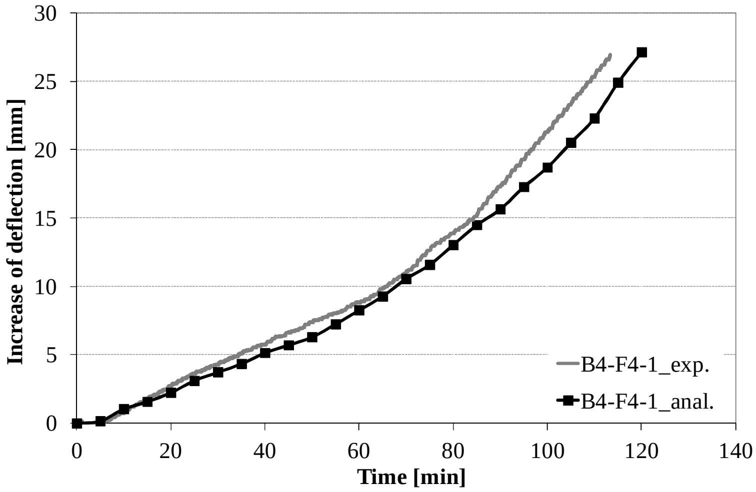

Figure C.181 – Experimental and analytical increase of midspan deflections as a function of time beam B4-F4-1

C.4.20 Beam S0-F4

C.4.20.1 Geometry of the specimen

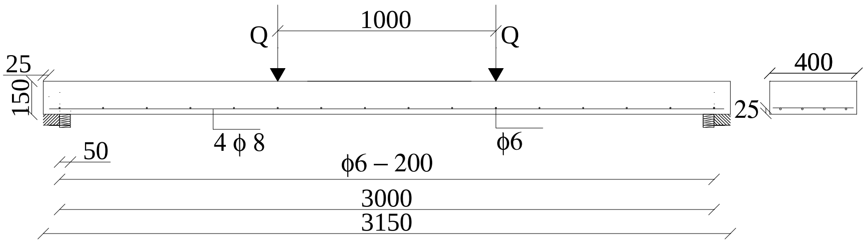

Figure C.182 – Geometry beam S0-F4

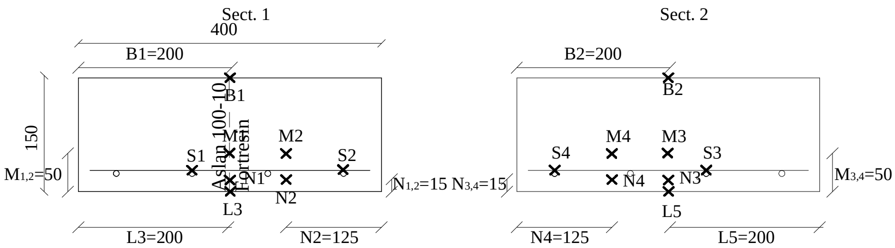

Figure C.183 – Insulation details and position thermocouples beam S0-F4

C.4.20.2 Time-temperatures and time- increase of deflection curves

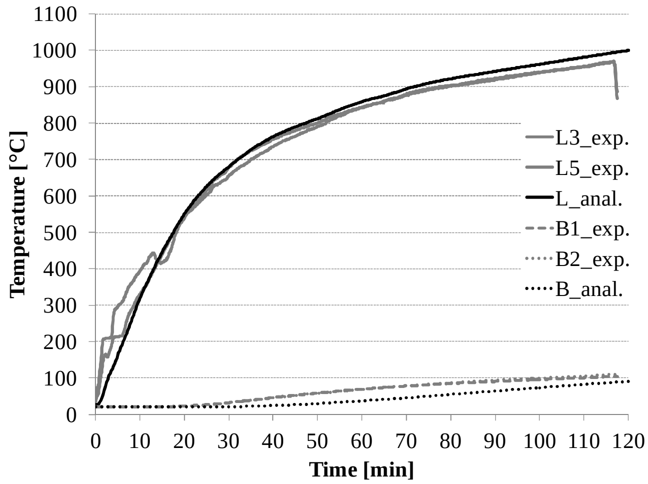

Figure C.184 – Experimental and analytical temperature-time curves thermocouples L and B

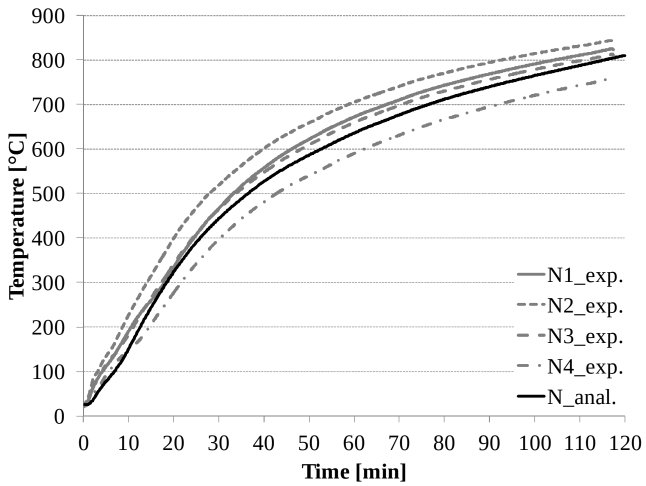

Figure C.185 – Experimental and analytical temperature-time curves thermocouples N

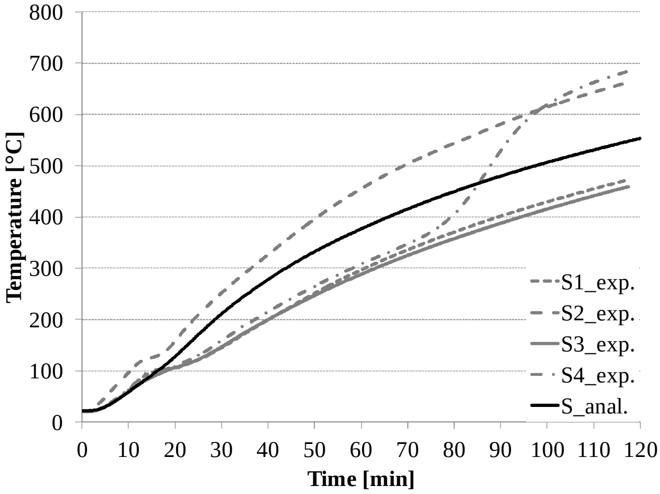

Figure C.186 – Experimental and analytical temperature-time curves thermocouples S

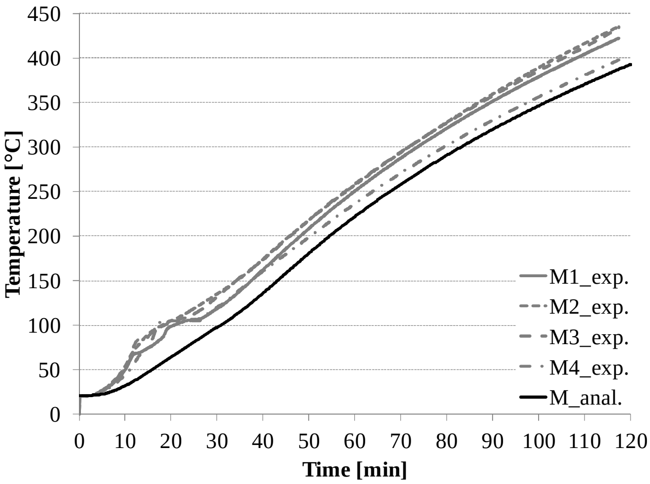

Figure C.187 – Experimental and analytical temperature-time curves thermocouples M

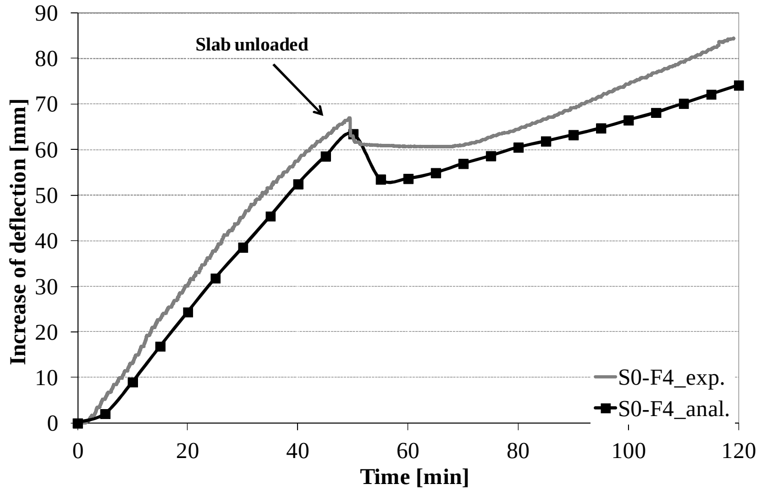

Figure C.188 – Experimental and analytical increase of midspan deflections as a function of time beam S0-F4

C.4.21 Beam S1-F4-1

C.4.21.1 Geometry of the specimen

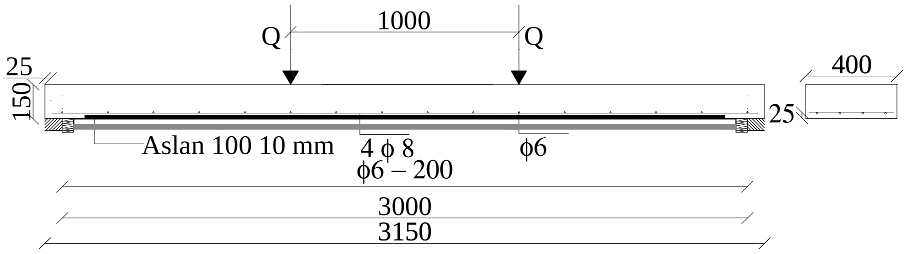

Figure C.189 – Geometry beam S1-F4-1

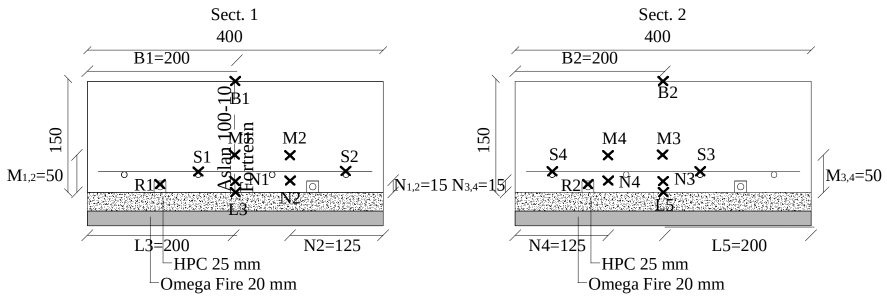

Figure C.190 – Insulation details and position thermocouples beam S1-F4-1

C.4.21.2 Time-temperatures and time- increase of deflection curves

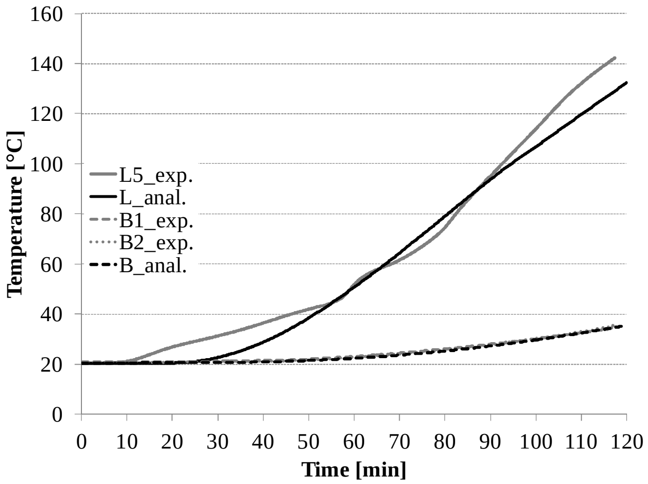

Figure C.191 – Experimental and analytical temperature-time curves thermocouples L and B

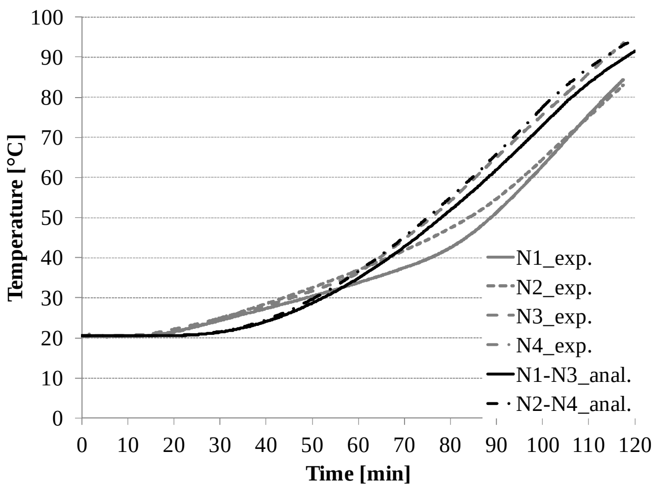

Figure C.192 – Experimental and analytical temperature-time curves thermocouples N

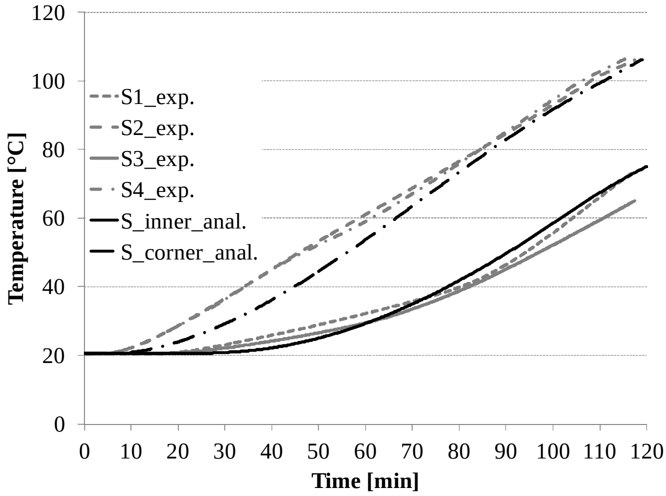

Figure C.193 – Experimental and analytical temperature-time curves thermocouples S

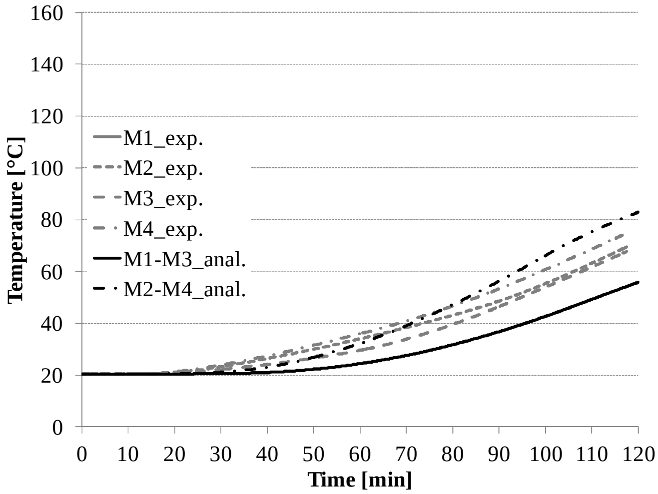

Figure C.194 – Experimental and analytical temperature-time curves thermocouples M

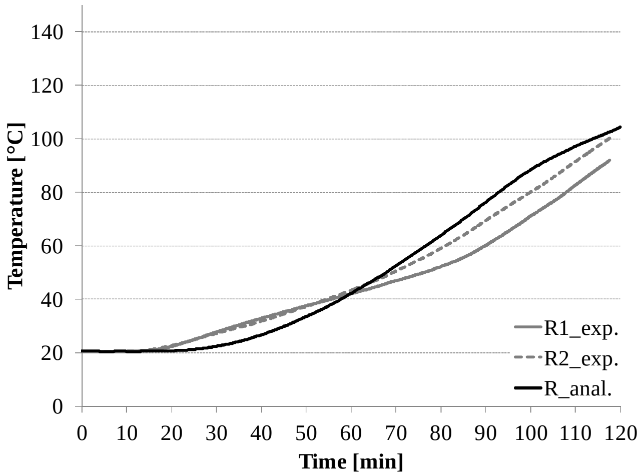

Figure C.195 – Experimental and analytical temperature-time curves thermocouples R

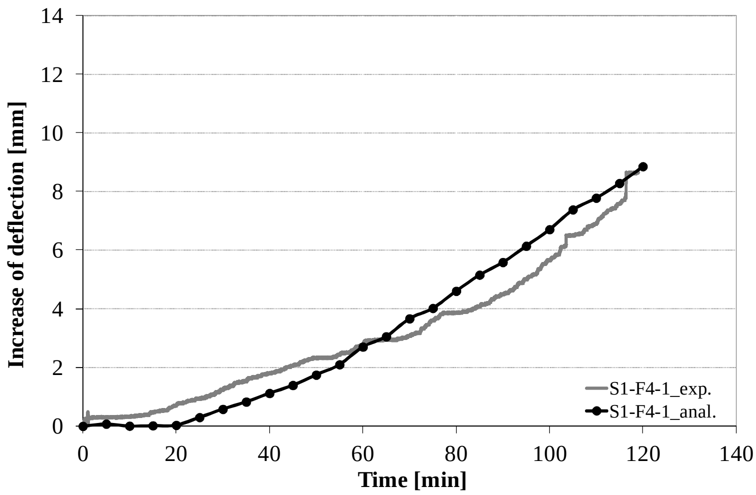

Figure C.196 – Experimental and analytical increase of midspan deflections as a function of time beam S1-F4-1

C.4.22 Beam S2-F4-1

C.4.22.1 Geometry of the specimen

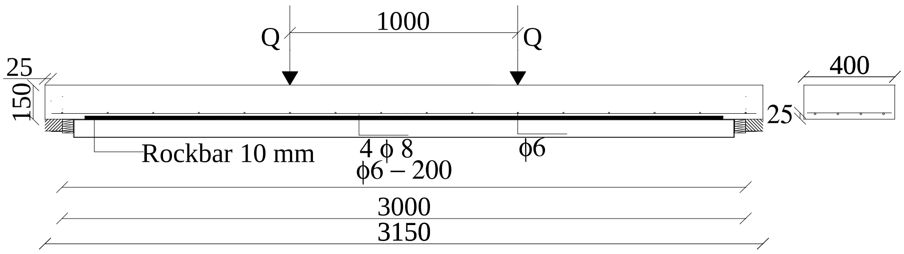

Figure C. 197 – Geometry beam S2-F4-1

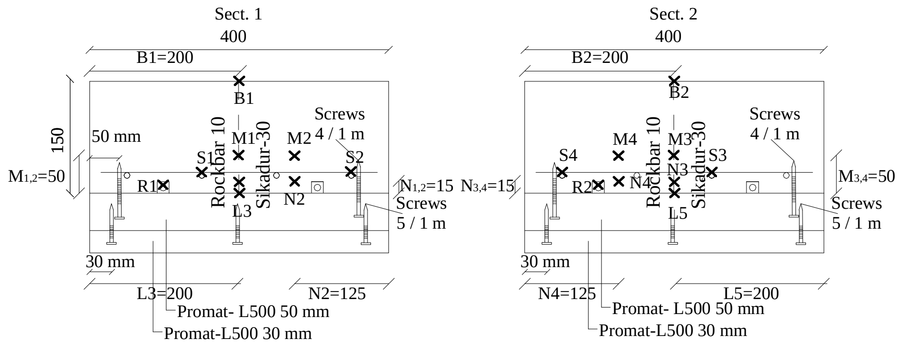

Figure C.198 – Insulation details and position thermocouples beam S2-F4-1

C.4.22.2 Time-temperatures and time- increase of deflection curves

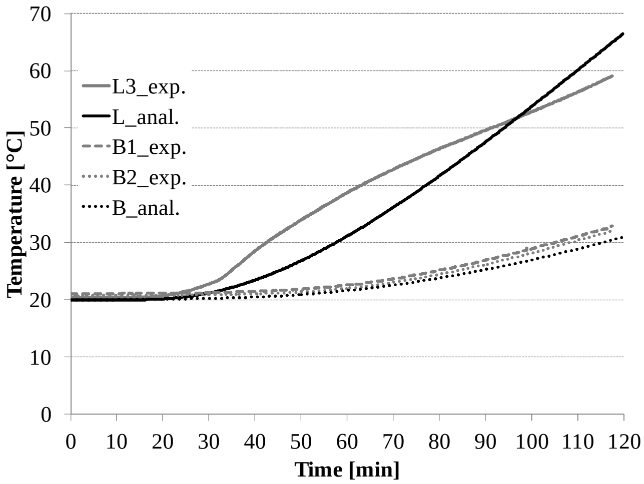

Figure C.199 – Experimental and analytical temperature-time curves thermocouples L and B

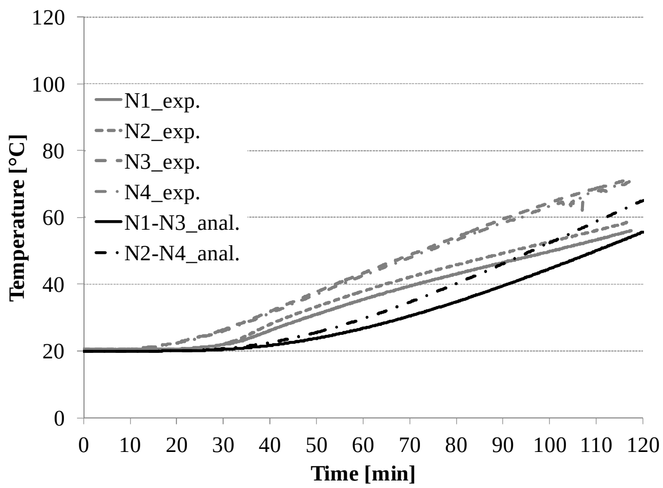

Figure C.200 – Experimental and analytical temperature-time curves thermocouples N

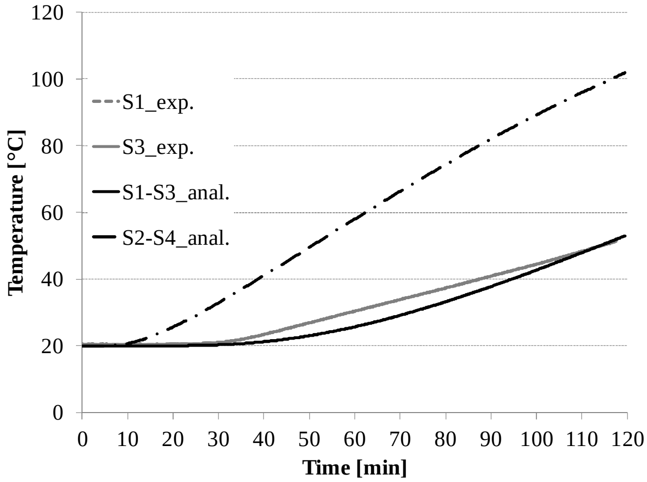

Figure C.201 – Experimental and analytical temperature-time curves thermocouples S

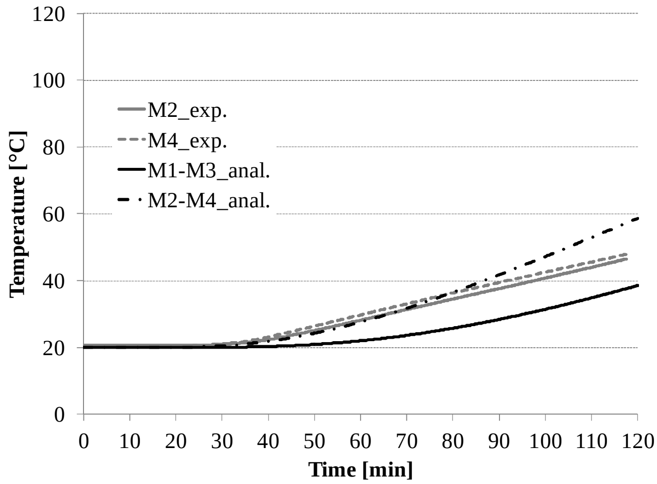

Figure C.202 – Experimental and analytical temperature-time curves thermocouples M

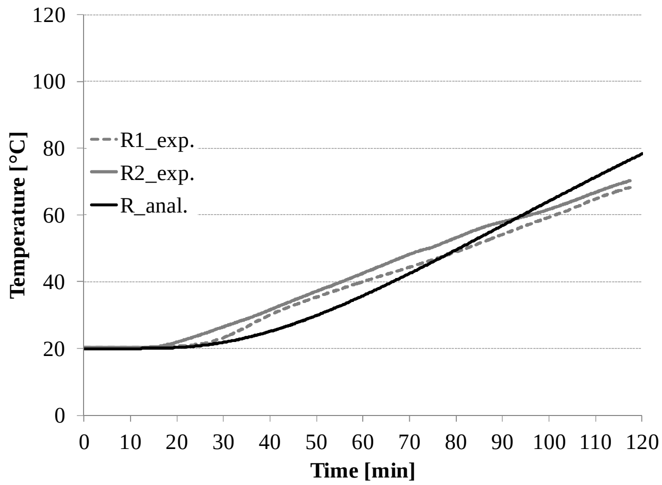

Figure C.203 – Experimental and analytical temperature-time curves thermocouples R

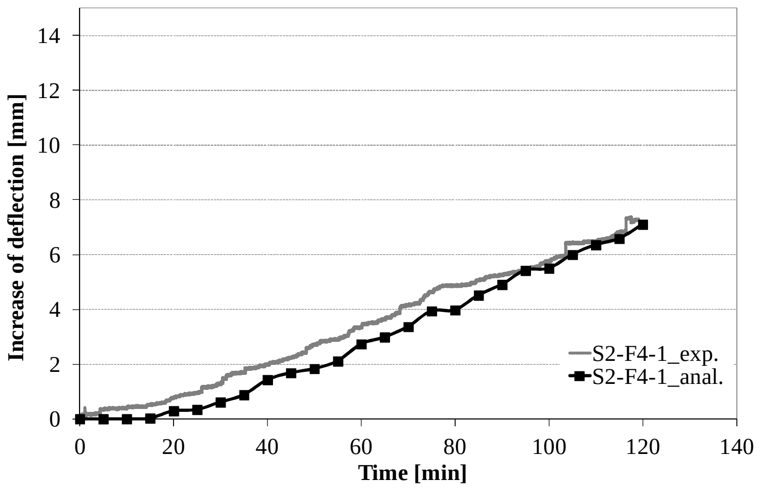

Figure C.204 – Experimental and analytical increase of midspan deflections as a function of time beam S2-F4-1

C.4.23 Beam S2-F4-2

C.4.23.1 Geometry of the specimen

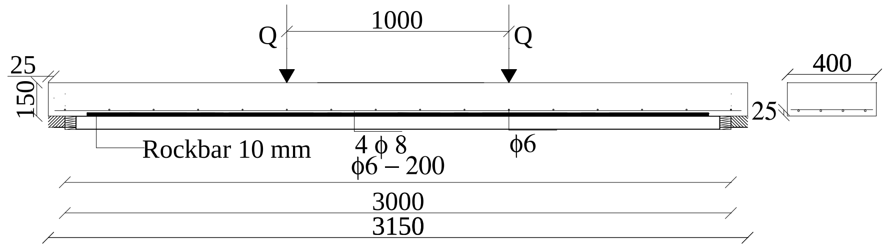

Figure C.205 – Geometry beam S2-F4-2

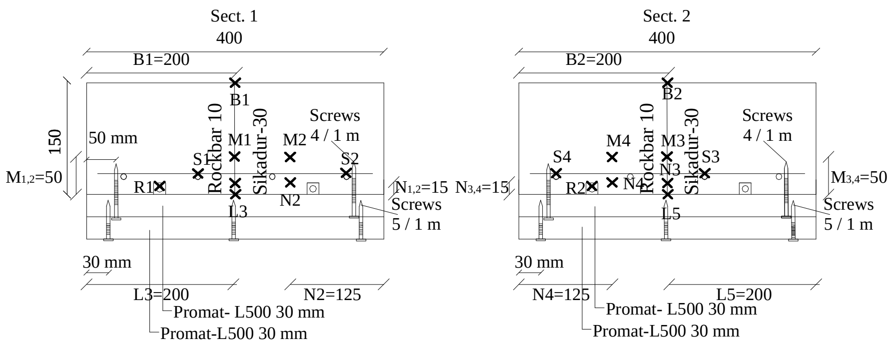

Figure C.206 – Insulation details and position thermocouples beam S2-F4-2

C.4.23.2 Time-temperatures and time- increase of deflection curves

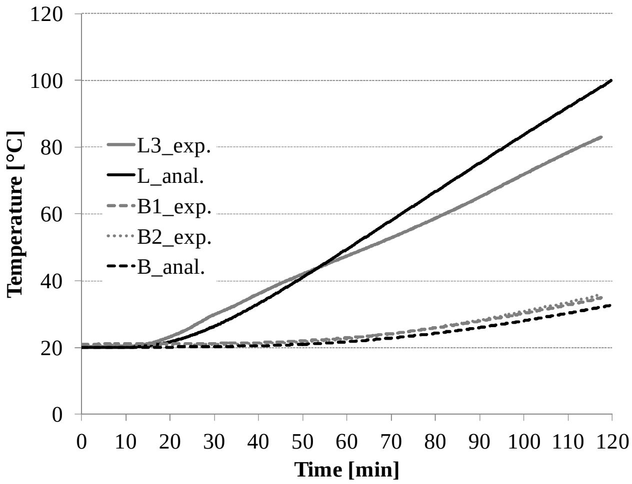

Figure C.207 – Experimental and analytical temperature-time curves thermocouples L and B

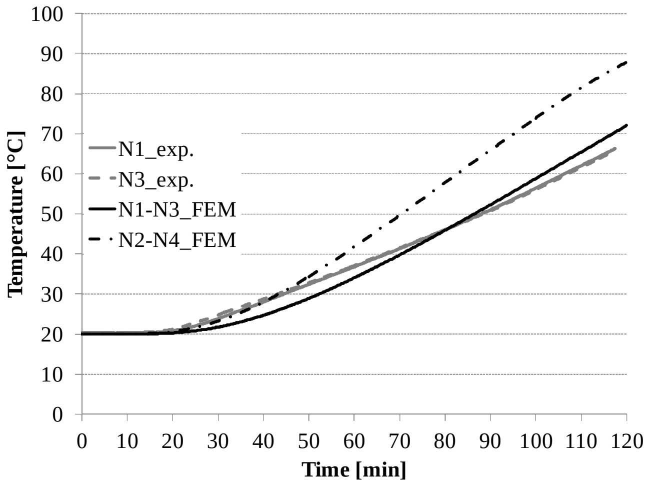

Figure C.208 – Experimental and analytical temperature-time curves thermocouples N

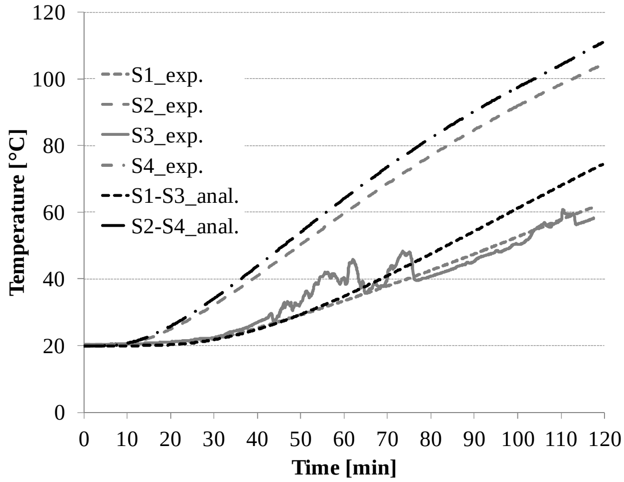

Figure C.209 – Experimental and analytical temperature-time curves thermocouples S

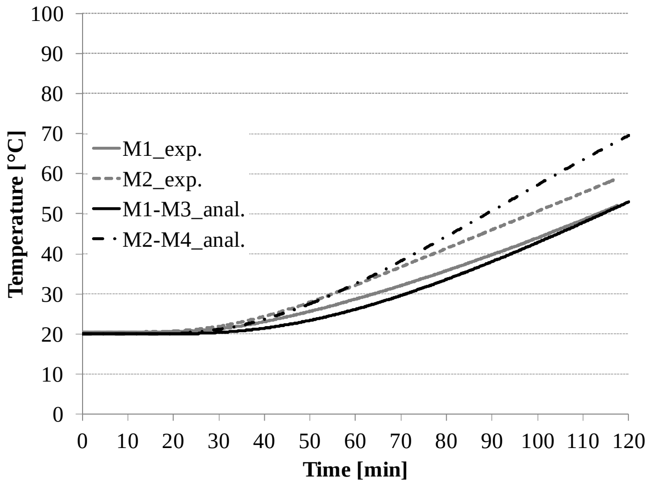

Figure C.210 – Experimental and analytical temperature-time curves thermocouples M

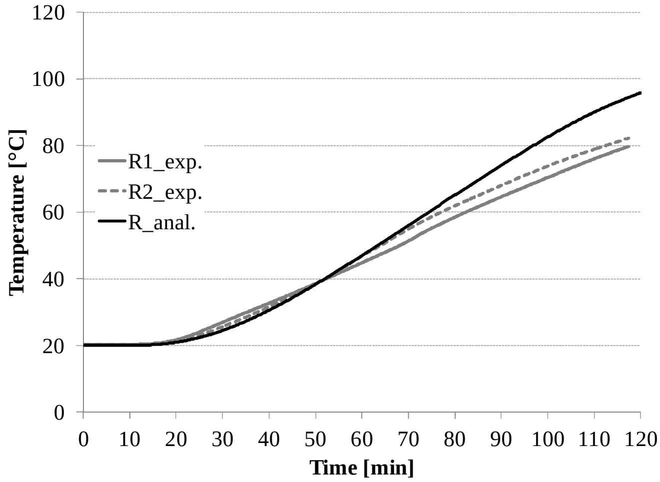

Figure C.211 – Experimental and analytical temperature-time curves thermocouples R

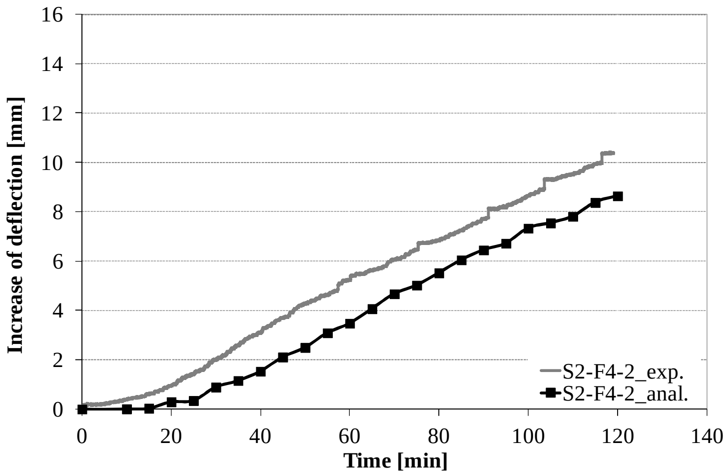

Figure C.212 – Experimental and analytical increase of midspan deflections as a function of time beam S2-F4-2

C.4.24 References

1. NBN-B15-220 (1990). "Proeven op beton- Bepaling van de druksterke".
2. NBN-B15-214 (1990). "Proven op beton-buigproef op betonprisma's".

APPENDIX D
ANALYSIS OF NSM FRP SHEAR STRESS DISTRIBUTION OF FIRE TESTED MEMBERS

D.1 Analysis of shear stresses

The differential equation governing bond of a round bar in a substrate material can be expressed as follow [1-3]:

$$\frac{d^2\tau(x)}{dx^2} - \alpha^2\tau(x) = 0 \qquad \text{(D.1)}$$

Equation D.1 comes from equilibrium and compatibility expressions of a finite element of rod with length dx, along with the assumption that the FRP rod is linearly elastic and that the concrete strain is negligible compared to the FRP strain. This will be explained in the following.

The analysis of a bonded joint (see Figure D.1) in the linear elastic range can be conducted by means of a simple "shear-lag approach".

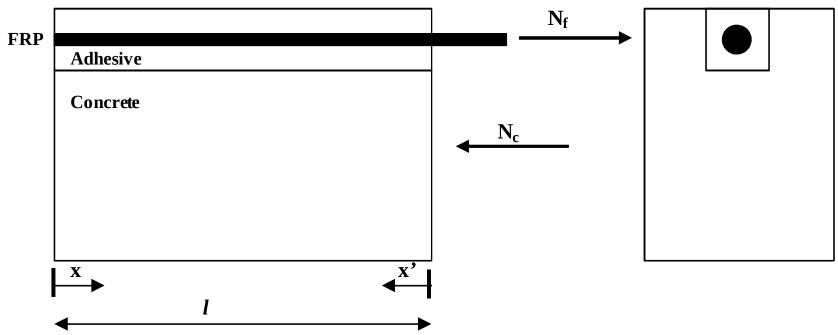

Figure D.1 – NSM FRP to concrete joint loaded in pure tension

The increase in normal force (N_f) in the NSM FRP over a small length dx has to be transferred via the shear stresses to the concrete (see Figure D.2). At moderate load levels a linear bond-slip behaviour can be adopted:

$$\frac{dN_f}{u_f dx} = \tau(x) = k_{el} s(x) \tag{D.2}$$

where:

- $\tau(x)$ are the shear stresses
- $s(x)$ is the slip
- k_{el} is the so-called slip modulus or modulus of displacement
- u_f is the perimenter of the NSM FRP bar

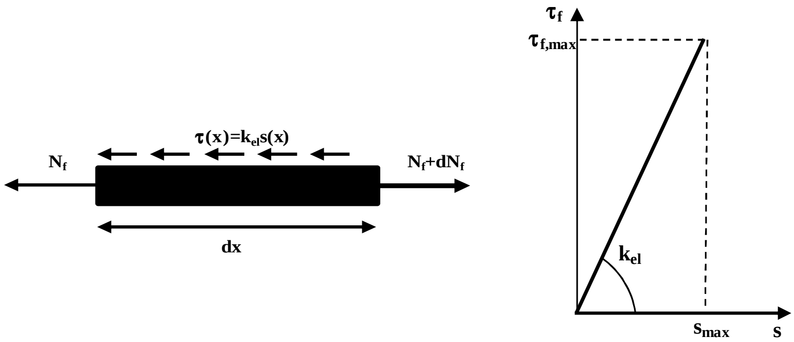

Figure D.2 – Equilibrium of an infinitesimal element and idealized bond slip law

The change in shear stresses over a length dx can be derived as:

$$\frac{d\tau(x)}{dx} = k_{el} \frac{ds(x)}{dx} \tag{D.3}$$

Considering that the FRP strain can be expressed as:

$$\varepsilon_f = \frac{ds(x)}{dx} = \frac{N_f}{E_f A_f} \tag{D.4}$$

where:

- E_f is the Young's modulus of the FRP
- A_f is the FRP cross-sectional area

Equation D.3 can be rewritten as:

$$\frac{d\tau(x)}{dx} = k_{el}\frac{N_f}{E_f A_f} \tag{D.5}$$

Differentiating equation D.5 with respect to x gives:

$$\frac{d^2\tau(x)}{dx^2} = \frac{k_{el}}{E_f A_f}\frac{dN_f}{dx} = \omega^2\frac{dN_f}{dx} \tag{D.6}$$

where: $\omega^2 = \dfrac{k_{el}}{E_f A_f}$ is a constant

Substituting equation D.2 in equation D.6 the following equation is obtained:

$$\frac{d^2\tau(x)}{dx^2} = \omega^2 u_f \tau(x) \tag{D.7}$$

Considering:

$$\alpha^2 = \omega^2 u_f \tag{D.8}$$

Equation D.7 can be written as follows:

$$\frac{d^2\tau(x)}{dx^2} - \alpha^2\tau(x) = 0 \tag{D.9}$$

or:

$$\tau'' - \alpha^2\tau = 0 \tag{D.10}$$

The solution of equation D.10 can be expressed as:

$$\tau(x) = C_1 e^{\alpha x} + C_2 e^{-\alpha x} \tag{D.11}$$

$$\frac{d\tau(x)}{dx} = \alpha C_1 e^{\alpha x} - \alpha C_2 e^{-\alpha x} \tag{D.12}$$

C_1 and C_2 can be determined by using the boundary conditions, assuming that the FRP force at x=0 is zero and that the FRP force at x=*l* is equal to the acting force.

For $$x = 0 \Rightarrow N_f(x) = 0 \tag{D.13}$$

equation D.5 gives:

$$\frac{d\tau(x=0)}{dx} = 0 \Rightarrow C_1 = C_2 = C \tag{D.14}$$

For $$x = l \Rightarrow N_f(x) = N_f(l) \qquad \text{(D.15)}$$

equation D.5 gives:

$$\frac{d\tau(x = l)}{dx} = \alpha C\left(e^{\alpha l} - e^{-\alpha l}\right) = \omega^2 N_f(l) \qquad \text{(D.16)}$$

Which gives:

$$C = \frac{\omega^2 N_f(l)}{\alpha\left(e^{\alpha l} - e^{-\alpha l}\right)} \qquad \text{(D.17)}$$

Considering equation D.8 and

$$\left(e^{\alpha l} - e^{-\alpha l}\right) = 2\sinh(\alpha l) \qquad \text{(D.18)}$$

the constant C can be written as:

$$C = \frac{\alpha N_f(l)}{2u_f \sinh(\alpha l)} \qquad \text{(D.19)}$$

Equation D.19 and D.11 gives the shear stresses as follows:

$$\tau(x) = \frac{\alpha N_f(l)}{2u_f \sinh(\alpha l)}\left(e^{\alpha l} + e^{-\alpha l}\right) = \alpha \frac{N_f(l)}{u_f} \frac{\cosh(\alpha x)}{\sinh(\alpha l)} \qquad \text{(D.20)}$$

And if the x-direction (see Figure D.1) is taken from the other side:

$$\tau(x') = \alpha \frac{N_f(l)}{u_f} \frac{\cosh(\alpha(l - x'))}{\sinh(\alpha l)} \qquad \text{(D.21)}$$

D.2 Shear stress distribution as a function of temperature

In the following sections the shear stress distribution over a distance from the NSM FRP bar/strip end up to the loading point (x=900 mm), as a function of fire exposure time, is given.

The calculated bond shear stresses, τ_f^*, are reported for each tested member up to the time in which they exceed the decreasing bond shear strength capacity with increasing temperature, τ_{limit}. At this point loss of composite action at the FRP/adhesive interface is assumed. The reduction of bond shear strength with increasing temperature is obtained from experimental results of the double bond shear tests at elevated temperature discussed in chapter 4.

A summary of the time of loss of composite action observed experimentally, $t_{deb,exp}$, the analytical assumed time of loss of composite action, $t_{deb,anal}$, the calculated bond shear stresses τ_f^* (at time of loss of composite action at the NSM FRP/concrete interface) and the bond strength at the FRP/adhesive interface τ_{limit} (at the analytical assumed time of loss of composite action at NSM FRP/concrete interface) is reported in Table D.1.

Table D.1 – Results of structural analysis for members exposed to fire

Specimen	$t_{deb,exp}$ [min]	$t_{deb,anal}$ [min]	τ_f^* [N/mm^2]	τ_{limit} [N/mm^2]
B1-F1-1	90	75	0.95	0.75
B2-F1-1	70	55	3.00	1.70
B2-F1-2	34	35	4.58*	5.20*
B3-F1-1	90	90	1.34	0.98
B1-F2-1	>120	>120	1.00	1.82
B1-F2-2	100	100**	1.77	3.15
B1-F2-3	>120	>120	0.60	0.65
B2-F2-1	25	25**	3.62	13.10
B2-F2-2	25	30**	4.02	13.10
B1-F3-1	>60	>60	3.80	4.75
B1-F3-2	>60	>60	1.50	1.80
B1-F3-3	>60	>60	2.82	3.15
B1-F3-4	>60	>60	1.48	1.82
B2-F3-1	>60	>60	4.48	4.52
B4-F3-1	>60	>60	-	-
B2-F4-1	-	-	-	-
B4-F4-1	>120	>120	-	-
S1-F4-1	>120	>120	0.75	2.00
S2-F4-1	>120	>120	1.47	4.98
S2-F4-2	>120	>120	1.06	3.25

** Values prior to detachment of fire insulation system*
***Values assumed based on experimental observation*

D.2.1 First fire test

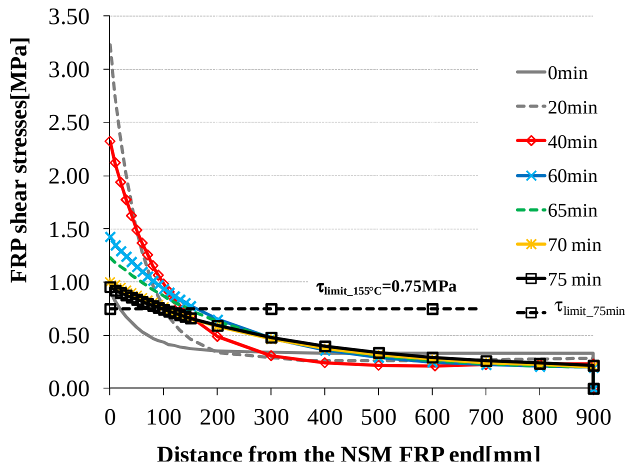

Figure D.3 – Variation of shear stress distribution as a function of the fire exposure time of beam B1-F1-1

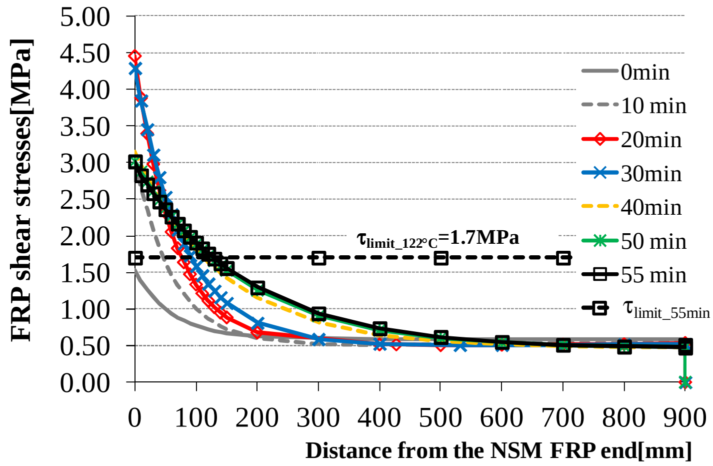

Figure D.4 – Variation of shear stress distribution as a function of the fire exposure time of beam B2-F1-1

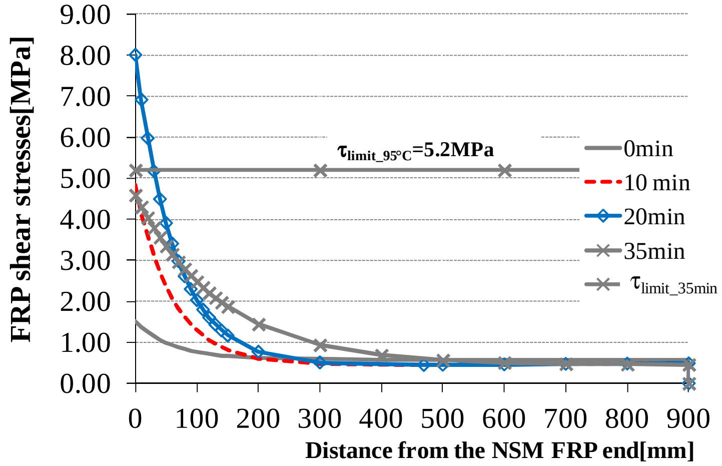

* *The shear stresses along the bond length of beam B2-F1-2 were calculated up to the time in which detachment of the fire insulation system was observed experimentally. At that time the loss of composite action, due to the fast increase of temperature, is assumed.*

Figure D.5 – Variation of shear stress distribution as a function of the fire exposure time of beam B2-F1-2

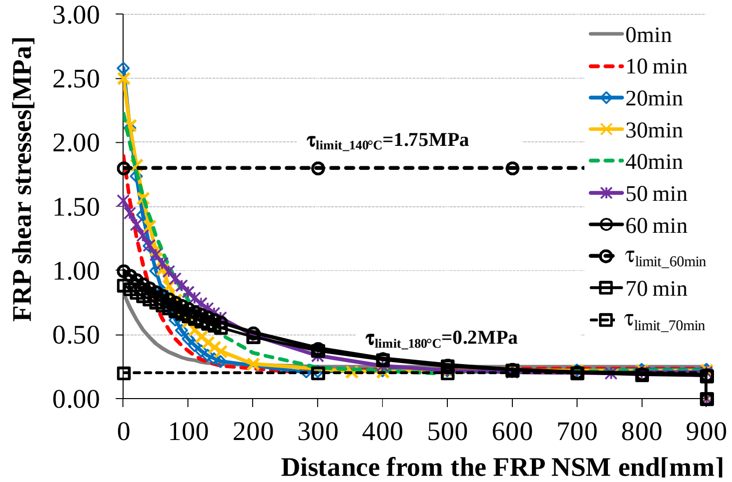

Figure D.6 – Variation of shear stress distribution strips at corners as a function of the fire exposure time of beam B3-F1-1

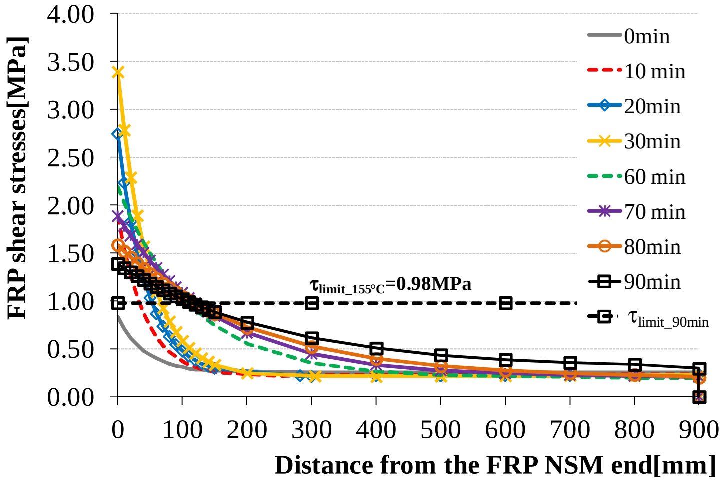

Figure D.7 – Variation of shear stress distribution inner strips as a function of the fire exposure time of beam B3-F1-1

D.2.2 Second fire test

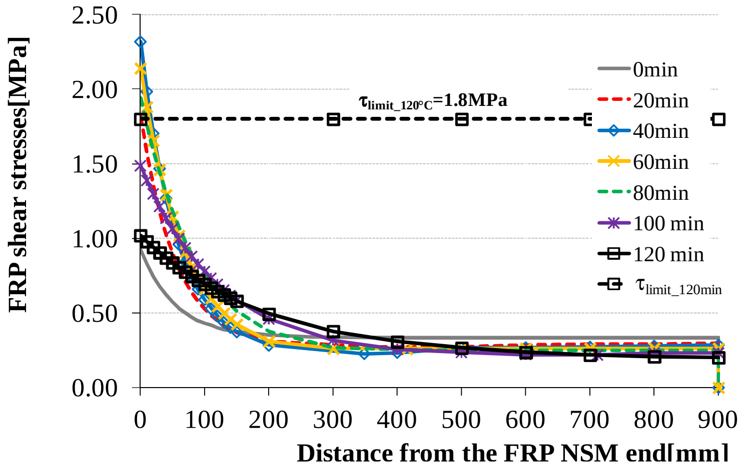

Figure D.8 – Variation of shear stress distribution inner strips as a function of the fire exposure time of beam B1-F2-1

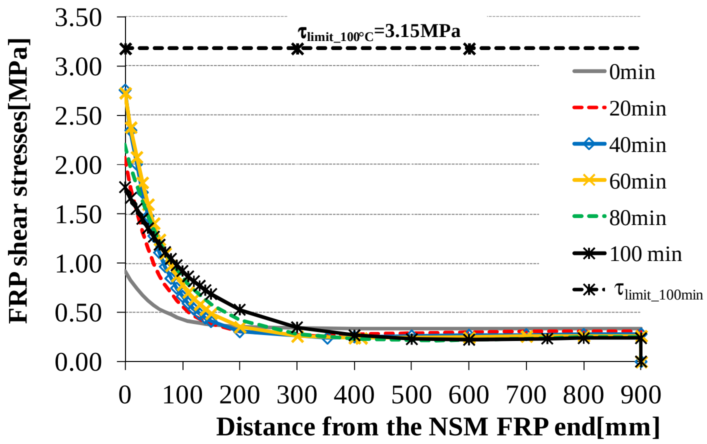

** The shear stresses along the bond length have been calculated up to the time in which a detachment of the fire insulation system is observed. At time of detachment the loss of composite action at FRP/concrete interface, due to the fast increase of temperature, is considered.*

Figure D.9 – Variation of shear stress distribution inner strips as a function of the fire exposure time of beam B1-F2-2

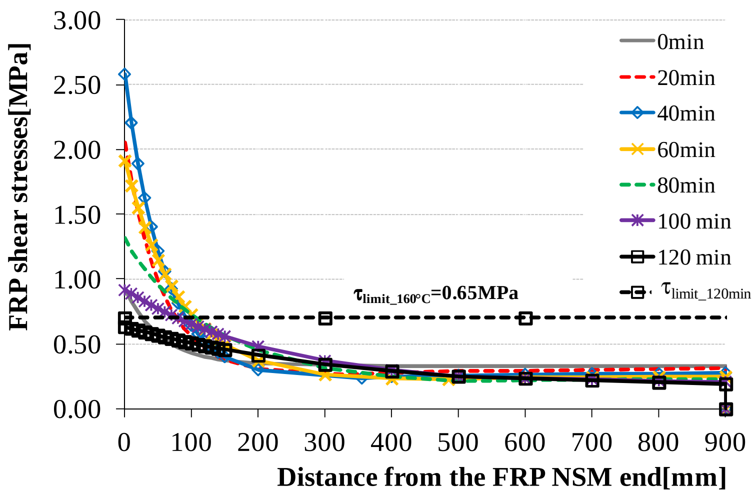

Figure D.10 – Variation of shear stress distribution inner strips as a function of the fire exposure time of beam B1-F2-3

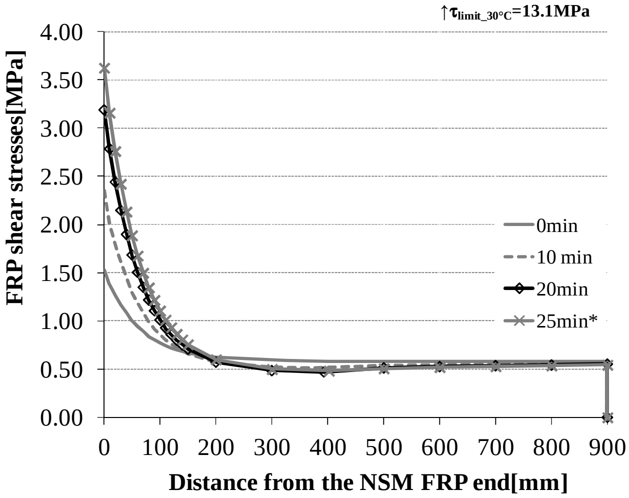

**The shear stresses along the bond length have been calculated up to the time in which cracks of the fire insulation system is observed (see chapter 6)*

Figure D.11 – Variation of shear stress distribution inner strips as a function of the fire exposure time of beam B2-F2-1

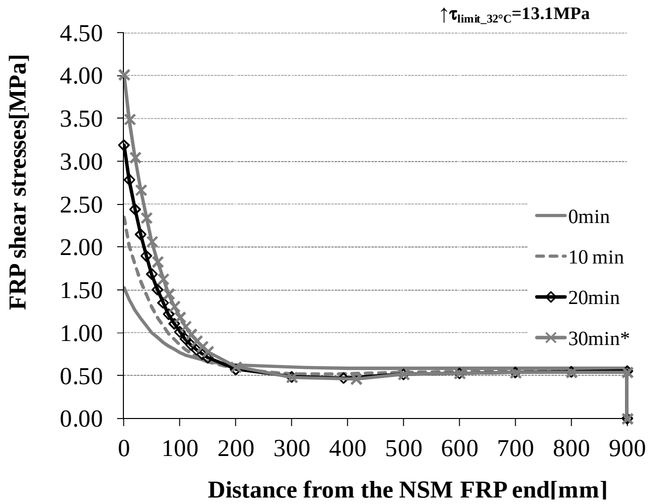

**The shear stresses along the bond length have been calculated up to the time in which cracks of the fire insulation system is observed (see chapter 6)*

Figure D.12 – Variation of shear stress distribution inner strips as a function of the fire exposure time of beam B2-F2-2

Third fire test

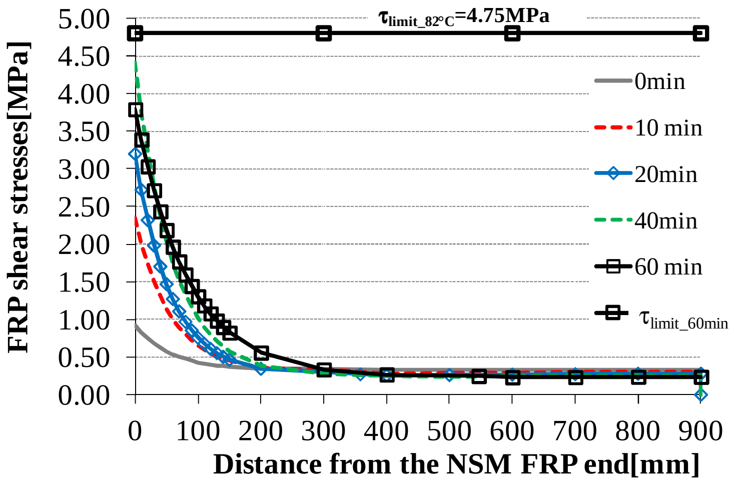

Figure D.13 – Variation of shear stress distribution as a function of the fire exposure time of beam B1-F3-1

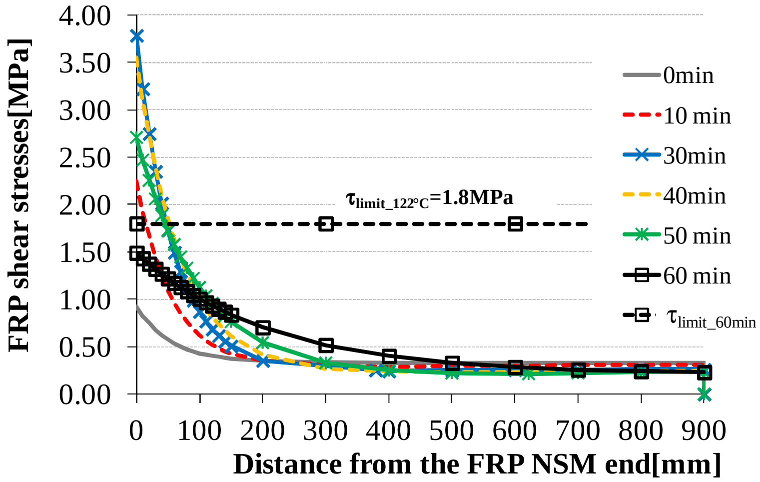

Figure D.14 – Variation of shear stress distribution as a function of the fire exposure time of beam B1-F3-2

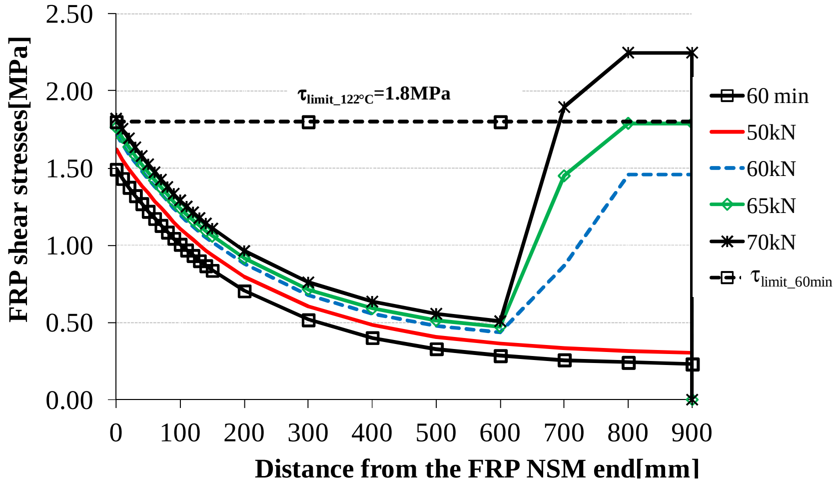

Figure D.15 – Variation of shear stress distribution with increasing load after fire exposure of beam B1-F3-2

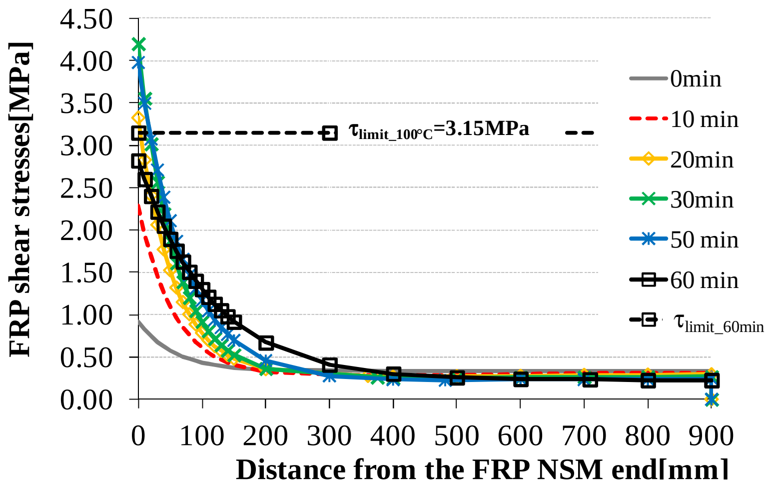

Figure D.16 – Variation of shear stress distribution with increasing load after fire exposure of beam B1-F3-3

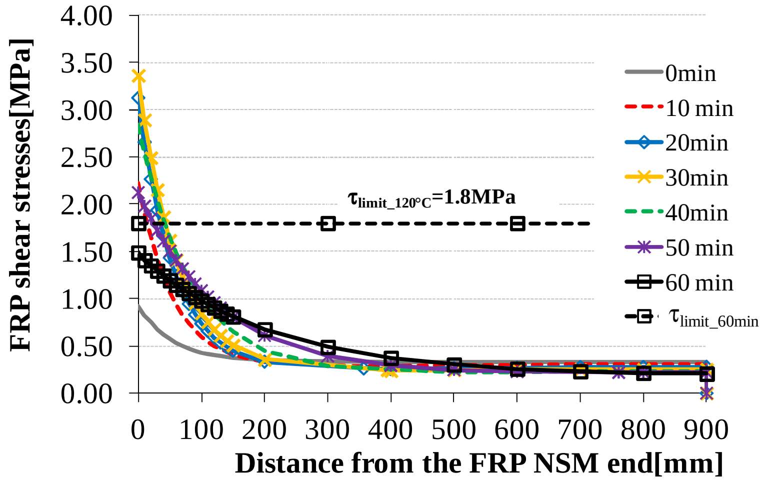

Figure D.17 – Variation of shear stress distribution with increasing load after fire exposure of beam B1-F3-4

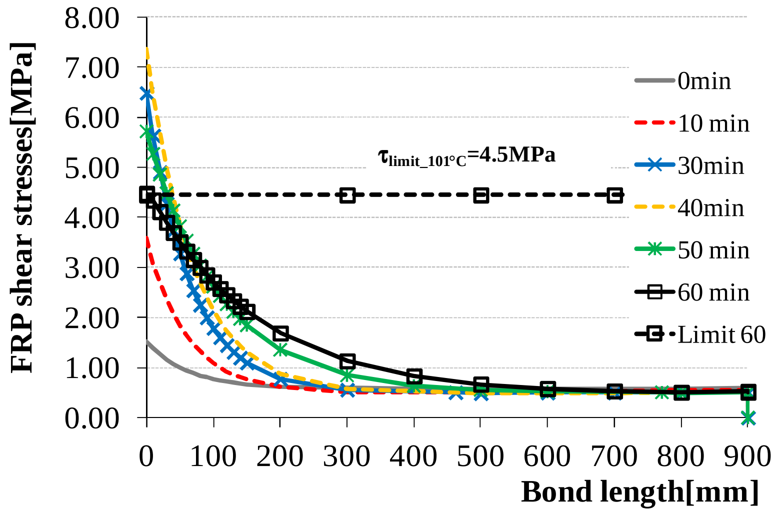

Figure D.18 – Variation of shear stress distribution with increasing load after fire exposure of beam B2-F3-1

D.2.3 Fourth fire test

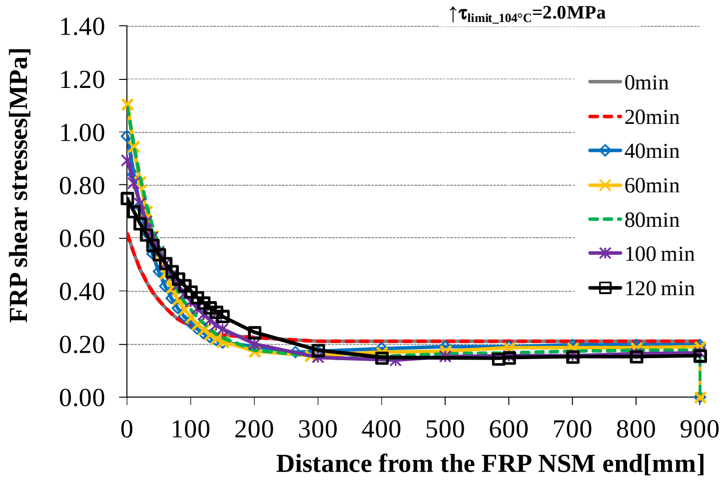

Figure D.19 – Variation of shear stress distribution with increasing load after fire exposure of beam S1-F4-1

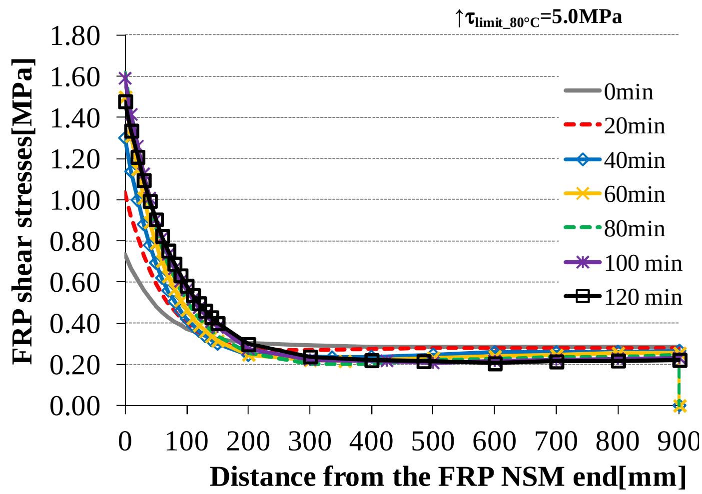

Figure D.20 – Variation of shear stress distribution with increasing load after fire exposure of beam S2-F4-1

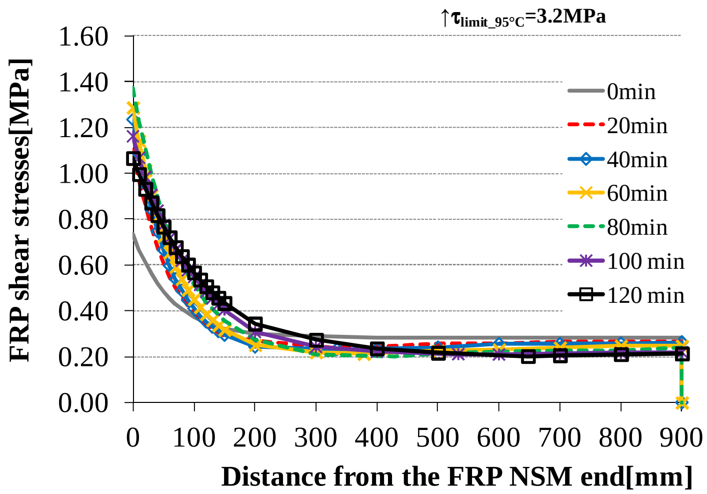

Figure D.21 – Variation of shear stress distribution with increasing load after fire exposure of beam S2-F4-2

D.3 References

1. Kaiser H. (1989). "Bewehren von Stahlbeton mit kohlenstoffaserverstarkten Epoxidharzen". (in German), *Ph-D thesis*, Thechnical University of Zurich, Switzerland, 224 pp.

2. Taljsten B. (1994). "Plate Bonding –Strengthening of Existing Concrete Structures with Epoxy Bonded Plates of Steel or Fibre Reinforced Plastics". *Ph-D thesis*, Lulea University of Technology, Sweden, 281 pp.

3. Faella C., Martinelli E., Nigro E. (2005). "Interface behaviour in FRP plates bonded to concrete: experimental tests and theoretical analyses". *In Proc. of 2003 ECI conference on advanced materials for construction of bridges, buildings, and other structures III*, vol. P5. Davos, Switzerland.